10th International Conference Series on

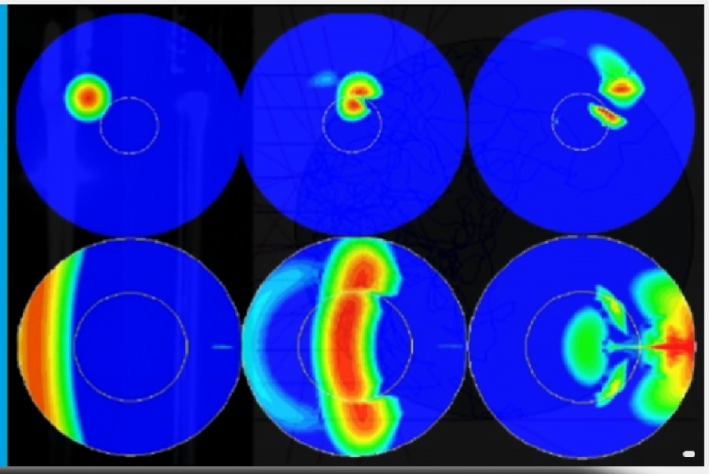
Laser-light and Interactions with Particles

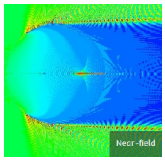
August 25-29th, 2014, Marseille, France.

LIP 2014

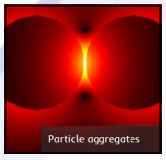
25-29th August 2014

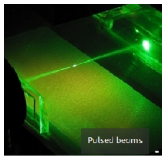
Marseille, France

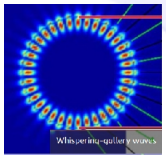


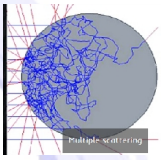


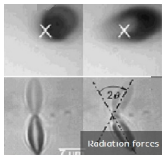






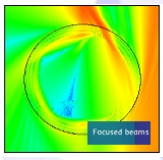


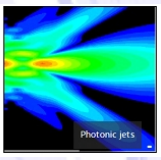


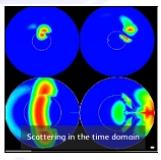


Laser-light and Interactions with Particles









Beam shape description

Time-resolved scattering

Far-field scattering

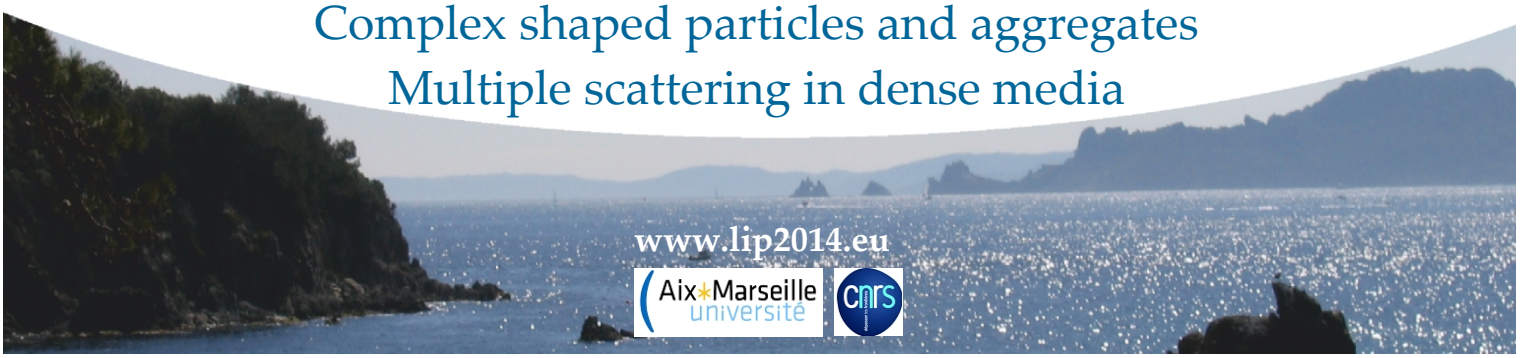
Mechanical effects of light,

Near-field scattering and resonances

Optical particle sizing and characterization methods

Complex shaped particles and aggregates

Multiple scattering in dense media



www.lip2014.eu

Aix*Marseille université

cnrs

BOOK of EXTENDED ABSTRACTS

www.lip2014.eu

10th edition of the international conferences series on

Laser-light and Interactions with Particles

(LIP2014)



25-29 August, 2014

Saint Charles Campus - Aix-Marseille University

Marseille, France

Proceedings of the 10th Int. Conf. on Laser-light and Interactions with Particles, F. Onofri and B. Stout, eds., (Aix-Marseille University, Marseille, 2014)
ISBN: 978-2-9548080-0-0



Preface

This volume contains the extended abstracts of the keynote lectures, oral communications, and posters presented at the 10th edition of the international conference series on Laser-light and Interactions with Particles (LIP2014), held in Marseille, France from August 25th to 29th 2014. This event was co-organized by the IUSTI laboratory and Fresnel Institute of Aix-Marseille University in partnership with the French National Center for Scientific Research (CNRS).

This conference series was initiated and founded by G. Gouesbet and G. Gréhan in 1987 at Rouen (France), under the title "Optical Particle Sizing, theory and practice (OPS)". In order to follow the developments and demands in this field, the title of the following editions was changed to "Optical Particle Characterization (OPC)": Phoenix, USA, 1990 (D. Hirleman); Yokohama, Japan, 1993 (M. Maeda); Nürnberg, Germany, 1995 (F. Durst); Minneapolis, USA, 1998 (A. Naqwi); Brighton, England, 2001 (A. Jones); Kyoto, Japan, 2004 (M. Itoh) and Graz, Austria, 2007 (O. Glätter). The conference returned to its roots in Rouen in 2012 where it was decided to change its title to "Laser-light and Interactions with Particles", and to expand its scope to cover: laser and acoustic beam shape descriptions; far-field, near-field, resonant and time-resolved scattering; mechanical effects of light; complex particle shapes and aggregates; and optical particle sizing and characterization methods. Covered applications range from multiphase flows, aerosol and atmospheric environment sciences, biomedical optical engineering, remote manipulation of objects, plasma and soft matter physics, etc.

A special issue of full-size papers, documenting research either reported at the conference or pertaining to the main topics of LIP2014, is planned for publication in Journal of Quantitative Spectroscopy and Radiative Transfer.

We would like to take this opportunity to express our thanks to those who contributed to the success of the conference. The assistance provided by the Honorary, Scientific, and Advisory committees in assessing abstracts, was highly appreciated. We gratefully acknowledge the companies who participated in the exhibition of scientific equipment, and all the institutions that financially sponsored this event. Our final thanks go to the regular and new participants who are essential to the success of this LIP conference.

For the organizing committee, Marseille France, June 24th 2014,

Fabrice R.A. Onofri



Directeur de Recherche
Laboratoire IUSTI, UMR 7343 AMU/CNRS
Co-Chairman of LIP2014
fabrice.onofri@univ-amu.fr

Brian Stout



Professor of Physics
Institut Fresnel, UMR 7249 AMU/CNRS
Co-Chairman of LIP2014
brian.stout@fresnel.fr

SPONSORING ORGANIZATIONS*

AIR FRANCE & KLM

Aix-Marseille University

French National Research Agency (ANR)

French National Scientific Research Center (CNRS)

Competitiveness cluster "Optics & Photonics" (Optitec)

Fédération Fabri de Peiresc (FR3515)

Laboratory of excellence "Mechanics and Complexity" (LabEx MEC)

CILAS - Particle Size Analyser division (CILAS)

LaVision - We count on photons (LaVision)

The Optical Society of America (OSA)

EXHIBITORS

European Optical Society (ESO)

French Optical Society (SFO)

LS Instruments AG

NKT Photonics

Oxford Lasers

Spectra-Physics

Springer Verlag

*at the present date: June 23rd, 2014

HONORARY COMMITTEE

W. BACHALO
Artium technologies Inc, CA, Sunnyvale, USA.
wbachalo@artium.com - http://www.artium.com/

X.S. CAI
University of Shanghai for Science and Technology, Shanghai, China.
caixs@sh163.net - http://www.at0086.com/USST/

G. GOUESBET
National Institute of Applied Sciences, Rouen, France.
gerard.gouesbet@coria.fr - http://www.coria.fr/spip.php?auteur33

G. GRÉHAN
National Center for Scientific Research, Rouen, France.
Grehan@coria.fr- http://www.coria.fr/spip.php?auteur51&lang=en

J.A. LOCK
Cleveland State University, Cleveland, OH, USA.
j.lock@csuohio.edu - http://works.bepress.com/james_lock/

M. MAEDA
Keio University, Yokohama, Japan.
ms-maeda@tkc.att.ne.jp - http://www.keio.ac.jp/

Z.S. WU
School of Science, Xidian University, Xidian, China
wuzhs@mail.xidian.edu.cn - http://old.xidian.edu.cn/../EliteofXidianUniversity/wuzhensen.htm

SCIENTIFIC COMMITTEE

Y.P. HAN
School of Science, Xidian University, Xidian, China
yphan@xidian.edu.cn - http://www.xidian.edu.cn/... /EliteofXidianUniversity/hangyiping.htm

P. L. MARSTON
Depart. Physics & Astronomy, Washington State University, Pullman, USA
marston@wsu.edu - http://www.physics.wsu.edu /~/People-Faculty-Marston.html

F.R.A. ONOFRI
IUSTI, National Center for Scientific Research, Marseille, France
fabrice.onofri@univ-amu.fr - http://iusti.univ-provence.fr/document.php?pagendx=12070

C.M. SORENSEN
Physics Department, Kansas State University, Manhattan, KS, USA
sor@phys.ksu.edu - https://www.k-state.edu/cbpd/steering.html

B. STOUT
Fresnel Institute, Aix-Marseille University, Marseille, France
brian.stout@fresnel.fr - http://www.fresnel.fr/perso/stout/

C. TROPEA
SLA, Technical University of Darmstadt, Darmstadt, Germany.
ctropea@sla.tu-darmstadt.de; http://www.sla.tu-darmstadt.de/sla/index.de.jsp

G. VIDEEN
Army Research Laboratory, Adelphi, MD, USA
gorden.videen@gmail.com - http://www.arl.army.mil/www/default.cfm?page=188

T. WRIEDT
ITW, University of Bremen, Bremen, Germany.
thw@iwt.uni-bremen.de - www.iwt-bremen.de/.../powder-and-particle-measurement.html

ADVISORY COMMITTEE

Y. AIZU
Muroran Institute of Technology, Muroran, Japan
aizu@mmm.muroran-it.ac.jp

M. BRUNEL
Laser/particle(s) interaction, CORIA, University of Rouen, Rouen, France
marc.brunel@coria.fr

R. CHAKRABARTY
Division of Atmospheric Sciences - Desert Research Institute, Reno, USA
rajan.chakrabarty@dri.edu

Y.E. GEINTS
Zuev Institute of Atmospheric Optics, Russian Academy of Sciences, Tomsk, Russia
ygeints@iao.ru

D. GRIER
Department of Physics and Center for Soft Matter Research, New-York University, New-York, USA
david.grier@nyu.edu

S. HANNA
Nanophysics and Soft Matter, University of Bristol, Bristol, UK
phsh@bristol.ac.uk

M. KOLWAS
Institut of Physics, Polish Academy of Sciences, Warsaw, Poland
Maciej.Kolwas@ifpan.edu.pl

F. LEMOINE
Spray combustion and optical diagnostics, LEMTA, University of Lorraine, Nancy, France
fabrice.lemoine@ensem.inpl-nancy.fr

F. G. MITRI
Chevron, Area 52 Technology, Santa Fe, NM, USA
fmitri@gmail.com

A.A.R. NEVES
Federal University of ABC, Santo André, Brazil
antonio.neves@ufabc.edu.br

B. POULIGNY
CRPP, National Center for Scientific Research, Pessac, France
pouligny@crpp-bordeaux.cnrs.fr

T. NIEMINEN
Dept. of Physics, University of Queensland, Brisbane, Australia
timo@physics.uq.edu.au

K-F. REN
Laser sources and dense media diagnostics, CORIA, University of Rouen, France
fang.ren@coria.fr

N. ROTH
Institute of Aerospace Thermodynamics, Stuttgart University, Stuttgart, Germany
Norbert.Roth@itlr.uni-stuttgart.de

C. ROZÉ
Laser sources and dense media diagnostics, CORIA, University of Rouen, Rouen, France
roze@coria.fr

D. D. SAMPSON
CMCA, The University of Western Australia, Crawley, Australia
david.sampson@uwa.edu.au

M. ŠILER
Institute of Scientific Instruments of the ASCR, Brno, Czech Republic
siler@isibrno.cz

A.M.K.P. TAYLOR
Department of Mechanical Engineering, Imperial College, London, UK
a.m.taylor@imperial.ac.uk

M.R. VETRANO
Von Karman Institute for Fluid Dynamics, Rhode St-Genese, Belgium
vetrano@vki.ac.be

F. XU
Jet Propulsion Laboratory, California Institute of Technology, Pasadena, USA
Feng.Xu@jpl.nasa.gov

R. XU
Micromeritics Instrument Corp., Shanghai, China
Ren.Xu@micromeritics.com

ORGANIZING COMMITTEE AND LOCAL ORGANIZATION

F. ONOFRI (co-chair), IUSTI, CNRS, Marseille, France

B. STOUT (co-chair), Fresnel Institute, Aix-Marseille University, Marseille, France

S. BARBOSA, IUSTI, Aix-Marseille University, Marseille, France.

J. BARTOLINI, IUSTI, National Center for Scientific Research, Marseille, France.

J-M. GEFFRIN, Fresnel Institute, Aix-Marseille University, Marseille, France

C. GUENE, Fresnel Institute, Aix-Marseille University, Marseille, France

F. LAMADIE, LGCI, CEA - Centre de Marcoule, Bagnols-sur-Cèze, France.

C. MONTET , IUSTI, Aix-Marseille University, Marseille, France.

C. PELCE, IUSTI, Aix-Marseille University, Marseille, France.

M. SENTIS, IUSTI, Aix-Marseille University, Marseille, France.

Conference secretariat: Mrs BARTOLINI - IUSTI - UMR n°7343 CNRS/Aix-Marseille Université, Polytech'Marseille-Dept. Mécanique-Energétique, Technopôle Château Gombert, 5. r. Enrico Fermi, 13453 Marseille cedex 13, France - Ph:(+33) 4 91 10 68 82 / Fax:(+33) 4 91 10 69 69, Email: contact@lip2014.eu

LIST of CONTENTS

KEYNOTE LECTURES (AK)

(AK-1) Surprises and anomalies in acoustical and optical scattering, Philip L. MARSTON

(AK-2) From optical tweezers to optically self-arranged and propelled microstructures, Pavel ZEMANEK

(AK-3) Numerical techniques for shaped beam scattering by large and absorbing particle using variable separation methods, Kuan-Fang REN

(AK-4) Electromagnetic scattering by dense discrete random media: physics and numerically exact results, Michael I. MISHCHENKO

(AK-5) Laser scattering in particle characterization: application perspective, Renliang XU

BEAM SHAPE DESCRIPTION (BS)

(BS-1) On the Description of Electromagnetic Arbitrary Shaped Beams : Beam Shape Coefficients versus Plane Wave Spectra, and vice versa, Gérard GOUESBET and James A. LOCK

(BS-2) Scattering of the Evanescent Components in the Angular Spectrum of a Tightly Focused Electromagnetic Beam by a Spherical Particle, James A. LOCK

(BS-3) Acoustics of Finite-Aperture Vortex Beams, Farid G. MITRI

(BS-4) Superpositions of equal-frequency ordinary Bessel beams: frozen waves for optical trapping and micromanipulation, Leonardo A. AMBROSIO

COMPLEX SHAPED PARTICLES & AGGREGATES (CP)

(CP-1) On the electromagnetic scattering of arbitrary shaped beams by arbitrary shaped particles: a review, Gérard GOUESBET, James A. LOCK and Michael I. MISHCHENKO

(CP-2) Light scattering on single evaporating microdroplet of suspension: Fano resonances and surface pressure, Maciej KOLWAS, Genadij DERKACHOV, Daniel JAKUBCZYK, Krystyna KOLWAS and Justice ARCHER

(CP-3) Electromagnetic modeling of sunscreen protection, Marie LECUREUX, Carole DEUMIE and Stefan ENOCH

(CP-4) Helicity resonances in spheres, Xavier ZAMBRANA-PUYALTO, Gabriel MOLINA-TERRIZA

(CP-5) Scattering properties of mineral and soot-containing aerosols, Janna M. DLUGACH, Michael I. MISHCHENKO

(CP-6) Method of moment solution for the electric current volume integral equation, Johannes MARKKANEN, Antti PENTTILÄ, Jouni PELTONIEMI and Karri MUINONEN

(CP-7) T-matrix calculation with the Green's dyadic technique for electromagnetic scattering: a numerical approach using Dyson equation, Ugo TRICOLI, Klaus PFEILSTICKER

(CP-8) Light scattering by random irregular particles with different morphology, Yevgen GRYNKO, Evgenij ZUBKO

(CP-9) High-frequency Gaussian beam scattering by ice crystals, Patrick STEGMANN, Erion GJONAJ and Cameron TROPEA

(CP-10) Formation of spherical aggregate from micro droplet containing submicron inclusions, Mariusz WOŹNIAK, Justice ARCHER, Gennadiy DERKACHOV, Daniel JAKUBCZYK, Tomasz WOJCIECHOWSKI, Krystyna KOLWAS, Maciej KOLWAS

(CP-11) Thermometry of evaporating acetone droplets in near-critical conditions by combined phosphorescence/fluorescence measurements, Benjamin BORK, Thomas KÖNIG, Florian WECKENMANN, Grazia LAMANNA and Andreas DREIZLER

(CP-12) Role played by multiple scattering on the absorption and scattering properties of soot fractal aggregates, Jérôme YON, Damien Hebert, Alexandre BESCOND, Claude ROZE and Alexis COPPALLE

(CP-13) Characterization and application of laser light scattering by ice crystals, A.-K. GANSMANN, P. STEGMANN and C. TROPEA

(CP-14) Light scattering from helical microparticles, Rodrigo BECERRA-CARRILLO, Jian YANG and Kevin ROBBIE

(CP-15) T-matrix methods for scattering by cylinders in optical tweezers, Xiaoqiong QI, Timo A. NIEMINEN, Alexander B. STILGOE, Vincent L.Y. LOKE, and Halina RUBINSZTEIN-DUNLOP

FAR-FIELD SCATTERING (FF)

(FF-1) Discrete Dipole Approximation for Particles near Surface: a 3D-FFT-accelerated Implementation, Maxim A. YURKIN and Marcus HUNTEMANN

(FF-2) Analysis of chiral sphere rainbows in geometric optics model, Zhen-Sen WU, Qing-Chao SHANG, Tan QU, Zheng-Jun Li and Lei GONG

(FF-3) Generalized rainbow patterns for spheroidal droplet characterization, Haitao YU, Jianqi SHEN and Cameron TROPEA

(FF-4) Vectorial Complex Ray Model – from geometrical op-tics to ray theory of wave, Kuan Fang REN, Claude ROZÉ, Yijia YUAN

(FF-5) Scattering of a plane electromagnetic wave by a radially inhomogeneous generalized Luneburg lens, James A. LOCK, Philip LAVEN and John A. ADAM

(FF-6) Light Scattering of a non diffracting zero-order Bessel beam by uniaxial anisotropic bispheres, Zheng-Ju LI, Zhen-Sen WU, Tan. QU, Hai-Ying LI, Lu BAI and Lei GONG

(FF-7) Electromagnetic scattering by a general anisotropic dielectric nonspherical particle, Jia Jie WANG, Yi PING HAN, Zhe Feng WU and Lu HAN

(FF-8) Observation of laser light scattering by randomly oriented particles at exact backscattering angle, Alain MIFFRE , Gregory DAVID, Elodie COILLET, and Patrick RAIROUX

(FF-9) T-matrix based scattering model for bio-medical sensor, V. SCHMIDT, Y. EREMIN and T. WRIEDT

(FF-10) Coupling T-Matrix formalism with UV-VIS polarization Laser LIDAR to retrieve atmospheric particles backscattering from desert dust, sea-salt and water soluble particles mixture, Alain MIFFRE, Gregory DAVID, Elodie COILLET, and Patrick RAIROUX

(FF-11) Analytical solutions of plane wave scattering from a large sized chiral cylinder, Qing-Chao SHANG, Zhen-Sen WU, Tan QU, Zheng-Jun LI, and Lei GONG

(FF-12) An analytic solution for the Gaussian beam scattering from a moving uniaxial anisotropic sphere, Mingjun WANG, Huayong ZHANG, Xizheng KE, Pengfei WU

(FF-13) Numerical computation of the scattering properties of large arbitrary shaped particle by MLFMA and VCRM, Yue-Qian WU, Ming-Lin YANG, Kuan Fang REN and Xin-Qing SHENG

(FF-14) ABSphere - Software for calculation of all physical properties of any shaped Beam by a spherical particle, Kuan Fang REN

NEAR-FIELD AND RESONANCES (NR)

(NR-1) Laser Emission from Random Gain Media with Bubble Structures, Takashi OKAMOTO, Shouhei MATSUSHITA and Masanori TAKABAYASHI

(NR-2) Influence of sinter necks on the spectral behaviour of ITO aggregates, Thomas WRIEDT, Jens HELLMERS, Krzysztof SKORUPSKI and Janusz MROCZKA

(NR-3) Phohotonic Jet Generated by Spheroidal Particle, Yiping HAN, Lu HAN and Wenjuan ZHAO

(NR-4) Near and Far Field Light scattering from silicon nitride microdisks, David McCLOSKEY and John F. DONEGAN

(NR-5) Laser-Bubble Interactions under the Acoustic Field, Honoh SUZUKI and I-Yin Sandy LEE

MECHANICAL EFFECTS OF LIGHT (ME)

(ME-1) Optical trapping and manipulation of nanostructures, O. M. MARAGÓ, M. G. DONATO, A. MAGAZZU, A. IRRERA, C. D'ANDREA, E. MESSINA, B. FAZIO, M. A. IATI, P. H. JONES, and P. G. GUCCIARDI

(ME-2) Photonic Nanojet in Optical Tweezers, Antonio A. R. NEVES

(ME-3) As Diverse pathes leden diverse folk the righte way to radiation pressure, Timo A. NIEMINEN

(ME-4) Optical Torques for Alignment of Au Nanorods, Jiunn-Woei LIAW, Wei-Jiun LO, and Mao-Kuen KUO

(ME-5) Practical Tractor Beams, David G. GRIER and David B. RUFFNER

(ME-6) Optical trapping in secondary maxima of a tightly focused laser beam, Martin ŠILER, Petr JÁKL, Jan JEŽEK, Lukáš CHVÁTAL and Pavel ZEMÁNEK

(ME-7) Magnetic nanoparticles ring formation and dynamics, JanMASAJADand Marcin BACIA

(ME-8) Why do ellipsoidal particles oscillate in focused Gaussian beams? Jean-Christophe LOUDET, Bernard POULIGNY and Besira MIHIRETIE

(ME-9) Optical binding and hydrodynamic synchronization between non-spherical colloidal particles, Stephen H. SIMPSON, Stuart BOX, Luke DEBONO, Philip H. JONES, Onofrio M. MARAGÒ and Simon HANNA

(ME-10) Scattering of focused Laser beam in Zebrafish brain, Itia FAVRE-BULLE, Daryl PREECE, Timo A. NIEMINEN, Ethan K. SCOTT and Halina RUBINSZTEIN-DUNLOP

(ME-11) Polarization dependent optical trapping of chiral microresonators, M. G. DONATO, J. HERNANDEZ, A. MAZZULLA, C. PROVENZANO, R. SAIJA, M.A. IATI, A. MAGAZZÙ, P. PAGLIUSI, R. BARTOLINO, P. G. GUCCIARDI, O. M. MARAGÒ AND G. CIPPARRONE

(ME-12) The escape of spheres from optical tweezers, Alexander B. STILGOE, Nima KHATIBZADEH, Ann A. M. BUI, Timo A. NIEMINEN, Michael W. BERNS and Halina RUBINSZTEIN-DUNLOP

(ME-13) Brownian motion in speckle light fields: from anomalous diffusion to optical manipulation, Giorgio VOLPE, Giovanni VOLPE and Sylvain GIGAN

(ME-14) Theoretical aspects of single-beam multitrapping acoustical tweezers, Glauber T. SILVA

(ME-15) Kramers escape rate of silicon nanowires in a double optical trap, A. MAGAZZU, C. J. RICHARDS, T. J. SMART, A. IRRERA, M. G. DONATO, F. PRIOLO, P. G. GUCCIARDI, O. M. MARAGÓ and P. H. JONES

(ME-16) Non Conservative optical forces for silicon nanowires in optical traps, A. MAGAZZU, A. IRRERA, P. ARTONI, S. H. SIMPSON, S. HANNA, P. H. JONES, F. PRIOLO, P. G. GUCCIARDI, and O. M. MARAGÓ

(ME-17) Optical tweezers force calibration of chromosomes, Nima Khatibzadeh, Ann A. M. BUI, Alexander B. STILGOE, Timo A. NIEMINEN, Halina RUBINSZTEIN-DUNLOP and Michael W. BERNS

(ME-18) Radiation torque induced by Bessel beam, Renxian LI, Lixin GUO, Ruiping YANG, Chunying DING and Zhensen WU

(ME-19) Analysis of radiation force of a Laguerre Gaussian vortex beam on a uniaxial anisotropic sphere, Tan QU, Zhen-Sen WU, Qing-Chao SHANG, Zheng-Jun LI, Lei GONG

(ME-20) Angular momentum transfer between Laguerre-Gauss beams and purpose-built microrotors, Vincent L.Y. LOKE, Theodor ASAVEI, Timo A. NIEMINEN and Halina RUBINSZTEIN-DUNLOP

(ME-21) "Optical gas bubble management" at its Laser thermo-capillary trapping in an absorbing liquid, A.D. BUTENKO, N.A. KAZACHKOVA, O.I. KOFMAN and V.I. LYMAR

(ME-22) A new polarimetric indicator in sensing applications based on magneto-dielectric nanoparticles, Ángela I. BARREDA, Juan M. SANZ, José M. SAIZ, Fernando MORENO and Francisco GONZÁLEZ

(ME-23) Scattering matrix measurements for single particles, Antti PENTTILÄ, Hanna PENTIKÄINEN, Daniel GUIRADO RODRÍGUEZ, Jouni PELTONIEMI, and Karri MUINONEN

MISCELLANEOUS TOPICS (MT)

(MT-1) Intrinsic Method for the Evaluation of Beam Shape Coefficients in Spheroidal Coordinates for Oblique Illumination, Lu HAN, Yi Ping HAN, Gerard GOUESBET, and Jia Jie WANG

(MT-2) Effect of Fractal Parameters of Soot Aggregates on their Absorption and Scattering Properties Simulated by Discrete Dipole Approximation, Gizem OKYAY and Franck ENGUEHARD

(MT-3) Dynamic polarimeter for spectral imaging of scattering media, J. M. SANZ, F. CARMAGNOLA, A. FERNANDEZ, F. MORENO, F. GONZALEZ and J. M. SAIZ

(MT-4) Diffusion of a laser pulse in a particle medium with three-dimensional geometry, Feng XU and Anthony B. DAVIS

(MT-5) Dynamics of laser excited colloidal Au nanoparticles conjugated with cysteine, Alexandra FALAMAS, Nicoleta TOSA and Valer TOSA

(MT-6) Optical properties of core–shell gold–iron oxide and iron oxide–gold nanoparticles for near UV and visible radiation wavelengths, Victor PUSTOVALOV, Liudmila ASTAFYEVA and Galina LEDNEVA

(MT-7) Ideal absorption design in nanoparticles, Brian STOUT, Nicolas, BONOD, Jérôme WENGER, Victor GRIGORIEV

(MT-8) Polarized light extraction from light emitting diode using metallic nanostructures, Örs SEPSI, Tibor GÁL and Pál KOPPA

OPTICAL PARTICLE CHARACTERIZATION (PC)

(PC-1) Fast nanoparticle sizing by image dynamic light scattering, Chengze XU, Xiaoshu CAI, Jie ZHANG, Lili LIU

(PC-2) High-sensitivity low-coherence dynamic light scattering and particle sizing for nanoparticles(Ⅲ) : Particle size distribution of pigment particles, Katsuhiro ISHII, Sohichiro NAKAMURA and Yuki SATO

(PC-3) Light scattering in highly concentrated mono- and bimodal dispersions, Lena BRESSEL, Miren AGUIRRE, Mariano BARRADO, Jose RAMON LEIZA and Olivier REICH

(PC-4) Diffusing wave spectroscopy: a modern light scattering technique to characterize mixtures/soft matter systems, Frédéric MONDIOT, Mathias REUFER, and Andreas C. VOELKER

(PC-5) Digital In-line Holography for the characterization of inclusions in a suspended water droplet, Wisuttida WICHITWONG, Sébastien COETMELLEC, Denis LEBRUN, Daniel ALLANO, Gérard GREHAN, and Marc BRUNEL

(PC-6) Energy redistribution in single particle interference microscopy, Markus SELMKE, Irene NEUGEBAUER and Frank CICHOS

(PC-7) Identification and characterization of cell-Derived microparticles using light scattering, Anastasiya I. KONOKHOVA, Darya N. CHERNOVA, Dmitry I. STROKOTOV, Maxim A. YURKIN, and Valeri P. MALTSEV

(PC-8) Interferometric out-of-focus imaging simulator for irregular multi-emitters. Application to the characterization of irregular rough particles, Marc BRUNEL, Sébastien COETMELLEC, Gérard GREHAN and Huanhuan SHEN

(PC-9) Simultaneous mapping of droplets size and concentration in sprays using structured laser illumination planar imaging, Yogeshwar Nath MISHRA, Elias KRISTENSSON and Edouard BERROCAL

(PC-10) Determination of droplet velocity and size immediately before impacting into a liquid pool, Norbert ROTH and Bernhard WEIGAND

(PC-11) Particle characterization with digital holography, Matthew BERG, Nava SUBEDI and Nicholas FOWLER

(PC-12) Measurement of bubbles inside a droplet by digital in-line holography, DARAWAN PEJCHANG, Sébastien COETMELLEC, Gérard GREHAN, Daniel ALANO, Denis LEBRUN and Marc BRUNEL

(PC-13) Measurement of spray characteristics by FII: Experimental validation² on calibrated multijet, Sawitree SAENGKAEW, Siegfried MEUNIER-GUTTIN-CLUZEL and Gerard GREHAN

(PC-14) Transient evolution of refractive index gradients inside single isolated droplets with rainbow refractometry, Christopher ROSEBROCK, Thomas WRIEDT and Lutz MÄDLER

(PC-15) Measurement of laser rainbow of elliptical liquid jet, Ruliang ZHONG, Xiang'e HAN and He LIU

(PC-16) Digital in-line holography for near field observation of liquid-liquid flows, Fabrice LAMADIE, Laurent BRUEL and Lila OULDARBI

(PC-17) On the measurement of nano and micro particles by Fourier Interferometric imaging, Sawitree SAENGKAEW, Annie GARO, Siegfried MEUNIER-GUTTIN-CLUZEL and Gérard GREHAN

(PC-18) Numerical considerations on measurements of light-absorbing particles using polarized-type phase Doppler Method, Naomichi YOKOI and Yoshihisa AIZU

(PC-19) Ultrathermometry of Evaporating Droplets, Giennadiy DERKACHOV, Daniel JAKUBCZYK, Mariusz WOŹNIAK, Justice ARCHER and Maciej KOLWAS

(PC-20) Laser Speckle of Nanofluids and its Application in Velocity Distribution Measurement, Chuanlong XU, Zhihong DU, Shimin WANG

(PC-21) Ionisation of soot aggregates and primary particles i a laser field, Vivien BEYER, Douglas GREENHALGH, Yannis HARDALUPAS, Christopher HONG, Alex M K P TAYLOR

(PC-22) Fine particles sampling of light-scattering Laser photometer and air sampler with impaction sizer, C-H HUANG and Y-Y CHANG

(PC-23) Aerosol optical and microphysical properties retrieved from combination LIDAR with Sun/sky photometer: Preliminary results over Lille, Valentyn BOVCHALIUK, Thierry PODVIN, Augustin MORTIER, Philippe GOLOUB, Oleg DUBOVIK, Didier TANRE, Igor VESELOVSKII, Stéphane VICTORI

(PC-24) In situ individual aerosol particle composition: combining IR spectroscopy and coherent heterodyne scattering, Jay EVERSOLE, Brian SAAR, David WOLINSKI, Adam SHABSHELOWITZ, Matthew HART and William HERZOG

(PC-25) Conformable organic photo sensors for particle systems characterization, Matthias SENTIS, Fabrice R.A. ONOFRI, Fabien CHAUCHARD, Olivier DHEZ, Jean-Yves LAURENT

(PC-26) An improved Analysis of the Scattering Properties to the Half-Space Problem with Multiple Defect Particles for Optical Surface, Lei GONG, Zhen-Sen WU

(PC-27) Multiplex single particle and biological cell analysis in microfluidics, David DANNHAUSER, Domenico ROSSI, Filippo CAUSA and Paolo A. NETTI

(PC-28) Observation of red blood cells in bood coagulation using digital holographic microscopy, Hideki FUNAMIZU, Yuki WATANABE and Yoshihisa AIZU

(PC-29) Measurement of collected polarised light across a liquid-liquid extensional flow, Arab BELKADI, Dominique TARLET, Agnès MONTILLET, Jérôme BELLETTRE and Patrizio MASSOLI

(PC-30) Coupling environmental acoustic levitation cell and Micro-Raman spectroscopy for monitoring photoevolution and hygroscopicity of single particles with atmospheric interest, Myriam MOREAU, Yeny TOBON , Sophie SOBANSKA and Jacques BARBILLAT

(PC-31) Characterization of nanopaticles aggregates by static light scattering, Cedric MONTET, Matthias SENTIS and Fabrice ONOFRI

PLASMONICS (PL)

(PL-1) Au-fluorophore nanohybrids: experimental evidence of the plasmonic Dicke effect, Pierre FAUCHÉ, Miguel COMESAÑA-HERMO, Brahim LOUNIS, Serge RAVAINE and Renaud VALLÉE

(PL-2) Enhanced Spin-Hall and Goos-Hänchen shift(s) mediated by scattering in plasmonic nanoparticles, Jalpa SONI, Shampy MANSHA, S. Dutta GUPTA, Ayan BANERJEE and Nirmalaya GHOSH

(PL-3) Tailoring the spectral efficiency of gold nanospheres using size dependence of plasmon resonance frequencies and damping rates, Krystyna KOLWAS and Anastasiya DERKACHOVA

(PL-4) Analysis of the scattering behaviour of two spherical plasmonic particles, Wen FENG, Jens HELLMERS, Vladimir SCHMIDT, Lutz MÄDLER and Thomas WRIEDT

(PL-5) Multiple light scattering from ordered and disordered atomic clouds, Philippe COURTEILLE and Romain BACHELARD

(PL-6) Surface plasmon polaritons in linear chains of silver nanospheroids, Ilia L. RASSKAZOV, Sergei V. KARPOV and Vadim V. MARKEL

(PL-7) Multiple particle scattering approach applied to coupling effects in plasmonic aggregates: from hybrid dimer modes to quadrumer Fano resonances, Saïd BAKHTI, Nathalie DESTOUCHES and Alexandre TISHCHENKO

Keynotes lectures

Surprises and Anomalies in Acoustical and Optical Scattering

Philip L. MARSTON[1,*]

[1] Physics & Astronomy Dept., Washington State University, Pullman, WA, 99164-2814, USA

*Corresponding author: marston@wsu.edu

Abstract

Experiments on radiation torques and negative radiation forces by various researchers display how the underlying wave-field geometry influences radiation forces. Other situations strongly influenced by wave-field geometry include high-order caustics present in light scattering patterns of objects as simple as oblate drops of water or oblate bubbles of air in water. Related theoretical and experimental investigations are considered. Scattering enhancements associated with guided waves having negative group velocities are also examined.

1 Introduction

Summarized here are examples of scattering research from the past 35 years. Readers are encouraged to consult the referenced publications for the broader context.

2 Optical Angular Momentum and Torque

In about 1900 Sadowsky (and later Poynting) realized that circularly polarized plane waves should exert a torque in certain situations. Beth confirmed this in the 1930s. In 1983 the present author noticed that an analysis of the torque on an isotropic sphere predicted by Mie theory was unavailable. If the incident circularly polarized light has positive helicity, the torque (using the time-averaged Maxwell stress evaluated in the far field) was found to be [1]: $\Gamma = P_{abs}/\omega$ where P_{abs} is the absorbed power (but not for non-axisymmetric objects). The various special cases in [1] considered including enhancing Γ and P_{abs} by selecting ω to excite a surface plasmon mode of a small metallic sphere. This enhancement was recently used to spin gold nano-spheres in water at an angular frequency of a few kHz [2]. It may appear surprising that there is no torque on an isotropic non-absorbing sphere. To understand this Marston and Crichton [3] used Humblet's decomposition of field angular momentum (from the 1940s) to analyse the angular momentum carried by the scattered radiation. Part of the axial component of angular momentum of the scattered field is attributed to "spin" and is associated with part of the scattered power: $P_{spin} = r^2 \int (I_+ - I_-) \cos\theta \, d\Omega$ where I_+ and I_- denote positive and negative helicity components of the far-field scattered irradiance evaluated at a scattering angle θ, r is the distance to the observer, and the integration is over a solid angle of 4π sr. Evaluating I_+ and I_- using Mie theory and introducing the spin efficiency factor Q_{spin} where $P_{spin} = I_0 \, \pi \, a^2 \, Q_{spin}$ gives [3,4]:

$$Q_{spin} = [2/(ka)^2] \sum_{n=1}^{+\infty} \{ \left(|a_n|^2 + |b_n|^2 \right) (2n + 1)/[n(n + 1)] \} + \{ [2n(n + 2)/(n + 1)] \, \mathrm{Re}[a_{n+1} b^*_n + a_n b^*_{n+1}] \} , \quad (1)$$

where I_0 is the illumination irradiance, a is the sphere radius, $k = \omega/c$, and a_n and b_n are Mie coefficients in the usual notation [1]. The Humblet decomposition shows that there is a flux of *orbital* angular momentum having an efficiency factor ($Q_{sca} - Q_{spin}$) where Q_{sca} is the scattering efficiency [3,4]. Omitting the orbital angular momentum gives the incorrect impression of a torque on lossless isotropic spheres illuminated by circularly polarized light.

3 Negative Radiation Forces and Bessel Beams

Much 20th century research on scattering by acoustic beams concerned situations involving low frequencies (associated with monopole and dipole scattering terms) or situations in which the description of the beam was valid only at high frequencies. Subsequently Durnin's angular spectrum representation was used to express the scattering by an arbitrary isotropic sphere centered on the axis of a Bessel beam [5,6]. The scattering is expressed in terms of partial wave coefficients (s_n-1) for the corresponding plane wave scattering problem with a modified weighting factor that depends on the conic angle β of the Bessel beam. It was then possible to compute the scattering properties and the associated acoustic radiation force for a variety of spheres by appropriate selection of the s_n from prior results for plane waves [5-8]. Situations were found for appropriate values of β and material properties such that the direction of radiation force was predicted to be opposite the propagation direction of the beam. These results were extended to the case of spheres centered on the axis of a first-order Bessel *vortex* beam [9,10]. For both kinds of beams, negative radiation forces were associated with situations in which scattering into the backward hemisphere was greatly suppressed relative to the scattering into the forward hemisphere. (Mitri [11] and others provided other related derivations.) Consideration of a partially analogous optical situation [12] provided important insight into the momentum projected by a Bessel beam. Subsequently Zhang and Marston carried out a corresponding geometric analysis of the radiation force on spheres centered on the axis of an nth order acoustic Bessel beam giving a radiation force proportional to the following dimensionless function [13]:

$$Y_p = (b - \langle w \rangle) Q_{sca} + b Q_{abs}, \qquad (2)$$

where Q_{sca} and Q_{abs} are dimensionless scattering and absorption efficiencies and $\langle w \rangle$ is the scattering asymmetry (defined by extending Van de Hulst's terminology to the present situation) and $b = \cos\beta$ where β is the conic angle of the Bessel beam. The asymmetry $\langle w \rangle$ satisfies the condition $-1 \leqslant \langle w \rangle \leqslant 1$. Inspection of (2) shows that Y_p and the corresponding force is negative only when $\langle w \rangle$ is sufficiently positive and β is sufficiently large. Though (2) was analytically derived in [13] it is consistent with the geometrical interpretation in [12]. (The geometrical interpretation based on momentum projection has been used to demonstrate negative radiation forces for other types of optical [14] and acoustic [15,16] beams.) In (2) all of the factors depend implicitly on β. Absorption introduces a positive force explicitly proportional to $b\,Q_{abs}$ and the partial wave representation for Q_{abs} is such that the nth term is proportional to $(1-|s_n|^2)$ and a factor depending on β. For spheres with $ka \ll 1$ an approximation is available for the increase in $(1-|s_n|^2)$ due to viscous dissipation in the fluid surrounding the sphere [17].

4 Radiation Torque of Acoustic Vortex Beams

Hefner and Marston [18] demonstrated the production of a first-order vortex beam in water by the phased excitation of a 4-element transducer array. By restricting their analysis to paraxial nth-order vortex beams they found that the time averaged axial angular momentum *flux* is $\langle L_z \rangle = mP/\omega$ where P is the beam power. They noted that absorption produces a corresponding axial torque on the absorber. Zhang and Marston [19-21] generalized the torque analysis to axisymmetric objects in beams that were not necessarily paraxial (including the case of mth order vortex standing waves) and predicted that the torque becomes, $\Gamma = m P_{abs}/\omega$. This relationship was subsequently verified using beams with a wide range of m [22]. For the case of a sphere centred on a vortex Bessel beam P_{abs} is expressible using a series expansion [13]. Far-field scattering is useful in the analysis of acoustic torques [19-21,23]. If the fluid surrounding the object is sufficiently viscous, absorption in the fluid induces rotary streaming which complicates the measurement of the torque [24].

5 Scattering Extinction of Invariant Beams

Idealized mth-order Bessel beams are perhaps the simplest example of an invariant beam. While analyzing the axial radiation forces of such beams (corresponding to a generalization of Eq. (2)), the optical theorem was extended so as to express the extinction power using an appropriately weighted superposition of scattering amplitudes at angles determined by the incident beam [16,21]. For the case of a sphere placed on the axis of a Bessel beam the extinction efficiency Qext depends strongly on the conic angle of the beam as well as on ka. For the simple case of a rigid sphere Q_{ext} approximately scales as a function of $ka \sin\beta$ when ka is large [25].

6 Diffraction Catastrophes of Spheroidal Drops

Early measurements of the response of acoustically levitated liquid drops to modulated ultrasonic radiation pressure showed that modulation of the light scattered in the rainbow region reveals small changes in the drop's shape [26,27]. Eventually higher-order caustics were discovered in the far field scattering by sufficiently oblate drops [28]. Nye computed the drop's aspect ratio for a hyperbolic umbilic focal section by requiring simultaneously vanishing principal curvatures of the associated outgoing wave front. The method of analysis was applied to a variety of other cases and inverse problems and a series of observations were performed [30-35]. Other groups confirmed that related two-dimensional scattering patterns are useful for inverse scattering and that numerical ray tracing methods can be helpful [36,37].

7 Light Scattering by Bubbles in Liquids

Gas bubbles in liquids have a refractive index less than the surroundings and this results in diffraction related scattering processes differing from those for drops. Examples include critical [38-44] and Brewster [42] angle scattering and backward and forward glory scattering [45-48]. Bubbles freely rising in water can become sufficiently oblate that the glory axial caustic unfolds into a four-cusped asteroid [48]. Near the critical scattering angle modulation of interference features are useful for detecting feeble shape oscillations [49]. At the critical scattering angle convergence to geometrical optics is extremely slow [41], the diffraction correction being $O(ka)^{-1/4}$. Optical radiation forces and trapping of bubbles in laser beams are closely related to total reflection by the bubble [50].

8 Caustic-Merging Transitions for Cylinders

The location of rainbow scattering by the body of a tilted circular dielectric cylinder depends on the amount of tilt [51]. The rainbow caustics on opposing sides of the meridional plane were observed to merge for a critical tilt angle as predicted [52]. The associated caustic loci generate a cusp curve [52]. This process generates an optical backscattering enhancement for critically tilted flat-ended dielectric fibers [53]. An analogous acoustic backscattering enhancement has been demonstrated [54].

9 Acoustic Scattering Enhancement from Ordinary and Backwards Guided Waves

Waves guided by surfaces of smooth elastic objects in water ordinarily have group and phase velocities in the same direction. An example of such a guide wave is a

Rayleigh-like leaky wave on stiff solids in water or Lamb-like waves on elastic shells. (A Rayleigh wave is a two-dimensional surface guided wave on an elastic half space. Lamb waves are waves in an elastic plate in which the plate acts like a waveguide.) For spheres such waves circumnavigate the backside and cause a type of backward and forward directed glory scattering [55-57]. For elastic shells situations can be found giving a topological change in the ray diagram associated with a negative group velocity. A pronounced backscattering enhancement is produced by this guided wave because circumnavigation of the backside is no longer required [58,59]. At a relatively lower k*a* there is a more commonly studied backscattering enhancement for thin shells associated with the near coincidence of a guided wave phase velocity with the speed of sound in water [60].

10 End and Corner Guided Wave Enhancements

Leaky guided waves on flat-ended objects can produce pronounced backscattering enhancements of sound for appropriately tilted objects due to the partial reflection of the guided wave at the truncation. Examples include meridional and helical rays on cylinders [61-64] and corner reflections on cubes [65]. Franz waves guide by solid cylinders are usually unimportant at high k*a*, however they become a dominant scattering mechanism for a slightly exposed cylinder at a free surface [66]. Guided wave scattering contributes to sonar images [67,68] and to the transient response of cylindrical shells viewed in the time-frequency domain [69].

11 Fluctuations in Wavefields of Random Caustics

When a high frequency spreading wave reflects from a randomly curved surface, there are situations where the fluctuations of the associated reflected wavefield are dominated by random caustics [70,71]. Catastrophe theory was used to calculate the wavefield for an acoustic realization of this situation and the analysis was supported by numerical integration and the Kirchhoff approximation [72]. The reflected wavefield was measured by placing the corresponding reflecting surface in a large tank of water. The observed fluctuations agreed with predictions [72,73] and the observed third and fourth order intensity moments depended on the acoustic frequency in a way consistent with the theory of twinkling exponents of an Airy caustic [31,70,71,73,74].

12 Doubly Focused Echoes from Spheres Scanned Through Reflection Caustics of Curved Surfaces

A special example of the aforementioned situation is the case of a concave reflecting surface consisting of the inside of a half of a circular cylinder (a large cylindrical pipe cut in half along its diameter). Small spheres were scanned through the Airy caustic of the associated internally reflected wavefield of an ultrasonic wave in water [75]. The spheres were made of air-filled solid foam so as to partially simulate the simple case of perfectly reflecting spheres. The ultrasound backscattered by the sphere was recorded by using the source transducer also as a receiver. By using sufficiently short ultrasonic bursts the backscattering was separated into three contributions: (a) direct scattering by the sphere not influenced by the presence of the cylindrical reflector; (b) a relatively delayed echo which had reflected once from the cylindrical surface as well being scattered by the sphere; and (c) an even more delayed echo which had been scattered once by the sphere but reflected twice from the cylindrical surface (once prior to reaching the sphere and once afterward). The questions of interest were: how do the category (a), (b), and (c) echoes depend on the location of the sphere relative to the Airy reflection caustic of the circular cylinder, and what are their relative magnitudes? As expected the direct scattering (a) depends only weakly on the location of the sphere. The once-focused echo (b) is larger than echo (a) when the sphere is close to the caustic and the position dependence is approximately described using an Airy function. (It is noteworthy that a uniform approximation method was found to improve the description of echo (b) [75].) Echo (c) is even larger than echo (b) when the sphere is near the caustic because the scattered wave is focused back on the source just as the incident wave is also focused on the sphere. The position dependence of echo (c) was shown to be a function of a hyperbolic-umbilic diffraction integral [76]. (That integral was previously found to be useful for describing the scattering of laser beams by spheroidal drops of water [31,35].) In analogous optical situations similar two-way focal scattering enhancements are expected.

13 Acknowledgement

Numerous students and associates who contributed to this research are noted in the references. (Professors James H. Crichton and Robert E. Apfel regrettably are no longer living.) ONR and NASA provided most of the support. The Alfred P. Sloan Foundation provided early support.

14 References

[1] P. L. Marston and J. H. Crichton, Radiation torque on a sphere caused by a circularly polarized electromagnetic wave, Phys. Rev. A 30, 2508-16 (1984).

[2] A. Lehmuskero *et al.*, Ultrafast spinning of gold nanoparticles in water using circularly polarized light, Nano Letters 13, 3129–34 (2013).

[3] P. L. Marston and J. H. Crichton, Radiation torque on a sphere illuminated with circularly polarized light and the angular momentum of scattered radiation, *Proceedings of the Chemical Research and Development Center's 1984 Scientific Conference on Obscuration and Aerosol*

Research, pp. 233-8, 1985. .
http://www.dtic.mil/cgi-bin/GetTRDoc?AD=ADA159094

[4] J. H. Crichton and P. L. Marston, The measurable distinction between the spin and orbital angular momenta of electromagnetic radiation, Electronic Journal of Differential Equations, C04, 37-50 (2000). https://eudml.org/doc/121998

[5] P. L. Marston, Axial radiation force of a Bessel beam on a sphere and direction reversal of the force, J. Acoust. Soc. Am. 120, 3518-24 (2006).

[6] P. L. Marston, Scattering of a Bessel beam by a sphere, J. Acoust. Soc. Am. 121, 753-8 (2007).

[7] P. L. Marston, Acoustic beam scattering and excitation of sphere resonance: Bessel beam example, J. Acoust. Soc. Am. 122, 247-52 (2007).

[8] P. L. Marston, Negative axial radiation forces on solid spheres and shells in a Bessel beam, J. Acoust. Soc. Am. 122, 3162-5 (2007).

[9] P. L. Marston, Scattering of a Bessel beam by a sphere: II. Helicoidal case and spherical shell example, J. Acoust. Soc. Am. 124, 2905-10 (2008).

[10] P. L. Marston, Radiation force of a helicoidal Bessel beam on a sphere, J. Acoust. Soc. Am. 125, 3539-47 (2009).

[11] F. G. Mitri, Negative axial radiation force on a fluid and elastic spheres illuminated by a high-order Bessel beam of progressive waves, J. Phys. A. 42, 245202 (2009).

[12] J. Chen, J. Ng, Z. Lin, and C. T. Chan, Optical pulling force, Nature Photonics 5, 531-4 (2011).

[13] L.-K. Zhang and P. L. Marston, Geometrical interpretation of negative radiation forces of acoustical Bessel beams on spheres, Phys. Rev. E. 84, 035601(R) (2011).

[14] O. Brzobohatý *et al.*, Experimental demonstration of optical transport, sorting and self-arrangement using a 'tractor beam', Nature Photonics 7, 123-7 (2013).

[15] C. E. M. Démoré *et al.*, Acoustic tractor beam, Phys. Rev. Lett. 112, 174302 (2014).

[16] L.-K. Zhang and P. L. Marston, Axial radiation force exerted by general non-diffracting beams, J. Acoust. Soc. Am. 131, EL329-35 (2012).

[17] P. L. Marston, Viscous contributions to low-frequency scattering, power absorption, radiation force, and radiation torque for spheres in acoustic beams, Proc. of Meetings on Acoustics 19, 045005 (2013).

[18] B. T. Hefner and P. L. Marston, An acoustical helicoidal wave transducer with applications for the alignment of ultrasonic and underwater systems, J. Acoust. Soc. Am. 106, 3313-6 (1999).

[19] L.-K. Zhang and P. L. Marston, Angular momentum flux of nonparaxial acoustic vortex beams and torques on axisymmetric objects, Phys. Rev. E. 84, 065601(R) (2011).

[20] L.-K. Zhang and P. L. Marston, Radiation torque on a sphere centered on an acoustic helicoidal (vortex) Bessel beam, J. Acoust. Soc. Am. 125, 2552 (2009); P. L. Marston and L. Zhang, Radiation torques and forces in scattering from spheres and acoustical analogues, *Optical Trapping Applications, OSA Optics & Photonics Congress* (Vancouver, BC, 2009) http://dx.doi.org/10.1364/OTA.2009.OMB5.

[21] L.-K. Zhang and P. L. Marston, Optical theorem for acoustic non-diffracting beams and application to radiation force and torque, Biomed Opt. Express 4, 1610–7 (2013); (E) 4, 2988 (2013).

[22] C. E. M. Démoré *et al.*, Mechanical evidence of the orbital angular momentum to energy ratio of vortex beams, Phys. Rev. Lett. 108, 194301 (2012).

[23] L.-K. Zhang and P. L. Marston, Acoustic radiation torque and the conservation of angular momentum, J. Acoust. Soc. Am. 129, 1679-80 (2011).

[24] A. Anhauser, R. Wunenburger, and E. Brasselet, Acoustic rotational manipulation using orbital angular momentum transfer, Phys. Rev. Lett. 109, 034301 (2012).

[25] P. L. Marston, Quasi-scaling of the extinction efficiency of spheres in high frequency Bessel beams, J. Acoust. Soc. Am. 135, 1668-71 (2014).

[26] P. L. Marston and R. E. Apfel, Quadrupole resonance of drops driven by modulated acoustic radiation pressure — experimental properties, J. Acoust. Soc. Am. 67, 27-37 (1980).

[27] P. L. Marston, Rainbow phenomena and the detection of nonsphericity in drops, Applied Optics 19, 680-5 (1980).

[28] P. L. Marston and E. H. Trinh, Hyperbolic umbilic diffraction catastrophe and rainbow scattering from spheroidal drops, Nature 312, 529-31 (1984).

[29] J. F. Nye, Rainbow scattering from spheroidal drops — an explanation of the hyperbolic umbilic foci, Nature 312, 531-32 (1984).

[30] P. L. Marston, Cusp diffraction catastrophe from spheroids: generalized rainbows and inverse scattering, Optics Letters 10, 588-90 (1985).

[31] P. L. Marston, Geometrical and catastrophe optics methods in scattering, Physical Acoustics 21, 1–234 (1992).

[32] H. J. Simpson and P. L. Marston, Scattering of white light from levitated oblate water drops near rainbows and other diffraction catastrophes, Applied Optics 30, 3468-73 (1991); G. Kaduchak, P. L. Marston, and H. J. Simpson, E_6 diffraction catastrophe of the primary rainbow of oblate water drops: Observation with white light and laser illumination, Applied Optics 33, 4691-6 (1994).

[33] G. Kaduchak and P. L. Marston, Hyperbolic umbilic and E_6 diffraction catastrophes associated with the secondary rainbow of oblate water drops: Observations with laser illumination, Applied Optics 33, 4687-701 (1994).

[34] D. S. Langley and P. L. Marston, Generalized tertiary rainbow of slightly oblate drops: observations with laser illumination. Applied Optics 37, 1520-6 (1998).

[35] P. L. Marston, Catastrophe optics of spheroidal drops and generalized rainbows, J. Quant. Spectrosc. Radiat. Transf. 63, 341-51 (1999).

[36] S. Holler *et al.*, Two-dimensional angular optical scattering for the characterization of airborne microparticles, Optics Letters 23, 1489-91 (1998).

[37] H. Yu, F. Xu, and C. Tropea, Optical caustics associated with the primary rainbow of oblate droplets: simulation and application in non-sphericity measurement, Optics Express 21, 25761 (2013).

[38] P. L. Marston, Critical angle scattering by a bubble: physical-optics approximation and observations, J. Opt. Soc. Am. 69, 1205-11 (1979); (E) 70, 353 (1980).

[39] D. L. Kingsbury and P. L. Marston, Mie scattering near the critical angle of bubbles in water, J. Opt. Soc. Am. 71, 358-61 (1981); D. L. Kingsbury and P. L. Marston, Scattering by bubbles in glass: Mie theory and physical optics approximation, Applied Optics 20, 2348-50 (1981); P. L. Marston, D. S. Langley, and D. L. Kingsbury, Light scattering by bubbles in liquids: Mie theory, physical-optics approximations, and experiments, Applied Scientific Research 38, 373-84 (1982).

[40] D. S. Langley and P. L. Marston, Critical-angle scattering of laser light from bubbles in water: measurements, models, and applications to sizing of bubbles, Applied Optics 23, 1044-54 (1984); P. L. Marston and D. S. Langley, Bubbles in liquid ^{4}He and ^{3}He: Mie and physical-optics models of light scattering, and quantum tunneling and spinodal models of nucleation, *Near Zero: New Frontiers in Physics*, edited by J. D. Fairbank, B. S. Deaver, C. W. F. Everitt, and P. F. Michelson (Freeman, San Francisco, 1988) pp. 127-40.

[41] C. E. Dean and P. L. Marston, Critical angle light scattering from bubbles: an asymptotic series approximation, Applied Optics 30, 4764-76 (1991).

[42] P. L. Marston, Colors observed when sunlight is scattered by bubble clouds in sea water, Applied Optics 30, 3479-84 (1991).

[43] N. Fiedler-Ferrari, H. M. Nussenzweig, and W. J. Wiscombe, Theory of near-critical-angle scattering from a curved interface, Phys. Rev. A 43, 1005–38 (1991).

[44] F.R.A. Onofri, S. Radev, M. Sentis, S. Barbosa, A physical-optics approximation of the near-critical-angle scattering by spheroidal bubbles, Optics Letters 37, 4780-2 (2012).

[45] D. S. Langley and P. L. Marston, Glory in the optical backscattering from air bubbles, Phys. Rev. Lett. 47, 913-6 (1981).

[46] W. P. Arnott and P. L. Marston, Optical glory of small freely-rising gas bubbles in water: Observed and computed cross-polarized backscattering patterns, J. Opt. Soc. Am. A5, 496-506 (1988).

[47] D. S. Langley and P. L. Marston, Forward glory scattering from bubbles, Applied Optics 30, 3452-4 (1991).

[48] W. P. Arnott and P. L. Marston, Unfolded optical glory of spheroids: Backscattering of laser light from freely rising spheroidal air bubbles in water, Applied Optics 30, 3429-42 (1991).

[49] T. J. Asaki, P. L. Marston, and E. H. Trinh, Shape oscillations of bubbles in water driven by modulated ultrasonic radiation pressure: Observations and detection with scattered laser light, J. Acoust. Soc. Am. 93, 706-13 (1993).

[50] B. T. Unger and P. L. Marston, Optical levitation of bubbles in water by the radiation pressure of a laser beam: an acoustically quiet levitator, J. Acoust. Soc. Am. 83, 970-5 (1988).

[51] J. A. Lock and C. L. Adler, Debye-series analysis of the first-order rainbow produced in scattering of a diagonally incident plane wave by a circular cylinder, J. Opt. Soc. Am. A14, 1316-28 (1997).

[52] C. M. Mount, D. B. Thiessen, and P. L. Marston, Scattering observations for tilted transparent fibers: evolution of Airy caustics with cylinder tilt and the caustic merging transition, Applied Optics 37, 1534-9 (1998); P. L. Marston, Descartes glare points in scattering by icicles: color photographs and a tilted dielectric cylinder model of caustic and glare point evolution, Applied Optics 37, 1551-6 (1998).

[53] P. L. Marston, Y. Zhang, and D. B. Thiessen, Observation of the enhanced backscattering of light by the end of a tilted dielectric cylinder owing to the caustic merging transition, Applied Optics 42, 412-7 (2003).

[54] F. J. Blonigen and P. L. Marston, Backscattering enhancements for tilted solid plastic cylinders in water due to the caustic merging transition: Observations and theory, J. Acoust. Soc. Am. 107, 689-98 (2000).

[55] K. L. Williams and P. L. Marston, Axially focused (glory) scattering due to surface waves generated on spheres: model and experimental confirmation using tungsten carbide spheres, J. Acoust. Soc. Am. 78, 722-8 (1985).

[56] S. G. Kargl and P. L. Marston, Observations and modeling of the backscattering of short tone bursts from a spherical shell: Lamb wave echoes, glory, and axial reverberations, J. Acoust. Soc. Am. 85, 1014-28 (1989).

[57] S. G. Kargl and P. L. Marston, Ray synthesis of Lamb wave contributions to the total scattering cross section for an elastic spherical shell, J. Acoust. Soc. Am. 88, 1103-13 (1990).

[58] G. Kaduchak, D. H. Hughes, and P. L. Marston, Enhancement of the backscattering of high-frequency tone bursts by thin spherical shells associated with a backwards wave: Observations and ray approximation, J. Acoust. Soc. Am. 96, 3704–14 (1994).

[59] P. L. Marston, Negative group velocity Lamb waves on plates and applications to the scattering of sound by shells, J. Acoust. Soc. Am. 113, 2659–62 (2003).

[60] L. G. Zhang, N. H. Sun, and P. L. Marston, Midfrequency enhancement of the backscattering of tone bursts by thin spherical shells, J. Acoust. Soc. Am. 91, 1862-74 (1992).

[61] S. F. Morse, P. L. Marston, and G. Kaduchak, High frequency backscattering enhancements by thick finite cylindrical shells in water at oblique incidence: experiments, interpretation and calculations, J. Acoust. Soc. Am. 103, 785-94 (1998).

[62] K. Gipson and P. L. Marston, Backscattering enhancements due to reflection of meridional leaky Rayleigh waves at the blunt truncation of a tilted solid cylinder in water: Observations and theory, J. Acoust. Soc. Am. 106, 1673-80 (1999).

[63] F. J. Blonigen and P. L. Marston, Leaky helical flexural wave backscattering contributions from tilted cylindrical shells in water: Observations and modelling, J. Acoust. Soc. Am. 112, 528-36 (2002).

[64] S. F. Morse and P. L. Marston, Backscattering of transients by tilted truncated cylindrical shells: time-frequency identification of ray

contributions from measurements, J. Acoust. Soc. Am. 111, 1289-94 (2002).

[65] K. Gipson and P. L. Marston, Backscattering enhancements due to retroreflection of ultrasonic leaky Rayleigh waves at corners of solid elastic cubes in water, J. Acoust. Soc. Am. 105, 700-10 (1999).

[66] G. C. Eastland and P. L. Marston, Enhanced backscattering in water by partially exposed cylinders at free surfaces associated with an acoustic Franz wave, J. Acoust. Soc. Am. 135, 2489-92 (2014).

[67] K. L. Williams *et al.*, Acoustic scattering from a solid aluminam cylinder in contact with a sand sediment: Measurements, modeling, and interpretation, J. Acoust. Soc. Am. 127, 3356-71 (2010).

[68] K. Baik, C. Dudley, and P. L. Marston, Acoustic quasi-holographic images of scattering by vertical cylinders from one-dimensional bistatic scans, J. Acoust. Soc. Am. 130, 3838–3851 (2011).

[69] S. F. Morse and P. L. Marston, Backscattering of transients by tilted truncated cylindrical shells: time-frequency identification of ray contributions from measurements, J. Acoust. Soc. Am. 111, 1289-94 (2002).

[70] M. V. Berry and C. Upstill, Catastrophe optics: morphologies of caustics and their diffraction patterns, Progress in Optics 18, 257–346 (1980).

[71] J. F. Nye, *Natural Focusing and Fine Structure of Light; Caustics and Wave Dislocations* (IOP, Bristol, 1999).

[72] K. L. Williams, J. S. Stroud, and P. L. Marston, High frequency forward scattering from Gaussian spectrum, pressure release, corrugated surfaces. I: Catastrophe theory modeling, J. Acoust. Soc. Am. 96, 1687-1702 (1994).

[73] J. S. Stroud, P. L. Marston, and K. L. Williams, Intensity moments of underwater sound scattered by a Gaussian spectrum corrugated surface: Measurements and comparison with a catastrophe theory approximation, *High Frequency Acoustics in Shallow Water* (Conference Series CP-45, SACLANTCEN, 1997) pp. 525-32.

[74] M. V. Berry, Focusing and twinkling: critical exponents from catastrophes in non-Gaussian random short waves, J. Phys. A. Math. Gen. 10, 2061-81 (1977).

[75] B. R. Dzikowicz and P. L. Marston, Singly-focused backscattering from small targets in an Airy caustic formed by a curved reflecting surface, J. Acoust. Soc. Am. 116, 2751-8 (2004).

[76] B. R. Dzikowicz and P. L. Marston, Doubly-focused backscattering from finite targets in an Airy caustic formed by a curved reflecting surface, J. Acoust. Soc. Am. 118, 2811-9 (2005).

Electromagnetic Scattering by Dense Discrete Random Media: Physics and Numerically Exact Results

Michael I. MISHCHENKO

NASA Goddard Institute for Space Studies, 2880 Broadway, New York, NY 10025, USA

michael.i.mishchenko@nasa.gov

Abstract

While it is recognized that the Maxwell equations (MEs) control the transport of electromagnetic energy in particulate media (clouds, particulate surfaces, particle suspensions), direct solutions of the MEs for such media had been impracticable until quite recently. This has led to the widespread use of the radiative transfer (RT) equation in situations when its very applicability is questionable. This situation has now changed owing to the development of efficient computer solvers of the MEs applicable to macroscopic multi-particle groups. In fact, a new branch of statistical optics emerged several years ago wherein the scattering of light (and other electromagnetic radiation) by particulate media is modelled directly by using numerically exact computer solutions of the MEs without invoking any assumptions underlying the RT theory.

1 Introduction

By definition, a discrete random medium (DRM) is a scattering object in the form of an imaginary volume V populated by a large number N of particles in such a way that the spatial distribution of the particles throughout the volume is statistically uniform or quasi-uniform. Over time, particle positions and states change randomly, thereby resulting in random changes of the state of the entire object. Typical examples of a DRM are clouds and particle suspensions. In many cases a particulate surface can also be modelled as a DRM, since even minute changes of the source-of-light → object → detector configuration during the measurement are equivalent to multi-wavelength shifts in particle positions and, in essence, result in a stochastic scattering object. The volume packing density of a DRM can vary from almost zero for a cloud to more than 50% for a particulate surface.

Given their specific morphological traits and ubiquitous presence, scattering objects in the form of a DRM deserve a detailed theoretical study. Until recently, theoretical computations of electromagnetic scattering by a DRM had been based on *ad hoc* phenomenological approaches with unknown accuracy and ranges of applicability. However, recent advances in the development of direct computer solvers of the macroscopic Maxwell equations (MMEs) and the availability of powerful computers and computer clusters have made possible first-principle modelling of electromagnetic scattering by representative multi-particle groups with arbitrary packing densities. This research has brought the subject of electromagnetic energy transport in densely packed DRMs into the realm of physical optics and has unequivocally demonstrated the mesoscopic origin of relevant optical effects [1].

2 Numerical solvers of the MMEs

The first studies of electromagnetic scattering by densely packed, three-dimensional, random multi-particle groups based on direct computer solutions of the MMEs were based on the multi-sphere method (MSM) which is a particular case of the superposition T-matrix method (STMM) [2–5]. More recently, other techniques have been used, such as the pseudospherical time-domain method and its variations [6–9], the discrete-dipole approximation [10–12], the finite-difference time-domain method [13,14], and the hybrid finite element–boundary integral–characteristic basis function method [15–17]. However, the MSM and STMM remain the most frequently used techniques [12,18–52]. Studies of two-dimensional DRMs composed of parallel infinite cylinders have been based on the multi-cylinder solution of the MMEs [53–57].

3 Specific applications

Among the most important results of the publications referenced above are the following:

(i) Demonstration of the purely mathematical character of frequency-domain electromagnetic scattering by multi-particle groups [1,36];

(ii) Direct qualitative and quantitative validation of the microphysical approach to radiative transfer and coherent backscattering and its range of applicability [19, 20, 25, 28, 31, 33–36, 38, 41, 42, 44–46, 53–56];

(iii) Analysis of illumination by Bessel and Gaussian beams [13, 15, 17, 34];

(iv) Quantitative analysis of packing density effects [2–4, 21, 27, 30, 38, 43, 46];

(v) First-principle interpretation of opposition phenomena in planetary astrophysics [12, 27, 29, 39, 47, 49, 50, 52];

(vi) Biomedical applications [13, 14, 44].

4 Acknowledgement

This material is based upon work supported by the NASA Remote Sensing Theory Program managed by Lucia Tsaoussi and the NASA Radiation Sciences Program managed by Hal Maring.

5 References

[1] M.I. Mishchenko, *Electromagnetic Scattering by Particles and Particle Groups: An Introduction* (Cambridge University Press, Cambridge, UK, 2014).

[2] L. Tsang, C.E. Mandt, K.H. Ding, Monte Carlo simulations of the extinction rate of dense media with randomly distributed dielectric spheres based on solution of Maxwell's equations, Optics Letters 17:314–6 (1992).

[3] L.M. Zurk, L. Tsang, K.H. Ding, D.P. Winebrenner, Monte Carlo simulations of the extinction rate of densely packed spheres with clustered and nonclustered geometries, Journal of the Optical Society of America A 12:1772–81 (1995).

[4] L.M. Zurk, L. Tsang, D.P. Winebrenner, Scattering properties of dense media from Monte Carlo simulations with application to active remote sensing of snow, Radio Science 31:803–19 (1996).

[5] C.C. Lu, W.C. Chew, L. Tsang, The application of recursive aggregate T-matrix algorithm in the Monte Carlo simulations of the extinction rate of random distribution of particles, Radio Science 30: 25–8 (1995).

[6] S.H. Tseng, A. Taflove, D. Maitland, V. Backman, Pseudospectral time domain simulations of multiple light scattering in three-dimensional macroscopic random media, Radio Science 41:RS4009 (2006).

[7] S.H. Tseng, B. Huang, Comparing Monte Carlo simulation and pseudospectral time-domain numerical solutions of Maxwell's equations of light scattering by a macroscopic random medium, Applied Physics Letters 91:051114 (2007).

[8] S.H. Tseng, Optical characteristics of a cluster of closely-packed dielectric spheres, Optics Communications 281:1986–90 (2008).

[9] M. Ding, K. Chen, Numerical investigation on polarization characteristics of coherent enhanced backscattering using SLPSTD, Optics Express 18:27639–49 (2010).

[10] A. Penttilä, K. Lumme, Coherent backscattering effects with Discrete Dipole Approximation method. In G. Videen, M. Mishchenko, M.P. Mengüç, N. Zakharova, editors, *Peer-reviewed Abstracts of the Tenth Conference on Electromagnetic & Light Scattering*, p. 157–60 (Bodrum, 2008).

[11] A. Sukhov, D. Haefner, A. Dogariu, Coupled dipole method for modeling optical properties of large-scale random media, Physical Review E 77:066709 (2008).

[12] K. Lumme, A. Penttilä, Model of light scattering by dust particles in the solar system: applications to cometary comae and planetary regoliths, Journal of Quantitative Spectroscopy & Radiative Transfer 112:1658–70 (2011).

[13] M.S. Starosta, A.K. Dunn, Three-dimensional computation of focused beam propagation through multiple biological cells, Optics Express 17:12455–69 (2009).

[14] M.S. Starosta, A.K. Dunn, Far-field superposition method for three-dimensional computation of light scattering from multiple cells, Journal of Biomedical Optics 15:055006 (2010).

[15] Z. Cui, Y. Han, Q. Xu, Numerical simulation of multiple scattering by random discrete particles illuminated by Gaussian beams, Journal of the Optical Society of America A 28:2200–8 (2011).

[16] Z.-W. Cui, Y.-P. Han, C.-Y. Li, Simulation of electromagnetic scattering by random discrete particles using a hybrid FE-BI-CBFM technique, Waves in Random and Complex Media 22:234–48 (2012).

[17] Z. Cui, Y. Han, X. Ai, Multiple scattering of arbitrarily incident Bessel beams by random discrete particles, Journal of the Optical Society of America A 30:2320–7 (2013).

[18] M.I. Mishchenko, Coherent backscattering by two-sphere clusters, Optics Letters 21:623–5 (1996).

[19] M.I. Mishchenko, L. Liu, Weak localization of electromagnetic waves by densely packed many-particle groups: exact 3D results, Journal of Quantitative Spectroscopy & Radiative Transfer 106:616–21 (2007).

[20] M.I. Mishchenko, L. Liu, D.W. Mackowski, B Cairns, G. Videen, Multiple scattering by random particulate media: exact 3D results, Optics Express 15:2822–36 (2007).

[21] M.I. Mishchenko, L. Liu, G. Videen, Conditions of applicability of the single-scattering approximation, Optics Express 15:7522–7 (2007).

[22] M.I. Mishchenko, L. Liu, J.W. Hovenier, Effects of absorption on multiple scattering by random particulate media: exact results, Optics Express 15:13182–7 (2007).

[23] K.K. Tse, L. Tsang, C.H. Chan, K.H. Ding, Multiple scattering of waves by random distribution of particles for applications in light scattering by metal nanoparticles. In A.A. Maradudin, editor, *Light Scattering and Nanoscale Surface Roughness*, p. 341–70 (Springer, New York, 2007).

[24] T.E. Doyle, D.A. Robinson, S.B. Jones, K.H. Warnick, B.L. Carruth, Modeling the permittivity of two-phase media containing monodisperse spheres: effects of microstructure and multiple scattering, Physical Review B 76:054203 (2007).

[25] M.I. Mishchenko, Multiple scattering, radiative transfer, and weak localization in discrete random media: unified microphysical approach, Reviews of Geophysics 46:RG2003 (2008).

[26] Y. Okada, A.A. Kokhanovsky, Light scattering and absorption by densely packed groups of spherical particles, Journal of Quantitative Spectroscopy & Radiative Transfer 110:902–17 (2009).

[27] M.I. Mishchenko, L. Liu, Electromagnetic scattering by densely packed particulate ice at radar wavelengths: exact theoretical results and remote-sensing implications, Applied Optics 48:2421–6 (2009).

[28] F. Voit, J. Schäfer, A. Kienle, Light scattering by multiple spheres: comparison between Maxwell theory and radiative-transfer-theory calculations, Optics Letters 34:2593–5 (2009).

[29] M.I. Mishchenko, J.M. Dlugach, L. Liu, V.K. Rosenbush, N.N. Kiselev, Yu.G. Shkuratov, Direct solutions of the Maxwell equations explain opposition phenomena observed for high albedo solar system objects, Astrophysical Journal 705:L118–22 (2009).

[30] J.C. Auger, V.A. Martinez, B. Stout, Theoretical study of the scattering efficiency of rutile titanium dioxide pigments as a function of their spatial dispersion, Journal of Coatings Technology and Research

6:89–97 (2009).

[31] M.I. Mishchenko, J.M. Dlugach, L. Liu, Azimuthal asymmetry of the coherent backscattering cone: theoretical results, Physical Review A 80:053824 (2009).

[32] T.E. Doyle, A.T. Tew, R. Jain, D.A. Robinson, Effects of aggregation on the permittivity of random media containing monodisperse spheres, Journal of Applied Physics 106:114104 (2009).

[33] F. Voit, J. Schäfer, A. Kienle, Light scattering by multiple spheres: solutions of Maxwell theory compared to radiative transfer theory, Proceedings of SPIE 7371:73711G (2009).

[34] D.W. Mackowski, M.I. Mishchenko, Direct simulation of multiple scattering by discrete random media illuminated by Gaussian beams, Physical Review A 83:013804 (2011).

[35] M.I. Mishchenko, D.W. Mackowski, Coherent backscattering in the cross-polarized channel, Physical Review A 83:013829 (2011).

[36] M.I. Mishchenko, V.P. Tishkovets, L.D. Travis, B. Cairns, J.M. Dlugach, L. Liu, V.K. Rosenbush, N.N. Kiselev, Electromagnetic scattering by a morphologically complex object: fundamental concepts and common misconceptions. Journal of Quantitative Spectroscopy & Radiative Transfer 112:671–92 (1011).

[37] A. Penttilä, K. Lumme, Optimal cubature on the sphere and other orientation averaging schemes, Journal of Quantitative Spectroscopy & Radiative Transfer 112:1741–6 (2011).

[38] J.M. Dlugach, M.I. Mishchenko, L. Liu, D.W. Mackowski, Numerically exact computer simulations of light scattering by densely packed, random particulate media. Journal of Quantitative Spectroscopy & Radiative Transfer 112:2068–78 (2011).

[39] L. Kolokolova, L. Liu, B. Buratti, M.I. Mishchenko, Modeling variations in near-infrared caused by the coherent backscattering effect. Journal of Quantitative Spectroscopy & Radiative Transfer 112:2175–81 (2011).

[40] D.W. Mackowski, M.I. Mishchenko, A multiple sphere *T*-matrix Fortran code for use on parallel computer clusters, Journal of Quantitative Spectroscopy & Radiative Transfer 112:2182–92 (2011).

[41] M.I. Mishchenko, J.M. Dlugach, D.W. Mackowski, Coherent backscattering by polydisperse discrete random media: exact T-matrix results, Optics Letters 36:4350–2 (2011).

[42] K. Muinonen, M.I. Mishchenko, J.M. Dlugach, E. Zubko, A. Penttilä, G. Videen, Coherent backscattering verified numerically for a finite volume of spherical particles, Astrophysical Journal 760:118 (2012).

[43] J.-C. Auger, B. Stout, Dependent light scattering in white paint films: clarification and application of the theoretical concepts, Journal of Coatings Technology and Research 9:287–95 (2012).

[44] F. Voit, A. Hohmann, J. Schäfer, A. Kienle, Multiple scattering of polarized light: comparison of Maxwell theory and radiative transfer theory, Journal of Biomedical Optics 17:045003 (2012).

[45] A. Hohmann, F. Voit, J. Schäfer, A. Kienle, Comparison of Monte Carlo simulations with exact Maxwell solutions for polarized light scattering by multiple absorbing spheres, Journal of Physics: Conference Series 369:012007 (2012).

[46] D.W. Mackowski, M.I. Mishchenko, Direct simulation of extinction in a slab of spherical particles, Journal of Quantitative Spectroscopy & Radiative Transfer 123:103–12 (2013).

[47] V.P. Tishkovets, E.V. Petrova, Coherent backscattering by discrete random media composed of clusters of spherical particles, Journal of Quantitative Spectroscopy & Radiative Transfer 127:192–206 (2013).

[48] A. Penttilä, Quasi-specular reflection from particulate media, Journal of Quantitative Spectroscopy & Radiative Transfer 131:130–7 (2013).

[49] Zh.M. Dlugach, M.I. Mishchenko, Coherent backscattering and opposition effects observed in some atmosphereless bodies of the Solar system, Solar System Research 47:454–62 (2013).

[50] C. Ejeta, K. Muinonen, H. Boehnhardt, S. Bagnulo, L. Kolokolova, D. Guirado, G.P. Tozzi. Polarization of Saturn's moon Iapetus. III. Models of the bright and the dark sides. Astronomy & Astrophysics 554:A117 (2013).

[51] A. Hohmann, F. Voit, J. Schäfer, A. Kienle, Multiple scattering of polarized light: influence of absorption, Physics in Medicine and Biology 59:2583–97 (2014).

[52] A. Virkki, K. Muinonen, A. Penttilä. Inferring asteroid surface properties from radar albedos and circular-polarization ratios, Meteoritics and Planetary Science 49:86–94 (2014).

[53] L. Roux, P. Mareschal, N. Vukadinovic, J.-B. Thibaud, J.-J. Greffet, Scattering by a slab containing randomly located cylinders: comparison between radiative transfer and electromagnetic simulation, Journal of the Optical Society of America A 18:374–84 (2001).

[54] J.-J. Greffet, J.-B. Thibaud, L. Roux, P. Mareschal, N. Vukadinovic, Scattering by a thin slab: comparison between radiative transfer and electromagnetic simulation. In *Waves and Imaging through Complex Media*, p. 299–305 (Springer, Dordrecht, 2001).

[55] S.H. Tseng, J.H. Greene, A. Taflove, D. Maitland, V. Backman, J.T. Walsh Jr., Exact solution of Maxwell's equations for optical interactions with a macroscopic random medium, Optics Letters 29:1393–5 (2004).

[56] S.H. Tseng, Y.L. Kim, A. Taflove, D. Maitland, V. Backman, J.T. Walsh Jr., Simulation of enhanced backscattering of light by numerically solving Maxwell's equations without heuristic approximations, Optics Express 13:3666–72 (2005).

[57] S.-C. Lee, Wave propagation through a dielectric layer containing densely packed fibers, Journal of Quantitative Spectroscopy & Radiative Transfer 112:143–50 (2011).

Numerical techniques for shaped beam scattering by large and absorbing particle using variable separation methods

Kuan Fang REN

UMR 6614/CORIA, CNRS - Université et INSA de Rouen, Rouen, 76801, France

*Corresponding author: fang.ren@coria.fr

Abstract

Shaped beam scattering and numerical computations are two very active domains of research in light interaction with particles. The shaped beams may invoke special effects when interacting with particles which are essence of many applications. The variable separation methods, typically the Generalized Lorenz-Mie theory, solve the problem rigorously, but the numerical evaluation of relevant physical quantities is always a challenge for practical applications. To deal with these difficulties it is often necessary to combine physical understandings, mathematical skills and algorithmic faculties. Sophisticated techniques will be presented to solve numerical problems arising in the calculation of the scattering and absorption properties, the internal and near fields, the radiation pressure and torque exerted on very large and strong absorbing particles illuminated by circular and elliptical Gaussian beams, Bessel and Doughnut beams. Software integrating these experiences on the prediction of all the physical quantities of any shaped beam by a homogeneous or stratified sphere will be presented.

1 Introduction

Numerical computation occupies today a crucial place in the scientific research and its role is even primordial for many theoretical researches and their applications. It permits, and it is often the only means, to reveal physical laws and to discover new phenomena of the nature based on the developed theories. The applications of new theories depend also much on our capacity to realize the reliable "computation" in a reasonable time.

In the point view of scientific research, especially in the field we are concerned, the numerical computations may be classified into two categories: a). discretising the equations, i.e. Maxwell equations, governing the physical phenomena and solving the problem numerically, such as the T-matrix, the discrete dipole approximation (DDA), the finite element method (FEM), the finite-difference time-domain method (FDTD), the method of moment (MoM); b). resolving the equations to obtain "analytical expressions" and then calculating the physical quantities numerically, such as the variable separation method in the light scattering. The first is usually more flexible but needs great computer resource. The latter is often considered to be rigorous and easier, but the reality is not always the case. Furthermore, the complexity of the problem, i.e. the particle shape, inhomogeneity, etc., are also limited due to the availability of mathematical tools. The numerical techniques attract much attention in the first category but less for the second. However, the numerical problem in the second category is neither much easier, nor less important. It is true that the boom in the computer technology in the last centuries provides formidable facility for scientific research, but the development of stable and reliable algorithms remains still a challenge in the field of the light interaction with particles and its applications.

The simplest case in this field is the scattering of the plane wave by a homogeneous sphere. Theory has been established more than a century [1,2] but the first practical algorithm is known [3-5] in 1980's. The physical mysteries behind this simplest model are extremely rich and attract the attention of a great number of researchers [6-8]. The scattering of the plane wave by a circular infinite cylinder is similar [9]. These are the two only cases we can calculate for a particle almost as large as we want and they are served as reference to valid the results of theoretical/numerical results for other theories or for other particles. Nevertheless, all the "numerical" problems are not resolved for the simplest particles [10]. When the particle is neither spherical nor circular infinite cylindrical, an analytical solution is possible if its shape corresponds to a mathematical coordinate system, but the numerical problem is often difficulty.

The invention of the laser provides a revolutionary development in the optics, certainly also for the light scattering by small particles and its applications to the optical metrology in the fluid mechanics [11,12], the environmental control [13] as well as in the optical manipulation of micro- and nanoparticle in life science and in material research (see [14-16] and references therein). At the same time, it provides a means to reveal particular phenomena which cannot be observed when a particle is illuminated homogeneously (plane wave). To describe the scattering of a laser beam or other inhomogeneous wave (e.g. evanescent wave) by a particle the shape of the beam are described by the beam shape coefficients (BSC). The most successful theory lies in the framework of the classical Lorenz-Mie theory, so called Generalized Lorenz-Mie Theories (GLMT). Many authors have contributed in different manners to these theories. A general description of these theories will be given with emphasis on the

numerical techniques in the evaluation of the beam shape coefficients.

The rest of the paper will be organized in four sections. The theoretical framework of the variable separation method will be first described in Section 2. Sections 3 and 4 are devoted respectively to the numerical techniques for the evaluation of the scattering coefficients and the beam shape coefficients. The special problems encountered in the calculation of the physical quantities by combining the above mentioned two kinds of coefficients will dealt with in Section 5.

2 Theoretical framework of variable separation method

The variable separation method is based on the fact that the wave functions of three variables $\psi(x_1, x_2, x_3)$ can be, in general, expressed as a product of the functions of one variable $X_1(x_1)$, $X_2(x_2)$ and $X_3(x_3)$, where x_1, x_2 and x_3 are the spatial coordinates. Each of the three functions satisfies a differential equation and they are related by two indices (n, m), discrete or continuous. The incident wave, the scattered waves as well as the waves in the particle are expanded in the eigen functions of $X_i(x_i)$. The expansion coefficients depend therefore on the properties of the particle and the shape of the incident beam. In general case, the coefficients depending on the particle's properties, called hereafter as scattering coefficients, are independent of the beam parameters, and in the counterpart, the beam shape coefficients should not contain any particle's properties. The fundamentals of the theories can be found in the monographs [17-20].

3 Scattering coefficients

The scattering coefficients are function of the particle properties, such as the size, the refractive index and the morphology parameters (e.g. aspect ratio for spheroidal, ellipsoidal sphere, or elliptical cylinder).

For a spherical particle (homogeneous or stratified), we need two series of coefficients a_n and b_n for the external field and two series coefficients c_n and d_n for the internal field [14,15]. Here, only one expansion index n is necessary because of the symmetry of the problem, and it extends theoretical from 0 to infinity. In practice, for the calculation of the scattering diagram or integral quantities such as the cross sections, the radiation pressure and torque, the summation on n is truncated to

$$n_{stop} = x + 4.05x^{1/3} + 2 \qquad (1)$$

where $x = 2\pi a / \lambda$ is the particle size parameter with a the particle radius and λ the wavelength. This criterion has been proposed by Wiscombe [4] and largely used in the Mie calculation [15]. It is in fact because the spherical Bessel function involved in the scattering coefficients decreases rapidly to less than 10^{-8} when n exceeds n_{stop}. If more precision (e.g. double or quadruple precision for example) is needed more terms should be taken in the calculation.

The scattering coefficients of a homogeneous sphere are expressed simply as function of Riccati-Bessel functions and we can calculate for very large and absorbing particles. Nevertheless, if we want to isolate different mode by using the Debye theory, the problem becomes more delicate since both the first and the second Hankel functions are involved [10].

The scattering coefficients of a stratified sphere are formulated in determinant by Kerker [17] and those for a coated sphere are coded by Bohren [19]. But to simulate a temperature/refractive index gradient, many layers are needed; the algorithm in matrix form [17] is limited in number of layers N_l and size. Li et al have proposed to calculate the coefficients by the ratios of the Bessel function between successive layers [21], the performance was still not sufficient to reply the real demand. Wu et al [22] then proposed to calculate the logarithmic derivatives of the Bessel function. This algorithm is proved to be very stable. With some improvement [23], we can calculate for a very large particle of many layers, $x \cdot N_l > 10^8$ on a personal computer. And this number is limited only by the computer resources. However, the attention must be paid to the fact that if eq. (1) is applied, the results may be erroneous. The summation number should calculated according to the product of the refractive index and the size parameters of all layers by

$$n_{stop} = \max(|m_j x_j| + 4.05|m_j x_j|^{1/3}) + 16 \qquad (2)$$

Furthermore, some astuteness is also necessary to avoid the numerical problem when two successive layers have the (quasi)equal refractive index [24]. This algorithm has also been applied to the scattering of shaped beam [25]

The scattering of the plane wave by an infinite circular cylinder is similar to a spherical particle. But four series of coefficients are necessary for the external field and four series of coefficients for the internal field because of the cross polarization in the case of oblique incidence [19]. The numerical techniques are similar to the spherical particle. Here another numerical problem may occur when the incident angle tends to zero; this is inevitable case for the scattering of a shaped beam by using the plane wave expansion [26,27] and the asymptotic expression for the Bessel functions are used [28]. The Debye theory for a stratified circular cylinder at oblique incident is much more complicated. Li et al proposed a very intelligent schema [29].

If the particle is neither a sphere nor a circular infinite cylinder, the problem becomes much more complicated. Even though the solution of variable separation method is still possible for particles of simple shape (spheroid, elliptical infinite cylinder, ellipsoid, etc.), the calculable particle size is seriously limited. The scattering of the plane wave or a shaped beam by a homogeneous or stratified, isotropic or anisotropic spheroidal particle are well documented [30-41]. Much effort has also devoted to the numerical calculation, the calculable size parameter can be as big as 650, same order as the capacity of pure numerical methods [42].

The scattering of elliptical infinite cylinder has been extensively studied by Yeh[43], Gouesbet et al [34-46]. But the numerical calculation is still more difficulty for two reasons: the first is due to difficulty in the calculation of the Mathieu functions for large argument which limit the size parameter and the other is the evaluation of the scattered wave in far zone for shaped beam scattering (see section 5).

4 Beam shape coefficients in different coordinate systems

When the spatial variation of the beam on the particle is not negligible, the incident wave can no longer be considered as the plane wave and it is taken into account by the so-called the beam shape coefficients.

In fact, in the variable separation methods, the plane wave is also expanded as partial waves, but the expansion coefficients are only function of the summation indices. For all shaped beam, the BSC depend not only on the geometry of the beam, i.e. the form, the waist radius, the polarization state, the axicon, the mode, etc., but also the position of the beam and the coordinate system in which the BSC are calculated. However they must be independent of the particle properties. The particle size, for example, must not intervene in the BSC calculation. The BSC are usually series of two indices which can be both discrete as in the spherical or ellipsoidal coordinate system, or one discrete and the other continuous as in the case of the infinite cylinder.

4.1 BSC in spherical coodinate system

This is the case the most studied and well developed (see [20, 47] and references therein). It is also the basis for the scattering of shaped beam by a spheroidal particle.

Two series of BSC are necessary to describe an arbitrarily shaped beam in spherical coordinate system. We find different definitions in the literature [48-51] and they are proved equivalent [52]. The definitions in the GLMT noted by $g_{n,TM}^{m}$ and $g_{n,TE}^{m}$ have a clear physical signification and are the most used. They are calculated respectively by the radial components of electric and magnetic fields. Theoretically, they are defined by the double or triple integrations. The double integration form for $g_{n,TM}^{m}$ is given by [20,50,51]

$$g_{n,TM}^{m}=\frac{kri^{n+1}}{4\pi j_n(kr)}\int_0^{2\pi}\int_0^{\pi}\frac{E_r(r,\theta,\phi)}{E_0}P_n^{|m|}(\cos\theta)e^{-im\phi}\sin\theta d\theta d\phi \quad (2)$$

We observe that the coefficients depend explicitely on the coordinate r but it should not. In fact, if the electromagnetic field satisfies strictly the Maxwell equations, the BSC calculated by eq. (2) are independent of r as we can demonstrate theoretically for the plane wave [52]. However, Analytical expressions of shaped beams often do not satisfy strictly the Maxwell equations [53], for example the Gaussian beam [54,55]. Fortunitely, this dependence is weak for well defined beam. It may also be eliminated by the integration on r [51-53]. In the point view of numerical calculation, the precision and the performance of the algorithm for the evaluation of the integration in eq. (2) depend much on the choice of the value r. Ren et al [51,52] have shown that the best choice is $kr=n+1/2$ because the oscillation of the integral kernal as function of θ is the weakest so the integration covegres the most rapidely[52].

It is worth to note that for any given BSC, the reconstructed field satisfies perfactly the Maxwell equation and any means to calculate the BSC are just to find the BSC which are the most faithful to the given analytical field expression. Four methods have been developed for the evaluation of the BSC in the spherical coordinate system: i). integration, ii). Localized Approximation, iii). Finite series iv). Standard beam.

The integration method is issued directely from the definition of the BSC, it is rigorous, flexible and ued as reference to evaluate the other methods but it is the most costly in term of the computer resources and time.

The localized approximation (LA) is not rigorously established but the precision is usually sufficient. Therefore, it is the most used in the practical calculation, especilly for Gaussian beam [38]. It is based on the localization principle [18]: the spherical wave component n corresponds to the ray arriving at a distance $r=(n+1/2)/k$ (k being the wave number) from z axis. The procedure of the LA consists of replacing the coodinate r by $(n+1/2)/k$ and θ by π/2. The BSC are the expansion cofficients of the incident wave as function of $e^{im\phi}$ ajusted with a prefactor Z_n^m [56]. The original version is for circular Gaussian beam in infinite series and has been largely used in the calculation of the scattering of the shaped beam [57]. Ren et al have extended it to the elliptical Gaussian beam [58]. However, when n is large, the series are not numerically stable because of limit of the precision [52]. Doicu et al [59] have demonstrated by the addition theorem that the BSC can be expressed as the cylindrical Bessel function. In fact if we compare the infinite series of the BSC and the definition of the Bessel function [60], it is easy to observe that the two terms in the infinite series of the BSC are just two Bessel function. This can be proved more easily by the localized approximation in integral form given by [61]

$$g_{n,TM}^{m}=\frac{Z_n^m}{2\pi E_0}\int_0^{2\pi}E_r(kr=n+1/2,\theta=\pi/2,\phi)e^{-im\phi}d\phi \quad (3)$$

called therefore as the integral localized approximation (ILA). This combined the advantage of the flexibility of integration method and the rapidity of the localized appximaation. ILA can be applied directly to evaluate the BSC of any collimated beam propagating along z axis. The BSC of the fifth order Gaussian beam are with eleven terms of Bessel function [62]. The BSC of the Bessel beam [8] and the doughnut beam[63] can also be obtained easily.

Theoretically, the index n goes from 0 to infinity and m from $-n$ to $+n$. But in the numerical calculation they are truncted according to both the particle size and the beam parameters.

The finite series [52,64] and the standard beam [20,47] have also developped for different orders of Gaussian beam. However, the finite series becomes very rapidely

unstable for large index n so it is raely used in the beam scattering.

4.2 BSC in other coodinate system

The BSC in spheroidal coordinate can be obtained from the BSC in spherical coodinate system by using the relation between the spheroidal vector wave functions and the spherical vector wave functions [33,37-39].

In the plane wave expansion method, the BSC in cylindrical coordinate system $I_{m,TM}(\gamma)$ and $I_{m,TE}(\gamma)$ are defined respectively by the z components of the electric and magnetic fields in the similar way as the BSC in the spherical coordinates. For example, $I_{m,TM}(\gamma)$ reads as [26]

$$I_{m,TM}(\gamma)=\frac{i^m}{4\pi^2 J_m(R)}\int_0^{2\pi} e^{-im\phi}\int_{-\infty}^{\infty}\frac{E_z(Z,R,\phi)}{E_0}e^{-i\gamma Z}dZd\phi \quad (4)$$

with $Z=kz$ and $R=k\rho(1-\gamma^2)$. But the expansion index γ is continuous which can be understood as the cosine of the incident angle of the plane wave component. So in the expansion of a wave by these coefficients in the framework of GLMT [26], the integration over γ goes from –1 to 1 while Lock extended this integration from -∞ to ∞ [27]. Ren et al have introduced also the localized approximation to evaluate the BSC [26,64,65]. This localized approximation for cylindrical coordinate system has later been applied to the BSC in the elliptical coordinate system for arbitrary shaped beam [44-46].

5 Calculation of physical quantities and general ramarks

In principle, once we possess the scattering coefficients and the BSC we can calculate all the physical quantities, such as the cross scattering section, the radiation pressure forces and torques, the scattering diagram (or scattering matrix), the internal field, and the external field in near or far zone. However, certain caution should be paid to the combination of the coefficients, especially the choice of the limits in the truncation of the summation indices. If they are not sufficient the results are not correct if they are too big, we will encounter the problem of overflow or underflow. This choice depends not only the properties of the particles, the beam shape and its position, but also the physical quantity to be calculated

The integral quantities are often expressed as the summation product of the scattering coefficients and the BSC, the truncation terms are to be examined according to their product. The scattering diagram needs also the angular functions, their variation as function of the summation index is essential for the determination of the number of terms. In the calculation of the internal and near fields, we need to calculate the internal coefficients (e.g. c_n and d_n for spherical particle) and Bessel/Hankel functions with the position as argument. Each term is therefore the product of four factors and it's their combination weight in the summation.

In the case of shaped beam illumination, the scattered field of an infinite cylinder is neither spherical nor cylindrical; there is no asymptotic expression for the scattered wave in far zone. So *stricto sensu* to obtain the scattered wave at a distance ρ for the cylinder, the Bessel functions with arguments $k\rho$ must be calculated [26]. Lock [27] has used a method of stationary phase to evaluate the intensity in far zone and given the physical interpretation of the results, but no numerical results are shown. So this is still an open problem.

To conclude, some general remarks may be made for the numerical calculation light interaction with particle:

1) The results of the special functions are to be checked by comparing with standard tools. Codes found on internet, even in the literature or routines of standard libraries may be incorrect or imprecise, especially in the extreme case (usually for very large or very small argument). It is suggested to compare with the results of Maple or Mathematica at least for some special cases since it standard mathematical tools, the precision of the results is ensured and we can calculate with any precision we want.
2) Before implementation of an algorithm, it is worth to study the properties of the function to be calculated, for example, the kernel of the integration for the calculation of the BSC for a given beam, then to choose adequate parameters and integration procedure.
3) If possible, avoid series form which are often unstable or reformulate the mathematical expressions to improve the convergence of the series.
4) Try to understand the physical significance of the parameters to help its choice. For example, in the point of view of localization, the index n in the spherical BSC stands for a ray at distance $r=(n+1/2)/k$, the summation terms should be increased if the beam is far off axis. The index m stands for the azimuth component and the summation terms must be adjusted according to the symmetry of the problem. It may take only ±1 for the plane wave until 30 or 50 for an off-axis Gaussian bean, or even bigger if the dissymmetry of the problem is important.
5) In case of underflow or overflow, try to store the exponent to a variable and then count it in the final calculation.

Software **ABSphere** with friendly graphical interface has been developed for the calculation of all physical quantities of the scattering of any shaped beam by a spherical particle [67,68]. It is available by request to the author.

6 Acknowledgement

This work has been also partially supported by substantial computation facilities from CRIHAN (Centre de Ressources Informatiques de Haute-Normandie) and the French National Research Agency (ANR) grant ANR-13-BS09-0008-01.

7 References

[1] L. Lorenz, Lysbevaege i og uder en plane lysbolger belyst kulge, Vidensk. Selk. Skr. 6, 1-62 (1890).

[2] G. Mie, Beiträge zur Optik Truber Medien, speziell Kolloidaler Metalösungen, Ann. Phys. 25, 377-452 (1908).

[3] W. J. Lentz, "Generating Bessel functions in Mie scattering calculations using continued fractions," Appl. Opt. 15, 668-671 (1976).

[4] W. J. Wiscombe, Improved Mie scattering algorithms, Appl. Opt. 19, 1505-1509 (1980)

[5] A. R. Jones, Calculations of the ratio of complex Ricatti-Bessel functions for Mie scattering, J. Phys. D 16, 149-152 (1983)

[6] E. A. Hovenac and J. A. Lock, Assessing the contributions of surface waves and complex rays to far-field scattering by use of the Debye series, J. Opt. Soc. Am. A 9, 781–795 (1992)

[7] H. M. Nussenzveig, Diffraction Effects in Semiclassical Scattering, Cambridge University Press (2006)

[8] R. Li, X. Han, K. F. Ren, Z. Wu, L. Guo, S. Gong, "Analysis of radiation pressure force exerted on a biological cell induced by high-order Bessel beams using Debye series", J. Quant. Spectrosc. Radiat. Transfer 126:69-77, 2013

[9] R. Li, X. Han and K. F. Ren, "Generalized Debye series expansion of electromagnetic plane wave scattering by an infinite multilayered cylinder at oblique incidence, Phys. Rev. E 79, 036602 (2009)

[10] J. Shen and H. Wang, "Calculation of Debye series expansion of light scattering," Appl. Opt. 49, 2422-2428 (2010).

[11] F. Onofri, S. Barbosa, Chapter 1: Basics on light scattering properties of small particles, in *Laser Metrology in Fluid Mechanics*, A. Boutier (ed.), Wiley-ISTE, London (2012)

[12] F. Onofri, S. Barbosa, Chapter 2: Optical particle characterization, in *Laser Metrology in Fluid Mechanics*, A. Boutier (ed.), Wiley-ISTE, London (2012)

[13] Mishchenko, M. I., L. D. Travis, and A. A. Lacis (2002): Scattering, Absorption, and Emission of Light by Small Particles, Cambridge University Press, Cambridge.

[14] B. Mihiretie, P. Snabre, J. C. Loudet and B. Pouligny, Radiation pressure makes ellipsoidal particles tumble, *Europhys. Lett.*, 100 48005 (2012)

[15] B. Mihiretie, J. C. Loudet and B. Pouligny, Optical levitation and long-working distance trapping: from spheres up to large aspect ratio ellipsoids, *J. Quant. Spectrosc. Radiat. Transfer*, 126, 61-68 (2013)

[16] P. Tuersun, X Han, Optical absorption analysis and optimization of gold nanoshells, *Appl. Opt.* 52:1325-1329 (2013)

[17] M. Kerker, The Scattering of Light and Other Electromagnetic Radiation (Academic New York, 1969).

[18] H. C. van de Hulst, Light Scattering by Small Particles (Wiley, New York, 1957).

[19] C. F. Bohren, and D.R. Huffman, Absorption and scattering of light by small particles (Wiley, New-York, 1983).

[20] G. Gouesbet and G. Gréhan, Generalized Lorenz-Mie Theories, (Springer, 2011)

[21] L. Kai and P. Massoli, Scattering of electromagnetic plane waves by radially inhomogeneous spheres: a finely stratified sphere model, Appl. Opt. 33, 501–511 (1994)

[22] Z. S. Wu and Y. P. Wang, Electromagnetic scattering for multilayered sphere: recursive algorithms, *Radio Sci.* 26, 1393–1401 (1991)

[23] Z. S. Wu, L. X. Guo, K. F. Ren, G. Gouesbet and G. Grehan, "Improved algorithm for electromagnetic scattering of plane waves and shaped beams by multilayered spheres, Appl. Opt., 36(21), 5188-5198 (1997)

[24] K. F. Ren, Light Scattering from a Stratified particle, internal report, CORIA – URA 230 CNRS - Rouen University, 2004

[25] Onofri F., Gréhan G. and Gouesbet G., Electromagnetic scattering from a multilayered sphere located in an arbitrary beam, *Applied Optics*, 34(30):7113-7124 (1995)

[26] K. F. Ren, G. Gréhan, and G. Gouesbet, Scattering of a Gaussian beam by an infinite cylinder in GLMT-framework, formulation and numerical results, *J. Opt. Soc. Am. A* 14, 3014–3025 (1997)

[27] J. Lock, Scattering of a diagonally incident focused Gaussian beam by an infinitely long homogeneous circular cylinder, J. Opt. Soc. Am. A 14(3):640-652 (1997)

[28] K. F. Ren, Scattering of an arbitrary beam by an infinite cylinder: off-axis case, Internal report, CORIA/UMR 6614 CNRS - Université & INSA de Rouen, (2002)

[29] R. Li, X. Han and K. F. Ren, "Generalized Debye series expansion of electromagnetic plane wave scattering by an infinite multilayered cylinder at oblique incidence, *Phys. Rev. E* 79, 036602 (2009)

[30] S. Asano and G. Yamamoto, Light scattering by a spheroidal particle, *Appl. Opt.* 14:29–49 (1975).

[31] J. P. Barton, "Internal and near-surface electromagnetic fields for a spheroidal particle with arbitrary illumination," Appl. Opt. 34 , 5542–5551 (1995).

[32] J. P. Barton, Internal, near-surface, and scattered electromagnetic fields for a layered spheroid with arbitrary illumination, Appl. Opt. 40, 3596–3607 (2001).

[33] Y. Han and Z. Wu. Scattering of a spheroidal particle illuminated by a Gaussian beam. *Appl. Opt.*, 40(15):2501-2509, (2001).

[34] Y. Han, Loic Méès, and K. Ren, Scattering of light by spheroids: the far field case. *Opt. Commun.* 210:1-9 (2002).

[35] Y. Han and Z. Wu. Absorption and scattering by an oblate particle. *J. Opt. A: Pure Appl. Opt.*, 4:74-77 (2002).

[36] Y. Han, L. Mees, K. F. Ren, G. Grehan, S. Wu and G. Gouesbet, "Far Scattered field from a spheroid under a femtosecond pulsed illumination in a generalized Lorenz-Mie theory framework, *Opt. Commun*. 231:71-77 (2004)

[37] F. Xu, K. F. Ren, X. Cai, Expansion of arbitrarily oriented, located and shaped beam in spheroidal coordinates, *J. Opt. Soc. Am. A*. 24(1):109-118 (2007)

[38] F. Xu, K. F. Ren, G. Gouesbet and G. Grehan and X. Cai, Generalized Lorenz-Mie theory for arbitrarily oriented, located and shaped beam scattering by a homogeneous spheroid', *J. Opt. Soc. Am. A* 24 (1), 119-131 (2007)

[39] F. Xu, K. F. Ren, G. Gouesbet, X. Cai and G. Grehan, Theoretical prediction of radiation pressure force exerted on a spheroid by an arbitrarily shaped beam, *Phys Rev. E*, 75, 026613 (2007)

[40] Z. Li, Z. Wu, Q. Shang, L. Bai, and C. Cao, Calculation of radiation force and torque exerted on a uniaxial anisotropic sphere by an incident Gaussian beam with arbitrary propagation and polarization directions, *Opt. Exp.*, 20, 16421-16435 (2012)

[41] Zhen-sen Wu, Zheng-jun Li, Qiong-kun Yuan, and Hai-Ying Li, Off-axis Gaussian Beam Scattering by an Anisotropic Coated Sphere, *IEEE Transact. Anten. & Propag.*, 59(12), 4740-4748, (2011)

[42] M. Yang, K. F. Ren, Y Wu and X. Sheng, Computation of stress on the surface of a soft homogeneous arbitrarily shaped particle, *Phys. Rev. E* 89, 043310, 2014

[43] C. Yeh: Backscattering cross section of a dielectric elliptical cylinder. *J. Opt. Soc Am. A.*, 55: 309±314 (1965)

[44] G. Gouesbet, L. Méès, G. Gréhan, K. F. Ren. Description of arbitrary shaped beams in elliptical cylinder coordinates, by using a plan e wave spectrum approach. *Opt. Commun.* 161:63-78 (1999)

[45] G. Gouesbet, L. Mees, G. Gréhan, and K. F. Ren, Description of arbitrary beams in elliptical cylinder coordinates, by using a plane wave spectrum approach, *Opt. Commun.* 161, 63–78 (1999).

[46] G. Gouesbet, L. Mees, G. Grehan, and K. F. Ren, Localized approximation for Gaussian beams in elliptical cylinder coordinates, *Appl. Opt.*, 39(6):1008-1025 (2000).

[47] Gouesbet G., J. A. Lock and Grehan G., Generalized Lorenz–Mie theories and description of electromagnetic arbitrary shaped beams: Localized approximations and localized beam models, a review, *J. Quantit. Spectros. Radiat.Transfer*, 112(1):1-27 (2011)

[48] J. P. Barton. Electromagnetic-field calculations for a sphere illuminated by a higher-order Gaussian beam. I. Internal and near-field effects. Appl. Opt. 36(6):1303-1311 (1997)

[49] B. Maheu, G. Grehan, G. Gouesbet, Generalized Lorenz-Mie theory: first exact values and comparisons with the localized approximation, Appl. Opt. 26, 23-25 (1987).

[50] G. Gouesbet, B. Maheu, and G. Gréhan, Light scattering from a sphere arbitrarily located in a Gaussian beam, using a Bromwich formulation, *J. Opt. Soc. Am. A* 5, 1427–1443 (1988).

[51] G. Gouesbet, C. Letellier, K. F. Ren, and G. Gréhan, Discussion of two quadrature methods of evaluating beam shape coefficients in generalized Lorenz–Mie theory, *Appl. Opt*. 35, 1537–1542 (1996)

[52] K. F. Ren, Diffusion des Faisceaux Feuille Laser par une Particule Sphérique et Applications aux Ecoulements Diphasiques, PhD thesis, Rouen University, (1995)

[53] K. F. Ren, G. Grehan and G. Gouesbet, "Electromagnetic field expression of laser sheet and its order of approximation, J. Opt. (Paris), 25(4), pp. 165-176, 1994

[54] L. W. Davis, Theory of electromagnetic beams, *Phys. Rev. A* 19, 1177-1179 (1979).

[55] J. P. Barton and D. R. Alexander, Fifth-order corrected electromagnetic field components for fundamental Gaussian beam, *J. Appl. Phys.* 66, 2800–2802 (1989).

[56] G. Gouesbet, G. Gréhan, and B. Maheu, A localized interpretation to compute all the coefficients gnm in the generalized Lorenz–Mie theory, J. Opt. Soc. Am. A 7, 998–1007 (1990)

[57] K. F. Ren, G. Gréhan, and G. Gouesbet, Localized approximation of generalized Lorenz–Mie theory. Faster algorithm for computations of the beam shape coefficients, Part. Part. Syst. Charact. 9, 144–150 (1992).

[58] K. F. Ren, G. Gréhan, and G. Gouesbet, Evaluation of laser sheet beam shape coefficients in generalized Lorenz–Mie theory by using a localized approximation, J. Opt. Soc. Am. A 11, 2072–2079 (1994).

[59] A. Doicu, T. Wriedt, Computation of the beam-shape coefficients in the generalized Lorenz-Mie theory by using the translational addition theorem for spherical vector wave functions, *Appl. Opt. 36,2971-2978 (1997)*

[60] M. Abramowitz and I. A. Stegun, Handbook of Mathematical Functions (Dover, New York, 1972),

[61] K. F. Ren, G. Gouesbet, and G. Gréhan, The integral localized approximation in generalized Lorenz–Mie theory, Appl. Opt. 37, 4218–4225 (1998).

[62] K. F. Ren, X. Han and R. Li, Computation of beam shape coefficients of fifth order Gaussian beam, 8th Int. Congr. Opt. Part. Charact., Graz, Austria, July 9-13 (2007)

[63] K. F. Ren, Pression de radiation et couple exercées sur une sphère par un faisceau type doughnut, Internal report, Rouen University (2010)

[64] G. Gouesbet, G. Gréhan, and B. Maheu, Expressions to compute the coefficients gnm in the generalized Lorenz–Mie theory using finite series, *J. Opt.* (Paris) 19, 35–48 (1988)

[65] L. Méès, K. F. Ren, G. Gréhan and G. Gouesbet. Scattering of a Gaussian beam by an infinite cylinder, with arbitrary location and arbitrary orientation, numerical results. *Appl. Opt.* 38, No 9 (1999)

[66] G. Gouesbet, K. F. Ren, L. Mees, and G. Gréhan, The cylindrical localized approximation, to speed up computations for Gaussian beams in the GLMT for cylinders, with arbitrary location and orientation of the scatterer, *Appl. Opt.* 38, 2647–2665 (1999).

[67] K. F. Ren, ABSphere – Software for calculation of all physical properties of any shaped beam by a spherical particle, LIP2014, Marseille, France (2014)

[68] K. F. Ren, ABSphere - Calcul scientifique d'interaction faisceau laser de forme quelconque avec une particule sphérique, vers. 1.0 du 25 sept. 2012, référencé le 24 mars 2014 sous n°IDDN.FR.001.130022.000.R.P.2014.000.30000

From Optical Tweezers To Optically Self-arranged and Propelled Microstructures

Oto BRZOBOHATÝ, Lukáš CHVÁTAL, Martin ŠILER, Petr JÁKL, Alejandro ARZOLA, Pavel ZEMÁNEK*

Institute of Scientific Instruments of the ASCR, v.v.i., Brno, 612 64, Czech Republic

*Corresponding author: zemanek@isibrno.cz

Abstract

It is now well-known that illumination of a colloidal suspension by laser beams leads to a force interaction between light and objects. Such objects can be locally trapped in a single beam trap, in an array of single beam traps or they can be rotated, delivered, sorted or self-arranged in more complex spatial distribution of electromagnetic field. Several selected topics will be discussed from the point of theoretical predictions based on Generalized Lorenz-Mie theories and experimental observations. Attention will be paid to angular momentum transfer from light to particles, pulling and pushing forces in "tractor" beam trap geometry, and various forms of self-arrangements of microparticles into so-called optically-bound matter.

1 Introduction

Scattering of light by particles leads to transfer of momentum and angular momentum of light to particles and occurrence of so-called optical force and torque. The basic theoretical background has been established in 19th and 20th century by Ludvig Lorenz, Gustav Mie and Peter Debye. Their approaches assuming a single spherical particle illuminated by a plane wave were rapidly developed to descriptions considering many interacting (and even non-spherical particles) illuminated by light fields with very complex spatial amplitude and phase distribution. Modern computers and algorithms provide fast and reliable prediction for majority of experiments performed in the domain of optical manipulation with particles. With the accessibility of powerful enough lasers within the last 20 years the pioneering experiments of Arthur Ashkin [1] have been repeated many times and put to another level of complexity, experiment control and data acquisition. Therefore, the domain of optical micromanipulation should be ready for precise comparison of theoretical predictions with quantitative experimental measurements and to verify the applied approaches.

2 Optical vortex beams

It is now also well-known that light carries except momentum also angular momentum. Circularly or elliptically polarized beams carry spin angular momentum that is transferred to absorbing or birefringent object causing its rotation around its axis [2]. Orbital angular momentum is a property of optical vortex beams having a spiral wavefront [3] and induces particle orbiting around the vortex beam axis. Figure 1 shows the experimental arrangement for detection of particle motion in an optical vortex beam. Since we used spatial light modulator, the properties of the beam can be changed dynamically in a contactless way. We performed experiments with Laguerre-Gaussian and Bessel beams with various topological charges m, beam waists w_0 or beam radii ρ.

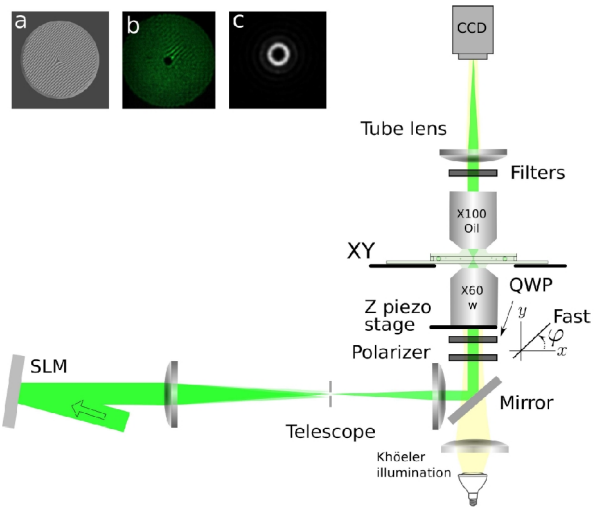


Figure 1 *An example of the geometry of the experiment where the single focused Laguerre-Gaussian vortex beam (a-phase mask, b-real beam) was used to propel the particle in the high intensity vortex ring (c) in the focal plane. Spatial light modulator was used to modify the beam topological charge and beam waist. Similar set-up was also used for experiments with Bessel beam.*

Figure 2 demonstrates the comparison of the measured radius of the particle trajectory in the Bessel vortex beam for different beam parameters. It is seen that in this case the coincidence between the theory and experiment is persuading but not perfect. In the subsequent series of experiments we improved the stability of the system and beam properties to obtain coincidence in the particle position better than 10 nm without any parameter fitting.

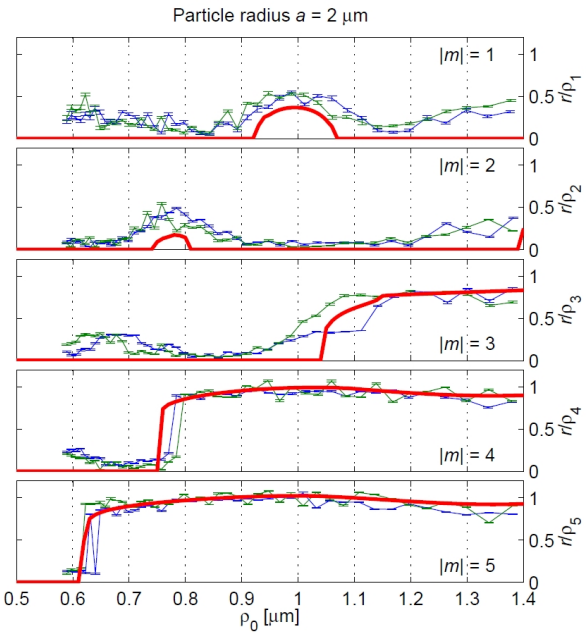


Figure 2 *Measured stable radial position r of the particle in the Bessel vortex beam relative to the radius of the innermost vortex ring ρ_m corresponding to different initial zero-order (m=0) Bessel beam core radius ρ_0. Blue (positive topological charge m>0) and green (negative topological charge m<0) points correspond to the measured data, the error-bars indicate 95 % confidence level of the average. The red curves denote the theoretical prediction for measured beam parameters. The beams were generated by the setup described in Fig. 1. [4]*

3 Optical binding

Optical binding presents an original method for self-arrangement of solid microparticles in liquid or air [5] by pure illumination with a laser beam. The resulting equilibrium positions of the particles in an optically bound structure are not only influenced by the spatial intensity profiles of the incident laser beams but also by the light scattered from all the bound particles [6]. In contrast to widely spread multiple optical trapping based on computer generated holograms or deflections of a trapping laser beam, individual particles in the optically bound structure cannot be positioned as one wishes. However, the inter-particle distances in optically bound structures can be externally controlled by changing the refractive index of the medium or the spatial intensity distribution of the caging laser beams. Figure 3 shows tunable optically-bound structures self-arranged in two counter-propagating elliptical Guassian beams (light-sheets). Beams properties were changed using a spatial light modulator [7,8] dynamically. As the beams widths increased, the optically bound structure enlarged but kept its initial shape. After several cycles of the field modifications various spatial configuration of optically bound structures can be observed in the rows of Fig. 3.

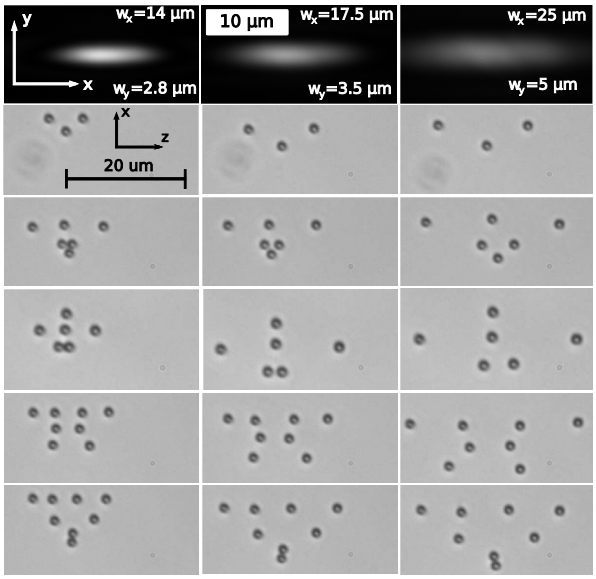


Figure 3 *Size control of two-dimensional optically bound structure. The first row shows the beam waist profiles of three different pairs of counter-propagating elliptical Gaussian beams. The following rows show dynamic size tuning of the structure with various initial configurations of particles (1070 nm in diameter) self-arranged in the above depicted beams. The total power of a single beam at the sample plane varied between 80 mW and 35 mW for the narrowest and widest beam, respectively.*

4 "Tractor" beam

Another experimental method used the geometry of the optical "tractor" beam [9]. The incident beam of diameter tens of micrometers is retro-reflected at the bottom mirror and creates a system of interference fringes parallel to the mirror surface (pancake traps). Particles are locked to the fringes in vertical direction but tent to self-arrange optically in horizontal direction. Due to different scattering patterns the particles of different sizes or even the whole self-arranged structures can be pulled against the direction of final wavevector if the polarization of the incident beam is changed from p to s. Figure 4 presents the geometry of the experiment and indicates that particles of different sizes can be propelled in opposite direction if the beam polarization is switched. Figure 5 presents the theoretical calculations for plane wave showing the optimal angles giving maximal pulling force for s and p polarizations. Figure 6 demonstrates the record of the particle motion if the polarization is switched from p to s. Consequently the force changes its sigh from positive pushing force to negative pulling force and this was utilized for passive optical sorting of tens of particles at the same time. Figure 7 illustrates this behaviour using particles of radii 400 nm and 500 nm. When the polarization of the incident beam was switched from p to s, the larger particles moved to the left due to the pulling force because the experimental parameters were selected according to Fig. 5.

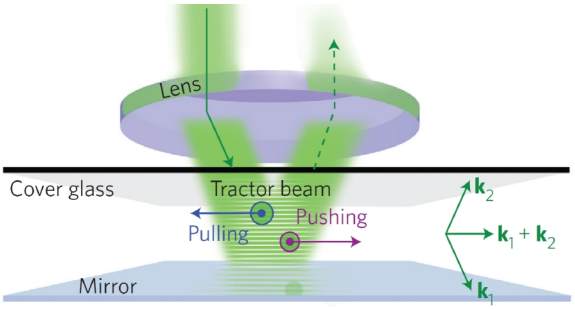


Figure 4 *Geometry of the experiment. Larger particle scatter light differently than a smaller particle and thus moves in opposite direction.*

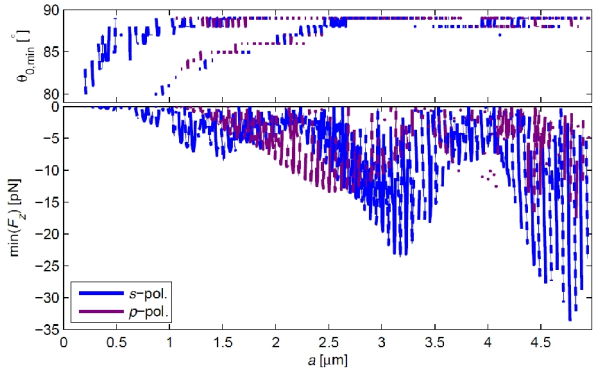


Figure 5 *Incident angles $\theta_{0,min}$ giving minimal force F_z (i.e. maximal pulling force pointing in Fig. 4 to the left) displayed for polystyrene particles of different radii a. Polystyrene particles with radii larger than 1μm can be pulled also by p-polarized beams.*

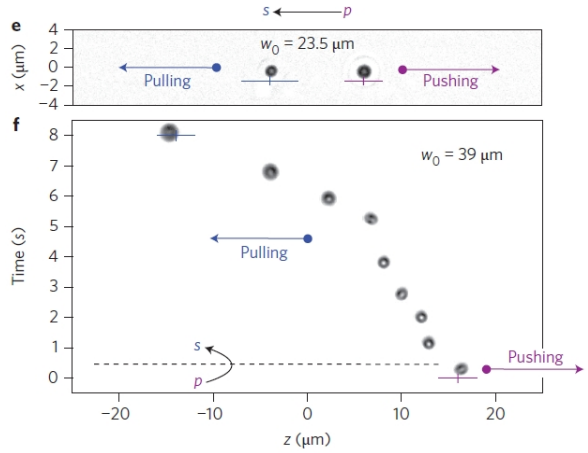


Figure 6 *Top: Stable positions of a polystyrene particle with a radius of 410 nm illuminated by an s- or p-polarized beam with a beam waist of w0=23.5 μm. Bottom: Time record of the motion of a single polystyrene particle of radius 410 nm illuminated by a wider initially p-polarized beam that is switched to an s polarized beam at t=0.5 s.*

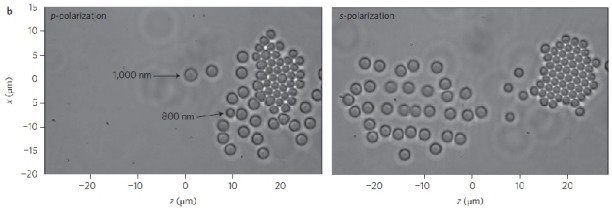


Figure 7 *Separation of polystyrene particles of radii 400 nm and 500 nm using the geometry of Fig. 4 and polarization switching of the beam from p (left) to s (right) polarization,.*

5 Acknowledgement

The authors acknowledge support from the Czech Science Foundation (14-36681G, 14-16195S), Technology Agency of the Czech Republic (TE01020233, TA03010642), Ministry of Education, Youth and Sports of the Czech Republic (LO1212) together with the European Commission (CZ.1.05/2.1.00/01.0017).

6 References

[1] A. Ashkin, *Optical trapping and manipulation of neutral particles* (World Scientific Publishing Company, 2006).

[2] Friese M.E.J, Nieminen T.A., Heckenberg N.R., Rubinsztein-Dunlop H., Optical alignment and spinning of laser-trapped microscopic particles, Nature 394:348-350 (1998)

[3] Allen, L., Padgett, M.J., Babiker, M., The orbital angular momentum of light. Progress In Optics: Vol XXXIX, 39:291-372 (1999)

[4] Šiler M., Jákl P., Brzobohatý O., Zemánek, P., Optical forces induced behavior of a particle in a non-diffracting vortex beam, Optics Express 20:24304-24319 (2012)

[5] Burns M.M.,, Fournier J.-M., Golovchenko, J. A., Optical binding, Physical Review Letters 63:1233-1236 (1989).

[6] Dholakia K., Zemánek P., Colloquium: Gripped by light: Optical binding, Reviews of Modern Physics 82:1767-1791 (2010).

[7] Brzobohatý O., Karásek V., Čižmár T., Zemánek, P., Dynamic size tuning of multidimensional optically bound matter, Applied Physics Letters 99:101105 (2011)

[8] Čižmár T., Brzobohatý O., Dholakia, K., Zemánek P., The holographic optical micro-manipulation system based on counter-propagating beams, Laser Physics Letters 8:50-56 (2011)

[9] Brzobohatý O., Karásek V., Šiler M., Chvátal L., Čižmár T., Zemánek P., Experimental demonstration of optical transport, sorting and self-arrangement using a 'tractor beam', Nature Photonics 7:123-127 (2013)

LASER SCATTERING IN PARTICLE CHARACTERIZATION: APPLICATION PERSPECTIVES

Renliang XU

Micromeritics Instrument (Shanghai), Ltd., China

ren.xu@micromeritics.com

Abstract

The science and technology of light scattering touches a very broad range of fields, from cosmology, meteorology, oceanography, all the way to nanotechnology and produces an enormous amount of research and application literatures. This review intends to only cover the progresses of light scattering applications in the field of particle characterization in the past decade. It is divided into three sections, static light scattering, i.e., scattering intensities as result of light-particle interaction at various spatial locations, dynamic light scattering, i.e., scattering intensities as result of light-particle interaction as a function of time, and scattering tracking that tracks particle movement through scattering.

1 Static Light Scattering (SLS)

Light scattering intensity measurement instruments can be categorized mainly into three types, i.e., optical particle counters (OPC) that measure scattering from individual particles; granulometers or goniometers, often being referred as multiangle light scattering (MALS) or static light scattering (SLS), that measure particles in liquid suspension in a broad angular range, typically can be continuously from near zero degree to 180 degrees using a rotating arm or fixed detectors throughout the entire angular range; and angular scattering intensity measurement instruments, commonly known as laser diffraction instruments (LD), that measure dry powders, sprays, or particles in liquid, using a set of fixed detectors at small angles with some additional detectors at large angles. Because the intended uses in research and industrial applications are different, the three types of instruments are designed differently. Particle counters, even though they can size individual particles, are mainly used for counting particles as a monitoring means for particular matters in oil, water, and air. Goniometers are used to measure macromolecules such as proteins and polymers in solution and mostly in research environment. On the other hand, laser diffraction has become the most popular tool in sizing solid particles, liquid droplets, or even air pockets from submicron to millimeter in various media, liquid, air, film, gel etc., due to its broad dynamic sizing range, high reproducibility, rapid measurement, few required known physical parameters, instrument automation and intelligence, and capability of on-line measurement. The major limitation is that it is not a direct sizing method and the size retrieval is limited to spherical model assumption. With approximately annual dispersion of several thousand new laser diffraction instruments, LD has been transformed in practice from a modern technology innovation to a common working horse or tool box in many industries, for example, in pharmaceutical and cement industries where it is widely used in Process Analytical Technology (PAT), both in-line and off line, and in food science and production, just name a few. The progresses of these three types of scattering technologies are to be reviewed in the presentation [1,2,3,4].

2 Dynamic Light Scattering (DLS)

With the advancement and popularization of nano-science and technology, various nanoparticles or molecules, such as fullerenes, carbon nanotubes, quantum dots and carbenes, which are small, fast moving in liquid and scatter weakly individually but often in more concentrated suspensions, have become the subjects of DLS measurement. DLS instruments are no longer limited to the laboratories of academics but have entered industrial laboratories in coating industry, rare earth materials, fluorescent powders, pharmaceuticals, food science, and even for diagnosing pathological conditions of body fluid. DLS is often used in combination with other techniques to simultaneously obtain more sample characters. For example, when combined with scanning probe microscopy (SPM), reorganization process during multi-stage self-assembly of a liposome-based delivery system can be studied statistically using DLS and in detail by SPM.

With the annual dispersion of new DLS instrument may surpass four digits, operators of DLS instruments are often industrial technicians or undergraduate students who require easy operating and rugged instruments. The DLS hardware has being evolved accordingly [5].

As a variation of DLS, electrophoretic light scattering (ELS) has also become a mature technology through the development during the past three decades and has been incorporated in an ISO Standard. ELS measures scattering intensity fluctuation from particles as a function of time while particles under both random Brownian motion and oriented electrophoretic motion in a well-defined electric field. Particle electrophoretic mobility is measured from which particle zeta potential can be derived. Past ELS configurations were mainly for measuring particles in dilute suspension or solution. Zeta potential is a property involving not only particle surface but also their environment, e.g., pH, ionic strength, and even the type of ions in the medium. Therefore, measurements of zeta

potential of particles in concentrated suspensions become a must in many occasions. A unique sample cell was designed in which a transparent electrode is attached to a thick window to transmit both incident light and scattered light through multiple refractions. Particles move electrophoretically in the field created by this electrode and another ordinary electrode. Light scattered from particles near the window surface are refracted twice before exiting from the other side of the window. This configuration enables a short light path length at a small scattering angle (~35°) so as to avoid the interference from Brownian broadening [6].

3 Particle Tracking Analysis (PTA)

This is an emerging branch of scattering technology applying to particle analysis. It is based on dynamically tracking particle movement through scattering from individual particles using image recording. Even though single particle tracking or time-resolved particle trajectory analysis from sequences of video images has been proposed for two-dimensional diffusion of particles in membranes more than two decades ago [7], only within the last decade, it has been used for particles in suspension and latterly for nanoparticles. Since it is a static measurement for the purpose of tracking particle dynamically, it is treated in this review separately.

Even though the principle is simple, for small particles or biomolecules such as bacterial and viruses, its scattering is typically not strong enough so it can be imaged as scattering spots individually. Carr uses a transparent substrate partially coated with a thin film of metal and illuminates a beam at a point adjacent or close to the metal coated region. The beam propagates above but close and substantially parallel to the metal surface defining a measurement zone where scattering from suspended particles can be detected in the far field by conventional photo detection systems [8].

4 References

[1] Strickland M.L., Olivier J. P., Conklin W. B., Hendrix W. P., US Patent No. 6,091,492 (2000)

[2] Chen J., Wang H., Shen J., Light scattering of particles illuminated by a divergent beam, Opt. Laser Eng., 50: 1410-1415 (2012)

[3] Fan J., Dong Q., China Patent No. 2012 2 0051682.5 (2012)

[4] Zhang F., China Patent No. CN201020163606 (2011)

[5] Xu R., Progress in nanoparticles characterization: Sizing and zeta potential measurement, Particuology, 6(2): 112-115 (2008)

[6] Sekiwa M., Tsutsui K., Morisawa K., Fujimoto T., Toyoshima A., US Patent No. 7,449,097 B2 (2008)

[7] Qian H., Sheetz M.P., Elson E.L., Single particle tracking, Biophys. J., 60: 910-921 (1991)

[8] Carr R. J., US Patent No. 7,751,053 B2 (2010)

Beam shape description

On the Description of Electromagnetic Arbitrary Shaped Beams : Beam Shape Coefficients versus Plane Wave Spectra, and vice versa

Gérard GOUESBET[1] and James A. LOCK[2]

[1] Département : Optique et Lasers, CORIA UMR 6614 CNRS/INSA et Université de Rouen, Saint-Etienne-du Rouvray, 76801, France.

[2] Department of Physics, Cleveland State University, Cleveland, Ohio, 44115, USA

*Corresponding author: Gouesbet@coria.fr

Abstract

A strong effort has been devoted during the three last decades, and more, to the study of electromagnetic scattering of arbitrary shaped beams by particles. For this topic, the most important issue concerns the description of the illuminating beam as an expansion over a basis of functions. There are essentially two kinds of expansion which have been used (i) a discrete expansion involving beam shape coefficients and (ii) a continuous expansion in terms of plane wave spectra. In this paper, we provide a formal relationship between these two kinds of expansion.

1 Beam shape coefficients.

Discrete expansions may be found for instance in spherical [1] or in spheroidal coordinates [2]. We restrict ourselves to spherical coordinates. The electric field **E** of the illuminating beam can then be expanded in terms of vector spherical wave functions according to, e.g. [3] for the first presentation of such expansions :

$$\mathbf{E}=\sum_{n=1}^{\infty}\sum_{m=-n}^{+n}\left[a_{mn}\mathbf{M}_{mn}^{(1)}(k\mathbf{r})+b_{mn}\mathbf{N}_{mn}^{(1)}(k\mathbf{r})\right] \tag{1}$$

in which **M** and **N** are Vector Spherical Wave Functions (VSWFs), a_{mn} and b_{mn} are expansion coefficients, k is the wave-number and **r** is the vector positition, with a similar expansion for the magnetic field **H** . In the original formulation of the generalized Lorenz-Mie theory (GLMT) describing the interaction between an Arbitrary Shaped Beam (ABS) and a homogeneous sphere defined by its diameter d and its complex refractive index M , the field expansions are provided in a "scalar" Bromwich formulation, e.g. [1] and references therein, introducing two sets of beam shape coefficients (BSCs) $g_{n,TM}^{m}$ and $g_{n,TE}^{m}$, which are defined in such a way that they exhibit simple appealing expressions in the case of axisymmetric beams, in particular plane waves [4], and are related to the expansion coefficients a_{mn} and b_{mn} . The relationship between expansion coefficients and BSCs is available from [5]. In the "scalar" formulation, the expansion of radial component of the electric field only involves $TM-$ BSCs according to [1], p 41 :

$$E_r=E_0\sum_{n=1}^{\infty}\sum_{m=-n}^{+n}c_n^{pw}g_{n,TM}^{m}\frac{n(n+1)}{r}j_n(kr)P_n^{|m|}(\cos\theta)\exp(im\phi) \tag{2}$$

in which c_n^{pw} (" pw " standing for plane wave) are subcoefficients of the classical LMT, j_n 's are spherical Bessel functions and P_n^m 's are associated Legendre functions. There exist a similar expression relating the radial component H_r of the magnetic field and the $TE-$ BSCs. The TM -BSCs can be evaluated from E_r by using different methods, including using quadratures reading as [1] :

$$g_{n,TM}^{m}=\frac{1}{E_0c_n^{pw}}\frac{2n+1}{4\pi n(n+1)}\frac{(n-|m|)!}{(n+|m|)!}\frac{r}{j_n(kr)}\int_0^{\pi}\int_0^{2\pi}E_rP_n^{|m|}(\cos\theta)\exp(-im\phi)\sin\theta d\theta d\phi \tag{3}$$

with a similar relationship between the TE -BSCs and the radial component H_r .

2 Plane wave Spectra.

The transverse component of the field **E** in the plane $z=0$ may be expressed in terms of two basic electric plane wave spectral components $S_x(k_x,k_y)$ and $S_y(k_x,k_y)$ using Fourier transforms, according to [6] :

$$\begin{pmatrix}E_x(x,y,0)\\E_y(x,y,0)\end{pmatrix}=\frac{1}{k^2}\int_{-\infty}^{+\infty}\int_{-\infty}^{+\infty}\begin{pmatrix}S_x^E(k_x,k_y)\\S_y^E(k_x,k_y)\end{pmatrix}\exp\left[i(k_xx+k_yy)\right]dk_xdk_y \tag{4}$$

with the inverse Fourier transforms reading as :

$$\begin{pmatrix}S_x^E(k_x,k_y)\\S_y^E(k_x,k_y)\end{pmatrix}=\frac{k^2}{4\pi^2}\int_{-\infty}^{+\infty}\int_{-\infty}^{+\infty}\begin{pmatrix}E_x(x,y,0)\\E_y(x,y,0)\end{pmatrix}\exp\left[-i(k_xx+k_yy)\right]dxdy \tag{5}$$

Because the propagation of the field satisfies the Helmholtz equation, one finds that Eq. 4 generalizes to [6] :

$$\begin{pmatrix} E_x(x,y,z) \\ E_y(x,y,z) \end{pmatrix} = \frac{1}{k^2}\int_{-\infty}^{+\infty}\int_{-\infty}^{+\infty}\begin{pmatrix} S_x^E(k_x,k_y) \\ S_y^E(k_x,k_y) \end{pmatrix}\exp\left[i(k_x x + k_y y + k_z z)\right]dk_x dk_y \quad (6)$$

The other spectral component S_z^E and the components of the magnetic spectral vector $\mathbf{S}_i^H (i = x, y, z)$ can then be obtained by using Maxwell's equations, e.g.[7].

3 Relationship between BSCs and spectra.

The description of the illumating beam may then be expressed in terms of *two* sets of BSCs or in terms of *two* sets of plane wave spectral components. From the formulation presented above, the paper associated with this abstract will establish the relationship between these two sets, namely expressing BSCs versus basic spectral components, and the basic spectral components versus BSCs. The results will involve several integrals that will be evaluated in closed forms.

In a companion review paper, it will be made clear that the formulation established in the present paper allows for an extensive discussion on the topic of electromagnetic scattering of arbitrary shaped beams by arbitrary shaped particles. It also allows one to discuss a few problems listed in [8].

4 References

[1] G. Gouesbet and G. Gréhan. *Generalized Lorenz-Mie theories* (Springer-Verlag , Berlin, 2011).

[2] G. Gouesbet, F. Xu, and Y.P. Han. Expanded description of electromagnetic arbitrary shaped beam in spheroidal coordinates for use in light scattering theories : A review. *Journal of Quantitative Spectroscopy and Radiative Transfer,* 112:2249.2267 (2011).

[3] G. Gouesbet and G. Gréhan. Generalized Lorenz-Mie theory for assemblies of spheres and aggregates. *Journal of Optics A : Pure and Applied Optics*, 1:706.712 (1999).

[4] G. Gouesbet. Partial wave expansions and properties of axisymmetric light beams. *Applied Optics* 35,9:1543.1555 (1996).

[5] G. Gouesbet. T-matrix formulation and generalized Lorenz-Mie theories in spherical coordinates. *Optics Communications* 283:517.521 (2010)

[6] S. Colak, C. Yeh, and L.W. Casperson. Scattering of focused beams by tenuous particles. *Applied Optics* 18:294.302 (1979)

[7] J.A. Lock. Angular spectrum and localized model of Davis-type beam. *Journal of the Optical Society of America A* 30, 3:489.500, (2013)

[8] G. Gouesbet and J.A. Lock. A list of problems for future research in generalized Lorenz-Mie theories and related topics, review and prospectus; commemorative invited paper, for the 50th anniversary of Applied Optics, *Applied Optics* 52, 5:897.916 (2013)

Scattering of the Evanescent Components in the Angular Spectrum of a Tightly Focused Electromagnetic Beam by a Spherical Particle

James A. LOCK[1,*]

[1] Physics Dept., Cleveland State University, Cleveland OH 44115, USA

*Corresponding author: j.lock@csuohio.edu

Abstract

In previous studies where a tightly focused beam is scattered by a spherical particle, either the experimental conditions were such that evanescent components were absent from the angular spectrum of the beam, or if they were present, it was assumed that their contribution to scattering was small and could safely be ignored. In this presentation the contribution of the evanescent components is explicitly considered and the validity their neglect is assessed. It is found that angular spectrum components just inside the evanescent regime may, under certain circumstances, have a minor but noticeable influence on either the scattered intensity or the trapping force on a spherical particle when it is near the wall of the sample cell.

1. Introduction

When a monochromatic electromagnetic beam propagating in the z direction and having wavelength λ and wave number $k=2\pi/\lambda$ is incident on a spherical particle of radius a and refractive index N, the interaction of the beam with the particle produces outgoing scattered waves. The fields of the incident beam can be written [1] as a sum of transverse electric (TE) and transverse magnetic (TM) spherical multipole waves $\mathbf{M}_{n,m}(k\mathbf{r})$ and $\mathbf{N}_{n,m}(k\mathbf{r})$,

$$\mathbf{E}(\mathbf{r}) = \sum_n \sum_m i^n (-1)^m \{\pi(2n+1)(n+m)! / [n(n+1)(n-m)!]\}^{1/2} \times [-i\, g^{\mathrm{TE}}_{n,m}\, \mathbf{M}_{n,m}(k\mathbf{r}) - g^{\mathrm{TM}}_{n,m}\, \mathbf{N}_{n,m}(k\mathbf{r})]$$

$$c\mathbf{B}(\mathbf{r}) = \sum_n \sum_m i^n (-1)^m \{\pi(2n+1)(n+m)! / [n(n+1)(n-m)!]\}^{1/2} \times [\, i\, g^{\mathrm{TM}}_{n,m}\, \mathbf{M}_{n,m}(k\mathbf{r}) - g^{\mathrm{TE}}_{n,m}\, \mathbf{N}_{n,m}(k\mathbf{r})] \quad (1)$$

where $g^{\mathrm{TE}}_{n,m}$ and $g^{\mathrm{TM}}_{n,m}$ are the shape coefficients of the incident beam, n is the integer partial wave number with $1\le n<\infty$, and m is the integer azimuthal mode number with $-n\le m\le n$. The spherical mutipole wave $\mathbf{M}_{n,m}(k\mathbf{r})$ is proportional to [1] the transverse vector spherical harmonic $\mathbf{X}_{n,m}(\theta,\phi)$, and $\mathbf{N}_{n,m}(k\mathbf{r})$ is proportional to a combination of the radial and transverse vector spherical harmonics $\mathbf{Y}_{n,m}(\theta,\phi)$ and $\mathbf{Z}_{n,m}(\theta,\phi)$. In generalized Lorenz-Mie theory, the outgoing scattered waves may also be decomposed into a sum of TE and TM spherical multipole waves. The weighting factor of each scattered partial wave is [2]

$$G^{\mathrm{TE}}_{n,m} = g^{\mathrm{TE}}_{n,m}\, b_n$$
$$G^{\mathrm{TM}}_{n,m} = g^{\mathrm{TM}}_{n,m}\, a_n \quad , \quad (2)$$

where a_n and b_n are the partial wave scattering amplitudes of Lorenz-Mie theory for an incident plane wave. Given the functional form of the fields of the incident beam, the shape coefficients may be calculated by inverting Eqs.(1),

$$g^{\mathrm{TE}}_{n,m} = -(-i)^{n+1}(-1)^m \{n(n+1)(n-m)!/[\pi(2n+1)(n+m)!]\}^{1/2} [1/j_n(kr)] \times \int_0^{\pi} \sin(\theta)\, d\theta \int_0^{2\pi} d\phi\, \mathbf{X}^*_{n,m}(\theta,\phi) \cdot \mathbf{E}(r,\theta,\phi)$$

$$g^{\mathrm{TM}}_{n,m} = (-i)^{n+1}(-1)^m \{n(n+1)(n-m)!/[\pi(2n+1)(n+m)!]\}^{1/2} [1/j_n(kr)] \times \int_0^{\pi} \sin(\theta)\, d\theta \int_0^{2\pi} d\phi\, \mathbf{X}^*_{n,m}(\theta,\phi) \cdot c\mathbf{B}(r,\theta,\phi) \, . \quad (3)$$

Over the years, much effort has gone into calculating $g^{\mathrm{TE}}_{n,m}$ and $g^{\mathrm{TM}}_{n,m}$ for a number of transversely localized beams, most notably for various models of a nominally Gaussian beam.

2. Background

There are other beam possibilities, however. For example consider the yz plane being an interface between glass with refractive index N_1 for $x<0$ and air with refractive index N_2 for $x>0$. If a single plane wave in the glass were incident on the interface past the critical angle for total internal reflection, an evanescent wave that is oscillatory in the z direction and damped in the x direction is created in the $x>0$ half-space. If a spherical particle were located a within few wavelengths of the N_1/N_2 interface in the air at the coordinates $(x_0, 0, 0)$, the evanescent wave incident on it produces oscillatory scattered waves. This situation has been treated in detail by a number of authors [3]. The evanescent wave may be interpreted as a linearly polarized plane wave whose propagation direction makes the angle $\theta_k=0+i\delta$ with respect to the z axis, so that $\cos(\theta_k)=\cosh(\theta_k)+0i$. The beam shape coefficients in this case are expressed in terms of associated Legendre functions $P_n^m[\cos(\theta_k)]$ of a complex argument [4]. The complex $\cos(\theta_k)$ plane for these functions contains a cut along the $\mathrm{Re}[\cos(\theta_k)]$ axis extending from $-\infty<\cos(\theta_k)\le 1$.

These associated Legendre functions are discontinuous from immediately above the cut to on the cut itself, and from on the cut to immediately beneath it. Fortunately, the complications associated with the cut in the complex plane are avoided for this geometry. The price to be paid for this, however, is that the scattering particle is off-axis with respect to the beam, so that all azimuthal modes m contribute to the scattered wave.

This presentation reports the calculation of $g^{TE}_{n,m}$ and $g^{TM}_{n,m}$ for a different evanescent wave geometry. Consider a plane wave or a mildly focused Gaussian beam propagating in the z direction and incident on a high numerical aperture (NA) microscope objective lens of refractive index N_1 which is optically connected to a microscope cover slip by an index matching oil. A sample cell containing either water or air of refractive index N_2 is in the converging region of the beam on the other side of the cover slip. This is the standard geometry for laser tweezers applications [5]. The center of the scattering particle is taken to be at the origin of coordinates, and the paraxial focal point of the beam is located at (x_0, y_0, z_0) with $z_0>0$. If the numerical aperture of the microscope objective lens is suitably large, the angular spectrum of the beam in the sample cell incident on the particle contains both oscillatory components with $0\le\theta_k\le\pi/2$ and evanescent components with $\theta_k=\pi/2-i\varepsilon$. For this geometry $\cos(\theta_k)=0+i\sinh(\varepsilon)$, which lies on the imaginary axis immediately above the cut in the complex plane. Thus much care in this evanescent wave geometry must be exercised in dealing with the associated Legendre functions in the complex plane. The advantage of this geometry, however, is that if $x_0=y_0=0$, the beam is on-axis with respect to the scattering particle and only the $m=\pm1$ azimuthal modes will contribute.

3. Calculation of the Beam Shape Coefficients

The angular spectrum of the incident beam [6] will in general contain plane wave components having all propagation angles θ_k (complex) and ϕ_k (real), and all polarization directions γ. The shape coefficients $g^{TE}_{n,m}(\theta_k, \phi_k, \gamma)$ and $g^{TM}_{n,m}(\theta_k, \phi_k, \gamma)$ for an arbitrary component in the spectrum of a beam was calculated in the following way. First, the fields of a plane wave in the angular spectrum having amplitude E_0, propagating in the z direction, and polarized in the xy plane at the angle γ with respect to the x axis, was rotated to the arbitrary θ_k, ϕ_k direction. The $\exp(i\mathbf{k}.\mathbf{r})$ phase factor of the rotated plane wave was then expanded in terms of spherical Bessel functions $j_n(kr)$, spherical harmonics of the coordinate space angles $Y_n^m(\theta,\phi)$, the azimuthal dependence of the plane wave component $\exp(im\phi_k)$, and associated Legendre functions $P_n^m[\cos(\theta_k)]$ of the complex angle θ_k. These fields were then substituted into Eqs.(3), the integrals were performed, and a number of symmetry and recursion properties of associated Legendre functions of a complex argument were used to simplify the result. The shape coefficients of the component were found to depend on the angular functions of the complex argument z,

$$\Pi_n^m(z) = S\, P_n^m(z) / (1 - z^2)^{1/2}$$
$$T_n^m(z) = -\, S\, (1 - z^2)^{1/2}\, (d/dz)\, P_n^m(z) \qquad (4)$$

where

$$S = (-1)^m \text{ if } z \text{ is real and } -1\le z\le 1$$
$$(-i)^m \text{ if } z \text{ is imaginary and } \mathrm{Im}(z)>0$$
$$(i)^m \text{ if } z \text{ is imaginary and } \mathrm{Im}(z)<0 \quad . \qquad (5)$$

These functions are continuous across the cut in the complex plane, thus insuring that as the angle θ_k in the angular spectrum of the beam continuously varies from real to complex values, $g^{TE}_{n,m}(\theta_k, \phi_k, \gamma)$ and $g^{TM}_{n,m}(\theta_k, \phi_k, \gamma)$ are also continuous functions of θ_k, despite the discontinuity of $P_n^m[\cos(\theta_k)]$ across the cut. They thus provide the analytic continuation of the beam shape coefficients from real angles θ_k to complex angles.

If the two-dimensional Fourier transform of the incident beam in its paraxial focal plane has the simple form

$$\mathbf{F}(\rho_k, \phi_k) = V(\theta_k)\, \mathbf{u}_x \qquad (6)$$

where $\rho_k=k\sin(\theta_k)$, the $m=1$ shape coefficients of the beam a distance Δ into the sample cell reduce to

$$g^{TE}_{n,1} = -i/[2\pi\, n(n+1)] \int_0^\infty [\rho_k\, d\rho_k / \cos(\theta_k)]$$
$$\times\ \exp[iN_2 k\Delta\cos(\theta_k)]\, V(\theta_k)$$
$$\times\ \{\Pi_n^1[\cos(\theta_k)] + \cos(\theta_k)\, T_n^1[\cos(\theta_k)]\}$$

$$g^{TM}_{n,1} = 1/[2\pi\, n(n+1)] \int_0^\infty [\rho_k\, d\rho_k / \cos(\theta_k)]$$
$$\times\ \exp[iN_2 k\Delta\cos(\theta_k)]\, V(\theta_k)$$
$$\times\ \{\cos(\theta_k)\, \Pi_n^1[\cos(\theta_k)] + T_n^1[\cos(\theta_k)]\} \qquad (7)$$

The expressions for the only other non-zero beam shape coefficients $g^{TE}_{n,-1}$ and $g^{TM}_{n,-1}$ are similar. If $\mathbf{F}(\rho_k, \phi_k)$ has both an x component and a y component, which is more realistic for the laser tweezers geometry [7], Eqs.(7) become only slightly more complicated. The same holds true for the shape coefficients of a tightly focused freely diffracting beam, such as the remodeled fifth-order Davis Gaussian beam. The major difference for the evanescent components in this geometry is that $\cos(\theta_k)$ lies below the cut in the complex plane in the converging portion of the beam before focus, while it lies above the cut in the diverging portion of the beam after focus. In Eqs.(7), the phase factor $\exp[iN_2k\Delta\cos(\theta_k)]$ indicates that when the particle is more than a few wavelengths from the wall of the sample cell, the contribution of the evanescent

components generated at the wall are rapidly damped and can safely be ignored.

As long as $\cos(\theta_k)$ is real, both Π_n^1 and T_n^1 are oscillatory in θ_k in the integrand of Eqs.(7). But in the evanescent regime when $\cos(\theta_k)=i\sinh(\varepsilon)$, both Π_n^1 and T_n^1 are asymptotically exponentially rising as a function of ε. Deep in the evanescent regime when ε is large, this increase will be more than compensated for by both the rapid decrease in the Fourier transform V as a function of ε, the and the much faster than exponential decay of the damping factor $\exp[-N_2 k\Delta \sinh(\varepsilon)]$. These effects rapidly damp out the integrands for large ε in the integral of Eqs.(7), and give no appreciable contribution to the beam shape coefficients. On the other hand, just inside the evanescent regime when ε is small, $\Pi_n^1[i\sinh(\varepsilon)]$ and $T_n^1[i\sinh(\varepsilon)]$ are nonzero and roughly independent of ε for odd n and even n, respectively. The Fourier transform V is roughly constant in ε, and the damping factor falls off only exponentially. This slower damping may, especially when the scattering particle is within a few wavelengths of the sample cell wall, produce a noticeable contribution of the small-ε evanescent waves to the beam shape coefficients $g^{TE}_{n,\pm1}$ and $g^{TM}_{n,\pm1}$. Similar conclusions were found for a different, much simpler evanescent wave system in [8].

4. References

[1] J.D. Jackson, *Classical Electrodynamics* (Wiley, New York, 1962).

[2] G. Gouesbet, B. Maheu, and G. Gréhan, Light scattering from a sphere arbitrarily located in a Gaussian beam, using a Bromwich formulation, Journal of the Optical Society of America A5(9):1427-43 (1988)

[3] H. Chew, D.-S. Wang, and M. Kerker, Elastic scattering of evanescent electromagnetic waves, Applied Optics 18(15):2679-87 (1979)

[4] W.Magnus, F. Oberhettinger, and R.P Soni, *Formulas and Theorems for the Special Functions of Mathematical Physics* (Springer-Verlag, New York, 1966).

[5] A.A.R. Neves, A. Fontes, C.L. Cesar, A. Composeo, R. Cingolani, and D. Pisignano, Axial optical trapping efficiency through a dielectric interface, Physical Review E76:061917 (2007)

[6] J.A. Lock, Angular spectrum and localized model of Davis-type beam, Journal of the Optical Society of America, A30(3):489-500 (2013)

[7] B. Richards and E. Wolf, Electromagnetic diffraction in optical systems II. Structure of the image field in an aplanatic system, Proceedings of the Royal Society (London) 253:358-79 (1959)

[8] W.H. Carter, Bandlimited angular spectrum approximation to a scalar dipole field, Optics Communications, 2(3):142-8 (1970)

Acoustics of Finite-Aperture Vortex Beams

Farid G. MITRI[1,*]

[1] Chevron – Area 52 Technology, Santa Fe, 87508, United States

*Corresponding author: mitri@chevron.com, fmitri@gmail.com

Abstract

A method based on the Rayleigh-Sommerfeld surface integral is provided, which makes it feasible to rigorously model, evaluate and compute the acoustic scattering and other mechanical effects of finite-aperture vortex beams such as the acoustic radiation force and torque on a viscoelastic sphere in various applications in acoustic tweezers and microfluidics, particle entrapment, manipulation and rotation. Partial-wave series expansions are derived for the incident field of acoustic spiraling (vortex) beams, comprising high-order Bessel and Bessel-Gauss beams.

1 Introduction

Considering the fact that practically every acoustic source (except a point source radiating omnidirectional waves) produces a finite beam, it is necessary to devise a method which enables modelling the incident pressure field for applications in beam-forming design, and other areas including imaging, scattering and dynamic effects caused by acoustic beams emanating from a finite aperture. Previous developments considered the cases of finite piston sources with uniform vibration [1], or clamped edges, Gaussian [2, 3] and others [4-7], to the zero-order Bessel beam [8, 9], for which both the axial scattering [10] and radiation force [11] on a sphere have been recently evaluated. The aim here is to extend the previous developments and provide partial-wave series expansions (PWSEs) for the acoustic pressure (scalar) field of vortex beams. In the present analysis, high-order Bessel and Bessel-Gauss beams are considered, however, the analysis can be directly extended to other types of vortex beams, such as the Laguerre-Gauss beam and other high-order Gaussian beams. The PWSEs are useful for further development related to the scattering and radiation forces by such beams, which will be the subject of future investigations.

2 Method

Consider a finite circular transducer with a surface of radius b in a non-viscous fluid medium. A spherical coordinates system (r, θ, ϕ) is chosen to coincide with the center O of the Cartesian coordinates system (x, y, z) (Fig. 1). The coordinates systems are situated at an axial distance r_0 from the center of the circular transducer. The description of the incident acoustic field produced by the finite source, and represented by its scalar velocity potential field Φ_i, is obtained from the Rayleigh-Sommerfeld integral as [12],

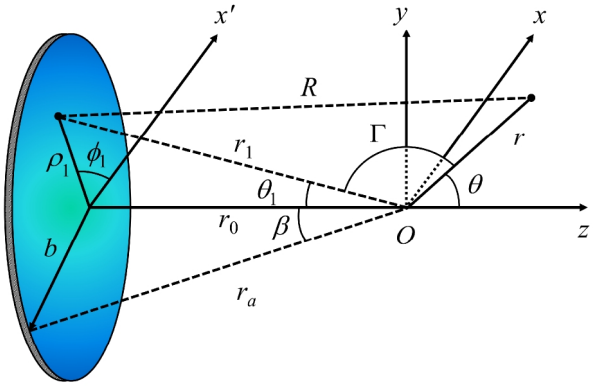


Figure 1 *Geometry of the problem used in the derivation of the incident acoustic fields of finite vortex beams.*

$$\Phi_i = \frac{1}{2\pi}\iint_{S_r} \frac{v e^{i(kR-\omega t)}}{R} dS_r, \qquad (1)$$

where R is the distance from the observation point to the finite source of circular surface S_r , the parameter k is the wave number of the acoustic radiation, ω is the angular frequency, and v is the normal velocity at $z = 0$. In the case of a uniform vibrational surface, v is unitary [3-5, 7, 13], but takes particular values when the radiator is simply supported [3, 4, 6], clamped [3, 4], described by a rotating (propeller) [14] or ring [15] source, apodized by a Gaussian distribution [4, 16], or excited according to its radially-symmetric vibrational modes describing zero-order Bessel beams [8-11].

For the purpose of the present study, apodizations of the normal velocity at $z = 0$, proportional to $\exp(im\phi)$ describing a vortex beam are considered. Current related research is investigating the scattering [17-26], radiation forces [27-30] and torques [31-33] on a spherical particle, in which infinite high-order Bessel beams were considered. However, acoustical vortex beams which carry an orbital angular momentum and emanate from a finite aperture are practically used in particle manipulation and rotation applications [34-38], and the present investigation could be potentially useful in modelling the mechanical effects (i.e. scattering, radiation forces and torques) of finite sound beams on a sphere, as opposed to waves of infinite extent.

First, the analysis treats the case of a high-order Bessel-Gaussian beam which reduces under a special limit to the case of a high-order Bessel vortex beam.

2.1 High-order Bessel-Gauss vortex beam

Consider an acoustic vortex for which the normal velocity is expressed as,

$$v\big|_{z=0} = V_0 J_m\left(k_\rho \rho_1\right) e^{-\left(\rho_1^2/w_0^2\right)} e^{im\phi_1}, \tag{2}$$

where V_0 is the velocity amplitude, ρ_1 is the distance from the center of the radiator to a point on its flat surface, $k_\rho = k\sin\beta$, with β corresponding to the half-cone angle of the beam, w_0 is the beam's waist, the parameter $m \neq 0$ is a positive or negative integer describing the order of the beam, and $J_m(.)$ is the cylindrical Bessel function of the first kind of order m, and ϕ_1 is the azimuthal angle at the surface of the finite source (Fig. 1).

Suppressing the time dependence $e^{-i\omega t}$ for convenience, and using the addition theorem for the spherical functions, i.e. (10.1.45) and (10.1.46) in [39] such that $r \le r_1$, Eq.(1) is expressed as,

$$\begin{aligned}\Phi_i = {} & \frac{ikV_0}{2\pi}\sum_{n=0}^{\infty}(2n+1)\, j_n(kr) \\ & \times\iint_{S_r} J_m\left(k_\rho\rho_1\right) e^{-\left(\rho_1^2/w_0^2\right)} h_n^{(1)}(kr_1) e^{im\phi_1} P_n(\cos\Gamma)\, dS_r,\end{aligned} \tag{3}$$

where $j_n(\cdot)$ and $h_n^{(1)}(\cdot)$ are the spherical Bessel and Hankel functions of the first kind, $P_n(\cdot)$ are the Legendre functions, and the differential surface $dS_r = \rho_1 d\rho_1 d\phi_1 = r_1 dr_1 d\phi_1$, since $r_1^2 = \rho_1^2 + r_0^2$.

Making use of the addition theorem for the Legendre functions [40, 41] using the definition of the angles as given in Fig. 1, $P_n(\cos\Gamma)$ can be expressed as ((3.19), p. 65 in [42]),

$$\begin{aligned}P_n(\cos\Gamma) = {} & \sum_{\ell=0}^{n}\left(2-\delta_{\ell,0}\right)\frac{(n-\ell)!}{(n+\ell)!} \\ & \times P_n^\ell\left(\cos(\pi-\theta)\right) P_n^\ell(\cos\theta_1)\cos\ell(\phi-\phi_1),\end{aligned} \tag{4}$$

where $\delta_{i,j}$ is the Kronecker delta function, and $P_n^\ell(\cdot)$ are the associated Legendre functions. Integrating both sides of Eq.(4) with respect to ϕ_1 using the property of the following integral,

$$\int_0^{2\pi} e^{im\phi_1}\cos\ell(\phi-\phi_1)\, d\phi_1 = \begin{cases} 0, & \ell \neq m \\ 2\pi, & \ell = m = 0 \\ \pi e^{im\phi}, & \ell = m \neq 0 \end{cases} \tag{5}$$

gives for $\ell = m \neq 0$ after substituting Eq.(4) and Eq.(5) into Eq.(3), the incident velocity potential as,

$$\begin{aligned}\Phi_i = {} & \frac{V_0 i e^{im\phi}}{k} \\ & \times\sum_{n=|m|}^{\infty}\Lambda_m(-1)^{n+m}(2n+1)\, j_n(kr)\frac{(n-m)!}{(n+m)!}P_n^m(\cos\theta),\end{aligned} \tag{6}$$

where,

$$\Lambda_m = \int_{kr_0}^{kr_a}(kr_1) J_m\left(k_\rho\sqrt{r_1^2-r_0^2}\right) e^{-\left[\left(r_1^2-r_0^2\right)/w_0^2\right]} h_n^{(1)}(kr_1) P_n^m\left(\frac{r_0}{r_1}\right) d(kr_1). \tag{7}$$

Eq.(6) represents the incident velocity potential for an acoustic high-order Bessel-Gauss vortex beam beam with its axis of wave propagation coinciding with the z-axis. The integral in Eq.(7) can be evaluated numerically as no closed-form solution is available yet. If m = 0, the field corresponds to a circular disk with uniform vibration.

2.2 High-order Bessel vortex beam

It can be easily noticed that for wide beams, the beam's waist $w_0 \to \infty$. Thus, Eq.(7) becomes,

$$\Lambda_m\big|_{w_0\to\infty} = \int_{kr_0}^{kr_a}(kr_1) J_m\left(k_\rho\sqrt{r_1^2-r_0^2}\right) h_n^{(1)}(kr_1) P_n^m\left(\frac{r_0}{r_1}\right) d(kr_1), \tag{8}$$

and the corresponding incident velocity potential of a high-order Bessel vortex beam can be obtained by inserting Eq.(8) into Eq.(6).

3 Discussion and conclusion

In this work, a method based on the Rayleigh-Sommerfeld surface integral is provided, which makes it feasible to rigorously obtain partial-wave series expansions for the incident field of acoustic spiraling (vortex) beams, comprising high-order Bessel and Bessel-Gauss beams. Those expressions are useful in the study of the axial and arbitrary scattering, radiation force and torque of finite-aperture vortex beams on a viscoelastic sphere in various applications in acoustic tweezers and microfluidics, particle entrapment, manipulation and rotation. From the expressions of the incident velocity potential (or pressure) fields, the beam-shape coefficients can be obtained and used to advantage in the numerical evaluation of the scattering and other mechanical effects of acoustical beams, especially in situations where the sphere is shifted off the beam's axis.

4 References

[1] H. Seki, A. Granato, and R. Truell, "Diffraction Effects in the Ultrasonic Field of a Piston Source and Their Importance in the Accurate Measurement of Attenuation," *The Journal of the Acoustical Society of America*, vol. 28, no. 2, pp. 230-238, 1956.

[2] E. P. Papadakis, "Effects of Input Amplitude Profile upon Diffraction Loss and Phase Change in a Pulse-Echo System," *The Journal of the Acoustical Society of America*, vol. 49, no. 1B, pp. 166-168, 1971.

[3] D. L. Dekker, R. L. Piziali, and J. E. Dong, "Effect of boundary conditions on the ultrasonic-beam characteristics of circular disks," *The Journal of the Acoustical Society of America*, vol. 56, no. 1, pp. 87-93, 1974.

[4] M. Greenspan, "Piston radiator: Some extensions of the theory," *The Journal of the Acoustical Society of America*, vol. 65, no. 3, pp. 608-621, 1979.

[5] T. Hasegawa, N. Inoue, and K. Matsuzawa, "A new rigorous expansion for the velocity potential of a circular piston source," *The Journal of the Acoustical Society of America,* vol. 74, no. 3, pp. 1044-1047, 1983.
[6] C. He and A. E. Hay, "Near-field characteristics of circular piston radiators with simple support," *The Journal of the Acoustical Society of America,* vol. 94, no. 1, pp. 554-561, 1993.
[7] T. D. Mast and F. Yu, "Simplified expansions for radiation from a baffled circular piston," *The Journal of the Acoustical Society of America,* vol. 118, no. 6, pp. 3457-3464, 2005.
[8] E. W. Guptill and A. D. Macdonald, "The acoustical field near a circular transducer," *Canadian Journal of Physics,* vol. 30, no. 2, pp. 119-122, 1952.
[9] E. W. Guptill, "The sound field of a piston source," *Canadian Journal of Physics,* vol. 31, no. 3, pp. 393-401, 1953.
[10] F. G. Mitri, "Near-Field Acoustic Resonance Scattering of a Finite Bessel Beam by an Elastic Sphere," *IEEE Transactions on Ultrasonics Ferroelectrics and Frequency Control,* vol. 61, no. 4, 2014.
[11] F. G. Mitri, "Single Bessel tractor-beam tweezers," *Wave Motion,* vol. submitted, 2014.
[12] J. W. S. Rayleigh, *The theory of sound* vol. 2. New York: Dover publications, 1945.
[13] T. Hasegawa, N. Inoue, and K. Matsuzawa, "Fresnel diffraction: Some extensions of the theory," *The Journal of the Acoustical Society of America,* vol. 75, no. 4, pp. 1048-1051, 1984.
[14] M. Carley, "Series expansion for the sound field of rotating sources," *The Journal of the Acoustical Society of America,* vol. 120, no. 3, pp. 1252-1256, 2006.
[15] M. J. Carley, "Series expansion for the sound field of a ring source," *The Journal of the Acoustical Society of America,* vol. 128, no. 6, pp. 3375-3380, 2010.
[16] G. C. Gaunaurd and H. Uberall, "Acoustics of finite beams," *The Journal of the Acoustical Society of America,* vol. 63, no. 1, pp. 5-16, 1978.
[17] F. G. Mitri, "Acoustic scattering of a high-order Bessel beam by an elastic sphere," *Annals of Physics,* vol. 323, no. 11, pp. 2840-2850, 2008.
[18] F. G. Mitri, "Equivalence of Expressions for the Acoustic Scattering of a Progressive High-Order Bessel Beam by an Elastic Sphere," *IEEE Transactions on Ultrasonics Ferroelectrics and Frequency Control,* vol. 56, no. 5, pp. 1100-1103, 2009.
[19] F. G. Mitri, "Interaction of a high-order Bessel beam with a submerged spherical ultrasound contrast agent shell - Scattering theory," *Ultrasonics,* vol. 50, no. 3, pp. 387-396, 2010.
[20] F. G. Mitri, "Interaction of a Nondiffracting High-Order Bessel (Vortex) Beam of Fractional Type alpha and Integer Order m With a Rigid Sphere: Linear Acoustic Scattering and Net Instantaneous Axial Force," *IEEE Transactions on Ultrasonics Ferroelectrics and Frequency Control,* vol. 57, no. 2, pp. 395-404, 2010.
[21] F. G. Mitri, "Acoustic beam interaction with a rigid sphere: The case of a first-order non-diffracting Bessel trigonometric beam," *Journal of Sound and Vibration,* vol. 330, no. 24, pp. 6053-6060, 2011.
[22] F. G. Mitri, "Linear axial scattering of an acoustical high-order Bessel trigonometric beam by compressible soft fluid spheres," *Journal of Applied Physics,* vol. 109, no. 1, p. 014916, 2011.
[23] F. G. Mitri and G. T. Silva, "Off-axial acoustic scattering of a high-order Bessel vortex beam by a rigid sphere," *Wave Motion,* vol. 48, no. 5, pp. 392-400, 2011.
[24] G. T. Silva, "Off-axis scattering of an ultrasound Bessel beam by a sphere," *IEEE Transactions on Ultrasonics Ferroelectrics and Frequency Control,* vol. 58, no. 2, pp. 298-304, 2011.
[25] F. G. Mitri, "Generalized theory of resonance excitation by sound scattering from an elastic spherical shell in a nonviscous fluid," *IEEE Transactions on Ultrasonics, Ferroelectrics and Frequency Control,* vol. 59, no. 8, pp. 1781-1790, 2012.
[26] F. G. Mitri, "Arbitrary scattering of an acoustical high-order Bessel trigonometric (non-vortex) beam by a compressible soft fluid sphere," *Ultrasonics,* vol. 53, no. 5, pp. 956-961, 2013.
[27] F. G. Mitri, "Negative axial radiation force on a fluid and elastic spheres illuminated by a high-order Bessel beam of progressive waves," *Journal of Physics a-Mathematical and Theoretical,* vol. 42, no. 24, p. 245202, 2009.
[28] F. G. Mitri, "Langevin Acoustic Radiation Force of a High-Order Bessel Beam on a Rigid Sphere," *IEEE Transactions on Ultrasonics Ferroelectrics and Frequency Control,* vol. 56, no. 5, pp. 1059-1064, 2009.
[29] M. Azarpeyvand, "Acoustic radiation force of a Bessel beam on a porous sphere," *The Journal of the Acoustical Society of America,* vol. 131, no. 6, pp. 4337-4348, 2012.
[30] G. T. Silva, J. H. Lopes, and F. G. Mitri, "Off-axial acoustic radiation force of repulsor and tractor bessel beams on a sphere," *IEEE Transactions on Ultrasonics, Ferroelectrics and Frequency Control,* vol. 60, no. 6, pp. 1207-1212, 2013.
[31] F. G. Mitri, T. P. Lobo, and G. T. Silva, "Axial acoustic radiation torque of a Bessel vortex beam on spherical shells," *Physical Review E,* vol. 85, no. 2, p. 026602, 2012.
[32] F. G. Mitri, T. P. Lobo, and G. T. Silva, "Erratum: Axial acoustic radiation torque of a Bessel vortex beam on spherical shells [Phys. Rev. E, 026602 (2012)]," *Physical Review E,* vol. 86, no. 5, p. 059902, 2012.
[33] G. T. Silva, T. P. Lobo, and F. G. Mitri, "Radiation torque produced by an arbitrary acoustic wave," *Epl,* vol. 97, no. 5, p. 54003, 2012.
[34] B. T. Hefner and P. L. Marston, "An acoustical helicoidal wave transducer with applications for the alignment of ultrasonic and underwater systems," *Journal of the Acoustical Society of America,* vol. 106, no. 6, pp. 3313-3316, 1999.
[35] K. Volke-Sepulveda, A. O. Santillan, and R. R. Boullosa, "Transfer of angular momentum to matter from acoustical vortices in free space," *Physical Review Letters,* vol. 100, no. 2, p. 024302, 2008.
[36] J. L. Ealo, J. J. Camacho, and C. Fritsch, "Airborne ultrasonic phased arrays using ferroelectrets: a new fabrication approach," *IEEE Transactions on Ultrasonics, Ferroelectrics and Frequency Control,* vol. 56, no. 4, pp. 848-858, 2009.
[37] A. O. Santillán and K. Volke-Sepúlveda, "A demonstration of rotating sound waves in free space and the transfer of their angular momentum to matter," *American Journal of Physics,* vol. 77, no. 3, p. 209, 2009.
[38] A. Anhäuser, R. Wunenburger, and E. Brasselet, "Acoustic Rotational Manipulation Using Orbital Angular Momentum Transfer," *Physical Review Letters,* vol. 109, no. 3, p. 034301, 2012.
[39] M. Abramowitz and I. A. Stegun, *Handbook of Mathematical Functions: with Formulas, Graphs, and Mathematical Tables*: Dover Publications, 1965.
[40] J. A. Stratton, *Electromagnetic Theory*: McGraw-Hill, New York, 1941.
[41] G. B. Arfken and H. J. Weber, *Mathematical Methods for Physicists*, 6th ed. San Diego, California: Academic Press, 2005.
[42] P. A. Martin, *Multiple Scattering - Interaction of Time-Harmonic Waves with N Obstacles*. Cambridge: Cambridge University Press, 2006.

Superpositions of Equal-Frequency Ordinary Bessel Beams: Frozen Waves for Optical Trapping and Micromanipulation

Leonardo A. AMBROSIO

Department of Electrical Engineering (SEL), São Carlos School of Engineering (EESC), University of São Paulo (USP), São Carlos, 13566-590, Brazil

leouspsc@gmail.com

Abstract

The theoretical description and characteristics of suitable superposition of equal-frequency ordinary Bessel beams, usually called *Frozen Waves*, are investigated for the first time in the framework of the generalized Lorenz-Mie theory. These types of waves, besides possessing all the properties intrinsically related to non-diffracting beams, are also capable of providing virtually any (arbitrarily chosen) longitudinal intensity patterns, which makes them attractive for optical trapping and manipulation systems.

1 Introduction

We are all very familiar with Bessel beams (BBs) and their optical trapping properties, particularly for their simplest (zero-order) version [1-3]. Their multi-ringed structure allows for multiple trapping along transverse planes relative to their optical axis with the advantage of self-reconstruction and long-range properties, for example.

However, single Bessel beams are not capable of providing any control over the longitudinal intensity pattern, i.e., once it is generated by a finite aperture at z = 0, we can no longer manipulate its longitudinal intensity within the range $0 \le z \le Z_{max}$, where Z_{max} (wich is intrinsically related to the aperture radius R) is the limit above which the BB loses its non-diffractive characteristic.

Recently, it has been proposed that Bessel beams can be superposed in order to achieve any desired longitudinal intensity pattern $F(z)$ along lossless or absorbent media. For example, in cylindrical coordinates (ρ,ϕ,z) the pattern of interest could be previously specified along $\rho = 0$. In this case, the BBs are endowed with the same operating frequency but, in order to add a new degree of freedom in the design and, simultaneously, to maintain some of the fundamental properties of each BB individually (*viz.*, non-diffractive or relative long-range nature and self-reconstruction), the longitudinal (transverse) wave numbers assume distinct values [4-7]. These types of waves have been called *Frozen Waves* (FWs) and can be easily generated by conventional methods such as computer generated holograms and spatial light modulators for applications including, but not limited to, long-range communication, atom guides, optical tweezers and bistouries, and so on [8].

Considering their advantages and potential applications in optical trapping and (micro)manipulating systems, in this work the generalized Lorenz-Mie theory (GLMT) is adopted in order to describe these Frozen Waves by means of the so-called beam-shape coefficients (BSCs) [9]. Then, the BSCs and GLMT are used to evaluate some field patterns and optical forces.

2 Theoretical Background

Under the *paraxial* approximation, let us superpose (2N+1) +z-propagating BBs, all with the same operating frequency but with distinct longitudinal or, equivalently, transverse wave numbers ($\exp(+i\omega t)$ is assumed). In cylindrical coordinates (ρ,ϕ,z) one can displace the composed beam by an amount (ρ_0,ϕ_0,z_0) in such a way that if the original BBs are linearly polarized either all along x or y, then the total **E** field is written, for lossless media, as

$$\mathbf{E} = \sum_{q=-N}^{N} A_q J_0\left(k_{\rho q}\sqrt{\rho^2+\rho_0^2-2\rho\rho_0\cos(\phi-\phi_0)}\right)\times e^{-ik_{zq}(z-z_0)}\begin{Bmatrix}\hat{x}\\ \hat{y}\end{Bmatrix} \tag{1}$$

where [4,5]

$$k_{zq} = Q + \frac{2\pi}{L}q \quad \left(0 \le Q \pm \frac{2\pi}{L}q \le \frac{n_{ref}\omega}{c}\right)$$
$$k_{\rho q} = \left(\frac{n_{ref}\omega}{c}\right)^2 - k_{zq}^2 \tag{2}$$
$$A_q = \frac{1}{L}\int_{-L/2}^{L/2} F(z)e^{i(2\pi/L)qz}dz$$

In Eqs. (1) and (2), $J_0(.)$ is the ordinary Bessel function, n_{ref} the real refractive index of the medium through which the wave propagates, c the speed of light in vacuum and k_{zq} and $k_{\rho q}$ the longitudinal and transverse wave numbers of the q-th BB, respectively. The desired longitudinal intensity pattern $F(z)$ along $\rho = 0$, limited within $-L/2 \le z \le +L/2$, is taken into account by the complex coefficients A_q, *i.e.*, each BB is suitably weighted with specific complex coefficients so that the amplitude and phase of the resulting pattern at the aperture located at the plane $z = z_a$ ($z_a < -L/2$) exactly reproduces $F(z)$.

Absorbent media could also be taken into account by assuming a complex wave vector, the implication of which being an additional exponential factor on the integrand of A_q [6,7].

In the framework of the GLMT, Eq. (1) must be described in terms of the BSCs [9]. In this work we chose the integral localized approximation (ILA) description due to its simplicity and because it does give us reliable physical insights, even though any other approach or technique would lead to similar results [10]. Using the results of a previous paper of the author for single ordinary Bessel beams [11], after some algebra one eventually gets

$$g_{n,TM\begin{Bmatrix}x\\y\end{Bmatrix}}^{0\,(FW)} = i\frac{2n(n+1)}{2n+1}\begin{Bmatrix}\cos\phi_0\\ \sin\phi_0\end{Bmatrix}\times \sum_{q=-N}^{N} A_q J_1(\varpi_q) J_1(\xi_q)\exp(ik_{zq}z_0), \tag{3}$$

$$g_{n,TE\begin{Bmatrix}x\\y\end{Bmatrix}}^{0\,(FW)} = i\frac{2n(n+1)}{2n+1}\begin{Bmatrix}\sin\phi_0\\ -\cos\phi_0\end{Bmatrix}\times \sum_{q=-N}^{N} A_q J_1(\varpi_q) J_1(\xi_q)\exp(ik_{zq}z_0), \tag{4}$$

$$\begin{aligned} g_{n,TM\begin{Bmatrix}x\\y\end{Bmatrix}}^{m\neq 0\,(FW)} = {} & \frac{1}{2}\left(\frac{-2i}{2n+1}\right)^{|m|-1}\times \sum_{q=-N}^{N} A_q \begin{Bmatrix}1\\ \mp i\end{Bmatrix} J_{|m|-1}(\varpi_q) J_{|m|-1}(\xi_q)\times \\ & \left[\cos(|m|-1)\phi_0 \mp i\sin(|m|-1)\phi_0\right] + \\ & \begin{Bmatrix}1\\ \pm i\end{Bmatrix} J_{|m|+1}(\varpi_q) J_{|m|+1}(\xi_q)\times \\ & \left[\cos(|m|+1)\phi_0 \mp i\sin(|m|+1)\phi_0\right]\times \\ & \exp(ik_{zq}z_0), \end{aligned} \tag{5}$$

$$\begin{aligned} g_{n,TE\begin{Bmatrix}x\\y\end{Bmatrix}}^{m\neq 0\,(FW)} = {} & \frac{1}{2}\left(\frac{-2i}{2n+1}\right)^{|m|-1}\times \sum_{q=-N}^{N} A_q \begin{Bmatrix}\mp i\\ -1\end{Bmatrix} J_{|m|-1}(\varpi_q) J_{|m|-1}(\xi_q)\times \\ & \left[\cos(|m|-1)\phi_0 \mp i\sin(|m|-1)\phi_0\right] + \\ & \begin{Bmatrix}\pm i\\ -1\end{Bmatrix} J_{|m|+1}(\varpi_q) J_{|m|+1}(\xi_q)\times \\ & \left[\cos(|m|+1)\phi_0 \mp i\sin(|m|+1)\phi_0\right]\times \\ & \exp(ik_{zq}z_0), \end{aligned} \tag{6}$$

where $\varpi_q = \sin\theta_{aq}(n+1/2)$ and $\xi = \rho_0 k\sin\theta_{aq}$, θ_{aq} being the axicon angle of the q-th BB. The usual nomenclature for the BSCs has been adopted [9]. Some normalization factors may be introduced in Eqs. (3)-(6) to emphasize the fact that we are not summing up (2N+1) beams individually generated by (2N+1) distinct power sources. The above equations, after normalization, should reproduce the plane wave *on-axis* case when one imposes $\rho_0 = 0, \phi_0 = 0, z_0 = 0$.

Eqs. (3)-(6) can be simplified for particular polarizations and spatial orientations of the beam. For example, an *on-axis* $(\rho_0 = 0, \phi_0 = 0, z_0 = 0)$ y-polarized FW is identified with conditions $g_{n,TE}^{m\neq\pm1} = g_{n,TM}^{m\neq\pm1} = 0$ and

$$g_{n,TM}^{m=\pm1} = \mp i0.5\sum_{q=-N}^{N} A_q\left(J_0(\varpi_q) - J_2(\varpi_q)\right) \tag{7}$$

$$g_{n,TE}^{m=\pm1} = \mp i g_{n,TM}^{m=\pm1}, \tag{8}$$

Eq. (8) being expected due to the symmetry relative to the z axis (axisymmetric case). Notice that the plane wave case can be recovered after imposing $\theta_{aq} \to 0$ and dividing Eqs. (7) and (8) by $\sum_{q=-N}^{N} A_q$.

3 Numerical Examples

Several interesting longitudinal intensity patterns may be chosen for trapping and manipulation purposes, such as $F(z)$ = *constant*, $F(z) = \exp(az)$ with $a > 0$ (a growing exponential), etc. Let us consider an x-polarized on-axis FW for which $F(z,\ \rho = 0) = \sin(3.25\pi z/L)$ within $-0.35L \le z \le 0.35L$, $L = 10^{-4}$ m. To create such a spatial pattern, one choice of parameters is $N = 25$, $Q = 0.8 n_{ref}\omega/c$ with $\omega = 1.77\times10^{15}$ rad/s and $n_{ref} = 1.33$ (water). Figure. 1 shows the three-dimensional intensity profile of the ideal (infinite energy) FW, while Figure. 2 is the FW expected from the (normalized) BSCs derived in this work in the context of the GLMT. Considering that the ILA, although extremely simple, is not an exact method to extract the BSCs from the GLMT, the similarity is quite remarkable. It is readily seen that points of stable equilibrium along z can be easily created. It must be emphasized, however, that the intensity patterns observed are created by ordinary propagating (not evanescent) BBs only, all of them with ideally constant intensity profile up to $z = 0.35L$. Thus, we have achieved longitudinal control over the field distribution, *i.e.*, for all practical purposes a new degree of freedom, from azimuthally symmetric non-diffracting beams.

The FW of Figure. 2 is now assumed to impinge on a simple spherical particle with three distinct diameters: d = 6, 12 and 18 μm. The longitudinal radiation pressure cross section $C_{pr,z}$ (in a.u.) for a relative refractive index of 1.05 (relative to $n_{ref} = 1.33$) as the FW is shifted along z by z_0 is shown in Figure. 3. It clearly reveals points of stable equilibrium and, consequently, effective trapping points. For each diameter, two such points are observed. Obviously, changing the argument of the sine function may increase the number of stable points even further.

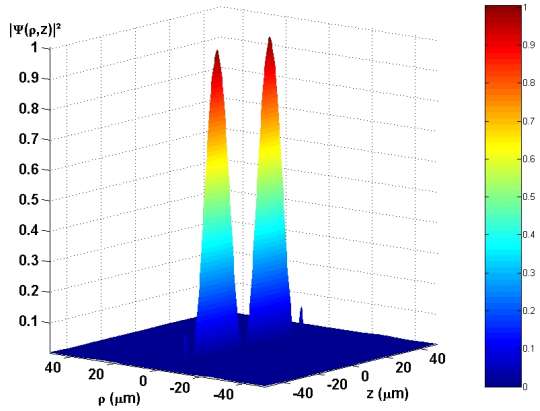


Figure 1 *Intensity pattern* $|\Psi(\rho,z)|^2$ *for a FW with F(z) =* $sin(3.25\pi z/L)$ *generated by an aperture with infinite radius (infinite energy)*

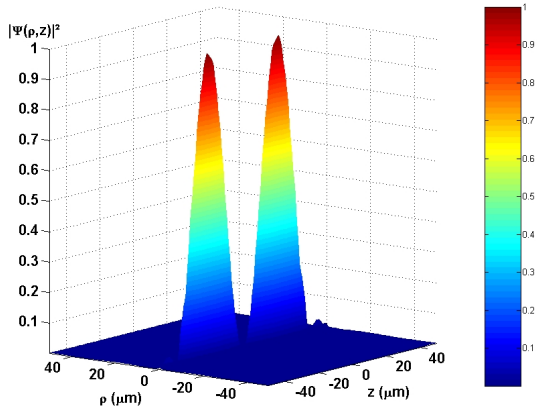


Figure 2 *Intensity pattern* $|\Psi(\rho,z)|^2$ *for a FW with F(z) =* $sin(3.25\pi z/L)$ *using the GLMT and the BSCs of Eqs. (3)-(6).*

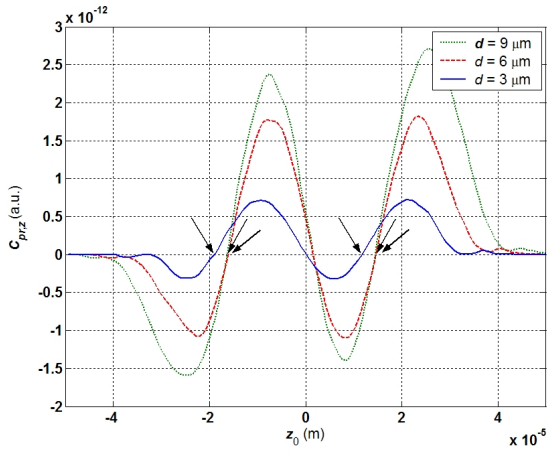


Figure 3 *Longitudinal forces over a spherical particle with d = 6, 12 and 18 μm for a relative refractive index of 1.05. Well-designed FWs can furnish several points of stable equilibrium (see the arrows) in concomitance with the relative long-range (non-diffracting) capabilities offered by Bessel beams.*

A certain transverse control over the intensity pattern can also be achieved by replacing the ordinary BBs by their higher-order versions. As a result $F(z)$ shifts from $\rho = 0$ to $\rho = a$, giving rise to a bright annular disk extending along z within the specified range $-Z_{max} \le z \le Z_{max}$ ($Z_{max} \le L/2$) [5,7]. I intend to comment on these points.

FWs present a high degree of flexibility in the design of virtually any $F(z)$ and are easy to generate using simple and current techniques. Besides, they carry the non-diffracting and self-reconstruction properties associated with Bessel beams, thus presenting themselves as strong candidates for laser beams in optical trapping and micro-manipulating systems.

4 Acknowledgement

The author would like to thank Michel Zamboni Rached for his kind comments and suggestions. Fapesp (*Fundação de Amparo à Pesquisa do Estado de São Paulo*), finantially supports this work.

5 References

[1] Garces-Chavez V., McGloin D., Melville H., Sibbett W., Dholakia K., Simultaneous micromanipulation in multiple planes using a self-reconstructing light beam, Nature 419:145-147 (2002).

[2] Garces-Chavez V., Roskey D., Summers M. D., Melville H., McGloin D., Wright E. M., Dholakia K., Optical levitation in a Bessel light beam, Appl. Phys. Lett. 85(18):4001-4003 (2004).

[3] Milne G., Dholakia K., McGloin D., Volke-Sepulveda K., Zemánek P., Transverse particle dynamics in a Bessel beam, Opt. Express 15(21):13972-13987 (2007).

[4] Zamboni-Rached M., Stationary optical wavefields with arbitrary longitudinal shape, by superposing equal frequency Bessel beams: Frozen Waves, Opt. Express 12(17):4001-4006 (2004).

[5] Zamboni-Rached M., Recami E., Hernández-Figueroa H. E., Theory of "frozen waves": modeling the shape of stationary wave fields, J. Opt. Soc. Am. A 22(11):2465-2475 (2005).

[6] Zamboni-Rached M., Diffraction-Attenuation resistant beams in absorbing media, Opt. Express 14(5):1804-1809 (2006).

[7] Zamboni-Rached M., Ambrosio L. A., Hernández-Figueroa H. E., Diffraction-attenuation resistant beams: their higher-order versions and finite-aperture generations, Appl. Opt. 49(30):5861-5869 (2011).

[8] Vieira T. A., Gesualdi M. R. R., Zamboni-Rached M., Frozen waves: experimental generation, Optics Letters 37(11):2034-2036 (2012).

[9] G. Gouesbet, and G. Gréhan, *Generalized Lorenz-Mie Theories*, (Springer-Verlag, Berlin-Heidelberg, 2011).

[10] Ren K. F., Gouesbet G., Gréhan G., Integral localized approximation in generalized Lorenz-Mie theory, Appl. Optics 37(19):4218-4225 (1998).

[11] Ambrosio L. A., Hernández-Figueroa H. E., Integral localized approximation description of ordinary Bessel beams and application to optical trapping forces, Biomed. Opt. Express 2(7):1893-1906 (2011).

Complex shaped particles & aggregates

On the electromagnetic scattering of arbitrary shaped beams by arbitrary shaped particles : a review

Gérard GOUESBET[1] , James A. LOCK[2]

[1] Département : Optique et Lasers, CORIA UMR 6614 CNRS/INSA et Université de Rouen, Saint-Etienne-du Rouvray, 76801, France.

[2] Department of Physics, Cleveland State University, Cleveland, Ohio, 44115, USA

*Corresponding author: Gouesbet@coria.fr

Abstract

Since the Lorenz-Mie theory describing the electromagnetic scattering of a plane wave by a homogeneous spherical particle, light scattering theories (and applications) based upon it have essentially developed along two streams (i) from plane waves to arbitrary shaped beams and, (ii) from homogeneous spherical particles to arbitrary shaped particles. The present paper presents a review devoted to a synthetic and unified view of these two streams.

1 T-matrix methods.

The unified view mentioned in the abstract relies on two ingredients (i) an up-to-dated definition of the expression "T-matrix method" and (ii) the relationship between expansions of electromagnetic beams in terms of elementary basis functions such as spherical multipoles or plane waves.

Regarding the expression "T-matrix method", it is traditionally considered as synonymous with the Extended Boundary Condition Method (EBCM). This is somewhat confusing and misleading as discussed in [1]. We believe that from now on, a strong clarification of the terminology is required. A good definition, adapted from a series of T-matrix reference databases, e.g. [2], may be as follows : In "*a*" T-matrix method, the incident and scattered fields are expanded in series of suitable vector spherical wave functions (*or in an equivalent form*), and the relation between the columns of the respective expansion coefficients is established by means of a transition matrix (or T-matrix).

As stated in [2], this definition is more inclusive than the original notion of the EBCM. Therefore, any method allowing one to evaluate the components of the T-matrix may be called "*a*" T-matrix method. Any scattering theory relying on "*a*" T-matrix method then may be said to pertain to "*the*" T-matrix formulation. In this paper, we shall essentially deal with two T-matrix methods, namely EBCM and GLMT (generalized Lorenz-Mie theory). The second issue of unification (item (ii) above) will then consist in a formal way to express the beam shape coefficients of the GLMT versus the plane wave spectra of EBCM, and vice versa.

2 Beam shape coefficients and GLMT.

The GLMT deals with the scattering of an arbitrary shaped beam by a homogeneous spherical particle defined by its diameter d and its complex refractive index M , by relying on the method of separation of variables. The illuminating beam may be described in terms of scalar potentials, such as the Bromwich scalar potentials, or in terms of vector spherical wave functions (VSWFs). The expansion of the illuminating beam in terms of VSWFs reads as (limiting ourselves to expressions related to the electric field) [1] :

$$\mathbf{E}^i = \sum_{n=1}^{\infty}\sum_{m=-n}^{+n}[a_{mn}\mathbf{M}_{mn}^{(1)}(k\mathbf{r}) + b_{mn}\mathbf{N}_{mn}^{(1)}(k\mathbf{r})] \qquad (1)$$

in which $\mathbf{M}^{(1)}$ and $\mathbf{N}^{(1)}$ are Vector Spherical Wave Functions (VSWFs) of the first type, a_{mn} and b_{mn} are expansion coefficients, k is the wave-number and $\mathbf{r}$ is the position vector. It is valid for any arbitrary beam description in spherical coordinates, independent of the shape of the particular scattering particle under consideration. In the Bromwich scalar formalism of the GLMT, already introduced in 1982 [3], field expansions are expressed by using two sets of beam shape coefficients (BSCs) $g_{n,TM}^{m}$ (associated with the radial component of the electric field) and $g_{n,TE}^{m}$ (associated with the radial component of the magnetic field) which have been originally defined in such a way that they reduce to simple expressions in the case of axisymmetric beams, including plane waves [4]. There exists a relationship between the expansion coefficients of Eq. 1 and the BSCs, e.g. :

$$b_{mn} = kE_0 c_n^{pw}(-1)^m(-1)^{(m-|m|)/2}\frac{(n-m)!}{(n-|m|)!}g_{n,TM}^{m} \qquad (2)$$

in which c_n^{pw} ("pw" standing for plane wave) are coefficients naturally appearing in the Bromwich formulation of the LMT [3]. Eq.2 shows that the expansion coefficients b_{mn} are of the TM -kind (associated with the electric field). There exists a similar relation between the TE -expansion coefficients a_{mn} (associated with the magnetic field) and the BSCs $g_{n,TE}^{m}$.

The expansion in terms of VSWFs of the scattered beam reads [1] :

$$\mathbf{E}^s = \sum_{n=1}^{\infty}\sum_{m=-n}^{+n}[r_{mn}\mathbf{M}_{mn}^{(4)}(k\mathbf{r}) + s_{mn}\mathbf{N}_{mn}^{(4)}(k\mathbf{r})] \quad (3)$$

in which VSWFs are now of the fourth-type where the time dependence is assumed to be $\exp(i\omega t)$.

From Eqs. 1 and 3, and using the results obtained in the framework of the GLMT for a homogeneous spherical particle, we obtain [1] :

$$\begin{pmatrix} r_{mn} \\ s_{mn} \end{pmatrix} = \mathbf{T}\begin{pmatrix} a_{mn} \\ b_{mn} \end{pmatrix} \quad (4)$$

in which the matrix $\mathbf{T}$ reads as :

$$\mathbf{T} = -\begin{pmatrix} b_n & 0 \\ 0 & a_n \end{pmatrix} \quad (5)$$

in which a_n and b_n are the usual scattering coefficients of the classical LMT, depending only on the particle, and $\mathbf{T}$ is a "degenerate" T-matrix. Actually, because the expansion coefficients possess two subscripts, the non-degenerate T-matrix is not a 2x2 matrix but the form of Eq.5 is here sufficient for our purpose. In particular, we observe that it does not depend on the arbitrary shaped beam under discussion, illustrating that ([5], p41) : *the elements of the T-matrix are independent of the incident and scattered fields.* Therefore, problems associated with the shape of the particles are disconnected from problems associated with the shape of the beams. The first kind of problems are solved by any T-matrix method. The second kind of problems are specific to the illuminating beam description. In spherical coordinates, this description may be encoded by the two sets of BSCs $g_{n,TM}^m$ and $g_{n,TE}^m$ associated with a set of discrete basis of functions. Another description may be encoded by two plane wave spectral components $S_x^E(k_x,k_y)$ and $S_y^E(k_x,k_y)$.

3 Plane wave spectra and EBCM.

The use of plane wave spectra is the standard method to express arbitrary shaped beams in EBCM. We may introduce two vectorial plane wave spectra, one $\mathbf{S}^E$ associated with the electric field and the other one $\mathbf{S}^H$ associated with the magnetic field. The two plane wave spectral components $S_x^E(k_x,k_y)$ and $S_y^E(k_x,k_y)$ may be defined by Fourier transforms of the transverse components of the field $\mathbf{E}$ in the plane $z=0$ according to [6] :

$$\begin{pmatrix} S_x^E(k_x,k_y) \\ S_y^E(k_x,k_y) \end{pmatrix} = \frac{k^2}{4\pi^2}\int_{-\infty}^{+\infty}\int_{-\infty}^{+\infty}\begin{pmatrix} E_x(x,y,0) \\ E_y(x,y,0) \end{pmatrix}\exp\left[-i(k_x x + k_y y)\right]dxdy \quad (6)$$

The other spectral component S_z^E and the components of the magnetic spectral vector $\mathbf{S}_i^H\,(i=x,y,z)$ can then be obtained by using Maxwell's equations, e.g.[7].

4 Relationship between BSCs and spectra.

The description of the illumating beam may then be expressed in terms of *two* sets of BSCs or in terms of *two* sets of plane wave spectral components. The formal relationship between these two different descriptions is established in a companion paper [8]. The results (not the demonstrations) obtained will be reproduced here and commented on. In particular the relationship between BSCs and spectra immediately establishes a relationship between GLMT and EBCM whose consequences will be discussed.

5 Reviews.

A better understanding of the material introduced above will afterward be provided by putting it in perspective, reviewing different issues as follows.

1. A historical background of the use of plane wave spectra will be reviewed, particularly in connection with its use in EBCM.

2. The different particle shapes which have been investigated by using GLMTs (arbitrary shaped beams) will be reviewed.

3. The use of EBCM for arbitrary shaped beams will be reviewed.

4. Different kinds of expansions used to describe illuminating shaped beams (discrete or continuous basis), associated with different coordinate systems, including the distinction between intrinsic and extrinsic methods (e.g. [6]), will be reviewed, illustrating different aspects of the theory of representations of arbitrary shaped beams.

5. The different T-matrix methods, beside EBCM and GLMTs will be reviewed.

6 Problems and solutions to problems.

Recently, a list of problems for future research in generalized Lorenz-Mie theories and related topics has been published [10]. The material provided in this paper and the companion paper [8] provides solutions or hints to solutions for some problems. These are :

Problem 1 : "Develop a general theory of coordinate transformations for extrinsic evaluations of beam shape coefficients". This problem may be better relabeled as "Develop a general theory of representations for the description of illuminating beams". The relationship between BSCs in GLMT and plane wave spectra, as well as many associated comments, contribute to this problem.

Problem 12 : "Study computational issues related to the plane-wave spectrum approach". Elements of information for this problem will be provided in Review 3 above.

Problem 12 : "Implement a localized model in EBCM". The new material obtained provides a better understanding of the problem, and actually also provides a solution to it.

Problem 14 : "Extend the EBCM to arbitrary-shaped beams with the use of beam shape coefficients". Similarly, this problem is now much better understood and new comments will be provided.

Problem 15 : "Examine the remodeling process of the angular-spectrum representation". This problem now has a very clear solution.

Problem 16 : "Examination of the remodeling process of the angular-spectrum representation for the particular case of a Gaussian beam ". This problem now also has a solution.

7 References

[1] G. Gouesbet. T-matrix formulation and generalized Lorenz-Mie theories in spherical coordinates. *Optics Communications*, 283:517-521 (2010)

[2] N. T. Zakharova, G. Videen, and N.G. Khlebtsov. Comprehensive T-matrix reference database : A 2009-2011 update. *Journal of Quantitative Spectroscopy and Radiative Transfer*, 113:1844-1852 (2012)

[3] G. Gouesbet and G. Gréhan. Sur la généralisation de la théorie de Lorenz-Mie. *Journal of Optics*, 13, 2:97-103 (1982)

[4] G. Gouesbet. Partial wave expansions and properties of axisymmetric light beams. *Applied Optics*, 35,9:1543-1555 (1996)

[5] M.I. Mishchenko, J.W. Hovenier, and L.D. Travis, editors. Light scattering by nonspherical particles. Theory, measurements and applications (Academic Press 2000)

[6] S. Colak, C. Yeh, and L.W. Casperson. Scattering of focused beams by tenuous particles. *Applied Optics*, 18:294-302 (1979)

[7] J.A. Lock. Angular spectrum and localized model of Davis-type beam. *Journal of the Optical Society of America A*, 30, 3:489-500 (2013)

[8] G. Gouesbet and J.A. Lock. On the description of electromagnetic arbitrary shaped beams : beam shape coefficients versus plane wave spectra, and vice versa. Abstract submitted to LIP2014, Marseille. *Paper under preparation* (2014)

[9] G. Gouesbet, F. Xu, and Y.P. Han. Expanded description of electromagnetic arbitrary shaped beam in spheroidal coordinates for use in light scattering theories : A review. *Journal of Quantitative Spectroscopy and Ra-diative Transfer*, 112:2249-2267 (2011)

[10] G. Gouesbet and J.A. Lock. A list of problems for future research in generalized Lorenz-Mie theories and related topics, review and prospectus; commemorative invited paper, for the 50th anniversary of "Applied Optics", Applied Optics, 52, 5 : 897-916 (2013)

Light scattering on single evaporating microdroplet of suspension: Fano resonances and surface pressure

Maciej KOLWAS*, Genadij DERKACHOV, Daniel JAKUBCZYK, Krystyna KOLWAS and Justice ARCHER

Institute of Physics of the Polish Academy of Sciences, al Lotnikow 32/46, 02-668 Warszawa, Poland

*Corresponding author: kolwas@ifpan.edu.pl

Abstract

We study light scattering on single microdroplet of suspension composed of SiO_2 spherical inclusions (225 nm radius) in ethylene glycol. Fano resonances were observed during formation of inclusion's surface on the wet object. The phenomenon is interpreted as interference of single scattering with multiple scattering on inclusions when their distances approach light wavelength. The evolution of effective surface pressure (isotherm) found from droplet radius evolution shows that the Fano profile is coinciding with the region of compression of inclusions being in a state of surface gas.

1 Introduction

The resonance phenomenon is one of the most fundamental physical phenomena present in all branches of science. The efficiency of most modern optoelectronic devices [e.g. 1] is based on different kinds of resonances. Among few important notions of resonance phenomena, the Fano resonance [2] – an overlap of constructive and destructive interferences when narrow, discrete band resonance coincide with broadband one [3] has been found in plasmonic nanoparticles, photonic crystals, and electromagnetic metamaterials [4].

The interference of narrow structures with broadband one seems to be present and is observable in significant part of photonics and especially in the scattering of light on composite media [e.g. 5].

In diagnostics of all scale materials - micro and nano, the propagation and scattering of light plays crucial role. Metamaterials [6], layered materials [7], photonic crystals [8] and generally materials with sophisticated effective index of refraction [9] seem to be the future of optoelectronics and photonics. The spectral efficiency of these materials is often based on superposition of narrow-band and broad band phenomena. This makes the Fano type resonances an inherent part of such phenomena.

We observed Fano resonance in intensity of light scattered on evaporating droplet, during the stage of formation of surface layer formed by inclusions, when scattering on separate inclusions transforms into scattering on rough surface of aggregate.

2 Experiment and results

We investigated evaporation of microdroplet of glycol solution of SiO_2 standardized spherical inclusions. The process of evaporation of liquid led to aggregation [10, 11] of inclusions. Single droplets were trapped inside stabilized electrodynamic trap [12, 13, 14].

The index of refraction of used glycols was comparable with the index of inclusions, hence, inclusions scattered light only when they were at the droplet surface. Therefore, at the beginning of evaporation, the scattering was just due to the scattering on the droplet. As evaporation progresses, inclusions appear on the droplet surface leading to scattering on aggregates of inclusions [10, 11].

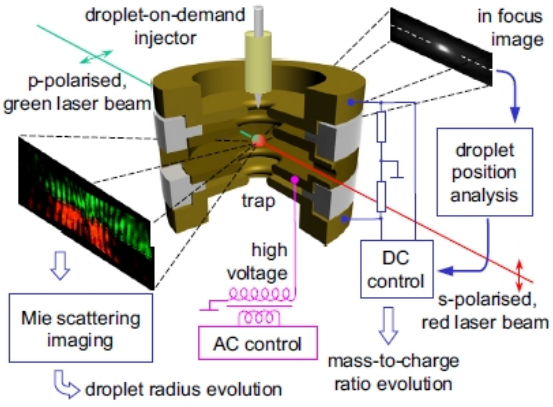


Figure 1 *Experimental set-up.*

Our experimental set-up allowed observing scattering of two laser lights on freely levitating droplet of suspension [12, 13]. We used red vertically (s) polarized laser light with the observation of vertically polarized scattered light I_{VV} and red cross polarized light I_{VH}; and green horizontally (p) polarized laser light with the observation of horizontally polarized scattered light I_{HH} and green cross polarized light I_{HV}.

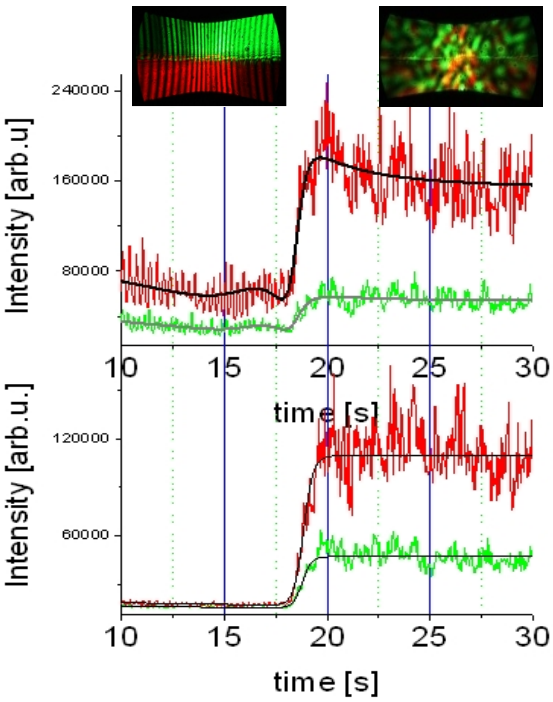


Figure 2 *The intensities of scattered light I_{VV} and I_{HH} (top) and cross-polarize I_{HV} and I_{VH} (bottom) together with fitted model. Inset – observed scattering pattern for given time as function of angle ϕ (vertical) and Θ. Left inset – interference fringes (t=0), right –speckles seen at the end of evaporation.*

The scattering intensities I (ϕ, Θ, t) were observed at an angle Θ=90±16.24° (azimuth) and ϕ=0±5.33° (elevation). Their interference patterns (fringes) were fitted to Mie theory to find droplet radius evolution, and then they were integrated over angles of observation ϕ and Θ to obtain time dependent signals I_{VV}, I_{HH}, I_{VH} and I_{HV}. Additionally, measurements of droplet position stabilization voltage was used to observe droplet mass evolution [12] and made possible the determination of droplet radius when speckled scattering on rough surface excluded application of Mie theory.

Examples of time evolution of scattered light intensities I_{VV} and I_{HH} and intensities of cross polarized scattered light I_{VH} and I_{HV} together with fitted evolution are shown in the Figure 2.

We simulate intensities of scattered light as sigmoid (logistic) function of time B (t) (Figure 2, 3),

$$B(t) = P2(t) + (P1(t) - P2(t))/(1 + \exp((t - P3)/P4))$$

showing transition from one linear in time region (described with P1(t) - scattering on droplet of liquid ca. 0-15 s)) to the second linear in time region (P2(t)) – the scattering on aggregate (beyond 25s). The additional structure before (ca.17s) and after fast increase (ca. 20s) of intensities I_{VV} and I_{HH} is described as the Fano profile function F(t) added to B(t):

$$F(t) = P5 \cdot (P6 \cdot P7 + t - P8)^2 / (P7^2 + (t - P8)^2$$

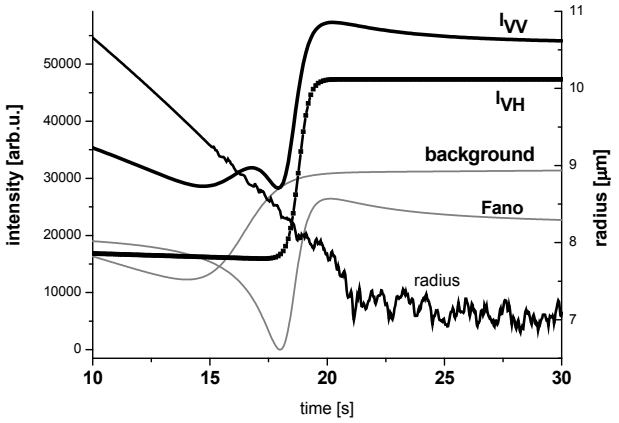


Figure 3 *Fitted intensities I_{VV} and I_{VH} and the decomposition of I_{VV} on Fano profile and background B(t) (gray). The experimental time evolution of droplet radius is shown for comparison.*

3 Fano resonance and surface isotherm

From evolution of droplet radius, the effective surface pressure (activity) isotherm of surface layer of inclusions - can be found [15, 11]. The surface pressure ***sp*** can be found as the difference between surface tension of "pure" glycol and surface tension of solution:

$$sp \equiv \sigma_L - \sigma \propto a(t) \cdot \ln\left(\frac{a(t_0)a'(t_0)}{a(t)a'(t)}\right)$$

Where a is droplet radius; $a' = da/dt$

We assumed that at the beginning of evaporation ($t=t_0$) the droplet was evaporating as droplet of pure liquid. For slowly evaporating liquids like all glycols the humidity of its vapor far from droplet is extremely low and can be equated to 0.

Surface pressure starts to grow when scattering on inclusions starts to be visible on polarization I_{VV} or I_{HH} (ca. 10 μm). The formation of surface seen as sudden increase of intensity I_{VH} (and I_{HV}) due to the multiple scattering (8.7-7.7 μm) is appearing when the phase transition surface gas-liquid (region with "constant" pressure between gas and liquid) is present.

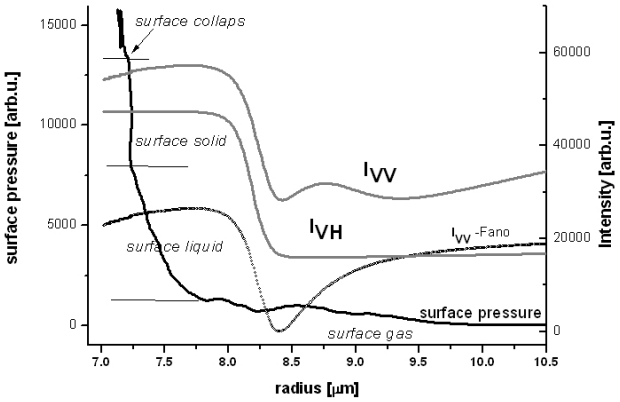


Figure 3 *The surface pressure isotherm. Surface pressure evolution as function of droplet radius. Fitted Intensity* I_{VV} *and Fano resonance part of* I_{VV} *and* I_{VH} *showing coincidence with compression part of surface evolution.*

Then the succeeding formation of less compressible state of surface liquid is seen in cross polarized light (here I_{VH}) as stabilization of signal (below ca 7.75 μm). The maximum of the Fano profile at ca. 7.75 μm coincides with the beginning of the state of surface liquid as well.

4 Conclusion

The formation of surface layer on evaporating droplet of suspension can lead to several resonance phenomena observed in light scattering. This phenomena results in a part from adjusting of distances of inclusions and their structure to light wavelength. This can be observed and measured with light scattering. Especially interesting seems to be phenomena of Fano type visualizing the creation of coherent scattering. We observed Fano resonance during the stage of formation of surface, when scattering on separate inclusions transforms into scattering on rough surface of aggregate.

The narrow-band (in time/radius) scattering was appearing when loose inclusions formed surface on the droplet with their distances <x> close to the light wavelength λ . At this stage of evaporation the surface behaves similarly to a layered structure. This phenomenon of enhancement of scattering can be called superscattering [16, 17]. It can be understood as a synchronization of (multiple) scattering on different inclusions (compare [5, 10]).The interference of superscattering with the broad band (single) scattering on inclusions can lead to interference and appearance of the Fano profile.

5 References

[1] K.F. Brennan, *The physics of semiconductors with applications to optoelectronic devices*(Cambridge University Press, NewYork 1999)

[2] U. Fano, *Sullo spettro di assorbimento dei gas nobili presso il l imite dello spettro d'arco* Nuovo Cimento 12, 154–161 (1935)

[3] A. Miroshnichenko, S Flach, Y.Kivshar, *Fano resonances in nanoscale structures*Rev. Mod. Phys., 82, 2257 - 2290 (2010)

[4] B. Luk'yanchuk, N. Zheludev, S. A. Maier, N.J. Halas, P. Nordlander, H. Giessen and Chong Tow Chong, *The Fano resonance in plasmonic nanostructures and metamaterials*, Nature Materials 9, 707–715 (2010)

[5] V.L. Shalaev (ed) *Optical Properties of Nanostructured Random Media* (Springer, Berlin2010)

[6] V.L. Shalaev *Optical negative-index metamaterials* Nature Photonics 1,41-48 (2007)

[7] SM Auerbach, KA Carrado, PK Dutta Ed.S.M. Auerbach, K.A. Carrado, P.K. Dutta *Handbook of Layered Materials*(Marcel Dekker, Inc., New York 2004)

[8] R. D. Joannopoulos, S.G Johnson, R.D.Meade, *Photonic crystals molding the flow of light* (Princeton University Press, Princeton 2008)

[9] E.Wolf, *Progress in Optics 51* (Elsevier 2008)

[10] G. Derkachov, K. Kolwas, D. Jakubczyk, M. Zientara, and M. Kolwas, *Drying of a Microdroplet of Water Suspension of Nanoparticles: from Surface Aggregates to Microcrystal* J. Phys. Chem. C 112, 16919–16923 (2008)

[11] D. Jakubczyk, M. Kolwas, G. Derkachov, and K. Kolwas, *Surface States of Microdroplet of Suspension* J. Phys. Chem. C 113, 10598–10602(2009)

[12] D. Jakubczyk, G.Derkachov, M.Kolwas, K.Kolwas, *Combining weighting and scatterometry: Application to a levitated droplet of suspension* JQSRT , 126 99–104(2013)

[13] M. Kolwas, D.Jakubczyk, G.Derkachov, K.Kolwas, *Interaction of optical Whispering Gallery Modes with the surface layer of evaporating droplet of suspension,* JQSRT 131, 138(2013)

[14] D. Jakubczyk, G. Derkachov, M. Zientara, M. Kolwas, and K. Kolwas, *Local-field resonance in light scattering by a single water droplet with spherical dielectric inclusions* J. Opt. Soc. Am. A 21, 2320 – 2323 (2004)

[15] A. Adamson, A. P Gast, *Physical Chemistry of Surfaces*,(Wiley New York, 1997)

[16] Z. Ruan and S. Fan, *Design of subwavelength superscattering nanospheres,* Appl. Phys. Lett.98, 043101(2011).

[17] Z. Ruan and S. Fan, *Superscattering of light from subwavelength nanostructures,* PRL 105, 013901 (2010)

ELECTROMAGNETIC MODELING OF SUNSCREEN PROTECTION

Marie LECUREUX[1-2*], Carole DEUMIE[2] and Stefan ENOCH[2]

[1] Naos Recherche, Aix-en-Provence, 13856, France
[2] Aix-Marseille Université, CNRS, Centrale Marseille, Fresnel Institut, UMR 7249, Marseille, 1013, France
* marie.lecureux@fresnel.fr

Abstract

Sunscreens are used as UV filters, in order to protect people from sun damages. The sunscreen quality is given by the sun protection factor (SPF), measured *in vivo*. In order to avoid long and complicated tests, a quick and simple *in vitro* method has been established, which gives an approximation of the SPF. Going a little further, we have elaborated a calculation method, using differential method for solving Maxwell equations, which allow us to know the transmission of light through sunscreen applied on a substrate. We compared our results to an other calculation method but also to *in vitro* measurements.

1 System studied

A sunblock is an emulsion of several phases, containing many ingredients such as filters, emulsifier, solvent or conservative. Filters are the main compounds that provide the sunscreen efficiency. They are divided in two types: the chemical ones (organic molecules that absorb UV light) and inorganic particulates (such as TiO2) scattering UV light.

The whole system is spread on the skin for *in vivo* tests. *In vitro,* the sunscreen efficiency evaluation consists in the measurement of the transmission of the cream applied on a Polymethyl Methacrylate (PMMA) substrate [1].

The transmission measurements are highly dependent on the distribution of the sunscreen on the substrate [2,3]. In order to take into account this distribution, we observe the samples by using an Optical Coherence Tomography device [4] (Figure. 1). The PMMA surface is metalized before the sunscreen deposition in order to increase the optical contrast between the sunscreen and the PMMA.

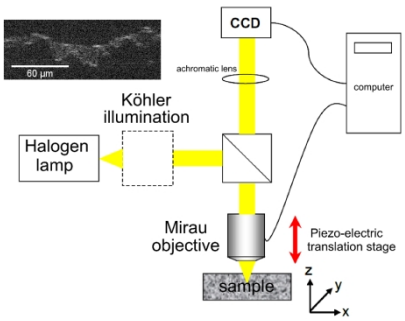


Figure 1 *Optical Coherence Tomography device configuration and example of one image*

2 Simulation of the suncreen protection

2.1 The differential method

We choose to use, as our first calculation method, a differential method to solve the Maxwell equations. This method calculates the transmission of 2D structures [5]. We consider three areas (Figure. 2). The superstrate (the air), above the cream, and the substrate below are supposed to be homogenous, linear and isotropic.

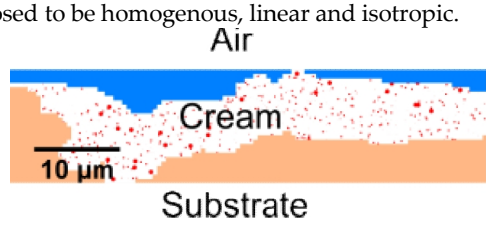


Figure 2 *Example of a matrix used in the differential method*

Substantial differences can be observed depending on the location on the image: the distribution and the quantity of cream are not the same on all the areas on the PMMA plate [6]. Here we can find some images obtained by OCT device (Figure. 3).



Figure 3 *15 figures from images of 55µm long of the OCT device. The air is represented in blue, the sunscreen is white and the substrate (the PMMA plate) the salmon color.*

From the images on each area, we calculate the transmission, and we keep the extinction of the mean transmission as the relevant value. The extinction is defined by Eq. (1) :

$$\text{Extinction} = -\log(T) \tag{1}$$

where T is defined by Eq. (2) :

$$T = \sum_{transmitted} Eff \tag{2}$$

Eff is the Poynting vector flux through a parallel surface of the average plane of the structure divided by the incident flux. The sum is taken over all the transmitted modes.

Given the sunscreen repartition on substrate and the characteristics of the filters, we were able to compare our simulated results to measurements and another model: the Step-Film model (Figure. 4).

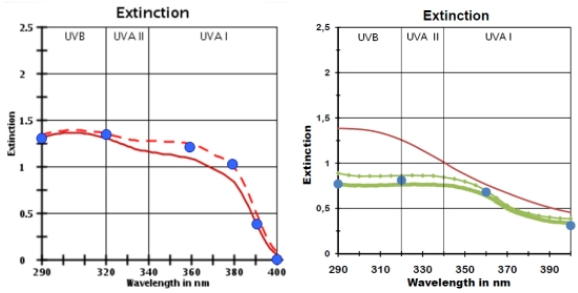


Figure 4 *Left: Extinction of a chemical sunscreen. The dashed and continuous red lines correspond to the step-film model (with resp. the chemicals compounds degraded and not degraded). The blue points correspond to the results of our electromagnetic simulations. Right: Extinction of a physical sunscreen. The green lines correspond to spectrometer measurements on two different samples. The blue points correspond to the results of our simulations. We choose to compare our simulations with measurements because in this case the step-film model (represented by the red line) did not match the measurements.*

2.2 . Calculation model improvement

The method used is rather slow (it takes approximately 130 hours per wavelength) and it cannot be used to anticipate every type of particles (metals cannot be taken into account for example – because it's a 2D method). In order to improve our model that is to say to find faster methods with a domain of validity more extended we tried several techniques: scattering by a set of parallel cylinder [7], Mie scattering [8] [9] or the finite element method [10].

In order to do so, we have separated the influence of the cream and the interface (Figure. 5)

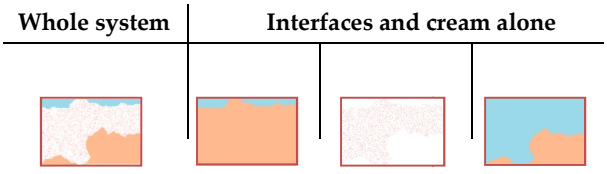


Figure 5 *Decomposition of the system in order to simplify our model*

3 Study of the influence of some parameters on the UV protection

Using the electromagnetic model, we have been able to study the impact of changes in the substrate (PMMA, skin hydrate or dehydrate Figure. 6).

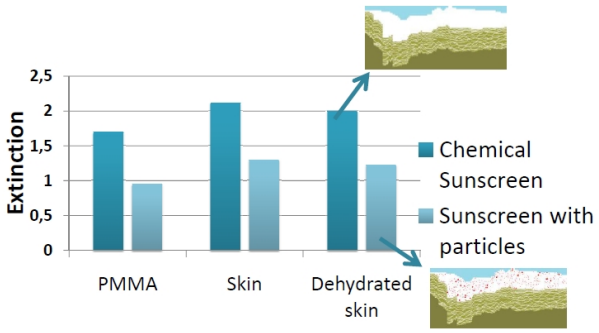


Figure 6 *Extinction of two sunscreens applied on different substrates*

We also studied the influence of some of the particles characteristics: diameters (Figure. 7), refractive index, shape or distribution inside the sunscreen.

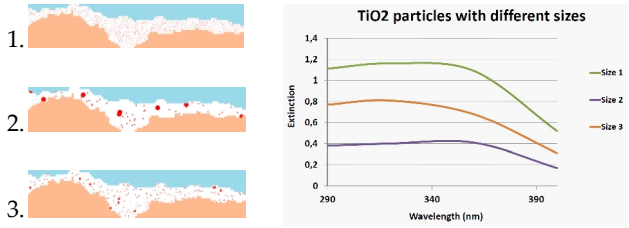


Figure 7 *The same cream and particles with 3 different sizes. We can note that as we put the same quantity of TiO2, the number of particles varies a lot.*

4 References

[1] B. L. Diffey and J. Robson, A new substrate to measure sunscreen protection factors throughout the ultraviolet spectrum, J. Soc. Cosmet. Chem. 40:127-133 (1989).

[2] L. Ferrero, M. Pissavini and O. Doucet, How a calculated model of sunscreen film geometry can explain *in vitro* and *in vivo* SPF variation, Photochem. Photobiol. Sci. 9:540-551 (2010).

[3] L. Ferrero, M. Pissavini, S. Marguerie and L. Zastrow, Efficiency of a continuous height distribution model of sunscreen film geometry to predict a realistic sun protection factor, J. Cosmet. Sci. 54:463-481 (2003).

[4] D. Huang, E.A. Swanson, C. P. Lin, J. S. Schuman, W. G. Stinson, W. Chang, M. R. Hee, T. Flotte, K. Gregory, C. A. Puliafito and J. G. Fujimoto, Optical Coherence Tomography, Science 254:1178-1181 (1991) .

[5] L. Arnaud,G. Georges, C. Deumie and C. Amra, Discrimination of surface and bulk scattering of arbitrary level based on angle-resolved ellipsometry: Theorical analysis, Optics Communications 281:1739-1744 (2008).

[6] M. Pissavini, B. Diffey, S. Marguerie, T. Carayol and O. Doucet, Predicting the efficacy of sunscreens in vivo veritas, International Journal of Cosmetic Science 34 :44-48 (2011).

[7] D. Felbacq, G. Tayeb and D. Maystre, Scattering by a random set of parallel cylinders, J. Opt. Soc. Am. 11:2526-2538 (1994)

[8] C.F. Bohren, and D.R. Huffman, *Absorption and scattering of light by small particles* (Wiley, New-York, 1983).

[9] H.C. vand de Hulst, *Light Scattering by Small Particles* (Dover Publications, New-York, 1981)

[10] J. Jin, *The Finite Element Method in Electromagnetics* (Wiley, New-York, 2002)

HELICITY RESONANCES IN SPHERES

Xavier ZAMBRANA-PUYALTO[1,2*], Gabriel MOLINA-TERRIZA[1,2]

[1] Department of Physics and Astronomy, Macquarie University, 2109 NSW, Australia
[2] ARC Center of Excellence for Engineered Quantum Systems, Macquarie University, 2109 NSW, Australia
Corresponding author: xavier.zambranapuyalto@mq.edu.au

Abstract

We present a framework to systematically study the duality properties of scatterers. The duality properties of a scatterer are related to the polarization change that a particle excerpts on a light beam. Our formalism can be applied to any geometry and material, but we develop it in the context of spherical scatterers. Due to their symmetries, we can formulate the problem semi-analytically using the Generalized Lorenz-Mie Theory.

1 Introduction

The Generalized Lorenz-Mie Theory (GLMT) has proved to be very useful to study a myriad of electromagnetic (EM) problems [1]. However, its formulation in terms of scalar potentials usually blurs the symmetries of the systems. Here, not only we exploit those symmetries but also introduce a symmetry that usually has been overlooked in scattering problems: EM duality symmetry. Duality symmetry compares the behaviour of electric and magnetic fields on an arbitrary medium [2]. Due to the lack of magnetic monopoles in nature, this symmetry is intrinsically broken for any medium different from vacuum [2]. However, as it was proven in [3], this symmetry can be restored in an isotropic medium when the ratio between the electric and magnetic constants is constant, *i.e.*

$$\varepsilon(\boldsymbol{r})/\mu(\boldsymbol{r}) = const. \tag{1}$$

We will denote a system that fulfils Eq. (1) as ``dual". Dual media are interesting, among many other things, because they can be used to make perfect light rotators [4] or to preserve the polarization of the EM field upon interaction [3,4,5]. In fact, in order to derive these last two results, it is important to link duality symmetry to the helicity of light. It can be proven that a medium is dual when it preserves the helicity content of any arbitrary light beam [3]. The link between duality symmetry and helicity in vacuum was done by Calkin in 1965 and Zwanziger in 1968 [6,7]. But it was not until very recently that helicity has been used to study light-matter interactions [3,8]. The helicity of light is defined as the projection of the angular momentum (AM) on the direction of linear momentum. Using operators: $\Lambda = \mathbf{J}\cdot\mathbf{P}/|\mathbf{P}|$ [8]. Here, it will be shown that this last definition is very useful for practical applications and suitable for theoretical predictions. In addition, we will see that highly non-dual materials such as TiO_2 can behave as dual for some resonant wavelengths. Finally, we will show that our formalism is applicable to any geometry.

2 Multipolar fields with a well-defined helicity

To study the dual behaviour of a scatterer, it will be useful to probe it using beams that are eigenvectors of the helicity operator Λ. These beams can be constructed as superpositions of plane waves, where each of the plane waves is an eigenvector of Λ. A plane wave $\mathbf{u}$ is an eigenvector of Λ when it can be expressed as $\mathbf{u} = \mathbf{e}_p\, e^{(ik\cdot r)}$, where $\mathbf{e}_p = (\mathbf{s} + p\mathbf{p})/\sqrt{2}$, where $\mathbf{s}$ and $\mathbf{p}$ are two orthogonal linear polarizations [8,9]. It can be proven that $\Lambda[\mathbf{u}] = p\mathbf{u}$, where the values of p have been restricted to p=-1,1. Then, if $\mathbf{u}$ is an eigenstate of Λ, we will say that it has a well-defined helicity. If a convenient superposition of plane waves is carried out, the multipolar fields are obtained [10]. The multipolar fields are widely used in different fields such as astrophysics, nuclear physics or optics. Their definition varies a little bit depending on the field, but in essence they can be defined as EM modes which are invariant under the Hamiltonian, the angular momentum (AM) squared J^2, a projection of the AM along the z axis J_z, and parity Π [11]:

$$J^2[\boldsymbol{A}^{y}_{jm_z}] = j(j+1)\boldsymbol{A}^{y}_{jm_z} \tag{2}$$
$$J_z[\boldsymbol{A}^{y}_{jm_z}] = m_z\boldsymbol{A}^{y}_{jm_z} \tag{3}$$
$$\Pi[\boldsymbol{A}^{e}_{jm_z}] = -^{j+1}\boldsymbol{A}^{e}_{jm_z} \tag{4}$$
$$\Pi[\boldsymbol{A}^{m}_{jm_z}] = -^{j}\boldsymbol{A}^{m}_{jm_z} \tag{5}$$

where $y = m, (e)$ depending on the parity of the multipolar field. However, a new set of multipolar fields can be obtained if the two multipolar modes with different parity are added or subtracted. We will denote these as multipolar modes with a well-defined helicity, as it can be proven that they are eigenstates of the helicity operator Λ [12]:

$$J^2[\boldsymbol{A}^{p}_{jm_z}] = j(j+1)\boldsymbol{A}^{p}_{jm_z} \tag{2}$$
$$J_z[\boldsymbol{A}^{p}_{jm_z}] = m_z\boldsymbol{A}^{p}_{jm_z} \tag{3}$$
$$\Lambda[\boldsymbol{A}^{p}_{jm_z}] = p\boldsymbol{A}^{p}_{jm_z} \tag{4}$$

where $p = \pm 1$ are the two possible values of helicity

3 Helicity preservation in scattering

The Generalized Lorenz-Mie problem is typically solved in the multipolar basis. That is, all the fields are

decomposed in the multipolar basis and then the boundary conditions are used to match the different fields on the surface of the sphere [1,13]. Another possibility is to use the multipoles with a well-defined helicity as a basis. Then, all the fields in the problem have to be decomposed as a superposition of $A^{+}_{jm_z}, A^{-}_{jm_z}$ [12]. This choice of basis has been overlooked in the literature. Notwithstanding, its choice has enabled us to demonstrate different effects in a very straightforward manner [5,12]. First, we give the analytical expression of the three electric fields in the problem in this basis, where the incident field is supposed to have a well-defined helicity:

$$\boldsymbol{E}^{i} = \sum_{j,m_z} \alpha^{p}_{jm_z} \boldsymbol{A}^{p}_{jm_z} \quad (5)$$

$$\boldsymbol{E}^{s} = \sum_{j,m_z} \alpha^{p}_{jm_z} \frac{a_j+b_j}{\sqrt{2}} \boldsymbol{A}^{p}_{jm_z} + \frac{a_j-b_j}{\sqrt{2}} \boldsymbol{A}^{-p}_{jm_z} \quad (6)$$

$$\boldsymbol{E}^{s} = \sum_{j,m_z} \alpha^{p}_{jm_z} \frac{a_j+b_j}{\sqrt{2}} \boldsymbol{A}^{p}_{jm_z} + \frac{a_j-b_j}{\sqrt{2}} \boldsymbol{A}^{-p}_{jm_z} \quad (7)$$

Then, the energy per unit length associated to each of the fields can be computed as:

$$W = \int_{\Omega} \frac{1}{16\pi} \varepsilon|\boldsymbol{E}|^2 + \mu|\boldsymbol{H}|^2 \, d\Omega \quad (8)$$

In particular, the scattered energy is [5]:

$$W^{s} = \sum_{jm_z} \left|\alpha^{p}_{jm_z}\right|^2 \left(|a_j|^2 + |b_j|^2 \right) \quad (9)$$

Now, it can be proven that the scattered energy can be divided into two orthogonal components. One of them (W^{s}_{p}) has the same helicity value as the incident beam. This is what we call the `direct' component. The other one ($W^{s}_{-p}$) has the opposite value of helicity, and we denote it as `crossed' component. Thanks to this decomposition in its two orthogonal components, a transfer function can be defined, and the duality properties of the scatterer can be studied. We will study these properties with the transfer function T_p [5]:

$$T_p = \frac{W^{s}_{-p}}{W^{s}_{p}} = \frac{\sum_{jm_z} \left|\alpha^{p}_{jm_z}\right|^2 |a_j-b_j|^2}{\sum_{jm_z} \left|\alpha^{p}_{jm_z}\right|^2 |a_j+b_j|^2} \quad (10)$$

T_p is the ratio between the scattered light going into the crossed component and the direct one. Thus, T_p varies from 0 to infinity. When T_p tends to zero, it means that the light in the crossed helicity component is zero, which means that the particle is dual, as the helicity is preserved. On the other hand, when T_p tends to infinity, it means that no light is being scattered in the direct component, which means that the particle is behaving as anti-dual. These two regimes can be used to generalize the so-called Kerker conditions [12]. Moreover, due to the fact that GLMT is analytical, the transfer function can be computed for different combinations of λ, R, n_r that make the particle behave as dual, where λ is the wavelength, $R$the radius of the sphere and $n_r$the relative index of refraction [5]. For example, in Fig.(1) we can observe that once the wavelength of our laser is fixed at 633nm, a sphere can behave as dual for many resonant combinations of R, n_r .

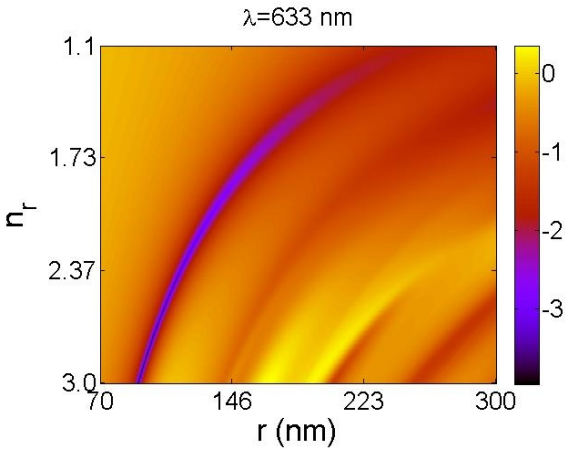


Figure 1 *Plot of* $log\,(T_p)$ *as a function of* R *and* n_r.

Finally, T_p can be generalized when the scatterer is not a sphere. Thus, our method of analysing the duality properties of scatterers remains valid independently of the geometry of the scatterer and the material it is made of. The generalization is done as:

$$T_p = \frac{\|\boldsymbol{E}^{s} - ip\boldsymbol{H}^{s}\|}{\|\boldsymbol{E}^{s} + ip\boldsymbol{H}^{s}\|}$$

4 Conclusions

A new method to study scattering interactions has been presented. The method uses analytical techniques to study the duality behaviour of scatterers. Even though the method is shown for spheres, it can be applied to scatterers of arbitrary shape. The results have implications in the field of optical activity, metamaterials and nanophotonics [4,5,12,14].

5 Acknowledgements

This work was funded by the Australian Research Council Discovery Project DP110103697 and the Centre of Excellence in Engineered Quantum Systems (EQuS). G.M.-T. is the recipient of an Australian Research Council Future Fellowship (project number FT110100924).

6 References

[1] G. Gouesbet, and G. Gréhan, *Generalized Lorenz-Mie Theories* (Springer, Berlin, 2011).

[2] J. D. Jackson, *Classical Electrodynamics* (John Wiley & Sons, New York, 1998).

[3] Fernandez-Corbaton I., Zambrana-Puyalto X., Tischler N., Vidal X., Juan M.L., and Molina-Terriza G., Electromagnetic Duality Symmetry

and Helicity Conservation for the Macroscopic Maxwell's Equations, Phys. Rev. Lett. 111(6):060401 (2013).

[4] Fernandez-Corbaton I., Vidal X., Tischler N., and Molina-Terriza G., Necessary symmetry conditions for the rotation of light, J. Chem. Phys. 138:214311 (2013).

[5] Zambrana-Puyalto X., Vidal X., Juan M. L., and Molina-Terriza G., Dual and anti-dual modes in dielectric spheres, Opt. Express 21(15):17520-17530 (2013).

[6] Calkin, M. G., An Invariance Property of the Free Electromagnetic Field, Am. J. Phys. 33:958-960 (1965).

[7] Zwanzinger D., Quantum field theory of particles with both electric and magnetic charges, Physical Review 176(5):1489 (1968)

[8] Fernandez-Corbaton I., Zambrana-Puyalto X., and Molina-Terriza G., Helicity and angular momentum: A symmetry-based framework for the study of light-matter interactions, Phys. Rev. A 86(4):042103 (2012).

[9] Fernandez-Corbaton I., Zambrana-Puyalto X., and Molina-Terriza G., On the transformations generated by the electromagnetic spin and orbital angular momentum operators, arXiv:1308.1729 (2013).

[10] W.-K. Tung, *Group Theory in Physics* (World Scientific, Singapore, 1985).

[11] M.E. Rose, *Multipole Fields* (Wiley, New York, 1955)

[12] Zambrana-Puyalto X., Fernandez-Corbaton I., Juan M. L., Vidal X., and Molina-Terriza G., Duality symmetry and Kerker conditions, Opt. Lett. 38:1857-1859 (2013).

[13] C.F. Bohren, and D.R. Huffman, *Absorption and scattering of light by small particles* (Wiley, New-York, 1983).

[14] Fernandez-Corbaton I., Molina-Terriza G., Role of duality symmetry in transformation optics, Phys. Rev. B 88(8):085111 (2013)

Scattering Properties of Mineral and Soot-Containing Aerosols

Janna M. Dlugach[1,*], Michael I. Mishchenko[2].

[1] Main Astronomical Observatory of the National Academy of Sciences of Ukraine, Kyiv, 03680, Ukraine
[2] NASA Goddard Institute for Space Studies, New York, NY 10025, U.S.A.

**Corresponding author: zhanna.dlugach@gmail.com, dl@mao.kiev.ua*

Abstract

We analyze the results of numerically exact computer modelling of the scattering properties of polydisperse compound aerosols composed of spherical soot grains placed on the surface or encapsulated in a much larger spherical mineral particle. The computations were performed by using the superposition *T*-matrix method. These results are also compared with the Lorenz-Mie data obtained for a uniform external mixture of mineral and soot particles. We show that the presence of soot grains can significantly change both the integral and differential scattering characteristics of the compound aerosols.

1 Introduction

Mineral and soot particles are ubiquitous constituents of natural and artificial environments [1–4]. Such particles can stick to each other and form various types of compound aerosols. Whether the optical properties of a mixture of mineral and soot particles change upon aggregation depends on the strength of the electromagnetic interaction between the mineral and soot components, which can now be in direct physical contact instead of being widely separated. This interaction and the resulting optical effects are still insufficiently understood and poorly quantified, and so constitute the main subject of this work.

Previously [5], we studied potential effect of the presence of small soot particles adhering to the surfaces of larger mineral hosts, and this effect was shown to be quite substantial. Here, we analyze the behaviour of the light scattering characteristics for the compound particles in the case when soot grains are embedded in a larger mineral host.

2 Methodology and Computational Results

Our model of a compound mineral-soot aerosol is a spherical mineral host particle with N_g encapsulated identical non-overlapping small spherical grains. Such model allows us to compute all scattering properties using the highly efficient, numerically exact superposition *T*-matrix method [6, 7] and the parallelized computer program posted on-line [8]. In our computations, the ratio of the radius of the mineral host to that of the small soot particles is kept constant at $R/r \equiv 10$, and soot particles are placed inside a large mineral host using a random-number generator. The scattering and absorption characteristics of the compound aerosol are averaged over the uniform orientation distribution of the resulting particle as well as over a standard power law distribution $n(R)$ = constant × R^{-3} [9] with an effective radius $R_{\rm eff}$ = 1 μm, the resulting effective radius of the soot particles is $r_{\rm eff}$ = 0.1 μm. The refractive index of the mineral hosts is adopted to be equal to 1.55 + i0.0003, while that of the soot particles is 1.75 + i0.435. The wavelength is fixed at 0.62832 μm. The numerical size averaging is based on the Gauss–Legendre quadrature formula with 100 nodes. The size averaging has a dual purpose of (i) better representing polydisperse particle ensembles encountered in various applications, and (ii) smoothing out sharp resonance features typical of monodisperse spherical scatterers [9]. In order to compare the effect of the soot particles encapsulated in mineral host with that produced by a uniform external mixture of mineral and soot aerosols or soot grains adhering to the surface of mineral particle considered in [5], the computations have been performed for N_g =49 and 149.

N_g	$C_{\rm ext}$	$C_{\rm sca}$	$C_{\rm abs}$	ω	g
host	6.314	6.265	0.049	0.9923	0.668
$49_{\rm ind}$	8.279	6.924	1.355	0.836	0.635
$149_{\rm ind}$	12.291	8.268	4.023	0.673	0.585
$49_{\rm cov}$	6.925	5.678	1.247	0.820	0.730
$149_{\rm cov}$	7.832	5.161	2.671	0.659	0.819
$49_{\rm enc}$	6.596	4.599	1.997	0.697	0.773
$149_{\rm enc}$	7.168	3.845	3.323	0.536	0.878

Table 1. Ensemble-averaged extinction, scattering, and absorption cross sections (in μm²) per compound aerosol particle, single-scattering albedo ω, and asymmetry parameter g

Table 1 lists ensemble-averaged integral radiometric characteristics, viz., the extinction, $C_{\rm ext}$, scattering, $C_{\rm sca}$, and absorption, $C_{\rm abs}$, cross sections as well as the single scattering albedo ω and the asymmetry parameter g. The subscript indicates the location of soot grains relative to the mineral host ("ind" denotes the case of uniform external mixture of mineral and soot particles; "cov" applies to the case of soot grains covering the surface of mineral host; "enc" denotes the case of encapsulated soot grains). The data presented in the first five rows of the table were obtained in [5]. It is seen that embedding strongly absorbing soot particles results in a substantial

decrease of the values of the cross sections C_{ext}, C_{sca} and single scattering albedo ω. At the same time the absorption cross section C_{abs} and asymmetry parameter g increase. The subsequent increasing the number of encapsulated soot particles N_g increases the extinction and absorption cross sections and the asymmetry parameter, and decreases the scattering cross section and the single scattering albedo. This can be explained by the fact that in the case of compound aerosol, increasing N_g results in suppressing the contribution of the weakly absorbing host to the scattering cross section.

differ noticeably from those obtained in [5] for soot grains located on the surface of mineral particle. The upper middle panel is also indicative of a potentially strong effect of encapsulated particles on the degree of linear polarization for unpolarized incident light given by $P(\theta) = -F_{12}(\theta) / F_{11}(\theta)$. In particular, this is seen when $N_g = 149$.

The ratio $F_{22}(\theta) / F_{11}(\theta)$ (the upper right-hand panel) is identically equal to 100% for a mineral spherical particle or the external mixture of spherical mineral and soot particles but deviates from 100% for the compound aerosols, signifying the behaviour typical of nonspherical scatters.

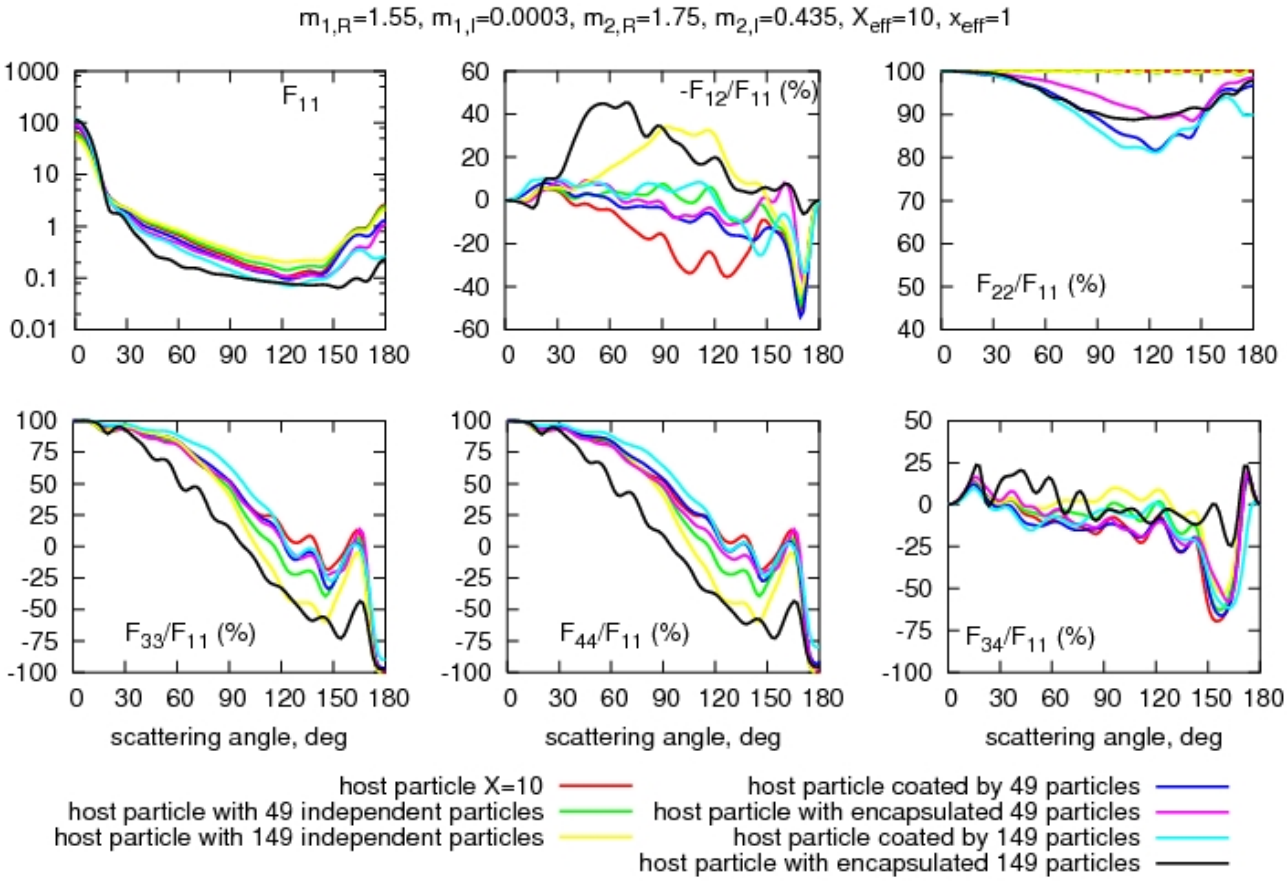


Figure 1. *Elements of the normalized Stokes scattering matrix for a large mineral particle, an external mixture of mineral and different number of soot particles, and different models of a composition-equivalent mineral-soot particles.*

For all models of compound particles listed in the first column of Table 1, Figure 1 depicts non-zero elements F_{ij} of the 4 x 4 normalized Stokes scattering matrix [9] relating the Stokes parameters of the incident quasi-monochromatic light and those of the scattered light (the scattering angle is the angle between the incidence and scattering directions). The upper left-hand panel demonstrates a strong effect of the presence of encapsulated soot particles on the behaviour of the phase function (the element F_{11}) in the range of scattering angles $\theta \geq 30^0$. But at the exactly backscattering direction, for the same number of soot particles N_g the values of F_{11} do not

But it is seen that the presence of encapsulated soot grains results in smaller deviation from 100% compared the case of soot grains covering the surface of the mineral particle. The data presented in the bottom panels show sufficiently strong effects produced by encapsulated soot submicron particles on the behaviour of the scattering matrix elements F_{33}, F_{44} and F_{34} (especially for $N_g = 149$).

In summary, the results of our computations performed by using the superposition T-matrix method demonstrate substantial effects of small soot grains encapsulated in large mineral particle on the optical cross sections, single scattering albedo and asymmetry parameter. The effect on

the scattering properties defined by the elements of the Stokes scattering matrix can also be significant.

3 Acknowledgement

We acknowledge support from the National Academy of Sciences of Ukraine under the Main Astronomical Observatory GRAPE/GPU/GRID Computer Cluster Project.

4 References

[1] E.J. Daivs and G. Schweiger, *The Airborne Microparticle* (Springer, 2002).

[2] Li J., Anderson J.R., and Buseck P.R., TEM study of aerosol particles from clean and polluted marine boundary layers over the North Atlantic, J. Geophys. Res. 108(D6): 4189 (2003).

[3] Reid E.A., Reid J.S., Meier M.M., Dunlap M.R., Cliff S.S., Broumas A., Perry K., and Maring H., Characterization of African dust transported to Puerto Rico by individual particle and size segregated bulk analysis, . Geophys. Res. 108(D19): 8591 (2003).

[4] P. Kukri, P.A. Baron, and K. Willeke, *Aerosol Measurement* (Wiley, 2011).

[5] Mishchenko M.I., Dlugach J.M., Adhesion of mineral and soot aerosols can strongly affect their scattering and absorption properties, Optics Letters 37(4):704-6 (2012).

[6] Mackowski D.W., Mishhchenko M.I., Calculation of the *T* matrix and scattering matrix for ensembles of spheres, J. Opt. Soc. Am. A 13(11): 2266-78 (1996).

[7] Mackowski D.W., Mishhchenko M.I., A multiple sphere *T* matrix Fortran code for use on parallel computer clusters, J. Quant. Spectrosc. Radiat. Transfer 112: 2182-92 (2011).

[8] Mackowski D.W. <http://www.eng.auburn.edu/users/dmckwski/scatcodes>.

[9] M.I. Mishchenko, L.D. Travis, and A.A. Lacis, *Scattering, Absorption, and Emission of Light by Small Particles* (Cambridge University, 2002).

Method of moment solution for the electric current volume integral equation

Johannes MARKKANEN[1,*], Antti PENTTILÄ [1], Jouni PELTONIEMI[1-2] and Karri MUINONEN[1-2]

[1] Department of Physics, University of Helsinki, Helsinki, 00014, Finland
[2] Finnish Geodetic Institute, Masala, 02431, Finland
Corresponding author: johannes.markkanen@helsinki.fi

Abstract

We present a novel discretization scheme for the electric current volume integral equation formulation of electromagnetic scattering. The method can be used for analyzing electromagnetic scattering by arbitrarily shaped three-dimensional objects. The scheme utilizes the method of moments with fully linear basis and testing functions. The solution accuracy of the proposed discretization scheme is compared to the standard scheme with the piecewise constant approximations as well as to the commonly used discrete-dipole approximation code. The preliminary results show that the method provides superior solution accuracy with respect to the number of unknowns.

1 Introduction

A full-wave numerical solution for the electromagnetic wave scattering by arbitrarily shaped inhomogeneous or anisotropic particles can be found through various numerical methods, such as the finite-element (FEM), finite-difference time-domain (FDTD), and the integral-equation methods (IEM). IEMs are the most attractive methods for open region scattering problems due to their inherent capability of modelling unbounded domains. In the IEMs, only the scatterers are modelled, and the integral equation automatically satisfies the radiation condition. Thus, the IEMs avoid modeling free space around the particle as opposed to the differential equation based methods in which the whole region of interest needs to be modelled and terminated by some boundary condition. In addition, the Green's function in the IEMs is an exact propagator, and therefore, the solution does not suffer from numerical dispersion.

For inhomogeneous or anisotropic materials, different types of volume integral equation (VIE) methods have been applied in the past [1-3]. Some VIEs are called as the discrete-dipole approximation DDA [4,5]. However, all of them are essentially based on the same integral equations, but the difference is how the numerical approximation scheme is constructed. The projection method is a commonly used technique to solve VIEs. The basic idea is to expand the unknown function/functions, e.g. electric/magnetic current, field or flux with a set of basis functions, and then force the approximation error to be orthogonal to some space. This can be considered as the best projection from the continuous space to the discrete one in some sense, and it requires defining a proper inner product as well as a set of testing functions. Hence, it is obvious that the choice of the formulation, the inner product, and the basis and testing functions must be made carefully, and it has a major effect on the accuracy of the numerical solution.

The discretization procedure leads to a system of linear equations, which can be solved numerically. Unfortunately, the resulting system matrix is full which means that the memory requirement increases quadratically and the solution time cubically with respect to the problem size. However, the development of the fast algorithms such as the multilevel fast multipole algorithm MLFMA [6,7], and the FFT-based algorithms [8,9] has made it possible to solve large problems with a reasonable amount of computational capacity. The fast methods employ iterative solvers in which the matrix-vector multiplication is accelerated by the abovementioned algorithms, giving O(N)-O(N log N) complexity for the memory and O(N log N) for the computing time.

In this abstract, we investigate the accuracy of the novel discretization of the electric current volume integral equation (JVIE) utilizing tetrahedral elements and piecewise linear approximations as basis and testing functions. The accuracy and the stability of the method is studied and compared with the previous discretization employing piecewise constant functions [10] as well as the commonly used DDA code [11].

2 Discretization of JVIE

Consider time-harmonic ($\exp(i\omega t)$) electromagnetic scattering by a dielectric object bounded by a volume D located in free space. The object is described by the electric permittivity dyad $\bar{\bar{\epsilon}}_r$. The electric current volume integral equation (JVIE) formulation is written as

$$\boldsymbol{J}^{inc} = \boldsymbol{J} - \left(\bar{\bar{\epsilon}}_r - \bar{\bar{I}}\right) \cdot (\nabla\nabla + k^2) \cdot \boldsymbol{V}(\boldsymbol{J}), \tag{1}$$

where the unknown is the equivalent electric polarization current

$$\boldsymbol{J} = -i\,\omega\epsilon_0 \left(\bar{\bar{\epsilon}}_r - \bar{\bar{I}}\right) \cdot \boldsymbol{E}\,, \tag{2}$$

in which $\boldsymbol{E}$ is the total electric field. The volume potential operator is defined as follows:

$$\boldsymbol{V}(\boldsymbol{f}) = \int_V G(\mathbf{r},\mathbf{r}')\mathbf{f}(\mathbf{r}')\,d\mathbf{r}', \quad (3)$$

where G is the free space Green's function, i.e., the fundamental solution for the Helmholtz equation. It is known that the above integral equation is solvable in L_2 (the vector space of square integrable functions) if the permittivity function satisfies some additional conditions [12]. This means that we can use L_2-conforming basis and testing functions as well as an L_2-inner product to obtain a convergent numerical method.

The discretization scheme follows the same fundamental principles presented in [10], although some modifications are required due to the higher-order basis and testing functions. First, the scatterer is discretized with linear tetrahedral elements, and then the unknown current is expanded by piecewise linear L_2 -conforming basis functions associated to the tetrahedral elements as follows:

$$\mathbf{J} \approx \sum_{p=1}^{4}\sum_{k=1}^{N\_tet}(c_k^{x,p}N_p\hat{\mathbf{e}}_x + c_k^{y,p}N_p\hat{\mathbf{e}}_y + c_k^{z,p}N_p\hat{\mathbf{e}}_z) \quad (4)$$

where $\hat{\boldsymbol{e}}_x$, $\hat{\boldsymbol{e}}_y$, and $\hat{\boldsymbol{e}}_z$ are the unit vectors N_p are the standard linear nodal shape functions and $c_k^{x,y,z,p}$ are the unknown coefficients. Therefore, each tetrahedron contains 12 basis functions (four functions for each component). The Galerkin testing (basis and testing functions are the same functions) procedure is applied with respect to the L_2-inner product, and the derivatives are moved into the basis and testing functions. The details are omitted due to the lack of space, but all the arising integrals are weakly singular, and can be computed with the singularity extraction technique [13].

3 Preliminary results

In this section, we study the accuracy of the linear JVIE solver. The results are computed by using the JVIE solver with either piecewise linear or constant basis functions and compared with the results computed by ADDA (Amsterdam discrete-dipole approximation) code [11].

Our first example is a dielectric sphere of size $ka = 2$ with the relative permittivity $\epsilon_r = 6$. Figure 1 shows the scattering efficiencies as functions of degrees of freedom (DoF) as well as the exact Mie solution. Clearly, the JVIE with the linear basis functions gives the fastest convergence, and the DDA the slowest. Similar conclusions can be made for different spheres, too. As another example, Figure 2 presents the relative RMS error in far field scattering integrated over the surface of a unit sphere.

It is important to note that these comparisons are not so straightforward since the DDA uses cubic elements and they introduce larger geometric errors than the tetrahedral elements used in JVIE. Also, the convergence of the solution should be investigated in case of more complicated objects. Moreover, the computational time and memory requirements per DoF are quite different in each method. In general, the DDA is the fastest and least memory consuming per DoF. However, asymptotically the scaling for each method is the same, O(N) for the memory and O(N log N) for the computing time when the FFT type acceleration technique is used.

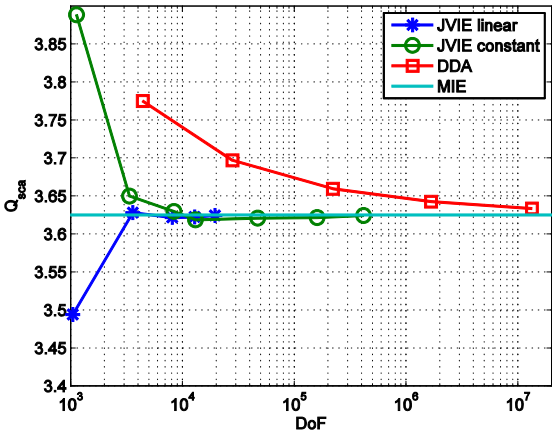


Figure 1 *Scattering efficiency vs. degrees of freedom (DoF). The scatterer is a sphere of size* $ka = 2$ *with* $\epsilon_r = 6$.

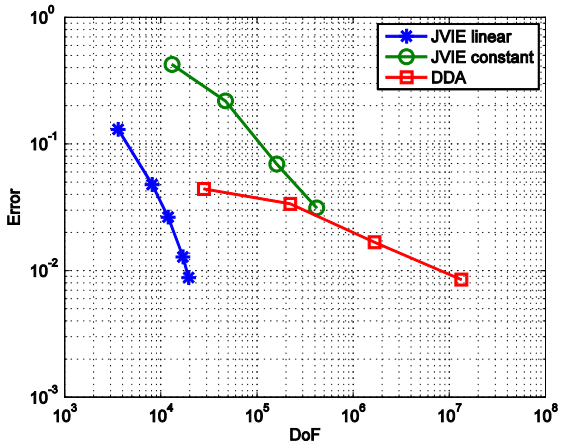


Figure *Relative error in the far field scattering as a function of DoFs. The scatterer is a sphere of size* $ka = 4$ *with* $\epsilon_r = 4$

4 Conclusions

The volume integral equation for the electric current has been discretized in L_2 by using tetrahedral elements and piecewise linear approximations. The method can be applied to analyze electromagnetic wave scattering by

arbitrarily inhomogeneous three-dimensional objects. The preliminary results show improvements in the solution accuracy compared to the previous discretization of the JVIE utilizing piecewise constant functions, as well as compared to the commonly used DDA solver.

5 Ackowledgement

The research has been funded by the ERC Advanced Grant No 320773 entitled "Scattering and Absorption of Electromagnetic Waves in Particulate Media" (SAEMPL).

6 References

[1] W.C. Chew, J. M. Jin, E. Michielssen, and J. Song, F*ast and efficient algorithms in computational electromagnetics* (Artech house, Boston, 2001).

[2] D, Schaubert, D Wilton, and A. Glisson. A tetrahedral modelling method for electromagnetic scattering by arbitrarily inhomogeneous dielectric bodies, IEEE Trans. Antennas and Propagation, vol. 31 no. 1, pp. 77-85, 1984.

[3] M. Botha, Solving the volume integral equations of electromagnetic scattering, Journal of Computational Physics, vol. 32, pp. 141-158, 2006.

[4] B.T. Draine, and P. J. Flatau, Discrete-dipole approximation for scattering calculations, Journal of the Optical Society of America A, vol. 11, no. 4, pp. 1491- 1499, 1994.

[5] M..A. Yurkin, A.G. Hoekstra, The discrete dipole approximation: An overview and recent developments, Journal of Quantitative Spectroscopy and Radiative Transfer, vol. 106, iss. 1-3, pp. 558-589, 2007.

[6] V. Rokhlin, Rapid solution of integral equations of scattering theory in two dimensions, Journal of Computational Physics, vol. 86, no. 2 pp. 414-439, 1990.

[7] C.C. Lu, A fast algorithm based on volume integral equation for analysis of arbitrarily shaped dielectric radomes, IEEE Trans. Antennas and Progation, vol 51, no. 3 pp. 606-612, 2003.

[8] E. Bleszynski, M. Bleszynski, and T. Jaroszewicz, AIM: Adaptive integral method for solving large-scale electromagnetic scattering and radiation problems, Radio Science, vol. 31, no. 5, pp. 1225-1251, 1996.

[9] J.R. Phillips, and J.K. White, A precorrected-FFT method for electrostatic analysis of complicated 3-D structures, IEEE Trans. Computer-Aided Design of Integrated Circuits and Systems, vol. 16, no. 10, pp.1059-1072, 1997.

[10] J. Markkanen, P. Ylä-Oijala, and A. Sihvola, Discretization of volume integral equation formulations for extremely anisotropic materials, IEEE Trans. Antennas and Propagation, vol. 60, no. 11, pp. 5195-5202, 2012.

[11] M. A. Yurkin, and A.G. Hoekstra, The discrete-dipole-approximation code ADDA: capabilities and known limitations, Journal of Quantitative Spectroscopy and Radiative Transfer, vol. 112, pp. 2234-2247, 2011.

[12] M.C. van Beurden, and S.J.L. Eijndhoven, Well-posedness of domain integral equations for a dielectric object in homogeneous background, Journal of Engineering Mathematics, vol. 62, pp. 289-302, 2008.

[13] S. Järvenpää, M. Taskinen, and P. Ylä-Oijala, Singularity extraction technique for integral equation methods with higher order basis functions on plane triangles and tetrahedra, International Journal for Numerical Methods in Engineering, vol. 58, pp. 1149-1165, 2003.

T-matrix calculation with the Green's dyadic technique for electromagnetic scattering: a numerical approach using Dyson equation

Ugo TRICOLI[1,*], Klaus PFEILSTICKER[1]

[1] Institute of Environmental Physics, University of Heidelberg, Heidelberg, 69120, Germany

Corresponding author: ugo.tricoli@iup.uni-heidelberg.de

Abstract

Results from a novel numerical technique to calculate the T-matrix are presented. The method exploits the volume integral equation for electromagnetic scattering of a single particle. It is based on the CDA and uses its Green's function formulation, see O. J. F. Martin *et al*. [1]. The basic procedure includes the parallel use of the Lippmann-Schwinger and the Dyson equations to iteratively solve for the T-matrix and the Green's function dyadic respectively. No boundary conditions need to be specified. The method can be used for the evaluation of the optical properties (e.g. Müller matrix) of anisotropic, inhomogeneous and asymmetric particles, both in far and near field, giving as output the T-matrix, which depends only on the scatterer itself and is independent from the polarization and direction of the incoming field. Estimation of the accuracy of the method is provided through comparison with the analytical spherical case (Mie theory) as well as non-spherical ice particles.

1 Method

It is assumed that the scattering system is formed by a dielectric, nonmagnetic particle, characterized by the dielectric constant ε embedded into an infinite homogeneous background medium of dielectric constant ε_0. The scattering problem can be expressed through the T-matrix in an integral form given in [2], the total field is then obtained from

$$\boldsymbol{E}(\boldsymbol{r}) = \boldsymbol{E}_0(\boldsymbol{r}) + \int_V d\boldsymbol{r}' \boldsymbol{G}_0(\boldsymbol{r},\boldsymbol{r}') \int_V d\boldsymbol{r}'' \boldsymbol{T}(\boldsymbol{r}',\boldsymbol{r}'') \boldsymbol{E}_0(\boldsymbol{r}'')$$

where **T** is the dyadic transition operator and **r** can run all over the system (i.e. scatterer and background). The integrals run over the internal volume of the particle V. Then, the T-matrix is calculated via the Lippmann-Schwinger equation for the T-matrix ,with $k_0 = \omega / c$

$$\boldsymbol{T}(\boldsymbol{r},\boldsymbol{r}') = \boldsymbol{T}_0(\boldsymbol{r},\boldsymbol{r}') + \int_V d\boldsymbol{r}'' \boldsymbol{G}_0(\boldsymbol{r},\boldsymbol{r}'') k_0^2 \Delta\varepsilon(\boldsymbol{r}'') \boldsymbol{T}(\boldsymbol{r}'',\boldsymbol{r}')$$

From quantum theory of scattering [3], we can also infer the Dyson equation for the Green's function dyadic,

$$\boldsymbol{G}(\boldsymbol{r},\boldsymbol{r}') = \boldsymbol{G}_0(\boldsymbol{r},\boldsymbol{r}') + \int_V d\boldsymbol{r}'' \boldsymbol{G}_0(\boldsymbol{r},\boldsymbol{r}'') k_0^2 \Delta\varepsilon(\boldsymbol{r}'') \boldsymbol{G}(\boldsymbol{r}'',\boldsymbol{r}')$$

The core of the algorithm lies in the parallel use of the Dyson equation and of the integral equation for the T-matrix, following the scheme proposed by O. J. F. Martin *et al*. [1]. It is based on a discretization of the involved integrals over a cubic voxelization of the particle. No Born approximation is imposed. The output is the T-matrix of the particle from which, one can get the field inside the scatterer as well as the near and far field solutions just employing the integral equation for the field.

2 Validation: Mie-theory comparison

The algorithm is validated through analytical results for a sphere (Mie theory) made of ice $\varepsilon = 1.1535 + i0.392$. Figure. 1 shows the first element of the Müller matrix for parallel polarization.

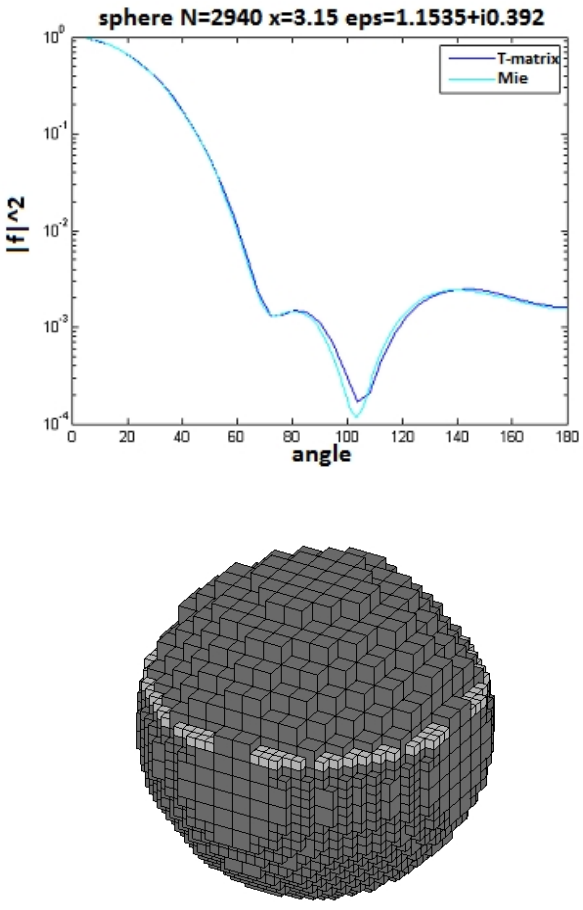


Figure 1 *Top: comparison of ice sphere phase functions calculated with Mie theory and our T-matrix technique for parallel polarized light ($\hat{z}$). Vertical axis: phase function (arbitrary units). Horizontal axis: scattering angle. Bottom: sparse-octree voxelization of the unit-sphere.*

3 Results: non-spherical particles

Results are shown for a ice cube (for incident direction see the subplot of the central panel in Figure. 2) and a ice cross (incident field direction along the longest direction). In the talk other interesting results will be presented for sharp edges particles like rectangular solids, torus, hexagonal plates as well as for particles with rough surface for which measurements in the laboratory exist.

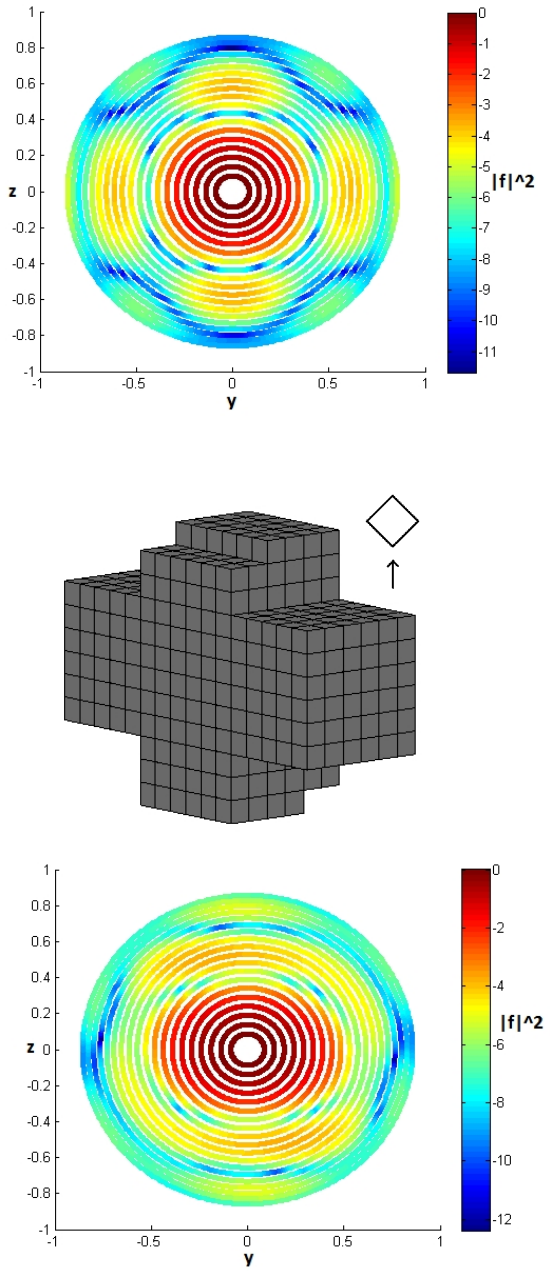


Figure 2 *Polar scattering pattern in logarithmic scale for vertical $\hat{z}$ linear polarization (normalized to the maximum). First row: cube with x=8. Second row: voxelization of a cross. Last row: cross with x=8. The axes are cartesian coordinates on the z-y plane. The scattering angle is in [5°, 60°] from center.*

4 Conclusions

The talk will report on (1) the technique to use in parallel two Lippmann-Schwinger equations, their discretization using sparse-octrees in order to calculate the Green's function dyadic and the related T-matrix for an arbitrary particle when an electromagnetic wave is incident on it (2) results for a sphere, and novel cases including sharp edges as well as rough-surface particles (3) comparison with recent experimental data from the SID instrument at IMK-KIT (Karlsruhe, Germany) for single forward scattering polar pattern.

4.1 Abbreviations and Acronyms

CDA: Coupled Dipole Approximation.
GDT: Green's Dyadic Technique.
SID: Small Ice Detector.
KIT: Karlsruhe Institute of Technology
IMK: Institute for Meteorology and Climate Research

5 Acknowledgement

Part of the research has been funded through the Deutsche Forschungsgemeinschaft (DFG) through grants Pf-384 7-1, 7-2, and Pf-384 9-1. Special thanks go to T. Deutschmann (IUP) for fruitful discussions.

6 References

[1] Martin O. J. F., Dereux A., and Girard C., Iterative scheme for computing exactly the total field propagating in dielectric structures of arbitrary shape, J. Opt. Soc. Am. A, Vol. 11, No.3, 1073 (1994).

[2] M. I. Mishchenko, L. D. Travis, A. A. Lacis, *Scattering, absorption, and emission of light by small particles* (Cambridge, UK, Cambridge University Press, 2002).

[3] E. N. Economou, *Green's Functions in Quantum Physics* (2nd ed., Springer-Verlag, Berlin, 1990).

[4] Martin O. J. F., Girard C., and Dereux A., Generalized Field Propagator for Electromagnetic Scattering and Light Confinement, Phys. Rev. Lett., Vol. 74, N. 4, 526, (1995).

[5] Yaghjian A. D., Electric dyadic Green's functions in the source region, Proc. IEEE 68, 248-263 (1980).

[6] C.F. Bohren, and D.R. Huffman, *Absorption and scattering of light by small particles* (Wiley, New-York, 1983).

[7] Grainger Roy G., Lucas J., Thomas G. E., and Ewen G. B. L., Calculation of Mie derivatives, Applied Optics ,Vol. 43, No. 28, (2004).

[8] Draine B. T., and Flatau P. J., Discrete-dipole approximation for scattering calculations, J. Opt. Soc. Am. A Vol. 11, 1491, (1994).

[9] E. Akkermans, and G. Montambaux, Mesoscopic Physics of Electrons and Photons (EDP Sciences-CNRS, Paris, 2004).

[10] [Martin O. J. F., Piller N. B., Electromagnetic scattering in polarizable backgrounds, Physical Review E, Vol. 58, N. 3, (1998).

[11] Martinez-OrtizC., http://www.mathworks.com/matlabcentral/fileexchange/21044-3d-voxelizer, (Copyright © 2009).

Light Scattering by Random Irregular Particles with Different Morphology

Yevgen GRYNKO[1,*], Evgenij ZUBKO[2]

[1] Department of Electrical Engeneering, University of Paderborn, Warburger Str. 100, Paderborn, 33100, Germany
[2] Institute of Astronomy, Kharkov National University, 35 Sumskaya St, Kharkov, 61022, Ukraine

*Corresponding author: yevgen.grynko@upb.de

Abstract

We simulate numerically light scattering by random irregular particles of two classes of shape: Gaussian random field particles and agglomerated debri particles. Comparison of the angular dependencies of the scattering matrix elements for the case of non-absorbing material shows qualitative similarity of optical properties of both types despite different morphology of scatterers. Absorbing particles result in the difference in linear polarization. However, a strong similarty remains for the intensity curves.

1 Introduction

Numerical simulation of light scattering by realistic particles is a problem that has many scientific and industrial applications. In practice one has to deal with isolated grains or powders consisting of particles that have random irregular shape. Examples are natural and artificial aerosols, soils, planetary regoliths and cosmic dust.

Very often spheres, ellipsoids and other regularly shaped and symmetric forms are used in numerical simulations to approximate more complicated shapes (e.g., [1]). This may, however, introduce unacceptable errors. Random irregular model shapes that are much closer to reality can also be considered. Usually they require larger computational resources but their obvious advantage is their realistic geometry and, either for grains or agglomerated clusters, one can avoid shape approximations.

There exist different classes of random shapes that can be generated numerically, e. g. prisms with random lengths of the diagonals, roughly faceted ellipsoids or random spheres with fluctuations of their radius and so on (e.g., [2,3]). The key problems here are generation algorithms and numerical description of particles.

In this work we study scattering properties of particles of two classes of random shapes using numerical simulations. First class is the so-called agglomerated debris particles (ADP) [4,5] (Fig. 1a) that have porous structure. Second class is Gaussian random field particles (GRF) [2,]. This type of shapes represents solid shapes (Fig. 1b) that are very similar to compact grains of different minerals that can be found in nature. We studied light scattering properties of GRF particles in the geometrical optics approximation [2,6,7] and recently with wave optics using Discontinuous Galerkin Time Domain method (DGTD) [8]. Here we also use DGTD for this class.

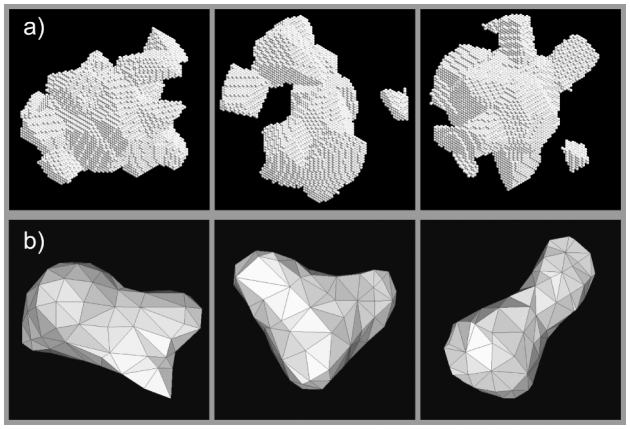


Figure 1 *Examples of particle geometries: a) agglomerated debri particles, b) Gaussian random field particles.*

2 Model desription

The algorithm for generation of agglomerated debris particles is discussed in [4,5]. The key features of ADPs are their irregular morphology and fluffy structure. Examples of such particles are shown in Fig. 1a and they also can be found in [4,5].

We use the discrete dipole approximation (DDA) method to calculate light scattering by the ADP particles (e.g., [9]). In the DDA, the scatterer is discretized on a cubic lattice. Each point is assigned the optical properties of the particle, and the spacing between lattice points is sufficiently small that each element of the lattice can be considered as an electric dipole. The total scattered field is the superposition of the scattered fields from all the dipoles in the system. Using the DDA algorithm, the light scattering from an arbitrarily shaped particle may be found.

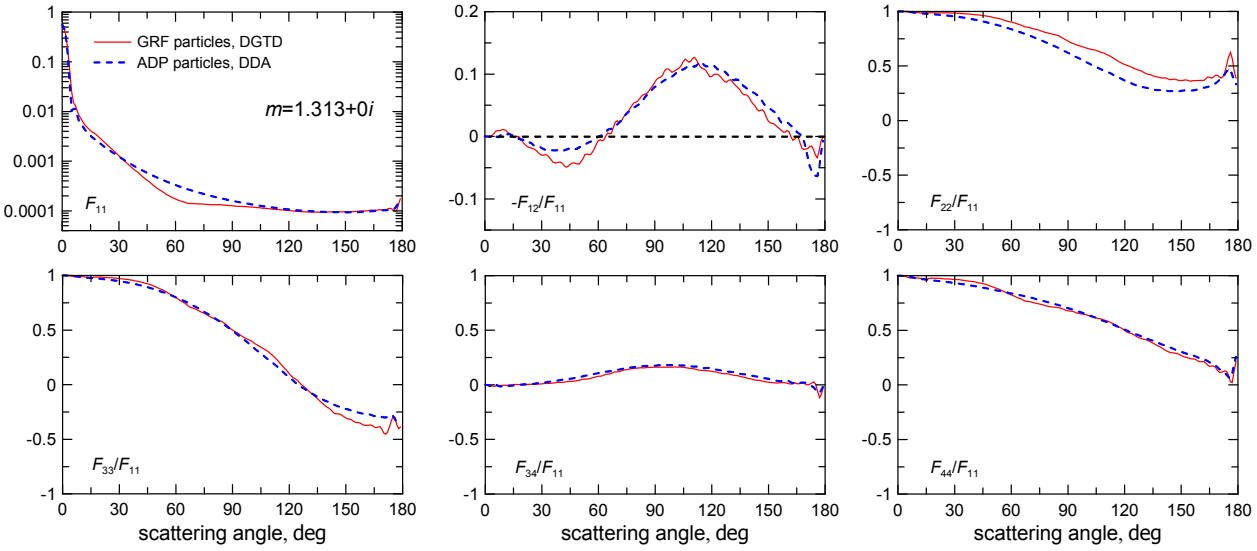


Figure 2 *Non-zero elements of scattering matrix calculated for GRF (solid lines) and ADP (dashed lines) particles (all averaged over samples) at X = 50, m = 1.313 + 0.0i.*

To generate model GRF particles we use a method based on the utilization of a 3-D random field with Gaussian probability density and correlation functions. It is discussed in [2,7,8]. Tuning the algorith parameters one can obtain compact shapes that are similar to solid mineral grains (Fig. 1b). For the application of the DGTD method the interfaces on particles are represented by sets of trianglar facets (200-300 facets per particle) that can be easily placed in the unstructured mesh of the computational domain. DGTD is a relatively new numerical method [10,11] that has proved its efficiency in different optical applications where Maxwell equations are solved for large-scale structures [8]. It is based on unstructured meshing that perfectly suits for arbitrary shapes and allows local mesh refinement for flexible control of the mesh resolution.

We take also a fixed size parameter for particles $X = \pi d/\lambda$ where d is the particle size (measured along the largest dimension of a particle) and λ is the wavelength. For all results it equals 50 which is a relatively large size for numerical simulations in terms of computer resources.

3 Results and discussion

Below we present and discuss the results of our simulations for two types of shapes of particles. We consider two materials expressed through two complex refractive indices, $m = 1.313 + 0i$ which corresponds to water ice and and an absorbing material with $m = 1.313 + 0.1i$. The results are averaged over many samples, $N = 500$ for ADP and $N = 300$ for GRF. For each sample the curves are averaged also over 180 scattering planes along the incidence direction.

Fig. 2 shows angular dependencies of six non-zero matrix elements calculated for an 'icy' material with complex refractive index $m = 1.313 + 0i$. We note surprisingly good agreement between such morphologically different particle sets for all matrix elements. One can assume that in a non-absorbing material the process of random electromagnetic scattering does not „feel" the shape of the scatterer. It is just strongly stochastic and averaging over samples of two kinds results in similar solutions. In the intensity (F_{11} the curves are normalized at 0°) we see, however, an expected difference at scattering angles < 90°. The curve corresponding to porous ADP particles is more smooth in this range which indicates diffraction and scattering on the constituent elements of such particles which broaden the curve. At the same time compact GRF particles act at this size parameter more like a lens and simply refract the incident ligth in forward direction.

In the polarization ($-F_{12}/F_{11}$) all typical features are reproduced for both types of shapes. First of all, this regards the positive polarization maxima. We expected them to be sensitive to the morphology of particles. However, their levels and positions almost coincide.

Again we see the evidence of forward refraction by GRF particles expressed in the stronger negative polarization at the angles smaller than 60. We note also a stronger depolarization ability for ADPs (F_{22}/F_{11}) which can also be attributed to their cluster-like morphology.

The other curves in Fig. 2 (F_{33}/F_{11}, F_{34}/F_{11}, F_{44}/F_{11}) are also very close to each other and do not show any significant difference between the shape classes.

The situation significantly changes if we introduce absorption in the material (Fig. 3) The complex refractive index $m = 1.313 + 0.1i$ at the size $X = 50$ makes a compact GRF particle opaque so that the light interacts mostly with the external surface and gets reflected. The fraction that penetrates the particle is almost totally absorbed. This is seen very well in the polarization panel ($-F_{12}/F_{11}$) where polarization curve looks like the one corresponding to simple Fresnelian reflection with maximum at Brewster angle. This is an indication of external reflection that dominates all other mechanisms. The positive maximum for ADPs is noticably lower than 100% and is shifted

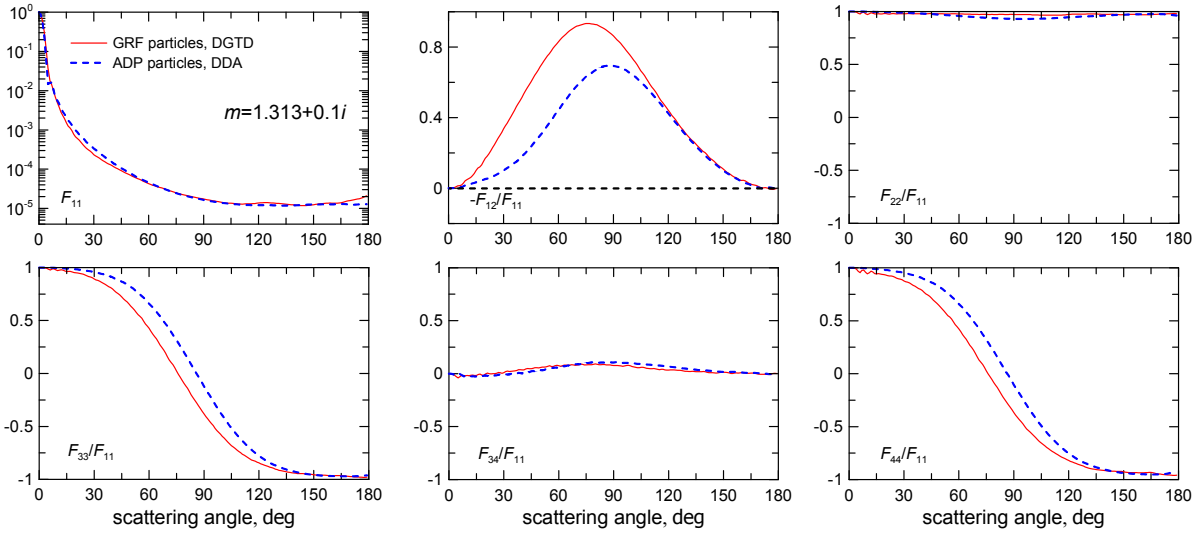


Figure 3 *Non-zero elements of scattering matrix calculated for GRF (solid lines) and ADP (dashed lines) particles (all averaged over samples) at X = 50, m = 1.313 + 0.1i.*

towards larger scattering angles. This is an evidence of scattering by smaller building blocks of theADP particles.

The intensity curves are very close for both classes. They are not influenced by the scattering component correponding to the internal wave propagation that must be different for each kind of shape as we see this in the non-absorbing case.

The depolarization power (F_{22}/F_{11}) for absrbing particles of both types is insignificant. There is, however, a difference in F_{33}/F_{11} and F_{44}/F_{11}.

Following our results we can conclude the following. Non-absorbing material obviously leads to a stochastic field distribution in particles. As a consequence, we observe very similar angular profiles of the scattering matrxi elements. This means that in practice, measuring scattering matrix elements at single wavelength one can hardly distinguish the morphology of transparent particles if they have similar refractive indices, whether the particles are compact (GRF) or they are porous agglomerates (ADP). Therefore multiwavelength photopolarimetry must be used if morpohology of particles is of interested.

For highly absorbing compact particles with X = 50 external scattering becomes dominant that results in almost 100% positive polarization whereas porous ADPs show results of scattering by structures of smaller scales. However, intensity curves remain similar in this case.

4 References

[1] G. Videen, Y. Yatskiv, and M. Mishchenko, Eds. *Photopolarimetry in remote sensing* (Kluwer Academic Publishers, 2004).

[2] Grynko Ye., and Shkuratov Yu., Scattering matrix calculated in geometric optics approximation faceted with various shapes, J. Quant. Spectrosc. Radiat. Transfer 78: 319-340 (2003).

[3] Muinonen K., Zubko E., Tyynelä J., Shkuratov Yu. G., and Videen, G., Light scattering by Gaussian random particles with discrete-dipole approximation, J. Quant. Spectrosc. Radiat. Transfer 106: 360-377 (2007).

[4] Zubko E., Shkuratov Yu., Kiselev N. N., Videen G., DDA simulations of light scattering by small irregular particles with various structure, J. Quant. Spec-trosc. Radiat. Transfer 101: 416-434 (2006).

[5] Zubko E., in Kokhanovsky A. A., ed., *Light Scattering Reviews, Vol. 6: Light Scattering and Remote Sensing of Atmosphere and Surface* (Springer-Verlag, Berlin, 2012).

[6] Shkuratov Yu., and Grynko Ye., Light scattering by media composed of semitransparent particles of different shapes in ray optics approximation: consequences for spectroscopy, photometry, and polarimetry of planetary regoliths, Icarus 173: 16-28 (2005).

[7] Grynko Ye., and Shkuratov Yu., Light scattering from particulate surfaces in geometrical optics approximation, in *Light scattering reviews, vol. III*, A. Kokhanovsky, ed. (Springer, 2008), pp. 329–382.

[8] Grynko Ye., Shkuratov Yu., and Foerstner Je., Light scattering by randomly irregular dielectric particles larger than the wavelength, Optics Letters 38: 5153-5156 (2013).

[9] Zubko E., Petrov D., Grynko Ye., Shkuratov, Yu., Okamot H., Muinonen K., Nousiainen T., Kimura H., Yamamoto T., and Videen G., Validity criteria of the discrete dipole approximation, Appl. Opt. 49: 1267- 1279 (2010).

[10] Hesthaven J. S., and Warburton T., Nodal High-Order Methods on Unstructured Grids: I. Time-Domain Solution of Maxwell's Equations, J. Comp. Phys. 181: 186-221 (2002).

[11] Busch K., König M., and Niegemann J., Discontinuous Galerkin Methods in Nanophotonics, Laser & Phot. Rev.. 5: 773-809 (2011).

High-frequency Gaussian beam scattering by ice crystals

Patrick STEGMANN[1,*], Erion GJONAJ[1-2] and Cameron TROPEA [1]

[1] Institute of Fluid Mechanics and Aerodynamics, Technische Universität Darmstadt, 64287, Germany
[2] Institute for the Theory of Electromagnetic Fields, Technische Universität Darmstadt, 64289, Germany
Corresponding author: pstegmann@sla.tu-darmstadt.de

Abstract

Airplanes passing the incuda (anvil-) regions of tropical cumulonimbi-clouds are at risk of suffering an engine power-loss event and engine damage due to ice ingestion [1]. In an attempt to forward-model the single scattering properties of typical ice crystal shapes illuminated by a Gaussian beam, a C++ code has been developed based on the geometrical optics approximation. Its results are compared to Finite-Difference-Time-Domain- (FDTD) simulations at intermediate ice particle sizes.

1 Introduction

It has been known since the mid-90s that the incus region of tropical cumulonimbus clouds poses a certain threat to commercial jet-powered aircraft [2]. The dominant types of aerosols under these atmospheric conditions are ice crystals and ice crystal aggregates [1]. Thus, measurement devices capable of acquiring specific data about the ice particles in flight and which are robust and compact enough for use in commercial airliners are highly desirable. As a prerequisite for the use of optical measurement devices, similar to those already employed for monitoring liquid water droplets in aerodynamic flows [3], a forward model of the laser-light scattering by a single ice crystal is created.

2 Geometrical Optics Approximation for Maxwell's Equations

For particles with a large Mie parameter and for complex irregular scattering shapes exact GLMT-methods [4] as well as numerical schemes like FDTD fail. The only viable option for high frequency, -large -size scattering problems is the geometrical-optics approximation. Given an expansion of the fields in terms of inverse powers of the wavenumber k proposed by Debye [5], the macroscopic form of Maxwell's equations as the basis for optics [6] can be split up into a succession of approximate equations whose solutions deliver an increasing degree of fidelity with respect to the exact solution. The zeroth order approximation is the well-known eikonal equation and the first order approximation includes two equations governing the amplitude transport for a plane vector-wave. As a consequence of this approximation, the electromagnetic field behaves like a stream of sharply localized particles [7]. Nevertheless the result is still a field theory [5] governed by the so-called *optical* Lagrangian.

In order to trace the behavior of the electromagnetic field inside the ice particle, a suitable surface triangulation of the polyhedral ice crystal is chosen and standard methods of computer graphics involving ray-tracing [8] are applied. These algorithms also allow one to consider fully three-dimensional particles in a quasi-dynamic setting. Although the initial situation is similar and the pure ray-tracing -procedure is identical to the work of Macke [9], the calculation of phase and amplitude along the rays is a generalization of the more sophisticated techniques proposed by Deschamps [10] and Ren [11].

3 Modelling of Gaussian Beam Incidence

To accommodate for the influence of the Gaussian beam shape on amplitude and phase of the rays incident upon the ice crystal, the straightforward procedure of Xu [12] is adapted to the present case. The amplitude and phase are calculated directly from the electromagnetic field of a zeroth order Davis-beam [13] while the wave-vector is given as the gradient of the phase. The same technique is studied extensively by Berry [14] in a different context.

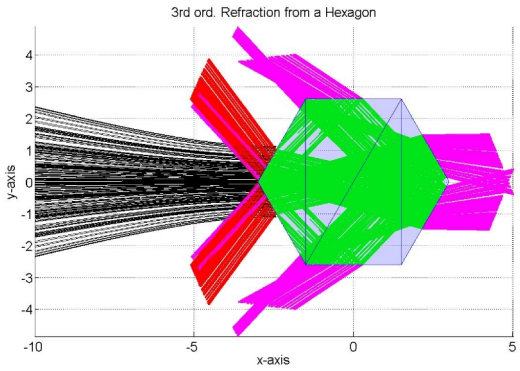


Figure 1 *Third order refraction (cumulative) of a sharply focused Gaussian beam by a hexahedral particle.*

3.1 Implementation

The code implementation itself was carried out in C++. The meta-template library blitz++ [15] was used in order to support high-performance vector- and matrix –operations.

4 FDTD Simulation and Experiment

Efforts to validate the geometrical optics results include a FDTD simulation for a comparable scattering configuration at intermediate sizes with the commercial CST studio suite [16] and an experiment with lab-grown water ice crystals. The details of the FDTD-method employed are explained in the classic paper by Yee [17]. A sample result of the FDTD simulation is shown below.

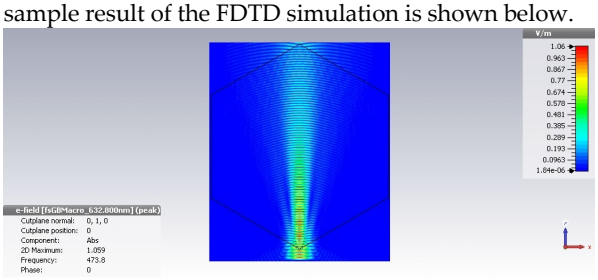


Figure 2 *Electric field strength in the x-z-plane of a Gaussian beam incident on a hexahedral particle.*

5 Acknowledgement

P. Stegmann would like to thank the Graduate School Computational Engineering and the Research Training Group GRK 1114 at the Technische Universität Darmstadt for supporting his Ph.D.-program.

6 References

[1] J. Mason, J. W. Strapp, P. Chow. The Ice Particle Threat to Engines in Flight. 44th AIAA Aerospace Sciences Meeting and Exhibit, Reno (2006).

[2] R. Lawson, L. Angus. Cloud Particle Measurements in Thunderstorm Anvils and Possible Weather Threat to Aviation. Journal of Aircraft Vol. 35, No. 1 (1998).

[3] H.-E. Albrecht, M. Borys, N. Damaschke, C. Tropea. Laser Doppler and Phase Doppler Measurement Techniques. (Springer Berlin-Heidelberg, 2006).

[4] G. Gouesbet, G. Gréhan. Generalized Lorenz-Mie theories. (Springer Berlin-Heidelberg, 2011)

[5] Yu. Kravtsov, Yu. Orlov. Geometrical Optics of Inhomogeneous Media. (Springer Series on Wave Phenomena, 1990).

[6] M. Born, E. Wolf. Principles of optics: Electromagnetic theory of propagation, interference and diffraction of light. (Cambridge University Press, 1999)

[7] D. Gloge, D. Marcuse. Formal Quantum Theory of Light Rays. Journal of the Optical Society of America 59, p. 1629-1631 (1969).

[8] T. Akenine-Möller, E. Haines, N. Hoffman. Real-Time Rendering. (CRC-Press, 2008).

[9] A. Macke. Modellierung der optischen Eigenschaften von Cirruswolken. Dissertation im Fachbereich Geowissenschaften der Universität Hamburg (1994).

[10] G. Deschamps. Ray Techniques in Electromagnetics. Proceedings of the IEEE, Vol. 60, p. 1022-1035 (1972).

[11] K.-F. Ren, F. Onofri, C Rozé, T. Girasole. Vectorial complex ray model and application to two-dimensional scattering of plane wave by a spheroidal particle. Optics Letters, Vol. 36, p. 370-372 (2011)

[12] F. Xu, K. F. Ren, X. Cai, J. Shen. Extension of geometrical optics approximation to on-axis Gaussian beam scattering. II. By a spheroidal particle with end-on incidence. Applied Optics, Vol. 45, p. 5000-5009 (2006).

[13] L. W. Davis. Theory of electromagnetic beams. Physical Review A, Vol. 19, p. 1177-1179 (1977).

[14] M. Berry. Exact and geometrical optics energy trajectories in twisted beams. J. Opt. A, Vol. 10 (2008).

[15] T. L. Veldhuizen.. Arrays in Blitz++. In Proceedings of the 2nd International Scientific Computing in Object-Oriented Parallel Environments (ISCOPE'98), Santa Fe, New Mexico (December 8-11, 1998)

[16] R. Sjiariel. CST STUDIO SUITE 2012 and the EDA workflow. Application note, CST AG (2012).

[17] K. S. Yee. Numerical Solution of Initial Boundary Value Problems Involving Maxwell's Equations in Isotropic Media. IEEE Transactions on antennas and propagation, Vol. AP-14, p. 302-307.

Formation of Spherical Aggregate from Micodroplet Containing Submicron Inclusions

Mariusz WOŹNIAK*, Justice ARCHER, Gennadiy DERKACHOV, Daniel JAKUBCZYK, Tomasz WOJCIECHOWSKI, Krystyna KOLWAS, Maciej KOLWAS

Institute of Physics, Polish Academy of Sciences, Al. Lotników 32/46, 02-668 Warsaw, Poland

**Corresponding author: mwozniak@ifpan.edu.pl*

Abstract

We have investigated formation of ordered aggregates of spherical nanosilica particles in evaporating droplets of aqueous colloidal suspension. Droplets have been freely suspended in the electrodynamic quadrupole trap. Slow drying process and the successive states of the aggregate formation have been investigated using static light scattering method. Modification made to the typical configuration of the electrodynamic quadrupole trap enables us to deposit the final (and the semi-final) structures and to investigate them with SEM methods.

1 Introduction

Evaporation process on a flat surface leading to formation of drop-deposited nanoparticle films and self-assembled monolayers of nano-crystals have been recently widely observed and discussed in the literature [1]. By means of the aggregation phenomenon it is possible to create composites whose physical properties are determined not only by their chemical composition but also by the specific morphology. This new kind of structures, known as metamaterials, exhibit unique (optical) properties not present in conventional materials.

However, much less is known about aggregation process in systems with spherical geometry such as drying microdroplets of suspension (e.g. [2]). Few studies concerning shell-structured or densely-packed aggregates of spheres appear in the literature (e.g. [3]) and even fewer have reported as regular, as dense or as large aggregates that we can observe and model [4,5]. Similar self-assembled structures, but generated by means of a fast spray drying method, were investigated in our former collaborative work [6].

In contrast to evaporation of a film of suspension leading to nanoparticle films, evaporation process of levitated microdroplets is unaffected by flat bulk surface. This particular geometry enables production of truly 3D photonic metamaterials and quasi-photonic crystals with spherical or quasi-spherical symmetry. In order to produce and diagnose this kind of objects it is necessary to build highly specialized equipment. These requirements are satisfied by electrodynamic traps with climatic chambers and additional control instruments built in our laboratory. To analyse and measure liquid microdroplets and particles aggregating within them we use static light scattering methods. Our modifications and improvements made to the typically used geometry of the electrodynamic quadrupole trap gives us a possibility to deposit aggregates one-by-one on a flat silicon substrate and to investigate them additionally with SEM.

2 Evaporation process and surface phenomena

Aggregation in a micodroplet of suspension is caused by evaporation process of liquid phase. The droplet evaporation process is driven by mass and heat transport through the droplet surface. A convenient expressions of the evaporation dynamics of a spherical droplet of pure liquid can be found [5,7]:

$$a\frac{da}{dt} \equiv a\dot{a} = \Lambda D\left[\frac{p_{cc}(T_{cc})}{T_{cc}} - \frac{p_a(T_a)}{T_a}\right] \tag{1}$$

where a is a droplet radius, p_a and p_{cc} are the vapour pressure near the droplet surface and far from the droplet respectively, T_a and T_{cc} are the temperatures of the droplet surface and the reservoir. D is the diffusion constant of vapour in the ambient gas and $\Lambda = M/(R\rho)$, where M and ρ are the molecular weight and density respectively, R is the universal gas constant.

The surface activity $\Delta\sigma$, describing the change of surface tension with respect to the surface tension of a pure liquid σ_w can be expressed as:

$$\Delta\sigma = \sigma_w - \frac{aT_a}{2\Lambda}\ln\left[1 - T_a\frac{a\dot{a} - (a\dot{a})(t_0)}{\Lambda D p_s T_a}\right] \tag{2}$$

It is worth noticing that using Eq. (2) we can find the temporal evolution of the surface pressure $\Delta\sigma(t)$ from the temporal evolution of the droplet radius a(t).

3 Experiment

Our experimental setup consists of a quadrupole electrodynamic trap with 4 linear electrodes in a vertical alignment. The electrodes provide alternating (AC) electric field in quadruple configuration. Separate annular electrodes around the vertical ones provide static (DC) field balancing the particles weight. The trap is kept in a small thermostatic chamber, which allows us to control parameters of the internal atmosphere by choosing ambient gas and adjusting temperature (from -40 up to +50°C). Figure 1 shows schematic drawing of the experimental setup. For graphic purposes climatic chamber is not shown.

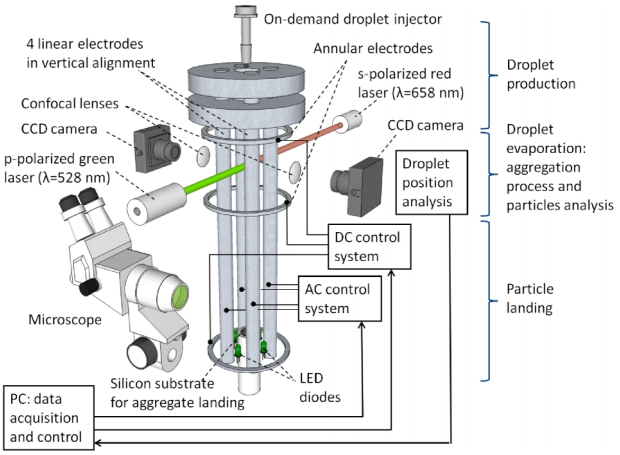


Figure 1. *Schematic drawing of the experimental setup.*

Droplets are injected by on-demand injector and charged by charge separation in the external field. Two coaxial, counter propagating lasers are used simultaneously for droplet illumination: green (532 nm) p-polarized and red (654 nm). The entirely defocused image is used for scatterometry. The focused image is used for droplet position stabilization with a PID type loop. The temporal evolution of the droplets is obtained with the Mie Scattering Lookup Table Method [8]. It is based on the fitting of the complete Mie theory predictions (stored in the lookup table) to the experimentally obtained scattering patterns. Our method provides accuracy of ±10 nm [8].

Additionally, it is worth noticing that vertical alignment of the quadrupole trap allows us to progressively reduce DC field without changes of the AC field constraining droplet (aggregate) horizontal position and thus soft-landing of the aggregating structure on the silicon substrate at the bottom part of the trap. It is also possible to shift the substrate inside the trap up to the stabilization point. Deposition allows us to further analyse aggregates with microscopic methods (SEM, TEM, AFM).

4 Results and discussion

The experiment was conducted at the temperature of 288.2 K, the initial humidity of 94% and the atmospheric pressure of 1006 hPa. We used aqueous suspension of SiO_2 spheres with diameter of 450 nm (MP-4540, Nissan Chemical Industries). The suspension obtained from the manufacturers was diluted with ultrapure water (Milli-Q Plus, Millipore) in 250:1 proportion resulting in the initial volume concentration of nanoparticles ~0.1%. Stabilizing agent introduced by the manufacturer was not removed.

Figure 2 shows experimental evolution of the droplet radius $a(t)$ obtained with the Mie Scattering Lookup Table Method as well as the numerical results of our evaporation model for pure water and water with solid inclusions (fraction of ~0.1%).

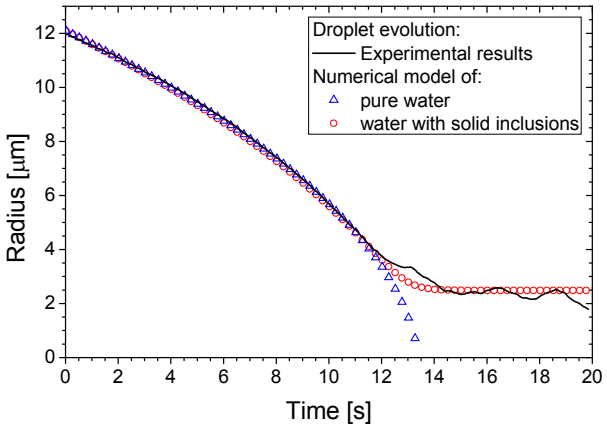


Figure 2. *Evolution of the droplet of aqueous suspension of 450 nm silica spheres (experimental and numerical results) and numerical results for droplet containing pure water.*

Using Eq. (2) we can express the surface pressure as a function of the droplet radius $\Delta\sigma(a)$. Figure 3 shows $\Delta\sigma(a)$ together with visualisation of the selected stages of our simulation of the evolution of an evaporating droplet of nanosilica suspension (droplet size scaled for clarity) [4].

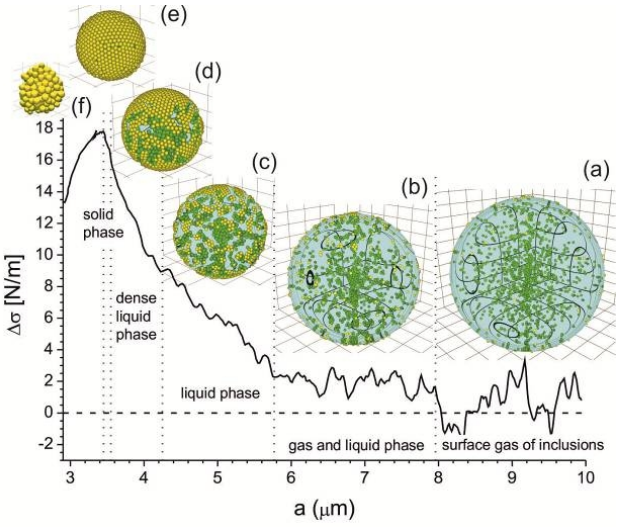


Figure 3. *Surface pressure isotherm together with visualisations of the selected stages of our simulations [4] of the evolution of a droplet of suspension (droplet size scaled freely for clarity).*

We have observed and also modelled different thermodynamic states of the surface layer of inclusions, occurring during evaporation of liquid with silica inclusions. They have been separated in Figure 3 with vertical, doted lines.

For relatively large droplet (a > 7.9 μm) when the fraction of inclusions is smaller than ~3%, there is a surface gas of inclusions on the droplet surface (Figure 3 (a)). Subsequently gas of inclusions is becoming denser (Figure 3 (b)). For 4.25 > a > 5.75 μm we observe the liquid-expanded phase (Figure 3 (c)). The surface is covered with large but dilute aggregates. Further evaporation of water compresses the surface structures while the number of inclu-

sions on the surface is further increasing. Additionally, this stage was investigated with SEM after deposition of the droplet with aggregating structure on the silicon surface (Figure 4 (a)). Due to the significant fraction of water deposited structure was not stable and disintegrated forming thin layer of silica nanoparticles.

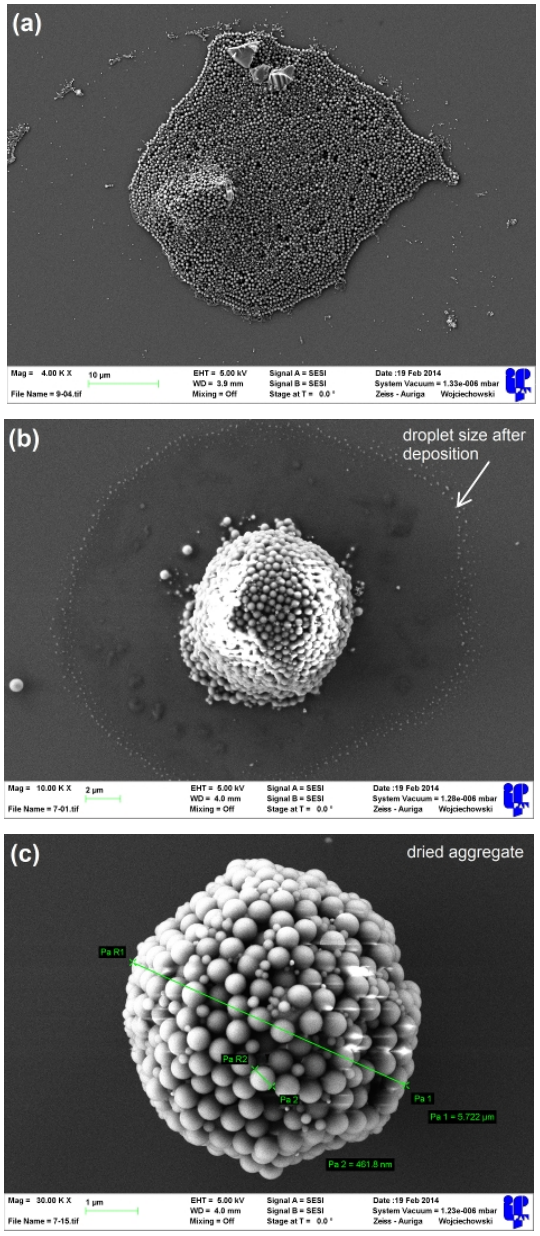


Figure 4. *SEM images of the deposited structures: (a) middle stage of the formation, (b) semi-final and (c) final (totally dried) stage of the aggregation/evaporation*

For a = ~4.25 μm a phase transition to liquid-condensed is possibly observed. Further compression leads to the surface liquid-solid transition for a = ~3.55 μm (Figure 3 (e)). This state can be possibly seen in Figure 4 (b). It can be inferred from careful observation of the SEM image that at the time of the deposition this structure was still containing a significant fraction of water, which totally dried out after landing. Therefore, we can see circular traces around the solid aggregate left by evaporating liquid. It can be noticed, that at this stage of aggregation, a well-organized structure, foreseen by our numerical model, appears on the aggregate surface. Subsequently, when the evaporation of the droplet continues, after the rapid growth of the surface pressure, a collapse of the surface layer takes place for a = ~3.45 μm (Figure 3 (f)). It is followed by the formation of a multilayered surface solid associated with the significant decrease in the surface pressure. The SEM image of the final structure observed after the deposition can be seen in Figure 4 (c). A transition from spherical symmetry to less regular structure can be identified by comparing Figure 4 (b) with Figure 4 (c).

5 Conclusion

We have shown that analysing the evolution of the droplet radius only, it is possible to derive enough information to determine surface states of inclusions of evaporating droplet of colloidal suspension. Our unique experimental setup gives us a possibility to deposit the aggregating structure at the selected stage of the evolution and analyse it with microscopic methods. Therefore, we were able to compare our numerical models of evaporation and aggregation with experimental results obtained with static light scattering method and SEM analysis. We found very good consistency between them.

However, application of SEM to the analysis of dynamic processes is limited. Hence, we were able to observe only to the final and the semi-final structures of drying aggregates because the previous stages were not stable enough and they disintegrated after deposition. Moreover, further evaporation on the surface of the substrate altered the evolution path.

Future perspectives for our research includes detailed consideration of the successive aggregation stages, utilization of various nanoparticles, as well as application of additional methods to "freeze" the evolution of the droplet at the earlier stages (e.g. by adding UV-active polymers).

6 References

[1] Rabani E., Reichman D. R., Geissler P. L., Brus L. E., Drying-mediated self-assembly of nanoparticles, Nature, 426: 271-274 (2003).

[2] Lee S. Y., Gradon L., Janeczko S., Iskandar F., Okuyama K., Formation of highly ordered nanostructures by drying micrometer colloidal droplets, ACS Nano, 4 (8): 4717–4724 (2010).

[3] Lauga E.. Brenner M. P., Evaporation-driven assembly of colloidal particles, Phys. Rev. Lett., 93: 238301 (2004).

[4] Derkachov G., Kolwas K., Jakubczyk D., Zientara M., Kolwas M., Drying of a Microdroplet of Water Suspension of Nanoparticles: from Surface Aggregates to Microcrystal, J. Phys. Chem. C, 112: 16919-16923 (2008).

[5] Jakubczyk D., Kolwas M., Derkachov G., Kolwas K., Surface states of micro-droplet of suspension, J. Phys. Chem. C, 113 (24): 10598-10602 (2009).

[6] Onofri F.R.A., Barbosa S., Toure O., Woźniak M., Grisolia C., Sizing highly-ordered buckyball-shaped aggregates of colloidal nano-particles by light extinction spectroscopy, J. Quant. Spectrosc. Radiat. Transfer, 126: 160–168 (2013).

[7] Pruppacher H., Klett J., Microphysics of Clouds and Precipitation (Kluwer, The Netherlands, 1997).

[8] Jakubczyk D., Derkachov G., Kolwas M., Kolwas K., Combining weighting and scatterometry: application to a levitated droplet of suspension. J. Quant. Spectrosc. Radiat. Transfer, 126: 99-104 (2013).

Thermometry of Evaporating Acetone Droplets in Near-Critical Conditions by Combined Phosphorescence/Fluorescencence Measurements

Benjamin BORK [1,*], Thomas KÖNIG [1], Florian WECKENMANN [2] Grazia LAMANNA [2] and Andreas DREIZLER [1]

[1] Reaktive Strömungen und Messtechnik, Technische Universität Darmstadt, Darmstadt, 64287, Germany
[2] Institut für Thermodynamik der Luft- und Raumfahrt, Universität Stuttgart, Stuttgart, 70569, Germany

Corresponding author: bork@csi.tu-darmstadt.de

Abstract

The scope of this work is the development of a measurement technique that enables contactless thermometry of single free-falling acetone droplets. A temperature dependence of the overall phosphorescence signal on the liquid acetone temperature is exploited. The fluorescence signal is merely influenced by acetone temperature. Therefore the phosphorescence/fluorescence signal ratio depends on a wide range of temperatures. The ratio is independent of pulse to pulse laser energy variations and fluctuations in the laser beam profile. For excitation a laser wavelength of 320 nm is chosen for an increased absorption length.

Liquid acetone phosphorescence shows strong nonlinearity upon excitation laser energy density. Therefore an extensive study in bulk liquid acetone is conducted to identify the parameters to prepare for well-controlled temperature measurements. These parameters and an estimate for the accuracy and precision of the measurement technique are given.

1 Introduction

Recent developments in combustion systems lead to increased ambient pressures and temperatures during fuel injection. The liquid fuel's thermodynamic critical point is sometimes exceeded by the ambient conditions in terms of pressure and temperature. Numerical and experimental methods to describe the transition from liquid fuel to gaseous fuel/air mixtures are scarce under these conditions.

An experiment with a single free-falling acetone droplet in nitrogen atmosphere at pressures and temperatures in the vicinity of acetone's critical point (p_c= 47 bar, T_c = 508 K) is set up. It is used to develop and adapt measurement techniques to the mentioned conditions and to gain a better understanding of the underlying droplet dynamics.

The temperature of the evaporating droplet during free-fall is a parameter of great interest. Well established optical methods for droplet temperature measurements cannot be applied due to different reasons. The rainbow technique [1] is limited to spherical droplets. The global rainbow method [2] is based on droplet ensembles. At near-critical conditions surface tension is reduced to such degree that even small droplets oscillate considerably. Two-colour laser-induced fluorescence (LIF) [3] requires the addition of a tracer dye. As the influence of such tracers on the thermodynamic equilibrium close to the critical point is unknown, results obtained by this technique require verification.

LIF of acetone vapour has been investigated in detailed by several groups [4-6] and it is widely used for concentration measurements and gas phase thermometry. Acetone absorbs uv light in a broad spectral region followed by emission of fluorescence (lifetime of a few nanoseconds) and phosphorescence (lifetime in the microsecond regime). If the gas surrounding the droplet contains oxygen it will quench only the phosphorescence but not the fluorescence of the acetone vapour due to significant difference in lifetimes. This mechanism was investigated by Tran et al. [7] aiming for a method to distinguish between liquid and gaseous phase at near-critical conditions.

The decay time of liquid acetone phosphorescence does not only depend on oxygen concentration but also on temperature. This temperature dependence potentially can be exploited for acetone droplet temperature measurements; this potential is investigated in this work.

2 Experimental Setup

For droplet experiments a pressure chamber is used that can be operated up to 60 bar. Optical access is provided from four directions. The chamber can be heated up to 550 K. The identical chamber can be used for calibration measurements in bulk pure liquid acetone. For this purpose it can be equipped with a special window that guides the laser beam to the measurement volume avoiding significant absorption by liquid acetone prior to the region of interest.

The ratio of phosphorescence and fluorescence signals induced by the same absorption event is measured. The signal ratio is insensitive to shot-to-shot laser energy fluctuations, inhomogeneities in the beam profile and lensing effects at the droplet surface. However, it is a prerequisite that both signals scale linearly with laser energy density.

The experimental setup is depicted in Figure. 1. The dye laser is operated with DCM in ethanol and allows wavelength tuning between 308 and 325 nm. The laser pulse energy is adjusted by a diffractive beam attenuator between 0.05 and 5 mJ/pulse without affecting the beam profile. The pulse length is approximately 5 ns.

The Gaussian beam is vertically extended by a cylindrical telescope and its maximum is cut out by a vertical slit (6 by 0.8 mm). 2 % of the laser pulse energy is reflected by a 20 mm thick quartz block onto a highly sensitive energy meter. The vertical slit is imaged into the measurement volume by two spherical lenses using a 4f-arrangement. The laser pulse energy in the measurement volume is up to 600 µJ corresponding to an average laser pulse energy density of 12 mJ/cm² while the beam profile is an almost ideal top-hat.

The signal is split by a 70/30 beam splitter. 70 % of the signal is imaged onto an image intensifier that is equipped with an interline CCD camera. 30 % is detected by an identical camera operated without an image intensifier. Both camera objective lenses are of identical type (180 mm, f/3.5). Fluorescence and phosphorescence of acetone have almost fully overlapping emission spectra and can only be separated temporally by gating in the nanosecond regime. The gated image intensifier is used to capture the phosphorescence signal with a 10 µs gate starting 20 ns after the laser pulse maximum. The second camera records the entire luminescence signal with an overall exposure time of 200 µs.

Recording the overall luminescence signal instead of fluorescence only simplifies the measurement setup as it requires one instead of two image intensifiers. Since the luminescence signal is dominated by fluorescence at elevated temperatures the result is expected to be identical if the signal ratio measured in droplet experiments is consistent with calibration.

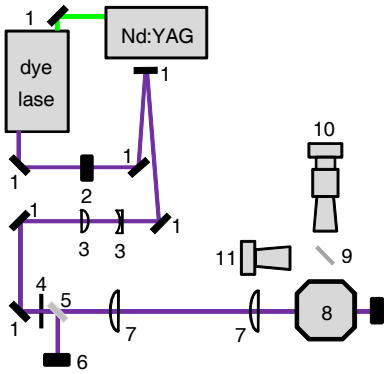


Figure 1 *Experimental setup: 1 mirror, 2 attenuator, 3 cylindrical lens, 4 slit aperture, 5 quartz plate, 6 energy meter, 7 spherical lens, 8 pressure chamber, 9 beam splitter, 10 intensified CCD camera, 11 CCD camera.*

3 Results and discussion

As the primary prerequisite the linearity of fluorescence and phosphorescence are investigated in bulk liquid acetone. The wavelength is set to 320 nm as this has been identified as a suitable wavelength in terms of absorption length for droplets with a diameter of approximately 1 mm. In previous measurements [8] the phosphorescence signal showed a strongly non-linear dependence on laser energy density already at values below 10 mJ/cm². In contrast, the fluorescence was observed to be linear up to the maximum laser energy tested (50 mJ/cm²).

The dependence of the overall phosphorescence signal on the laser energy density is displayed for different temperatures in Figure 2. Polynomials of first and fourth order are fit to the scatter plots by the least-square method. While the linear fit is applied to energy densities up to 0.5 mJ/cm² the fourth order polynomial is fit to the entire dataset. At 296 K a linear dependence is observed only for energy densities of less than 0.5 mJ/cm². With increasing temperature, at 383 K, the linear range extends to energy densities beyond 2 mJ/cm². Above 423 K phosphorescence signals become linear independent of laser energy density.

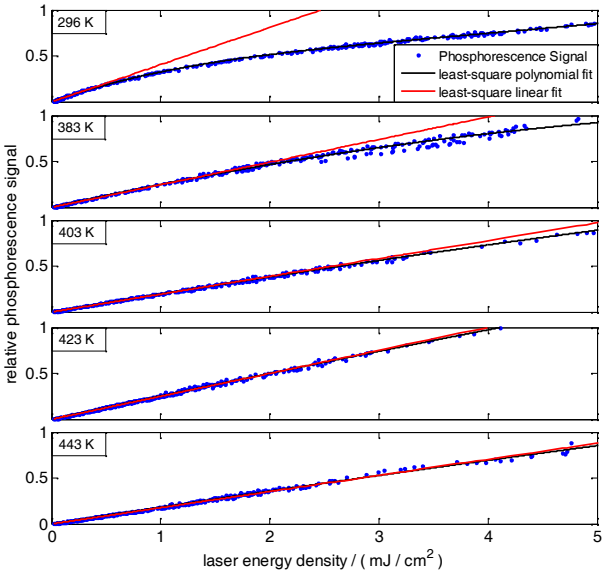


Figure 2 *Liquid acetone relative phosphorescence signal versus laser energy density at 58 bar.*

In Figure 3 the phosphorescence/luminescence signal ratio is plotted over the laser energy density for each laser shot. Each scatter plot consists of 350 measurements.

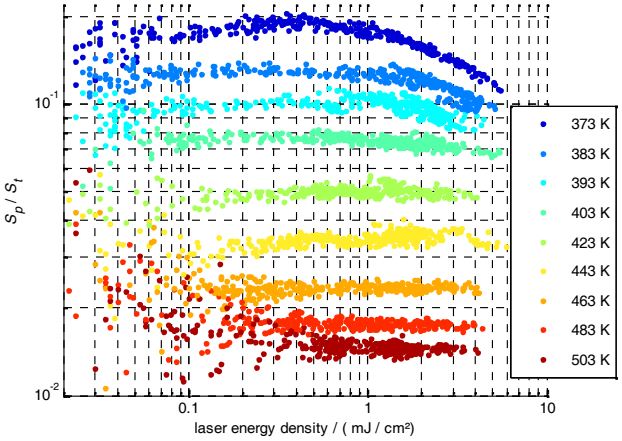


Figure 3 *Phosphorescence/luminescence signal ratio of liquid acetone at 58 bar for 320 nm excitation wavelength*

At laser energy densities below 0.1 mJ/cm² the scatter plots spread due to low signal to noise ratio. Close to the critical temperature (508 K) the spreading occurs already at 0.5 mJ/cm² due to the very low phosphorescence signal. For future single droplet temperature measurements in near-critical conditions the droplet temperature is expected to be at minimum 100 K below the critical point of acetone. Therefore, the laser energy density is chosen to a maximum of 1 mJ/cm² for the following considerations.

To convert measured phosphorescence/luminescence ratios to droplet temperatures, a calibration curve is required. This calibration curve is displayed in Figure. 4. It is based on measurements by the intensified camera only to make sure that no inaccuracies (slight differences in vignetting or any other disturbances) in the imaging cause any systematic errors in the calibration. Using a single camera the signal ratio is derived from individual laser shots because phosphorescence and luminescence signals are recorded from consecutive measurements. To obtain a calibration independent of pulse energy density the phosphorescence/luminescence signal ratios are averaged and corrected by the ratio of the corresponding average pulse energy densities. The calibration curve is fitted by a fourth order polynomial to interpolate in-between the discrete sampling points.

The deviation between calibration curves obtained from different regions of interest and laser pulse energy regimes is taken as an estimate for the accuracy of the presented temperature measurement technique. It yields values of 2 K maximum uncertainty up to 473 K, 3 K at 483 K and 5 K between 493 and 507 K. The precision is derived from laser pulse correlated signal ratios of both cameras at laser energy settings between 0.5 and 1 mJ/cm². The standard deviation of the signal ratio at constant temperature corresponds to an uncertainty in temperature of less than 2 K between 403 K and 473 K and increases to 7 K at 507 K.

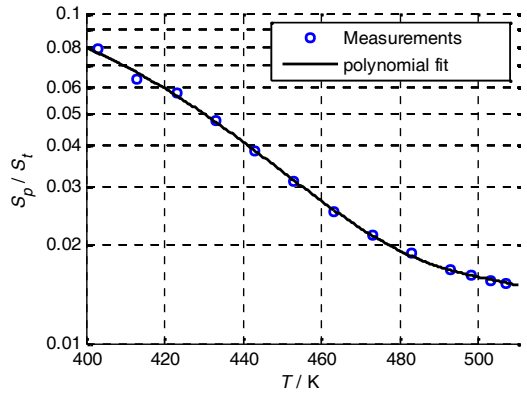


Figure 4 *Calibration curve for liquid acetone at 58 bar for 320 nm excitation wavelength*

4 Conclusions and Outlook

A novel technique is presented to measure temperatures of acetone droplets. The method is limited to a temperature range between 400 K and 508 K (T_c) and the laser excitation energy density has to be chosen carefully to guarantee a linear behaviour of the phosphorescence signal. In future experiments the technique is applied to droplets, both in non-evaporating conditions at constant temperature to further explore the limits of the new methodology and to evaporating droplets. An exemplary fluorescence droplet image is illustrated in Figure 5.

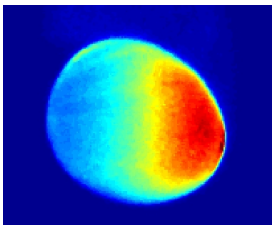


Figure 5 *Fluorescence of a single acetone droplet in nitrogen at 483 K and 58 bar for 320 nm excitation wavelength.*

5 Acknowledgement

We kindly acknowledge the financial support by Deutsche Forschungsgemeinschaft through SFB-TRR 75.

6 References

[1] Roth N., Anders K. and Frohn A., Simultaneous Measurement of Temperature and Size of Droplets in the Micrometer Range, Journal of Laser Applications 2(1):37-43 (1990)

[2] Saengkaew S., Godard G., Blaisot J. B., Gréhan G., Experimental analysis of global rainbow technique: sensitivity of temperature and size distribution measurements to non-spherical droplets, Experiments in Fluids 47(4-5):839-48 (2009)

[3] Lavieille P., Lemoine F., Lavergne G., Lebouché M., Evaporating and combusting droplet temperature measurements using two-color laser-induced fluorescence, Experiments in Fluids 31(1):45-55 (2001).

[4] Thurber M., Grisch F., Kirby, B., Votsmeier, M., Hanson, R., Measurements and modeling of acetone laser-induced fluorescence with implications for temperature-imaging diagnostics, Applied Optics 37(21):4963-78 (1998).

[5] Koch, J. D., Hanson, R. K., Koban, W., Schulz, C., Rayleigh–calibrated fluorescence quantum yield measurements of acetone and 3-pentanone, Applied Optics 43(31):5901-5910 (2004).

[6] Braeuer, A., Beyrau, F., Leipertz, A., Laser-induced fluorescence of ketones at elevated temperatures for pressures up to 20 bars by using a 248 nm excitation laser wavelength: experiments and model improvements, Applied Optics 45(20):4982-9 (2006).

[7] T. Tran, *Acetone Planar Laser-Induced Fluorescence and Phosphorescence for Mixing Studies of Multiphase Flows at High Pressure and Temperature*, (Ph.D. Thesis, Georgia Institute of Technology, USA, 2008).

[8] Bork B., Stritzke F., Weckenmann F., Lamanna G., Weigand B., Dreizler A., Acetone photophysics investigations for the application of PLIFP to droplet evaporation measurements under supercritical conditions, *25th European Conference on Liquid Atomization and Spray Systems (ILASS–Europe)*, 1-4 September, Chania, Greece, 2013

ROLE PLAYED BY MULTIPLE SCATTERING ON THE ABSORPTION AND SCATTERING PROPERTIES OF SOOT FRACTAL AGGREGATES

Jérôme YON*, Damien Hebert, Alexandre BESCOND, Claude ROZE and Alexis COPPALLE

[1] CORIA-UMR 6614- Normandie Université, CNRS-Université et INSA de Rouen
Campus Universitaire du Madrillet, 76801 Saint Etienne du Rouvray, France

Corresponding author: yon@coria.fr

1 Context of the study

It is well known that soot particles have a toxicological impact due to their ultrafine size and their content in carcinogenic molecules (PAH). More recently, it has been demonstrated that they have a strong influence on the global warming [1]. Transmission Electron Microscopy revealed the aggregated nature of these particles and their fractal properties corresponding to a power law relationship between the aggregate mass and its size.
The optical in-situ characterization of soot particles is very promising for many applications. Indeed, measurement of light extinction by soot particles is often considered as a reliable way to determine the soot volume fraction. Laser induced incandescence is widely used to measure soot volume fraction in many applications. Furthermore, angular light scattering allows to determine the particle size or fractal dimension [2].

Due to the complex morphology of these particles and the computation time needed for the evaluation of their exact radiative properties, the optical measurements are usually interpreted by the Rayleigh Debye Gans theory for fractal aggregates (RDG-FA). This simple theory predicts that light absorption is related to the number N_p of primary spheres in the aggregates (proportional to the particle volume) and the light scattering to N_p^2. The angular dependence of the scattered light is described by a structure factor which depends on the particle size and fractal dimension [3]. This theory appears to be reliable given the experimental uncertainties [4]; however, several important hypotheses are made including that radius of the primary sphere has to be smaller than the wavelength (Rayleigh regime), each primary spheres is supposed to be exposed to the incident light source and multiple scattering inside the aggregate is neglected.

2 Objectives of the study

Recently, we suggested to incorporate the multiple scattering effects inside aggregates in the RDG-FA theory by a phenomenological approach involving the scaling approach (q-region) introduced by Sorensen [5]. By comparing this approach with exact absorption and scattering properties of 150 aggregates computed by the discrete dipoles approximation (DDSCAT)[6] for 7 wavelengths (from 266 to 1064 nm), we were able to propose correction terms to the RDG-FA theory in order to take into account the multiple scattering effects [7].

In the present study, the impact of inclusion of multiple scattering effects on extinction spectra and angular scattering measurements is presented.

3 Main results

The figure 1 presents the impact of the inclusion of the multiple light scattering inside the aggregates on the extinction spectra calculated in case of Diesel soot particles [8]. It is shown that multiple scattering soften the decreasing of the light extinction as a function of the wavelength in the near UV spectrum. The multiple scattering also reduces contribution of the total scattering in the extinction coefficient.

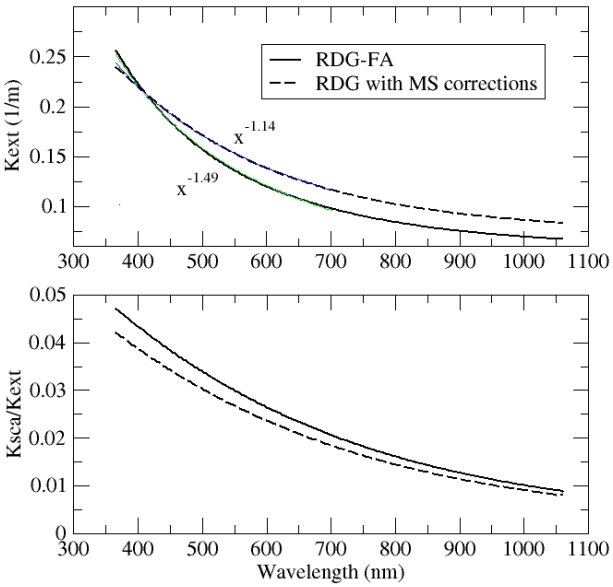


***Figure 1** Impact of aggregate internal multiple scattering on the evaluation of the extinction spectra.*

The impact of the multiple scattering on the angular light scattering is presented in figure 2. The dash line corresponds to the structure factor predicted by the RDG-FA (whatever the wavelength) whereas continuous curves takes into account multiple scattering for wavelengths 266, 532 and 1064 nm. We observe a moderated under prediction of the RDG-FA at any scattering angles for largest wavelengths whereas at lowest wavelengths multiple scattering causes an important over prediction of the RDG-FA. The slope of the power law regime for larger scattering angles (or corresponding norm of the scattering

vector q=4π/sin(θ/2) can also deviate from the theoretical value (equal to the opposite of the fractal dimension). This indicates that fractal dimension determined by angular scattering measurements at 266 nm can lead to an over prediction of the fractal dimension by a factor higher than 8%.

Nevertheless, we observe that measurements performed at 532 nm reduce the impact of the multiple scattering.

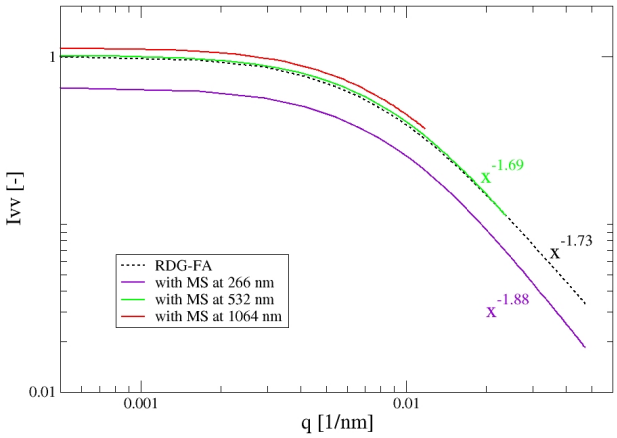


Figure 2 *Impact of aggregate internal multiple scattering on the evaluation of angular light scattering signal*

4 Conclusion

Correction terms of the RDG-FA theory were proposed using a phenomenological model, to take into account the multiple scattering inside the aggregates. They were adjusted by a comparison with rigourous results obtained by numerical computation using DDSCAT code. The influence of the multiple scattering on the extinction and scattering coefficients, and on the scattering angular distribution showed that this effect must be included for a more accrurate use for experimental data inversion.

5 Acknowledgement

This work has been supported by the French Civil Aviation Authority (DGAC).

References

[1] T. C. Bond, S. J. Doherty, D. W. Fahey, P. M. Forster, T. Berntsen, B. J. DeAngelo, M. G. Flanner, S. Ghan, B. Kärcher, D. Koch, S. Kinne, Y. Kondo, P. K. Quinn, M. C. Sarofim, M. G. Schultz, M. Schulz, C. Venkataraman, H. Zhang, S. Zhang, N. Bellouin, S. K. Guttikunda, P. K. Hopke, M. Z. Jacobson, J. W. Kaiser, Z. Klimont, U. Lohmann, J. P. Schwarz, D. Shindell, T. Storelvmo, S. G. Warren, and C. S. Zender, "Bounding the role of black carbon in the climate system: A scientific assessment," J. Geophys. Res. D: Atmos., 2013.

[2] C. Caumont-Prim, J. Yon, A. Coppalle, F.-X. Ouf, and K. Fang Ren, "Measurement of aggregates' size distribution by angular light scattering," Journal of Quantitative Spectroscopy and Radiative Transfer, vol. 126, pp. 140-149, 2013.

[3] R. A. Dobbins and C. M. Megaridis, "Absorption and scattering of light by polydisperse aggregates," Appl. Opt., vol. 30, pp. 4747-4754, 1991.

[4] R. K. Chakrabarty, H. Moosmüller, W. P. Arnott, M. A. Garro, J. G. Slowik, E. S. Cross, J. H. Han, P. Davidovits, T. B. Onasch, and D. R. Worsnop, "Light scattering and absorption by fractal-like carbonaceous chain aggregates: comparison of theories and experiment," Appl. Opt., vol. 46, pp. 6990-7006, 2007.

[5] C. M. Sorensen, "Q-space analysis of scattering by particles: A review," J. Quant. Spectrosc. Radiat. Transfer, 2013.

[6] B. T. Draine and P. J. Flatau, "User Guide for the Discrete Dipole Approximation Code DDSCAT 7.1 (http://arxiv.org/abs/1002.1505)," 2010.

[7] J. Yon, F. Liu, A. Bescond, C. Caumont-Prim, C. Rozé, F. X. Ouf, and A. Coppalle, "Effects of multiple scattering on radiative properties of soot fractal aggregates," Journal of Quantitative Spectroscopy and Radiative Transfer, vol. 133, pp. 374-381, 2014.

[8] J. Yon, R. Lemaire, E. Therssen, P. Desgroux, A. Coppalle, and K. Ren, "Examination of wavelength dependent soot optical properties of diesel and diesel/rapeseed methyl ester mixture by extinction spectra analysis and LII measurements (online first : DOI: 10.1007/s00340-011-4416-4)," Appl. Phys. B, vol. 104, pp. 253-271, 2011.

Characterization and Application of Laser-Light-Scattering by Ice Crystals

A.-K. GANSMANN*, P. STEGMANN and C. TROPEA

[1] *Fachgebiet für Strömungslehre und Aerodynamik, Technische Universität Darmstadt, Alarich-Weiß Straße 10, 64287 Darmstadt, Germany.*

Corresponding author: ann-kathrin.gansmann@stud.tu-darmstadt.de

Abstract

Under certain circumstances ice crystals in the atmosphere can be hazardous for air traffic [1]. Hence it is desirable to develop measurement devices to characterize the ice content in the air around the aircraft. In order to apply optical measurement techniques, the knowledge of the optical characteristics, especially polarisation and scattering, of ice crystals is essential. Those characteristics have been specifically examined in this study. An application in detecting and sizing ice crystals will be realized based on these results.

1 Introduction

In the past, cases have occurred in which airplanes passing through high convective clouds have suffered icing in the engines, especially the low-pressure compressor part. This has led to thrust decrease and even engine power loss events, since the compressor of a jet engine is prone to rotating stall and dangerous surge, if the flow conditions inside the compressor are perturbed [2]. Due to such events many measurement instruments for airborne detection and characterisation of the composition of clouds have been developed [1]. With an analytic solution for the light scattering by spherical particles (Mie-Theory [3]), water droplets can be detected and characterized by optical measurement techniques in a satisfactory manner. However, the situation for non-spherical particles like ice crystals is more complicated. The light scattering by these non-spherical particles, with the explicit purpose of developing a commercial in-situ measurement device, has only recently been the subject of detailed investigations.

At the Institute for Fluid Mechanics and Aerodynamics at the Technische Universität Darmstadt the scattering properties of ice crystals have been specifically studied and characterised. An application of this knowledge to a measurement device similar to those for water droplets will be realized.

2 Experiments on light scattering by ice crystals

Ice crystals are mostly of hexagonal basic structure, as Kepler has postulated in 1611 [4]. Other forms can occur (for example cubical), but these exist typically at conditions colder than -30°C and at high pressures [5].

2.1 Study on light scattering properties of a hexagon

With a hexagonal plate obtained by stereolithography it is possible to test the scattering properties of the hexagonal structure without the need of cooling. The plate has a height of 2.4 mm, an edge length of 2.54 mm and a refractive index of 1.6. With these characteristics it is not suitable for a quantitative comparison with light scattering experiments on real ice crystals. However, the main aim of this preliminary experiment is to test the general experimental set up (as can be seen in **Figure 1**), placed in a freezer chest.

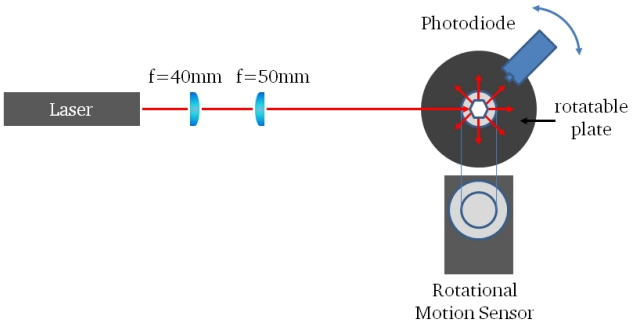


***Figure 1** Experimental set up*

The model crystal can be rotated through 360°. The position of the crystal is detected by a rotational motion sensor. At a crystal orientation of 0° the laser is aligned perpendicular to one facette of the hexagon. The scattered light is detected by a photodiode that can be placed at arbitrary scattering angles. The sample intensity distribution of the scattered light at a detector position of 95° relative to the laser as a function of the crystal orientation can be seen in **Figure 2** .

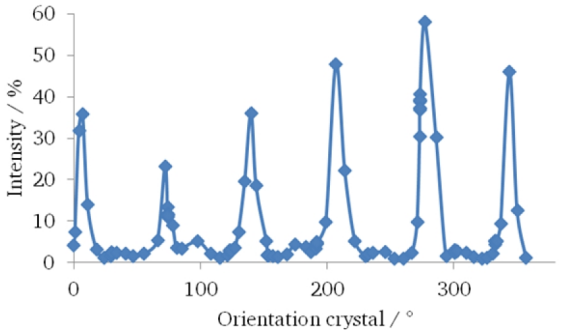


***Figure 2** Intensity of the scattered light as the model crystal is rotated by 360°*

The intensity achieves a maximum if two angles of the hexagon are facing each other. In-between there are far less distinct maxima if two edges are facing each other. The differences in the value of the maxima can be explained by the fact that the model crystal is not perfect. It has been polished by hand so that there is no guarantee that the edges are really parallel and that the angles are all identical and equally sharp.

2.2 Study on light scattering properties of ice crystals

In order to characterize real ice crystals, appearing on the side walls of the freezer due to the humidity in the air, the experimental set-up of section 2.1 is placed in a commercial laboratory freezer. The Helium-Neon laser cannot withstand such low temperatures (ca. -20°C), so a mirror periscope directs the Gaussian beam into the freezer.

A linear polarization filter is added to the detecting unit. The laser light is already polarized linearly so by turning the filter the polarization of the scattered light can be analyzed with the law of Malus [6]. This method is especially suitable for the limited space of the freezer.

An additional camera is focused onto the crystal to obtain the size of the ice crystal, using calibration of the magnification factor.

Future experiments are foreseen in which ice crystals are examined in an acoustic levitator, where they no longer have a defined stable orientation and light scattering characteristics correspond to an average over all crystal orientations.

2.3 Experiments on mixed phases

Not only ice crystals alone, but ice particles mixed in melting/freezing water droplets can be characterized as an extension of the previous experiment in the levitator. With the known light scattering characteristics of water droplets a distinction from the ice particles is possible.

2.4 Dynamical measurements

Ice and water particles in the atmosphere usually are in motion. There is an additional relative velocity if the particles are detected by a device on an airplane.

In a first step a velocity of the particles is added by simply turning the levitator off and letting them fall freely. A light barrier is added to the experimental set-up to record the droplet/crystal speed.

3 References

[1] D. Baumgardner, L. Avallone, A. Bansemer, S. Borrmann, P. Brown, U. Bundke, P. Y. Chuang, D. Cziczo, P. Field, M. Gallagher, J.-F. Gayet, A. Heymsfield, A. Korolev, M. Krämer, G. McFarquhar, S. Mertes, O. Möhler, S. Lance, P. Lawson, M. D. Petters, K. Pratt, G. Roberts, D. Rogers, O. Stetzer, J. Stith, W. Strapp, C. Twohy, and M. Wendisch, Meeting Summaries: In Situ, Airborne Instrumentation, *Workshop on In Situ, Airborne Instrumentation: Adressing and Solving Measurement Problems in Ice Clouds*, 25-27 June, Seaside, Oregon, 2010

[2] J. G. Mason, J. W. Strapp, P.Chow, The Ice Particle Threat to Engines in Flight, *44th AIAA Aerospace Sciences Meeting and Exhibit*, 9-12 January, Reno, Nevada, 2006

[3] H. C. Van de Hulst, *Light Scattering by Small Particles* (Dover Publications, Inc., New York, 1981)

[4] J. Kepler, J. Bromberg, *The Six-Cornered Snowflake* (Paul Dry Books, Inc., Philadelphia, Pennsylvania, 2010)

[5] W. F. Kuhs, Eiskalte Kristalle, Georgia Augusta 4: 28-33 (2005)

[6] E. Hecht, *Optik* (Oldenbourg Wissenschaftsverlag GmbH, München, 2009)

Light Scattering from Helical Microparticles

Rodrigo BECERRA-CARRILLO[1,*], Jian YANG[2] and Kevin ROBBIE[1]

[1] Department of Physics, Engineering Physics, and Astronomy, Queen's University, Kingston, Ontario K7L 3N6, Canada

[2] TDYE CFM Defect Engineering, GlobalFoundries Inc., Malta, NY 12020, USA

Corresponding author: rbecerra@physics.queensu.ca

Abstract

Helical thin films and microparticle suspensions were prepared with Glancing Angle Deposition. Differential circular transmittance measurements were performed on both. The films show the expected Bragg peak; the suspensions show it shifted towards shorter wavelengths, and also show a change in sign in the region where the film's Bragg peak appears. The Discrete Dipole approximation is used to study the scattering of a helical particle, and model the suspension as a medium with independent randomly oriented chiral scatterers.

1 Introduction

Glancing Angle Deposition (GLAD) is a specialized Physical Vapour Deposition technique that allows producing thin films with different morphologies: columnar, zigzag, and helical [1]. The helical thin films present two effects related to their structural chirality: optical rotation, and the Circular Bragg Phenomenon [2].

If the columns are detached from the film, one obtains a collection of helical microparticles. These have been used to fabricate nanostructured propellers [3]; however, their transmittance properties haven't been reported. The scattering properties of randomly oriented chiral spheres have been presented in [4]. In this work we describe the fabrication of the microparticles, how their transmittance properties vary from those of the films, and how we are modelling their scattering using the Discrete Dipole Approximation (DDA).

2 Experiment and simulation

Silicon thin film coatings were grown by GLAD, using a custom deposition chamber [1]. The material source was high purity silicon, and it was evaporated with an electron beam, and deposited on a glass substrate. The deposition angle was 85 degrees from the substrate normal, with a flux of 5 $Å s^{-1}$ measured by a quartz crystal microbalance. The helical particles were detached from the substrate by ultrasonic agitation, and suspensions in water were prepared. Differential circular transmittance (DCT) measurements were done using a custom spectrophotometer [5].

The scattering of a helical microparticle was studied numerically using DDA[6]. The simulations were done using Open DDA [7], in Mammouth Parallel II from Calcul Quebec (http://calculquebec.ca). The helical target consisted in a 5 turn, right handed helix, composed of ~10^5 dipoles. From the simulations the Extinction matrix **K** was calculated.

3 Results

Figure 1a and 1b show a SEM image with a cross-section of the right-handed (RH) and left-handed (LH) helical film, respectively. A comparison between RH and LH microparticles is shown in figure 1c. A powder of microparticles is shown in figure 1d. These films have a helical pitch (height of one turn) of 300 nm.

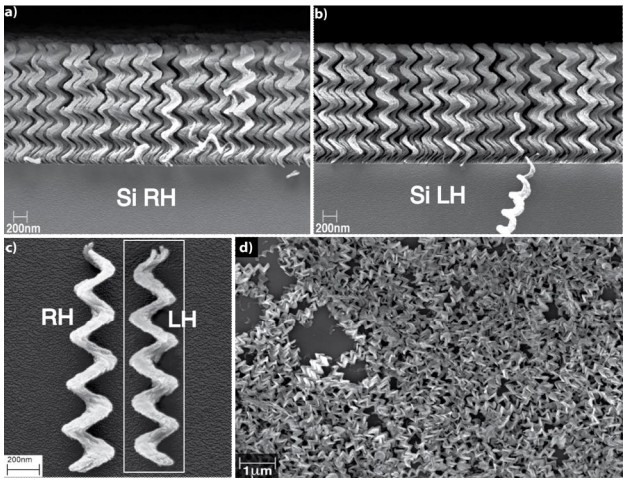


***Figure 1** SEM images of (a) RH, and (b) LH helical films. (c) Detail of a single RH and LH microparticle (d) Powder with helical microparticles. Adapted from [5].*

Figure 2 shows the measured DCT, for thin films and microparticle suspensions. We can see that the films produce the expected Circular Bragg Phenomenon [2]: a RH film transmits left circularly polarized light (LCP), and a LH film transmits right circularly polarized light (RCP). For the suspensions, we see that the Bragg peak shifts towards shorter wavelengths, and that the region where the film's original Bragg peak is located now shows a change in sign; therefore, the suspensions (in this region) transmit light with the same handedness as their structure.

A similar behaviour can also be seen for the measurements done in powders with helical microparticles, shown in figure 3. The plot also shows that

a racemic mixture of the powders does not produce any Bragg peaks.

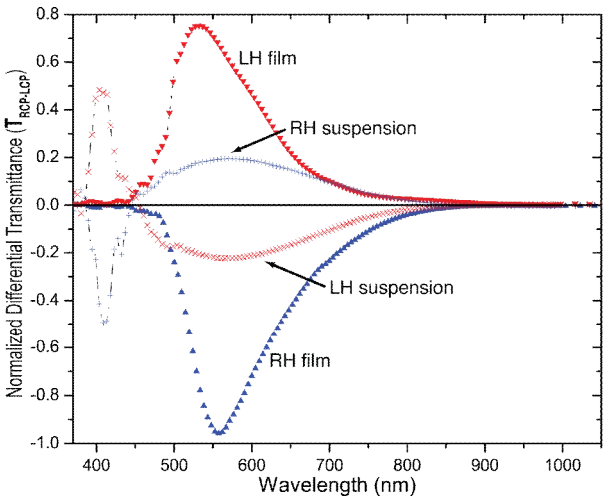


Figure 2 *Normalized DCT measurements for helical thin films and microparticle suspensions, adapted from [5].*

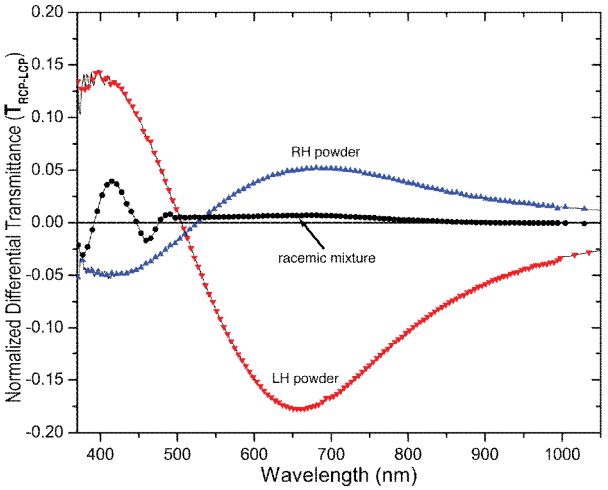


Figure 3 *Normalized DCT measurements for microparticle powders and racemic mixture, adapted from [5].*

The DCT is proportional to the K_{14} element of the extinction matrix [8]. Figure 4 shows the simulated K_{14} element, with light going through the helical axis of a RH microparticle, for several helical pitches. We see that the Bragg peak (where transmittance of LCP light is higher) shifts to longer wavelengths by increasing the helical pitch. This agrees with what we expected, as the Bragg wavelength is proportional to the product of the refractive index and the helical pitch [2].

For a helix with fixed pitch, the variation of the width also shifts the Bragg peak. Figure 5 shows this behaviour for a 350 nm pitch helix, varying the width relative to the helical axis, from 140 to 420 nm. As the width decreases, the Bragg peak shifts to shorter wavelengths, which resembles the effect observed in figure 4, when the helical pitch decreases.

The microparticle suspensions have an estimated concentration 10^8 particles cm^{-3}, so we can regard them as a medium containing independent chiral scatterers in random orientations. For such a medium, the extinction matrix **K** has the form [4,8]:

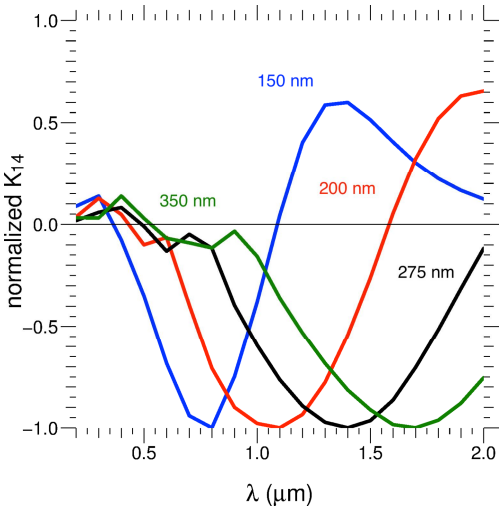


Figure 4 *Simulated K_{14} for a helical target with different helical pitches (see labels).*

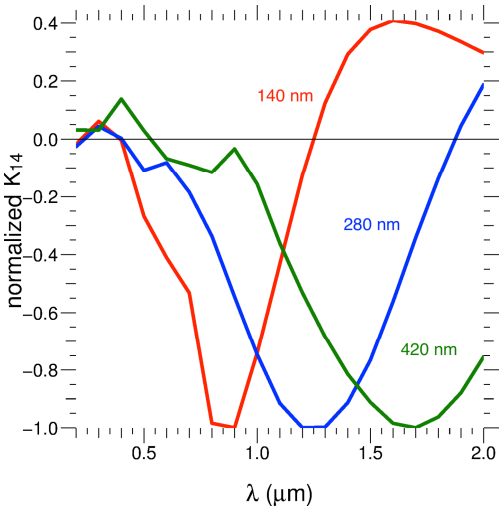


Figure 5 *Simulated K_{14} for three helices with a pitch of 350 nm, with different widths relative to the helical axis (see labels).*

$$\begin{pmatrix} K_{11} & 0 & 0 & K_{14} \\ 0 & K_{22} & K_{23} & 0 \\ 0 & -K_{23} & K_{33} & 0 \\ -K_{14} & 0 & 0 & K_{44} \end{pmatrix} \quad (1)$$

where all the non-zero elements are averaged over single particle orientations. In the previous equation we

are assuming all the particles are identical, so there is no averaging over particle sizes.

To study light incident at oblique angles relative to the helical axis, we need to identify the orientations that don't modify the scattering. From equation (1) we see that any rotation of the particle about the direction of the incident beam (described by the ϕ Euler angle) should not affect the value of K_{14}. The only Euler angles that should change the scattering, and contribute to the ensemble average in equation (1), are θ (tilt of helical axis with respect to the incident beam), and ψ (rotation about the helical axis).

As we vary θ from 0 to 90 (helical axis parallel and perpendicular to incident beam, respectively), we see in figure 6 that K_{14} changes sign. Simulations show that the reverse trend occurs by varying θ from 90 to 180.

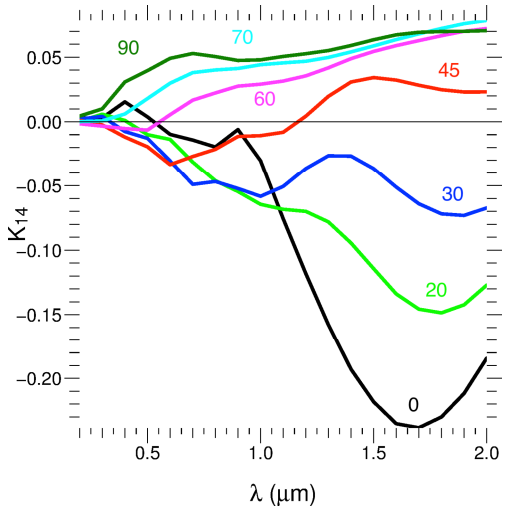


Figure 6 *Simulated K_{14} element for a helix with pitch 350 nm. Each colour corresponds to an orientation in θ (see labels).*

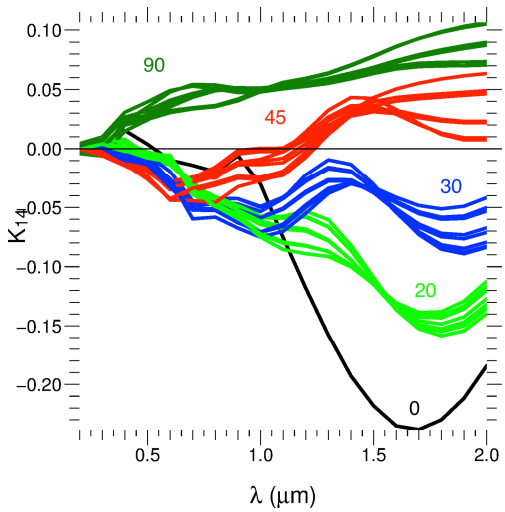


Figure 7 *Simulated K_{14} element for a helix with pitch 350 nm. Each set of coloured curves corresponds to a fixed θ (labelled in the figure), and varying ψ.*

In figure 7 it is shown that for fixed θ, and varying ψ the changes in the K_{14} element are approximately the same. Therefore, to a first approximation, the DCT can be described by only varying θ.

Literature shows the Bragg peak of a helical film shifts towards shorter wavelengths, when light is incident at oblique angles (with respect to the helical axis) [2]. In the case of the microparticle suspensions, if we assume they are all randomly oriented, then light is equally likely to encounter particles in any orientation. However, the orientations for which θ is different from 0 or 180 have a larger geometrical cross-section, so most of the light scattered by the medium comes by particles receiving light at oblique angles.

4 Future work

A size distribution function will be added, to yield a better approximation of the extinction matrix of a suspension of helical microparticles. Radiative transfer theory will then be used to study multiple scattering from these mediums, and compare with microparticle suspensions in higher concentrations.

5 Acknowledgement

Funding is provided by NSERC and the CREATE Chiral Materials Grant.

6 References

[1] Robbie K., et al., Ultrahigh vacuum glancing angle deposition system for thin films with controlled three-dimensional nanoscale structure, Review of Scientific Instruments, 75, 1089-97 (2004)

[2] A. Lakhtakia, and R. Messier, *Sculptured Thin Films: Nanoengineered Morphology and Optics* (SPIE Publications, 2005).

[3] Ghosh A., and Fischer P., Controlled Propulsion of Artificial Nanostructured Propellers, Nano Letters 9 (6), 2243 (2009).

[4] Kokhanovsky A. A., Radiative Transfer in chiral random media, Phys. Rev. E, 60: 4899-4907, 1999.

[5] J. Yang, *Optically Active Chiral Mediums Fabricated with Glancing Angle Deposition*, PhD thesis, Department of Physics, Engineering Physics, and Astronomy, Queen's University, 2012.

[6] Draine B. T., and Flatau P. J., Discrete-dipole approximation for scattering calculations, J. Opt. Soc. Am. A, 11(4): 1491-1499, Apr 1994.

[7] Mc Donald J., Golden A., and Jennings S. G., OpenDDA: A Novel High-Performance Computational Framework for the Discrete Dipole Approximation, IJHPCA, 23(1): 42-61, 2009.

[8] A. A. Kokhanovsky *Polarization Optics of Random Media* (Springer, 2003).

T-MATRIX METHODS FOR SCATTERING BY CYLINDERS IN OPTICAL TWEEZERS

Xiaoqiong QI[1,2*], Timo A. NIEMINEN[1], Alexander B. STILGOE[1], Vincent L.Y. LOKE[1], and Halina RUBINSZTEIN-DUNLOP[1]

[1] Quantum Science Laboratory, School of Mathematics and Physics, The University of Queensland, Queensland 4072, Australia

[2] State Key Laboratory on Integrated Optoelectronics, Institute of Semiconductors, Chinese Academy of Sciences, Beijing 100083, China

Corresponding author: x.qi1@uq.edu.au

Abstract

The applicability of the extended boundary condition method (EBCM) and pointing matching (PM) methods to calculate the T-matrix for scattering by cylinders in optical tweezers is explored. The normalized energy deviation (NED) of the axial optical forces obtained by the methods are compared with forces calculated using the discrete-dipole approximation (DDA) to measure their accuracy. We analyse and compare the relationship between NED and the aspect ratio for Rayleigh and wavelength-size cylinders, respectively. In addition, we determine ranges of sizes and aspect ratios giving errors below 1% and 10%. The results in this paper can help researchers to choose the most efficient method to calculate the T-matrix for nonspherical particles with acceptable accuracy.

1 Introduction

The near-infrared wavelength region of 800-1,100nm is commonly used in optical tweezers since the light is poorly absorbed by most living matter. Manipulating particles of sizes on the order of the illuminating wavelength has attracted intensive attention since it could be trapped more easily [1]. Furthermore, nonspherical micrometre-scale particles are an attractive choice for optically-trapped scanning probe microscopy. Unfortunately, the particles at such sizes are simultaneously too large for the Rayleigh approximation to be valid, and too small for the geometric optics approximation to be applied. Based on the full electromagnetic wave scattering calculation, the T-matrix method is widely used for the calculating of scattering by particles of sizes on the order of the illuminating wavelength [2-4]. The T-matrix is independent of the incident field, and only decided by the scattering properties of the particle. As a result, the T-matrix only need to be calculated once for any particular particle and can then be used for any other incident field or the particle in different positions or orientations within the trapping beam. This is a more efficient method compared with finite element method (FEM) and finite-difference time-domain (FDTD) method where the entire calculation needs to be repeated [3].

As a general description of the electromagnetic scattering by a particle, there are many methods could be used to calculate the T-matrix, which include the extended boundary condition method (EBCM), the point matching (PM) method, and the discrete-dipole approximation (DDA)[4]. The most commonly used method is EBCM, where only surface integrals are required so that it reduces to a 2D method and can be even be 1D for axially symmetric particles. However, the computation suffers from ill-conditioning for particles that become too non-spherical, such as highly elongated or flattened particles with aspect ratios very different from 1. The sizes and shapes for which the different methods become too inaccurate will vary with the different methods. Thus, a study of the accuracy of the different methods can allow a suitable method to be chosen.

The computational efficiency of the methods matters as well. In principle, DDA will work for particles of all aspect ratios, but as it is a volume-based method, it can be significantly slower than the surface-based methods (EBCM and PM). In turn, the point-matching method can outperform EBCM in terms of speed, by avoiding the time-consuming surface integrals required by the EBCM. Thus, knowledge of the relative accuracies of the methods allows the fastest sufficiently accurate method to be chosen.

The discrete-dipole approximation (DDA), also called the coupled-dipole method, has known to provide highly accurate results for scattering by particles of arbitrary shape, and provides a suitable benchmark to compare results from EBCM and PM. We use all three methods to calculate T-matrices, and use the T-matrices to calculate optical forces acting on the particles. We perform the calculation for cylinders of various sizes and aspect ratios, and determine size and aspect ratio regimes where EBCM and PM are accurate to better than 1% and 10%.

2 The T-matrix method

In the T-Matrix method, the incident field and scattered fields, E_{inc} and E_{scat}, can be expanded into the vector spherical wave function (VSWF) basis as follows:

$$E_{inc}(r) = \sum_{n=1}^{N_{\max}} \sum_{m=-n}^{n} a_{nm} RgM_{nm}(kr) + b_{nm} RgN_{nm}(kr)$$
$$E_{scat}(r) = \sum_{n=1}^{N_{\max}} \sum_{m=-n}^{n} p_{nm} RgM_{nm}^{(1)}(kr) + q_{nm} RgN_{nm}^{(1)}(kr) \quad (1)$$

where the VSWFs, M_{nm}, N_{nm}, and the regular VSWFs $RgM^{(1)}_{nm}$, $RgN^{(1)}_{nm}$ are defined in [2]. The incident beam coefficients a_{nm} and b_{nm} could be calculated by the overdetermined linear equations at multiple points in the field. The scattered field coefficients can be obtained by matrix multiplication with Eq. (2) once the T-matrix is calculated for a given particle:

$$[p_{nm}, q_{nm}] = T[a_{nm}, b_{nm}] \quad (2)$$

The expansion series for the incident and scattered waves are truncated at N_{max}, which is related to the size of the scattering particle. Accurate convergence requires $N_{max} > kr_0$ by including higher-order multipole modes, where $k=2n_p\pi/\lambda_0$ and r_0 is the radius of the particle. The T-matrix is truncated at the same N_{max}. The axial trapping force can be calculated by the equation describe in [2].

2.1 Different methods to calculate the T-matrix

In principle, T-matrix could be calculated by any method that could provide the relationship between the incident and scattered fields in a suitable form. EBCM attracted more attention than any other methods since it was developed with T-matrix simultaneously [4]. In the EBCM, the transfer functions between the incident and internal, and scattered and internal fields are calculated instead of the coupling of the incident and scattered fields directly. The internal field within the particle is expanded in terms of regular VSWFs. Consequently, the T-matrix could be obtained by multiplication of the transfer matrix mentioned above.

Alternatively, the expansion coefficients of the scattered field could be calculated by considering the scattering of an incident field consisting of a single VSWF mode. This results in the calculation of T-matrix column by column. Based on this, we can use over-determined point-matching or DDA to find the T-matrix. Our point-matching method finds the expansion coefficients of the scattered field that satisfy the boundary conditions for the the incident, internal, and scattered fields at points on the particle surface. The matching points are usually chosen as an equal angle grid on the particle surface; this grid can be coarse compared with the grids needed for surface integrals in EBCM. However, both EBCM and PM method suffer from ill-conditioning for large particles and extreme aspect ratios, since they use the same field expansions.

2.2 Comparisons of EBCM and PM method with DDA method

Lorenz-Mie theory provides an analytical solution to calculate the T-matrix for spherical particles (for which the T-matrix is a diagonal matrix). We use the Lorenz-Mie solution as the test method to test the convergence of DDA for spherical particles. We then assume that DDA will provide similar accuracy for cylinders when using the same dipole spacing. In this way, the DDA method provides accurate results, allowing comparison of EBCM and PM. The axial optical force F_z experienced by the particle in an optical trap (optical tweezers) provides a suitable parameter for comparison. The normalised energy deviation (NED) of F_z is defined to describe the accuracy of the studied method as shown below:

$$NED = \frac{\int |F_{DDA}(z) - F_T(z)|^2 \, dz}{\int |F_{DDA}(z)|^2 \, dz} \quad (3)$$

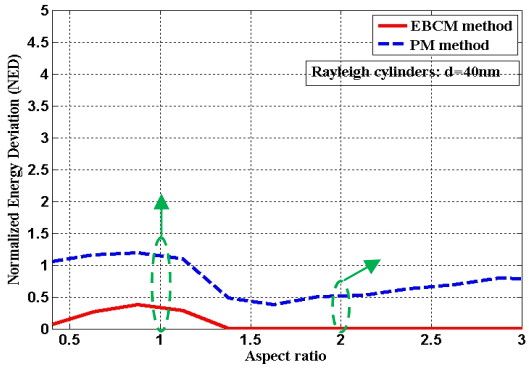
We have optimized EBCM method and PM method by choosing the accurate convergence truncation positions $N_{\max} = kr + 3\sqrt[3]{3}kr$, where r is the half of the diagonal length of cylinders. The incident beam is a Gaussian beam propagating along the positive z-axis in water background with free-space wavelength λ_0=1064nm and beam power P_0=100mw. The refractive index of the particles is chosen to be n_p=1.59, that of polystyrene. The numerical aperture of the objective lens forming the trap is NA=1.02.

2.3 The accuracy variations for Rayleigh and wavelength-scale cylinders

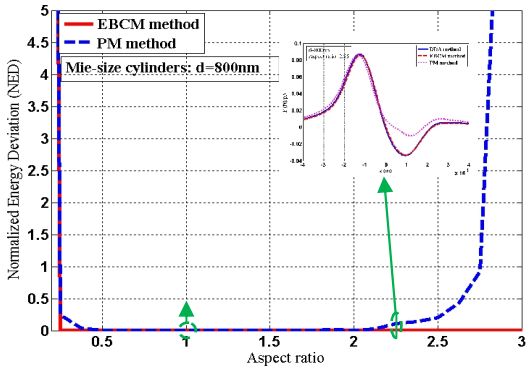
Extensive numeraical simulations results reveal that none of the NED caculated by EBCM and PM linearly increase with the aspect ratio for Rayleigh cylinders and wavelength-scale cylinders. Furthermore, the results for the accuracy for both EBCM and PM for varying aspect ratio are different for Rayleigh cylinders ($d < \lambda/10$) and wavelength-scale cylinders ($\lambda/10 < d < 5\lambda$). As shown in Fig. 1(a), EBCM is more accurate than PM method when calculating the axial optical force for the Rayleigh cylinders with the diameter d=40nm. Moreover, the flattened and enlongated cylinders with the aspect ratio at small and large regions, respectively, have relatively lower accuracy compared with the region in between. Compared with Fig.1 (b) where the NED vs. aspect ratio for wavelength-scale cylinders are given, the accuracy for Rayleigh cylinders varies slower when aspect ratio varies.

Furthermore, to directly reflect the differences of the axial optical force obtained by EBCM, PM, and DDA at various accuracy, the axial optical force profiles calculated by these three methods are shown as insets in Fig.1(a) and (b). For Rayleigh cylinders with aspect ratio of 1.0 (the length is 40nm correspondingly), NED are 0.33 and 1.15, namely, the error is 33% and 115%, repectively. It is observed that both of the F_z profiles from EBCM and PM are very different from the DDA result. However, when the aspect ratio is 2.0, the error for EBCM reduces to 0.0054%, which results in a nealy perfect match of F_z profile. But the PM result still suffers from an error of 51%. For wavelength-scale particles, both EBCM and PM have better accuruacy in most regions although flattened and enlongated cylinders in this case suffer from large errors. It is also noted that PM method has very good accuracy in the middle region of the aspect ratio, which can be further demonstrated by the F_z profiles from the insets in Fig.1(b). The error of EBCM and PM is 0.036% and 0.08%

respectively when the aspect ratio is 1.0, while that for aspect ratio of 2.25 is 0.02% and 11%, respectively. It is observed that the error is 11% is still acceptable. PM method quickly fails when aspect ratio is larger than 2.75.



(a) Rayleigh cylinders

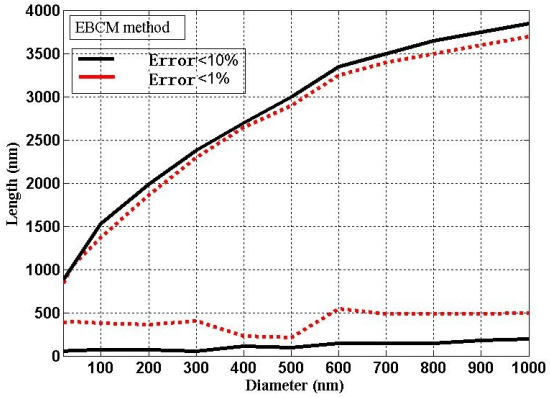


(b) Wavelength-scale cylinders

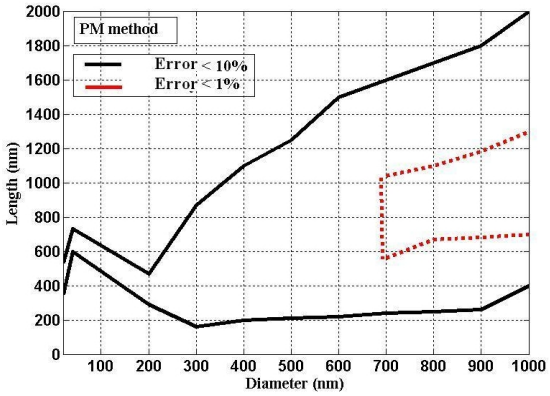
Figure 1 *The relationship between the accuracy of EBCM and PM method and the aspect ratio of cylinders*

2.4 The accuracy mapping in the size domain

In order to extensively present the accuracy of EBCM and PM method for calculating scattering by cylinders, Figure 2(a) and (b) give the accuracy mapping with 1% and 10% for EBCM and PM in its size domain, respectively. The black solid curves border the regions with error smaller than 10%. Within these, the red dotted lines circulate the regions with error below 1%. It should be noted that the region of error < 1% for PM is quite small, since we only plot the continuous region. There are still many tiny regions, for example, when the diameter is 150nm, the length between 450nm and 620nm, in which the error of PM is smaller than 1%. In addition, it is expected that the accuracy mapping of EBCM and PM on the size domain with 1% and 10% will result in closed regions when we include larger diameters. Considering the computation efficiency of calculating T-matrix is PM > EBCM > DDA method, one can choose the corresponding method for the specific particle size with acceptable accuracy.



(a) EBCM method



(b) PM method

Figure 2 *The accuracy mapping of scattering by cylinders*

3 Acknowledgement

This work was supported by the National Natural Science Foundation of China under Grant 61106049 and 61377071.

4 References

[1] Svoboda, K. & Block, S. M. Biological applications of optical forces Ann. Rev. Biophys. Biomol. Struct., **23**, 247–285 (1994).

[2] Nieminen T. A, Loke V. L. Y. Stilgoe A. B, Knöner G, Branczyk A. M, Heckenberg N. R. and Rubinsztein-Dunlop H, Optical tweezers computational toolbox, J. Opt. Soc. Am. A **9**, S196–S203 (2007).

[3] Nieminen T. A, Loke V.L.Y, Stilgoe A.B, Heckenberg. N.R, Rubinsztein-Dunlop H, T-matrix for modelling optical tweezers, Journal of Modern Optics **58**:5-6,528-544 (2011)

[4] Nieminen T. A, Rubinsztein-Dunlop H, Heckenberg. N.R, Calculation of the T-matrix: general considerations and application of the point-mathing method, Journal of Quantitative Spectroscopy & Radiative Transfer **79-80**, 1019-1029(2003)

Far-field scattering

Discrete Dipole Approximation for Particles near Surface: a 3D-FFT-accelerated Implementation

Maxim A. YURKIN[1-2,*] and Marcus HUNTEMANN[3]

[1] Institute of Chemical Kinetics and Combustion SB RAS, Institutskaya 3, Novosibirsk, 630090, Russia
[2] Novosibirsk State University, Pirogova 2, Novosibirsk, 630090, Russia
[3] Institute of Environmental Physics, University of Bremen, Otto-Hahn-Allee 1, Bremen, 28359, Germany
Corresponding author: yurkin@gmail.com

Abstract

We present a modification of the discrete dipole approximation (DDA) to simulate light scattering by particles of arbitrary shape and composition located above the plane homogeneous substrate. The modification retains the 3D-FFT acceleration scheme of the free-space DDA and hence its computational complexity. The modification is implemented in the recent version of the open-source ADDA code, available for anyone to use. The test simulations, compared with the T-matrix method, confirm the correctness of the implementation.

1 Introduction

The DDA is a general method to simulate light scattering by particles of arbitrary shape and composition [1]. It is mostly applied to finite particles in a homogeneous medium (e.g. vacuum). However, there are a multitude of applications, where a particle is located near a plane surface. The extension of the DDA to such problems is possible [2,3] but has two problems. First one is the calculation of interaction of two dipoles near the substrate, related to so-called Sommerfeld integrals [4]. Efficient evaluation of such integrals is still a field of active research, but we do not discuss it here. Instead we use the reliable albeit probably not the fastest routines [4], which were also used in previous DDA implementations.

Second problem is the lack of the translational symmetry of the dipole-dipole interaction (Green's tensor), which breaks standard 3D-FFT acceleration of the matrix–vector products used in the DDA [5]. As a result, existing DDA implementation either do not use FFT at all [3] or use only 2D-FFT due to the remaining translational symmetry parallel to the surface [2]. The computational complexity of the method is then $O(N_{\text{iter}}N^2)$ or $O(N_{\text{iter}}N^{4/3}\log N)$ respectively, where N is the number of dipoles used to discretize a particle and N_{iter} is the number of iterations required for the convergence of the iterative solver (typically, $N_{\text{iter}} \ll N$). A 3D-FFT acceleration for such cases, with complexity $O(N_{\text{iter}}N\log N)$, was presented for a similar volume-integral equation method [6], but has never been implemented in a DDA code.

In this extended abstract we present a way to retain 3D-FFT acceleration for the DDA applied to particles above the substrate, and describe the details of its implementation in the open-source ADDA code [7]. We also performed test simulations and compare the results with that of the T-matrix method.

2 DDA formulation

In principle, generalizing the DDA to particles on surface boils down to replacing the free-space Green's tensor $\overline{\mathbf{G}}$ by $\overline{\mathbf{G}}+\overline{\mathbf{R}}$, where $\overline{\mathbf{R}}$ is the "reflected" part. The main DDA equations [1] then become:

$$\overline{\boldsymbol{\alpha}}_i^{-1}\mathbf{P}_i - \sum_{j\neq i}\left(\overline{\mathbf{G}}_{ij}+\overline{\mathbf{R}}_{ij}\right)\mathbf{P}_j = \mathbf{E}_i^{\text{inc}}, \tag{1}$$

where $\overline{\boldsymbol{\alpha}}_i$ and $\mathbf{P}_i$ is the polarizability and total polarization of the dipole i, $\mathbf{E}_i^{\text{inc}}$ is the incident field at dipole position $\mathbf{r}_i$. To determine the unknown vector $\mathbf{P}$, system of linear equations (1) is solved by an iterative solver. Then the main computational bottleneck is the evaluation of matrix–vector product, the main part of which is the sum in Eq. (1).

The first part of the sum is the same as in the free-space DDA [1] and is evaluated using the translational symmetry

$$\overline{\mathbf{G}}_{ij} = \overline{\mathbf{G}}(\mathbf{r}_i,\mathbf{r}_j) = \overline{\mathbf{G}}(\mathbf{r}_i-\mathbf{r}_j) \equiv \overline{\mathbf{G}}'_{\mathbf{i}-\mathbf{j}}, \tag{2}$$

where we assumed that dipoles are located on a uniform cubical grid, and $\mathbf{i}$, $\mathbf{j}$ are vector indices. $\overline{\mathbf{G}}'_{\mathbf{i}} = \overline{\mathbf{G}}_{\mathbf{i0}} = \overline{\mathbf{G}}(\mathbf{i}d)$ for $|i_\mu| \le n_\mu$ ($\overline{\mathbf{G}}'_{\mathbf{0}} \equiv \overline{\mathbf{0}}$) and is assumed periodic with period $2n_\mu$ along axis μ (d is the dipole spacing, n_μ is the size of the dipole grid). The sum is transformed into a discrete convolution

$$\sum_{j=1,j\neq i}^{N}\overline{\mathbf{G}}_{ij}\mathbf{P}_j = \sum_{\mathbf{j}=(1,1,1)}^{(n_x,n_y,n_z)}\overline{\mathbf{G}}'_{\mathbf{i}-\mathbf{j}}\mathbf{P}_{\mathbf{j}} = \sum_{\mathbf{j}=(1,1,1)}^{(2n_x,2n_y,2n_z)}\overline{\mathbf{G}}'_{\mathbf{i}-\mathbf{j}}\mathbf{P}'_{\mathbf{j}}, \tag{3}$$

where $\mathbf{P}'$ is the periodic (same as $\overline{\mathbf{G}}'$) zero-padded extension of $\mathbf{P}$:

$$\mathbf{P}'_{\mathbf{j}} = \begin{cases}\mathbf{P}_{\mathbf{j}}, \forall\mu: 1\le j_\mu \le n_\mu;\\ 0, \text{otherwise},\end{cases} \tag{4}$$

Finally, the convolution is evaluated as:

$$[\overline{\mathbf{G}}_{ij}]\mathbf{P} = F^{-1}\left(F(\overline{\mathbf{G}}')F(\mathbf{P}')\right), \tag{5}$$

where F and F^{-1} are the direct and inverse discrete Fourier transforms applied to each component of the vector or tensor independently.

We limit ourselves to particle being fully above the semi-infinite substrate, which surface is assumed to be the xy-plane. Then the reflected part is a function of the

distance between evaluation point and the image of source:

$$\overline{\mathbf{R}}(\mathbf{r},\mathbf{r}') = \overline{\mathbf{R}}(x-x', y-y', z+z') = \overline{\mathbf{R}}(\boldsymbol{\rho}, Z), \quad (6)$$

where $\boldsymbol{\rho}$ is the distance along the surface. The simplest approximation is that of a single image dipole:

$$\overline{\mathbf{R}}_{\mathrm{im}}(\boldsymbol{\rho}, Z) = \frac{1-\varepsilon_{\mathrm{s}}}{1+\varepsilon_{\mathrm{s}}}\overline{\mathbf{G}}(\boldsymbol{\rho}, Z)(\bar{\mathbf{I}} - 2\bar{\mathbf{I}}_z), \quad (7)$$

where $\bar{\mathbf{I}}_z = \hat{e}_z\hat{e}_z$ is a projector on the z-axis and ε_{s} is the complex electric permittivity of the substrate. The rigorous expression for the reflection term is

$$\overline{\mathbf{R}}(\boldsymbol{\rho}, Z) = \frac{\hat{\rho}\hat{\rho}}{\rho^2}\left(I_\rho^{\mathrm{H}} + I_\varphi^{\mathrm{H}}\right) - \left(1-\bar{\mathbf{I}}_z\right)I_\varphi^{\mathrm{H}} + \frac{\hat{\rho}\hat{e}_z - \hat{e}_z\hat{\rho}}{\rho} I_\rho^{\mathrm{V}} + \bar{\mathbf{I}}_z I_z^{\mathrm{V}} + \overline{\mathbf{R}}_{\mathrm{im}}(\boldsymbol{\rho}, Z), \quad (8)$$

where I_ρ^{H}, I_φ^{H}, I_ρ^{V}, and I_z^{V} are the Sommerfeld integrals [4] that depend on ρ, Z, and ε_{s}.

Similar to Eq. (2) we define the auxiliary vector

$$\overline{\mathbf{R}}'_{\mathbf{i}} = \overline{\mathbf{R}}_{\mathbf{i}\{0,0,0\}} = \overline{\mathbf{R}}(i_x d, i_y d, i_z d + 2h_1) \quad (9)$$

for $|i_{x,y}| \le n_{x,y}$, $0 \le i_z < 2n_z-1$, $\overline{\mathbf{R}}'_{\mathbf{i}} \equiv 0$ for $i_z = 2n_z-1$, and is further extended periodically (same as $\overline{\mathbf{G}}'$). h_1 is a distance from the lowest dipole layer (their centres) to the surface. The sum over z-axis is now a discrete correlation, but it can be transformed to a convolution by inverting the order of z-components of $\mathbf{P}$:

$$\sum_{j=1}^{N} \overline{\mathbf{R}}_{ij}\mathbf{P}_j = \sum_{\mathbf{j}=(1,1,1)}^{(2n_x, 2n_y, 2n_z)} \overline{\mathbf{R}}'_{\mathbf{i}-\mathbf{j}}\widetilde{\mathbf{P}}_{\mathbf{j}}, \quad (10)$$

where

$$\widetilde{\mathbf{P}}_{\mathbf{j}} = \begin{cases} \mathbf{P}_{\{j_x, j_y, 1\}}, 1 \le j_{x,y} \le n_{x,y} \;\&\; j_z = 1; \\ \mathbf{P}_{\{j_x, j_y, 2n+2-j_z\}}, 1 \le j_{x,y} \le n_{x,y} \;\&\; n_z < j_z \le 2n_z; \\ 0, \text{ otherwise.} \end{cases} \quad (11)$$

Conveniently, $\widetilde{\mathbf{P}}$ satisfies

$$F(\widetilde{\mathbf{P}}) = F_z^{-1}F_yF_x(\mathbf{P}'), \quad (12)$$

where F_μ is the 1D discrete Fourier transform along the axis μ. Combining Eqs. (5), (10), and (12) we finally obtain

$$[\overline{\mathbf{G}}_{ij} + \overline{\mathbf{R}}_{ij}]\mathbf{P} = F^{-1}\left(\left(F(\overline{\mathbf{G}}')F_z + F(\overline{\mathbf{R}}')F_z^{-1}\right)F_xF_y(\mathbf{P}')\right). \quad (13)$$

Since $F(\overline{\mathbf{G}}')$ and $F(\overline{\mathbf{R}}')$ need to be calculated only once, the computational time for matrix–vector product is only slightly (by F_z^{-1} and a few O(N) operations) larger than that for the free-space DDA. In particular, it has the same complexity order O(Nlog$N$).

Certain changes in formulae to calculate the scattered fields (based on the determined $\mathbf{P}$) are also required, but they are straightforward and were published previously [2,3,8]. Less clear is the definition of the scattering matrices, e.g. the Mueller one [9], when either incident or scattered field is in the substrate. To the best of our knowledge, this issue is not covered in the literature. We propose to generalize the standard definition of the Mueller matrix as

$$\begin{pmatrix} I_{\mathrm{sca}} \\ Q_{\mathrm{sca}} \\ U_{\mathrm{sca}} \\ V_{\mathrm{sca}} \end{pmatrix} = \frac{1}{k_{\mathrm{sca}}^2 r^2} \begin{pmatrix} S_{11} & S_{12} & S_{13} & S_{14} \\ S_{21} & S_{22} & S_{23} & S_{24} \\ S_{31} & S_{32} & S_{33} & S_{34} \\ S_{41} & S_{42} & S_{43} & S_{44} \end{pmatrix} \begin{pmatrix} I_{\mathrm{in}} \\ Q_{\mathrm{in}} \\ U_{\mathrm{in}} \\ V_{\mathrm{in}} \end{pmatrix}, \quad (14)$$

where k_{sca} is the is the wave vector for the scattering direction, and we consider scattering into substrate only for non-absorbing one, i.e. k_{sca} is always real. The definitions of the Stokes vector (both incident and scattered) through the electric fields can be found in textbooks [9,10]. Important is that this definition contains the refractive index of the medium m as factor Re(m) [10].

3 Software implementation

The formulae described in Section 2 were implemented in the open-source code ADDA. In particular, these new features are included in the recently released version 1.3b4, available online [11]. Moreover, they are fully integrated with other parts of ADDA, including employed parallelization technologies. In particular, MPI parallelization allows one to solve huge problems (up to 1 billion dipoles [7]) using a large computer cluster. OpenCL mode allows one to significantly accelerate the code for moderately-sized problems using a modern video card (GPU) [12]. And a special (non-FFT) mode is available for very porous particles [13]. Details of the implementation are described in the manual [14].

4 Test simulations

We consider a single test case – an Ag sphere (radius R = 50 nm, refractive index 0.25 + 3.14i [15]) placed on glass substrate (m_{s} = 1.5), illuminated by plane wave from below propagating at 60° relative to the surface normal (evanescent illumination). Wavelength is 488 nm, and ADDA v.1.3b4 was used with two levels of discretization (64 and 128 dipoles per sphere diameter).

Figure 1 shows perpendicular and parallel scattering intensities ($S_{11} - S_{12}$ and $S_{11} + S_{12}$ respectively) in the main scattering plane (0° correspond to upward vertical direction) in comparison with the reference T-matrix results. The latter correspond to Fig. 4.10 of [15], but were recalculated by Vladimir Schmidt using NFM-DS 1.1 [16]. Moreover, the raw results of the NFM-DS, differential scattering efficiencies for unity amplitude of the incident electric field, were multiplied by a factor $\pi(kR)^2/m_{\mathrm{s}}$ = 0.86800, where k is the free-space wave vector.

The DDA accuracy is good – relative errors of angle-resolved quantities are within a few percent. Moreover, the errors for n_x = 128 are almost exactly twice smaller than that for n_x = 64, which indicates a smooth convergence. The latter can also be used to increase the accuracy using the extrapolation technique [17]. We had to use relatively fine discretization to obtain such accuracy, but that is not surprising for metallic nanoparticles [18]. The main practical problem, however, is that it is hard to predict the accuracy of the DDA for such problems *a priori*. No detailed accuracy studies exist for particles on surface, while transferability of free-space benchmarks is at least questionable.

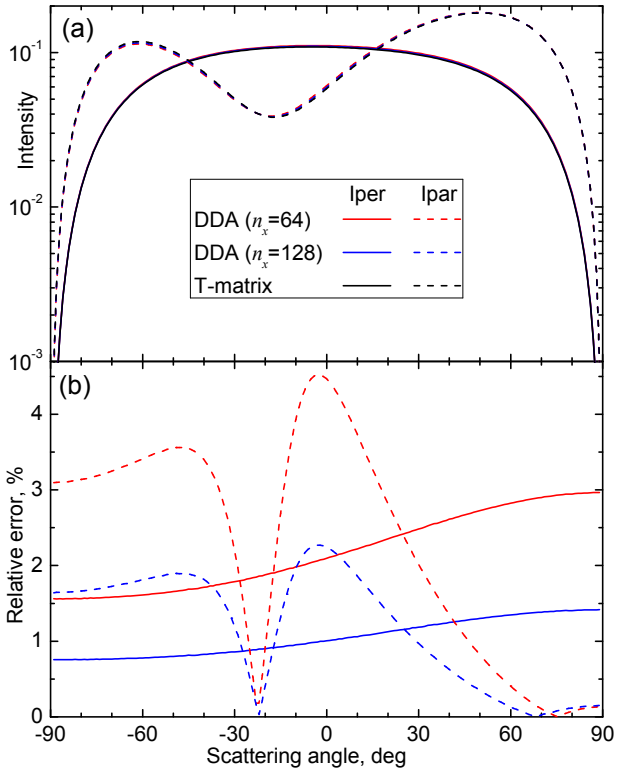


Figure 1 *(a) Light-scattering intensity for Ag sphere on a glass substrate under evanescent illumination (see text for details); (b) relative errors of DDA results in comparison with the T-matrix method.*

5 Conclusions

We presented a reliable, fast, open-source, and easy-to-use tool to simulate interaction of electromagnetic fields with particles of arbitrary shape and composition located on or near a semi-infinite plane substrate. In particular, only the particle itself needs to be discretized and the simulation time is not principally larger than that when no substrate is present. We believe this tool may find many applications in different fields, ranging, for example, from nanostructures on substrate to surface roughness on large dust particles.

6 Acknowledgement

We thank Vladimir Schmidt for providing reference T-matrix results.

7 References

[1] M.A. Yurkin and A.G. Hoekstra, "The discrete dipole approximation: an overview and recent developments," *J. Quant. Spectrosc. Radiat. Transfer* **106**, 558–589 (2007).

[2] R. Schmehl, B.M. Nebeker, and E.D. Hirleman, "Discrete-dipole approximation for scattering by features on surfaces by means of a two-dimensional fast Fourier transform technique," *J. Opt. Soc. Am. A* **14**, 3026–3036 (1997).

[3] V.L.Y. Loke, P.M. Mengüç, and T.A. Nieminen, "Discrete dipole approximation with surface interaction: Computational toolbox for MATLAB," *J. Quant. Spectrosc. Radiat. Transfer* **112**, 1711–1725 (2011).

[4] D.L. Lager and R.J. Lytle, *Fortran Subroutines for the Numerical Evaluation of Sommerfeld Integrals Unter Anderem*, Tech. Rep. UCRL-51821, Lawrence Livermore Lab., Livermore, USA (1975).

[5] J.J. Goodman, B.T. Draine, and P.J. Flatau, "Application of fast-Fourier-transform techniques to the discrete-dipole approximation," *Opt. Lett.* **16**, 1198–1200 (1991).

[6] Y.A. Eremin and V.I. Ivakhnenko, "Modeling of light scattering by non-spherical inhomogeneous particles," *J. Quant. Spectrosc. Radiat. Transfer* **60**, 475–482 (1998).

[7] M.A. Yurkin and A.G. Hoekstra, "The discrete-dipole-approximation code ADDA: capabilities and known limitations," *J. Quant. Spectrosc. Radiat. Transfer* **112**, 2234–2247 (2011).

[8] E. Bae, H. Zhang, and E.D. Hirleman, "Application of the discrete dipole approximation for dipoles embedded in film," *J. Opt. Soc. Am. A* **25**, 1728–1736 (2008).

[9] C.F. Bohren and D.R. Huffman, *Absorption and Scattering of Light by Small Particles*, Wiley, New York (1983).

[10] M.I. Mishchenko, L.D. Travis, and A.A. Lacis, *Scattering, Absorption, and Emission of Light by Small Particles*, Cambridge University Press, Cambridge (2002).

[11] ADDA – light scattering simulator using the discrete dipole approximation, http://code.google.com/p/a-dda/

[12] M. Huntemann, G. Heygster, and G. Hong, "Discrete dipole approximation simulations on GPUs using OpenCL--Application on cloud ice particles," *J. Comput. Sci.* **2**, 262–271 (2011).

[13] J. Leinonen, D. Moisseev, and T. Nousiainen, "Linking snowflake microstructure to multi-frequency radar observations," *J. Geophys. Res.: Atmos.* **118**, 3259–3270 (2013).

[14] M.A. Yurkin and A.G. Hoekstra, "User manual for the discrete dipole approximation code ADDA 1.3b4," http://a-dda.googlecode.com/svn/tags/rel_1.3b4/doc/manual.pdf (2014).

[15] A. Doicu, R. Schuh, and T. Wriedt, "Scattering by particles on or near a plane surface," in *Light Scattering Reviews 3*, A.A. Kokhanovsky, Ed., pp. 109–130, Springer, Berlin (2008).

[16] NFM-DS, http://www.scattport.org/index.php/light-scattering-software/t-matrix-codes/list/239-nfm-ds

[17] M.A. Yurkin, V.P. Maltsev, and A.G. Hoekstra, "Convergence of the discrete dipole approximation. II. An extrapolation technique to increase the accuracy," *J. Opt. Soc. Am. A* **23**, 2592–2601 (2006).

[18] M.A. Yurkin, D. de Kanter, and A.G. Hoekstra, "Accuracy of the discrete dipole approximation for simulation of optical properties of gold nanoparticles," *J. Nanophoton.* **4**, 041585 (2010).

Analysis of chiral sphere rainbows in geometric optics model

Zhen-Sen WU[1,*], Qing-Chao SHANG[1], Tan QU[1], Zheng-Jun LI[1], and Lei GONG[2]

[1] School of Physics Optoelectronic Engineering, Xidian University, Xi'an, 710071, China
[2] Xi'an Technological University, Xi'an, 710021, China

*Corresponding author: wuzhs@mail.xidian.edu.cn - chaoxidian@foxmail.com

Abstract

A geometric optics model is set up to analyze the rainbow phenomenon of chiral spheres. The ray traces inside the chiral sphere are determined by reflection and refraction laws of light at achiral-chiral interface and chiral-achiral interface. The calculated rainbow angles achieve good agreements with those obtained by analytical solutions. Effects of chirality parameter and refractive index of the sphere on rainbow angles are analyzed.

1 Introduction

Chiral media in nature at optical frequencies, also known as the "optical active media", are some solutions of substances with handed microstructure, such as grape sugar and tartaric acid.[1] Some biological particles with handed microstructure may be modelled by chiral spheres. Thus theory of light scattering from chiral spheres may help the study on biological particles. Numerical results from light scattering from large sized chiral spheres show that three first-order rainbows occur for a linearly polarized wave incidence [2, 3]. We make an attempt to present a geometric optics model for rainbows of a chiral sphere based on the optical property of chiral media. The traces of a ray travelling in a chiral sphere are analyzed and the three rainbow angles are calculated.

2 Reflection and refraction of light propagating through chiral slab

Figure 1 presents the reflection and refraction of a ray incident on a chiral medium from a general isotropic medium. Two transmitted rays are generated in chiral medium; one is RCP ray and the other is LCP ray [4, 5].

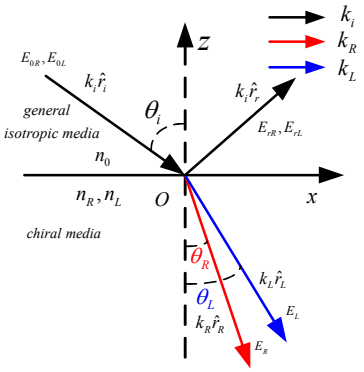


Figure 1 *light incident at an achiral-chiral interface.*

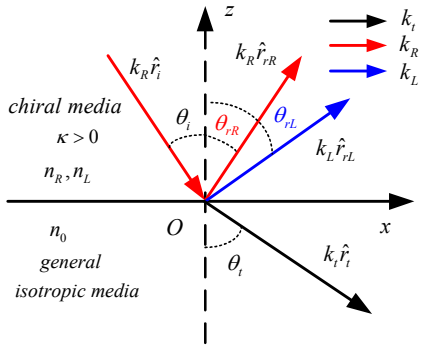


Figure 2 *light incident at a chiral-achiral interface.*

Figure 2 presents the reflection and refraction of an RCP ray incident on a general isotropic medium from a chiral medium. There are two reflected rays in the chiral medium; one is RCP ray and the other is LCP ray [4, 5].

3 Geometric optics model for chiral sphere rainbows

Figure 3 shows how a ray incident on a chiral sphere travels inside the sphere. It can be seen that there are three final transmitted rays after once internal reflection inside the sphere, corresponding to three rainbow structures of the chiral sphere.

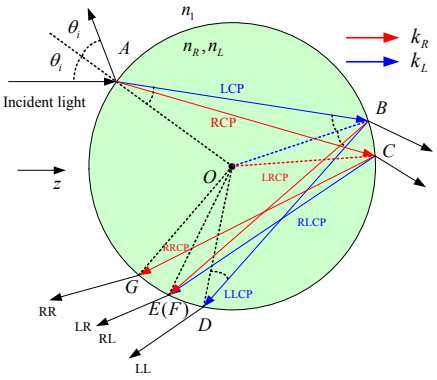


Figure 3 *ray traces inside the chiral sphere.*

Finally, the three deviation angles (angular displacements of transmitted directions from positive z axis) are obtained as:

$$\theta_{RR} = 2\theta_i + \pi - 4\arcsin\left(n_1 / n_R \sin\theta_i\right) \quad (1)$$

$$\theta_{LL} = 2\theta_i + \pi - 4\arcsin\left(n_1 / n_L \sin\theta_i\right) \quad (2)$$

$$\theta_{RL} = \theta_{LR} = 2\theta_i + \pi - 2\arcsin\left(n_1 / n_R \sin\theta_i\right) - 2\arcsin\left(n_1 / n_L \sin\theta_i\right) \quad (3)$$

The extrema of the three angles are the three first order rainbow angles of the chiral sphere.

4 Numerical results

Figure 4 shows a comparison between rainbow angles calculated by GO model and rainbow structures from analytical solutions.

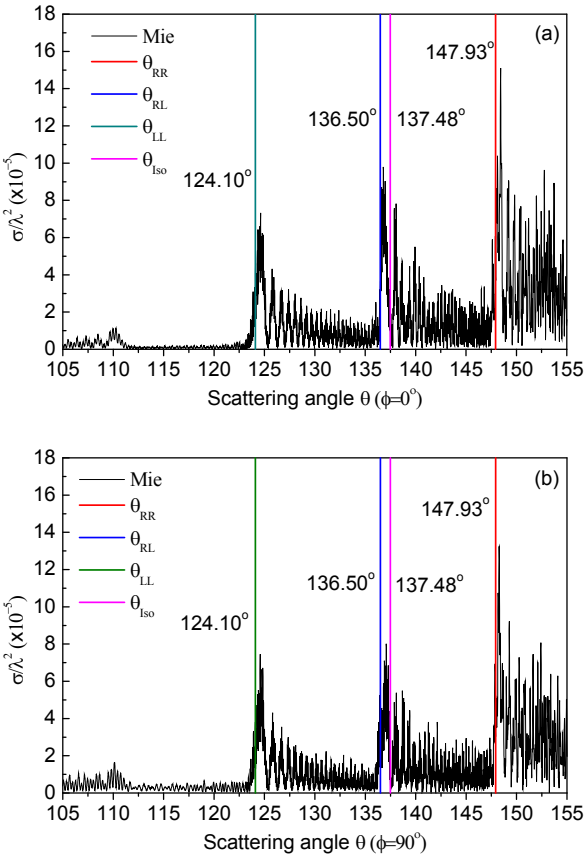


Figure 4 *Comparison of rainbow angles of chiral spheres between GO model and MIE theory.*

5 Acknowdgement

This work was supported by the National Natural Science Foundation of China under grants 61172031, 61308025 and 61108071 and the Fundamental Research Funds for the Central Universities.

6 References

[1] A. Lakhtakia, *et al.*, *Time-Harmonic Electromagnetic Fields in Chiral Media* vol. 335: Springer, 1989.

[2] Q.-C. Shang, *et al.*, "Analysis of rainbow scattering by a chiral sphere," *Opt. Express*, vol. 21, pp. 21879-21888, 2013.

[3] Z.-S. Wu, *et al.*, "Calculation of electromagnetic scattering by a large chiral sphere," *Appl. Opt.*, vol. 51, pp. 6661-6668, 2012.

[4] S. Bassiri, *et al.*, "Electromagnetic wave propagation through a dielectric-chiral interface and through a chiral slab," *J. Opt. Soc. Am. A.*, vol. 5, pp. 1450-1459, 1988.

[5] A. I. Miteva and I. J. Lalov, "Reflection of electromagnetic waves from isotropic optically active media," *Journal of Physics: Condensed Matter*, vol. 3, p. 529, 1991.

Generalized Rainbow Patterns for SpheroiDal Droplet Characterization

Haitao YU[1], Jianqi SHEN[1] and Cameron TROPEA[2*]

[1] College of Science, University of Shanghai for Science and Technology, Shanghai 200093, China
[2] Institute of Fluid Mechanics and Aerodynamics, Center of Smart Interfaces, Technische Universität Darmstadt, 64287, Germany

Corresponding author: ctropea@sla.tu-darmstadt.de

Abstract

In this work we present generalized rainbow patterns for spheroidal droplets as computed using a vector ray tracing approach. The structure and shape of these patterns allows the droplet size, refractive index and aspect ratio of the droplets to be inferred. Also results for droplets tilted with respect to the illuminating beam will be discussed.

1 Introduction

Light scattering from a spheroidal droplet in the vicinity of the primary rainbow region has been described by Marston and Trinh [1]. To distinguish such a rainbow from those arising from a spherical droplet, the pattern from spheroidal droplets is called a generalized rainbow pattern. It has been shown that both the equatorial diameter and the relative refractive index can be deduced from the generalized rainbow pattern of spheroidal water droplets [2]. Several salient optical caustics exist in generalized rainbow patterns. Optical caustics have also been observed in the light scattering with white light illumination, in a more complicated caustic's progression for highly oblate water droplets and inside of liquid droplets [3-8]. Recently, Lock and Xu [9] studied the formation of the rainbow caustic, transverse cusp and hyperbolic umbilic caustics of oblate spheroids by use of Debye series. In past studies the present authors have used a vector ray tracing (VRT) model to study the optical caustic structures near the primary rainbow angle of a spheroidal water droplet; characteristics of the pattern were used to measure the non-sphericity of the droplet [10].

In the present work, the evolution of the optical caustics in terms of the rainbow and hyperbolic umbilic (HU) limiting fringe will be presented. By use of VRT, a relation between rainbow fringe curvature and the droplet shape, in particular the aspect ratio, is established and compared with experimental results. Based on the VRT model and Airy approximation, the quantities size, shape and refractive index can be deduced from the generalized rainbow pattern of a spheroidal droplet. Also the effect of tilt angle of the spheroidal droplet with respect to the illuminating beam will be reported.

2 Results

The optical caustic structure near the primary rainbow scattering angle of a spheroidal water droplet, as simulated using the VRT model, reveals the shape of the rainbow and HU fringes. It can be seen from Fig.1 that the rainbow fringe folds gradually and then unfolds as the aspect ratio increases.

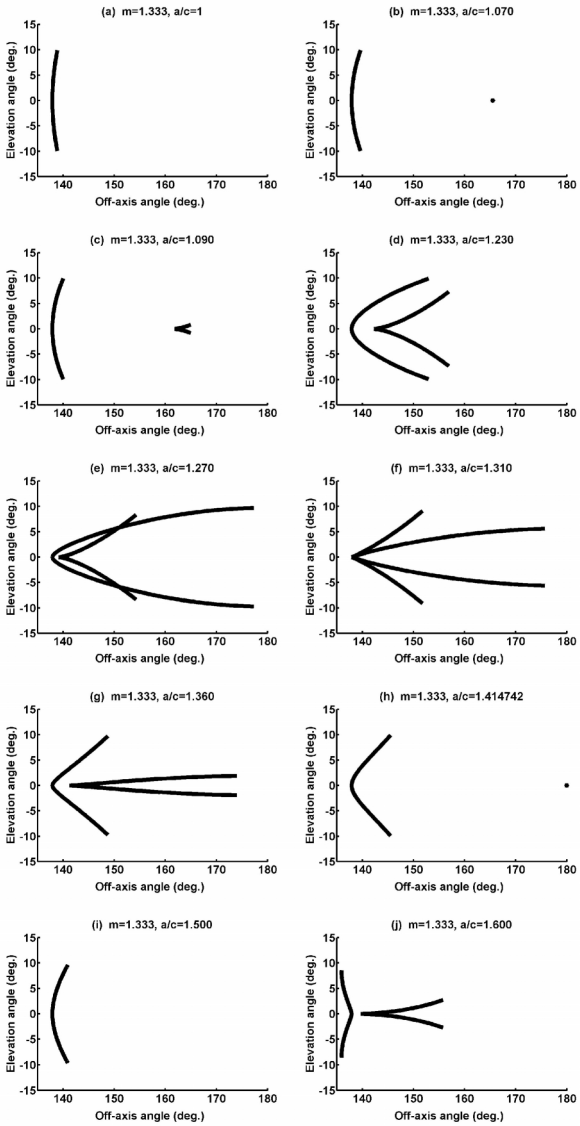


Figure 1 *Evolution of the primary rainbow fringe and the HU fringe as the aspect ratio of an oblate water droplet increases.*

The cusp caustic first appears on the right side of Fig. 1(b) for droplets with an aspect ratio a/c=1.07. Then the HU fringe unfolds with increasing aspect ratio. A comparison of the curvature of the rainbow fringes found with the VRT simulations to that obtained from experiments is shown in Fig. 2: the curvature has been computed at the apex point of the rainbow fringe.

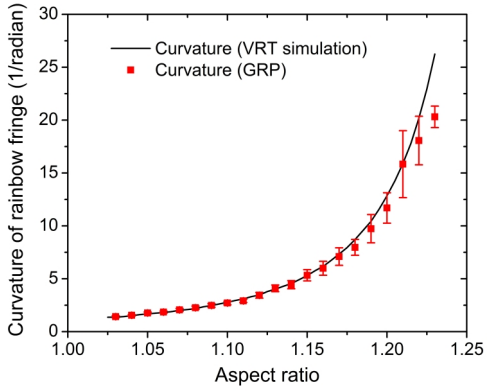


Figure 2 *Comparison of the curvature of the primary rainbow fringe calculated from VRT simulations and that from experimentally observed generalized rainbow patterns.*

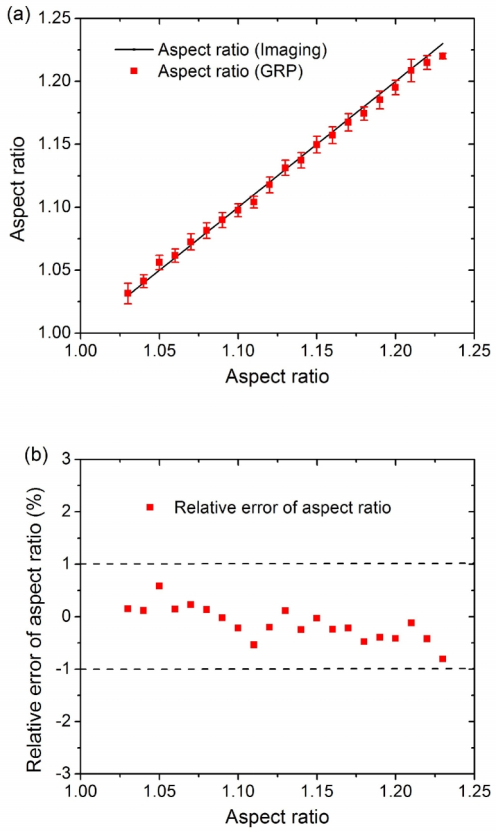


Figure 3 *a) Comparison of water droplet aspect ratio calculated from the generalized rainbow pattern (GRP) to that observed from direct imaging; b) Relative errors of water droplet aspect ratio calculated by the generalized rainbow technique.*

The curvatures calculated from experiment are shown with error bars corresponding to one standard deviation taken over an ensemble of independent measurements. It can be seen that the agreement between the VRT model and measurements is excellent: most deviations are within the experimental uncertainty. For large aspect ratios (e.g. a/c >1.23), the droplet jitters significantly in the acoustic levitator used to hold it and the generalized rainbow pattern becomes highly instable and blurry. So it is difficult to distinguish the rainbow fringe without using a high-.speed camera.

Based on the relation between the rainbow fringe curvature and the aspect ratio of oblate spheroidal droplets (Fig. 2), the aspect ratios (r_{GRP}) of spheroidal droplets are calculated from the generalized rainbow pattern and compared to values observed through direct imaging ($r_{Imaging}$), yielding excellent agreement(Fig. 3a). The error bars shown in this figure correspond to one standard deviation computed over many individual measurements. To evaluate the accuracy of computed r_{GRP}, the relative error in percentage ((r_{GRP} - $r_{Imaging}$)x100/$r_{Imaging}$) is given in Fig. 3b. The relative error lies between ±1%, indicating a high achievable accuracy.

3 Acknowledgements

The authors would like to thank the DFG Research Training Group 1114 “Optical Measurement Techniques for the Characterisation of Transport Process” for financial support of the first author.

4 References

[1] P. L. Marston and E. H.Trinh, Hyperbolic umbilic diffraction catastrophe and rainbow scattering from spheroidal drops, Nature 312, 529-531 (1984).

[2] H. T. Yu, F. Xu, and C. Tropea, Spheroidal droplet measurements based on generalized rainbow patterns, J. Quant. Spectr. Radiat. Transfer 126, 105–122 (2013).

[3] H. J. Simpson and P. L. Marston, Scattering of white light from levitated oblate water drops near rainbows and other diffraction catastrophes, Appl. Opt. 30(24), 3468-3473 (1991).

[4] G. Kaduchak, P. L. Marston, and H. J. Simpson, E_6 diffraction catastrophe of the primary rainbow of oblate water drops: observations with white-light and laser illumination, Appl. Opt. 33(21), 4691-4696 (1994).

[5] G. Kaduchak and P. L. Marston, Hyperbolic umbilic and E_6 diffraction catastrophes associated with the secondary rainbow of oblate water drops: observations with laser illumination, Appl. Opt. 33(21), 4697-4701 (1994).

[6] P. L. Marston and G. Kaduchak, Generalized rainbows and unfolded glories of oblate drops: organization for multiple internal reflections and extension of cusps into Alexander’s dark band, Appl. Opt. 33(21), 4702-4713 (1994).

[7] D. S. Langley and P. L. Marston, Generalized tertiary rainbow of slightly oblate drops: observations with laser illumination, Appl. Opt. 37(9), 1520-1526 (1998).

[8] J. A. Lock and E. A. Hovenac, Internal caustic structure of illuminated liquid droplets, J. Opt. Soc. Am. A 8(10), 1541-1552 (1991).

[9] J. A. Lock and F. Xu, Optical caustics observed in light scattered by an oblate spheroid, Appl. Opt. 49(8), 1288-1304 (2010).

[10] H. T. Yu, F. Xu, and C. Tropea, Optical caustics associated with the primary rainbow of oblate droplets: simulation and application in non-sphericity measurement, Optics Express, 21(22), 25761–25771 (2013).

Vectorial Complex Ray Model – from geometrical optics to ray theory of wave

Kuan Fang REN[1,*], Claude ROZÉ[1], Yijia YUAN[2]

[1] UMR 6614/CORIA, CNRS - Université et INSA de Rouen, Saint-Etienne du Rouvray, 76801, France
[2] Shanghai Jiao Tong University - Paris Tech Elite Institute of Technology, 800 Dongchuan Road, Shanghai, 200240, China

Corresponding author: fang.ren@coria.fr

Abstract

Numerical prediction of light interaction with large non-spherical particles is vital in many applications but no useful tool is presently able to reply this demand. The Vectorial Complex Ray Model (VCRM) we are developing permits to describe the scattering of large object of smooth surface and arbitrary shape. By introducing a new property – the curvature of the wave front in the ray model, VCRM predicts correctly the divergence or convergence of a wave at each interaction with the particle surface and the phase due to the focal line. Thanks to this new property, the wave effect near singularity regions such as the caustics, the critical angles as well as the diffraction may be included directly. The fundamentals of VCRM and Ray Theory of Wave are presented in this communication.

1 Introduction

The interaction between light (or electromagnetic wave) and an object concerns many fields of fundamental and application research, such as metrology of particles in atmosphere, diagnostics of the atomization/spray in two-phase flow, trapping and manipulation of cells in life science, sorting nanoparticles in material, even the design of antenna or the radar detection. Many methods have been developed for the prediction of different properties of ? this interaction. However, they are either valid for objects of very simple form or seriously limited in the size of the objects. The approximate methods such as geometrical optics or Monte-Carlo ray tracing can deal with the scattering of large objects with complex form but their precision is not sufficient for the applications. The Vectorial Complex Ray Model (VCRM) has been recently developed [1] to reply this need. We will present in this communication this model, the Monte-Carlo Ray Tracing of Wave [2] as its variety and Ray Theory of Wave (RTW) as their extension.

2 Desctiption of the models

In Geometrical Optics or classical ray tracing, a wave is described by bundles of rays which possess four properties: amplitude, phase, propagation direction and polarization. The wave form is not an intrinsic property of the rays. So the divergence or convergence of a wave on the surface of the particle as well as the phase due to the focal lines cannot be counted directly. In the special cases of spherical particles and circular cylinders, these effects are counted separately to deal with the phenomena of rainbow and the scattering near the critical angle. The models we present in this section include the curvature of the wave front as an intrinsic property of rays and therefore permit to treat the wavelike behaviour of light directly for large arbitrary shape particles.

2.1 Vectorial Complex Ray Model

In Vectorial Complex Ray Model, a ray is characterized by the amplitude, the phase, the propagation direction, the polarization and the wave front curvatures. All these features evolve at each interaction of ray with the particle surface. The direction of a ray is described by its wave vector $\vec{k}$. The directions of reflected and refracted rays are determined by the continuity of the tangent components of the wave vectors on the particle surface:

$$k_\tau^{'} = k_\tau \tag{1}$$

The wave front and the particle surface in the vicinity of the incident point are described by 2 × 2 matrices Q (before interaction), Q' (after interaction) and C (interface curvatures) (Figure 1). Their relation is given by the following wave front matrix equation.

$$(k'-k)\cdot nC = k'\Theta'^{T} Q'\Theta' - k\Theta^{T} Q\Theta \tag{2}$$

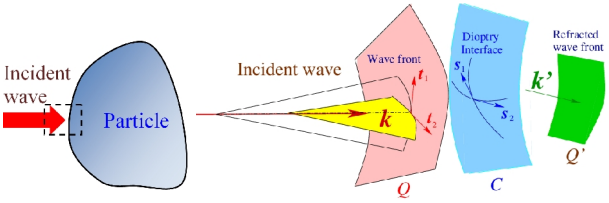


Figure 1 *Definition of the curvatures of wave fronts and dioptric surface.*

Eqs. (1) and (2) along with the Fresnel formulas permit to evaluate all five properties of the rays step by step. The wave divergence/convergence and the phase due to the focal lines are deduced directly from these values. The total scattered field is the superposition of the complex amplitude of all orders of the emergent rays. This model has been applied successfully to predict 2D (in the plane of symmetry) of an ellipsoid [1, 2, 3] and an elliptic cylinder

[4, 5]. Various new physical phenomena in light scattering by non-spherical particles are revealed.

Software has also been developed for the ray tracing and the calculation of the scattering diagram of an elliptical particle with any incident angle.

2.2 Monte-Carlo-Ray Tracing of Wave

The Monte Carlo Ray Tracing (MCRT) is a very flexible method and can be easily adapted to the particles of complex shape. It has been widely applied for the simulation of single and multiple scattering by large non-spherical particles. But the wave form is not counted in MCRT so its precision is limited.

Similar as in VCRM, we introduce also the curvatures of the wave in MCRT. This extended version of MCRT, called Monte-Carlo Ray Tracing of Wave (MCRTW) improves considerably the precision of the MCRT by taking into account the divergence or convergence and the phase shift due to the focal lines [3]. By comparison with the Mie theory for the scattering by a sphere, we proved that the MCRTW can correctly predict the scattering diagram in almost all the directions except in the forward direction due to the diffraction and near the rainbow or critical angles because of caustics. The MCRTW has been applied to the 2D scattering of the plane wave by a large spheroid.

2.3 Ray Theory of Wave

Ray model is practically the only way to deal with the interaction of light with a big non-spherical particle. It is conventionally admitted that the models based on ray tracing are valid when the particle is much larger than the wavelength. But this is only true if we are interested in the global properties or in the regions far from singularity. Near singularity regions, the wave effect must be counted even for very big particle. Since the two models described above permit to calculate precisely the all five properties of rays, particularly the wave form and phase, they are very suitable to be extended to deal with these singularities.

We recognize three types of singularity and each one is linked to a kind of measurement technique (Table 1). Until now these phenomena have been used in the optical metrology exclusively for spherical particles and circular cylinders. The concept introduced in VCRM and MCRTW will be casted into a more general theory – Ray Theory of Wave – to deal with the interaction of any wave with an object of smooth surface.

Singularity	Physical phenomena	Relevant techniques
Discontinuity of intensity	Diffraction	Diffractometry
Discontinuity of the intensity derivative	Critical angle scattering [7,8]	Refractometry of bubble[9]
Infinity of the intensity	Rainbow	Refractometry of rainbow

Table 1 *Singularities in the interaction of light with a particle, their relevant phenomena and measurement techniques*

The Ray Theory of Wave (RTW) in development is based on four principles:

1). All waves are described by rays and each ray is characterized by its direction, amplitude, phase, polarization and wave front curvature;
2). At interaction on a dioptric surface, the properties of the rays are governed by the Snell law given in Eq. (1), the Fresnel formulae and the wave front matrix equation (Eq. (2));
3). The total field is the summation of the complex amplitude of all the rays in the region far from the singularity points.
4). Near the singular regions, such the border of the particle (corresponding to forward diffraction), the caustics (rainbow angles) and the semi-caustics (critical angles), rays are considered as secondary sources and the total field is the contributions of the secondary rays near the singular angles.

The Airy theory [6] is a good example to deal with the singularity with ray model. In this theory the phase is expressed approximately by a cubic function and the amplitude is supposed constant, while in VCRM and MCRMW we predict precisely the phase and the amplitude of all rays even for a non-spherical particle.

3 Some results and discussion

We give in this section two typical results obtained with VCRM and MCRTW to show the applicability of these models and their potentials in the development of RTW.

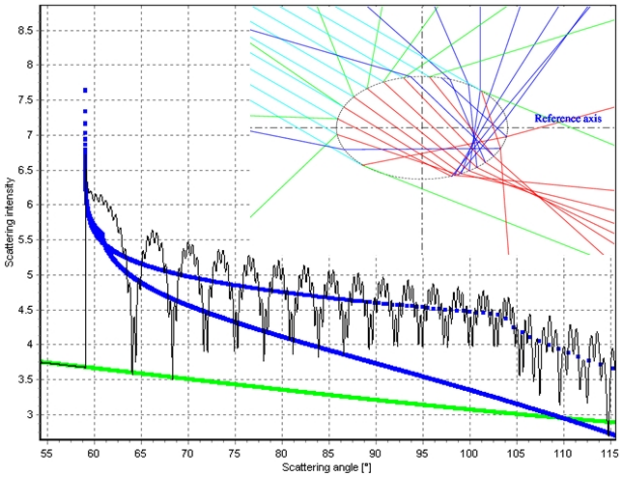


Figure 2 *Rainbow-like structure calculated by VCRM with the software VCRMEll2D for an ellipsoid of water droplet (m=1.33) with three semi-axis a=30 μm, b=40 μm and c=50 μm illuminated by a plane wave at 30° with long axis*

The first example is to show the behaviour of the scattering diagram near rainbow angle predicted by VCRM. Figure 2 shows the ray tracing (top right), the

intensity of each emergent rays of the reflected (green curve) and refracted rays blue curves) and the total intensity (black curve) for an elliptical water droplet (m=1.33). The rainbow angle is located at 59° where the intensity tends to infinity but the diagram at larger angles has Airy-like structure. We have compared with Debye theory for the scattering by a spherical particle and found that the agreement is almost perfect. We find also in Figure 2 that the derivative of the intensity of the second order ray is not continuous at 104°; this is due to the total reflection of the first internal reflection. Therefore to predict precisely the scattering diagram in these regions (less than 59° and near 104°), the principle 4). of RTW given above should be applied.

The second example concerns the comparison of the MCRMW with VCRM (Figure 3). In this simulation, the total intensity of MCRMW is calculated by superposition of the complex amplitudes of the emergent rays arriving in the same direction. The agreement between the two models is satisfactory. Evidently, the precision of MCRTW depends on the total number of rays (called also photons). The computation time on a personal computer with 4 core 4X2.5 GHz and a memory of 4 Go for 10^8 photons is about 1 hour. The precision is always better for low order rays because of the number of rays.

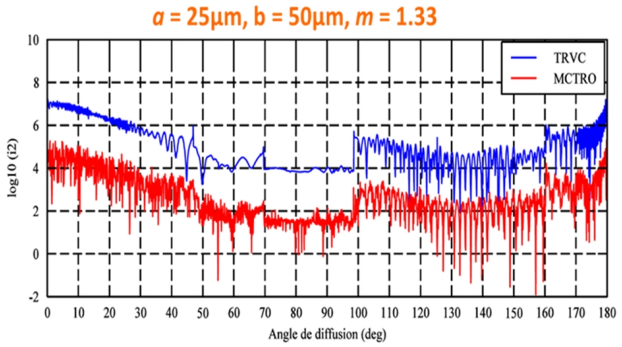


Figure 3 *Comparisons of the scattering patterns of a spheroidal droplet of transversal radius b=25 µm, symmetric radius a=50 µm and of refractive index m=1.33 illuminated by a polarized plane wave of wavelength λ = 0.6328 µm calculated by VCRM and MCRTW. The result of MCRTW is shifted by 10^2 for clarity.*

4 Acknowledgement

This work has been also partially supported by substantial computation facilities from CRIHAN (Centre de Ressources Informatiques de Haute-Normandie) and the French National Research Agency (ANR) grant ANR-13-BS09-0008-01.

5 References

[1] Ren K. F., Onofri F., Rozé C., and Girasole T., Vectorial complex ray model and application to two-dimensional scattering of plane wave by a spheroidal particle, Optics Letters 36(3):370–372 (2011)

[2] Ren K. F., Rozé C., and Girasole T., Scattering and transversal divergence of an ellipsoidal particle by using vectorial complex raymodel, Journal of Quantitative Spectroscopy and Radiative Transfer 113(18):2419–2423 (2012)

[3] Yuan Y., Diffusion de la lumière par un objet irrégulier pour l'application à l'imagerie des sprays, PhD thesis of Rouen University, France, 29 March 2012

[4] Jiang K., Han X., and Ren K. F., Scattering from an elliptical cylinder by using the vectorial complex ray model, Applied Optics 51(34):8159–8168 (2012)

[5] Jiang K., Han X., and Ren K. F., Scattering of a Gaussian beam by an elliptical cylinder using the vectorial complex ray model, J. Opt. Soc. Am. A. 30(8):1548-1556 (2013)

[6] van de Hulst, H. C. Light scattering by small particles, Dover Publications (1957)

[7] Marston P. L., Critical angle scattering by a bubble: physical-optics approximation and observations, J. Opt. Soc. Am. A, 69:1205-1211 (1979).

[8] Onofri F., Radev St., Sentis M., Barbosa S., A physical-optics approximation of the near-critical-angle scattering by spheroidal bubbles, Opt. Lett. 37(22):4780-4782 (2012)

[9] Onofri F., Krysiek M., Mroczka J., Critical Angle Refractometry and Sizing for Bubbly Flow Characterization, Opt. Lett. 32:2070-2072 (2007)

Scattering of a Plane Electromagnetic Wave by a Radially Inhomogeneous Generalized Luneburg Lens

James A. LOCK[1,*], Philip LAVEN[2] and John A. ADAM[3]

[1] Physics Dept., Cleveland State University, Cleveland, OH 44115, USA
[2] 9 Russells Crescent, Horley, RH6 7DJ, UK
[3] Dept. of Mathematics and Statistics, Old Dominion University, Norfolk, VA 23508, USA

Corresponding author: j.lock@csuohio.edu

Abstract

Much has been learned about the nature of the interaction of radiation with macroscopic matter by examining scattering of an electromagnetic plane wave or a transversely localized beam by a homogeneous dielectric spherical particle. It is also of both theoretical and practical interest to understand the details of electromagnetic scattering by a radially inhomogeneous sphere. In this new setting one would expect to encounter all the various phenomena observed in scattering by a homogeneous sphere. But in addition one would expect that new phenomena will occur, which are impossible for the more specialized homogeneous sphere geometry.

1 Introduction

We here consider scattering by a generalized Luneburg lens (GLL) of radius a whose refractive index profile is

$$n(r) = [2B - C\,(r/a)^2]^{1/2} \qquad (1)$$

where B and C are positive or negative constants subject to the constraint:

$$2B \geq C + 1 \text{ for } C > 0 \text{ and } 2B \leq C + 1 \text{ for } C < 0 \qquad (2)$$

We chose to study this refractive index profile because all aspects of its scattering in ray theory can be evaluated analytically in closed form. The light deflection problem in ray theory is identical to that of the motion of a classical particle [1] of energy E in a conservative central force field whose potential energy function is

$$U(r) = E\,[C\,(r/a)^2 + 1 - 2B] \qquad (3)$$

For $C > 0$, the force field is attractive, while for $C < 0$ it is repulsive. Thus one can use intuition obtained from classical potential scattering to understand the light scattering by a particle with a radially-variable refractive index profile.

2 Luneburg Particle in Ray Theory

When $C > 0$ the GLL is an example of a variable-density particle, while for $C < 0$ it resembles a variable-density gas bubble in water. The curved ray paths inside the sphere turn out to be sections of an ellipse when $C > 0$, and sections of a hyperbola when $C < 0$ – as shown in Figure 1 where the incident beam of light is represented by a set of parallel rays arriving from the left of each diagram.

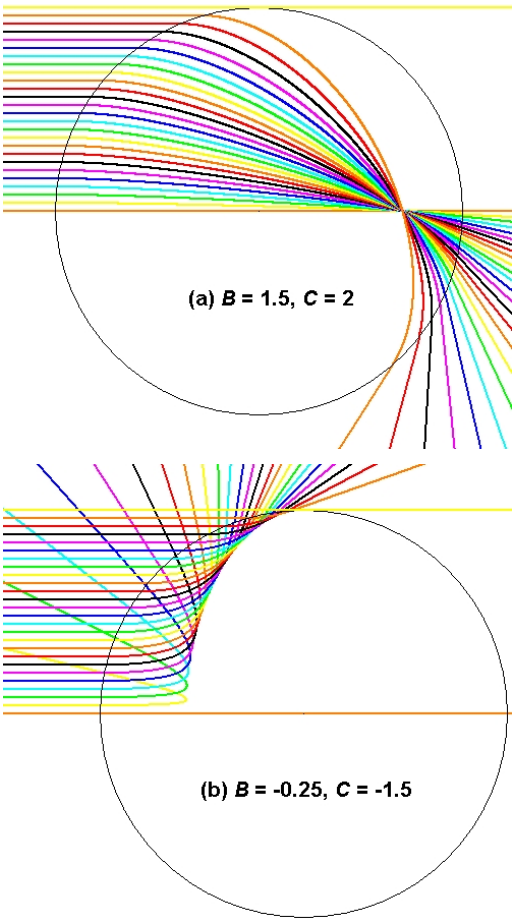


Figure 1 *Ray tracing for p = 1 rays passing through a GLL with (a) B = 1.5 and C = 2 and (b) B = -0.25 and C = -1.5.*

When $2B = C + 1$, as in both diagrams in Figure 1, the refractive index at the particle surface smoothly merges into that of the external medium, preventing both external and internal reflection at the particle surface. Thus the only Debye series scattering mechanisms remaining are

diffraction (a part of the Debye $p = 0$ term) and transmission ($p = 1$).

When $2B \neq C + 1$ there is a refractive index discontinuity at the particle surface which produces external reflection (the remaining part of the $p = 0$ term) and internal reflections (giving rise to the entire $p \geq 2$ Debye series of ray or wave interactions with the particle surface).

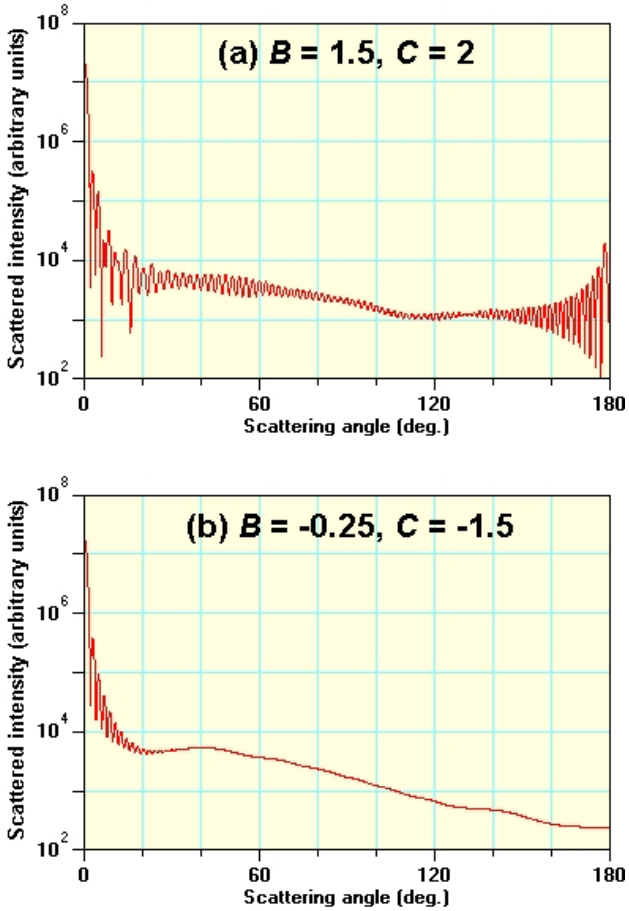


Figure 2 *Wave theory results showing intensity as a function of scattering angle for $\lambda = 0.65$ μm and a GLL of radius $a = 10$ μm with (a) $B = 1.5$ and $C = 2$ and (b) $B = -0.25$ and $C = -1.5$.*

The deflection angle Θ for $p \geq 1$ was calculated in ray theory as a function of the angle of incidence θ_i of an incoming light ray. The shape of the elliptical or hyperbolic ray trajectories inside the sphere was also calculated, as was the optical path length from the entrance plane to the exit plane and the scattered intensity. The scattering angle and optical path length were also plotted parametrically as a function of θ_i to produce ray theory time domain scattering graphs. It was found that for transmission in ray theory, in contrast to the case of scattering by a homogeneous sphere where $p = 1$ rainbows are impossible, one bow can occur when $2B = C + 1$, and either zero or two bows can occur when $2B \neq C + 1$. When this happens the first bow is of the usual type, a relative minimum of both the deflection angle and the optical path length as a function of θ_i. The second bow, however, is a relative maximum of both the deflection angle and optical path length, which for various other refractive index profiles is associated with the near-onset of the semi-classical phenomenon of orbiting.

3 Luneburg Particle in Wave Theory

Wave theory scattering was also numerically computed for both the transverse electric (TE) and transverse magnetic (TM) polarization using the parallel iteration version of the finely-stratified multi-layer sphere model [2] for inhomogeneous-sphere Mie scattering. Figure 2 shows results for the two conditions examined in Figure 1, but these reveal little information about the scattering processes, apart from the obvious forward-scattering peak due to diffraction.

Such results can be used to construct time domain scattering graphs produced when an incident femtosecond duration pulse is scattered by the particle. As shown in Figure 3, time domain scattering effectively performs a Debye series decomposition of the full Mie scattered intensity by reading the interference structure between two or more different p-value processes occurring at the same scattering angle, without having to explicitly evaluate the various Debye terms.

The predictions of ray theory were compared with those of wave theory. We found for values of B and C that predicted either one or two $p = 1$ bows in ray theory, the finely-stratified multi-layer sphere model easily reproduced the first bow. Its deflection angle agreed with the Descartes angle prediction of ray theory, except for a small Airy shift that depends on the particle size. However, wave theory computations failed to reproduce the second bow for those values of B and C for which it was expected in ray theory. We believe this is due to the extreme narrowness of the impact parameter interval responsible for the second ray theory bow of a GLL. Evidence that this is the case is provided by the fact that the finely-stratified multi-layer sphere model was easily able to reproduce both $p = 1$ bows for certain other carefully constructed monotonically decreasing refractive index profiles when ray theory predicted that two should occur. In addition, yet other monotonically decreasing refractive index profiles were found that predicted four $p = 1$ bows in ray theory. Lastly, Figure 3(a) shows that when $C > 1$, the diffraction fields can be separated from all other scattering processes in the time domain (in this case the $p = 1$ transmitted portion of the fields). This has previously been assumed to be impossible.

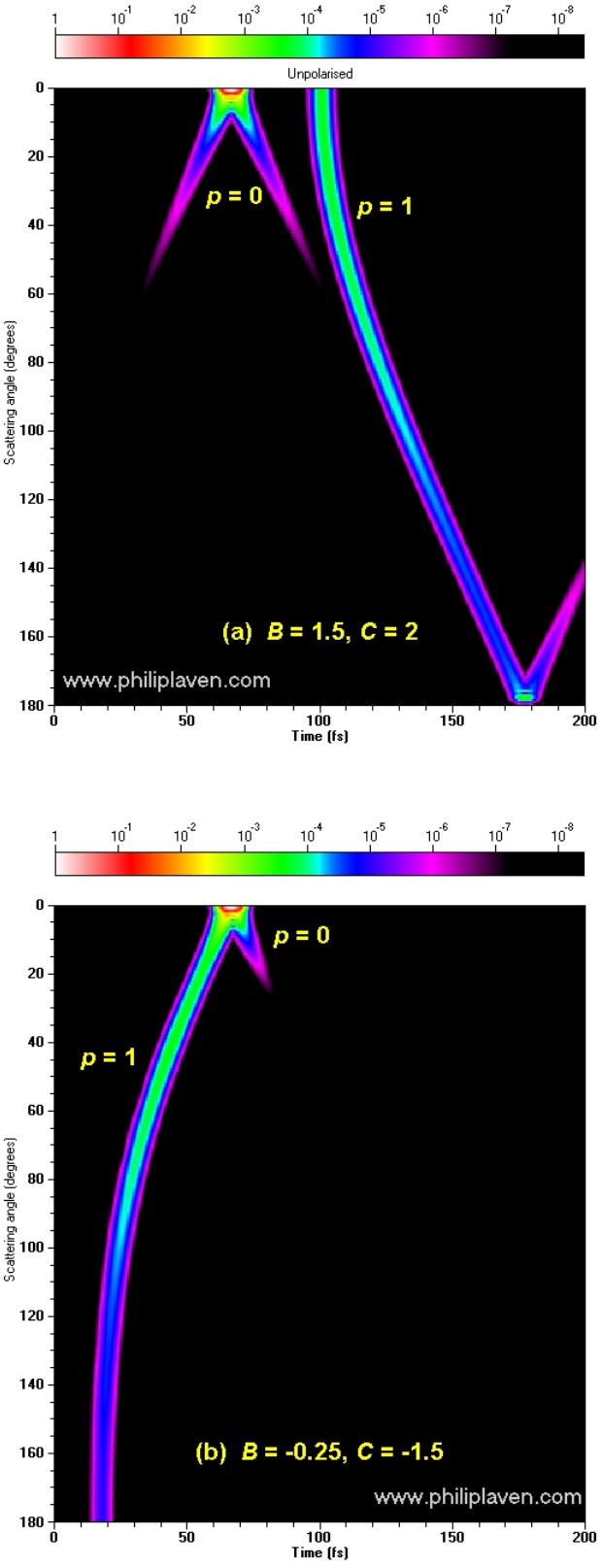


Figure 3 *False-colour map showing intensity in the time domain for λ = 0.65 μm for a GLL of radius a = 10 μm with (a) B = 1.5 and C = 2 and (b) B = -0.25 and C = -1.5.*

4 Luneburg Bubble

For the generalized Luneburg "variable density bubble", with $-1 < C < 0$ and $2B < C + 1$, incident rays with small impact parameters pass through the sphere, with the $p = 1$ transmitted rays being scattered at $\Theta \approx 0°$. In the potential scattering analogy this corresponds to a particle directly incident on a repulsive potential energy hill with sufficient energy to cross over the top of the hill and continue down the other side.

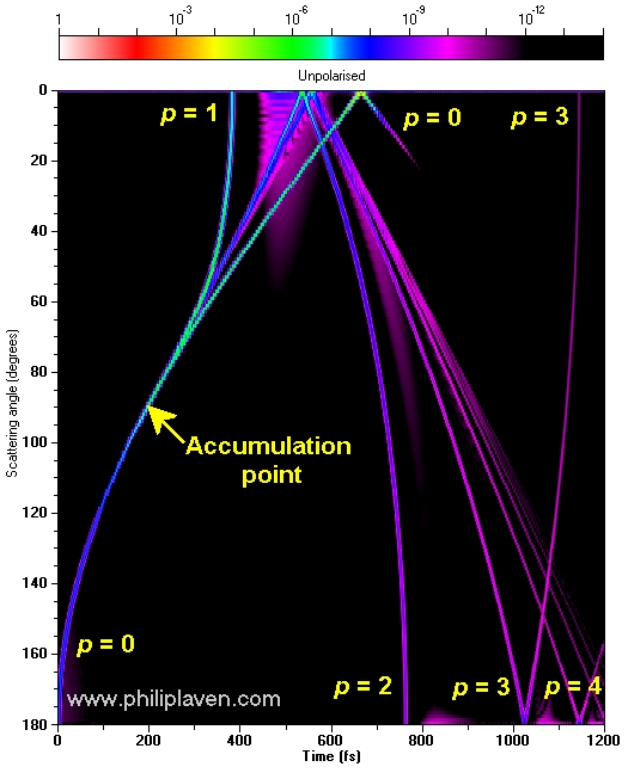


Figure 4 *Time domain results for λ = 0.65 μm for a GLL of radius a = 100 μm with B = 0.125 and C = -0.25.*

When $C < -1$, incident rays with very small impact parameters penetrate only part way into the sphere before they are reflected back from the interior at $\Theta \approx -180°$. In the potential scattering analogy, this corresponds to a directly incident particle not having enough energy to pass over the top of the repulsive potential energy hill. It travels part way up the hill, momentarily stops, and then travels back down in the direction it had come. This corresponds in wave theory to evanescent forward propagation beginning at the total internal reflection point.

For $C < 0$ and $2B < C + 1$, total external reflection is predicted in ray theory to occur when:

$$\sin(\theta_i) \geq (2B - C)^{1/2} \qquad (4)$$

The incident impact parameter interval in the vicinity of $\sin(\theta_{ic}) = (2B - C)^{1/2}$ corresponds to the transition between partial and total exterior reflection. This is an example of a weak external reflection caustic, which interferes with the

transmitted field to produce a two-ray-to-one-ray transition centered about the critical scattering angle Θ_c. This effect is prominently reproduced in our wave theory computations for $-1 < C < 0$. Another interesting feature of our time domain plots is the accumulation point of all the $p \geq 1$ Debye terms at:

$$\Theta = -\pi + 2 \arcsin[(2B - C)^{1/2}] \quad (5)$$

$$\Delta t = (2a/c)\,[1 - (1 - 2B + C)^{1/2}] \quad (6)$$

where c is the speed of light in vacuum.

Figure 4 shows such an accumulation point at $\Theta = 90°$ and $\Delta t = 195.3$ fs, which is a consequence of rays making a number of internal reflections with near-grazing incidence inside the sphere. [3] For $C = -1$ and $B = 0$, a weak caustic is also produced and is centred about $\Theta = 90°$, as shown in Figure 5. Lastly, Brewster angle effects were found in the TM polarization in both the scattered intensity and the time domain graphs.

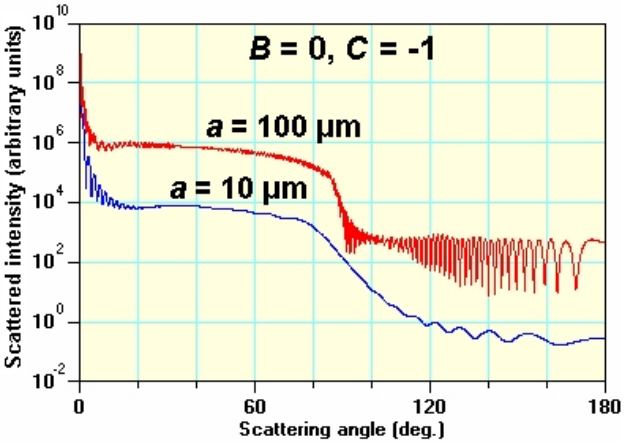


Figure 5 *Wave theory results showing intensity as a function of scattering angle for $\lambda = 0.65$ μm for a GLL of radius $a = 10$ μm (blue curve) and $a = 100$ μm (red curve) with $B = 0$ and $C = -1$.*

5 References

[1] H. M. Nussenzveig, *Diffraction Effects in Semiclassical Scattering* (Cambridge University, Cambridge, UK, 1992).

[2] J. A. Lock, "Scattering of an electromagnetic plane wave by a Luneburg lens. III. Finely stratified sphere model," J. Opt. Soc. Am. A **25**, 2991-3000 (2008).

[3] N. Fiedler-Ferrari, H.M. Nussenzveig, and W.J. Wiscombe, "Theory of near-critical-angle scattering from a curved surface," Phys. Rev. **A43**, 1005-1038 (1991).

Light Scattering of a Nondiffracting Zero-order Bessel Beam by Uniaxial Anisotropic Bispheres

Zheng-Jun LI[1,*], Zhen-Sen WU[1], Tan. QU[1], Hai-Ying LI[1], Lu. BAI[1] and Lei. GONG[2]

[1] School of physics optoelectronic engineering, Xidian University, Xi'an Shaanxi, 710071, China.
[2] School of Photoelectric Engineering, Xi'an Technological University, Xi'an, 710021, China

Corresponding author: lizj@xidian.edu.cn

Abstract

Based on the generalized multiparticle Mie theory and the Fourier transformation approach, light scattering of two interacting homogeneous uniaxial anisotropic spheres with parallel primary optical axes illuminated by a nondiffracting zero-order Bessel beam is investigated. The expansion expression of the zero-order Bessel beam is given in terms of the spherical vector wave functions (SVWFs). Utilizing the vector addition theorem of the SVWFs, the interactive scattering coefficients are derived through the continuous boundary conditions on which the interaction of the bispheres is considered. The effects of the conical angle of the wave vector components of the Bessel beam, beam center position, sphere separation distance, and anisotropic parameters on the field distributions can be numerically analyzed in detail. Some results are compared with those illuminate by a Gaussian beam. This investigation could provide an effective test for further research on the scattering characteristic of an aggregate of anisotropic spheres by a high-order Bessel vortex beam and radiation forces, which are important in optical tweezers and related particle manipulation applications.

1 Introduction

Because of its non-diffracting and self-constructing property, Bessel beam has gained growing attentions from scholars since its naissance by Durnin in 1987 [1]. The scattering problems of a zero-order Bessel beam by spherical particles are studied by many scholars. In 2007, Marston considered the scattering problem of Bessel beam by spherical particle [2]. Ma et al. investigated an unpolarized Bessel beam and Bessel-Gauss beam scattering by spheres [3]. F. G. Mitri investigated Arbitrary scattering of an electromagnetic zero-order Bessel beam by a dielectric sphere [4]. The scattering of a high-order vortex Bessel beam are also by many scholars. For most papers to which we have referred, the investigations focus on the scattering by single isotropic sphere. The study on anisotropic medium is exiguous. Recently, Qu researched scattering by a uniaxial anisotropic sphere located in an off-axis zero-order Bessel beam [5].

Due to recent advances in material science and technology etc., a great interest in the interaction between EM wave and anisotropic media is being grown. Many scholars have investigated the scattering characteristics of a uniaxial anisotropic spherical particles using analytical method [6-10]. Based on generalized multi-particle Mie theory developed by many people in past decades, researchers from our group recently studied the scattering characteristic of uniaxial bispheres [11], multiple uniaxial anisotropic spheres [12]. The scattering of uniaxial bispheres located in a Gaussian beam were also investigated. However, in most of the articles that we have referred, the investigations focus on a plane wave scattering by multiple isotropic or anisotropic spheres. However, the interaction of a Bessel beam with multiple anisotropic spheres is still a new problem but one of considerable merit.

In this paper, based on the GMM theory and our former work, a rigorous analytical solution on the scattering of uniaxial anisotropic bispheres with parallel primary optical axes illuminated by a zero-order Bessel beam will be derived. The scattering properties are numerically analyzed in detail. In the subsequent depiction, a time dependence of the form exp(-iωt) is assumed and suppressed, where ω is the circular frequency.

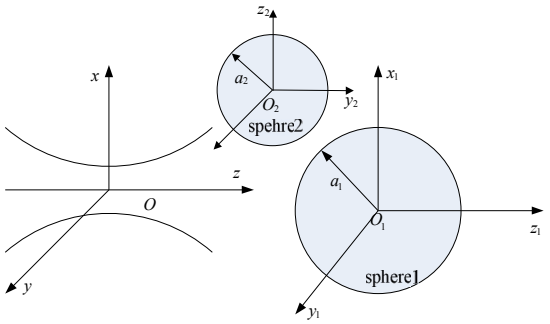


Figure 1 *Geometry for light scattering of a zero-order Bessel beam by uniaxial anisotropic bispheres*

2 Theory Formulae

Considering two uniaxial anisotropic spheres with radius $a_j\,(j=1,2)$ and the primary optical axes coincident with the z-axis in a global coordinate system *Oxyz* , as shown in Fig. 1, the centers of the spheres are located at (x_1,y_1,z_1) and (x_2,y_2,z_2) , respectively. The particles are illuminated by a polarized Bessel beam which can be

expressed in particle coordinate system $O_j x_j y_j z_j$ using integral form as:

$$\mathbf{E}_j^i(\mathbf{r}) = E_0 \int_0^{2\pi} \mathbf{e}_v(\alpha,\beta)\exp(i\mathbf{k}\cdot\mathbf{r})\exp(i\mathbf{k}\cdot\mathbf{r}_j)d\beta \quad (1)$$

where, E_0 is the peak amplitude, $\mathbf{e}_v(\alpha,\beta)$ indicates the unit polarization vectors, v represents polarization directions of x and y, $\exp(i\mathbf{k}\cdot\mathbf{r})$ denotes a plane wave with wave vector $\mathbf{k}=(k,\alpha,\beta)$, parameter α is being called conical angle of Bessel beam and $\mathbf{r}_j = -x_j\hat{x} - y_j\hat{y} - z_j\hat{z}$.

Utilizing integral localized approximation (ILA), the Bessel beam can be expanded in terms of SVWFs as [5]:

$$\begin{aligned}\mathbf{E}_j^i(\mathbf{r}) &= \sum_{n=1}^{\infty}\sum_{m=-n}^{n} E_{mn}\left[a_{jmn}^{iv}\mathbf{M}_{mn}^{(1)}(\mathbf{r},k_0) + b_{jmn}^{iv}\mathbf{N}_{mn}^{(1)}(\mathbf{r},k_0)\right] \\ \mathbf{H}_j^i(\mathbf{r}) &= \frac{k_0}{iw\mu_0}\sum_{n=1}^{\infty}\sum_{m=-n}^{n}\left[b_{jmn}^{iv}\mathbf{M}_{mn}^{(1)}(\mathbf{r}_j,k_0) + a_{jmn}^{iv}\mathbf{N}_{mn}^{(1)}(\mathbf{r}_j,k_0)\right]\end{aligned} \quad (2)$$

The expansion coefficients can be found in [5]. The scattered fields of the jth (j=1, 2) uniaxial anisotropic sphere can also be expanded in terms of SVWFs in the jth sphere coordinate system $O_j x_j y_j z_j$ as:

$$\begin{aligned}\mathbf{E}_j^s &= \sum_{n=1}^{\infty}\sum_{m=-n}^{n} E_{mn}\left[a_{jmn}^{s}\mathbf{M}_{mn}^{(3)}(\mathbf{r}_j,k_0) + b_{jmn}^{s}\mathbf{N}_{mn}^{(3)}(\mathbf{r}_j,k_0)\right] \\ \mathbf{H}_j^s &= \frac{k_0}{i\omega\mu_0}\sum_{n=1}^{\infty}\sum_{m=-n}^{n} E_{mn}\left[a_{jmn}^{s}\mathbf{N}_{mn}^{(3)}(\mathbf{r}_j,k_0) + b_{jmn}^{s}\mathbf{M}_{mn}^{(3)}(\mathbf{r}_j,k_0)\right]\end{aligned} \quad (3)$$

The uniaxial anisotropic medium is characterized by a permittivity and permeability with tensor $\bar{\varepsilon}_j$ and $\bar{\mu}_j$ (j=1, 2), respectively, expressed as:

$$\bar{\varepsilon}_j = \varepsilon_0\begin{bmatrix}\varepsilon_{jt} & 0 & 0\\ 0 & \varepsilon_{jt} & 0\\ 0 & 0 & \varepsilon_{jz}\end{bmatrix},\quad \bar{\mu}_j = \mu_0\begin{bmatrix}\mu_{jt} & 0 & 0\\ 0 & \mu_{jt} & 0\\ 0 & 0 & \mu_{jz}\end{bmatrix} \quad (4)$$

Applying Fourier transformation method, the EM fields in the jth uniaxial anisotropic spheres can be expanded in terms of the SVWFs [11].

On the spherical boundary at $r_j = a_j$, the tangential components (designated by the subscript t) of the EM fields continue as:

$$\mathbf{E}_j^I\big|_t = \mathbf{E}_j^{it}\big|_t + \mathbf{E}_j^s\big|_t, \qquad \mathbf{H}_j^I\big|_t = \mathbf{H}_j^{it}\big|_t + \mathbf{H}_j^s\big|_t \qquad (r_j = a_j) \quad (5)$$

where $\mathbf{E}_j^{it}$ and $\mathbf{H}_j^{it}$ represent the total EM fields incident on the jth(j=1, 2) uniaxial anisotropic sphere. The total incident field can be derived applying the addition theorem of the SVWFs, then substituting the expressions of the incident, internal and scattered fields into Eq. (5), we can derived the interacting scattering coefficients [11].

Known the scattering coefficients, the total scattered fields which are the vector superposition of the scattered field of every uniaxial anisotropic sphere can be derived by applying the addition theorem of the SVWFs again. The total scattered fields in the global coordinate system Oxyz can be derived,

$$\begin{aligned}\mathbf{E}^{st} &= \sum_{n=1}^{\infty}\sum_{m=-n}^{n} E_{mn}\left[a_{mn}^{st}\mathbf{M}_{mn}^{(3)}(\mathbf{r}_0,k_0) + b_{mn}^{st}\mathbf{N}_{mn}^{(3)}(\mathbf{r}_0,k_0)\right] \\ \mathbf{H}^{st} &= \frac{k_0}{i\omega\mu_0}\sum_{n=1}^{\infty}\sum_{m=-n}^{n} E_{mn}\left[a_{mn}^{st}\mathbf{N}_{mn}^{(3)}(\mathbf{r}_0,k_0) + b_{mn}^{st}\mathbf{M}_{mn}^{(3)}(\mathbf{r}_0,k_0)\right]\end{aligned} \quad (6)$$

where a_{mn}^{st} and b_{mn}^{st} are the total scattering coefficients [11]. Then according to the definition of the RCS, we can calculate the angular distribution of the RCS. The effects of the beam parameters, and anisotropic parameters on the field distributions will be numerically analyzed in detail. And some results are compared with those illuminate by a Gaussian beam.

3 Acknowledgement

The authors gratefully acknowledge support from the National Natural Science Foundation of China under Grant Nos. 61308025 and 61172031, the Natural Science Foundation in Shaanxi Province of China (2013JQ8018) and Fundamental Research Funds for the Central Universities.

4 References

[1] Durnin J., Exact solution for nondiffracting beams.I.The scalar theory, J. Opt. Soc. Am. A **4**(4):651-654 (1987).

[2] Marston. P.L., Scattering of a Bessel beam by a sphere, J.Acoust Soc Am **121**(2):753-738 (2007).

[3] Ma X.B., and Li E.B., Scattering of an unpolarized Bessel beam by spheres, Chin. Opt. Lett. **8**(12):1195-1198 (2010).

[4] Mitri F.G., Arbitrary scattering of an electromagnetic zero-order Bessel beam by a dielectric sphere, Opt. Lett. **36**(5):766-768 (2011).

[5] Qu T., Wu Z.S., Shang Q.C., Li Z.J., and Bai L., Electromagnetic scattering by a uniaxial anisotropic sphere located in an off-axis Bessel beam, J. Opt. Soc. Am. A **30**(8):1661-1669 (2013).

[6] Stout B., Michel N., and Evgeny. P, Mie scattering by an anisotropic object. Part I. Homogeneous sphere, J. Opt. Soc. Am. A **23**(5):1111-1123 (2006).

[7] Wong K.L., and Chen H.T., Electromagnetic scattering by a uniaxially anisotropic sphere, IEE PROCEEDINGS-H **139**(4):314-318 (1992).

[8] Qiu C.W., Li L.W., and Yeo T.S., Scattering by rotationally symmetric anisotropic spheres:Potential formulation and parametric studies, physical review E 75:026609 (2007).

[9] Geng Y.L., Wu X.B., and Li L.W., Mie scattering by a uniaxial anisotropic sphere, Phys. Rev. E 70:056609 (2004).

[10] Wu Z.S., Yuan. Q.K., Peng Y., and Li Z.J., Internal and external electromagnetic fields for on-axis Gaussian beam scattering from a uniaxial anisotropic sphere, J. Opt. Soc. Am. A **26**(8):1779-1788 (2009).

[11] Li Z.J., Wu Z.S., and LI H.Y., Analysis of electromagnetic scattering by uniaxial anisotropic bispheres, J. Opt. Soc. Am. A **28**(2):118-125 (2011).

[12] Li Z.J., Wu Z.S., Shi Y.E., Bai. L, and Li H.Y., Multiple scattering of electromagnetic waves by an aggregate of uniaxial anisotropic spheres, J. Opt. Soc. Am. A **29**(1):22-31 (2012).

ELECTROMAGNETIC SCATTERING BY A GENERAL ANISOTROPC DIELECTRIC NONSPHERICAL PARTICLE

Jia Jie WANG*, Yi Ping HAN, Zhe Feng WU and Lu HAN

School of Physics and Optoelectronic Engineering, Xidian University, Xi'an, 710071, China

Corresponding author: wangjiajie@xidian.edu.cn

Abstract

A theoretical treatment is implemented within the framework of the extended boundary condition method (EBCM) to predict the electromagnetic scattering properties of a general anisotropic dielectric particle. The anisotropic dielectric permittivity tensor is taken to be arbitrary. The unknown electromagnetic fields inside the anisotropic scatterer is expanded in terms of a system of quasi-spherical vector wave functions (qSVWFs), which are derived by using an inverse Fourier transform operation. As verification, special cases of typical anisotropic media, including gyroelectric anisotropic medium, biaxial anisotropic medium and uniaxial anisotropic medium, are reduced theoretically from the general derivations. Furthermore, numerical comparisons are made between results obtained using the presented method and those published data calculated using other methods. Very good agreements are achieved for the present cases, which partially indicate the correctness of the derived theoretical formulae and the home-made program. Specifically, influences of shape deformation as well as of anisotropy components in permittivity tensor upon the scattering properties will be analyzed later.

1 Theoretical treatments

To find a solution for the electromagnetic scattering problem in the framework of EBCM, an expansion representation of the electromagnetic fields inside the scatterer in terms of vector wave functions is needed. For instance, VSWFs are commonly used in the expansion of electromagnetic fields in isotropic media. To find an expansion representation of electromagnetic fields in the uniaxial anisotropic media, series of quasi-spherical vector wave functions (qSVWFs) were derived by Kiselev et al. [1] and by Doicu [2], respectively. And a series of qSVWFs for the expansion of electromagnetic fields in the biaxial anisotropic media was given by Schmidt and Wriedt [3].

As we know, either for a uniaxial medium, or for a biaxial medium, their permittivity tensors are diagonal matrix or could be transformed to diagonal matrix by rotating the principal coordinate system. Nevertheless, there are anisotropic medium whose permittivity tensors cannot be transformed into a diagonal matrix, e.g. gyrotropic anisotropic medium. Thus, to extend the EBCM based T-matrix method to be suitable for a wider range of anisotropic scatterers with arbitrary permittivity tensor is a necessary. Such an attempt could be found in a recent study by Schmidt and Wriedt [4]. Nevertheless, the extend in Ref.[4] seems to be not complete, for instance, the special case of gyrotropic anisotropic medium cannot be covered. Recently, solutions for the electromagnetic scattering by a gyroelectric particle were analyzed by Wang et al.[5], where a system of qSVWFs for expanding electromagnetic field insider gyrotropic anisotropic medium were presented.

In this present paper, based on the previous reported derivations [1-5], a general system of qSVWFs are rederived for an expansion representation of electromagnetic fields inside a general anisotropic scatterers with arbitrary permittivity tensors by using the inverse Fourier transform. Special cases for gyroelectric anisotropic medium, biaxial anisotropic medium and uniaxial anisotropic medium are discussed.

For cases of an electric anisotropic medium consist of the isotropic permeability $\bar{\mu}$ and the anisotropic permittivity $\bar{\varepsilon}$, the parameters are described as:

After some forward algebra, we could obtain an expansion representation for the electric and magnetic fields in a general anisotropic media:

$$\begin{aligned}\mathbf{E}(\mathbf{r}) &= \sum_{n=1}^{\infty}\sum_{m=-n}^{n}[c_{mn}\mathbf{X}_{mn}^{e}(\mathbf{r}) + d_{mn}\mathbf{Y}_{mn}^{e}(\mathbf{r})] \\ \mathbf{H}(\mathbf{r}) &= -i\sqrt{\frac{\varepsilon}{\mu}}\sum_{n=1}^{\infty}\sum_{m=-n}^{n}[c_{mn}\mathbf{X}_{mn}^{h}(\mathbf{r}) + d_{mn}\mathbf{Y}_{mn}^{h}(\mathbf{r})]\end{aligned} \tag{2}$$

where $\mathbf{X}_{mn}^{e,h}$, $\mathbf{Y}_{mn}^{e,h}$ are the newly derived quasi-spherical vector functions:

$$\begin{aligned}\mathbf{X}_{mn}^{e,h}(\mathbf{r}) &= \int_{\Omega}(-\frac{1}{1-ff'})[A_{mn}\mathbf{w}_1^{e,h}e^{ik_1\mathbf{e}_r\cdot\mathbf{r}} \\ &\quad + B_{mn}\mathbf{w}_2^{e,h}e^{ik_2\mathbf{e}_r\cdot\mathbf{r}}]dS(\Omega) \\ \mathbf{Y}_{mn}^{e,h}(\mathbf{r}) &= \int_{\Omega}(-\frac{1}{1-ff'})[A'_{mn}\mathbf{w}_1^{e,h}e^{ik_1\mathbf{e}_r\cdot\mathbf{r}} \\ &\quad + B'_{mn}\mathbf{w}_2^{e,h}e^{ik_2\mathbf{e}_r\cdot\mathbf{r}}]dS(\Omega)\end{aligned} \tag{3}$$

$$
\begin{aligned}
A_{mn} &= m\pi_n^{|m|}(\theta)(-f') + i\tau_n^{|m|}(\theta) \\
B_{mn} &= m\pi_n^{|m|}(\theta) + i\tau_n^{|m|}(\theta)(-f) \\
A'_{mn} &= im\pi_n^{|m|}(\theta)(-f) + \tau_n^{|m|}(\theta) \\
B'_{mn} &= im\pi_n^{|m|}(\theta) + \tau_n^{|m|}(\theta)(-f')
\end{aligned} \tag{4}
$$

where

$$
\begin{aligned}
\mathbf{w}_1^e &= \varepsilon\left\{[(\lambda_{r\theta}f + \lambda_{r\varphi})]\mathbf{e}_r + \lambda_1 \cdot \mathbf{v}_1\right\} \\
\mathbf{w}_2^e &= \varepsilon\left\{[(\lambda_{r\theta} + \lambda_{r\varphi}f')]\mathbf{e}_r + \lambda_2 \cdot \mathbf{v}_2\right\} \\
\mathbf{w}_1^h &= \sqrt{\lambda_1\varepsilon}(f\mathbf{e}_\varphi - \mathbf{e}_\theta) \\
\mathbf{w}_2^h &= \sqrt{\lambda_2\varepsilon}(\mathbf{e}_\varphi - f'\,\mathbf{e}_\theta)
\end{aligned} \tag{5}
$$

$$
\mathbf{v}_1 = f\mathbf{e}_\theta + \mathbf{e}_\varphi \qquad \mathbf{v}_2 = (\mathbf{e}_\theta + f'\,\mathbf{e}_\varphi) \tag{6}
$$

As verification, special cases of typical anisotropic media, including gyroelectric anisotropic medium, biaxial anisotropic medium and uniaxial anisotropic medium, could be reduced theoretically from the general derivations, which are not presented in this report.

2 Numerical validation

The theoretical formulae presented in Section 1 have been implemented into a FORTRAN program. To verify the correctness of the solution as well as the accuracy of our home-made program, numerical results for electromagnetic scattering from an anisotropic particle are calculated and compared with those data published in previous literature calculated using other methods.

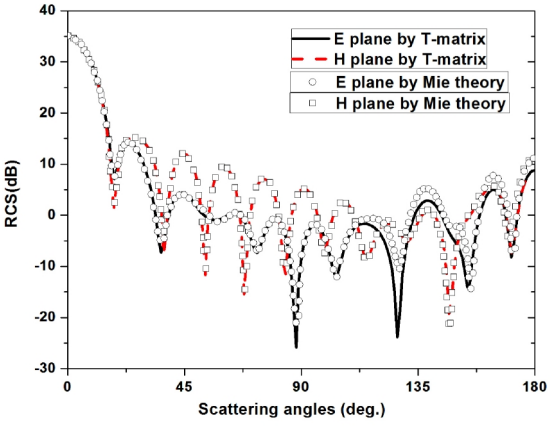


Figure 1. *Comparison of Radar cross sections (RCSs) for a lossy uniaxial sphere obtained from the present T-matrix method and those calculated using an extended Mie theory in Ref.[6]. The parameters for the uniaxial sphere used in the simulation are* $k_0 r = 4\pi$, $\varepsilon_{xx} = \varepsilon_{yy} = 2 + 0.1i$, $\varepsilon_{zz} = 4 + 0.2i$ *,respectively.*

Firstly, RCSs for a special case of a lossy uniaxial anisotropic spherical particle of the electrically large size are calculated. The size parameter of the particle is $k_0 r = 4\pi$. The components in electric permittivity tensor are $\varepsilon_{xx} = \varepsilon_{yy} = 2 + 0.1i$, $\varepsilon_{zz} = 4 + 0.2i$. In Fig.1, comparisons of RCSs in *E*-plane (*yoz* plane) and *H*-plane (*xoz* plane) calculated by the present method are compared with those calculated by using an extended Mie theory [6]. As we can see, the agreements between the results obtained in the present paper and those from Ref.[6] are obvious.

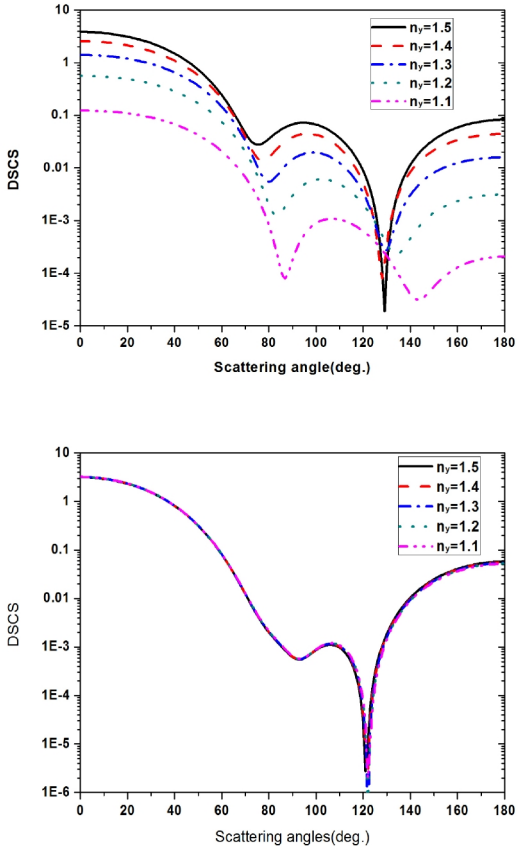


Figure 2. *Normalized differential scattering cross sections (DSCS) for an ellipsoid with* $k_s a = 2$ $k_s b = 3$ $k_s c = 4$ *, with parameters* $\varepsilon_{xx} = \sqrt{1.5}$ $\varepsilon_{yy} = \sqrt{1.3}$ $\varepsilon_{zz} = \sqrt{1.1}$ *in Ref.[3] are reproduced by the present T-matrix method*

As we know, one of the inherited advantages of solutions obtained in the framework of the EBCM is its capability in dealing with nonspherical particles. To further validate as well as to demonstrate the capability of the home-made program, normalized differential scattering cross sections (DSCS) for a biaxial anisotropic ellipsoid are calculated by using the present method. The size parameter of the ellipsoid are $k_s a = 2$, $k_s b = 3$, $k_s c = 4$ and the permittivity tensor is described by $\varepsilon_{xx} = \sqrt{1.5}$, $\varepsilon_{yy} = \sqrt{1.3}$, $\varepsilon_{zz} = \sqrt{1.1}$, which is the same parameters used in Ref.[3]. Almost an exact agreement is achieved between the results presented in Fig.3 and those given in Ref.[3] as expected since the general derivations

in the present paper are degenerated to the special case of biaxial anisotropic medium. It is interesting to notice that the perpendicular components of DSCS are independent of the effect of bianisotropic parameters, since in this case the electric field oscillates in a plane, which is perpendicular to the y-axis. While the parallel components of DSCS decrease as the bianisotropic parameters ε_{yy} decrease, and the scattering angles of minimum intensity peaks move to larger values.

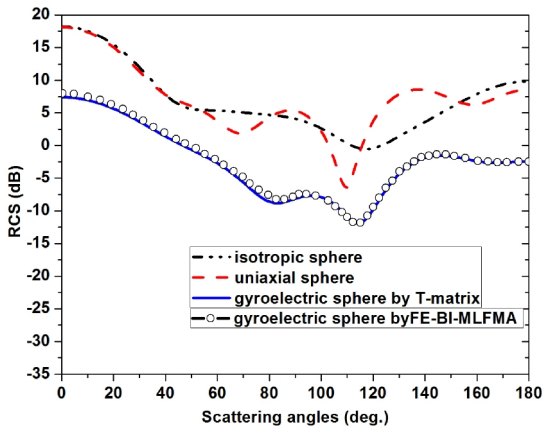


Figure 3. *Radar cross sections (RCSs) for a gyroelectric spherical particle with parameters* $k_0 r = 1.2\pi$, $\varepsilon = 3\varepsilon_0$ $\varepsilon_g = -2\varepsilon_0$ $\varepsilon_z = 4\varepsilon_0$ *from Ref.[7] calculated using FE-BI-MLFMA are reproduced by the present method.*

Among the general anisotropic medium, a special subclass which is known as gyrotropic anisotropic medium has attracted a lot of interests since the existence of natural gyrotropic crystals and possible realization of artificial gyrotropic composites, such as magnetized plasma, ferrite, and so on. Specifically, the plasma has shown its potential applications in the field of antennas and microwave, such as optical signal processing procedures, the control of radar cross sections for military objects, development of certain types of radar absorbers. To further demonstrate the capability of our code, RCSs of a magnetized plasma sphere with parameters $k_0 r = 1.2\pi$, $\varepsilon = 3\varepsilon_0$, $\varepsilon_g = -2\varepsilon_0$, $\varepsilon_z = 4\varepsilon_0$ are calculated by the present method and displayed in Fig.3. Comparison with the results from Ref.[7] calculated using FE-BI-MLFMA is made. As shown in Fig.3, a very good agreement is achieved.

3 Conclusion

A T-matrix solution is constructed for the aim of predicting the electromagnetic scattering behaviors from a nonspherical anisotropic particle with arbitrary permittivity tensor. The theoretical treatments is implemented within the framework of the extended boundary condition method (EBCM), where a system of quasi-spherical vector wave functions (qSVWFs) for expanding electromagnetic fields inside anisotropic media is derived by using an inverse Fourier transform operation. As verification, comparisons are made between numerical results obtained using the presented method and those published data calculated using other methods. Very good agreements are achieved for the present cases, which partially indicate the correctness of the derived theoretical formulae and the home-made program. Influences of shape deformation as well as of anisotropy components in permittivity tensor upon the scattering properties will be analyzed later.

4 Acknowledgement

The authors acknowlege the support by the "Fundamental Research Funds for the Central University" in China.

5 References

[1] Kiselev AD, Reshetnyak VYu, Sluckin TJ. Light scattering by optically anisotropic scatterers I: T-matrix theory for radial and uniform anisotropies. Phys. Rev. E. 2002; 65:056609.

[2] Doicu A. Null-field method to electromagnetic scattering from uniaxial anisotropic particles. Opt. Commun. 2003; 218:11-7

[3] Schmidt V, Wriedt T. T-matrix method for biaxial anisotropic particles. JQSRT 2009;110(14):1392-1397.

[4] Schmidt V, Wriedt T. The T-matrix for particle with arbitrary permittivity tensor and parallelization of the computational code, JQSRT, 2012; 113:1712-1718.

[5] Wang JJ, Han YP, Han L, Cui ZW, Electromagnetic scattering from gyroelectric anisotropic particle by T-matrix method; 2014. 135:20–29.

[6] Geng YL, Wu XB, Li LW, Guan BR, Mie scattering by a uniaxial anisotropic sphere, Phys. Rev. E, 2004; 70:056609.

[7] Sheng XQ, Peng Z, Analysis of scattering by large objects with off-diagonally anisotropic material using finite element-boundary integral-multilevel fast multipole algorithm, IET Microw. Antennas Propag., 2010; 4(4): 492-500.

Observation of Laser Light Scattering by Randomly Oriented Particles at Exact Backscattering Angle

Alain MIFFRE [1,*], Gregory DAVID [1-2], Elodie COILLET[1], and Patrick RAIROUX[1]

[1] Institute of Light and Matter, University Lyon, Lyon1, CNRS, Villeurbanne, 69622, France
[2] Laboratory of Physical Chemistry, Swiss Federal Institute of Technology ETHZ, Zurich, 8093, Switzerland
Corresponding author: alain.miffre@univ-lyon1.fr

Abstract

In this contribution, we propose a new laboratory experimental set-up to observe laser light scattering by an ensemble of randomly-oriented particles in ambient air, for the first time in the exact backscattering direction. This direction is one of the most sensitive directions to the particles microphysical properties. We then show how to retrieve the particles depolarization d_p from our laboratory observations and discuss the size and shape dependence of d_p, in agreement with scattering matrix theory and T-matrix numerical code. Several outlooks are proposed.

1 Introduction

Among all laser light scattering directions, the backscattering direction has gained interest in the last decades due to its handiness, and above all, as it is one of the most sensitive directions to the size and the shape of the sample. Hence, light backscattering has been used in various research fields, such as biomedicine, fundamental research or for environmental purposes. In the literature, light backscattering by randomly-oriented particles has been addressed in numerical simulations [1, 2], laboratory experiments [3], as well as field measurements, using passive [4] or active [5] remote sensing. In this contribution, a new laboratory experimental set-up is proposed to address light scattering by an ensemble of randomly-oriented particles, in the exact backscattering direction, within a small field of view [6]. As detailed below, this set-up allows evaluating the depolarization of light by a particles ensemble. Experimental results are proposed for non depolarizing particles, in agreement with Mie theory, then for nonspherical particles, by applying T-matrix numerical code.

2 Backscattering of light by randomly-oriented particles

Polarization-resolved backscattering is generally studied in the framework of the Mueller matrix or scattering phase matrix $\mathbf{F_P}$, relating the incident and scattered Stokes vectors [7]. For randomly-oriented particles, placed in an unbounded host surrounding medium, in the single scattering approximation, only $F_{11,P}$, $F_{22,P}$ and $F_{14,P} = F_{41,P}$ are not null and the particles depolarization, i.e. the particles deviation from isotropy, is $d_P = 1 - F_{22,P}/F_{11,P}$. To ease the comparison with numerical simulations and field experiments, our laboratory exact backscattering measurement fulfils the far-field approximation where the scattering volume can be treated as a point source of scattered radiation [8]. Figure 1 presents the principle of our exact backscattering measurement. The geometry is achieved by inserting a well-specified polarizing beam-splitter cube (PBC) on the optical pathway from a laser source to the particles scattering medium. After retroflection on the PBC, the s-polarization component of the backscattered light is detected and, as in lidar applications [5], this signal is discriminated from the background stray light by measuring the time-of-flight for a laser pulse to reach the photo-detector. In addition, a collection optics system (not represented in Figure 1) efficiently collects the particles backscattering, while minimizing any stray light, in a 3 mrad field of view. Hence, after accurate alignment procedure (1 mm.10 m^{-1}), this set-up fulfils the requirements for a high angular resolution (θ = 180.0 ± 0.2°, to avoid blocking light with the detector) and a high dynamical range (to discriminate low particles backscattering from background stray light), which is new in the exact backscattering direction.

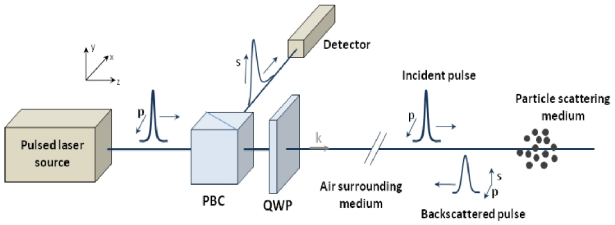


Figure 1 *Principle of our laboratory measurement at exact backscattering angle (θ = 180.0 ± 0.2°) for particles in air.*

The experiment is operated in the UV spectral range at λ = 355 nm, to increase our sensitivity to particles in the range of a few cents of nanometres, for which particles size parameters are close to unity. It consists in a two-stage procedure. Backscattering of light by ambient particles is first measured (i.e. signal S_0), then the nanoparticles are generated with a commercial atomizer (TSI 3079) and injected in the particles scattering volume (detected signal $S = S_0 + S_P$). The particles backscattering signal S_P can hence be measured as a function of the photon time-of-flight by

subtracting S(t) from $S_0(t)$, the laser trigger cavity being used to fix the time origin, as in range/time-resolved lidar applications. The distance from the PBC to the particles scattering medium corresponds to 40 ns pulsed laser time-of-flight, well above the 5 ns-laser pulse duration. Figure 2 shows an example of backscattering signal S_P for water droplets in ambient air.

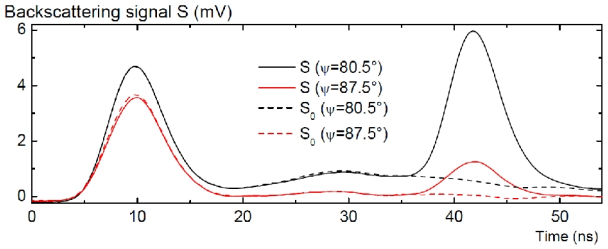


Figure 2 *Observation of exact backscattering of light by water droplets in ambient air (the angle ψ is related to the QWP).*

By modulating the laser linear polarization (using the ψ-angle of the quarter-wave plate (QWP)), S_P is modified as displayed in Figure 2. The variation of S_P with ψ can be calculated theoretically by taking into account the successive Mueller matrices encountered by the laser pulse on its optical path from the PBC to the particles medium then back to the detector. After a few calculations, we get for the detected light intensity:

$$S_p(\psi) \propto \left[F_{11,p} + F_{22,p} + (F_{11,p} - 3F_{22,p}) \times \cos(4\psi)\right] \quad (1)$$

Hence, the particles depolarization $d_P = 1 - F_{22,P}/F_{11,P}$ can be measured by adjusting the ψ-dependence of S_P. To minimize statistical errors, several ψ-values are chosen and S_P is averaged over 150 laser shots. Systematic errors are negligible, due to low laser intensity fluctuations and low particles number fluctuations.

3 Particles depolarization retrieval

By using the above methodology, we evaluate the particles depolarization in two case studies: for spherical water droplets, then for nonspherical sea-salt particles.

3.1 Non depolarizing particles

Figure 3 presents the variation of S_P as a function of ψ for spherical water droplets, used for calibrating our experimental set-up. To account for the amount of light backscattered during the whole pulse laser duration τ, the plotted quantity is $S_{P,\tau}$ (i.e. the integral of S_P over τ). Using Equation (1), we retrieved a particles depolarization d_P = (0.04 ± 0.08) %, compatible with Mie scattering theory. In turn, the single-scattering approximation appears to be realistic, and moreover, the state-of-the-art literature [9] provides quantitative evidence that at our particles number densities, this approximation is quite safe.

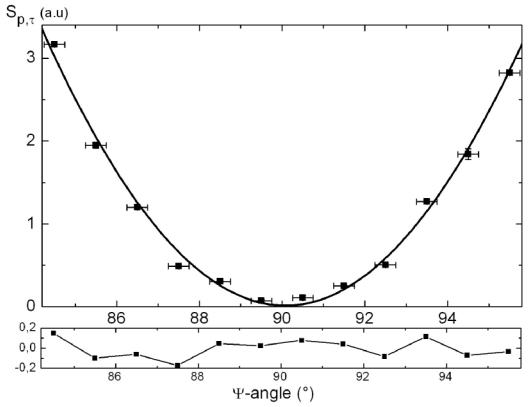


Figure 3 *Calibration with water droplets (Mie theory).*

3.2 Non spherical particles in ambient air

The depolarization of salt NaCℓ-particles in ambient air has been evaluated for different relative humidities (RH), as plotted in Figure 4. We hence retrieved d_P = (1.1 ± 0.4) % for RH = 90 %, then d_P = (9.6 ± 1.4) % for RH = 30 %.

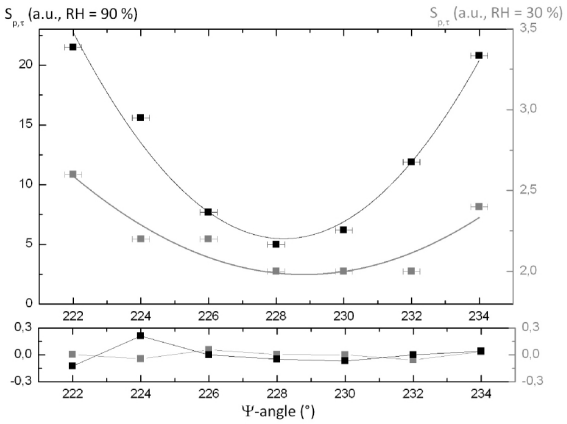


Figure 4 *Depolarization of salt particles at two different RH.*

Above the NaCℓ-deliquescence point (RH = 75 %), salt particles behave like spherical particles and d_P is close to zero. Below the 40 %-crystallization point, NaCℓ-particles exhibit a cubic shape so that d_P is higher. This result agrees with scattering matrix theory: as for $F_{11,P}$ and $F_{22,P}$, the retrieved d_P-value is shape-dependent.

4 Size dependence of the particles depolarization

Comparison with other laboratory experiments is not straightforward: none operates in the exact backscattering direction, and extrapolations up to 180.0° may lead to quite considerable errors [10]. Polarization-resolved lidar field measurements may provide d_P-values for sea-salt particles, but such particles may differ from our generated salt particles. Moreover, comparison with lidar devices should be done with care [5]. Nonetheless, as for $F_{11,P}$ and $F_{22,P}$, d_P is size-dependent, which can be characterized by addressing the particles size distribution of our generated salt particles with a scanning mobility particle sizer (TSI,

SMPS 3910). Figure 5 shows the variation of d_P with the mean NaCℓ-particles radius r (determined with a 10 %-uncertainty), for four different particle size distributions.

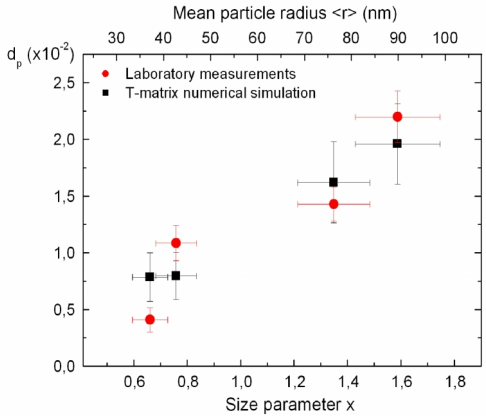


Figure 5 *Laboratory and T-matrix evaluation of salt particles depolarization at different mean particle radius r (or equivalently particles size parameter* $x = 2\pi r/\lambda$*).*

As the mean particles radius r increases from 37 to 90 nanometres, the particles depolarization increases by a factor of 5. By assuming our salt particles to behave like an ensemble of randomly-oriented spheroids (T-matrix code, [1]), we numerically evaluate $F_{11,P}$ and $F_{22,P}$, then d_P at the four mean particles radii (or equivalently four mean particles size parameters $x = 2\pi r/\lambda$). The results plotted in Figure 5 correspond to an aspect ratio $\varepsilon = 1.05$ and a salt particles complex refractive index $m = 1.51 - 0.0004 \times i$ at λ = 355 nm. Within error bars, the T-matrix numerical simulation agrees with our laboratory d_P-measurement, at least for particles radii in the range of 100 nanometres.

5 Conclusion and outlook

As a conclusion, we observed laser light backscattering by an ensemble of randomly oriented particles in ambient air, for the first time in the exact backscattering direction (θ = 180.0 ± 0.2°) and in the far-field single-scattering approximation. As this direction is one of the most sensitive to the particles microphysical properties, we used our new laboratory experimental set-up to evaluate the particles depolarization d_P of spherical water droplets, then nonspherical salt particles. Moreover, we studied the dependence of d_P with size and shape, originating from the size and the shape dependence of the scattering matrix elements themselves. Our laboratory experiment has been compared with T-matrix numerical simulation and further experiments are planned with nonspherical particles under different relative humidities. Otherwise, other numerical codes may then be applied [2,11], the latter being well-suited for particles with discrete symmetries such as cubic crystals like NaCℓ-crystals. Though d_P is a clear indicator of the particles deviation from isotropy, it cannot however be considered as a shape indicator. As an outlook, in addition to size and shape effects, surface roughness effects may be considered, as they are also included in the scattering matrix [12]. Observation of laser light scattering apart from the exact backscattering angle still remains a very efficient complementary tool for particles microphysical analysis. The potential oral presentation will present our most recent advances.

6 Acknowledgments

The authors thank Région Rhône-Alpes and CNRS for partly funding this work.

7 References

[1] Mishchenko, M.I. and Travis L.D.: Capabilities and limitations of a current Fortran implementation of the T-matrix method for randomly oriented rotationally symmetric scatterers, J. Quant. Spectrosc. Radiat. Transf., 60:309-324 (1998).

[2] Draine, B.T. and Flatau, P.J., Discrete-dipole approximation for scattering calculations, J Opt Soc Am.,11:1491–9 (1994).

[3] Muñoz, O., Volten, H., Hovenier, J. W., et al., Scattering matrices of volcanic ash particles of Mount St Helens, Redoubt, and Mount Spurr volcanoes, J. Geophys. Res., 109:D16201 (2004).

[4] Dubovik, O., Sinyuk, A., Lapyonok, T., et al., Application of spheroid models to account for aerosol particle nonsphericity in remote sensing of desert dust, J. Geophys. Res., 111:D11208 (2006).

[5] David D., Thomas B., Nousiainen T., Miffre A., and Rairoux P., Retrieving volcanic, desert dust, and sea-salt particle properties from two/three-component particle mixtures using UV-VIS polarization Lidar and T-Matrix, Atmos. Chem. Phys., 13: 6757-6776, (2013).

[6] David G., Thomas B., Coillet E., Miffre A. and Rairoux P., Polarization-resolved exact light backscattering by an ensemble of particles in air, Optics Express, 21(16):18624-28639 (2013).

[7] Mishchenko M.I., Travis L.D., and Lacis A.A., *Scattering, Absorption and Emission of Light by Small Particles* (Cambridge University Press, NASA, 2002).

[8] Mishchenko M.I., Hovenier J.W., and Mackowski D.W., Single scattering by a small volume element, J. Opt. Soc. Am. A, 21:71-87 (2004).

[9] Mishchenko M.I., Liu L., and Videen G., Conditions of applicability of the single-scattering approximation, Opt. Express, 15:7522-7527 (2007).

[10] Schnaiter M., Büttner S., Möhler O., Skrotzki J., Vragel M., and Wagner R., Influence of particle size and shape on the backscattering linear depolarization ratio of small ice crystals, Atmos. Chem. Phys., 12:10465-10484 (2012).

[11] Kahnert, M., The T-matrix code Tsym for homogeneous dielectric particles with finite symmetries, J. Quant. Spec. Rad. Transf., 123:62-72 (2013).

[12] Li C., Kattawar G.W., Yang P., Effects of surface roughness on light scattering by small particles, J. Quant. Spectrosc. Radiat. Transfer 89:123–31 (2004).

T-matrix Based Scattering Model for Bio-medical Sensor

V. SCHMIDT [1,*], Y. EREMIN [2] and T. WRIEDT [3]

[1] University Bremen, Bremen, 28359, Germany
[2] Institute für Werkstofftechnik, Bremen, 28359, Germany
[3] Lomonosov Moscow State University, Moscow, 119991, Russia

Corresponding author: vschmidt@iwt.uni-bremen.de

Abstract

To simulate the optical signal in a bio-medical sensor the Null-Field Method with Discrete Sources (NFM-DS) was extended to light scattering by a particle on or near a planar waveguide. The program is verified by comparison of scattering diagrams and extinction cross-sections with those computed using the Mie theory and the Discrete Source Method (DSM).

1. Model

An optical detection systems used in a biomarker sensor seems to be a very promising technique, which allows rapid and sensitive detection of molecules in a raw biological sample. Using a non-homogeneous electromagnetic field eq. an evanescent wave helps to discriminate biomarker-induced and non-biomarker-induced signals. If the marker is bio-chemically bonded to the surface inside the penetration depth of the evanescent wave on the waveguide, then it is excited and scatters light. Otherwise, the signal-over-background ratio has to be increased because the concentration of the bio-marker is usually very low and the real-life biological samples generate very high background signals. This requires further investigations of the light scattering process in a bio-medical sensor.

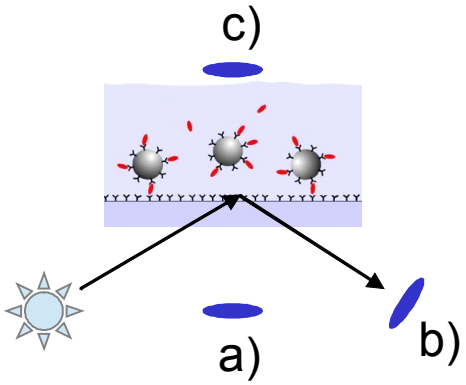


Figure 1 *Different detection techniques of a particle in the evanescent field a) dark field, b) total internal refraction method (TIRM) c) bright field.*

There are different detecting techniques schematically presented in the Figure 1. The detector can be positioned in the a) lower or c) upper half-space or b) it detects the extinction of the total internally reflected beam.

2. T-matrix method

The T-matrix method is a well known accurate method to simulate light scattering problems for scattering objects comparable with the wavelength [1, 2]. It is based on a semi-analytical solution of the Maxwell equations. In the frame of the method the electromagnetic fields are expressed in term of the Spherical Vector Wave Functions (SVWF) as follows

$$\mathbf{E}^i(\mathbf{r}) = \sum_{n=-\infty}^{\infty}\sum_{m=-n}^{n}\left\{a_{nm}\mathbf{M}_{nm}^{(1)}(k\mathbf{r}) + b_{nm}\mathbf{N}_{nm}^{(1)}(k\mathbf{r})\right\},$$

$$\mathbf{E}^s(\mathbf{r}) = \sum_{n=-\infty}^{\infty}\sum_{m=-n}^{n}\left\{p_{nm}\mathbf{M}_{nm}^{(3)}(k\mathbf{r}) + q_{nm}\mathbf{N}_{nm}^{(3)}(k\mathbf{r})\right\},$$

where a_{nm}, b_{nm} and p_{nm}, q_{nm} are the expression coefficients of the incident and scattering fields. The NFM-DS allows computing the interconnection between the coefficients in linear form using the T-matrix

$$\begin{pmatrix} p_{nm} \\ q_{nm} \end{pmatrix} = \mathbf{T}\cdot\begin{pmatrix} a_{nm} \\ b_{nm} \end{pmatrix}.$$

The method was originally suggested for single dielectric particles of arbitrary shape [3]. Nowadays it is extended to more complex cases like anisotropic material, clusters of particles, Gaussian beam or electron beam excitation and particles on or near a plane surface [2, 4]. Analytically including the particle-surface interaction into the T-matrix method leads to the following equation [2]

$$\begin{pmatrix} p_{nm} \\ q_{nm} \end{pmatrix} = \mathbf{T}\cdot\left\{\begin{pmatrix} a_{nm} \\ b_{nm} \end{pmatrix} + \begin{pmatrix} a_{nm}^R \\ b_{nm}^R \end{pmatrix} + \mathbf{R}\cdot\begin{pmatrix} p_{nm} \\ q_{nm} \end{pmatrix}\right\},$$

where p_{nm}, q_{nm} are the expansion coefficients of the scattering field in the upper half-space, $\mathbf{R}$ is the reflection matrix describing the linear transformation of the expansion coefficients by the reflection. The computation of the matrix $\mathbf{R}$ is based on the representation of the outgoing SVWF as an integral over plane waves and applying the Fresnel coefficients to each plane wave. To compute the scattering field in the lower half-space we use the transition matrix $\mathbf{R}'$

$$\begin{pmatrix} p_{nm}^T \\ q_{nm}^T \end{pmatrix} = \mathbf{R}' \cdot \begin{pmatrix} p_{nm} \\ q_{nm} \end{pmatrix},$$

where the matrix $\mathbf{R}'$ is computed in the similar way like $\mathbf{R}$.

Computation of the extinction cross-section C_{ext} for the particle illuminated by the evanescent wave differs slightly from the well known formula for the free space case [1]. Following the derivation by the referred book for the electromagnetic fields in the lower half-space the extinction cross-section can be computed as follows

$$C_{ext} = \frac{4\pi}{k_{sub}} \frac{\mathrm{Im}\left(E^{TR} \cdot E^{R}\right)}{|E_0|^2},$$

where E^R stands for the total internally refracted field, E^{TR} stands for the scattered light transmitted through the surface boundary in the direction of the E^R, k_{sub} is the refractive index of the substrate.

3. Numerical results

Differential Scattering Cross-Section (DSCS)

In order to validate the derived equations we compared the numerical results using the Discrete Source Method (DSM) [5].

In Figure 2 the scattering diagrams for the spherical particle on the plane surface are presented. The particle of diameter 600nm is placed near the surface with a particle-surface distance of 100nm and it is illuminated by the evanescent field. The refractive index of the particles is 1.5 and that of the ambient medium is 1.33. The evanescent wave is produced by a plane wave of wavelength 628.5 nm traveling in the substrate at an incident angle of 45 degree. The refractive index of the substrate is 1.5. The comparison of the scattering diagrams obtained by the T-matrix code and the DSM shows very good agreement for both polarizations.

Extinction Cross-Section

In Figure 3 the spectral extinction cross section of an spherical Ag particle on a plane surface is presented. The particle of diameter 200nm is illuminated by an evanescent field. The refractive index of the substrate is 1.5. The evanescent wave is produced by a plane wave of wavelength 628.5 nm traveling in the substrate at an incident angle of 70 degree. Three different approaches are compared a) illumination by a plane wave, b) solution by Quinten [6] (homogenous evanescent field incident on the particle) and c) exact solution using NFM-DS.

One can see that for larger wavelengths if the particle lies deeply inside the penetration depth there are no differences between the three approaches. Even illumination by a plane wave gives a good estimate of the signal. The smaller the wavelength, the smaller penetration depth. In this case, the evanescent field inside the particle region becomes strongly decaying and approximation by Quinten disagrees with the NFM-DS simulation.

4. Acknowledgement

This work was conducted in the framework of the project NextDx, funded within the European Commission FP7 program.

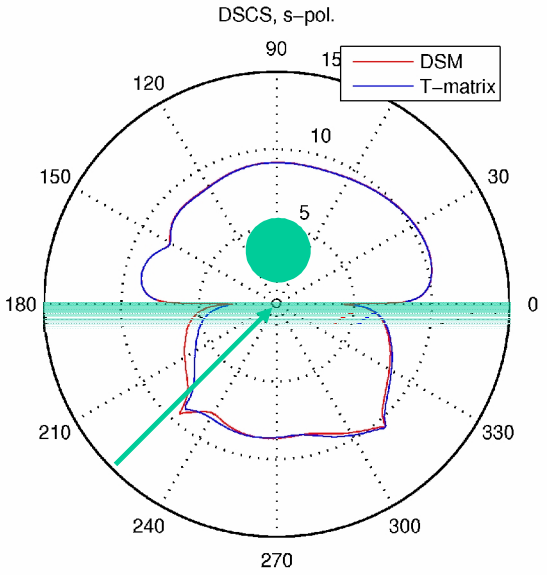


Figure 2 *Comparison of the differential scattering cross-sections for a spherical particle near the surface using the NFM-DS and the DSM method.*

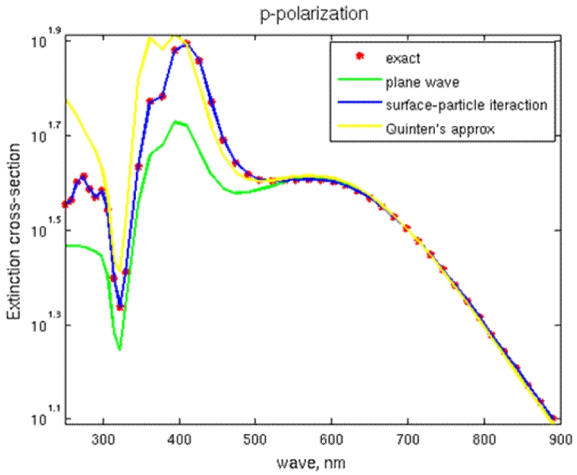


Figure 3 *Comparison of the extinction cross-sections for the spherical particle on the surface computed using different approaches.*

5. References

[1] M. Mishchenko, J. Hovenier, L. Travis, Light scattering by nonspherical particles. Theory, measurement and applications (Academic Press, 2000).

[2] A. Doicu, T. Wriedt, Y.A. Eremin, Light Scattering by Systems of Particles (Springer, 2006).

[3] P.C. Waterman, Matrix formulation of electromagnetic scattering, Proc IEEE 53:805–12 (1965).

[4] A. Doicu, Y.A. Eremin, T. Wriedt, Acoustic and electromagnetic scattering analysis using discrete sources (Academic Press, 2000).

[5] Y.A. Eremin, N.V. Orlov, A.G. Sveshnikov, Models of electromagnetic scattering problems based on discrete sources method. In: Wriedt T, editor. Generalized multipole techniques for electromagnetic and light scattering (Elsevier, Amsterdam, 1999).

[6] M. Quinten, A. Pack, R. Wannemacher, Scattering and extinction of evanescent waves by small particles, Applied Physics B 68:87-92 (1999)

Coupling T-Matrix Formalism with UV-VIS Polarization Laser *Lidar* to Retrieve Atmospheric Particles Backscattering From Desert Dust, Sea-Salt and Water Soluble Particles Mixture

Alain MIFFRE [1,*], Gregory DAVID [1-2], Elodie COILLET[1], and Patrick RAIROUX[1]

[1] Institute of Light and Matter, University Lyon, Lyon1, CNRS, Villeurbanne, 69622, France
[2] Laboratory of Physical Chemistry, Swiss Federal Institute of Technology ETHZ, Zurich, 8093, Switzerland

Corresponding author: alain.miffre@univ-lyon1.fr

Abstract

In this contribution, the polarization and spectral properties of atmospheric nonspherical particles, such as sub-micrometer desert dust or sea-salt particles, are addressed with UV-VIS polarization lidar backscattering field measurements. We show that three-component particles external mixtures can be partitioned into their nonspherical components, by numerically simulating the backscattering and depolarization properties of desert dust and sea-salt particles, using T-matrix numerical code. This combined methodology is new, as opposed to the traditional approach using lidar and T-matrix separately. It may be useful for radiative forcing assessment.

1 Introduction

Backscattering and extinction of laser light by atmospheric particles are the two physical processes in lidar remote sensing. The most frequently observed situation is relative to long-range transport by advection from a source region to a place where intrusion episodes occur. In this case, particles are highly dispersed and aged, and their size and their shape may be different from those observed in the source region. Hence, a complex vertical layering is generally observed at remote sites, in the form of two/three component particle mixtures. The case of two-component particles mixture has already been published in the literature by applying the scattering matrix formalism [1]. Here, we address the case of a three-component particle mixtures, as encountered during Saharan dust outbreaks, where desert dust (dd) particles mix with sea-salt (ss) particles and water-soluble (ws) species. We here develop a new methodology to retrieve range-resolved backscattering profiles, specific to each particles component in such a particles mixture (p) = {dd, ss, ws}. For this, a 2λ-polarization lidar is operated in combination with T-matrix numerical simulations specific to each nonspherical particles component, i.e. for dust then for sea-salt particles [2]. In Section 2, we present the polarization lidar and its link with the scattering matrix formalism. Then, in Section 3, T-matrix numerical simulations are performed on dust then sea-salt particles to combine both approaches in Section 4 where our new methodology is presented and applied.

2 Polarization lidar and scattering matrix

A polarization lidar experiment is sensitive to size-averaged particle backscattering cross-sections, which define the so-called volume particles backscattering coefficient β_P (in $Mm^{-1}sr^{-1}$):

$$\beta_{p,\pi}(\lambda) = \int_{PSD} (d\sigma / d\Omega)_p n_p(r) dr \qquad (1)$$

where the integral is performed over the particles size distribution (PSD) and the polarization $\pi = \{//,\perp\}$ is defined with respect to the incident laser linear polarization, n_P representing the particles number density. The particles depolarization ratio δ_P is then defined as $\beta_{P,\perp}/\beta_{P,//}$. Using Equation (1), the link between the polarization lidar and the scattering matrix **F** can be addressed as follows [1, 3]:

$$\beta_{p,//} = (F_{11,p} + F_{22,p})/2 \qquad \beta_{p,\perp} = (F_{11,p} - F_{22,p})/2 \qquad (2)$$

where $F_{11,P}$ and $F_{22,P}$ are the two non-vanishing scattering matrix elements for randomly-oriented particles, which depend on the particles size, shape and refractive index. The Lyon UV-VIS polarization lidar remote sensing experiment has been extensively described in [4]. In a few words, this elastic backscattering lidar operates at λ_{UV} = 355 nm and λ_{VIS} = 532 nm, and its home-built detector (see Figure 1) efficiently partitions backscattered photons as a function of their polarization and wavelength.

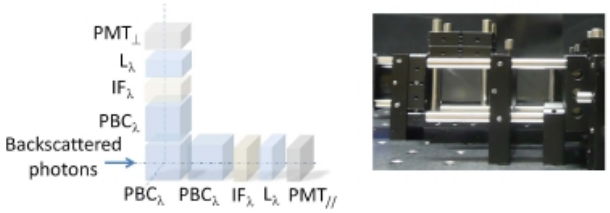


Figure 1 *Scheme of our polarization detector (PBC = polarizing beamsplitter cube, IF = Interference filter, PMT = photomultiplier tube) with picture of the cross-polarized channel.*

As specified on a dedicated test bench at our laboratory, polarization and wavelength cross-talks are fully

negligible with better than 10^{-7} accuracy, allowing a robust calibration of the particles depolarization ratio, as performed by J. Alvarez et al. [5]. Particle depolarization ratios, as low as 6×10^{-3}, close to the molecular depolarization, have been measured in the atmosphere. Then, by applying the Klett's algorithm to correct for the particles extinction, vertical profiles of $\beta_{p,//}$ and $\beta_{p,\perp}$ coefficients, then δ_p can be retrieved, as displayed in Figure 2 in the form of time-altitude maps.

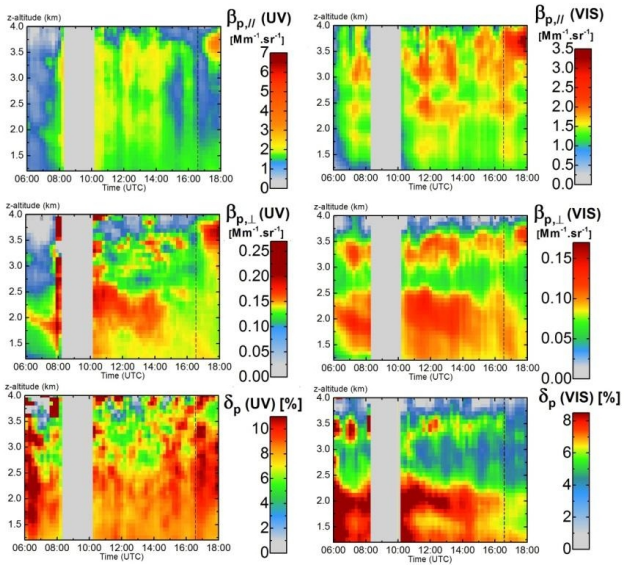


Figure 2*Time-altitude maps of particles backscattering retrieved from the Lyon polarization lidar at λ_{UV} and λ_{VIS}.*

3 T-matrix numerical simulations

In this section, numerical simulations are exploited to separate the specific contributions of each nonspherical component in the particles mixture. For desert dust particles, we applied the T-matrix numerical code [6], by mimicking the dust particles by size-shape distributions of homogeneous spheroids, assuming equal number of prolate and oblate spheroids. To account for polarization effects, aspect ratios were distributed through a power law n = 3 shape distribution [7]. Sea-salt particles, which are cubic below their crystallization point, were numerically simulated by applying an extension of the T-matrix code, developed by M. Kahnert [8] for targets with discrete symmetries such as cubes. Figure 3 presents the retrieved backscattering cross-sections (per unit volume) and depolarization as a function of the particle radius. In agreement with Equations (1) and (2), depolarization ratio δ_p, specific to dd and ss-particles, are then obtained by integration over the PSD, as given in Table 1 at λ_{UV} and λ_{VIS}. In the absence of complementary measurements, the two PSD were taken from the literature: Mallet et al. [9] for dd-particles, O'Dowd et al. [10] for ss-particles. Table 1 also contains the spectral dependence of the cross-polarized backscattering coefficient $\beta_{p,\perp}$, in the form of an Angström exponent $A_\perp$ [11].

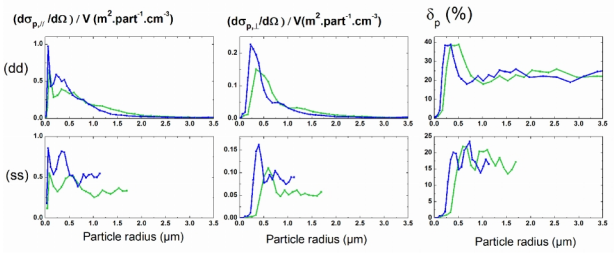


Figure 3 *Simulated backscattering cross-sections and depolarization for desert dust (dd) and sea-salt (ss) particles using T-matrix formalism at UV and VIS refractive indices.*

Particles	δ_p(UV) (%)	δ_p(VIS) (%)	$A_\perp$
Dust (dd)	18.1	13.8	1.326
Sea-salt (ss)	15.9	16.2	− 0.478

Table 1 *Output of our T-matrix numerical simulation.*

4 Backscattering in a three-component mixture

In this section, by combining the Sections 2 and 3 outputs, we propose a new methodology for nonspherical particles backscattering retrievals in a three-component particles mixture. As a case study, we consider the above external mixture (p) = {dd, ss, ws}.

4.1 Methodology : coupling lidar with T-matrix

In the presence of three particles populations, twelve unknowns have to be determined, namely $\beta_{p,\pi}(\lambda)$, with (p) = {dd, ss, ws}, π = {//,⊥} and λ = {λ_{UV}, λ_{VIS}}. Application of the superposition principle then allows to retrieve vertical profiles of $\beta_{dd}(\lambda)$, $\beta_{ss}(\lambda)$ and $\beta_{ws}(\lambda)$. Four equations can be derived from the lidar measurements at λ_{UV} and λ_{VIS}. In addition, assuming δ_{ws} = 0 at both wavelengths give two more equations, the remaining six quantities being given by the T-matrix numerical simulation output, as obtained in Table 1. Hence, the system of 12 equations can be solved to retrieve $\beta_{p,\pi}(\lambda)$ at both wavelengths and for both polarization, leading to $\beta_{dd}(\lambda)$, $\beta_{ss}(\lambda)$ and $\beta_{ws}(\lambda)$ retrievals.

4.2 Application to the mixing of dust with sea-salt and water soluble particles

We applied our {polarization lidar, T-matrix}-algorithm to the mixing of dust with sea-salt particles observed in Figure 2. As a stand-alone lidar does not provide chemistry, the possible presence of dust, sea-salt and water-soluble particles at the remote site was checked with air mass back-trajectories, while the relative humidity remained below 40 %, allowing ss-particles to be cubic. Hence, our algorithm provides separate backscattering profiles, once the chemistry is known. Figure 4 displays the retrieved vertical profiles of desert dust, sea-salt and

water-soluble particles at λ_{UV} and λ_{VIS}. For the first time, the nonsphericity of two components is taken into account in a three-component particles mixture. To test the robustness of this methodology, we affected error bars on the coefficients retrieved in Table 1. For dust particles, the model variability (± 10 % on the particles radius, equi-probable shape distribution) induces a 4 %-variability on $\beta_{P,\perp}$ (20 % on $\beta_{P,//}$). For sea-salt particles, error bars were below 10 %. Moreover, the $A_\perp$-coefficients were used as convergence criteria of our algorithm (negative backscattering were obtained for different $A_\perp$-values). It underlines the robustness of our methodology, as well as the need for a precise knowledge of the PSD's. We hence reveal in Figure 4 the complex vertical layering observed at Lyon. The β_{dd} and β_{ss} vertical profiles are not complementary, due to the presence of ws-particles.

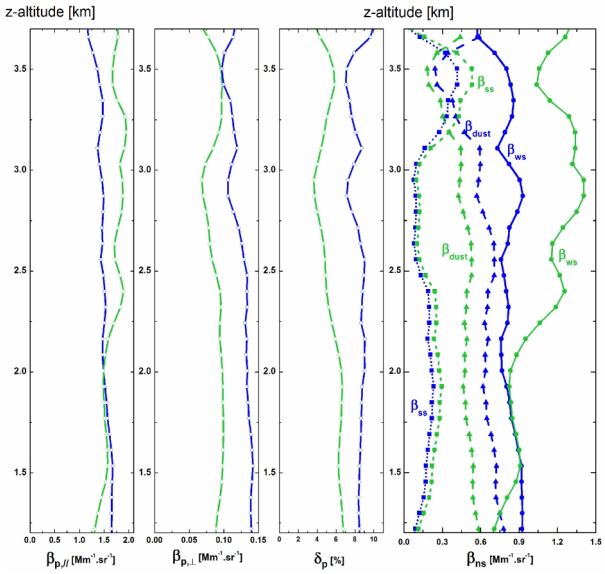


Figure 4 *Backscattering vertical profiles in the particles mixture at 16h15 UTC, then backscattering profiles specific to desert dust, sea-salt and water soluble particles at λ_{UV} and λ_{VIS}.*

5 Conclusion

As a conclusion, we have shown that polarization lidar, based on laser backscattering and extinction in the atmosphere, when used in combination with T-matrix numerical code, is a very powerful tool for providing information on the backscattering property of externally-mixed aerosols, having up to three components. To our knowledge, it is the first time that such a partitioning is achieved by considering the nonsphericity of each nonspherical component (i.e., both sea-salt and desert dust particles nonsphericity), while assuming particles as spherical may lead to quite considerable errors in radiative forcing assessment [12]. The poster will detail the inversion algorithm and the most recent advances in this field, where recent laboratory experiments now provide measurements of the particles depolarization [13].

6 Acknowledgments

The authors thank Région Rhône-Alpes and CNRS for partly funding this work.

7 References

[1] Miffre A., David G., Thomas B. and Rairoux P., Atmospheric non-spherical particles optical properties from UV-polarization lidar and scattering matrix, Geophys. Res. Lett., 38, L16804 (2011).

[2] David D., Thomas B., Nousiainen T., Miffre A., and Rairoux P., Retrieving volcanic, desert dust, and sea-salt particle properties from two/three-component particle mixtures using UV-VIS polarization Lidar and T-Matrix, Atmos. Chem. Phys., 13: 6757-6776, (2013).

[3] Mishchenko M.I., Travis L.D., and Lacis A.A., *Scattering, Absorption and Emission of Light by Small Particles* (Cambridge University Press, NASA, 2002).

[4] David G., Miffre A., Thomas B. and Rairoux P., Sensitive and accurate dual-wavelength UV-VIS polarization detector for optical remote sensing of tropospheric aerosols, Appl. Phys. B, 108:197–216 (2012).

[5] Alvarez J.M., Vaughan M. A., Hostelier C. A., Hunt W. H. and Winker D. M., Calibration technique for polarization-sensitive Lidars, J. Atm. Ocean. Tech., 23: 683-699 (2006).

[6] Mishchenko M.I. and Travis L.D.: Capabilities and limitations of a current Fortran implementation of the T-matrix method for randomly oriented rotationally symmetric scatterers, J. Quant. Spectrosc. Radiat. Transf., 60:309-324 (1998) .

[7] Merikallio S., Lindqvist H., Nousiainen T., and Kahnert M., Modelling light scattering by 1 mineral dust using spheroids: assessment of applicability, Atmos. Chem. Phys., 11:5347– 5363 (2011)

[8] Kahnert, M., The T-matrix code Tsym for homogeneous dielectric particles with finite symmetries, J. Quant. Spec. Rad. Transf., 123:62-72 (2013).

[9] Mallet M., Roger J. C., Despiau S., Putaud J. P. and Dubovik, O., A study of the mixing state of black carbon in urban zone, J. Geophys. Res, 109, D04202 (2004).

[10] O'Dowd C., Smith M.H., Consterdine I. E., and Lowe J. A., Marine aerosol, sea salt, and the marine sulfur cycle: a short review, Atm. Env., 31:73-80 (1997).

[11] Sasano Y., and Browell E.V., Light scattering characteristic of various aerosol types derived from multiple wavelength lidar observations, Appl. Opt., 28:1670-1679 (1989).

[12] Kahnert M., Nousiainen T., Räisänen P., Mie simulations as an error source in mineral aerosol radiative forcing calculations, QJR Meteorol. Soc. 307:133:299 (2007).

[13] David G., Thomas B., Coillet E., Miffre A. and Rairoux P., Polarization-resolved exact light backscattering by an ensemble of particles in air, Optics Express, 21(16):18624-28639 (2013).

Analytical solutions of plane wave scattering from a large sized chiral cylinder

Qing-Chao SHANG [1], Zhen-Sen WU [1,*], Tan QU [1], Zheng-Jun LI [1], and Lei GONG [2]

[1] School of Physics Optoelectronic Engineering, Xidian University, Xi'an, 710071, China
[2] Xi'an Technological University, Xi'an, 710021, China

*Corresponding author: wuzhs@mail.xidian.edu.cn; chaoxidian@foxmail.com

Abstract

Light scattering from a large sized chiral cylinder is resolved based on the Mie regime, in a similar way with the scattering problem of chiral spheres. The incident, internal, and scattered fields are expressed in terms of cylindrical vector wave functions. The scattering coefficients are obtained in forms of logarithmic derivatives of cylindrical Bessel functions according to the boundary conditions. Numerical results show that rainbow phenomenon similar to that of a chiral sphere also occurs for a large sized chiral cylinder.

1 Introduction

In recent years chiral media have caused great interests to researchers in both microwave region and optics. Light interaction with chiral particles is an important aspect of research on chiral media. Scattering problems of a chiral sphere [1] and a chiral cylinder [2] were solved by Bohren in 1970s. Since then, many problems in this area have been studied, including light scattering from a chiral sphere in chiral background media [3], scattering from a chiral spheroid [4, 5], and scattering from a stratified chiral sphere [6, 7]. Results of scattering from large sized chiral spheres show a special rainbow phenomenon for chiral sphere [8]. We resolve scattering by a chiral cylinder and calculate numerical results of the scattering width.

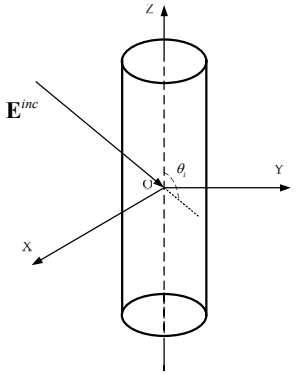


Figure 1 *Plane wave impinging on a chiral cylinder.*

2 Theory

Figure 1 presents a diagram of the problem that a plane wave impinges on an infinite circular chiral cylinder. The procedure is almost identical to that presented in [9], except that for chiral the expansion of internal fields is

$$\mathbf{E}=\sum_{n=1}^{\infty}\left[\begin{array}{l}A_n\mathbf{M}_n^{(1)}(\mathbf{r},k_1)+A_n\mathbf{N}_n^{(1)}(\mathbf{r},k_1)\\+B_n\mathbf{M}_n^{(1)}(\mathbf{r},k_2)-B_n\mathbf{N}_n^{(1)}(\mathbf{r},k_2)\end{array}\right], \tag{1}$$

$$\mathbf{H}=Q\sum_{n=1}^{\infty}\left[\begin{array}{l}A_n\mathbf{N}_n^{(1)}(\mathbf{r},k_1)+A_n\mathbf{M}_n^{(1)}(\mathbf{r},k_1)\\+B_n\mathbf{N}_n^{(1)}(\mathbf{r},k_2)-B_n\mathbf{M}_n^{(1)}(\mathbf{r},k_2)\end{array}\right], \tag{2}$$

where A_n and B_n are expansion coefficients of internal field; $\mathbf{M}_n^{(1)}(\mathbf{r},k_1)$ and $\mathbf{N}_n^{(1)}(\mathbf{r},k_2)$ are the cylindrical vector wave functions. And in the final expressions of the scattering coefficients, functions are written as in forms of logarithmic derivatives and ratios of cylindrical Bessel functions, all of which can be calculated conveniently by their recurrence relations.

3 Results

Figure 2 presents the angular distributions of scattering widths for a chiral cylinder illuminated by a normal plane wave incidence. It can be seen that three first order rainbow structures occurs for a chiral cylinder, similar to that of a chiral sphere.

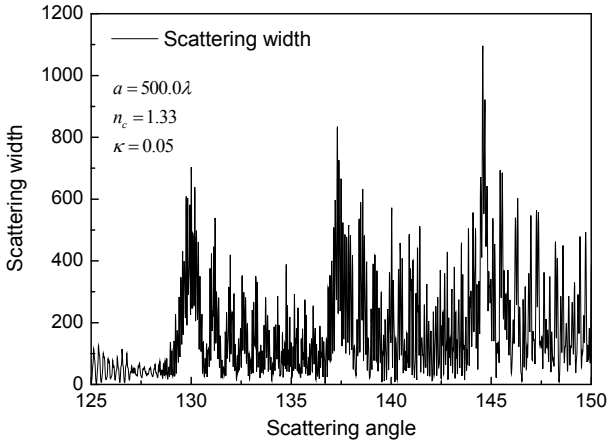


Figure 2 *Angular distributions of scattering widths for a chiral cylinder.*

4 Acknowledgement

This work was supported by the National Natural Science Foundation of China under grants 61172031, 61308025 and 61108071 and the Fundamental Research Funds for the Central Universities.

5 References

[1] F. Bohren, "Light scattering by an optically active sphere," *Chem. Phys. Lett.*, vol. 29, pp. 458-462, 1974.

[2] C. F. Bohren, "Scattering of electromagnetic waves by an optically active cylinder," *J. Colloid Interface Sci.*, vol. 66, pp. 105-109, 1978.

[3] M. Hinders and B. Rhodes, "Electromagnetic-wave scattering from chiral spheres in chiral media," *Il Nuovo Cimento D*, vol. 14, pp. 575-583, 1992.

[4] M. F. R. Cooray and I. R. Ciric, "Wave scattering by a chiral spheroid," *J. Opt. Soc. Am. A*, vol. 10, pp. 1197-1203, 1993.

[5] A. Lakhtakia, *et al.*, "Scattering and absorption characteristics of lossy dielectric, chiral, nonspherical objects," *Appl. Opt.*, vol. 24, pp. 4146-4154, 1985.

[6] D. L. Jaggard and J. C. Liu, "The matrix Riccati equation for scattering from stratified chiral spheres," *IEEE Trans. Antennas Propag.*, vol. 47, pp. 1201-1207, 1999.

[7] L. Li, *et al.*, "Electromagnetic scattering by an inhomogeneous chiral sphere of varying permittivity: A discrete analysis using multilayered model," *Progress In Electromagnetics Research*, vol. 13, pp. 1203-1206, 1999.

[8] Q.-C. Shang, *et al.*, "Analysis of rainbow scattering by a chiral sphere," *Opt. Express*, vol. 21, pp. 21879-21888, 2013.

[9] C. F. Bohren and D. R. Huffman, *Absorption and scattering of light by small particles*: Wiley, 1998.

An analytic solution for the Gaussian beam scattering from a moving uniaxial anisotropic sphere

Mingjun WANG[1,2*], Huayong ZHANG[3], Xizheng KE [2], Pengfei WU[2]

[1] School of Physics and Electronic Engineering, Xian Yang Normal College, Xian yang, Shaanxi, 712000, China
[2] School of Automation and Information Engineering, Xi'an University of Technology, Xian Shaanxi, 710048, China
[3] School of Electronic science and technology, Anhui university, Hefei, Anhui, 230039, China
*Corresponding author: wmjxd@aliyun.com

Abstract

The interaction between electromagnetic waves and uniaxial anisotropic materials has been studied over the years, and one interesting phenomenon is reported to cloak an object with rotationally symmetric anisotropic media whose axial permittivity and permeability parameters tend to zero. Based on the generalized Lorenz-Mie theory (GLMT), which is effective in describing the electromagnetic scattering of a shaped beam by a homogeneous isotropic sphere, An analytic solution to Gaussian beam scattering by a rotationally uniaxial anisotropic sphere is presented in this paper. The scattered fields as well as the fields within the anisotropic sphere are expanded in terms of infinite series with spherical vector wave functions by using an appropriate expansion of the incident Gaussian beam. The unknown expansion coefficients are determined from a system of linear equations derived from the boundary conditions. And according to the Lorentz transformations, we will be combined with the Scattering Fields to discuss the properties of a high-speed uniaxial anisotropic sphere. Numerical results of their scattering Fields and normalized differential scattering cross section are shown, and the scattering characteristics are discussed concisely.

1. The relations between moving system moving alone z axis relative to the static system and a Gaussian beam scattering from a uniaxial anisotropic sphere

As shown in Fig.1, observer Σ' moves with the velocity $\vec{v}$ relative to observer Σ. In Σ', A Gaussian beam propagates in free space and from the negative z'' to the positive z'' axis of the Cartesian coordinate systems $O''x''y''z''$, with the middle of its beam waist located at origin O''. The system $O'x'y'z'$ is parallel to $O''x''y''z''$. The center of a rotationally uniaxial anisotropic sphere is located at origin O' and has the Cartesian coordinates (x_0'', y_0'', z_0'') in $O''x''y''z''$.

2. Expansions of Gaussian beam and scattered fields in spherical coordinates in system Σ'

a).The electromagnetic fields of the incident Gaussian beam

Within the GLMT framework, the electromagnetic fields of the incident Gaussian beam, for the TM mode, can be expanded in terms of the spherical vector wave functions with respect to the system $O'x'y'z'$, as follows

$$\mathbf{E}'^{i} = E_0 \sum_{n=1}^{\infty} \sum_{m=-n}^{n} C_{nm} \left[i g_{n,TE}^{m} \mathbf{m}_{mn}^{r(1)}(kr) + g_{n,TM}^{m} \mathbf{n}_{mn}^{r(1)}(kr) \right] \quad (1)$$

$$\mathbf{H}'^{i} = \frac{E_0}{\eta_0} \sum_{n=1}^{\infty} \sum_{m=-n}^{n} C_{nm} \left[g_{n,TE}^{m} \mathbf{n}_{mn}^{r(1)}(kr) - i g_{n,TM}^{m} \mathbf{m}_{mn}^{r(1)}(kr) \right] \quad (2)$$

Where $\eta_0 = \sqrt{\mu_0/\varepsilon_0}$ is the free-space wave impedance, and C_{nm} the normalization factors for the index m.

For the TE mode, the corresponding expansions of the Gaussian beam can be obtained by replacing $g_{n,TE}^{m}$ in Eqs.(1), (2) by $-g_{n,TM}^{m}$, and $g_{n,TM}^{m}$ by $g_{n,TE}^{m}$.

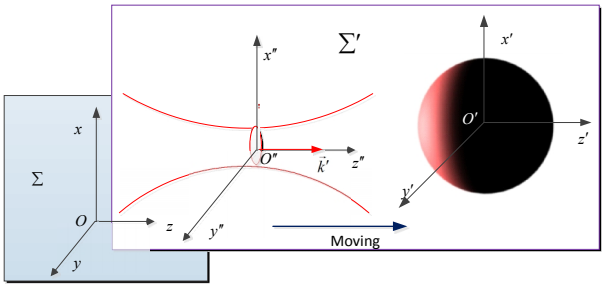


Figure 1 *The relations between moving system Σ' where observer lies in the and the static system Σ and a Gaussian beam scattering from a uniaxial anisotropic sphere in system Σ'*

The scattered fields can be expanded accordingly, as follows

$$\mathbf{E}'^{s} = E_0 \sum_{n=1}^{\infty} \sum_{m=-n}^{n} \left[i a_{mn} \mathbf{m}_{mn}^{r(3)}(kr) + b_{mn} \mathbf{n}_{mn}^{r(3)}(kr) \right] \quad (3)$$

$$\mathbf{H}'^{s} = \frac{E_0}{\eta_0} \sum_{n=1}^{\infty} \sum_{m=-n}^{n} \left[a_{mn} \mathbf{n}_{mn}^{r(3)}(kr) - i b_{mn} \mathbf{m}_{mn}^{r(3)}(kr) \right] \quad (4)$$

where a_{mn} and b_{mn} are the unknown expansion coefficients to be determined.

Description of electromagnetic fields within a rotationally uniaxial anisotropic sphere in Σ'

a rotationally uniaxial anisotropic medium, source-free Maxwell equations are written as

$$\nabla \times \mathbf{E}' = i\omega \mathbf{B}' \tag{5}$$

$$\nabla \times \mathbf{H}' = -i\omega \mathbf{D}' \tag{6}$$

and the constitutive relations for the medium as

$$\mathbf{D}' = \bar{\bar{\varepsilon}} \cdot \mathbf{E}' \tag{7}$$

$$\mathbf{B}' = \bar{\bar{\mu}} \cdot \mathbf{H}' \tag{8}$$

where the permittivity and permeability tensors $\bar{\bar{\varepsilon}}$ and $\bar{\bar{\mu}}$ are characterized by

$$\bar{\bar{\varepsilon}} = (\varepsilon_r \hat{r}\hat{r} + \varepsilon_t \hat{\theta}\hat{\theta} + \varepsilon_t \hat{\varphi}\hat{\varphi}) \tag{9}$$

$$\bar{\bar{\mu}} = (\mu_r \hat{r}\hat{r} + \mu_t \hat{\theta}\hat{\theta} + \mu_t \hat{\varphi}\hat{\varphi}) \tag{10}$$

The electromagnetic fields in the uniaxial anisotropic medium can be decomposed into the TE and TM modes (with respect to $\hat{r}$), by introducing the scalar potentials Φ_{TE} and Φ_{TM}.

$$\mathbf{D}' = -\nabla \times (\hat{r}\Phi_{TE}) \tag{11}$$

$$\mathbf{B}' = \nabla \times (\hat{r}\Phi_{TM}) \tag{12}$$

By combining Eqs.(5)-(10) and Eq.(11), after some algebraic manipulations we can have

$$\omega^2 \nabla\Phi_{TE} \times \hat{r} = \nabla \times \{\bar{\bar{\mu}}^{-1} \cdot \nabla \times [\bar{\bar{\varepsilon}}^{-1} \cdot (\nabla\Phi_{TE} \times \hat{r})]\} \tag{13}$$

the spherical vector wave functions are defined by

$$\begin{bmatrix} \mathbf{m}_{mv_{TM}(n)}(k_t r,\theta,\varphi) \\ \mathbf{m}_{mv_{TE}(n)}(k_t r,\theta,\varphi) \end{bmatrix} = \nabla \times \begin{bmatrix} \hat{r}\Phi_{TM} \\ \hat{r}\Phi_{TE} \end{bmatrix} \tag{14}$$

$$\begin{bmatrix} \mathbf{n}_{mv_{TM}(n)}(k_t r,\theta,\varphi) \\ \mathbf{n}_{mv_{TE}(n)}(k_t r,\theta,\varphi) \end{bmatrix} = \frac{1}{k_t} \nabla \times \begin{bmatrix} \mathbf{m}_{mv_{TM}(n)}(k_t r,\theta,\varphi) \\ \mathbf{m}_{mv_{TE}(n)}(k_t r,\theta,\varphi) \end{bmatrix} \tag{15}$$

The electromagnetic fields within the anisotropic sphere can be expanded in terms of Eqs.(14), (15), as follows

$$\mathbf{E}'^{w} = E_0 \sum_{n=1}^{\infty} \sum_{m=-n}^{n} \left[c_{mn} \frac{k_t}{\omega} \bar{\bar{\varepsilon}}^{-1} \cdot \mathbf{n}_{mv_{TM}(n)}(k_t r,\theta,\phi) + i d_{mn} \mathbf{m}_{mv_{TE}(n)}(k_t r,\theta,\phi) \right] \tag{16}$$

$$\mathbf{H}'^{w} = E_0 \sum_{n=1}^{\infty} \sum_{m=-n}^{n} \left[d_{mn} \frac{k_t}{\omega} \bar{\bar{\mu}}^{-1} \cdot \mathbf{n}_{mv_{TE}(n)}(k_t r,\theta,\phi) - i c_{mn} \mathbf{m}_{mv_{TM}(n)}(k_t r,\theta,\phi) \right] \tag{17}$$

Gaussian beam scattering by an anisotropic sphere and Its boundary condition

The unknown expansion coefficients a_{mn} and b_{mn} in Eqs.(3), (4) as well as c_{mn} and d_{mn} in Eqs.(16), (17) can be determined by applying the boundary conditions over the sphere surface

$$\left.\begin{aligned} E_\theta'^{i} + E_\theta'^{s} = E_\theta'^{w}, \quad E_\phi'^{i} + E_\phi'^{s} = E_\phi'^{w} \\ H_\theta'^{i} + H_\theta'^{s} = H_\theta'^{w}, \quad H_\phi'^{i} + H_\phi'^{s} = H_\phi'^{w} \end{aligned}\right\} \quad at \quad r = r_1' \tag{18}$$

where $r = r_1'$ is the radius of the anisotropic sphere.

Eq.(18) can be explicitly written as

$$C_{nm} g_{n,TE}^{m} j_n(kr_1') + a_{mn} h_n^{(1)}(kr_1') = d_{mn} j_{v_{TE}(n)}(k_t r_1') \tag{19}$$

$$C_{nm} g_{n,TM}^{m} \frac{1}{kr_1'} \frac{d}{d(kr_1')}[kr_1' j_n(kr_1')] + b_{mn} \frac{1}{kr_1'} \frac{d}{d(kr_1')}[kr_1 h_n^{(1)}(kr_1')] = c_{mn} \eta_t \frac{1}{k_t r_1'} \frac{d}{d(k_t r_1')}[k_t r_1' j_{v_{TM}(n)}(k_t r_1')] \tag{20}$$

$$C_{nm} g_{n,TE}^{m} \frac{1}{kr_1'} \frac{d}{d(kr_1')}[kr_1' j_n(kr_1')] + a_{mn} \frac{1}{kr_1'} \frac{d}{d(kr_1')}[kr_1' h_n^{(1)}(kr_1')] = d_{mn} \frac{\eta_0}{\eta_t} \frac{1}{k_t r_1'} \frac{d}{d(k_t r_1')}[k_t r_1' j_{v_{TE}(n)}(k_t r_1')] \tag{21}$$

$$C_{nm} g_{n,TM}^{m} j_n(kr_1') + b_{mn} h_n^{(1)}(kr_1') = \eta_0 c_{mn} j_{v_{TM}(n)}(k_t r_1') \tag{22}$$

where $\eta_t = \sqrt{\mu_t / \varepsilon_t}$.

3. Lorentz transformations and the fields of Gaussian beam scattering by an anisotropic sphere in system Σ

In static system Σ, the general representations for the four-dimensional vectors may be written as follows

$$a_{\mu\nu} = \begin{bmatrix} 1 & 0 & 0 & 0 \\ 0 & 1 & 0 & 0 \\ 0 & 0 & \gamma & i\beta\gamma \\ 0 & 0 & -i\beta\gamma & \gamma \end{bmatrix} \tag{23}$$

where $\gamma = \left(1-\beta^2\right)^{-1/2}, \beta = v/c$, $x_\mu = (r, ict)$, c is the speed of light in free space and r is the distance from the origin of the coordinates system to the observing point. The relations of the four-dimensional wave vectors are obtained as:

$$k_x' = k_x, k_y' = k_y, k_z' = \gamma(k_z - \frac{v}{c^2}\omega), \quad \omega' = \gamma\left(\omega - v k_z\right) \tag{24}$$

The electromagnetic fields make up two-step tensors in the four-dimensional space. The relations of the tensors can be written as

$$F'_{\mu\nu} = a_{\mu\lambda} a_{\nu\tau} F_{\lambda\tau} \tag{25}$$

where

$$F_{\mu\nu} = \begin{bmatrix} 0 & B_z & -B_y & -\frac{i}{c}E_x \\ -B_z & 0 & B_x & -\frac{i}{c}E_y \\ B_y & -B_x & 0 & -\frac{i}{c}E_z \\ \frac{i}{c}E_x & \frac{i}{c}E_y & \frac{i}{c}E_z & 0 \end{bmatrix} \tag{26}$$

Then the scattering field $\vec{E}_s$ in the system Σ and $\vec{E}'_s$ in the system Σ' are related by

$$E'_x = \gamma\left(E_x - vB_y\right), E'_y = \gamma\left(E_y + vB_x\right),$$
$$E'_z = E_z, B'_x = \gamma\left(B_x + \frac{v}{c^2}E_y\right), \quad (27)$$
$$B'_y = \gamma\left(B_y - \frac{v}{c^2}E_x\right), B'_z = B_z$$

Electromagnetic fields can be written as a Matrix form

$$\begin{bmatrix} E_x \\ E_y \\ E_z \end{bmatrix} = \begin{bmatrix} \gamma & 0 & 0 \\ 0 & \gamma & 0 \\ 0 & 0 & 1 \end{bmatrix}\begin{bmatrix} E'_x \\ E'_y \\ E'_z \end{bmatrix} + \begin{bmatrix} 0 & \gamma v & 0 \\ -\gamma v & 0 & 0 \\ 0 & 0 & 0 \end{bmatrix}\begin{bmatrix} B'_x \\ B'_y \\ B'_z \end{bmatrix}$$

The vector fields are related by from the above Matrix form:

$$\mathbf{E} = \mathbf{T}_1\mathbf{E}' + \mathbf{T}_2\mathbf{B}' \quad (28)$$

If the relation of vector fields between the spherical and rectangle coordinates system are as following

$$\mathbf{E} = \mathbf{P}\mathbf{E}_s, \mathbf{B} = \mathbf{P}\mathbf{B}_s \quad (29)$$

Put (29) in (27), we have

$$\mathbf{E}_s = \left(\mathbf{P}^{-1}\mathbf{T}_1\mathbf{P}'\right)\mathbf{E}'_s + \left(\mathbf{P}^{-1}\mathbf{T}_2\mathbf{P}'\right)\mathbf{B}'_s = \mathbf{M}\mathbf{E}'_s + \mathbf{N}\mathbf{B}'_s \quad (30)$$

The elements of Matrix M can be written as

$$m_{11} = \gamma\sin\theta\sin\theta' + \cos\theta\cos\theta',$$
$$m_{12} = \gamma\sin\theta\cos\theta' - \cos\theta\sin\theta',$$
$$m_{21} = \gamma\cos\theta\sin\theta' - \sin\theta\cos\theta', \quad (31)$$
$$m_{22} = \gamma\cos\theta\cos\theta' + \sin\theta\sin\theta',$$
$$m_{13} = 0, m_{23} = 0, m_{31} = 0, m_{32} = 0, m_{33} = \gamma$$

The elements of Matrix N can be written as

$$n_{11} = 0, n_{12} = 0, n_{21} = 0, n_{22} = 0$$
$$n_{13} = \gamma v\left(\cos\theta\cos\phi - \sin\theta\sin\phi\right), \quad (32)$$
$$n_{23} = \gamma v\cos\theta, n_{31} = -\gamma v\sin\theta',$$
$$n_{32} = -\gamma v\cos\theta', n_{33} = 0$$

Using (32)and(31)in（30）,we have the electric fields in system Σ

$$E_{\theta s} = m_{22}E'_{\theta' s} + m_{23}E'_{\varphi' s} + n_{22}B'_{\theta' s} + n_{23}B'_{\varphi' s}$$
$$E_{\varphi s} = m_{32}E'_{\theta' s} + m_{33}E'_{\varphi' s} + n_{32}B'_{\theta' s} + n_{33}B'_{\varphi' s} \quad (33)$$

According to (3),(4),(19)-(22)and(33),we can obtain an analytic solution for the Gaussian beam scattering from a moving uniaxial anisotropic sphere. Some numerical results of their normalized differential scattering fields and cross section will be shown, and the scattering characteristics will be discussed in detail.

4. Conclusion

Within the generalized Lorenz-Mie theory framework, an analytic solution to Gaussian beam scattering by a rotationally uniaxial anisotropic sphere is presented. The scattered fields as well as the fields within the anisotropic sphere are expanded in terms of infinite series with spherical vector wave functions by using an appropriate expansion of the incident Gaussian beam. The unknown expansion coefficients are determined from a system of linear equations derived from the boundary conditions. And according to the Lorentz transformations, we will be combined with Scattering Fields to discuss the properties of a high-speed uniaxial anisotropic sphere. Numerical results of their scattering fields and normalized differential cross section are shown, and the scattering characteristics are discussed concisely.

5. Acknowledgements

This works is partly supported by the National Natural Science Foundation of China (Grant No. 61271110, 60977054), New Scientific and Technological Star of Shaanxi Province funded project (Grant No. 2011KJXX39) and the Natural Science Foundation of Shaanxi Province education office, China (Grant No. 12Jk0955).

6. References

[1] G. Gouesbet, "Generalized Lorenz-Mie theories, the third decade: A perspective," Journal of Quantitative Spectroscopy and Radiative Transfer 110, 1223-1238 (2009).

[2] Mingjun Wang, Zhensen Wu, Yingle Li,Influnce of high-speed dielectric spherical particles movement on its scattering characteristics. Chinese Optics Letter. 5(4)：245-248(2007).

[3] Zheng-Jun Li, Zhen-Sen Wu, and Qing-Chao Shang, "Calculation of radiation forces exerted on a uniaxial anisotropic sphere by an off-axis incident Gaussian beam," Opt. Express 19, 16044-16057 (2011)

[4] J. A. Kong, Electromagnetic wave Theory (New York, John Wiley & Sons, 1986)

Numerical computation of the scattering properties of large arbitrary shaped particle by MLFMA and VCRM

Yue-Qian WU[1,2], Ming-Lin YANG[1,2], Kuan Fang REN [2,*] and Xin-Qing SHENG[1]

[1] Center for Electromagnetic Simulation, Beijing Institute of Technology, Beijing, 100081, China
[2] UMR 6614/CORIA, CNRS - Université et INSA de Rouen, Rouen, 76801, France

Corresponding author: fang.ren@coria.fr

Abstract

The Surface Integral Equation (SIE) with Multilevel Fast Multipole Algorithm (MLFMA) is an efficient full wave numerical method for computing scattering properties by a large particle of arbitrary shape. It can be well parallelized with Message Passing Interface (MPI) on a memory distributed computer system and obtain accurate results for relatively large particles with size parameter reach up more than 500 efficiently. The recently developed high frequency asymptotic method, called Vectorial Complex Rays Model (VCRM) is proved to be especially suitable for computing scattering by a large particle of arbitrary shape. Accuracy of these two methods on spherical particles has been well studied by comparisons with the rigorous Lorenz-Mie theory (LMT) but less on non spherical particles. In this paper, scattering properties by large elliptical particles with different aspect ratios are computed by using both the SIE with MLFMA and the VCRM. Good agreements between these two methods validate accuracy of them and show great capability of the SIE with MLFMA at the same time. At last, scattering by a large irregular shaped particle is also computed by the SIE with MLFMA.

1 Introduction

In various research fields, we need to solve light scattering problems by arbitrary particles, such as atmospheric radiative transfer, bio-optics and climatology. In fact, particles encountered in nature (ice crystals, dust aerosols, raindrops and cells in biophysical systems) are often irregularly shaped and have a wide range of sizes. In order to achieve accurate and efficient results, various methods are developed which can be classified in three categories: rigorous methods, numerical methods and approximate methods. LMT [1-2] is a rigorous method and has been widely used in light scattering problems by homogenous spheres, layered spherical particles and infinitely long cylinders. However, it is difficult to treat the scattering properties by realistically complex shaped particles. For this reason, numerical methods such as the discrete dipole approximation (DDA) [3], the finite difference time-domain technique (FDTD) [4, 5] and the T-matrix method [6, 7] have been developed and are used in practice. But for all these numerical methods, the computational requirements increase quickly with size, such that they become inapplicable when the particle size is extremely large. So the development of the efficient algorithm is crucial for each method.

SIE is one of the robust and accuracy full-electromagnetic wave methods for scattering of an arbitrary shaped particle. In this paper, the multilevel fast multipole algorithm (MLFMA) [8, 9, 10] based on the SIE was employed to reduce both the time and the memory complexity. To further improve the efficiency of MLFMA, MPI [8, 9] on a memory distributed computer system is used. This algorithm is of high accuracy and has capability to deal with arbitrary shaped particles of size parameter as large as 500.

Besides the above mentioned methods, various approximate approaches have been developed to obtain scattering properties of large particles, such as geometrical optics (GO) [11] and physical optics [12, 13]. These approaches are applicable when the size of the particle is much larger than the wavelength of the incident beam. VCRM [14, 15] developed by Ren et al. is suitable to deal with the scattering of irregular large particles of smooth surface. In VCRM, the waves are described by vectorial complex rays. By introducing a new property: the curvature of the wavefront and using the vectors in ray tracing, the method is more accurate and flexible than classical GO for arbitrary shaped particles. The accuracy of VCRM has been investigated by comparisons with LMT for spherical particles. It has been successfully applied to the calculation of scattering by ellipsoidal particles [14, 15, 16] and infinite elliptical cylinders [17, 18]. Various new physical phenomena in light scattering by non-spherical particles have been revealed.

Both MLFMA and VCRM have achieved good agreement with LMT on spherical particles. But there is no further discussion between these two methods for scattering by non spherical particle. Comparison between the MLFMA and VCRM for elliptical particles will be presented in this paper, along with computed results of scattering properties of a large complex shaped particle.

The body of the paper is organized as follows: VCRM and MLFMA will be briefly presented in Section 2. The numerical accuracy and capability of the two methods will be discussed in Section 3 with the computed results.

2 Theoretical basis

2.1 Vectorial Complex Ray Model – VCRM

Vectorial Complex Ray Model (VCRM) is based on the geometrical optics but a new property – the wave front curvatures – is introduced. This property permits to account the wavelike behaviour of light, the convergent or divergent of the wave. Thus, a ray is described not only by its amplitude, phase, polarization, propagation direction, but also by the curvatures of the wave front of the wave that the ray presents. All these features evolve at each interaction of ray with the particle surface. Particularly, the curvature matrix of the emergent wave after each interaction of the ray with the particle surface is calculated according to the curvature matrix of the incident wave and the local curvature of the particle surface by using the wave front equation.

The significant benefits of this approach are: a). the wave properties are integrated in the ray model; b). the divergence/convergence of the wave is deduced by the wave front curvature; c). the phase shift due to the focal lines is determined directly by the curvature of the wave front.

2.2 Multilevel Fast Multipole Algorithm – MLFMA

We consider the electromagnetic scattering problem of a homogeneous particle of any shape illuminated by a wave (Figure. 1). Let S be the surface of particle, (ε_1, μ_1) and (ε_2, μ_2) the permittivity and permeability in the outer and inner regions of the particle respectively. The scattered electromagnetic filed at any point can be obtained by the equivalent electric and magnetic currents **J** and **M** on the surface of the particle which are determined by the electric and magnetic field integral equations according to [19]:

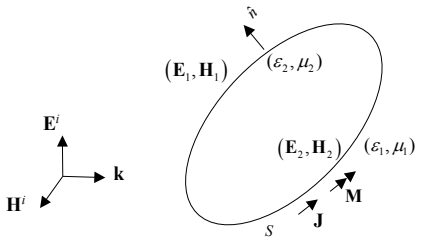


Figure 1 *Sketch map of homogeneous particle*

$$\mathbf{E}_1 - Z_1\mathbf{L}_1(\mathbf{J}) + \mathbf{K}_1(\mathbf{M}) = \mathbf{E}^i \quad (1)$$

$$\mathbf{H}_1 - Z_1^{-1}\mathbf{L}_1(\mathbf{M}) - \mathbf{K}_1(\mathbf{J}) = \mathbf{H}^i \quad (2)$$

$$\mathbf{E}_2 - Z_2\mathbf{L}_2(\mathbf{J}) + \mathbf{K}_2(\mathbf{M}) = 0 \quad (3)$$

$$\mathbf{H}_2 - Z_2^{-1}\mathbf{L}_2(\mathbf{M}) - \mathbf{K}_2(\mathbf{J}) = 0 \quad (4)$$

where $Z_1 = \sqrt{\mu_1/\varepsilon_1}$, $(\mathbf{E}^i, \mathbf{H}^i)$ denote the incident fields, and the operators and are defined as:

$$\mathbf{L}_l\{\mathbf{X}\}(r) = jk_l\int\left[\mathbf{X}(r') + \frac{1}{k_l^2}\nabla(\nabla'\cdot\mathbf{X}(r'))\right]G_l(r,r')dr' \quad (5)$$

$$\mathbf{K}_l\{\mathbf{X}\}(r) = \int dr'\mathbf{X}(r')\times\nabla' G_l(r,r') \quad (6)$$

Following the Combined Tangential Formulation (CTF) [5] we obtain following equations which are free of internal-resonance problem.

$$\hat{t}\cdot\left[\mathbf{L}_1 + \mathbf{L}_2\right]\{\mathbf{J}\} - \hat{t}\cdot\left[Z_1^{-1}\mathbf{K}_1 + Z_2^{-1}\mathbf{K}_2\right]\{\mathbf{M}\} = -Z_1^{-1}\hat{t}\cdot\mathbf{E}^i(\vec{r}) \quad (7)$$

$$\hat{t}\cdot\left[Z_1\mathbf{K}_1 + Z_2\mathbf{K}_2\right]\{\mathbf{J}\} + \hat{t}\cdot\left[\mathbf{L}_1 + \mathbf{L}_2\right]\{\mathbf{M}\} = -Z_1\hat{t}\cdot\mathbf{H}^i(\vec{r}) \quad (8)$$

where $\hat{t}$ is a tangential vector of the surface.

In the implementation, the dielectric surface is meshed by triangular patches. Within each patch, Rao, Wilton and Glisson (RWG) vector basis functions [19] are applied to expand the unknown equivalent electric and magnetic currents. With using the standard Galerkin's method, a complete matrix equation system can be obtained. The required matrix-vector multiplications are performed efficiently with the multilevel fast multipole algorithm (MLFMA) which can reduce both the time and the memory. MPI parallelization is applied to further improve the efficiency of MLFMA.

3 Numberical results and discussion

In this section, we just show numerical results on a sphere with radius of 50 μm and an ellipsoid having the same volume. Detailed computation information together with other results including scattering by an irregular shaped large particle will be presented during the LIP-2014 conference.

The elongation of the particles is characterized through a couple of aspect ratios, defined as $\kappa_1 = c/a$, $\kappa_2 = c/b$ with *a*, *b* and *c* denoting the semi-axes of the ellipsoid along the *x*, *y* and *z* directions respectively. We have $\kappa_1 = \kappa_2 = 1.0$ for sphere, $\kappa_1 = \kappa_2$ for spheroids and $\kappa_1 \neq \kappa_2$ for ellipsoids.

The first example is a spherical water droplet (*m*=1.33) with radius of 50 μm. The incident plane wave is polarized in *x* direction with wavelength of 0.785 μm. The scattering intensity in *xz* plane computed by MLFMA together with those obtained by LMT and VCRM are plotted in figure 2. It can be seen from this figure that both VCRM and MLFMA agree well with LMT. But there are slit differences between VCRM and LMT when the scattering angle ranged from about $60°\sim120°$ while MLFMA agrees with LMT well. This is because in VCRM the surface wave effect has not yet taken into consideration. But the overall accuracy of VCRM is good.

The next example is an ellipsoid with *a*=35.47, *b*=49.66, *c*=70.95 i.e. $\kappa_1 = 2.0$ and $\kappa_2 = 1.43$. This ellipsoid has the same volume of the sphere with radius of 50 μm. The computed scattering diagrams in *xz* plane computed by VCRM and MLFMA are shown in figure 3. As expected, these two results agree with each other, but a significant difference is observed for the scattering angles range from about $60°\sim120°$. Also, the difference is due to the surface wave effect and the diffraction effect near rainbow angle.

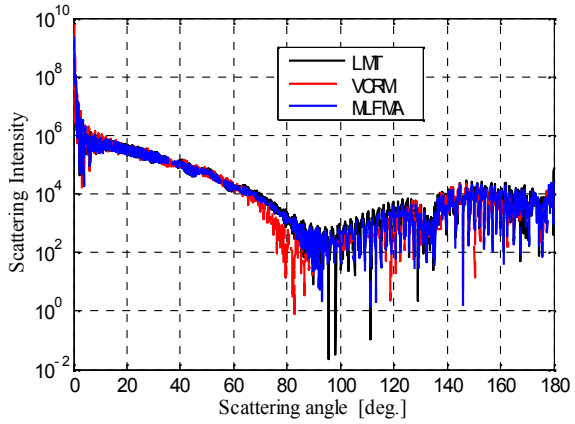


Figure 2 *Comparison of scattering diagrams computed by LMT, VCRM and MLFMA for a water droplet of refractive index m=1.33 and radius 50 μm illuminate by a plane wave of wavelength 0.785 μm for horizontal polarization.*

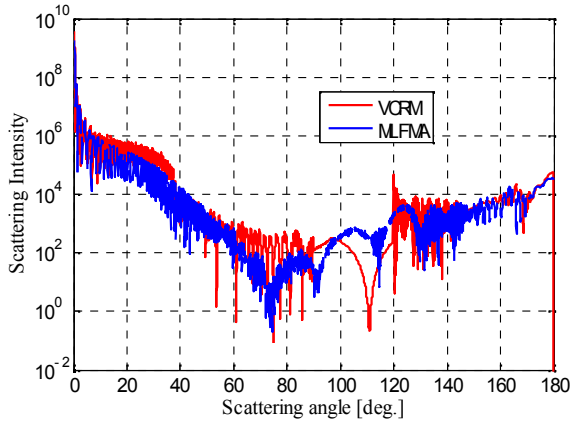


Figure 3 *Comparison of scattering diagrams computed by VCRM and MLFMA for an ellipsoidal water droplet with* $\kappa_1 = 2.0$ *and* $\kappa_2 = 1.43$ *having the same volume of a sphere with radius 50 μm. Other parameters are the same as in Figure 2.*

4 Acknowledgement

The authors acknowledge the support from the China Scholarship Council for the stay of Yueqian WU and Minglin Yang at CORIA. This work has been also partially supported by substantial computation facilities from CRIHAN (Centre de Ressources Informatiques de Haute-Normandie) and the French National Research Agency (ANR) grant ANR-13-BS09-0008-01.

5 References

[1] H. C. van de Hulst, *Light Scattering by Small Particles* (Dover, New-York, 1957).

[2] C. F. Bohren and D. R. Huffman, *Absorption and Scattering of Light by Small Particles* (Wiley, New-York, 1983).

[3] Draine B. T. and Flatau P. J., Discrete-dipole approximation for light calculations, Optical Society of America 11(4):1491–1499 (1994)

[4] Yang P. and Liou K. N., Finite-difference time domain method for light scattering by small ice crystals in three-dimensional space, Optical Society of America 13(10):2072–2085(1996)

[5] Sun W.-B., Fu Q., and Chen Z., Finite-difference time-domain solution of light scattering by dielectric particles with a perfectly matched layer absorbing boundary condition, Applied Optics 38(15):3141–3151 (1999)

[6] Waterman P. C. Matrix formulation of electromagnetic scattering. Proceedings of IEEE 53:805–812(1965)

[7] Mishchenko M. I. and Travis L. D., Capabilities and limitations of a current FORTRAN implementation of the T-matrix method for randomly oriented rotationally symmetric scatterers, Journal of Quantitative Spectroscopy and Radiative Transfer 60(3): 309–324 (1998).

[8] Fostier J. and Olyslager F., "An asynchronous parallel MLFMA for scattering at multiple dielectric objects," IEEE Transactions on Antennas and Propagation 56(8) : 2346-2355(2008)

[9] Ergül Ö., Parallel implementation of MLFMA for homogeneous objects with various material properties, Progress In Electromagnetics Research, 121:505-520(2011)

[10] Pan X. M., Pi W. C., Yang M. L., Peng Z. and Sheng X. Q., Solving problems with over one billion unknowns by the MLFMA, IEEE Transactions on Antennas and Propagation 60(5):2571-2574(2012)

[11] Ungut A., Grehan G., and Gouesbet G., Comparisons between geometrical optics and Lorenz-Mie theory, Applied Optics 20(17):2911-2918 (1981).

[12] Ravey J. C. and Mazeron P., Light scattering in the physical optics approximation: application to large spheroids, Journal of Optics 13(5): 273–282(1982)

[13] Ravey J. C. and Mazeron P., Light scattering in the physical optics approximation: numerical comparison with other approximate and exact results, Journal of Optics 14(1):29–41(1983)

[14] Ren K. F., Onofri F., Rozé C., and Girasole T., Vectorial complex ray model and application to two-dimensional scattering of plane wave by a spheroidal particle, Optics Letters 36(3):370–372 (2011)

[15] Ren K. F., Rozé C., and Girasole T., Scattering and transversal divergence of an ellipsoidal particle by using vectorial complex raymodel, Journal of Quantitative Spectroscopy and Radiative Transfer 113(18):2419–2423 (2012)

[16] Yuan Y., Diffusion de la lumière par un objet irrégulier pour l'application à l'imagerie des sprays, PhD thesis of Rouen University, France, 29 March 2012

[17] Jiang K., Han X., and Ren K. F., Scattering from an elliptical cylinder by using the vectorial complex ray model, Applied Optics 51(34):8159–8168 (2012)

[18] Jiang K., Han X., and Ren K. F., Scattering of a Gaussian beam by an elliptical cylinder using the vectorial complex ray model, J. Opt. Soc. Am. A. 30(8):1548-1556 (2013)

[19] R. F. Harrington, *Field Computation by Moment Methods*(2nd edition) (IEEE Press, New-York, 1993)

ABSphere - Software for calculation of all physical properties of Any shaped Beam by a Spherical particle

Kuan Fang REN

UMR 6614/CORIA, CNRS - Université et INSA de Rouen, Rouen, 76801, France

*Corresponding author: fang.ren@coria.fr

Abstract

Based on the rigorous solution of the Maxwell equation – the Generalized Lorenz-Mie Theory (GLMT), software ABSphere has been developed for the calculation of different physical properties concerning the interaction of a spherical particle and a shaped beam. The particle can be homogeneous or stratified. Five kinds of shaped beam are considered: circular Gaussian beam, elliptical Gaussian beam, Doughnut beam and Bessel beam. It is also possible for user to provide the beam shaped coefficients for any shaped beam. Five quantities can be calculated: 1). Scattering diagram, 2). Internal/near field intensity, 3). Efficient coefficients (sections), 4). Radiation forces 5). Radiation torques. The test on a conventional personal computer shows that the particle size can be as large as some millimetres (for visible light) and the number of layers can be some ten thousands.

1 Context of the development

In the field of light-particles interaction, the scattering of a spherical particle is the simplest and the most important since it is the only model that we can calculate rigorously all the physical properties for particles of almost any size illuminated by any shaped beam. Particularly, when the spherical particle is illuminated by different shaped beam we can reveal many physical phenomena and serves as reference to validate the models for other shaped particles.

In the framework of Generalized Lorenz-Mie Theory, the incident beam and the particle property are described respectively and independently by two series of the beam shaped coefficients (BSC) $g_{n,TM}^{m}$, $g_{n,TE}^{m}$ and four series of the Mie coefficients: a_n , b_n for the scattered fields and c_n , d_n for the internal fields. Once we know the beam shaped coefficients and the Mie coefficients we can calculates all physical quantities [1, 2].

2 Description of the software

The calculation of the Mie coefficients and the beam shape coefficients are essential. A brief description of the calculation of these coefficients is given in this section.

2.1 Mie Coefficents

The calculation of Mie coefficients is for a homogeneous particle is well documented [1] and without special problem even for large particle. However, the numerical evaluation of these coefficients for a stratified sphere is not an easy task [3]. Based on the work of Wu et al [4] the author has developed an algorithm which is more stable and efficient.

2.2 Shaped beams in ABSphere

The beam shape coefficients are at the core for the numerical prediction of the scattering of a shaped beam by a sphere. They are also essential for the scattering of a spheroid or other shape particle since the beam shaped coefficients in that coordinate system can be expressed as function of the beam shape coefficients in spherical coordinate system. Many authors have contributed to the numerical evaluation of these BSC (see [4] and the references therein).

In ABSphere, the Integral Localized Application (ILA) [5] is adopted since for commonly used shaped beams, the integral can be evaluated to the standard Bessel function (see Table 1). Therefore, there is no problem of numerical instability. By comparison with the rigorous quadrature methods it is proved that the precision of ILA is usually very satisfactory.

Shaped beams	Parameters	Beam shape coefficients
Circular Gaussian beam	Beam waist radius w_0	All beam shape coefficients are calculated by using Bessel function derived from ILA.
Elliptical Gaussian beam	Beam waist radii w_{0x} , w_{0y}	
Doughnut beam	Beam waist radius w_{0dn} Polarization: 4 states	
Bessel Beam	Any order υ with given angle of axicon α_0	
Any beam with known g_n^m	ABSpher reads the beam shape coefficients to calculate the physical quantities.	

Table 1 *Shaped beams considered in ABSphere*

Theoretically, any given double series of BSC $g_{n,TM}^{m}$, $g_{n,TE}^{m}$ describe a beam whose electromagnetic fields satisfy perfectly the Maxwell equations. The evaluation of the beam shape coefficients from given electromagnetic field is just to find the coefficients which describe a beam the most

"faithful" to the given one. To reply the needs of calculation for any shaped beams, ABSphere provides the possibility for the user to give the double series of BSC in order to calculate the quantities listed in the following section. For example, if the user wants to calculate the radiation pressure on a sphere in the evanescent wave, he can calculates its BSC independently by integral methods and then ABSphere reads the coefficients from a file to calculate the quantities at his will.

2.3 Quantities calculated by ABSphere

The actual version of ABSphere calculates the following quantities:

1). Scattering diagram $I(\theta)$ for given an azimuth angle φ (to define the observation plane).
2). Internal/near field $I(x,y,z)$
3). Efficient coefficients (sections) Q_{ext}, Q_{sca}, Q_{abs} as function of particle size.
4). Radiation forces section $C_{pr,x}, C_{pr,y}, C_{pr,z}$ as function of particle size or its position.
5). Radiation torques T_x, T_y, T_z as function of particle size or its position.

2.4 Some results

Some typical results are given in this section.

Figure 1 is a graph of ABSphere showing the scattering diagram of a particle of glass (m=1.5) of radius a=7.5 μm, illuminated by a circular Gaussian beam ($\lambda = 0.5\ \mu$m , $w_0 = 5\ \mu$m). The blue and the red curves are the total scattering intensities for the azimuth angle $\varphi = 0$ and 90° , while the black and the green curves are the intensities of the Debye series for diffraction plus reflection for the two observation planes at $\varphi = 0$ and 90° .

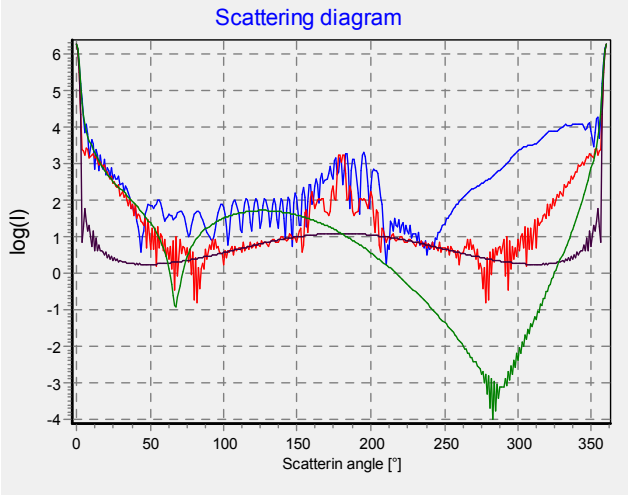
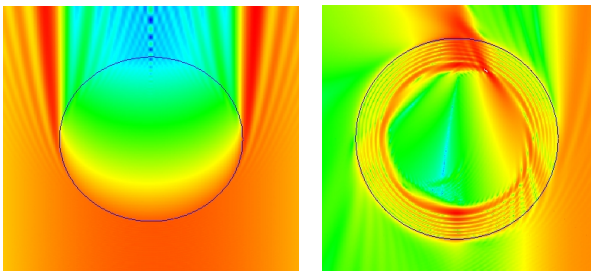


Figure 1 *. Scattering diagrams of a particle of glass located at* $x_0 = 5\ \mu$m *in a Gaussian beam.*

The second example is to show the calculation of the internal and near fields when a particle is illuminated by a shaped beam. Figure 2(a) shows the internal and near fields of a nano-sphere in SiO_2 (a=92.5nm) illuminated by Synchrotron ray of 248 eV and Figure 2(b) the internal and near fields of a glass sphere (a=7.5 μm) illuminated by a Gaussian Beam (w_0=5μm) at 10 μm off-axis.



(a) (b)

Figure 2 *. Internal and near fields of a particle: (a) a nano-sphere in SiO2 (a=92.5nm) illuminated by Synchrotron ray of 248 eV, (b) a glass sphere (a=7.5 μm) illuminated by a Gaussian Beam (w0=5μm) at 10μm off-axis.*

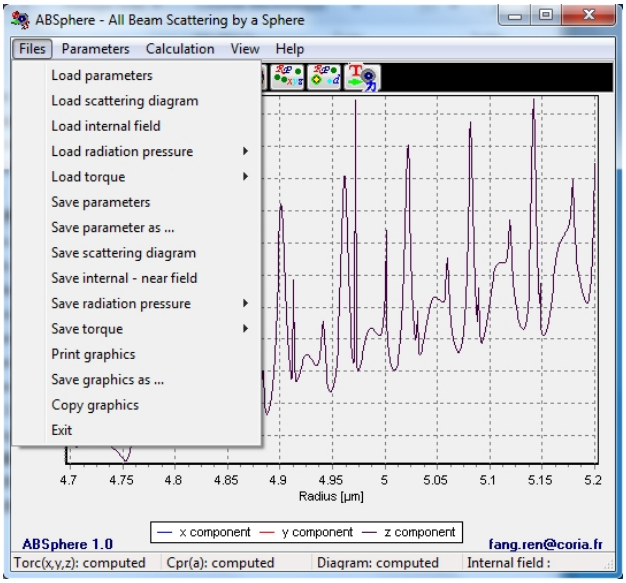


Figure 3*. Screen Shot of ABSPHERE - Software*

3 Acknowledgement

This work has been also partially supported by substantial computation facilities from CRIHAN (Centre de Ressources Informatiques de Haute-Normandie) and the French National Research Agency (ANR) grant ANR-13-BS09-0008-01.

4 References

[1] C. F. Bohren, and D.R. Huffman, Absorption and scattering of light by small particles (Wiley, New-York, 1983).

[2] G. Gouesbet and G. Gréhan, Generalized Lorenz-Mie Theories, (Springer, 2011)

[3] Onofri F., Gréhan G. and Gouesbet G., Electromagnetic scattering from a multilayered sphere located in an arbitrary beam, Applied Optics, 34(30):7113-7124 (1995)

[4] Wu Z. S., Guo L. X., Ren K. F., Gouesbet G. and Grehan G., Improved algorithm for electromagnetic scattering of plane waves and shaped beams by multilayered spheres, Appl. Opt., 36(21):5188-5198 (1997)

[5] Gouesbet G., J. A. Lock and Grehan G., Generalized Lorenz–Mie theories and description of electromagnetic arbitrary shaped beams: Localized approximations and localized beam models, a review, J. Quantit. Spectroscopy Radiative Transfer, 112(1):1-27 (2011)

[6] Ren K. F., Gouesbet G. and Grehan G., The integral localized approximation in generalized Lorenz-Mie theory, Appl. Opt., 37(19):4218-4225 (1998)

Mechanical effects of light

Optical trapping and manipulation of nanostructures

O. M. Maragó[1,*], M. G. Donato[1], A. Magazzu[1,2], A. Irrera[1], C. D'Andrea[1,3], E. Messina[1], B. Fazio[1], M. A. Iati[1], P. H. Jones[4], and P. G. Gucciardi[1]

[1] CNR-IPCF, Istituto per i Processi Chimico-Fisici, Messina, Italy
[2] Dottorato in Fisica, Università di Messina , Messina, Italy
[3] Matis CNR-IMM and Dipartimento di Fisica, Università di Catania, Catania, Italy
[4] Department of Physics and Astronomy, University College London, London, UK
Corresponding author: marago@me.cnr.it

Abstract

Optical trapping (OT) of nanostructures has acquired tremendous momentum in the last few years. Manipulating nanoparticles with standard OT is generally difficult because radiation forces scale approximately with particle volume and thermal fluctuations easily overwhelm trapping forces at the nanoscale. However carbon nanotubes, graphene, polymer nanofibers, plasmonic nanoparticles, and semiconductor nanowires, have been stably trapped thanks either to their highly anisotropic geometry or to their intrinsic resonant behavior. Here we discuss our recent results on OT of nanostructures with a focus on the role of shape on optical forces, spectroscopy measurements in optical traps, and implications in force and spectroscopic sensing at the nanoscale.

1 Introduction

Optical trapping and manipulation of micrometre-sized particles was first reported in 1970 [1]. Since then, it has been successfully implemented in two size ranges: the subnanometre scale, where light–matter mechanical coupling enables cooling of atoms [2], and the micrometre scale, where the momentum transfer resulting from light scattering allows manipulation of microscopic objects such as cells [3]. But it has been difficult to apply these techniques to the intermediate, nanoscale, range that includes structures such as quantum dots, nanowires, nanotubes, graphene and two-dimensional crystals, all of crucial importance for nanomaterials-based applications [4]. Recently, however, several new approaches have been developed and demonstrated for trapping plasmonic nanoparticles, semiconductor nanowires and carbon nanostructures [4]. Here we describe our experimental and theoretical efforts in the understanding and the exploitation of optical forces as applied to nanostructures.

2 Optical trapping of nanostructures

We have trapped and manipulated different type of nanostructures (Fig. 1) with a first goal to investigate optical forces through their accurate measure in the optical trap [5-8]. We have used nanostructures as probes for light-driven rotations [9-10], as well as accurately measure forces with resolution at the level of femto-Newtons [5] crucial for photonic force microscopy applications [4] combining the outstanding force-sensing capabilities of OT with increased nanometric precision and bridging the gap between micro and nanoscale in fluidic environments (Fig. 1). In this context the role of shape [5-8,13] and size-scaling [6,13] is crucial for understanding the interplay between optical forces and hydrodynamic interactions that change dramatically with size, hence much affecting both force-sensing and spatial resolution in precision applications [4,5].

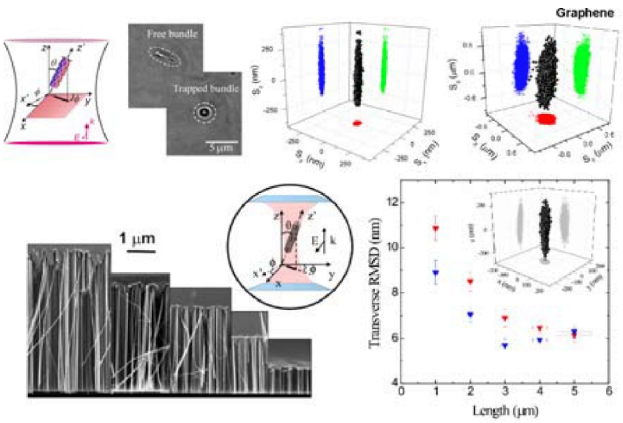


Figure 1 *(Top) Optical trapping and Brownian motion of carbon nanotubes and graphene [4,5,9]. (Bottom) Optical trapping of Silicon nanowires and size-scaling [6,13].*

Furthermore the integration of OT with Raman and SERS spectroscopy (Fig. 2) allowed us to perform ultra-sensitive chemical-physical analysis of trapped nanoparticles [8,11,12]. The use of optical forces to trap and manipulate metal nanoparticles and aggregates permits exploitation of the field-enhancement properties of these nanostructures for surface-enhanced Raman spectroscopy of molecules adsorbed on aggregates optically trapped in a Raman tweezers setup [11,12] (Fig. 2). Moreover, we also demonstrated the operation of a SERS sensor in liquid environment obtained by optical force induced aggregation of colloidal gold nanorods.

This is the result of an interplay between thermal and radiation pressure effects. The creation of highly efficient hot spot regions enables the Raman detection of proteins dissolved in a buffer solution at very low concentration (up to 10^{-7} M).

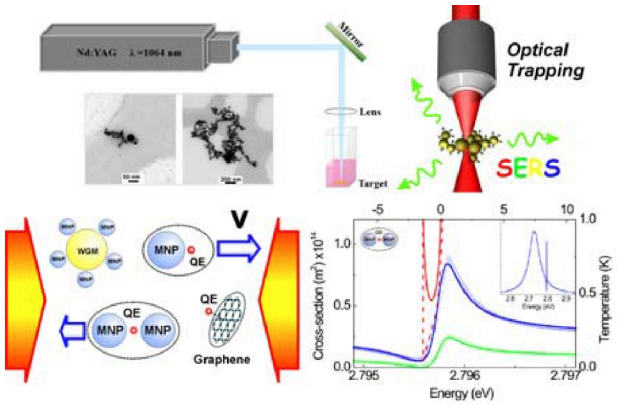


Figure 2 *Optical trapping of plasmonic nanoaggregates and SERS [8,11,12]. Fano-Doppler laser cooling of hybrid nanostructures [18].*

3 Conclusions

In conclusion, optical trapping of nanostructures offers a unique opportunity to trap, manipulate, probe, characterize, individual nanostructures with well defined optical, mechanical, thermal properties. The range of applications is huge and spans from photonic force microscopy with femtonewton resolution, Raman and SERS spectroscopy in liquid, to novel approaches in laser cooling [14] and optomechanics of levitated particles [4].

4 References

[1] A. Ashkin, Acceleration and trapping of particles by radiation pressure. *Phys. Rev. Lett.* **24,** 156–159 (1970).

[2] C. J. Foot, "Atomic Physics", *Oxford University Press* (2005).

[3] Ashkin, A., Dziedzic, J., Bjorkholm, J., and Chu, S. Observation of a single-beam gradient optical trap for dielectric particles. *Opt. Lett.* 11, 288 (1986).

[4] O. M. Maragò, P. J. Jones P. G. Gucciardi, G. Volpe, A. C. Ferrari, Optical trapping and manipulation of nanostructures. *Nature Nanotechnology*, **8**, 807-819 (2013)

[5] O. M. Maragò, Femtonewton force sensing with optically trapped nanotubes. *et al. Nano Lett.* **8,** 3211 (2008).

[6] A. Irrera, *et al.* Size-scaling in optical trapping of silicon nanowires. *Nano Lett.* **11,** 4879 (2011).

[7] M. G. Donato, *et al.* Optical trapping of nanotubes with cylindrical vector beams. *Opt. Lett.* **37,** 3381–3383 (2012).

[8] O. M. Maragò, *et al.*, Brownian motion of graphene. *ACS Nano* **4**, 7515 (2010).

[9] P. H. Jones, *et al.* Rotation detection in light-driven nanorotors. *ACS Nano* **3**, 3077 (2009).

[10] A. Neves, et al., Rotational dynamics of optically trapped nanofibers. *Opt. Express* **18,** 822 (2010).

[11] E. Messina, et al. Plasmon-enhanced optical trapping of gold nanoaggregates with selected optical properties. *ACS Nano* **5**, 905 (2011).

[12] E. Messina, et al. Manipulation and Raman spectroscopy with optically trapped metal nanoparticles obtained by pulsed laser ablation in liquids. *J. Phys. Chem C* **115** 5115 (2011).

[13] F. Borghese, *et al.* Radiation torque on non-spherical particles in the transition matrix formalism. *Phys. Rev. Lett.* **100,** 163903 (2008).

[14] A. Ridolfo, *et al.* Fano-doppler laser cooling of hybrid nanostructures. *ACS Nano* **5,** 7354 (2011).

Photonic Nanojet in Optical Tweezers

Antonio A. R. NEVES *

Centro de Ciências Naturais e Humanas, Universidade Federal do ABC (UFABC), Santo André – SP, 09210-170, Brazil

*Corresponding author: antonio.neves@ufabc.edu.br

Abstract

Photonic nanojets are currently being investigated, brought into attention ten years ago for potential application as ultramicroscopy technique, using its sub-wavelength resolution to enhance detection and interaction with matter. For these novel applications under development, optically trapping a sphere, acts as an ideal framework to employ these nanojets. In this case, the nanojet is generated by a highly focused beam contrary to the classical plane wave method, but it inherits the advantage from optical trapping, that the microsphere remains on the beam propagation axis, and that can be positioned arbitrarily in space especially for intracellular applications. Moreover, due to optical forces, there is an equilibrium position of the sphere centre with respect to the beam focus. This work, presents a detailed analysis of the formal relationship between the optical force on a microsphere and its photonic nanojet.

1 Photonic Nanojets

Photonic nanojet (PNJ) are none other than external caustics, spatially localized high energy density regions structured in the near-field of the shadow side surface of micro-scale dielectric cylinders or spheres, when illuminated by a plane wave [1,2].

The main features of PNJ are waists smaller than diffraction limit and propagation over several wavelengths without significant diffraction. This leads to potential spectroscopic methods with high spatial resolution and high detection sensitivity by backscattering enhancement. Therefore the characteristics of a nanojet can be described by a few parameters: the peak amplitude of the PNJ intensity, the radial distance from the peak amplitude to the sphere surface (radial shift), the radial distance from the peak amplitude to the point where the intensity decays to $1/e^2$ (decay length), and the PNJ width, which is the $1/e^2$ waist of the jet [3]. A simulation for a typical PNJ generated by a circularly polarized plane wave is presented in Figure. 1.

The current understandings of the behaviour of PNJ for a given wavelength are: the PNJ waist widening/shrinking as a function of increasing relative refractive index; and the PNJ lengthening due to increasing sphere radius. The modelling for plane wave PNJs have just four parameters: refractive index of the particle, and surrounding, wavelength of the incident wave, and radius of the sphere.

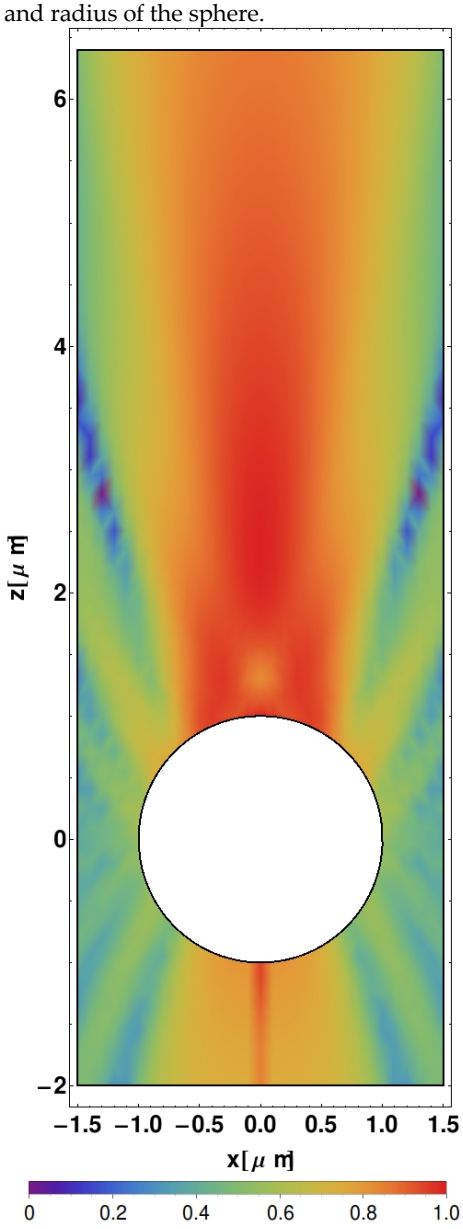


Figure 1 *PNJ (in red) illustrated by the colour map of the normalized scaling of the logarithmic magnitude of time-averaged Poynting vector, for a 2μm latex sphere in a circularly polarized plane wave propagating along the positive z-direction.*

Meanwhile for a focused incident beam on a sphere, it has been shown that the resulting PNJ decreases the confocal volume by an order of magnitude and enhances the fluorescence brightness by a factor of five, outperforming a classical confocal microscope [4]. Hence, for a focused incident beam instead of a plan wave, the new additional focused beam parameters increases the complexity of the problem. In the special case of an optically trapped sphere, the highly focused incident beam focus cannot be positioned arbitrarily with respect to the sphere centre, to maximize energy confinement, but is in a stable equilibrium position a few wavelengths away from the sphere centre along the propagation axis, balancing the scattering and gradient force components.

2 Beam description and optical forces

To present a complete study of PNJ in optical tweezers we start with a description of the incident highly focused beam in the framework of generalized Lorenz–Mie theory (GLMT) [5]. The basic idea of GLMT is that a beam, that is a solution to Maxwell's equations (Maxwellian beam), can be written as an infinite series of spherical functions and spherical harmonics, each multiplied by a coefficient that is called a beam shape coefficient (BSC). These BSCs completely describes the incident, the internal, and the scattered electromagnetic fields in terms of partial waves series. The correct determination of these radially independent BSCs, allows for precise determination of the observed electromagnetic phenomena. However, contrary to the employed Davis description of Gaussian beams, a perturbation method introduces higher-order corrections to the paraxial approximation, which for a strong focusing (as in optical tweezers), yields a condition that is rarely meet and there is a need to go beyond a paraxial expansion. To this aim, we resort to an early development based on the angular spectrum representation, later applied to optical trapping that led to a final solution of describing a completely arbitrary vectorial Maxwellian beam [6]. This new approach has the benefit of providing an analytical expression for the BSCs as a function of beam position with respect to the sphere directly, without the need to rely on costly vector translation theorems.

Once the BSCs are determined, we apply the Maxwell stress tensor formalism to determine the force components on an optically trapped microsphere, providing new insights, given the analytical nature of the solution, concerning the electromagnetic description of laser beams.

Finally to determine the PNJ due to an optically trapped micro-sphere, we first determine the location along the propagation axis where stable equilibrium condition is verified. The position is found from an optical force curve with respect to the trap position from microsphere centre. This type of force profile has been applied previously in the investigation of morphology dependent resonances of an optically trapped microsphere [7]. At this stable position, an energy density plot could be done to identify the existence/location of PNJs, for different optical trapping characteristics (wavelength, refractive indexes, polarization).

As a result, an understanding between the interaction of an optically trapped micro-sphere and its PNJ field structure is of fundamental importance for the study of optical physics, and has practical significance for applications such as imaging, nano-lithography, detection, metrology, biophotonics, and especially spectroscopy.

3 Acknowledgement

The present work received support from CNPq (308627/2012-1), Conselho Nacional de Desenvolvimento Científico e Tecnológico and FAPESP (2014/07191-9), Fundação de Amparo à Pesquisa do Estado de São Paulo, Brazil.

4 References

[1] Chen Z., Taflove A., and Backman V., Photonic nanojet enhancement of backscattering of light by nanoparticles: a potential novel visible-light ultramicroscopy technique, Optics Express 12(7):1214-20(2004)

[2] Lock J.A., Adler C.L., and Hovenac E.A., Exterior caustics produced in scattering of a diagonally incident plane wave by a circular cylinder: semiclassical scattering theory analysis, J. Opt. Soc. Am. A 17(10):1846-56(2000)

[3] Itagi A.V., Challener W.A., Optics of photonic nanojets, J. Opt. Soc. Am. A 22(12):2847-58(2005)

[4] Gérard D., Wenger J., Devilez A., Gachet D., Stout B., Bonod N., Popov E., and Rigneault H., Strong electromagnetic confinement near dieletric microsphere to enhance single-molecule fluorescence, Optics Express 16(19):15297-303(2008)

[5] G. Gouesbet, and G. Gréhan, [1] Generalized Lorenz-Mie Theories ([1] Springer, [1] Berlin, 2011).

[6] Neves A.A.R., Fontes A., Padilha L.A., Rodriguez E., Cruz C.H.B., Barbosa L.C., and Cesar C.L., Exact partial wave expansion of optical beams with respect to an arbitrary origin, Optics Letters 31(16):2477-79(2006)

[7] Neves A.A.R., Fontes A., Pozzo L.Y., de Thomaz A.A., Chillce E., Rodriguez E., Barbosa L.C., and Cesar C.L., Electromagnetic forces for an arbitrary optical trapping of a spherical dielectric, Optics Express 14(26):13101-106(2006)

As Diverse Pathes Leden Diverse Folk the Righte Way to Radiation Pressure

Timo A. NIEMINEN

School of Mathematics and Physics, The University of Queensland, Brisbane, QLD 4072, Australia

Corresponding author: timo@physics.uq.edu.au

Abstract

Radiation pressure has a long history, from Kepler to modern applications such as optical tweezers. The underlying principle—the inertia of energy—shows essential links between classical mechanics, thermodynamics, and relativity, and we can use a diverse range of theoretical roads to explain and understand radiation pressure.

1 Introduction

Geoffrey Chaucer, better known for his literary work *The Canterbury Tales*, commented in his scientific work [1] on the diversity of paths to knowledge, comparing these paths to roads leading to Rome: "as diverse pathes leden diverse folk the righte way to Rome". However, science tends to compartmentalisation, with specialised fields dealing with specialised knowledge and theories, and we are often faced with single roads rather than diverse paths. Therefore, it is refreshing to find an idea that has a truly diverse range of paths leading to it: radiation pressure. Indeed, if we consider the main branches of theoretical physics, as shown in Figure 1, we can find explanations that lead to radiation pressure in classical mechanics, relativistic mechanics, quantum mechanics, classical and quantum field theory, classical thermodynamics, and statistical mechanics.

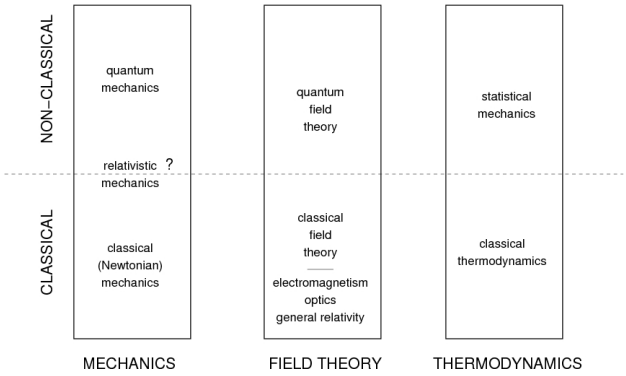


Figure 1 *The major fields of theoretical physics. The division in classical and non-classical parts of mechanics, field theory, and thermodynamics gives us 6 fields. Every one of these fields can be used to explain radiation pressure.*

The development of optical tweezers changed the radiation pressure of light from a curiosity of physics to a commonly used experimental tool [2]. This led to renewed interest in both fundamental theory [3] and the history of the phenomenon. The essentially theoretical principle is the inertia of energy, made famous by Einstein's $E = mc^2$, [4]. While this is usually considered a relativistic concept, marking a break with earlier theories, the inertia of energy was obtained well before 1900 on the basis of classical optics and mechanics [5] and thermodynamics [6], showing the unity of a broad range of physics, and showing evolutionary, rather than revolutionary, aspects of the theory of relativity.

2 The early history of radiation pressure

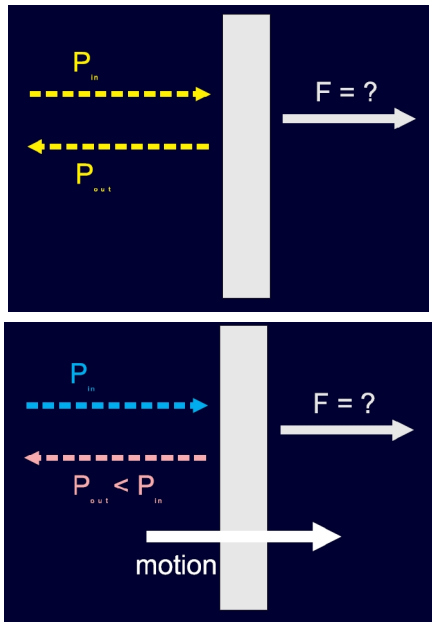
The earliest mention of radiation pressure is often said to be Kepler's suggestion that comet tails were pushed away from the sun by an emission from the sun [7]. (However, it is not clear whether Kepler meant that the force repelling comet tails from the sun was due to light, or whether his "emissions" were intended as a Cartesian explanation of what we would today call "action at a distance".) Newton used the idea of the momentum of light in his theory of the refraction of light, and was misled into believing that light travelled faster in media with higher refractive index (because the momentum of light in such media must be greater). However, he notably avoided radiation pressure as his explanation of comet tails. This may well have been due to uncertainty about the amount of momentum carried by light—all that was known was that it was, terrestrially, unobservably small. Consequently, Newton explained the fact that comet tails were directed away from the sun in terms of buoyancy in the ether which must be denser near the sun.

The first unambiguous theory of radiation pressure appears to be due to Euler, who theoretically predicted radiation pressure, on the basis of a theory of light as pressure waves in the ether (following Huyghens' theory of light) [8]. As translated by Beyer [9], Euler wrote that "While a sound vigorously excites not only a vibratory motion in the air particles, but one also observes a real motion in small, very light dust particles which tumble in the air, it cannot be doubted that the vibratory motion caused by the light produces a similar effect." It is interesting to note that radiation pressure should be expected from either the particle or the wave theories of light considered at that time. However, this appears to have been overlooked, and the lack of observed radiation pressure was used by 19th century proponents of the wave theory of light as evidence for the wave theory over the particle theory [10].

The next major step was the appearance, in quick succession, of explanations of radiation pressure based on each of classical mechanics, classical field theory, and classical thermodynamics. Unlike earlier work, all three provided correct quantitative models. The first of these was Maxwell's prediction of radiation pressure [11]. Maxwell noted that the force exerted by radiation—the momentum flux—was numerically equal to the energy density. Thus, the relationship between energy and momentum depended on the speed of the wave, with the magnitude of the momentum being

$$|\mathbf{p}| = E/c, \quad (1)$$

where E is the energy of the wave. Thus, an explanation in terms of classical field theory had arrived. Poynting and Heaviside, working independently, would clarify the transport of energy and momentum by electromagnetic fields after Maxwell's death.



Shortly after Maxwell's *Treatise* was published, Bartoli give a simple and satisfying explanation based on classical mechanics [12]. If we consider a wave incident on a stationary mirror, no work is done, and the reflected wave has the same power as the incident wave. However, if the mirror is moving, the incident wave is doing work on the mirror, and the force can be determined from the rate of doing work. The redshifts and blueshifts of the incident and reflected waves give the rate of doing work, and the force due to the radiation pressure can be found. Unsurprisingly, the quantitative result is the same as Maxwell's: the momentum and the energy are related by the speed of the wave.

The third major classical explanation was by Umov [6], who showed on thermodynamic grounds, that the transport of energy was accompanied by the transport of momentum. Again, the momentum and energy are related by the speed of the transport of energy. This was a highly significant paper, because the result is very general—it does not depend on specific details of the type of energy.

3 Non-classical theories

The non-classical parts of the branches of theoretical physics shown in Figure 1 are varied; in each branch, "non-classical" carries a different meaning. Indeed, in mechanics, we can find two different types of "non-classical" mechanics: relativistic mechanics and quantum mechanics. Both of these give rise to explanations of radiation pressure. The relativistic explanation can be stated simply as Einstein's famous $E = mc^2$ [4]. A deeper look can be taken at the energy-momentum 4-vector; the magnitude of this 4-vector is, in appropriate units, the rest mass, and we can see that any energy in motion, whether the rest mass is zero or non-zero, has momentum. Again, the result is quantitatively the same as obtained from the classical theories.

The simplest explanation from quantum mechanics is simply de Broglie's relationship between momentum $\mathbf{p}$ and wavevector $\mathbf{k}$ of matter waves [13],

$$\mathbf{p} = \hbar\mathbf{k}.$$

The story of the how we can arrive at radiation pressure from statistical mechanics is rather more complicated. Essentially, we can consider the pressure exerted by a photon gas, and the work needed to compress such a gas in reflective and absorbing/emitting cylinders. The experimental foundation is the blackbody spectrum—and we should not be surprised to find experimental foundations lurking in physics—which drove the early quantum revolution and led to the 1911 Nobel Prize in Physics being awarded to Wien. The available space does not allow a full analysis, so we must be content with the observation that the blackbody spectrum requires the aforementioned relationship between energy and momentum of light. Finally, we can turn to quantum field theory. If we identify the quantum theory of light from the development of quantum electrodynamics (QED), the 1965 Nobel Prize in Physics (Feynman, Schwinger, Tomonaga) provides a convenient date, making this the most recent of our non-classical fields of physics. However, the experimental basis (again, experimental results matter!) is older [14]. The key observation is the annihilation of particles and antiparticles; the product of this annihilation is photons, and if the consider this event in any reference frame other than the zero momentum frame of the particle/anti-particle pair, conservation of momentum requires that our initial momentum not simply disappear. Thus, the photons, the light produced by the annihilation event, must carry momentum.

Thus, we find that every major branch of physics leads to explanations of radiation pressure. As radiation pressure involves work done on matter by fields, and

therefore involves mechanics, field theory, and thermodynamics, we can readily understand this in hindsight. Nonetheless, it is surprising and interesting to discover such a range of theoretical roads which we can travel towards our understanding of radiation pressure.

Apart from modern applications of radiation forces (such as optical tweezers [2]), these theoretical roads have proved very productive. With the recognition that electromagnetic fields can carry momentum, the idea of inertia of electromagnetic energy led to the concept of electromagnetic mass, and a search for a theory uniting electromagnetics and mechanics. The unifying theory was not the theory that was expected; rather than a straightforward explanation of the origin of mass on the basis of electromagnetism, the theory that emerged was the special theory of relativity, which was unexpected in many ways, and was viewed as revolutionary. The best-known result of the theory, simply expressed as $E = mc^2$ is fundamentally a statement of the inertia of energy. The relationship between energy, (rest) mass, and momentum was concisely expressed in Minkowski's formulation of the theory.

However, this relationship, apart from the definition of rest mass as the norm of the energy–momentum 4-vector, had already been expressed by Umov [6], and was implicit in much of the other work in the field. Therefore, we can emphasise the evolutionary, rather than revolutionary, aspect of special relativity.

4 References

[1] G. Chaucer, *A treatise on the astrolabe* (1391).

[2] A. Ashkin, J. M. Dziedzic, J. E. Bjorkholm and S. Chu Observation of a single-beam gradient force optical trap for dielectric particles, Optics Letters 11, 288–290 (1986)

[3] R. N. C. Pfeifer, T. A. Nieminen, N. R. Heckenberg, and H. Rubinsztein-Dunlop, Momentum of an electromagnetic wave in dielectric media, Reviews of Modern Physics 79, 1197–1216 (2007)

[4] A. Einstein, Ist die Trägheit eines Körpers von seinem Energieinhalt abhängig?, Annalen der Physik 18, 639–643 (1905)

[5] A. Bartoli, Il calorico raggiante e il secondo principio di termodynamica, Nuovo Cimento 15, 196–202 (1884)

[6] N. Umow, Ableitung der Bewegungagleichungen der Energie in continuirlichen Körpern, Zeitschrift für Mathematik und Physik 19, 418–431 (1974)

[7] J. Kepler, *De cometis libelle tres* (Augustae Vindelicorum, Augsburg, 1619)

[8] L. Euler, Recherches physiques sur la cause de la queüe des cometes, de la lumiere boreale, et de la lumiere zodiacale, Mémoires de l'académie des sciences de Berlin, 117–140 (1746)

[9] R. T. Beyer, Radiation pressure—the history of a mislabeled tensor. Journal of the Acoustical Society of America 63, 1025–1030 (1978)

[10] J. Worrall, The pressure of light: the strange case of the vacillating 'crucial experiment', Studies in the History and Philosophy of Science 13, 133–171 (1982)

[11] J. C. Maxwell, *A treatise on electricity and magnetism* (Clarendon Press, Oxford, 1873)

[12] A. Bartoli, Il calorico raggiante e il secondo principio di termodinamica, Nuovo Cimento 15, 193–202 (1884)

[13] L. de Broglie, Recherches sur la théorie des quanta, Ann. De Phys. 3, 22 (1925)

[14] H. Kragh, *Quantum generations: A history of physics in the twentieth century* (Princeton University Press, Princeton, 1999)

Optical Torques for Alignment of Au Nanorods

Jiunn-Woei LIAW[1-2], Wei-Jiun LO[3], and Mao-Kuen KUO[3*]

[1]Department of Mechanical Engineering, Chang Gung University, Taoyuan 333, Taiwan
[2]Center for Biomedical Engineering, Chang Gung University, Taoyuan 333, Taiwan
[3] Institute of Applied Mechanics, National Taiwan University, Taipei 106, Taiwan
Corresponding author: mkkuo@ntu.edu.tw

Abstract

The optical torque exerted on a gold nanorod (Au-NR) as irradiated by a polarized laser beam is theoretically studied. Using the multiple multipole (MMP) method, the EM field around an Au-NR irradiated by a polarized plane wave is simulated, and then the wavelength-dependent optical torque in terms of Maxwell stress tensor is analysed. In addition, the plasmonic heating of the laser on Au-NR is also studied. The numerical results can help us to evaluate the resultant torque exerted on an Au-NR of specific size and aspect ratio by a laser of specific wavelength and fluence quantitatively. Our results show that the optical torque is dependent on the wavelength and the angle between the laser's polarization and Au-NR's orientation. Moreover, the optical torque depends on the size and aspect ratio of Au-NR. According to our analysis, the 1064-nm laser is applicable to rotate and align an Au-NR with less plasmonic heating.

1 Introduction

Using a focused and polarized CW laser beam to provide optical force and torque is an important approach of optical tweezers for optical manipulation and fabrication of nanostructures. Recently, this technology has been used to rotate and align gold nanorod (Au-NR), gold nanowire, silver nanorod and nanowire [1-6]. Due to the surface plasmon resonance (SPR) of Au-NR, the optical trapping and rotation of optical tweezers exerted on Au-NR are different from the dielectric anisotropic structures. For a gold nanorod (Au-NR), there are two different optical behaviours: transverse surface plasmon resonance (TSPR) and longitudinal surface plasmon resonance (LSPR), where LSPR is tuneable according to its aspect ratio (AR). The Nd: YAG laser of 1064 nm is usually used to rotate and align Au-NRs, because 1064 nm is off-resonant and red-shifted from the peak of Au-NR's LSPR so the plasmonic heating on Au-NR is very small to avoid the thermal deformation of Au-NR. In contrast, the laser of 532 nm, close to the interband transition of gold (the TSRP overlaps with the absorption band), is not suitable for the alignment of Au-NR, because the plasmonic heating is severe.

In this paper, we used MMP method to simulate the EM field of Au-NR irradiated by a plane wave. In the previous works, this method has been proven its applicability for the simulation of nanorod's optical responses [7-10]. Subsequently, we calculated the Maxwell's stress tensor of the external field to obtain the resultant torque.

2 Theory

The orientation angle of an Au-NR with respect to the laser's polarization direction is denoted by θ. For a harmonic field, the average Maxwell stress tensor T of the external field is defined as

$$\mathbf{T} = \frac{1}{2}\mathrm{Re}\left\{\varepsilon\mathbf{E}\mathbf{E}^* + \mu\mathbf{H}\mathbf{H}^* - \frac{1}{2}\left(\varepsilon\mathbf{E}\cdot\mathbf{E}^* + \mu\mathbf{H}\cdot\mathbf{H}^*\right)\mathbf{I}\right\} \quad (1)$$

where ε the μ permittivity and permeability of the surrounding medium are used. The external electric and magnetic fields are the total fields outside the nanoparticle; i.e. the combination of the incident and scattered fields. In Eq. (1), the symbol * denotes the complex conjugate, and Re is the real part of a complex number. The induced optical torque M exerted on Au-NR by the incident field are

$$\mathbf{M} = \int_S \mathbf{r}\times(\mathbf{T}\cdot\mathbf{n})ds \quad (2)$$

3 Results and Discussion

In the following simulation, the surrounding medium is water. We assume that the shape of Au-NR is a cylinder with two semi-spheres at the two ends as depicted in Figure 1. The optical torques exerted on this Au-NR of $\mathrm{AR} = 4$ and $r = 20$ nm irradiated by a laser with fluence of 25 MW/cm^2 are shown in Figure 2 for various θ (15°, 30°, 45°, 60°, 75°). In addition, the absorption efficiency is shown in Figure 3. For these cases, the order of magnitude of optical torque exerted on Au-NR is about 10^2 pN-nm. Figure 3 shows that the peak of the absorption efficiency is at LSPR, 955 nm. Both optical torque and the absorption efficiency depend on θ. The maximum torque occurs at a smaller θ. However, the plasmonic heating is more severe for a smaller θ. Moreover, the maximum optical torque can be obtained when the laser's wavelength is closed to LSPR. However, the most severe plasmonic heating is also at LSPR. Therefore, it is a trade-off problem to choose the optimal laser for rotating an Au-NR of specific size and AR. According to our analysis, the 1064-nm laser is applicable to rotate and align an Au-NR with a compatible torque and less plasmonic heating.

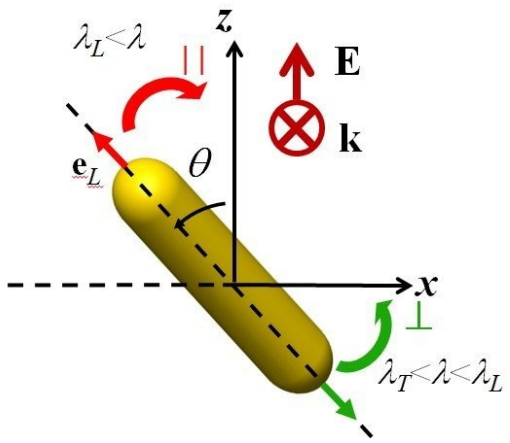


Figure 1 *Configuration of Au-NR irradiated by a z-polarized plane wave with y-incidence. The angle between the long axis of Au-NR and z axis is* θ.

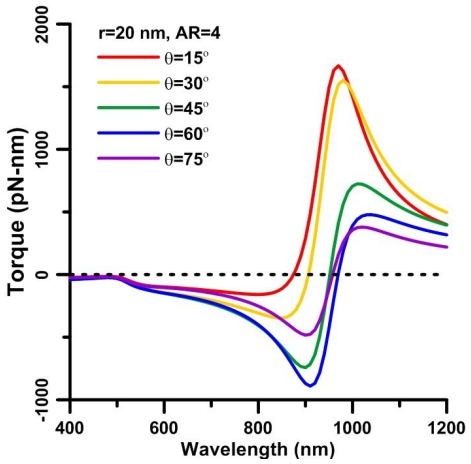


Figure 2 *Optical torque exerted on Au-NR of* $r = 20$ nm *and* $\mathrm{AR} = 4$ *at different angles in water irradiated by laser with fluence of 25 MW/cm² at various wavelengths.*

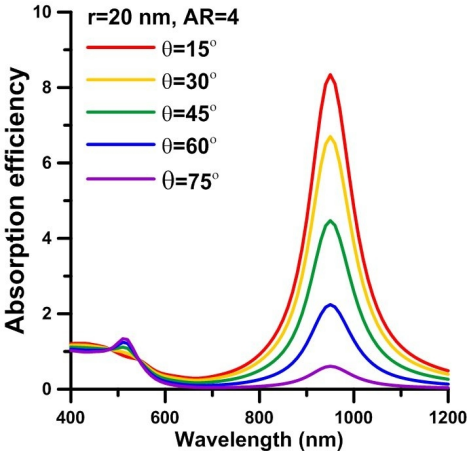


Figure 3 *Absorption efficiency of Au-NR of* $r = 20$ nm *and* $\mathrm{AR} = 4$ *at different angles in water versus wavelength.*

4 Conclusions

The wavelength-dependent optical torque exerted on an Au-NR irradiated by a polarized laser beam was studied theoretically. We used MMP method to simulate the EM field of Au-NR irradiated by a plane wave. Subsequently, we calculated the Maxwell's stress tensor of the external field to obtain the resultant torque. Our numerical results illustrate that the induced optical torque depends on the size and AR of Au-NR. For example, for Au-NR of AR= 3 and r= 20 nm with different orientations with respect to the laser's polarization, the optical torques exerted by lasers of different wavelengths were demonstrated.

5 Acknowledgement

The research was supported by National Science Council, Taiwan (NSC 102-2221-E-182-049, 100-2221-E-002-041-MY2) and Chang Gung Memorial Hospital (CMRPD 290043).

6 References

[1] Selhuber-Unkel C., Zins I., Schubert O., Sönnichsen C., Oddershede L. B., Quantitative optical trapping of single gold nanorods, Nano Lett. 8: 2998–3003 (2008)

[2] Tong L., Miljković V. D., Ka¨ll M., Alignment, rotation, and spinning of single plasmonic nanoparticles and nanowires using polarization dependent optical forces, Nano Lett. 10: 268–273 (2010.)

[3] Do J., Fedoruk M., Ja¨ckel F., Feldmann J., Two-color laser printing of individual gold nanorods, Nano Lett. 13: 4164–4168 (2013)

[4] Ruijgrok P. V., Verhart N. R., Zijlstra P., Tchebotareva A. L., Orrit M., Brownian fluctuations and heating of an optically aligned gold nanorod, Phys. Rev. Lett. 107: 037401 (2011)

[5] Yan Z., Sweet J., Jureller J. E., Guffey M. J., Pelton M., Scherer N. F., Controlling the position and orientation of single silver nanowires on a surface using structured optical fields, ACS Nano 6: 8144–8155 (2012)

[6] Yan Z., Pelton M., Vigderman L., Zubarev E. R., Scherer N. F., Why single-beam optical tweezers trap gold nanowires in three dimensions, ACS Nano 7: 8794–8800 (2013)

[7] Liaw J.-W., Chen J.-H., Chen C.-S., Kuo M.-K., Purcell effect of nanoshell dimer on single molecule's fluorescence, Opt. Express 17: 13532-13540 (2009)

[8] Liaw J.-W., Tsai H.-Y., Huang C.-H., Size-dependent surface enhanced fluorescence of gold nanorod: enhancement or quenching, Plasmonics 7: 543-553 (2012)

[9] Liaw J.-W., Huang C.-H., Chen B.-R., Kuo M.-K., Subwavelength Fabry-Perot resonator: a pair of quantum dots incorporated with gold nanorod, Nanoscale Res. Lett. 7: 546 (2012.)

[10] Liaw J.-W., Huang C.-H., Kuo M.-K., Longitudinal plasmon modes of Ag nanorod coupled with a pair of quantum dots, J. Nanosci. Nanotechnol. 13: 6627–6634 (2013)

Practical Tractor Beams

David G. GRIER* and David B. RUFFNER

Department of Physics and Center for Soft Matter Research, New York University, New York, NY 10003, USA

*Corresponding author: david.grier@nyu.edu

Abstract

A tractor beam is a traveling wave that transports illuminated objects back to its source, opposite to the direction in which the wave's energy flows. The recently developed theory of photokinetic effects clarifies the circumstances under which a collimated beam of light can act as a tractor beam. Its lessons are then used to create optical conveyors, a class of active tractor beams capable of long-range bidirectional transport [1], and solenoidal waves that act as true tractor beams with no active intervention [2]. These practical tractor beams are implemented experimentally with the holographic optical trapping technique.

1 Photokinetic Effects

The forces exerted by a beam of light on a small object arise from the object's response to the light's electromagnetic field. This field may be described with its vector potential

$$\mathbf{A}(\mathbf{r},t) = u(\mathbf{r})\, e^{i\varphi(\mathbf{r})}\, e^{-i\omega t}\, \hat{\varepsilon}(\mathbf{r}), \tag{1}$$

where $u(\mathbf{r})$ is the amplitude, $\varphi(\mathbf{r})$ is the phase, and $\hat{\varepsilon}(\mathbf{r})$ is the polarization, each of which can be controlled experimentally. Equation (1) is specialized to the case of a monochromatic wave at angular frequency ω. We will adopt the further simplifying assumption that the polarization is uniform throughout the beam, $\hat{\varepsilon}(\mathbf{r}) = \hat{\varepsilon}$, which is reasonable for a nominally collimated beam. The electric and magnetic fields are obtained from $\mathbf{A}(\mathbf{r},t)$ as

$$\mathbf{E}(\mathbf{r},t) = -\partial_t \mathbf{A}(\mathbf{r},t) = i\omega\, \mathbf{A}(\mathbf{r},t) \text{ and} \tag{2}$$

$$\mathbf{H}(\mathbf{r},t) = \frac{1}{\mu} \nabla \times \mathbf{A}(\mathbf{r},t), \tag{3}$$

where μ is the magnetic permeability of the medium.

A neutral isotropic particle couples to these fields through induced multipole moments. For small particles, this response is dominated by the electric dipole term,

$$\mathbf{p}(\mathbf{r},t) = i\omega\alpha\, \mathbf{A}(\mathbf{r},t), \tag{4}$$

where $\alpha = \alpha' + i\alpha''$ is the particle's complex polarizability, and gives rise to the time-averaged Lorentz force [3,4]

$$\begin{aligned} \mathbf{F}(\mathbf{r}) &= \frac{1}{2}\Re\left\{(\mathbf{p}\cdot\nabla)\mathbf{E}^*(\mathbf{r},t) + \mu\partial_t \mathbf{p}\times\mathbf{H}^*(\mathbf{r},t)\right\} \\ &= \frac{\omega^2}{2}\Re\left\{\alpha \sum A_j(\mathbf{r},t)\nabla\mathbf{A}_j^*(\mathbf{r},t)\right\} \\ &= \frac{\mu c}{2}\alpha'\nabla I(\mathbf{r}) + \mu c\alpha'' I(\mathbf{r})\nabla\varphi(\mathbf{r}), \end{aligned} \tag{5}$$

where

$$I(\mathbf{r}) = \frac{\omega^2}{2\mu c} u^2(\mathbf{r}) \tag{6}$$

is the local intensity. The first term in Eq. (5) is the manifestly conservative intensity-gradient force that is responsible for trapping by single-beam optical traps [5]. The second describes a non-conservative force proportional to phase gradients that describes the radiation pressure acting on the particle [6,7]. It is proportional to the momentum density carried by the beam of light,

$$\mathbf{g}(\mathbf{r}) = \frac{1}{\omega c} I(\mathbf{r}) \nabla\varphi(\mathbf{r}) \tag{7}$$

and therefore is directed substantially downstream along the optical axis. Because Eq. (5) incorporates redirection of the light's momentum by scattering, it demonstrates that beams with uniform axial intensity cannot act as tractor beams for dipolar objects. This may account for the difficulty of observing proposed tractor-beam action in uniform Bessel beams [8–10], which nonetheless may arise at higher orders in multipole scattering. Beams with axial intensity gradients, however, can take advantage of competition between trapping and radiation pressure to create tractor beams for dipolar objects.

2 Optical Conveyors

The vector potential of an optical conveyor [7] is the superposition of two coaxial Bessel beams [11],

$$\mathbf{A}(\mathbf{r},t) = u_0\, e^{-i\omega t}\left[b_1(k\mathbf{r}) + e^{i\phi(t)} b_2(k\mathbf{r})\right]\hat{\varepsilon}, \tag{8}$$

each of the form

$$b_j(k\mathbf{r}) = J_0\left(\sqrt{1-\beta_j^2}\, kr\right) e^{i\beta_j kz}, \tag{9}$$

where $k = n_m\omega/c$ is the wavenumber of light in a medium of refractive index n_m, and where β_j is a dimensionless factor with a value between 0 and 1 that reduces the axial wavenumber relative to a plane wave. Equation (9) is written in cylindrical coordinates $\mathbf{r} = (r,\theta,z)$ aligned with the $\hat{z}$ axis. The transverse amplitude profile takes the form of a Bessel function of the first kind of order zero. The two component Bessel beams differ in their axial factors, $\beta_2 > \beta_1$, so that the conveyor's axial intensity has a sinusoidal profile with maxima located at positions

$$z_n(t) = \frac{2\pi n + \phi(t)}{(\beta_2 - \beta_1)\, k} \tag{10}$$

indexed by the integer n. Applying Eq. (5), the force field associated with this intensity pattern features stable equilibria at axial positions

$$Z_n(t) = z_n(t) + \frac{\pi}{\Delta\beta k} - \frac{2}{\Delta\beta k}\tan^{-1}\left(\frac{\alpha'}{\alpha''}\frac{\Delta\beta}{2\beta}\right), \qquad (11)$$

each of which can act as a trap for a dipolar particle. Here, $\Delta\beta = \beta_2 - \beta_1$ and $\beta = (\beta_2 + \beta_1)/2$. Ramping the relative phase $\phi(t)$ translates the traps and therefore transports trapped objects.

Figure 1(a) shows the volumetric reconstruction [12] of an optical conveyor with $\beta_1 = 0.94$ and $\beta_2 = 0.96$ projected with the holographic optical trapping technique [1,13,14]. This conveyor was used to trap 1.5-μm-diameter silica spheres dispersed in water, and to transport them both up and down the optical axis over a range of more than 60 μm. Figure 1(b) shows the trajectory of one such particle measured with holographic video microscopy [15,16].

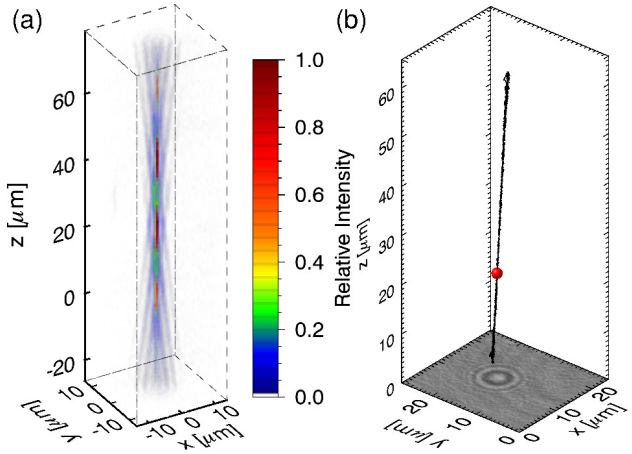


Figure 1 *(a) Measured intensity of an optical conveyor. (b) Measured trajectory of a colloidal sphere (drawn to scale) in an optical conveyor.*

Unlike an optical tweezer, whose range is inherently limited, an optical conveyor can capture objects anywhere along its length. Its interferometric structure enables it to capture both light-seeking and dark-seeking particles, as demonstrated by the existence of the solutions to Eq. (11) for all values of α' and α''. The self-healing nature of the constituent Bessel beams [17] furthermore enables a conveyor to capture multiple particles simultaneously at different positions along its length [1]. All captured particles move in the same direction and with the same speed, set by $\phi(t)$, up to a limit set by the maximum value of $\mathbf{F}(\mathbf{r})\cdot\hat{z}$.

The optical conveyor in Fig. 1 was projected with 3.5 W of light at a vacuum wavelength of 532 nm (Coherent Verdi 5W). The hologram encoding the optical conveyor was imprinted on the wavefronts of the Gaussian beam using a liquid crystal spatial light modulator (SLM, Holoeye PLUTO). The beam then was projected into the sample using a microscope objective lens (Nikon PlanApo, 60× numerical aperture 1.4, oil immersion). This system yielded a peak intensity of 0.93 mW/μm² along the axis of the optical conveyor.

The same objective lens was used to acquire in-line holograms of trapped particles using the collimated beam of a second laser at a vacuum wavelength of 447 nm (Coherent Cube) at an intensity of 8 mW/mm², roughly 5 orders of magnitude dimmer than the trapping beam. Interference between light scattered by trapped particles and the unscattered portion of the illuminating beam was recorded with a video camera (NEC TI-324A) at 30 frames/sec, and was analysed frame-by-frame with predictions of the Lorenz-Mie theory of light scattering [18,19] to obtain the particles' time-resolved three-dimensional trajectories [15,16]. These measurements yield an axial resolution of roughly 3 nm over a range of more than 100 μm [20].

The ultimate range of an optical conveyor is limited by diffraction of the Bessel beam with the smaller axial wavenumber to roughly

$$R_{\max} \le \frac{A}{\sqrt{1-\beta_1^2}} \qquad (12)$$

where A is the radius of the optical train's aperture. Truly long-range bidirectional transport therefore is possible with optical conveyors. The larger values of β_1 required for such applications limit the maximum value of $\Delta\beta$ and therefore the maximum axial force that can be applied. The ultimate limit is set by the real part of the target particle's polarizability and the influence of higher-order multipole scattering.

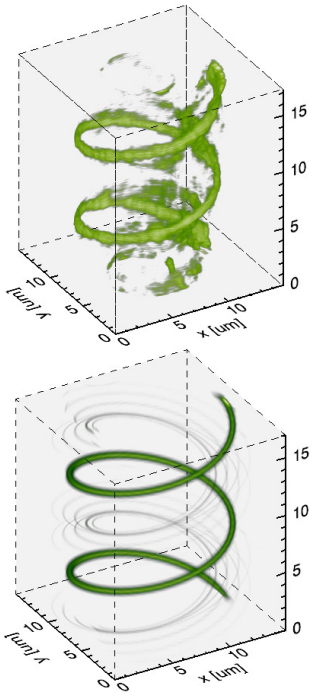


Figure 2 *Predicted and measured intensity distributions of an optical solenoid beam.*

3 Solenoidal Tractor Beams

Although optical conveyors satisfy our definition of a tractor beam, their operation requires active variation in the relative phase $\phi(t)$. An ideal tractor beam should transport material back to its source with no intervention at all. This more stringent condition is satisfied by optical solenoids [2]. Unlike conventional beams of light, the maximum intensity of an optical solenoid spirals around the optical axis in a helix of radius R and axial pitch Δz. Remarkably, these are non-diffracting solutions to the Helmholtz equation. Like optical conveyors, the vector potential of an optical solenoid beam is conveniently expressed as a superposition of Bessel modes, in this case

$$A_{\nu\ell}(\mathbf{r},t) = \sum_{m=\lfloor \ell-\nu \rfloor}^{\ell} c_{\ell m} J_m\left(\sqrt{1-\beta_{\ell m}^2}kr\right) e^{im\theta} e^{i\beta_{\ell m}kz} e^{-i\omega t}\hat{\varepsilon} \qquad (13)$$

where the expansion coefficients $c_{\ell m} = \beta_{\ell m} J_m\left(\sqrt{1-\beta_{\ell m}^2}kR\right)$ depend on the radius of the solenoid, and the axial factors $\beta_{\ell m} = (\ell - m)/(k\Delta z)$ are selected from a set that is parameterized by the solenoid's pitch. Figure 2 shows the predicted and measured intensity distributions for a typical optical solenoid described by Eq. (13).

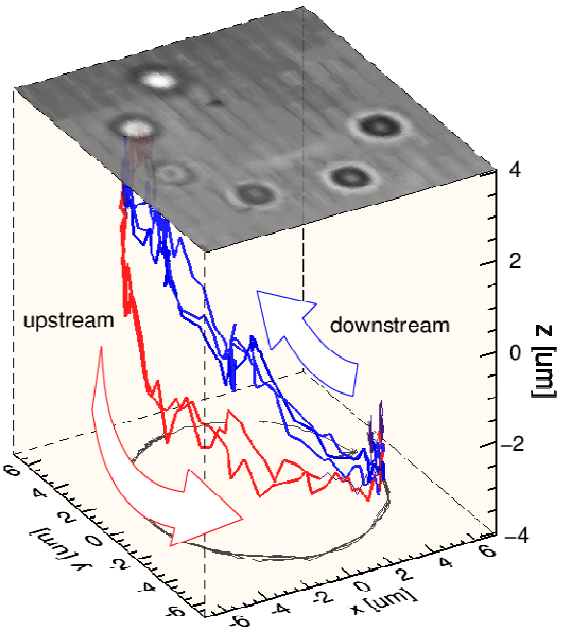


Figure 3 *Trajectory of a colloidal sphere in a solenoid beam.*

Each solenoidal mode is characterized by an integer radial index $\nu = k\Delta z$ and an azimuthal index ℓ. The azimuthal index endows solenoid's wavefronts with a helical pitch that is independent of the pitch of the intensity spiral. This helicity endows the solenoid with an orbital angular momentum density

$$\mathbf{l}(\mathbf{r}) = \mathbf{r} \times \mathbf{g}(\mathbf{r}) \qquad (14)$$

that exerts a torque on an illuminated particle at **r**. If the axial intensity gradient balances the axial component of the radiation pressure, then the transfer of orbital angular momentum can transport an illuminated object up the solenoid's helical intensity profile, thereby giving rise to retrograde motion. Because such a solenoid is a diffractionless mode, it therefore acts as a tractor beam along its entire length, with no intervention whatsoever.

The data in Fig. 3 show the three-dimensional trajectory of a 1.5 μm-diameter silica sphere in water moving along a solenoid with a radius of R = 5 μm and a pitch of Δz = 8 μm. Setting $\ell = +30$ causes the particle to spiral downstream along the optical axis. Reversing the helical pitch to $\ell = -30$ draws the bead upstream, confirming that the solenoid acts as a tractor beam. Whereas the optical conveyor requires $\phi(t)$ to be varied in order to transport material, the solenoidal tractor beam operates entirely unattended. In that sense, it is a practical realization of a true tractor beam.

4 Acknowledgements

This work was supported by the National Science Foundation by Grant Number DMR-1305875, and in part by a supplementary grant from NASA.

5 References

D.B. Ruffner, D.G. Grier, Optical Conveyors: A Class of Active Tractor Beams, Phys. Rev. Lett. 109:163903 (2012).

[1] S. Lee, Y. Roichman, D. Grier, Optical solenoid beams, Opt. Express. 18:6988–6993 (2010).

[2] J.P. Gordon, Radiation Forces and Momenta in Dielectric Media, Phys. Rev. A. 8 :14–21 (1973).

[3] P.C. Chaumet, M. Nieto-Vesperinas, Time-averaged total force on a dipolar sphere in an electromagnetic field., Opt. Lett. 25:1065–1067 (2000).

[4] A. Ashkin, J.M. Dziedzic, J.E. Bjorkholm, S. Chu, Observation of a single-beam gradient force optical trap for dielectric particles, Opt. Lett. 11:288–290 (1986).

[5] Y. Roichman, B. Sun, J. Amato-Grill, D.G. Grier, Optical forces arising from phase gradients, Phys. Rev. Lett. 100:013602 (2008).

[6] D. Ruffner, D. Grier, Optical Forces and Torques in Nonuniform Beams of Light, Phys. Rev. Lett. 108:1–4 (2012).

[7] P.L. Marston, Axial radiation force of a Bessel beam on a sphere and direction reversal of the force, J. Acoust. Soc. Am. 120:3518 (2006).

[8] J. Chen, J. Ng, Z. Lin, Optical pulling force, Nat. Photonics. 5:531–534 (2011).

[9] A. Novitsky, C.-W. Qiu, H. Wang, Single Gradientless Light Beam Drags Particles as Tractor Beams, Phys. Rev. Lett. 107:1–4 (2011).

[10] J. Durnin, Exact solutions for nondiffracting beams. I. The scalar theory, J. Opt. Soc. Am. A. 4:651-654 (1987).

[11] Y. Roichman, I. Cholis, D. Grier, Volumetric imaging of holographic optical traps, Opt. Express. 14:10907–10912 (2006).

[12] E. Dufresne, D. Grier, Optical tweezer arrays and optical substrates created with diffractive optics, Rev. Sci. Instrum. 69:1974–1977 (1998).

[13] D. Grier, A revolution in optical manipulation, Nature. 424:810–816 (2003).

[14] S.-H. Lee, Y. Roichman, G.-R. Yi, S.-H. Kim, S.-M. Yang, A. van Blaaderen, et al., Characterizing and tracking single colloidal particles with video holographic microscopy, Opt. Express. 15:18275–18282 (2007).

[15] F.C. Cheong, B.J. Krishnatreya, D.G. Grier, Strategies for three-dimensional particle tracking with holographic video microscopy Abstract :, Opt. Express. 18:13563–13573 (2010).

[16] J. Arlt, V. Garcés-Chávez, W. Sibbett, K. Dholakia, Optical micromanipulation using a Bessel light beam, 197:239–245 (2001).

[17] C.H. Bohren, D.R. Huffman, *Absorption and Scattering of Light by Small Particles* (J. Wiley & Sons, New York, 1983).

[18] M.I. Mishchenko, L.D. Travis, A.A. Lacis, *Scattering, Absorption and Emission of Light by Small Particles*, (Cambridge University Press, Cambridge, 2001).

[19] B.J. Krishnatreya, A. Colen-Landy, P. Hasebe, B.A. Bell, J.R. Jones, A. Sunda-Meya, et al., Measuring Boltzmann's constant through holographic video microscopy of a single colloidal sphere, Am. J. Phys. 82:23-31 (2014).

Optical trapping in secondary maxima of a tightly focused laser beam

Martin Šiler[1,*], Petr Jákl[1], Jan Ježek[1], Lukáš Chvátal[1] and Pavel Zemánek[1]

[1] Institute of Scientific Instruments of the ASCR, v.v.i., Brno, 61264, Czech Republic

Corresponding author: siler@isibrno.cz

Abstract

Single beam optical tweezers hold particles behind the focal plane due to the high gradients of optical intensity present in a focused laser beam. However, description of this optical field based on a vectorial theory of diffraction reveals that the high intensity focal area is accompanied by several secondary maxima on the optical axis as well as by a structure of rings away of the optical axis. Here, we discuss possibility to use these secondary maxima as the optical traps. We present the properties of such traps created by focusing using water immersion objective lens of numerical aperture 1.2.

1 Introduction

Nano- or micro-particle exposed to a focused laser light is affected by the forces originating in the transfer of light momentum. Optical tweezers [1, 2] is a tool of choice for many applications because it enables to hold and move micro particles in microscopes or lab-on-a-chip systems. The angular spectrum description of light focusing through objective lens corresponds to the Debye approximation of the diffraction of a convergent spherical wave on a circular aperture [3, 4]. In this description several oscillations of light intensity along beam propagation axis are present and in the transversal planes out of focus the light rings exist. Similarly, these rings can be also observed experimentally; however, the distribution of light intensity near focus is usually broadened and changed by the spherical aberrations originating from the refractive index mismatch in between air or immersion oil behind microscope objective and other media where observation is performed. Such aberrations may be supressed in the experiment using several methods based on a spatial light modulator [5, 6] and, therefore the spatial intensity distribution of such a beam is expected to be close to the theoretical assumption ignoring aberrations. Recently, Kyrsting et al. [7] observed a trapping of golden nanoparticles in front of beam focal plane as well as out of the beam axis. Similarly our group reported[8] trapping of air of liquid nanodroplets in in different planes and different positions with respect to beam axis using a single beam focused with a lens with low numerical aperture (NA).

In this paper, we will study the force interaction of a microparticle placed into focused laser beam described by an angular spectrum method. We will show that in this description the field near focal point includes these oscillations and rings. These inhomogeneities enhance possibilities of particle trapping and, moreover, such local maxima of intensity create several new locations, where microparticle may be trapped. We analyse occurrences and properties of these new trapping sites.

2 Beam properties and optical forces

The Debye approximation of the diffraction of a convergent spherical wave on a circular aperture [3, 4] is considered as highly appropriate for the description of a strongly focused beam without aberrations. Figure 1 shows the sections of optical intensity near focal points of objective NA = 1.2. We considered water immersion objective (n = 1.33) and wavelength λ = 1064 nm. The sections along beam propagation axis are shown in logarithmic scale while transversal sections are plotted in linear scale but normalized to one in each transversal plane. One can see that the intensity oscillates and creates sets of local maxima and minima. In the transversal direction sets of light rings are created. These rings may have high or low (even zero) intensity points on the optical axes. Moreover, the intensity of these rings is uneven and highest on the y axis, i.e. in the direction perpendicular to the beam polarization and, further, the focal spot is elliptical and tighter in the y direction.

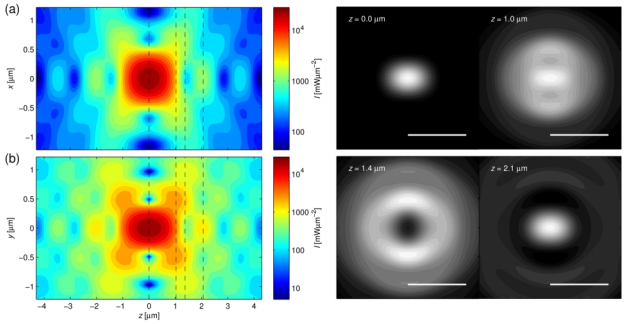


Figure 1 *(left) Optical intensity I in logarithmic scale in* x-z *(a) and* y-z *(b) planes calculated for field focused by an objective having numerical aperture NA = 1.2. Right part shows transversal sections of field (in* x-y *planes) for several* z*. Intensity in each section is normalized to 1 and white bar depicts distance of 1 μm.*

2.1 Calulation of optical forces

To express the optical force acting upon a spherical dielectric particle placed into the focused beam we use the Generalized Lorenz-Mie Theory in Barton's approach [9].

The key step is to expand the incident field into series of spherical harmonic functions which are described by the scattered field coefficients A_{lm} and B_{lm}. We have previously showed that these coefficients may be expressed analytically in case of non-diffracting Bessel beam [10]. This approach may be used even in the case of focused Gaussian beam. Therefore, the calculation of incident field coefficients requires only single numerical integration over an angular spectrum instead of triple integration including the particle surface and angular spectrum.

Figure 2 shows trajectories of particles of various radii placed into such focused beam. The trajectories were calculated numerically for motion of a single particle in force fields F_z and F_y that were calculated by the above mentioned approach. Moreover, contours depicting zero levels of these forces are shown by white and magenta curves. The intersections of both types of contours mark locations where the particle may be stably trapped. However, in order to create a trapping location the slopes of both F_z and F_y have to be negative, i.e. $\partial F_y / \partial y < 0$ and $\partial F_z / \partial z < 0$. One can see that the particle trajectories converge to these places. Parts of Fig. 2 show evolution of trajectories with changing particle radii. For the particle radius 100 nm, stable trapping locations exist in every local maximum of optical intensity, see Fig. 2 left. As the particle size increases, the weak optical gradients near maxima away from optical axis cannot trap such particle anymore and these off-axis trapping locations cease to exist, see Fig. 2 right (particle radius 400 nm) and only the trapping sites on the optical axis survive. With further increase of the particle radius, only "classical" trapping location exist nearby the focal point.

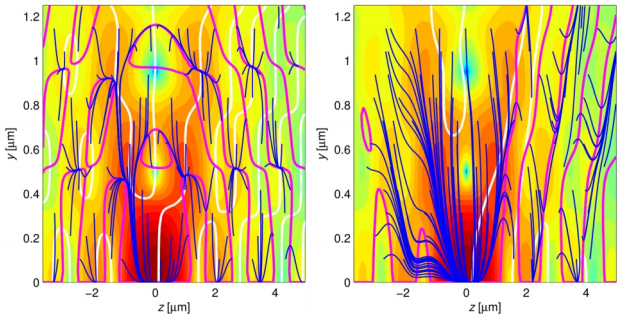


Figure 2 *Trajectories (blue curves) of polystyrene particles (n = 1.59, water immersed) in a focused beam (NA = 1.2). Particle radii are 100 nm (a) and 400 nm (b). White contours separate regions of positive or negative force* F_z *along* z*-direction and magenta contours separate regions of positive or negative radial force* F_y.

2.2 Locations of optical traps and their properties

We calculated optical forces on a regular mesh of ~ 3600 points in *y*-*z* plane for polystyrene particles having radii 25 nm up to 500 nm (step 25 nm). Further, we calculated particle trajectories in this 2D force field and we localized approximate stable particle positions. We repeated the force calculations in the vicinity of these points on finer mesh in 3D. Figure 3 shows locations of these stable points by circles of increasing sizes. We denote each of these stable particle locations according the following scheme depicted in Fig. 3, i.e. the "classical" trap site behind beam focus is labelled as "0." Other traps behind and in front of the beam focal plane are denoted by sings "+/-", respectively and increasing number indicates increasing relative distance from the focal plane. Off axis traps in the first line closest to the optical axis are denoted by letter "A" and traps in the second line are denoted by letter "B."

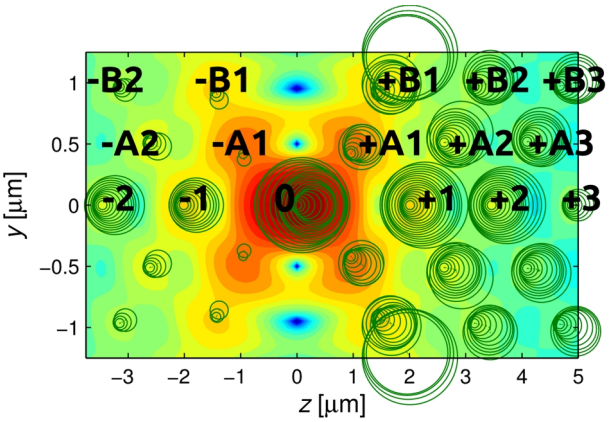


Figure 3 *Stable trapping sites in beams focused by objective lens of NA = 1.2. Background map shows the optical intensity distribution in logarithmic scale (see Fig. 1). Green circles denote the stable location of a polystyrene particle having radius 25 nm (smallest circles) up to 500 nm (largest circles). The step in particle radii is 25 nm. Trapping sites denomination is illustrated by text labels.*

Figure 3 shows that the smallest particles of radius 25 nm can be trapped in any local maximum. This is in accordance with the so-called Rayleigh approximation of optical forces which is applicable only for particles much smaller than the wavelength. The nanoparticles are held in the places of high optical intensity by gradient forces while forces caused by radiation pressure are negligible. Particles of all sizes up to 500 nm radius are trapped on the optical axis in trapping site 0. In the other axial trapping sites particles of radii up to 450 nm can be trapped in site +1, 400 nm in +2, 300 nm in -1, 275 nm in -2 and 150 nm in +3. Largest particles can be trapped off axis in trapping sites +A2 (up to 325 nm) and +B1 (up to 500 nm with a gap between 300 and 425 nm). Particles of radius only up to 225 nm can be trapped in trapping location +A1 which is the strongest of the secondary maxima out of the optical axis. This is caused by the fact that bigger particles are pulled into the main maximum 0. Only smaller particles may be trapped in front of the main maximum 0 both on and out of the optical axis. Again local gradients are overcome by the highest intensity and steepest gradient in location 0.

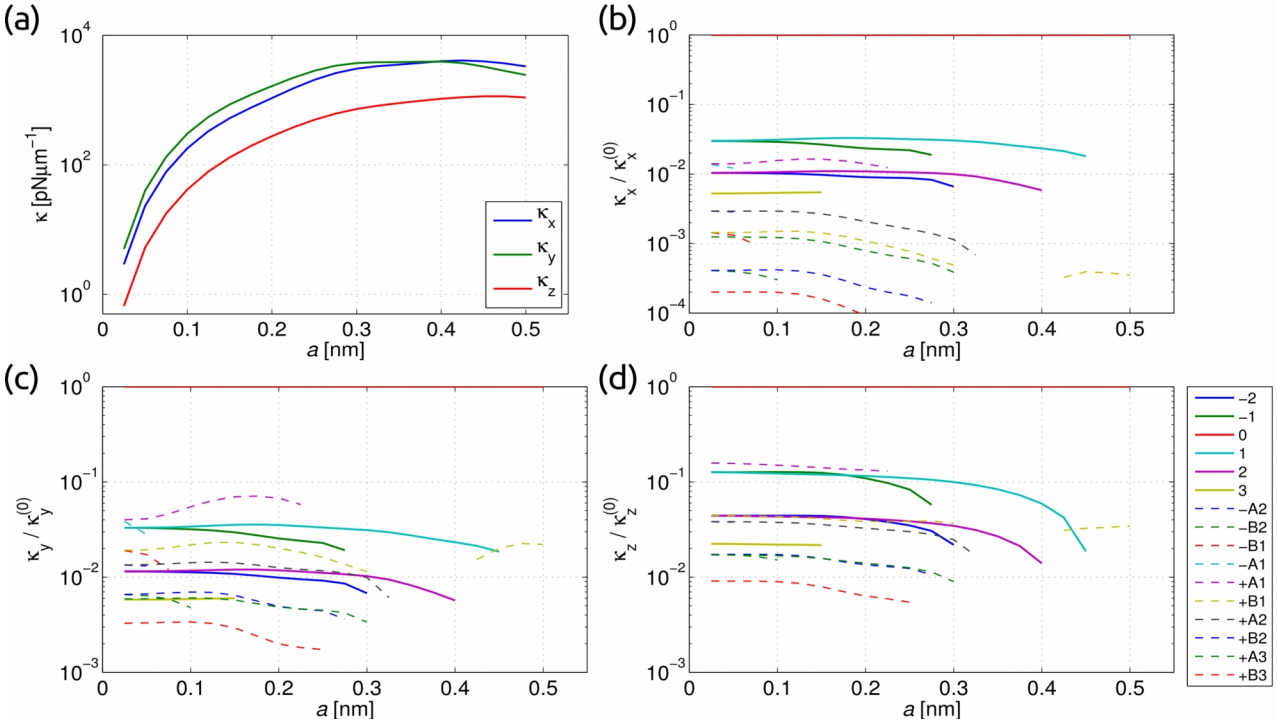


Figure 4 *(a) Trap stiffnesses in* x, y, *and* z *directions for particles of radii from 25 nm up to 500 nm placed in trapping site 0. Parts (b-d) depict relative trapping stiffnesses in various trapping sites in* x *(b),* y *(c) and* z *(d) directions, respectively.*

Further on, we calculated the trap stiffnesses $\kappa_{x;y;z}$ in the above mentioned stable locations by means of numerical differentiation. Figure 4a shows the trap stiffness $\kappa^{(0)}_{x;y;z}$ in the trapping location 0 and Figs. 4b-d show the trapping stiffnesses in the secondary trapping locations relative to the values in location 0. Solid curves show the axial trapping sites and dashed curves show the off-axis trapping sites. From the data presented in Fig. 4 we find following conclusions:

- All stiffnesses in location 0 are at least one order of magnitude higher than in any other trapping site.
- Trapping locations behind focal plane (+) are slightly stronger than locations in front of the focal plane (-).
- Highest stiffnesses in off axis traps can be found in site +A1. The stiffnesses in this site are even higher than in the secondary axial sites.
- Stiffnesses in *x* direction are almost one order of magnitude lower than in *y* direction for off-axis traps.
- This is caused by the weak gradients along light rings near these traps.
- Trap stiffnesses in *y* direction are slightly higher than in *x* direction for all axial trapping sites.

3 Conclusions

The optical intensity field near the focus of a focused beam described by an angular spectrum consists of the central maximum accompanied by several oscillations on the optical axis and several intensity rings further out of the focal plane [3, 4]. Moreover, the intensity distribution along these rings is not constant but has two local maxima in direction perpendicular to the beam polarization and the transverse intensity profile in the focal plane is elliptic. Both of these effects are connected to the focusing of the polarized light. We considered focusing by objective lens of numerical apertures NA = 1.2 (water immersion) with vacuum wavelength λ = 1064 nm.

We calculated the optical forces acting on a polystyrene particle placed in such focused beam. The local secondary maxima may serve as optical traps as well for small particles with radius smaller than λ /2. Particle may be trapped in several spots on axis either in in front or behind the beam focal plane. Also trapping spots away off the optical axis exist in a plane perpendicular to beam polarization. Compared to the "classical" trapping spot on the optical axis just behind focal plane the trap stiffnesses of these secondary maxima are at least one order of magnitude smaller. The results presented in this paper confirm experimental and theoretical observations of A. Kyrsting [7] which were obtained for golden nanoparticles. We applied this formalism to explain behaviour of water droplets in optical tweezers [8]. In our future activities we plan to confirm the results of this study by experiments.

4 Acknowledgement

The authors acknowledge the support from the Czech Science Foundation (GPP205/12/P868), Ministry of Education, Youth and Sports of the Czech Republic together with the European Commission (project No. CZ.1.05/2.1.00/01.0017).

5 References

[1] Ashkin A., Dziedzic J.M., Bjorkholm J. E., Chu S., Observation of a single-beam gradient force optical trap for dielectric particles, Opt. Lett. 11: 288-290(1986).

[2] Fazal F. M., Block S. M., Optical tweezers study life under tension, Nature Phot. 5: 318-321 (2011).

[3] Richards B., Wolf E., Electromagnetic diffraction in optical systems. 2. Structure of the image field in an aplanatic system, Proc. Royal Soc. London A 253(1274): 358-379 (1959).

[4] J.J. Stamnes J., *Waves in focal regions* (IOP Publishing, Bristol 1986).

[5] Čižmár T., Mazilu M., Dholakia K., In situ wavefront correction and its application to micromanipulation, Nature Phot. 4:388-394 (2010).

[6] Mosk A. P., Lagendijk A., Lerosey G., Fink M., Controlling waves in space and time for imaging and focusing in complex media, Nature Phot. 6: 283-292(2012).

[7] Kyrsting A., Bendix P. M., Oddershede L. B., Mapping 3d focal intensity exposes the stable trapping positions of single nanoparticles, Nano Letters 13:31-35 (2013).

[8] Brzobohatý O., Šiler M., Ježek J., Jákl P., Zemánek P., Optical manipulation of aerosol droplets using a holographic dual and single beam trap," Opt. Lett. 38: 4601-4604 (2013).

[9] Barton J. P., Alexander D. R., Schaub S. A., Theoretical determination of net radiation force and torque for a spherical particle illuminated by a focused laser beam, J. Appl. Phys. 66: 4594-4602 (1989).

[10] Šiler M. and Zemánek P., Optical forces in a non-diffracting vortex beam," Journal of Quantitative Spectroscopy and Radiative Transfer 126: 78- 83 (2013).

MAGNETIC NANOPARTICLES RING FORMATION AND DYNAMICS

Jan MASAJADA[1*] and Marcin BACIA[1]

[1] Institute of Physics, Wroclaw University of Technology, Wroclaw, 50-370, Poland

Corresponding author: jan.masajada@pwr.wroc.pl

Abstract

The holographic optical tweezers were used to show the interaction between strongly focused laser beam and magnetic nanoparticles in ferrofluid. When the light intensity was high enough magnetic nanoparticles were removed from the beam center and formed a dark ring. The same behavior was observed when focusing the vortex or Bessel beams. The interactions between two or more separated rings of magnetic nanoparticles born by independent optical traps were also observed.

1 Introduction

Ferrofluids are colloidal suspensions of magnetic particles having size about 10nm dispersed into liquid (organic or water) [1, 2]. The magnetic particles are coated with a surfactant to inhibit their aggregation and sedimentation. Ferrofluids have both liquid and magnetic properties, which are useful for various applications.

Optical tweezers are used for optical manipulation of micro and nano objects [3]. Holographic optical tweezers [4, 5] allows for creation of few tens of optical traps within the area of tightly focused laser beam. The traps can be moved independently in x-y-z direction. Different kind of traps (light, dark, Bessel) can be generated simultaneously. Figure 1 shows scheme of the holographic optical tweezers made in our laboratory. It is based on inverted biological microscope Olympus IX71. The spatial light modulator Holoeye-Pluto was used for optical traps generation. We used: laser diode 980nm with the output beam power up to 300mW. We have used beam power up to 70-100mW (measured before the microscope objective lens). The beam was focused with immersion objective Olympus UPlanFL N 100x/1.30 Oil with NA=1.3. The focused spot had radius ~2μm. The images of the sample were taken under white light illumination. We used halogen projection lamp made by Philips (type 7023).

The optical tweezers have been already used for nanofluids investigations (see [6] for references). The light action on the ferrofluids was also described in [7-9]. In paper [10] we reported on the new phenomenon discovered when investigating the ferrofluids with the holographic optical tweezers. The advantages of the holographic system are high energy density and the possibility to work with many different optical traps in the same time. We showed that when the light energy density is strong enough the magnetic nanoparticles are organized into a ring. The central part of the ring becomes transparent (the ferrofluid transparency is low). In multitrap mode each trap generates its own ring and these rings interact with each other in a complicated way.

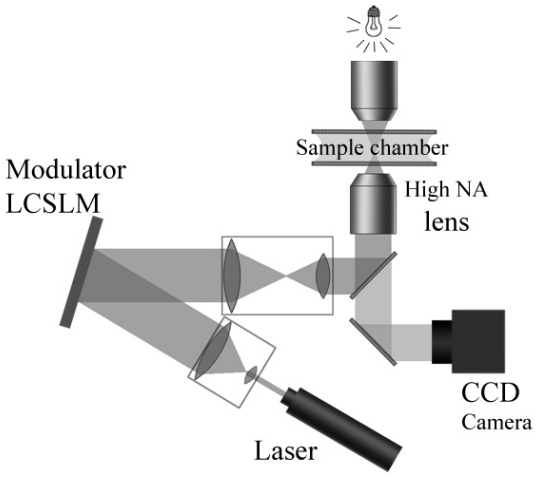


Figure 1. *Optical tweezers scheme. The optical traps were created and controlled by the spatial light modulator (LCSLM). Images were taken by camera under white-light illumination*

2 Sample results

We have observed the process of dark ring formation using fast camera (Microtron Inspecta MC1362) with a frame rate 3000fps. The ring formation appears to be very fast, because it cannot be observed even with mentioned frame rate. Time separation between frames was about 330μs and still the whole process was taking place in time when the two successive frames were captured (Fig. 2).

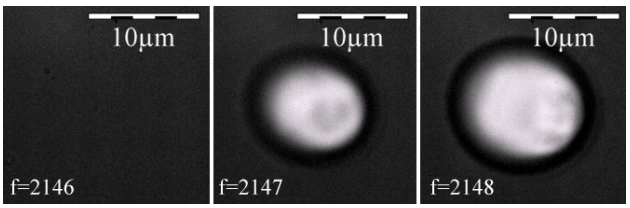


Figure 2. *Three successive frames from a movie showing flash ring formation (f on the picture is frame number)*

Another interesting feature was a light tail emerging from the dark ring (Fig. 3). The stronger laser beam was used the more often such a tail was observed. The rings were associated with a stream of nanoparticles which was particularly strong inside a bright tails.

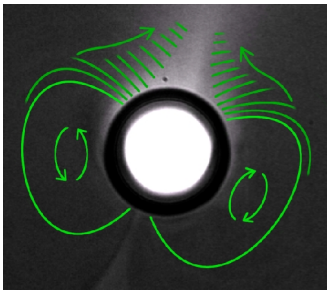


***Figure 3**. Illustration of nanoparticles transport in the ring neighbourhood areas*

Adding more traps results in similar effects. The central part of each trap becomes transparent. The transparent areas are encircled by a dark ring of magnetic nanoparticles Fig. 4

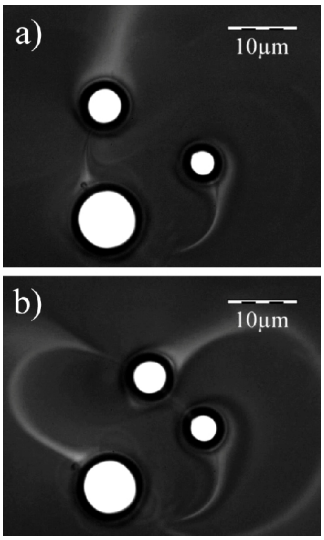


***Figure 4.** Three traps create three rings of magnetic nanoparticles. The rings interact with each other*

The dark rings are joined with the curved bright lines. These connecting lines were always observed when two or more bright spots were generated. We also observed dynamical reconfiguration of the bright lines when moving the optical trap

It is interesting that by moving the optical trap we could join and separate bright spots in a smooth way. The experiment has also showed that the dark rings geometry was changing with the geometry of the laser spot; Figure 5

In our presentation we plan to show more experimental results on the specific behavior of magnetic nano-particles in the strong laser field

3 Conclusions

We reported on the new phenomenon in ferrofluids observed with holographic optical tweezers equipped with fast video camera. The physical mechanisms that are responsible for these effects are difficult to interpret. What we could claim is that the trapping effects play a significant role in the observed phenomena. The two others groups of effects which are reported in papers devoted to dynamics observed in ferrofluids: are thermal effects and intermolecular interactions. All these effects are mutually related and the whole picture becomes complicated. At the present stage we do not offer any clear physical model for the observed effects. Our main goal was to communicate these interesting phenomena to a wider scientific audience.

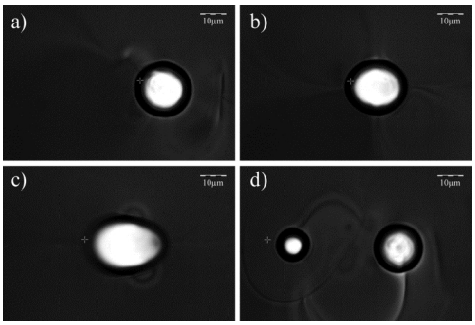


***Figure 5.** Trap overlapping experiment. a) two overlapping traps of different power formed the single bright spot; b-d the trap of smaller power was shifted left.*

4 References

[1] J. Philip, JM. Laskar, J. Nanofluids, Optical properties and applications of ferrofluids – a review, **1**, 3-20 (2012)

[2] K. Raj, B. Moskowitz, R. Casciari, J.Magn. Magn. Mater. *Advances in ferro fluid technology*, **149**, 174 (1995)

[3] D. G. Grier, Nature, *A revolution in optical manipulation*, **424**, 21 (2003)

[4] A. Jonas and P. Zemanek, Light at work: the use of optical forces for particle manipulation, sorting and analysis, Electrophoresis **29**, 4813 (2008)

[5] J. E. Curtis, B. A. Koss, D. G. Grier, *Dynamic holographic optical tweezers*, Opt. Commun., **207**, 169, (2002)

[6] T. Sugiyama, K. Yuyama and H. Masuhara, *Laser trapping chemistry: from polymer assembly to amino acid crystallization*, Accounts of Chemical Research, **45** 1946, (2012)

[7] J. Philip, JM. Laskar, J. Nanofluids, Optical properties and applications of ferrofluids – a review, **1**, 3-20 (2012)

[8] B. Hoffmann, W. Köhler, *Reversible light-induced cluster formation of magnetic colloids*, J. Magn. Magn. Mater. **262**, 289, (2003)

[9] R. R. Kellner, W. Köhler, *Short time aggregation dynamics of reversible light-induced cluster formation in ferrofluids*, J. Appl. Phys. **97**, 034910, (2005)

[10] J. Masajada, M. Bacia, S. Drobczyński, Cluster formation in ferrofluids induced by holographic optical tweezers, Opt. Lett., **38** 3910-3913 (2013)

Why do ellipsoidal particles oscillate in focused Gaussian beams?

Jean-Christophe LOUDET[1,*], Bernard POULIGNY[1] and Besira MIHIRETIE[1,2]

[1] Université de Bordeaux, CNRS Centre de recherche Paul Pascal, Pessac, 33600, France
[2] Department of Physics, University of Gothenburg, Sweden

Corresponding author: loudet@crpp-bordeaux.cnrs.fr

Abstract

Recently dielectric particles of ellipsoidal shapes have been observed to undergo sustained oscillations driven by laser radiation pressure forces and torques. We show that the observed particle dynamics can be understood through a simple ray-optics model, including the influence of beam divergence.

1 Introduction

Spherical dielectric particles are commonly manipulated with laser beams. Within certain limits (size and refractive index) a little sphere can be locked around the focus of a large aperture beam, as in optical tweezers [1]. An alternate – and historically earlier - configuration is that of optical levitation, whereby a vertical moderately focused beam is used to lift the particle against its own weight [2]. The particle may be stopped near the beam-waist: the equilibrium so obtained is not strictly stable, but may be easily maintained by tuning the laser power.

We recently carried out levitation experiments with ellipsoidal particles, and observed behaviours that were drastically different from those of spheres [3]. Below we shortly report the main experimental observations and we offer a qualitative interpretation of the observed particles dynamics.

2 Experimental hardware

The particles were fabricated starting from polystyrene spheres, 10 µm in diameter. Prolate ellipsoids (average aspect ratio $k > 1$) were generated by uniaxial stretching, and oblate ones ($k < 1$) by biaxial stretching of the spheres. We thus obtained ellipsoids with dimensions between a few µm and several 10 µm. We studied the behaviours of these particles in a classical levitation experiment, with a vertical laser beam, inside a glass cell filled with water.

The beam waist diameter was 2.6 µm, with a corresponding diffraction length ≈ 14 µm.

3 Observations

We collected many observations with particles of different aspect ratios located near the beam waist, in bulk water (true levitation configuration) and when the particle was pushed up to contact with the top boundary of the sample cell (a water-glass interface; in some experiments, a water-air or a water-oil interface). Near the beam-waist, particles which were not too far from a sphere got trapped on the laser beam axis in static configurations, with their long axes lying vertical. Conversely, we found that particles of high ellipticity, either rod-like ($k \gg 1$) or disk-like ($k \ll 1$) never came to static configurations: they were seen to undergo sustained oscillations, in the form of coupled translation and tilt motions; see Fig. 1.

Sustained oscillations were observed in all circumstances, be the particle in bulk or in contact to a boundary surface. The data evidence a bifurcating behaviour, from static to oscillating, at $k \approx 3$ for prolate particles and $k \approx 0.3$ for oblate ones. We observed oscillations that were periodic (Fig. 2), bi-periodic or irregular (Fig. 3), depending on particle parameters and position along the beam axis.

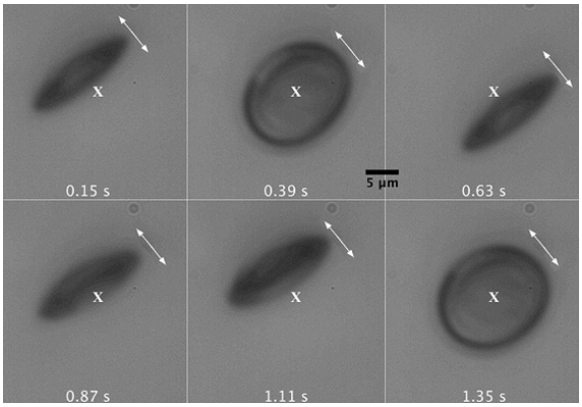


Figure 1 *Top view of an oscillating oblate ellipsoid in bulk water. The white cross 'X' – represents the position of the beam center. The arrows represent the direction of oscillation.*

3 Ray-optics model

We propose an interpretation of the observed dynamical behaviours on the basis of a simple 2-dimensional (2d) model for the interaction of an ellipsoid with light, using the ray-optics (RO) approximation. A first version of the model, for prolate ellipsoids and a simply parallel beam (as in Fig. 4 below), was reported in [3].

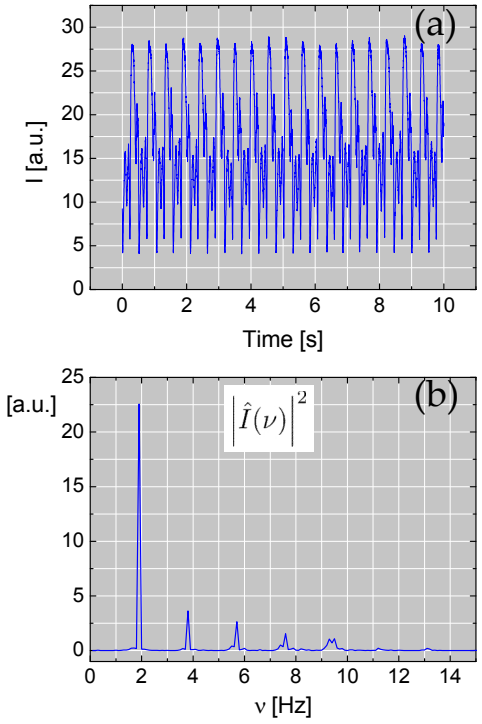


Figure 2 ***(a)*** *Example of an experimental periodic signal recorded with a photodiode analyzing the on-axis signal losses due to the scattering of light by the oscillating particle.* ***(b)*** *Corresponding power spectrum density exhibiting peaks at integral multiples of the fundamental frequency ≈ 2 Hz. Prolate ellipsoid located at the beam waist plane with aspect ratios k_1=k_2=3.8. Laser power: 19mW.*

For a given position and orientation of the ellipsoid with respect to the beam axis (see Fig. 4), we compute the radiation pressure forces (**F**) and torques (**Γ**) experienced by the particle – due to numerous momentum transfers through refraction and reflection– using standard ray-tracing algorithms. These forces and torques are then fed into the equations of motion (written in the limit of small particle tilt angle, θ << π/2) which are further integrated to access the particle dynamics. In the model we suppose that the optical forces **F** and torque **Γ** are balanced by corresponding Stokes drag terms in translation and rotation:

$$\mathbf{F}\cdot\hat{\mathbf{z}} - \tilde{m}\mathbf{g} - \varsigma_{\parallel}\dot{z} = 0 \qquad (1a)$$

$$\mathbf{F}\cdot\hat{\mathbf{x}} - -\varsigma_{\perp}\dot{x} = 0 \qquad (1b)$$

$$\mathbf{\Gamma} + \psi_{\perp}\dot{\theta}\hat{\mathbf{y}} = 0 \qquad (1c)$$

In Eqs. (1), x , z and α are the axial, transverse and angular coordinates of the particle and the dot stands for time derivative. $\varsigma_{\parallel}$, $\varsigma_{\perp}$ and $\psi_{\perp}$ are the corresponding translational and rotational drag coefficients which are available in the literature for ellipsoids. This simple model reproduces fairly well the observed bifurcation between static states and limit cycles when k increases.

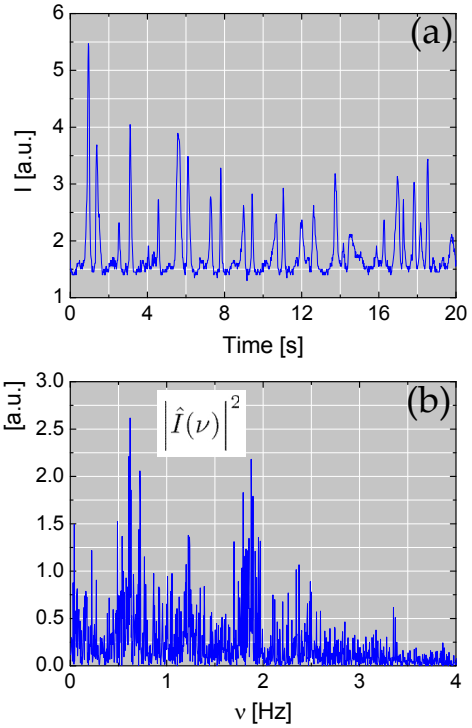


Figure 3 *Same as in Figure 2 but for a non-periodic signal obtained with a prolate ellipsoid located at the beam waist plane with k_1=5.1 and k_2=4.5.*

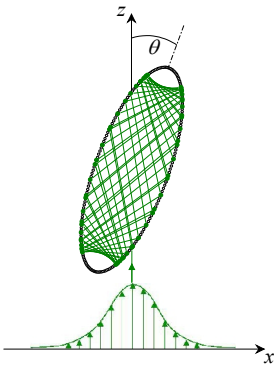


Figure 4 *2d ray optics (RO) model in the xz plane. The ellipsoid long axis makes an angle θ with respect to the z-axis. 60 reflections inside the ellipsoid are shown here for illustration. The laser beam has a Gaussian intensity profile.*

In order to explore the effect of beam diffraction, we recently generalized the simulation to the case of a divergent/convergent beam striking the ellipsoid. We still find oscillations except that the particle dynamics now depends on the particle axial position (z). State diagrams summarizing the particle dynamics in the (k, z) plane for various beam parameters will be presented. As a salient result we find that much fewer oscillating configurations

occur upon increasing the beam divergence. Occasionally, a bifurcation between two limit cycles emerges out of the calculations (Fig. 5). We also computed force and torque maps for various particle configurations (x, θ, z) and several ellipsoid aspect ratios (Fig. 6). These maps help us identify the underlying k-dependent mechanisms responsible for the onset of oscillations. In particular, the amplitude of the optical torque appears as a key parameter driving the bifurcation.

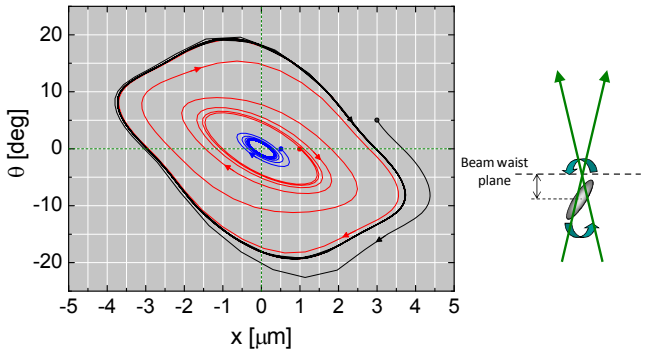


Figure 5 *Example of computed particle dynamics in phase space for two different initial conditions and for a convergent beam hitting the particle (see schematic on the right). The ellipsoid bifurcates here between two limit cycles.*

As an essential outcome, our simple RO model shows that the non linear dependence of the radiation pressure forces versus the particle position and angle coordinates is good enough to reproduce the observed oscillations.

4 Acknowledgement

This work was financially supported by ITN Comploids and Agence Nationale de la Recherche through AMOCOPS project. We thank P. Merzeau, L. Buisson, P. Barboteau, E. Texier and J.Y. Juanico for technical help.

5 References

[1] Jonáš A., Zemánek P., Light at work: the use of optical forces for particle manipulation, sorting, and analysis, Electrophoresis, 29(24):4813-51 (2008)

[2] Ashkin A., Acceleration and Trapping of Particles by Radiation Pressure, Phys. Rev. Lett. 24(4):156-9 (1970)

[3] Mihiretie B., Snabre P., Loudet J.C., Pouligny B., Radiation pressure makes ellipsoidal particles tumble, Europhys. Lett. 100, 48005-1-6 (2012); Mihiretie B., Snabre P., Loudet J.C., Pouligny B., Optical levitation and long-working distance trapping: from spheres up to large aspect ratio ellipsoids, J. Quant. Spectrosc. Radiat. Transfer 126:61-68 (2013)

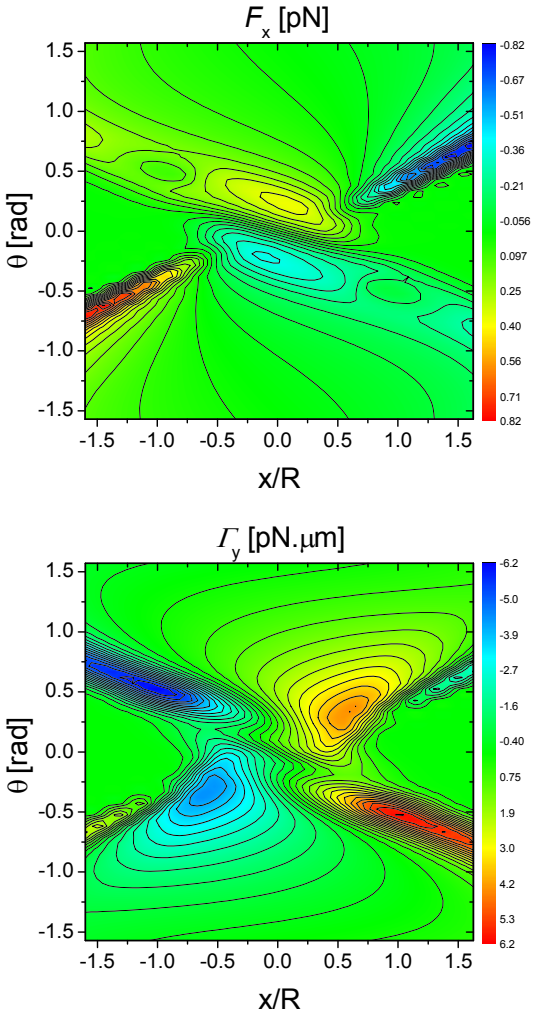


Figure 6 *Exemplary maps of total force (F_x) and torque (Γ_y) as a function of off-centering (x/R) and tilt (θ) of the ellipsoid (TE polarization mode; R is the radius of the mother sphere from which the ellipsoid is derived). The ellipsoid is located below the beam waist plane as shown in Fig. 3 (schematic). Aspect ratio k=4.25, beam waist radius w_0=1.3 μm, far-field beam divergence angle: 5.4°.*

Optical Binding and Hydrodynamic Synchronization Between Non-Spherical Colloidal Particles

Stephen H. SIMPSON[1], Stuart BOX[1], Luke DEBONO[1], Philip H. JONES[2], Onofrio M. MARAGÒ[3] and Simon HANNA [1,*]

[1] H.H. Wills Physics Laboratory, University of Bristol, Bristol, BS8 1TL, UK
[2] Department of Physics and Astronomy, University College London, London WC1E 6BT, UK
[3] CNR-IPCF, Istituto per i Processi Chimico-Fisici, I-98158 Messina, Italy

Corresponding author: s.hanna@bristol.ac.uk

Abstract

The optical binding forces and hydrodynamic coupling between clusters of non-spherical particles of varying symmetry are examined both computationally and experimentally in two systems. In one case, arrays of nanowires are examined in counter-propagating plane waves, and the conditions required for optical binding are deduced. In the other case, non-spherical "rotors" are held in an array of optical traps, and the conditions for synchronisation between different parts of the array are established. In both cases, hydrodynamic interactions play a key role in the observed dynamical behaviour.

1 Optical Binding in Nanowires and Nano-structures

Optical binding was first observed a quarter of a century ago [1]. The effect is due to optical forces arising from multiple scattering, that tend to arrange matter into regular arrays [2]. Most studies of optical binding have involved dielectric spheres [3,4]. Reduction in particle symmetry adds further complexity to these systems. Unlike dielectric spheres, torques can be generated both the external field and by the field scattered by neighbouring objects. Arranging, orienting and dispersing nanowires, and nanostructures in general is becoming an increasingly sought after goal [5,6]; optical binding provides a novel method for achieving this.

1.1 Methods

We consider high-aspect ratio dielectric nanowires of several microns length and 10 nm diameter, in counter-propagating plane waves. This is a complex, highly coupled system: the nanowires interact with the external optical field and with the surrounding fluid, but also interact optically and hydrodynamically with each other.

In our optical model, the nanostructures are represented by aggregates of small beads. The "coupled dipole method" is used to give the forces on the beads via the Lorentz force law. These contributions are summed to give the resultant forces and torques on the complete nanostructures.

For the hydrodynamic coupling, the diffusion matrix is computed for the *same* collection of beads. This is then reduced to a diffusion matrix for collection of rigid nanostructures, and then a Brownian dynamics approach is used to obtain the fully coupled deterministic motion and the thermal fluctuations.

1.2 Single nanowires

For single nanowires, the stable configurations are first established by computing the optical forces and torques as the particles are translated and rotated in the light field. The preferred orientations are determined by maximising the overlap of the particle with the intensity maxima, resulting in parallel and oblique configurations (see e.g. Figure 1). When the nanowire is wholely contained in a single intensity maximum, the polarisation direction provides a secondary orientation preference.



Figure 1 *Example configurations of nanowires in counter-propagating plane waves.*

1.3 Two or more nanowires

When two nanowires are placed side-by-side in a single intensity maximum, optical interactions are observed that cause a preference for the nanowires to orient parallel, with a separation ~0.9 times the light wavelength in the medium. As more nanowires are introduced, the preference is for them to stack, like steps on a ladder, and the nanowire separation increases slightly (Figure 2) [7].

Brownian dynamics simulations indicate that the stability of the nanowire ladder that results increases with the number of steps in the ladder, even when steps are missing. For example, two short ladders will typically coalesce to form a single long ladder, as shown in Figure 3.

Preliminary experimental studies on carbon nanotubes in counter-propagating beams have indicated the presence of optical binding [8], as have quantum mechanical calculations [9]. Work is continuing to study the influence

of particle shape and symmetry on the optical binding forces and configurations.

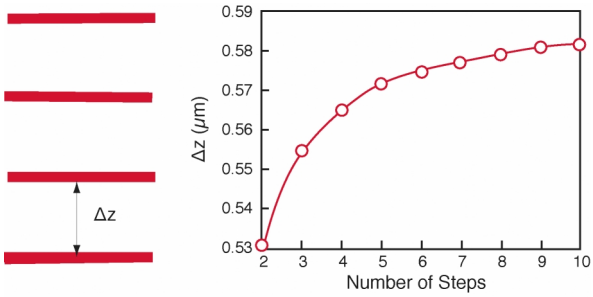


Figure 2 *Step separation in an optically bound ladder of nanowires.*



Figure 3 *Two snapshots from a Brownian dynamics simulation of two ladders, before and after coalescence. After they have merged, there is a missing step, but the longer ladder remains stable.*

2 Hydrodynamic Synchronisation

Hydrodynamic coupling plays an important role in the coordinated beating of cilia and flagellae, and is likely to play an important role in the design of future microscopic machines, artificial swimmers and pumps. A very simple model for hydrodynamic synchronization in cilia and flagellae consists of two hydrodynamically coupled spheres, following circular trajectories. The phase-locking of this system has been studied both theoretically and experimentally [10-12].

Now we consider an extension of this model to arrays of rotors. Instead of treating the rotors as spheres, we use rigid microparticles of varying symmetry, of which the simplest is approximated by an ellipsoid (see Figure 4). The rotors are fabricated using 2-photon polymerisation, and are held in an array of optical traps generated using holographic optical tweezers [13]. Rotation is induced by introducing asymmetry either into the optical fields, e.g. with Laguerre-Gaussian beams, or into the shape of the particles.

The model has been simulated using Brownian dynamics with a simplified optical force-field. Full hydrodynamic coupling has been employed using the method described in the previous section.

Both the symmetry of the particles and the symmetry of the lattice have been varied in the simulations, as have the directions of rotation e.g. co-rotating or counter-rotating in various patterns. The strength of the hydrodynamic coupling, and the resultant synchronisation, was found to depend on all of these factors. Intriguingly, specific couplings were observed between distant, but symmetrically related, rotors. For example in Figure 4, there were preferential couplings between the rotors at the corners, those along the edges of the lattice, and those in the central region.

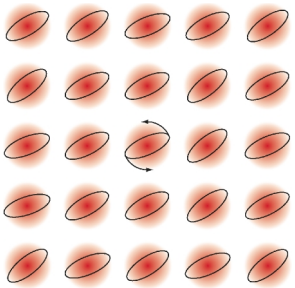


Figure 4 *Schematic showing an array of rigid rotors held in optical traps.*

Work is continuing to understand the mechanisms of phase-locking and synchronization, by drawing together the results from simulations and the ongoing experiments.

3 Acknowledgement

The authors thank the EPSRC (UK) for funding of this research and the Advanced Computing Research Centre (ACRC) of the University of Bristol for access to computing resources.

4 References

[1] Burns M.M., Fournier J.-M. and Golovchenko J.A., Phys. Rev. Lett. 63(12): 1233 (1989).

[2] Singer W., Frick M., Bernet S. and Ritsch-Marte, M., J. Opt. Soc. Am. B 20(7): 1568–1574 (2003).

[3] Karásek V., Brzobohatỳ O. and Zemánek P., J. Opt. A: Pure and Applied Optics 11(3): 034009 (2009).

[4] Čižmár T., Romero L.D., Dholakia K. and Andrews D., J. Phys. B: Atomic, Molecular and Optical Physics 43(10): 102001 (2010).

[5] Cölfen H. and Mann S., Angewandte Chemie Int. Ed. 42(21): 2350–2365 (2003).

[6] Mann S., Nature Materials 8(10): 781–792 (2009).

[7] Simpson S.H., Jones P.H., Maragò O.M., Hanna S. and Miles M.J., Proc. of SPIE 8810: 881026 (2013).

[8] Maragò O.M., Jones P.H., Gucciardi P.G., Volpe G. and Ferrari A.C., Nature Nanotechnology 8(11): 807-819 (2013).

[9] Andrews D.L. and Bradshaw D.S., Laser-induced forces between carbon nanotubes, Optics Letters 30(7): 783–785 (2005).

[10] Niedermayer T., Eckhardt B. and Lenz P., Chaos 18: 037128 (2008).

[11] Uchida N. and Golestanian R., Phys. Rev. Lett. 106: 058104 (2011).

[12] Kotar J., Debono L., Bruot N., Box S., Phillips D., Simpson S., Hanna S. and Cicuta P., Phys. Rev. Lett. 111: 228103 (2013).

[13] Phillips D.B., Padgett M.J., Hanna S., Ho Y.-L.D., Carberry D.M., Miles M.J. and Simpson S.H., Nature Photonics, in press (2014).

Scattering of Focussed Laser Beam in Zebrafish Brain

Itia FAVRE-BULLE[1,*], Daryl PREECE[1], Timo A. NIEMINEN[1], Ethan K. SCOTT[2] and Halina RUBINSZTEIN-DUNLOP[1]

[1] School of Mathematics and Physics, The University of Queensland, Brisbane, QLD 4072, Australia
[2] School of Biomedical Sciences, The University of Queensland, Brisbane, QLD 4072, Australia
Corresponding author: itia.favrebulle@gmail.com

Abstract

We study the spreading by of a focussed laser beam by scattering in a zebrafish brain. We compare experimental results and modelling using generalised Lorenz-Mie theory.

1 Introduction

Optogenetic methods use light to manipulate neural activity in genetically or functionally defined neurons with high precision. Larval zebrafish are widely used in optogenetics studies as they are easily grown, are a convenient size, and are relatively transparent. In order to study neural activity optogenetic methods use fluorescent proteins. In our study, we use GCamp5 protein. GCamp5 proteins are expressed in the zebrafish brain and convert blue light into green light when neurons are activated. As zebrafish neurons are about 5µm in size, it is essential to be able to manipulate light precisely. Indeed, focussing light on one neuron and observing firing in the whole brain (around 400×400×200 µm^3) requires a wide field of view and good 3D imaging precision at the same time. A wide enough field of view can be obtained with a 40× microscope objective. Such objectives have an Airy disk around 0.7µm. However, scattering in the brain tissue can significantly limit imaging. Here, we study the spreading by of a focussed laser beam by scattering in a zebrafish brain.

2 Experiment

A spatial light modulator (SLM) is an ideal tool for imaging, as it can be computer-controlled and used to modulate both the phase and amplitude of an incoming beam. Essentially, an SLM functions as a digital hologram. With the set-up shown in Figure 1, we can use the SLM to steer and manipulate the beam. An example of this is shown in Figure 2. Ideally, we would focus the beam so that we can excite a single neuron. However, we observe that the beam is considerably broadened by scattering in the brain tissue, with the width of the beam increasing with depth, as shown in Figure 3 and Figure 4.

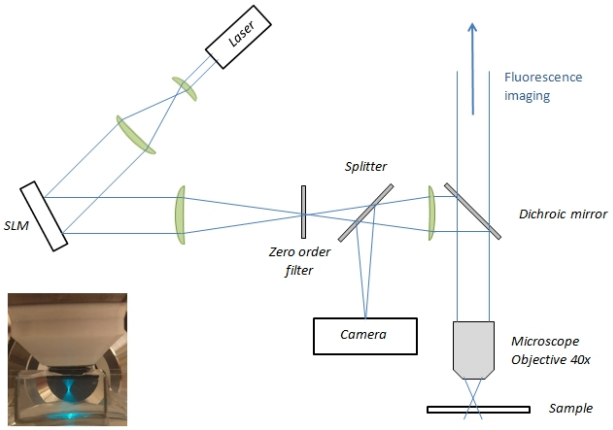


Figure 1 *Experimental set-up for optogenetics studies. A 533nm laser is used for excitation of fluorescent proteins. A beam expander collimates the light from the laser onto a spatial light modulator (SLM). A telescope configuration of lenses images the SLM screen on the back focal plane of the microscope objective. A zero order filter is placed in the first lens focal plane to stop zero order light from the SLM. Finally a beam splitter splits the light coming out from the microscope objective and scattering from the sample is measured using a CCD camera.*

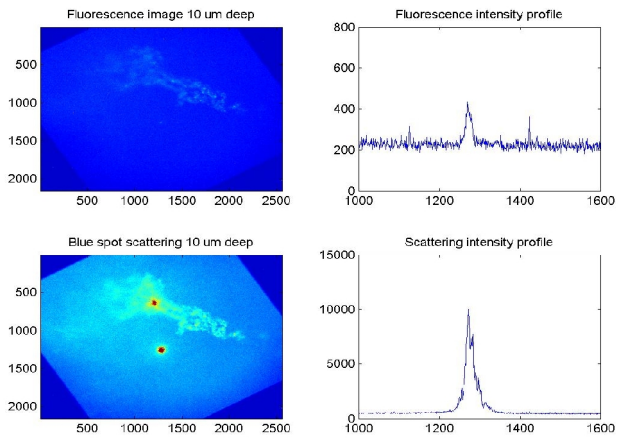


Figure 2 *Intensity profiles of a spot at the depth of 10µm in the tectum region of a zebrafish brain. Bottom left: Blue light image of the zebrafish brain; the center dark spot is the spot displayed in the brain. Bottom right: Blue light intensity profile of the spot (cut from left image). Top left: Corresponding fluorescence image. Top right: Fluorescence intensity profile of the spot (cut from left image).*

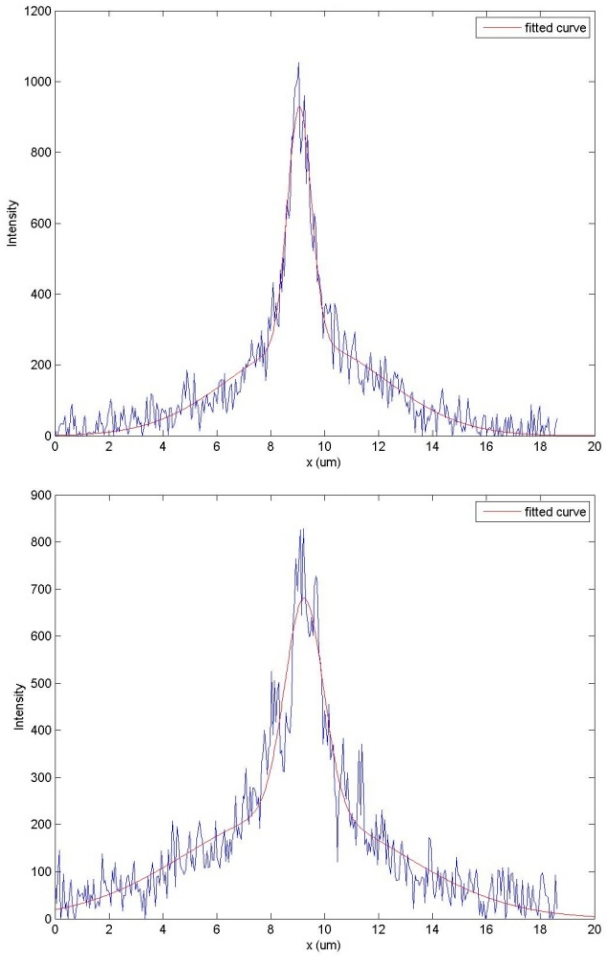


Figure 3 *Blue curves: Blue light intensity profiles for depths of 100μm deep (top) and 200μm (bottom) within a zebrafish brain. Red curves: Sum of two Gaussian curves fitted to data. The fitted curves allow us to easily quantify the width of the core and wings of the beam as it spreads.*

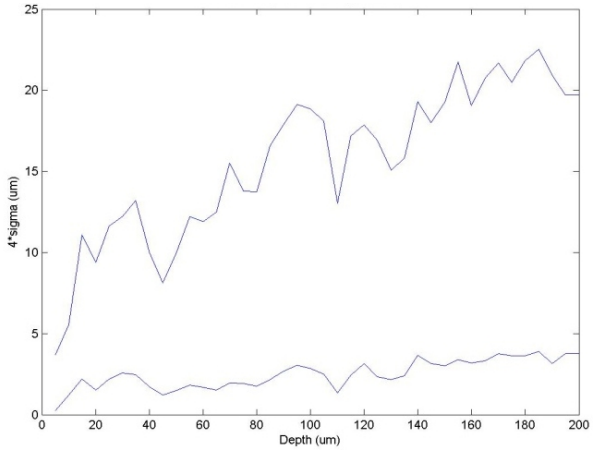


Figure 4 *Evolution of the size of each Gaussian with depth. Top curve: wider Gaussian (wings of beam). Bottom curve: narrow Gaussian (core of beam).*

3 Modelling

Compared with many animal tissues, zebrafish brain is highly transparent. However, even in the absence of absorption, there are still refractive index variations that will result in light passing through the tissue being scattered. In animal cells such as these, there are two components that dominate scattering: mitochondria, which are the main source of large-angle scattering, and nuclei, which are the main contribution to forward scattering [1]; these are the major high refractive index contrast structures within the cells. Since it is forward scattering that results in the spreading of the beam as it propagates through the zebrafish brain, a reasonable approximation of the scattering properties of the brain tissue can be obtained by modelling scattering by nuclei.

Assuming a cell density of 0.014 cells per μm^3, as measured by counting cells in microscope images, a nuclear refractive index of 1.4, a background medium refractive index of 1.36, and a mean nuclear radius of 1.25μm, we calculated the scattering and spread of a focussed laser beam of free-space wavelength 0.48μm. A simple approximation was used to model the scattering medium: we assumed that the average effect of the scattering by a volume element of the medium was the same as the scattering effect of a cell nucleus weighted by the probability of a nucleus being in that volume element.

Calculation of the spreading of the beam is shown in Figure 5. This is a first-principles calculation, with no fitted parameters. The calculation only accounts for single scattering.

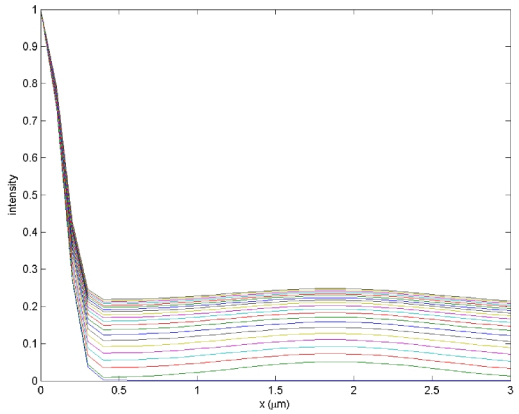


Figure 5 *Calculation of spreading of beam with propagation through zebrafish brain. Each higher line corresponds to a deeper depth, to a maximum depth of 80μm. That the broadening of the beam results from scattering of the core of the beam into the wings, with the core (other than the reduction of energy) being little affected, is clearly shown.*

The calculated spreading of the beam approximately reproduces the observed spreading. However, the calculation does not match important details. This probably indicates that either the initial parameters

assumed for the calculation are incorrect, or that multiple scattering cannot be ignored. In the first case, we can obtain more quantitative information about the scattering properties of the scattering medium by improving the match between calculations and observations. In the second case, we can, again, obtain more quantitative information about the scattering properties of the scattering medium.

4 References

[1] Drezek R., Dunn A., Richards-Kortum R. Light Scattering from Cells: Finite-difference time-domain simulations and goniometric measurements, Applied Optics 38(16) 3651-61 (1999)

POLARIZATION DEPENDENT OPTICAL TRAPPING OF CHIRAL MICRORESONATORS

M. G. DONATO[1], J. HERNANDEZ[2], A. MAZZULLA[3], C. PROVENZANO[2], R. SAIJA[4], M.A. IATI[1], A. MAGAZZÙ[1,4], P. PAGLIUSI[2,3], R. BARTOLINO[2,3], P. G. GUCCIARDI[1], O. M. MARAGÒ[1] and G. CIPPARRONE[2,3*]

[1]CNR-IPCF, Istituto per i Processi Chimico-Fisici, I-98158 Messina, Italy.
[2]Physics Department, University of Calabria, Ponte P. Bucci, Cubo 33B, 87036 Rende (CS), Italy
[3]CNR-IPCF, UOS Cosenza, Ponte P. Bucci, Cubo 33B, 87036 Rende (CS), Italy
[4]Dipartimento di Fisica e Scienze della Terra, Università di Messina, Messina, Italy

Corresponding authors: donato@me.cnr.it, gabriella.cipparrone@fis.unical.it

Abstract

We perform an experimental and theoretical investigation of the simultaneous optical trapping and rotation of spherulite-like chiral microparticles. The coupling of linear and angular momentum, mediated by the light spin and the microparticles chiral reflectance, allows for fine tuning of chirality-induced optical forces and torques. This offers novel tools for optomechanics, optical sorting and sensing, and optofluidics.

1 Introduction

The development of optical tweezers [1] (OT) brought to the exploitation of optical forces and torques in several areas as biophysics, nanotechnology, complex fluids, microrheology and microfluidics [2]. In particular, several methods have been used to induce optically controlled rotations and alignment [3]. In optical manipulation experiments, the radiation forces and torques exerted by a circularly polarized (CP) beam are generally decoupled. However, recent experiments involving chiral particles have demonstrated the occurrence of polarization-dependent radiation forces, opening a route for chiral optomechanics [4,5].

In this work, we measure optical trapping forces and torques on left-handed (L-)chiral microparticles. We optically trap spherical, non-absorbing, spherulite-like solid microparticles obtained by photopolymerization of cholesteric liquid crystal (CLC) droplets (see Figure 1). Correlation function analysis is used to measure polarization-dependent trapping forces and torques originating from the coupling between the transferred linear momentum (LM) and angular momentum (AM). From the ratio between the transverse trapping force constants of the two light CP states and rotation frequency measurements, we infer the onset of chirality-controlled photonic effects that occur for specific ratio between the particle radius and the inner helical pitch.

2 Optical trapping of chiral microparticles.

Chiral mirrors have been developed employing chiral materials such as Cholesteric Liquid Crystals (CLC) to provide additional degree of freedom for the design processes via the chirality parameter. Such CLC mirrors work differently from standard ones. In fact, depending on the left or right handed chiral structure of the CLC material, they display circular Bragg reflection, *i.e.*, CP light having the same handedness of the chiral arrangement (parallel spin) and wavelength inside a specific photonic band gap, is reflected maintaining unchanged its spin state, while light having opposite handedness (antiparallel spin) is transmitted unaffected. This feature allows the transfer of angular momentum upon reflection from the chiral mirror.

Optical trapping experiments are conducted using spherical polymeric particles with spherulite-like arrangement in which the inner structure consists of supramolecular helices originating from the centre (see Figure 1). The molecular director spontaneously twists about a direction perpendicular to the long molecular axis with a pitch, p, defined as the distance over which the director rotates 2π. This helicoidal arrangement leads to Bragg reflection for light propagating along the helical axis and wavelength within the stop band (Fig. 1a, inset). Reflectance depends on the microparticles radius R_0.

Optical trapping is carried out at different wavelengths (λ=830 nm and λ=785 nm), both of them fulfilling the selective reflection condition. The optical forces and torques on trapped particles are measured by detecting the thermal fluctuations and light-induced rotations by back focal plane interferometry on a quadrant photodiode (QPD). The particle tracking signals are then processed by correlation function analysis [3]. The autocorrelation functions (ACFs) of the signals give a full account of the particle translational and rotational motion in the optical trap. In fact, thermal positional fluctuations of the trapped particle are described by a Langevin equation [3] and yield a single exponential decay in the ACFs. Moreover, rotations about the z-axis appear on the transverse fluctuating signals on the QPD, yielding a cosinusoidal modulation in the transverse ACFs [3]. Thus we have:

$$C_{ii}(\tau) \approx A\left(k_B T/\kappa_i\right)e^{-\omega_i \tau} + B\cos(\Omega\tau) \qquad (1)$$

where $\omega_i=\kappa_i/\gamma$ (i=x,y,z) are relaxation frequencies related to the trap spring constants κ_i and viscous translational damping $\gamma=6\pi\eta R_0$, with η=1.002 mPa s for water at 20

°C. For rotating particles, the fit of ACFs with Eq. 1 gives a direct measurement of the particle rotational frequency, Ω, which is used to evaluate the averaged optical torque transferred to the trapped particle. Since Ω is set by the equilibrium between optical and rotational drag torques, the optical torque modulus, Γ^{+}_{rad}, is equal to the rotational drag torque on a sphere rotating in a fluid at low Reynolds number, $\Gamma_{drag} = 8\pi\eta R_0^3\Omega$ [6].

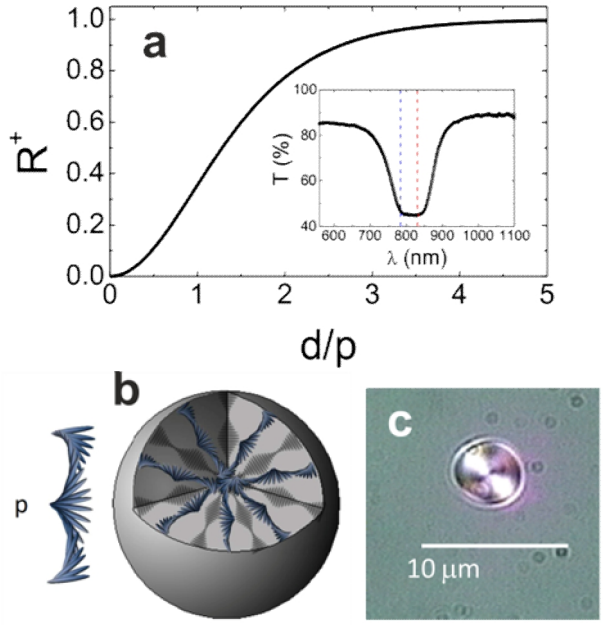


***Figure 1**. **a,** Calculated reflection, R^+, from an L-chiral layer with pitch p and variable thickness, d (Eq. 2) and measured transmission spectrum of a polymerized CLC film for linearly polarized light and a thickness 20 μm (inset). The dashed lines are trapping wavelengths used in the optical trapping experiments. **b,** Sketch of a polymeric particle with spherulite-like (radial) configuration of the helical structure. **c,** Optical microscope image of the particle between crossed polarizers.*

The dynamics of about twenty different micro-particles, trapped by right-handed CP (RCP) and left-handed CP (LCP) light, has been investigated as a function of their size. We observe that for RCP light, the particles are always trapped independently of their size and do not rotate. When the polarization state of the trap is switched to LCP, a size dependent behaviour occurs. In particular, the particles with R_0 >2 μm are expelled from the trap; when R_0 <1 μm they are trapped and do not rotate. For 1<R_0<2 μm the micro-particles are trapped and simultaneously rotate. Thus, depending on the particle size, two main phenomena originate from the interaction between chiral particles and light carrying spin angular momentum (SAM). The first one is related to the optical forces, that can be attractive or repulsive depending on the light spin state. The second one is related to the optical torque that originates from chirality mediated transfer of SAM.

We acquired five tracking signals for each trapped particle and each polarization state, averaging the results on all measurements made for each particle. In particular, by applying ACFs analysis to each tracking signals we get the transverse optical force constants for each spin state, κ^+ (LCP) and κ^- (RCP). Thus, the change in the averaged transverse force constant, $\kappa^{\pm} = (\kappa_x^{\pm} + \kappa_y^{\pm})/2$, is obtained as a function of particle radius.

Figure 2a shows the ratio κ^+/κ_- as a function of the particle radius normalized to the trapping wavelength. This gives a direct evidence of the coupling between spin and optical trapping forces. In fact, as the particle radius grows and the selective reflectance increases, the trapping force constants κ^+ lowers with respect to κ^- due to the consequent increase of the scattering force. In particular, for particles with $R_0/\lambda < 1$ (corresponding to R_0 < 1.6 *p*) the chiral structure is just formed or even absent. Thus, the reflectivity R^+ is negligible (Fig. 1a) and we expect the trapping forces to be independent on the light spin state, *i.e.* $\kappa^+ \cong \kappa^-$. On the contrary, when the particle radius grows so that enough chiral layers are formed, photonic effects become relevant and the net optical trapping force exerted by LCP beam is lower than the one with opposite spin. In fact, in the former case a portion of the impinging power is selectively reflected increasing the detrimental effect of the radiation pressure on the trapping itself. Thus, the force constant degeneracy is lifted and $\kappa^+ < \kappa^-$. In the limit case of a perfect chiral photonic structure (R^+=1, T^+=0) the total optical force of LCP light field becomes negative because only the radiation pressure due to the reflected light is present. Trapping of such particles with LCP light beam is not possible [4,5]. Thus transmitted light transfer only LM, and AM transfer occurs by the light reflected from the L-chiral microparticles. This, in turn, causes a torque on the particle itself, yielding a stable rotation. The effect can occur only if the total LM exchanged preserves the trapping action of the light beam. The size-scaling of the ratio κ^+/κ^- (Fig. 2a) and the radiation torque displays this behaviour, *i.e.*, the onset of spin-dependent optomechanics.

We model optical trapping forces in our experiments using both a ray-optics approach [7] and exact electromagnetic calculations based on the use of the Maxwell stress tensor in the T-matrix formalism [8,9]. The chiral polymer refractive indices, $n_{\parallel}$ and $n_{\perp}$, at each trapping wavelength are evaluated by the Cauchy formula. In the case of LCP light, the Fresnel reflection coefficient (Fig. 1) near the centre of the stop band strongly depends on the effective thickness of the chiral polymer layer, *d*, so that the reflectance is:

$$R^+ = \left[\tanh(\beta d)\right]^2 \qquad (2)$$

where

$$\beta = \pi(n_{\parallel}^2 - n_{\perp}^2)\sqrt{2}/2\lambda(n_{\parallel}^2 + n_{\perp}^2)^{1/2} \quad (3)$$

For radially isotropic particles the presence of the defect in the centre of the precursor droplet breaks the photonic structure. As a consequence, the thickness we need to consider to correctly model the photonic effects for the spherical particle is close to R_0. Additionally, a form factor of 2/3, related to the spherical shape, must be also considered. Thus, R^+ for the radial particles is evaluated by using an effective thickness $d=(2/3)R_0$ in Eq. 2. We used these values of reflectance and transmittance to calculate optical forces on the chiral particles in ray optics calculations. Results are shown as the green dashed line in Fig. 2a. The discrepancy between experiment and theory is accounted for the inadequacy of the ray-optics approach for a truthful description of optical forces [10]. A more accurate approach is based on T-matrix formalism. For RCP illumination, particles are modelled as homogeneous dielectric with a real refractive index, $\bar{n}=(n_{\parallel}+n_{\perp})/2$, whereas, for LCP illumination, they are considered as core-shell particles[46]. In the latter case, the core has a real refractive index $n_{core}=\bar{n}$, while the reflecting properties of the chiral microresonators are embedded in the thin shell having a complex size dependent refractive index, $n_{shell}=n(R_0)[1+i\alpha]$, that is needed to model the size dependent reflectance (based on Eq. 2) of the chiral particles. T-matrix calculation gives a very good agreement with experimental results (solid green line in Figure 2a). In addition, the measured torque for LCP light is compared with the torque calculated using the reflectance from Eq. 2 and a T-matrix based calculation. Again, the T-matrix approach gives a better agreement with experimental data.

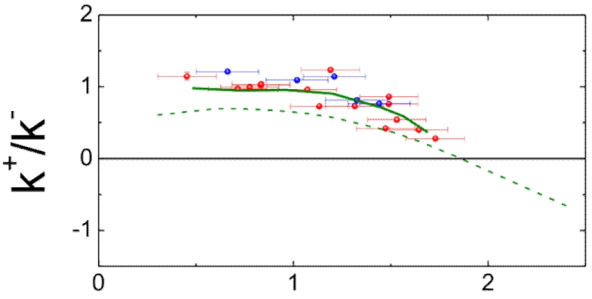


Figure 2 : *Onset of chiral optomechanics. Lines are calculations obtained by ray-optics (dashed green line) and exact T-matrix (solid green line) modeling of optical forces on spherical particles.*

3 Conclusions

In conclusion, we have reported an experimental investigation of polarization-dependent optical forces and torques on chiral microparticles. We have observed optomechanical effects originating from the coupling of transferred LM and AM mediated by the particle chirality. We have shown simultaneous optical trapping and rotation connected to light spin selective reflection exhibited by the chiral particles and their control by means of the particle reflectance and light spin. Chirality-controlled optical trapping and manipulation opens novel strategies for optomechanics and optical sorting. The method used to create chiral microparticles allows for embedding resonant nanoparticles at the central defect, with prospects for microcavity optomechanics.

4 References

[1] Ashkin, A., Dziedzic, J. M., Bjorkholm, J. E., Chu, S. Observation of a Single-Beam Gradient Force Optical Trap for Dielectric Particles, Optics Letters 11(5):288–290 (1986).

[2] Maragò, O. M., Jones, P. H., Gucciardi, P. G., Volpe, G., Ferrari, A. C. Optical trapping and manipulation of nanostructures, Nature Nanotechnology 8:807-819 (2013).

[3] Jones, P. H., Palmisano, F., Bonaccorso, F., Gucciardi, P.G., Calogero, G., Ferrari, A.C., Marago, O.M. Rotation detection in light-driven nanorotors. ACS Nano 3(10):3077–3084 (2009)

[4] Hernández, R. J., Mazzulla, A., Pane, A., Volke-Sepúlveda, K., Cipparrone, G. Attractive-repulsive dynamics on light-responsive chiral microparticles induced by polarized tweezers, Lab on a Chip 13: 459 (2013).

[5] Cipparrone, G., Mazzulla A., Pane A., Hernandez R.J., Bartolino R., Chiral Self-Assembled Solid Microspheres: a novel multifunctional microphotonic device. Adv. Mater. **23**, 5773 (2011).

[6] Nieminen, T. A., Asavei, T., Loke, V. L. Y., Heckenberg, N. R., Rubinsztein-Dunlop, H. Symmetry and the generation and measurement of optical torque. Journal of Quantitative Spectroscopy & Radiative Transfer **110**, 1472–1482 (2009).

[7] Ashkin, A. Forces of a single-beam gradient laser trap on a dielectric sphere in the ray optics regime, Methods in Cell Biology 55:1–27 (1998).

[8] Borghese, F., Denti, P., Saija, R. & Iatì, M. A. Optical trapping of non-spherical particles in the T-matrix formalism, Optics Express 15:11984–11998 (2007).

[9] Borghese, F., Denti, P., Saija, R., & Iati, M. A. Radiation torque on nonspherical particles in the transition matrix formalism, Optics Express, 14:9508-9521 (2006).

[10] Nieminen, T. A., Stilgoe, A. B., Heckenberg, N. R., & Rubinsztein-Dunlop, H. H. (2010). Approximate and exact modeling of optical trapping. In SPIE NanoScience + Engineering (art. 77622V).

THE ESCAPE OF SPHERES FROM OPTICAL TWEEZERS

Alexander B. STILGOE[1], Nima KHATIBZADEH[2], Ann A. M. BUI[1,*], Timo A. NIEMINEN[1], Michael W. BERNS[2-3], and Halina RUBINSZTEIN-DUNLOP[1]

[1] School of Mathematics and Physics, The University of Queensland, St Lucia, 4072, Australia
[2] Beckman Laser Institute and Medical Clinic, University of California, Irvine, 92612, USA
[3] Institute of Engineering in Medicine, University of California, San Diego, 92093, USA

Corresponding author: a.bui@uq.edu.au

Abstract

Force calibration of optical tweezers allows quantitative force measurements. Here we investigate the escape force calibration method, which finds the escape force from the escape velocity. It was found that sphere escapes from the trap on a different path depending on how long it takes to reach escape velocity. Escape force varies to about 30 percent, dependent on how fast the escape force is applied.

1 Introduction

Optical tweezers use scattering and gradient forces to trap microscopic particles in a laser beam. The optical forces are on the piconewton scale, which is ideal for cellular environments. Calibrating optical tweezers allows one to quantify the forces acting in such environments. In the central trapping region, the force can be approximated as that of a linear spring as shown in Figure 1. The calculations are done for a 4.5 micron diameter polystyrene bead in water. The linear approximation breaks as the particle reaches the limits of the trap at the peaks. It is this force at the peak that tells us the greatest force that could be exerted by the trap onto that particle. Beyond the peaks, the particle is no longer trapped.

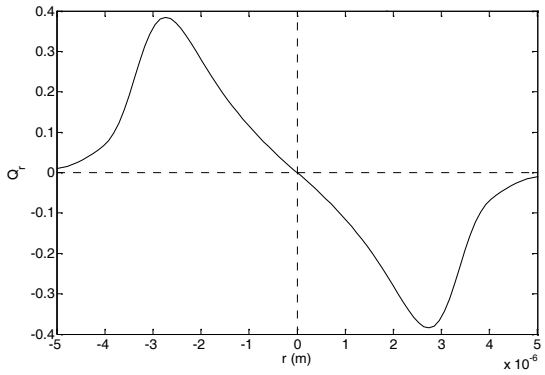


Figure 1 *Lateral force-position curve. This the (dimensionless) force exerted on a 4.5 micron polystyrene bead in water. At the centre of the trap, there is no force acting on the particle, thus is stably trapped there. As the particle moves away from the centre, along a lateral axis (r), the lateral optical force (Q_r) increases roughly linearly. The peaks represent the greatest force of the trap on such a particle.*

To find a relation like that of Figure 1, the trap needs to be calibrated. There are several calibration methods. The escape force method calibrates a trap by using the viscous drag of the medium to see how much force is required for the particle to escape from the trap. This is shown in Figure 2.

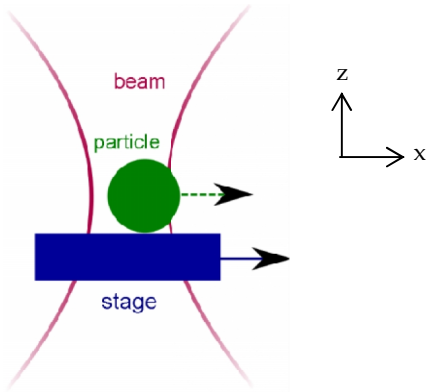


Figure 2 *Escape force calibration of the trap. A bead is trapped then the stage, with the surrounding medium, is moved with the viscous drag force pushing the bead out of the trap, thus finding its escape force. It is generally assumed that this escape force corresponds to the peak forces of Figure 1.*

To find the escape force, a bead is first trapped in a medium, such as water. The stage is moved to drag the particle out of the trap. The stage velocity, $\mathbf{v}$, corresponds to a drag force, $\mathbf{F}$, which is related through Stokes' law: $\mathbf{F} = \Gamma\mathbf{v}$. In general, Γ is the particle's drag tensor, but in this case for a spherical bead, we have a scalar where $\Gamma = 6\pi\eta r$ where η is the dynamic viscosity of the medium and r is the radius of the bead.

It was noticed that experimental measurement of escape force on cylinders, then checked with spheres, did not line up with the usual force-position curve, like Figure 1. The escape force was lower than expected.

Here, we use simulation to vary the time it takes for the stage to reach escape velocity, from rest; equivalent to varying how long it takes to apply the drag force.

2 Experiment

The experiment involved trapping the bead and moving the stage until that the particle can no longer follow the trap. To find the escape velocity, the position of

the particle and position of the stage can be tracked. The stage velocity increases linearly with time. The escape of the particle can be determined as the point where the particle's position changes from being relatively still around the centre of the trap to following the quadratic motion of the stage. This is more obvious when looking at its time derivative, i.e. velocity, as the particle's velocity will change from almost zero to increasing linearly to match the stage velocity. Experiments are done by accelerating a stage. Viscous drag force is applied to the trapped particle due to relative motion of the fluid around the particle. The experiment was performed by two groups. The acceleration rates for the stage to reach escape velocity, from rest, were 1×10^{-6} ms^{-2} and 8.33×10^{-5} ms^{-2}, which are close to the slower limit.

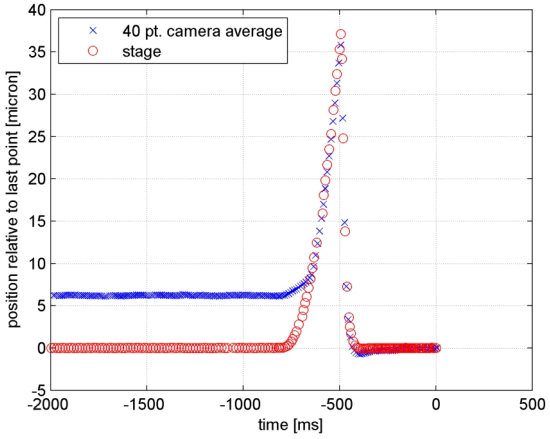


Figure 3 *Tracking position of particle and stage. The particle position has been shifted so that the escaped part lines up with the stage. This is done for analysis purposes.*

However, the experimental calibration does not tell us the greatest possible force in trap: it tells us how much force was required to remove the particle from the trap, which may still be the greatest force for that run, but the runs change. Unlike experiment, with simulation, it is straightforward to record force and position for the entire escape.

3 Simulation

We simulate the behaviour of a bead and a trap with the T-matrix method with the toolbox [1]. The position of the particle, $\mathbf{x_i}$, can be described as

$$\mathbf{x_i} = \mathbf{x_{i-1}} + \mathbf{\Gamma}^{-1}\,\mathbf{f_o}\,\mathbf{x_{i-1}} + \mathbf{g} + \mathbf{v_{i-1}}\,\Delta t \qquad (1)$$

where $\mathbf{\Gamma}$ is the particle's drag tensor, the position is altered by the optical force, $\mathbf{f_o}\,\mathbf{x_{i-1}}$, the gravitational buoyancy of the particle in the medium, $\mathbf{g}$, and the velocity of the stage, $\mathbf{v_{i-1}}$. These forces act for a time interval of Δt. The difference between experiment and simulation is that the simulation can record position and forces acting on the particle for the entire run, thus revealing the escape trajectories, as in Figure 4. We can see that the particle does not come out of the trap on-axis, as would be suggested by the usual force-position curve like Figure 1.

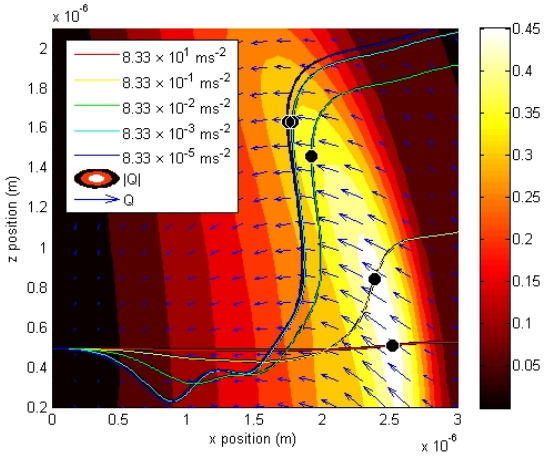


Figure 4 *Particle doesn't come straight out of the trap. If escape force applied slowly, tends to follow the zero contour out of the trap. If escape force applied quickly, tends to go straight out of the trap. This is for a 4.5 μm particle escaping from a 4 mW trap.*

By varying the acceleration of the stage, the time taken to apply the escape force is varied. In Figure 4, we can see that for greater accelerations, red curve, the particle escapes almost straight out of the trap, the hard trajectory. This corresponds to a force curve which essentially matches the expected force curve, red curve in Figure 5.

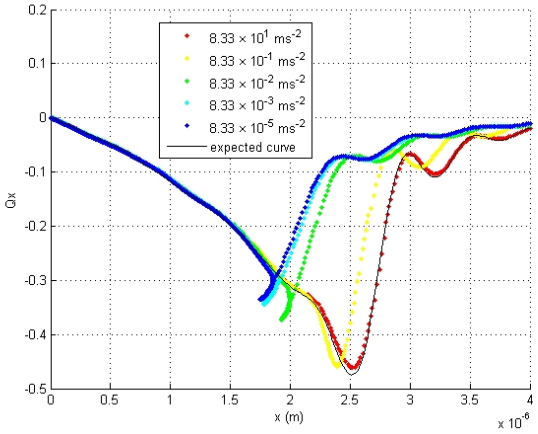


Figure 5 *Variation of escape force (Q_x) for different rates of applying the escape force. For fast force (red), the particle escapes along axis and almost matches the expected curve in Figure 4. For slow force (blue), the particle does not escape along axis and we see the resulting lower magnitude of Q_x which occurs earlier along the transverse axis.*

However, consider the case of slow acceleration, i.e. the drag force is increased slowly, blue curves. The particle does not go straight out of the trap, but instead has a trajectory following lowest axial force, the easy trajectory. The effect of this trajectory deviation on the escape force

can be seen in Figure 5. The slow curve, blue, has its greatest force earlier and of smaller magnitude than the fast curve, red.

For accelerations between the two extremes (yellow, green and cyan curves), the trajectories and forces also lie somewhere between those two corresponding extremes.

We can see that there is a general curve for the escape Q over different accelerations, which under scaling, is common over trapping powers, as shown in Figure 6. This shows that there is a variation of about 30 % for the value of the escape Q, dependent on how quickly the escape force is applied.

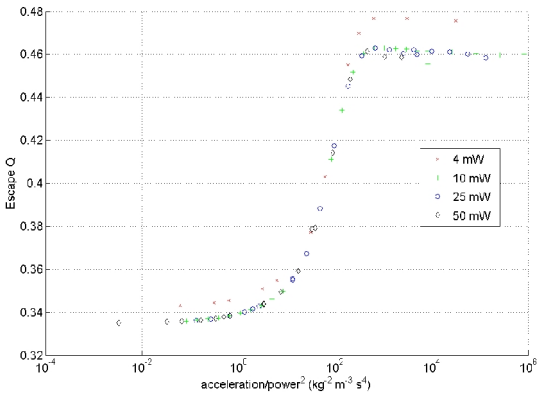


Figure 6 *The high and low escape Q corresponds to the hard and the easy trajectory. This is the 4.5 µm particle escaping from a trap with different trapping powers. The same high and low escape Q exists for different trapping powers.*

4 Conclusion

Escape force calibration of optical tweezers does not necessarily give the greatest possible force from the trap onto the particle, but actually gives the greatest force as the particle escapes from the trap. There are the two extreme rates of applying escape force, with most resulting in trajectories and escape force values between the two corresponding to the extreme rates. Which trajectory we want and the importance of such choice depends on how the calibration will be used: do we just wish to find how much force there is when we pull something out or do we wish to find the greatest force applied by the trap?

5 References

[1] Nieminen T.A, Loke, V.L.Y., Stilgoe, A.B., Knöner, G., Brańczyk, A.M., Heckenberg, N.R., Rubinsztein-Dunlop, H. , Optical tweezers computational, Journal of Optics A: Pure and Applied Optics 9(8): S196-S203 (2007)

Brownian Motion in Speckle Light Fields: From Anomalous Diffusion to Optical Manipulation

Giorgio VOLPE[1*], Giovanni VOLPE[2,3] & Sylvain GIGAN[1]

[1] Institut Langevin, UMR7587 of CNRS and ESPCI ParisTech, 1 rue Jussieu, 75005 Paris, France
[2] Soft Matter Lab, Physics Department, Bilkent University, Cankaya, 06800 Ankara, Turkey
[3] UNAM – National Nanotechnology Research Center, Bilkent University, Cankaya, 06800 Ankara, Turkey

Corresponding author: giorgio.volpe@espci.fr

Various phenomena rely on particles performing stochastic motion in random potentials. Examples range from the nanoscopic world of molecules undergoing anomalous diffusion within the cytoplasm of a cell [1] to the Brownian motion of stars within galaxies [2]. Another example of this kind of phenomena is given by the motion of a Brownian particle in a random optical potential generated by a speckle pattern, i.e., the random light field resulting from complex light scattering in optically complex media, such as biological tissues, turbid liquids and rough surfaces (see background in Figure 1a-c) [3-4]. This latter example is particularly suited to work as a model system because its parameters (e.g, particle size and material, illumination light) are easily controllable and its dynamics are easily accessible by standard optical microscopy techniques [5]. Earlier experimental works showed the possibility of trapping particles in high-intensity speckle light fields [6-9], the simplest optical manipulation task, and the emergence of superdiffusion in an active media constituted by a dense solution of microparticles that generates a time-varying speckle field [10]. However, apart from these previous studies, there is little understanding of the interaction of Brownian motion with random light potentials and the intrinsic randomness of speckle patterns is largely considered a nuisance to be minimized for most purposes, e.g., in optical manipulation [11-12]. In fact, similar and even more complex effects have been extensively studied using periodic potentials rather than random potentials: these studies include the observation of giant diffusion induced by an oscillating periodic potential, and the demonstration of guiding and sorting particles using either moving periodic potentials [13-15] or static periodic potentials in microfluidic flows [16-18]. It is not a priori obvious that the same phenomena that have been observed with periodic potentials can also arise with random potentials, as the statistical properties of random potentials fundamentally differ from those of periodic potentials. For example, in non-equilibrium statistical physics, the dynamics of a Brownian particle in a moving periodic potential can be described as a straightforward generalization of the dynamics of a Brownian particle in static not out-of-equilibrium potentials, while this is no longer the case for random potentials for which a full out-of-equilibrium description is still required [19].

Here, we study the Brownian motion of a particle in a speckle pattern and, in particular, we derive the characteristic timescale τ of such motion [21], which is universal as it depends only on the universal properties of speckle light fields[3]. This theoretical insight permits us to demonstrate both theoretically and experimentally that random potentials can also be used instead of more regular potentials to control the dynamics of a Brownian particle in a very accurate way, despite their intrinsic randomness. First of all, while the emergence of superdiffusion in time-varying speckle patterns has already been observed [10], we demonstrate that speckle fields provide a tunable and controllable model system to study anomalous diffusion by relating τ to the emergence of subdiffusion and superdiffusion in time-varying speckle patterns. Moreover, we demonstrate the possibility of harnessing the *memory effect* of speckle fields to perform basic optical manipulation tasks such as guiding and sorting, which go beyond selective optical trapping in high-intensity speckle grains [7-8].

References

[1] Barkai, E., Garini, Y., & Metzler, R. Strange kinetics of single molecules in living cells, *Phys. Today* **65**, 29-35 (2012).

[2] Chandrasekhar, S. Brownian motion, dynamical friction, and stellar dynamics, *Rev. Mod. Phys.* **21**, 383-388 (1949).

[3] Goodman, J. W. Some fundamental properties of speckle, *J. Opt. Soc. Am.* **66**, 1145 1150 (1976).

[4] Mosk, A. P., Lagendijk, A., Lerosey, G., & Fink, M. Controlling waves in space and time for imaging and focusing in complex media, *Nature Photon.* **6**, 283-292 (2012).

[5] Babic, D., Schmitt, C., & Bechinger, C. Colloids as model systems for problems in statistical physics, *Chaos* **15**, 026114 (2005).

[6] Boiron, D., *et al.* Trapping and cooling cesium atoms in a speckle field, *Eur. Phys. J. D* **7**, 373-377 (1999).

[7] Shvedov, V. G., *et al.* Laser speckle field as a multiple particle trap, *J. Opt.* **12**, 124003 (2010).

[8] Shvedov, V. G., *et al.* Selective trapping of multiple particles by volume speckle field, *Opt. Express* **18**, 3137-3142 (2010).

[9] Staforelli, J. P., Brito, J. M., Vera, E., Solano, P., & Lencina, A. A clustered speckle approach to optical trapping, *Opt. Commun.* **283**, 4722-4726 (2010).

[10] Douglass, K. M., Sukhov, S., & Dogariu, A. Superdiffusion in optically controlled active media, *Nature Photon.* **6**, 834-837 (2012).

[11] Čižmár, T., Mazilu, M., & Dholakia, K. *In situ* wavefront correction and its application to micromanipulation, *Nature Photon.* **4**, 388-394 (2010).

[12] Dholakia, K., & Čižmár, T. Shaping the future of optical manipulation, *Nature Photon.* **5**, 335-342 (2011).

[13] Ricárdez-Vargas, I., Rodríguez-Montero, P., Ramos-García, R., & Volke-Sepúlveda, K. Modulated optical sieve for sorting of polydisperse microparticles, *Appl. Phys. Lett.* **88**, 121116 (2006).

[14] Demergis, V., & Florin, E.L. High precision and continuous optical transport using a standing wave optical line trap, *Opt. Express* **19**, 20833-20848 (2011).

[15] Šiler, M., Čižmár, T., & Zemánek, P. Speed enhancement of multi-particle chain in a traveling standing wave, *Appl. Phys. Lett.* **100**, 051103 (2012).

[16] McDonald, M.P., Spalding, G.C., & Dholakia, K. Fractionation of polydispersed colloid with acousto-optically generated potential energy landscapes, *Nature* **426**, 421-424 (2003).

[17] Milne, G., Rhodes, D., McDonald, M., & Dholakia, K. Microfluidic sorting in an optical lattice, *Opt. Lett.* **32**, 1144-1146 (2007).

[18] Xiao, K. & Grier, D.G. Multidimensional optical fractionation of colloidal particles with holographic verification, *Phys. Rev. Lett.* **104**, 028302 (2010).

[19] De Groot, S.R. & Mazur, P. *Non-equilibrium thermodynamics* (Dover, New York, 1984).

[20] Volpe, G., Volpe, G., & Gigan, S. Brownian motion in a speckle light field: Tunable anomalous diffusion and selective optical manipulation, *Sci. Rep.* **4**, 3936 (2014).

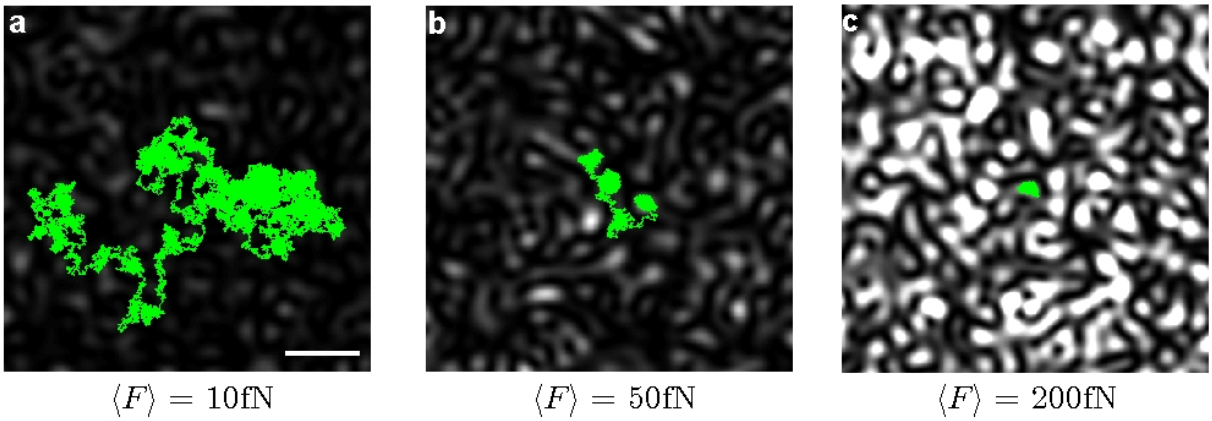


Figure 1: *Subdiffusion in a static speckle pattern. (**a-c**) The background represents a speckle pattern generated by a circular aperture (λ = 1064 nm, speckle grain 490 nm); the white scale bar corresponds to 2 μm. The trajectories (green solid lines) show progressive confinement of a polystyrene bead (R = 250 nm, n_p = 1.59) in water (n_m = 1.33, η = 0.001 Ns/m², T = 300 K) as a function of the increasing speckle intensity corresponding to an average force on the particle of (**a**) <F> = 10fN, (**b**) <F> = 50fN, (**c**) <F> = 200fN.*

Theoretical Aspects of Single-beam Multitrapping Acoustical Tweezers

Glauber T. SILVA[1,*]

[1] Physical Acoustics Group, Institute of Physics, Federal University of Alagoas, Maceió AL, 57072-900, Brazil

Corresponding author: glauber@pq.cnpq.br

Abstract

The concept of a multitrapping acoustical tweezer based on a focused ultrasound beam is presented and theoretically investigated. The beam is described in the paraxial approximation and it is generated by a concave transducer. The resulting focused beam exerts a radiation force on a small particle that is much smaller than the incident wavelength (i.e. the so-called Rayleigh scattering regime). It is shown that several trapping points are developed in the pre-focal zone (i.e. the region between the transducer and its geometric focus point) along the beam axial direction. Additionally, the possibility of using a zeroth-order Bessel and a Gaussian focused beam as a multitrapping acoustical tweezer is analysed.

1 Introduction

Noncontact particle handling based on optical [1] and acoustica [2] radiation forces is promoting a revolution in biotechnlogy and biomedical applications. In acoustics, different schemes to produce the radiation force such as standing wave [2] and focused beams [3] have been employed or proposed. Recently, Mitri [4] demonstrated that a negative acoustic radiation force (i.e. the radiation force and the wave propagation are in opposite directions) can be produced by a circular piston radiator on a sphere in the source nearfield at different depths along the beam axis. This result has motivated us to analyse the possibility of producing an acoustical tweezer with multitrapping points in 3D.

In particular, we are interested on investigating if an ultrasound focused beam can trap small particles (i.e. the particle is much smaller that the incident wavelength) in the pre-focal zone. This leads to the concept of single-beam multitrapping acoustical tweezer. Obviously this device has an advantage of trapping different particles simultaneously at different depths by the acoustic radiation force generated with the ultrasound focused beam.

In this work, a theoretical analysis of the radiation force of a multitrapping acoustical tweezer acting on a small particle (fused quartz and benzene) suspended in water is performed through computational simulations. An spherically focused ultrasound transducer uniformly excited generates the incident beam. The particle can be located anywhere in the radiated ultrasound field. Moreover, nonuniform excitation of the transducer is used to produce focused zeroth-order Bessel and Guassian beams.

Resuts show that several trapping points (axially and transversely) arise in the pre-focal zone of the transducer. In addition, we will discuss the stability of the trapping points in terms of the particle parameters such as density, compressibility, and ultrasound absorption.

2 Acoustic radiation force on a Rayleigh particle

The acoustic radiation force arises on the suspended particle due to the momentum transferring from the incident beam to the particle. In second-order approximation of the pressure amplitude, the radiation force is the result of the normal component of the radiation stress tensor integrated over the particle surface. It can be shown that in the Rayleigh scattering regime, the acoustic radiation force exerted on a particle has three components as follows [5] $\boldsymbol{F}^{\mathrm{rad}} = \boldsymbol{F}^{\mathrm{abs}} + \boldsymbol{F}^{\mathrm{grad}} + \boldsymbol{F}^{\mathrm{scat}}$, where $\boldsymbol{F}^{\mathrm{abs}}$ is due to ultrasound absorption in the particle, $\boldsymbol{F}^{\mathrm{grad}}$ depends on the gradient of the acoustic potential and kinetic energy densities of the incident beam, and $\boldsymbol{F}^{\mathrm{scat}}$ is related to the scattered waves by the particle. Both absorbing and scattering radiation forces depend on the time-averaged incident intensity.

To calculate the acoustic energy density and the intensity of the incident beam to the particle for a concave transducer, we use the integral solution for a focused beam in the paraxial approximation given in Ref. [6].

3 Numerical results and conclusion

To illustrate the feasibility of multitrapping acoustical tweezer, we compute the axial and transverse radiation force on benzene droplet of radius suspended in water. The radius of the droplet is 58 mu m. The focused transducer has aperture 50 mm and curvature radius of 70 mm. The transducer is driven at 1 MHz.

In Fig. 1, we show the axial radiation force. We notice three trapping points in the pre-focal zone. The scattering and the absorbing radiation forces push the particle forwardly along the beam propagation direction. This tends to weaken the axial stability of the

trapping points. In this case, these forces are too weak to break the axial stability seen in the pre-focal zone.

In conclusion, feasibility of a single-beam multitrapping acoustical tweezer was theoretically demonstrated. We believe that this concept represents an advance in the design of acoustical tweezer devices.

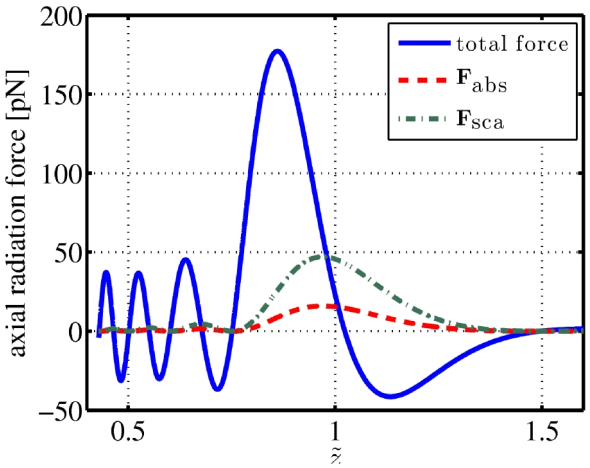


Figure 1 *The axial radiation force exerted by a focused beam on a benzene droplet. In the pre-focal zone ~z < 1, we notice at least three trapping points. The absorbing and the scattering radiation forces are also illustrated.*

4 Acknowledgement

This work was supported by grant n.o 481284/2012-5 CNPq (Brazilian Agency).

5 References

[1] D. G. Grier, A revolution in optical manipulation, *Nature* 424:810-816 (2003).

[2] J. Wu, Acoustical tweezer, *J. Acoust. Soc. Am.* 89:2140 (1991)

[3] J. Lee, S.-Y. The, A. Lee, H. H. Kim, C. Lee, K. K. Shung, Single beam acoustic trapping, *Appl. Phys. Lett.* 95: 073701 (2009).

[4] F. G. Mitri, Near-field single tractor-beam acoustical tweezer, *Appl. Phys. Lett.*103:114102 (2013).

[5] G. T. Silva, Acoustic radiation force and torque on an absorbing compressible particle in an inviscid fluid, ArXiv:1307.4705v2 [physics.class-ph] (2014).

[6] B. G. Lucas and T. G. Muir, The field of a focusing source, *J. Acoust. Soc. Am.* 72:1289 (1982).

Kramers escape rate of Silicon Nanowires in a double optical trap

A. MAGAZZU[1,2,*], C. J. RICHARDS[3], T. J. SMART[3], A. IRRERA[1], M. G. DONATO[1], F. PRIOLO[4], P. G. GUCCIARDI[1], O. M. MARAGÓ[1] and P. H. JONES[3,*]

[1] CNR-IPCF, Istituto per i Processi Chimico-Fisici, Messina, Italy
[2] Dottorato in Fisica, Università di Messina , Messina, Italy
[3] Department of Physics and Astronomy, University College London, London, UK
[4] Matis CNR-IMM and Dipartimento di Fisica, Università di Catania, Catania, Italy
Corresponding authors: mago.alex@gmail.com, philip.jones@ucl.ac.uk

Abstract

We studied, by videomicroscopy, thermally activated hopping of Silicon Nanowires (SiNWs) in a bistable potential well. We investigated how the activated hopping depends on the SiNWs length, inter-well distances and optical intensities.

1 Introduction

Optical tweezers (OT) are powerful tools to understand, detect and measure forces in soft-matter systems at the micro and nanoscale [1]. They are commonly used in areas as diverse as biophysics, colloidal physics, and hydrodynamics of small systems.

A particle optically trapped in a potential well is subject to the stochastic forces due to the surrounding medium in thermal equilibrium (Brownian motion). If the force fluctuations are strong enough the trapped particle can escape in the course of time by overtaking the potential barrier. In 1940 H. A. Kramers [2] first studied and calculated the probability of escape depending on temperature, for known the viscosity of the medium surrounding the particle. This scenario becomes still more interesting if we consider a set of two closely-separated traps that give rise to a double-well potential. In this case the trapped particle will feel an energy barrier between the two traps that depends on the separation, *d*, of the two traps, and on the height of the potential wells. This scenario represents an activated escape from a metastable state and is currently used as a suitable model for physical, chemical, and biological processes.

Kramers in 1940 also presented a quantitative calculation of the residence time in a double-well potential for spherical particles, immersed in a fluid of known viscosity.

2 Kramers escape rate of Silicon Nano Wires in a double optical trap

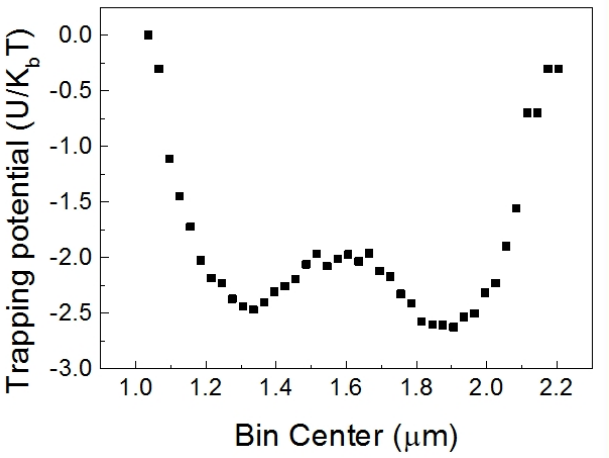
McCann et al [3] made an experimental verification of the Kramer's escape rate of a colloidal spherical particle by observing the dynamics of the particle in a double-well formed by two closely-separated optical tweezers. Subsequently Hayashi et al experimentally investigated the variation in escape rate for various particle sizes, inter-well distances and optical intensities, suggesting that the differing Kramers esacape rates could be applied to particle sorting. Starting from these works we created a double optical tweezers in order to study the Kramers rate of non-spherical particles. Differently to spherical particles, non-spherical particles in an optical tweezers experience a non-negligible non-conservative contribution to the optical force [4] which may be expected to alter their dynamics in this potential landscape.

A double optical trap has two equilibrium positions specified by the locations of the laser foci. For a small potential barrier between the traps a trapped particle will have bistable dynamics that will be crucially depend on parameters such as laser power, distance between the traps, relative intensity (trap depth) and size of the trapped particle. In our expriment we created a double optical trap by focusing two parallel laser beams through a single objective lens creating a bistable three-dimensional potential well. The laser source used during our experiments was a Nd:YAG with a wavelength of 1064nm, and maximum power of 3W, of which at most 80mW was used to make the optical traps. In this double optical trap the particle feels both the potential minima, and it hops continuously back and forth between them, as illustrated in Figure 1. The two samples investigated consisted of ultra-thin silicon nanowires (SiNWs) with a diameter of 10 nm and nominal lengths of 3.6μm and 5.3μm respectively [5,6]. We studied how the activated hopping depends on the SiNWs length, inter-well distances and optical intensities.

Because a theory for the Kramer's escape rate of non spherical particles is currently lacking, we used the representation developed for spherical particles [1,2]:

$$\tau = \frac{2\pi\gamma_{\perp}}{\omega_b \omega_a} \exp\left(\frac{\Delta E}{K_B T}\right) \qquad (1)$$

Where $\gamma_{\perp}$ is the viscous drag coefficient for a rod moving perpendicular to its axis, and ω_b and ω_a are the associated quadratic frequencies of the potential $U \propto 1/2\omega^2 x^2$ at position x_a and x_b.



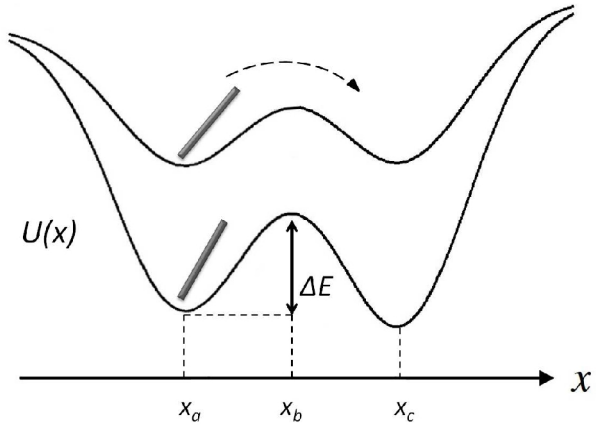


Figure 1: Hopping motion of a SiNW in a double well potential

Tracking signals of the particle hopping motion were, acquired by videomicroscopy and subsequent particle tracking analysis. An example of the position track obtained in this way is shown in Figure 2. The profile of the optical potential was then calculated as:

$$U(r) = -K_B T \ln \rho(y) \qquad (2)$$

Where $K_B T$ is the thermal energy, and ρ(y) the frequency of points recorded in the tracking signal at location r., an example of which is shown in Figure 3.

Figure 2: *Experimental videomicroscopy tracking signal of a 2.17 um long SiNW in a double optical trap.*

Here we report on the first observation of Kramer's escape rate of non-spherical particles in a double optical trap. We find that the dwell times for SiNWs in the two traps scales exponentially with the trapping power and with the distance, d, between the two potential wells, Figure 4. This is easily understood because when the energy barrier decreases, it is more probable that fluctuations of the Brownian motion transfer to the particle the minimum momentum required to overcome the energy barrier.

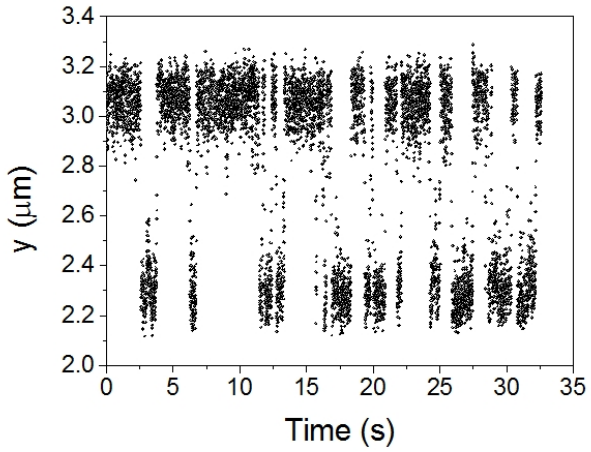


Figure 3: *Trapping potential at d=0.9 um for a 5.3 um SINWs*

This is easily understood because when the energy barrier decreases, it is more probable that fluctuations of the Brownian motion transfer to the particle the minimum momentum required to overcome the energy barrier. This result is in accord with the theoretical prediction for spherical particles [7]. When the length of the SiNWs increases the situation becomes more complex. We noted that that the distance at which the bistable behavior has been noticed increases with the SiNWs length. This is because the longer SiNWs exceed the size of the laser waist. This fact, in conjunction with the radiation pressure, and with a misalignment with the optical axis, promotes the escape of the SiNWs from the rear of a trap and it is immediately trapped by the adjacent trap.

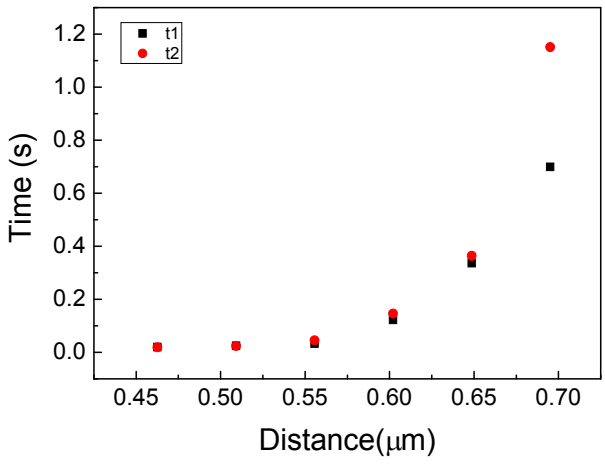


Figure 4: Dwell time of a 2.15 um SiNW in the two traps (t1,t2) varying the inter traps distance d.

When the distance between traps is reduced, we observe that at a critical value of separation the energy barrier seem to be so small that the SiNW appears trapped

in a single potential well. This trap is sited between the two single traps and it has a width that is the sum of the two individual widths. The critical value of separation scales with the SiNWs length for the same reason that we explained previously explaining the distance at which the bistable behavior has been noticed.

3 Acknowledgement

We acknowledge MPNS COST Action 1205 "Advances in Optofluidics: Integration of Optical Control and Photonics with Microfluidics" for support.

4 References

[1] O. M. Maragò, P. J. Jones P. G. Gucciardi, G. Volpe, A. C. Ferrari, Nature Nanotechnology, 8, 807-819 (2013)

[2] H. A. Kramers, Physica VII, 4 (1940).

[3] L. I. McCann, M. Dykman & B. Golding, Nature, 402, 785-787, (1999).

[4] Simpson, S. and Hanna, S. Nanotechnology 23(20),205502 (2012).

[5] A. Irrera et al., Nano Lett. 11, 4879–4884 (2011).

[6] A. Irrera, et al., Nanotechnology 23(7), 075204 (2012).

[7] Y. Hayashi, S. Ashihara, T. Shimura, K. Kurod, Opt. Commun. 281, 3792-3798 (2008).

Non Conservative Optical Forces For Silicon Nanowires in Optical Traps

A. MAGAZZU[1,2,*], A. IRRERA[1], P. ARTONI[3], S. H. SIMPSON[4], S. HANNA[4], P. H. JONES[5], F. PRIOLO[3], P. G. GUCCIARDI[1], and O. M. MARAGÓ[1,*]

[1] CNR-IPCF, Istituto per i Processi Chimico-Fisici, Messina, Italy
[2] Dottorato in Fisica, Università di Messina , Messina, Italy
[3] Matis CNR-IMM and Dipartimento di Fisica, Università di Catania, Catania, Italy
[4] H. H. Wills Physics Laboratory, University of Bristol, Bristol, UK
[5] Department of Physics and Astronomy, University College London, London, UK

Corresponding authors: mago.alex@gmail.com, marago@me.cnr.it

Abstract

We measure non-conservative forces in optical trapping of ultra-thin Silicon nanowires by photonic force and torque microscopy. We reveal how the extreme non-spherical shape generates a transverse component of the radiation pressure that results in a thermally activated non-conservative rotation of the nanowire about the trap axis. We explore the behavior with trapping power and scaling with nanowire length. This has implications for optical force calibration and optomechanics with levitated non-spherical particles.

1 Introduction

Optical tweezers (OT) are powerful tools to understand, detect and measure forces in soft-matter systems at the micro and nanoscale [1]. They are commonly used in areas as diverse as biophysics, colloidal physics, and hydrodynamics of small systems. One of the crucial enabling step of OT is the accurate calibration of the applied optical forces. An implicit assumption of all calibration methods is that, for small displacements of a particle from the center of a Gaussian beam optical trap, the restoring force is proportional to the displacement, i.e., the optical trap is assumed to act as a Hookeian spring with a fixed stiffness. This condition implies that the optical force-field produced by optical forces must be conservative, excluding the possibility of a rotational (non-conservative) component [2]. This is not strictly correct since scattering forces are intrinsically non-conservative and this has some measurable consequences.

2 Optical forces

For a generic particle in optical tweezers the optical forces are essentially the sum of two types: the gradient (conservative) force is responsible for trapping [2], while the non-conservative part generally has a destabilizing effect [3,4,5]:

$$\boldsymbol{F} = -\nabla \boldsymbol{U} + \boldsymbol{F}_{NC}$$

For a non-spherical particle the non-conservative forces can be considered composed by two contributions. A first contribution depends on the standard non-homogeneous radiation pressure due to the gaussian geometry of the laser beam that may yield a rotational force in ρ-z plane even for a spherical trapped particle [4,5]. The second contribution, manifest for nonspherical objects, depends on alignment along the axial direction, that generates a transverse force (optical lift effect) [6] that causes rotations and precessions in the ρ-z plane.

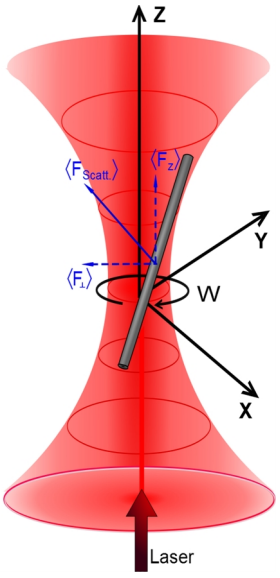


Figure 1 *depiction of a SiNW in an optical trap and forces* acting on it.

3 Non-conservative effects

For an optically trapped spherical particle, non conservative effects are only experienced when the laser power, and hence optical potential depth, is sufficiently low to permit the (thermally fluctuating) sphere to explore a large trapping volume, and to feel the inhomogeneity of the scattering force which is greater

nearer the edges of the optical potential well. Under these conditions the thermal motion displays a toroidal bias coupling the directions transverse (ρ) and parallel (z) to the beam propagation axis. By increasing the laser power the non-conservative effects tend to vanish, being of second-order with respect to the gradient (conservative) forces [7]. However for non-spherical particles, such effects have been predicted to be first-order, hence non-vanishing with the laser power and affecting optical force calibration.

In the case of nanowires increasing the length of the SiNWs the transverse stiffness tends to L^{-3}. Instead the rotational term, initially increases with L for parts of SiNWs outside the focus point and when L is great enough, to cause the orientation and constrainment of the nanowire in the transverse direction, it tends to L^{-1} [8]. The rotational term decreases slower and is more dominant than the translational term. For this reason we can infer that non conservative rotation in xy plane is a roto-translation of the nanowire about the optical axis, rather than a precession of the wire about the centre-of-mass point.

Here we report the first observation of non-conservative effects on non-spherical particles, specifically on ultra-thin silicon nanowires (SiNWs) with a diameter of 10 nm and several lengths (L = 1.00±0.05, 2.08±0.04, 3.1±0.1,4.0±0.2 and 5.0±0.5 μm) [9,10]. These SiNWs are held in an optical tweezers where optical forces align the axis of the NW close to the propagation direction of the trapping laser beam as shown in Figure 1.

We show how the non-conservative effects depend on shape and size of the trapped particle and on laser power. We detect two different kinds of thermal motion in the trap, a toroidal motion coupling the ρ-z directions and a roto-translation coupling the x-y directions, Figure 1. We characterize the two dimensional motion of SiNWs, by the Differential Cross Correlations (DCCFs) [3] of particle tracking signals, that highlight roto-translation and toroidal bias. We explore the scaling behavior of these non conservative effects with trapping power and with nanowire length

We also calculated the non conservative component of the force-field, shown in Figure. 2, that takes account of the amount of the non conservative effects and is defined as the ratio of the rotational and the average of the relaxation frequencies in the x-y plane:, $\varepsilon_{ij} = \omega_{ij}/\omega_{\rho}$. Typically the non-conservative contribution to the trapping force is of the order of a few percent of the total optical force acting on the particle.

We find that the non-conservative contribution scales as $1/L$ represented in figure 2 by the black line assuming large L, $L \gg z_R$ where z_R is the Rayleigh range of the strongly focused trapping laser beam which measures the length of the focal region parallel to the beam axis.

We conclude that non-conservative effects on non-spherical particles are linked to the occurrence of a transverse component of the radiation pressure. Although we measured non-conservative effects in the order of few percent of the trap dynamics, we were able to detect them at any available laser power, implying that this needs to be take into account when dealing with calibration of optical trapping forces based on effective potentials [11,12]. Moreover non-conservative forces can have a more dramatic effect when dealing with optomechanics of levitated non-spherical particles [1].

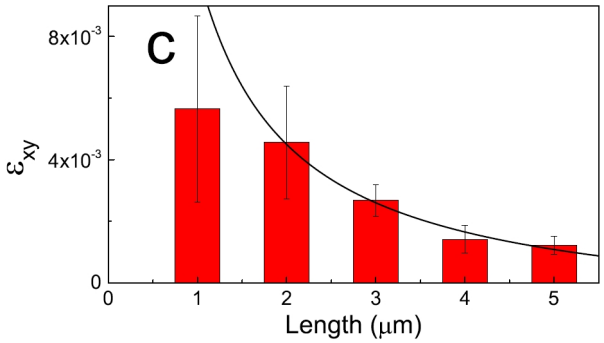


Figure 2 *Non-conservative component of the force-field as function of the SiNWs length.*

4 References

[1] O. M. Maragò, P. J. Jones P. G. Gucciardi, G. Volpe et al, *Nature Nanotechnology*, 8, 807-819 (2013)

[2] Ashkin, A., Dziedzic, J., Bjorkholm, J., and Chu, S. *Opt. Lett.* 11, 288 (1986).

[3] Volpe Giorgio, V. G. and Petrov, D. *Physical Review* **E 76,** 061118 (2007).

[4] David G. Grier et al. *Physical Review Letters 101,* 128301 (2008)

[5] G. Pesce, G. Volpe, *Europhysics Letters*, 86 38002, (2009)

[6] Simpson, S. H., Hanna, S., Peterson, T. J., and Swartzlander, G. A. *Optics Letters* 37(19), 4038–4040 (2012).

[7] Simpson, S. H. and Hanna, S. *J. Opt. Soc. Am. A* 27(9), 2061–2071 Sep (2010).

[8] Simpson, S. and Hanna, S. *Nanotechnology* **23**(20),205502 (2012).

[9] Irrera, A. and et al. *Nano Lett.* 11, 4879–4884 (2011).

[10] Irrera, A., Artoni, P., Iacona, F., Pecora, E., Franzo, G., Galli, M., Fazio, B., Boninelli, S., and Priolo, F. *Nanotechnology* 23(7), 075204 (2012).

[11] Nieminen, T., Rubinsztein-Dunlop, H., and Heckenberg, N. Journal of Quantitative Spectroscopy and Radiative *Transfer* 70(4), 627–637 (2001).

[12] Bishop, A. I., Nieminen, T. A., Heckenberg, N. R., and Rubinsztein-Dunlop, H. *Physical Review A* 68(3), 033802 (2003).

Optical tweezers force calibration of chromosomes

Nima KHATIBZADEH[1], Ann A. M. BUI[2,*], Alexander B. STILGOE[2], Timo A. NIEMINEN[2], Halina RUBINSZTEIN-DUNLOP[2] and Michael W. BERNS [1,3]

[1] Beckman Laser Institute and Medical Clinic, University of California, Irvine, 92612, USA
[2] School of Mathematics and Physics, The University of Queensland, St Lucia, 4072, Australia
[3] Institute of Engineering in Medicine, University of California, San Diego,
9500 Gilman Drive, La Jolla, California 92093, USA

Corresponding author: a.bui@uq.edu.au

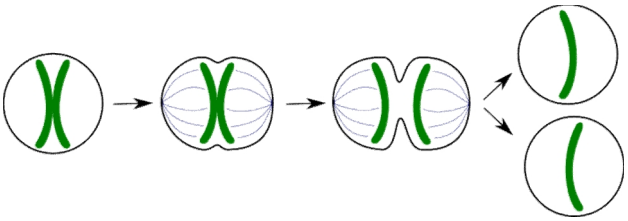
Abstract

Cell division is a necessary process which involves the chromosomes being split to form new cells. The force required to split chromosomes is a mystery. Here, optical tweezers are used to determine the force required to stop chromosome movement during cell division. Escape force measurement on isolated Chinese hamster ovary chromosomes determined the force efficiency, which allowed trapping power to be converted to force. We find a force value of around 0.1-10 pN was required for chromosome movement, consistent with other estimates.

1 Introduction

Genetic information in eukaryotic organisms is stored in DNA, which is arranged into chromosomes who reside in the nucleus of the cell. For organisms to survive, cells must reproduce to pass on their genetic information. To do this, the DNA replicates and arranges itself into the legs which form the chromosome. The legs of the chromosome are pulled in opposite direction, thereby pulling the chromosome apart. Each of the legs becomes wrapped inside their own nucleus, creating the daughter cells of the original cell (Figure 1).

Figure 1 *Cell division. During mitosis, the chromosomes align and the (two) legs are pulled apart. Each leg is surrounded to make the (two) daughter cells who can then continue with the whole division process again.*



It is established that the chromosomes are pulled apart, but the quantity of force required to do this has not been agreed upon. There have been previous estimates and measurements, but the value of the force required varies by orders of magnitude from 700 pN to 0.1-1 pN [1]. The 700 pN estimate was taken from an experiment hooking a flexible glass needle to chromosome grasshopper spermatocytes to find an upper limit on the force required. The 0.1-10 pN was an estimate from hydrodynamic calculations. There are other estimates for this separation force from other methods, such as looking at the elasticity of the chromosomes. Here we consider using optical tweezers to determine what force is needed to pull the chromosome out of the trap.

Optical tweezers use scattering and gradient forces to trap microscopic particles in a medium with a single laser beam. These forces are on the order of piconewtons, making them ideal for handling biologicals on the cellular scale. The advantage of using optical tweezers for a chromosome calibration, over other mechanical methods, is that we can noninvasively exert piconewton forces on the chromosome, which would normally float in nuclear fluid medium.

2 Method

It is planned to conduct an experiment in which the optical tweezers hold the chromosomes as they undergo cell division. When the chromosomes are pulled apart by microtubules, the tweezers hold a leg of the chromosome. The trapping power is applied to completely stop the movement of the chromosome. However, this trapping power is not a force. Thus, we need to convert the power quantity to a force quantity, which can be done through the consideration of force efficiency. Thus, the main task is to find the force efficiency of the chromosome at the point at which the chromosome escapes the trap.

2.1 Force efficiency

It is common with optical tweezers to work with a dimensionless force efficiently quantity, Q, which can be considered as the force in units of $n\hbar k$ per photon where n is the refractive index of the medium, $\hbar$ is the reduced Planck constant and k is the wavenumber of the trapping beam. This Q is independent of the trapping power and is characteristic of the beam and particle.

The expression for force, F, in terms of dimensionless force efficiency is given by:

$$F = \frac{nQ}{c}P \qquad (1)$$

where P is the power of the trapping beam at the focal point, and c is the speed of light in a vacuum. Power (P) is controlled by the input power for the trapping beam. The medium's refractive index and n can be assumed to be constant and have been found. The only unknowns left are the force and trapping efficiency. We can find the force for a given power by looking at the escape force, which will then give us an expression for the force efficiency.

2.2 Escape force

We are interested in the force it takes to split a chromosome, which is the force required for the chromosome to escape the trap. Here will call it escape force. To find the escape force, we start with the chromosome being trapped then the stage is moved in a lateral direction, as shown in Figure 2.

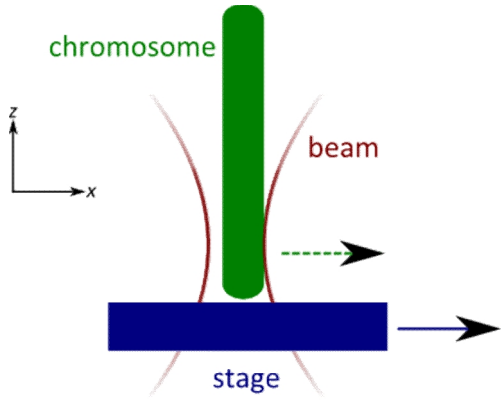


Figure 2 *Escape force calibration of trap with cylinder. The cylinder is trapped then the stage is moved to create viscous drag force to pull the cylinder out of the trap.*

The stage movement results in a viscous drag force, from the medium thus pushing the chromosome out of the trap. The velocity of the stage at which the chromosome escapes, the escape velocity, v_{esc}, is related to the escape force, F_{esc}, through Stokes' Law:

$$F_{esc} = \Gamma v_{esc} \qquad (2)$$

where Γ is the drag tensor of the chromosome which depends on the dimensions of the chromosome and the viscosity of the medium.
Combining Eq. (1) and (2), we have an expression to find the force efficiency at the point of escape, Q_{esc}. .

3 Measurement

Isolated Chinese hamster ovary chromosomes were suspended in viscous media of various viscosities. The escape velocities of these chromosomes were found for different trapping powers. The escape forces were found using Eq. (2) from the escape velocities, which then give the escape force efficiencies from Eq. (1). The escape force efficiencies are shown in Figure 1.

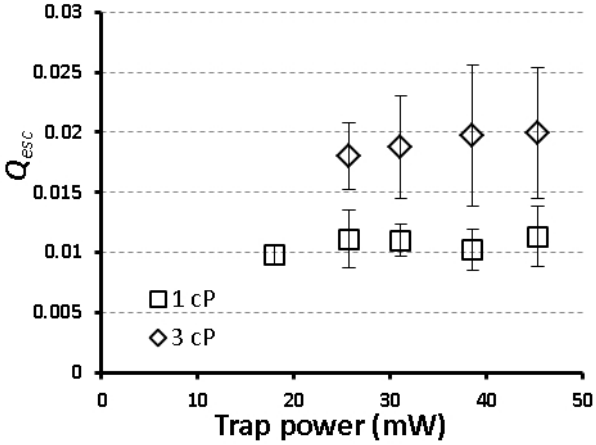


Figure 3 *Escape trapping efficiency (Q_{esc}) versus trapping power for Chinese hamster ovary chromosomes suspended in 1 and 3cP viscous media.*

This value for Q_{esc}. translates to chromosome splitting forces on the order of 0.1 pN to 10 pN, which is consistent with theoretical estimates, but falls far short of the mechanical measure of 700 pN.

4 Acknowledgement

The authors would like to acknowledge the support from the Australian Research Council for this project (DP140100753).

RADIATION TORQUE INDUCED BY BESSEL BEAM

Renxian LI *, Lixin GUO, Ruiping YANG, Chunying DING and Zhensen WU

School of Physics and Optoelectronic Engineering, Xidian University, Xi'an 710071, China

**Corresponding author: rxli@mail.xidian.edu.cn*

Abstract

Radiation torque exerted on a sphere induced by a Bessel beam is expressed using the generalized Lorenz-Mie theory (GLMT). The Beam Shape Coefficients (BSCs) is calculated using Integral Localized Approximation (ILA). Numerical results of radiation torque are presented for various position of beam centre, order of beam, and angle α_0 of beam.

1 Introduction

It is well known that transfer of angular momentum from a laser beam to a particle can produce radiation torques, which can be employed to the manipulation of microscopic objects[1], and have been widely used in the fields of biology, physics, optofluidics, etc. The torque may be caused by circularly polarized plane wave, which carries spin angular momentum[2-3]. In this case, the particle needs to be absorbing. The torque may also occur for the case of a sphere illuminated by an off-axis shaped beam[4]. In this case, the off-axis beam has orbit angular momentum. It is obvious that when an absorbing particle is illuminated by an off-axis circularly polarized focused beam, both the spin angular momentum and orbit one will be transferred from beam to the particle.

Many researchers have been devoted to the theoretical prediction of radiation torque, and different approaches have been developed. When the particle is much larger than the wavelength of incident beam, i.e. d>10λ with d the diameter of the particle and λ the wavelength, the Geometrical optics can be employed to the prediction of radiation torque[5]. Conversely, the Rayleigh model[6] can be employed to the prediction of radiation torque exerted on a particle which is much small than the wavelength, i.e. d<<λ. Both geometrical optics and Rayleigh model are approximation approaches. These two limiting cases can be unified by the rigorous theory "Generalized Lorenz-Mie Theory (GLMT)"[7-8], which is the solution to the Maxwell's equations and is suitable for any d/λ.

Bessel beam has characteristics of non-diffraction and self-reconstruction, and it consists of a series of concentric rings of decreasing intensity[9-10]. So it can be employed to simultaneously trap and manipulate many particles[11-15]. In our previous work, we have discussed the scattering of a Bessel beam by a spherical particle[16] and the radiation pressure force induced by a Bessel beam[17]. In this presentation, we will extend our work to the study of radiation torque exerted on a sphere induced by a Bessel beam.

2 Theoretical background

The radiation torque exerted on a particle of arbitrary shape can be expressed as[18]:

$$<\mathbf{T}>=-\int_S \hat{n}\cdot<\vec{\vec{A}}>\times\mathbf{r}dS \tag{1}$$

where the symbol <> denotes time average and $\vec{\vec{A}}$ is the Maxwell stress tensor:

$$\vec{\vec{A}}=\varepsilon\mathbf{EE}^*+\mu\mathbf{HH}^*-\frac{1}{2}\left(\varepsilon|\mathbf{E}|^2+\mu|\mathbf{H}|^2\right)\vec{\vec{I}} \tag{2}$$

When a sphere is illuminated by a Bessel beam, radiation torque has a longitudinal component T_z and two transverse components T_x and T_y:

$$T_x=\frac{4\hat{m}}{c}\frac{\pi}{k^3}\sum_{n=1}^{\infty}\sum_{m=1}^{n}C_n^m\Re(A_n^m) \tag{3}$$

$$T_y=\frac{4\hat{m}}{c}\frac{\pi}{k^3}\sum_{n=1}^{\infty}\sum_{m=1}^{n}C_n^m\Im(A_n^m) \tag{4}$$

$$T_z=-\frac{4\hat{m}}{c}\frac{\pi}{k^3}\sum_{n=1}^{\infty}\sum_{m=1}^{n}mC_n^mB_n^m \tag{5}$$

with

$$C_n^m=\frac{2n+1}{n(n+1)}\frac{(n+|m|)!}{(n-|m|)!} \tag{6}$$

$$\begin{aligned}A_n^m &= A_n(g_{n,TM}^{m-1}g_{n,TM}^{m*}-g_{n,TM}^{-m}g_{n,TM}^{-m+1*})\\ &+B_n(g_{n,TE}^{m-1}g_{n,TE}^{m*}-g_{n,TE}^{-m}g_{n,TE}^{-m+1*})\end{aligned} \tag{7}$$

$$B_n^m = A_n(|g_{n,TM}^{m}|^2-|g_{n,TM}^{-m}|^2)+B_n(|g_{n,TE}^{m}|^2-|g_{n,TE}^{-m}|^2) \tag{8}$$

$$A_n=\Re(a_n)-|a_n|^2 \tag{9}$$

$$B_n=\Re(b_n)-|b_n|^2 \tag{10}$$

Where, a_n and b_n are traditional Mie scattering coefficients, and $g_{mn,TM}$ and $g_{mn,TE}$ are so-called Beam Shaped Coefficients (BSCs). The BSCs for a Bessel beam of arbitrary order has been derived using the integrated

localized approximation in our previous work. They can be expressed as

$$g_{n,TM}^{0} = \frac{Z_n^0}{2} e^{ik\cos\alpha_0 z_0} \left[J_1(\varpi) J_{1-\nu}(\xi) e^{-i\phi_0} + J_{-1}(\varpi) J_{-1-\nu}(\xi) e^{i\phi_0} \right] \tag{11}$$

$$g_{n,TE}^{0} = \frac{Z_n^0}{2} e^{ik\cos\alpha_0 z_0} \left[iJ_1(\varpi) J_{1-\nu}(\xi) e^{-i\phi_0} - iJ_{-1}(\varpi) J_{-1-\nu}(\xi) e^{i\phi_0} \right] \tag{12}$$

$$g_{n,TM}^{m} = \frac{Z_n^m}{2} \left[J_{1+m}(\varpi) J_{1+m-\nu}(\xi) e^{-i(1+m)\phi_0} + J_{-1+m}(\varpi) J_{-1+m-\nu}(\xi) e^{-i(-1+m)\phi_0} \right] \times e^{ik\cos\alpha_0 z_0} \tag{13}$$

$$g_{n,TE}^{m} = \frac{iZ_n^m}{2} \left[J_{1+m}(\varpi) J_{1+m-\nu}(\xi) e^{-i(1+m)\phi_0} - J_{-1+m}(\varpi) J_{-1+m-\nu}(\xi) e^{-i(-1+m)\phi_0} \right] \times e^{ik\cos\alpha_0 z_0} \tag{14}$$

Here ν is the order of beam, and the definition of other parameters can be found in our previous papers. In this presentation we will present numerical results of radiatin torque for various position of beam centre, order of beam, and angle α_0 of beam.

3 Acknowledgement

This study is supported by the Natural Science Foundation of China (Grant No. 61101068 and 61172031), the National Science Foundation for Distinguished Young Scholars of China (Grant No.61225002), and the Fundamental Research Funds for the Central Universities.

4 References

[1] A. ASHKIN, J. M. DZIEDZIC, Optical Trapping and Manipulation of Viruses and Bacteria [J], Science 1987, 235:1517-1520.

[2] M. E. J. FRIESE, T. A. NIEMINEN, N. R. HECKENBERG, et al., Optical alignment and spinning of laser-trapped microscopic particles [J], Nature 1998, 394: 348-350.

[3] A. M. STEWART, Angular momentum of the electromagnetic field: the plane wave paradox resolved [J], Eur. J. Phys. 2005, 26: 635-641.

[4] S. CHANG, S. S. LEE, Optical torque exerted on a homogeneous sphere levitated in the circularly polarized fundamental-mode laser beam [J], J. Opt. Soc. Am. B 1985, 2: 1853–1860.

[5] R. C. GAUTHIER, Trapping model for the low index ring shaped micro-object in a focused lowest order Gaussian beam profile [J], J. Opt. Soc. Am. B 1997, 14 (4): 782-789.

[6] A. ROHRBACH, E. H. K. STELZER, Optical trapping of dielectric particles in arbitrary fields [J], J. Opt. Soc. Am. A 2001, 18: 839-853.

[7] H. POLAERT, G. GREHAN, G. GOUESBET, Forces and torques exerted on a multilayered spherical particle by a focused Gaussian beam [J]. Opt. Commun., 1998, 155:169～179.

[8] G. GOUESBET, B. MAHEU, G. GREHAN. Light scattering from a sphere arbitrarily located in a Gaussian beam, using a Bromwich formulation [J]. J. Opt. Soc. Am. A, 1988, 5:1427～1443.

[9] Durnin J. Exact solutions for nondiffracting beams. I. The scalar theory. J Opt Soc Am A 1987; 4(4): 651–4.

[10] Mc Gloin D, Dholakia K. Bessel beams: diffraction in a new light, Contemp Phys 2005; 46(1): 15–28.

[11] Garce´s-Cha´vez V, Mc Gloin D, Melville H, Sibbett W, Dholakia K. Simultaneous micromanipulation in multiple planes using a self-reconstructing light beam. Nature 2002; 419 (6903): 145–7.

[12] Arlt J, Garces-Chavez V, Sibbett W, Dholakia K. Optical micromanipulation using a Bessel light beam. Opt Commun 2001; 197 (4–6): 239–45.

[13] Arlt J, Dholakia K, Soneson J, Wright E. Optical dipole traps and atomic waveguides based on Bessel light beams. Phys Rev A 2001; 63 (6): 063602.

[14] Garce´s-Cha´vez V, Roskey D, Summers M, Melville H, McGloin D, Wright E, et al. Optical levitation in a Bessel light beam. Appl Phys Lett 2004; 85: 4001.

[15] Khonina S, Kotlyar V, Skidanov R, Soifer V, Jefimovs K, Simonen J, et al. Rotation of microparticles with Bessel beams generated by diffractive elements. J Mod Opt 2000; 51 (14): 2167 – 84.

[16] Renxian LI, Lixin Guo, Chunying Ding, Zhensen Wu, Scattering of an axicon-generated Bessel beam by a sphere, Opt. Commun. 2013, Vol. 307, PP 25–31

[17] Renxian LI,, Xiang'e Han, Kuan Fang Ren, Zhensen Wu, Lixin Guo, Shuxi Gong, Analysis of radiation pressure force exerted on a biological cell induced by high-order Bessel beams using Debye series, J. Quant. Spectrosc. Ra. 2013, vol. 126, PP 69–77

[18] Xu, F.; Lock, J. A.; Gouesbet, G. & Tropea, C. Radiation torque exerted on a spheroid: Analytical solution Physical Review A, APS, 2008, 78, 013843

Analysis of radiation force of a Laguerre Gaussian vortex beam on a uniaxial anisotropic sphere

Tan QU [1,*], Zhen-Sen WU[1,*], Qing-Chao SHANG [1], Zheng-Jun LI [1], Lei GONG [2]

[1] Xidian University, Xi'an, 710071, China
[2] Xi'an Technological University, Xi'an, 710021, China
Corresponding author: wuzhs@mail.xidian.edu.cn

Abstract

Based on the expansion of Hermite Gaussian (HG) beam in terms of spherical vector wave functions (SVWFs) utilizing Complex Source Point Method (CSPM) and the relation between HG beam and Laguerre Gaussian (LG) vortex beam, derived the expansion of LG beam in terms of SVWFs. Using Generalized Lorenz Mie Theory (GLMT) calculated the radiation force exerted on a uniaxial anisotropic sphere by a LG vortex beam with spiral phase distribution. The effects of the radial and azimuthal mode index of LG vortex beam on the transverse and axial radiation force have been numerically analysed in detailed.

1 Introduction

Since the discovery by Ashkin, optical tweezers have become an indispensable tool for manipulating small particles by exertion of forces as low as several piconewtons without mechanical contact. It is a transfer of the momentum from the laser beam to the particles encountered. In addition to the spin momentum associated with the polarization state of the photons, some beams having phase fronts also possess orbital angular momentum (OAM) which will rotate the particles along the propagation axis. The concept of OAM associated with azimuthal phase term is now leading to new applications in optical tweezing and microscopy. The signature of the OAM appears in the phase singularity which can be found in the centre of LG vortex beams. The generation of this optical tweezers operating with LG vortex beams has very captivating application prospects because it presents some advantages over conventional Gaussian beams, such as the ability to trap particles over an extended distance with limited-diffraction.

Although there has been extensive study of the interaction of a LG vortex beam with a sphere, the detailed theoretical analysis of the radiation force of LG vortex beam on a sphere with the same size order of incident beam wavelength, especially a uniaxial anisotropic one has been much more limited because of its complexity.

2 Theoretical Formulas

Because higher order HG beam and LG vortex beam are the differential of fundamental Gaussian beam in Cartesian coordinate and circular cylinder coordinate system, respectively[1]. In this paper, the expansion of HG beam based on the CSPM in terms of SVWFs[2] has been used,

$$\begin{aligned}&\mathbf{A}_{HG}(u,v)=\hat{x}\psi_{HG}(u,v)\\&=\sum_{n=1}^{\infty}\sum_{m=-n}^{n}[\alpha^{(1)}(u,v,n,m)\mathbf{M}_{mn}^{(1)}+\beta^{(1)}(u,v,m,n)\mathbf{N}_{mn}^{(1)}]\end{aligned}\tag{1}$$

where u and v represent the beam order of HG beam; $\mathbf{A}_{HG}(u,v)$ and $\psi_{HG}(u,v)$ are the vector potential and the slowly varying function of the HG beam, respectively; $\alpha^{(1)}(u,v,n,m)$ and $\beta^{(1)}(u,v,n,m)$ are the expansion coefficients, $\mathbf{M}_{mn}^{(1)}$ and $\mathbf{N}_{mn}^{(1)}$ are the SVWFs; the superscript (1) denotes the first kind spherical Bessel function.

Consider the relation between the HG beam slowly varying function and LG vortex beam slowly varying function [3],

$$\begin{aligned}\psi_{LG}(p,l)=(-2i)^{-n}\sum_{r=0}^{p}\sum_{s=0}^{l}\binom{p}{r}\binom{l}{s}\\\times i^{l-s}\psi_{HG}(2r+s,2p+l-2r-s)\end{aligned}\tag{2}$$

where, p and l are radial and azimuthal mode index of LG vortex beam; $\psi_{LG}(n,m)$ is the slowly varying function of LG vortex beam.

An appropriate description of the vector potential $A_{LG}(p,l)$ of an x-axis polarized LG vortex beam in terms of SVWFs is derived as:

$$\begin{aligned}&A_{LG}(p,l)=\hat{x}\psi_{LG}(p,l)\\&=(-2i)^{p}\sum_{r=0}^{p}\sum_{s=0}^{l}\binom{p}{l}\binom{l}{s}i^{l-s}\\&\times\left\{\sum_{n=1}^{\infty}\sum_{m=-n}^{n}[\alpha^{(1)}(2r+s,2p+l-2r-s,n,m)\mathbf{M}_{mn}^{(1)}\right.\\&\left.+\beta^{(1)}(2r+s,2p+l-2r-s,m,n)\mathbf{N}_{mn}^{(1)}]\right\}\end{aligned}\tag{3}$$

Based on the relation between electric and magnetic field and the vector potential[4], the electric and magnetic field of the incident LG vortex beam can be expressed as:

$$\begin{aligned}\vec{E}_{LG}^{i}(p,l)=(-2i)^{p}\sum_{r=0}^{p}\sum_{s=0}^{l}\binom{p}{l}\binom{l}{s}i^{l-s}\\\times i\omega\sum_{n=1}^{\infty}\sum_{m=-n}^{n}\begin{bmatrix}\alpha^{(1)}(2r+s,2p+l-2r-s,n,m)\vec{M}_{mn}^{(1)}\\+\beta^{(1)}(2r+s,2p+l-2r-s,n,m)\vec{N}_{mn}^{(1)}\end{bmatrix}\end{aligned}\tag{4}$$

$$\vec{H}^{i}_{LG}(p,l)=(-2i)^{p}\sum_{r=0}^{p}\sum_{s=0}^{l}\binom{p}{l}\binom{l}{s}i^{l-s}$$
$$\times\omega\sum_{n=1}^{\infty}\sum_{m=-n}^{n}\begin{bmatrix}\beta^{(1)}(2r+s,2p+l-2r-s,n,m)\vec{M}^{(1)}_{mn}\\+\alpha^{(1)}(2r+s,2p+l-2r-s,n,m)\vec{N}^{(1)}_{mn}\end{bmatrix} \quad (5)$$

Combing with the scattering theory of electromagnetic beams[5], the analytical expression of radiation force of LG vortex beam on a uniaxial anisotropic sphere is presented here using GLMT. Compared with the Ray optics method and Rayleigh dipole scattering model which are suitable for the particles in limited size related to the incident beam wavelength, GLMT can be applied for the particles of any size, especially those in the intermediate regime($D\sim\lambda$) that probably represent the most typical situation in biological applications.

Numerical calculations of the effects of the radial and azimuthal mode index of LG vortex beam on the transverse and axial radiation force are given. The results might be helpful for illustrating the azimuthal phase dependence of the LG vortex modes which is the origin of the orbital angular momentum associated with these modes. Radiation force curve varied with beam waist radius and particle dielectric parameters have been investigated in detailed.

3 Conclusion

Using the transformation from HG beam to LG vortex beam, the radiation force characteristics of a LG vortex beam exerted on a uniaxial anisotropic sphere are investigated. The theory presented here is useful for the validation of the experiment of the optical tweezers and be helpful for the interpretation of the physical process of the trapping and manipulation of with LG vortex beam.

4 Acknowledgement

This work was supported by the National Natural Science Foundation of China under grants 61172031, 61308025 and 61108071 and the Fundamental Research Funds for the Central Universities.

5 References

[1] I. Kimel, and L. R.Elias, "Relations Between Hermite and Laguerre Gaussian Modes", IEEE Journal of Quantum Electronics 1993,vol. 29 pp. 2562-2567.

[2] J. S. Kim, and S. S. Lee, "Scattering of laser beams and the optical potential well for a homogenous sphere", J.Opt.Soc.Am., 1983,vol. 73 pp. 303-311.

[3] E. Zauderer, "Complex argument Hermite-Gaussian and Laguerre -Gaussian beams", J.Opt. Soc. Am. A, 1985,vol. 3 pp. 465-469.

[4] L.W.Davis, "Theory of electromagnetic beams", Phys. Rev. A, 1979,vol. 19 pp. 1177-1179.

[5] Y. Geng, X. Wu, and L. Li, "Analysis of electromagnetic scattering by a plasma anisotropic sphere", Radio Sci., 2003,vol. 38 pp. 991-997.

Angular Momentum Transfer Between Laguerre-Gauss Beams and Purpose-Built Microrotors

Vincent L.Y. LOKE[1,*], Theodor ASAVEI[1-2], Timo A. NIEMINEN[1] and Halina RUBINSZTEIN-DUNLOP[1]

[1] School of Mathematics and Physics, The University of Queensland, 4072, Australia
[2] ELI-NP Centre, Magurele, 077125, Romania

Corresponding author: loke@physics.uq.edu.au

Abstract

We investigate the torque efficiency in the angular momentum transfer between Laguerre-Gauss beams and purpose-built microrotors with discrete rotational symmetry. The microrotors are fabricated using two-photon photopolymerization. To aid the design of the microrotors, we employ the discrete dipole approximation and the T-matrix methods to model the torque imparted by the driving beam, in parallel with experimental verification.

1 Introduction

The development of optically-driven microrotors is motivated by a number of applications. In lab-on-a-chip applications they function as pumps or impellers [1, 2]. Microrotors have also been used as a viscometer in the picolitre scale [3]. They can also be used to directly agitate a biological cell in the study of its response to stimulation.

We have design optically-driven microrotors in the past with a stalk-like structure [3]. However, lab-on-a-chip applications may require a flatter, disc-shape rotor. Thus, we embarked on designing a microrotor with such a shape.

2 Laguerre-Gauss beams

For this study, we use the Laguerre-Gauss LG_{04} beam to drive the microrotor. The beam is generated by passing a Gaussian laser beam through a hologram (figure 1) [4]. As a result, the beam acquires a phase structure made up of a quadruple helix and it possesses orbital angular momentum (OAM).

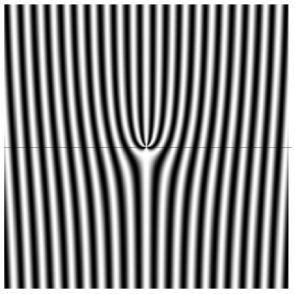


Figure 1 *An off axis hologram for generating the LG04 beam.*

The beam, tightly focussed using a high numerical aperture lens (NA=1.3), is used to trap and rotate the microrotor.

3 The corrugated donut rotor

Since the LG beam has a phase singularity at its core and the rotor is required to have disc-like dimensions, we embark on designing a rotor with a donut shape. Additionally, the donut requires some corrugation so that it can couple to the LG azimuthal modes, hence the corrugated donut rotor (CDR).

As a consequence of Floquet's theorem [17, 18], when a CDR with p-fold discrete rotational symmetry is trapped with an LG_{0l} beam, the scattered modes will be $l_j = l_0 + j_p$, where l_0 is the azimuthal mode of the incident beam and j is an integer. The incident beam carries OAM of l_0 ħ per photon whereas the CDR scatters into modes with l_j ħ angular momentum per photon.

Since we use the LG_{04} beam, we designed the CDR with 8-fold discrete rotational symmetry, i.e., p = 8, where the scattered light couples to $LG_{0,-12}$, LG_{04}, $LG_{0,12}$. The mode overlap at LG_{04} is primarily responsible for producing torque.

4 Two-photon photo-polymerization and micromanipulation

The CDR is made via two-photon photopolymerization. Details of the process are outlined in [5]. Basically, it involves 3D raster scanning, in the x, y and z directions, using a femtosecond pulse laser focussed onto UV-curing resin encased between cover slips (fig. 2). The uncured portion is flushed away with acetone. The finished product is shown in figure 3.

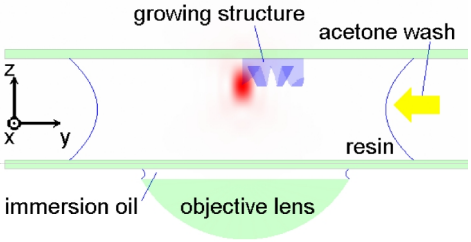


Figure 2 *Schematic diagram of the 2PP process.*

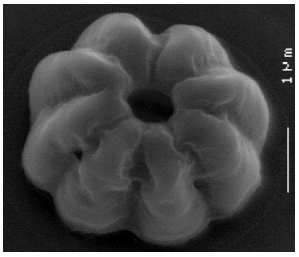


Figure 3 *Electron micrograph of a corrugated donut rotor, 3D-printed using two-photon photopolymerization.*

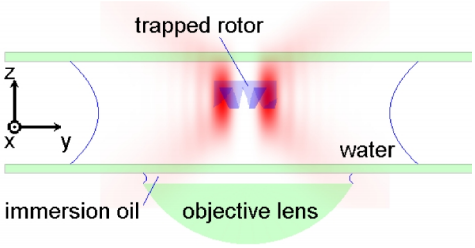


Figure 4 *Schematic diagram of the CDR beam trapped and rotated by the Laguerre-Gauss beam.*

With the CDR in place, the chamber is then filled with deionized water (fig. 4). The tightly-focussed LG beam is then used to trap and spin the CDR. The orbital torque is determined by measuring the rotation rate for incident beams with left-circular, right-circular and linear polarizations [3].

5 Discrete dipole approximation and the T-matrix

In parallel with the experiments, we perform computational calculations of the forces and torques on the CDR. Discrete dipole approximation (DDA) [6] is the method of choice due to its capability in modelling arbitrary shapes. Figure 5 shows the CDR represented as polarizable dipoles arranged in a cubic lattice, illuminated by and LG_{04} beam which is modelled using vector spherical wave function (VSWF) expansion.

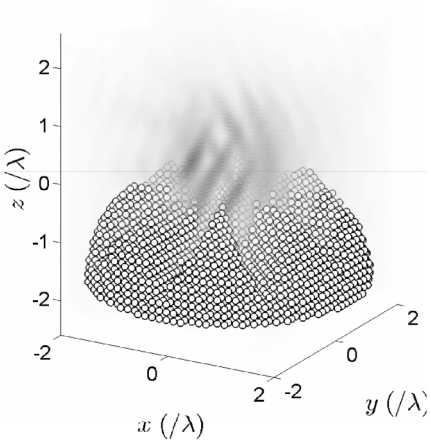


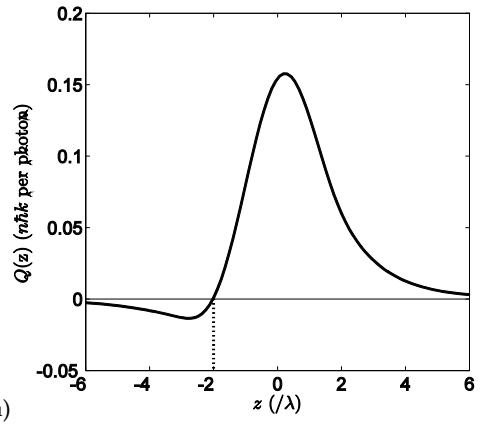
Figure 5 *Dipole model of the CDR trapped and driven by an LG_{04} beam with a convergence angle of 78°.*

We perform repeated calculations of the forces on the CDR so as to find its equilibrium position. Because of this requirement we use a DDA T-matrix [7] method to save computational time. The method also exploits the discrete rotational symmetry to further reduce computational time and memory footprint.

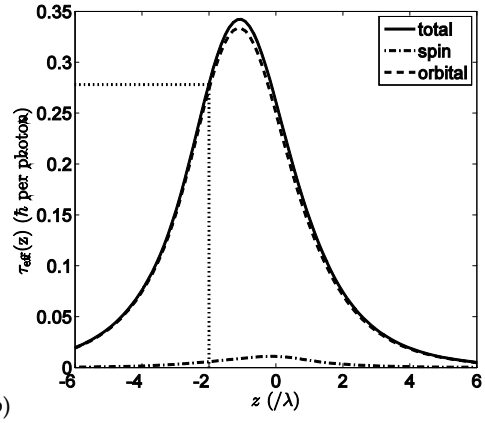
6 Results

In the experiment, we used the LG_{04} beam, focussed at the convergence angle of 78°, to trap and rotate the CDR similar to that shown in figure 3. The measured orbital torque was 0.3 ± 0.03 ħ per photon.

Using the DDA T-matrix method we performed force and torque calculations for the CDR along the beam axis. The beam propagates in the –z direction and its linear momentum pushes the CDR away from the focus whereas the field gradient works to pull it close to the focus. The axial force profile in figure 6a suggests that the CDR will be trapped at the -2λ position. Taking the value at equilibrium (fig. 6b), the orbital torque is approximately 0.28 ħ per photon.



(a)



(b)

Figure 6 *a) The axial force efficiency versus displacement along the beam axis (focus at 0) of the CDR driven by an LG_{04} beam. The equilibrium is where the force is zero, in this case, approximately -2λ. b) The torque efficiency versus displacement along the beam axis. The value at equilibrium is taken for comparison with the experimental result.*

7 Conclusion

A donut-shaped corrugated rotor with 8-fold discrete symmetry was proven viable, experimentally and computationally, to be trapped and rotated by a tightly-focussed LG_{04} beam, inspired by the beam shape as well as the application of Floquet's theorem to achieve optimal azimuthal mode coupling. The shape of the CDR provides a design for a rotor suitable for a flat, disc-like spatial requirement for a lab-on-a-chip application.

The DDA T-matrix method was used to model the CDR being manipulated by LG beams. The torque results of the model and experiment where in good agreement, i.e., within 7% error.

8 References

[1] P. Galajda and P. Ormos, Complex micromachines produced and driven by light, App. Phys. Lett. 78:249–251 (2001).

[2] S. Maruo, A. Takaura, and Y. Saito, Optically driven micropump with a twin spiral microrotor, Optics Exp. 17:18525–18532 (2009).

[3] T. Asavei, T. A. Nieminen, V. L. Y. Loke, A. B. Stilgoe, R. Bowman, D. Preece, M. J. Padgett, N. R. Heckenberg, and H. Rubinsztein-Dunlop, "Optically trapped and driven paddle-wheel," New J. of Phys. 15:063016 (2013).

[4] N. R. Heckenberg, R. Mcduff, C. P. Smith, and A. G. White, Generation of optical-phase singularities by computer-generated holograms, Optics Lett. 17:221–223 (1992).

[5] T. Asavei, T. A. Nieminen, N. R. Heckenberg, and H. Rubinsztein-Dunlop, Fabrication of micro-structures for optically driven micromachines using two-photon photopolymerization of UV curing resins, J. of Opt. A 11:034001 (7pp) (2009).

[6] B. T. Draine and P. J. Flatau, Discrete-dipole approximation for scattering calculations, J. Opt. Soc. Am. A 11:1491–1499 (1994).

[7] V. L. Y. Loke, T. A. Nieminen, N. R. Heckenberg, and H. Rubinsztein-Dunlop, T-matrix calculation via discrete dipole approximation, point matching and exploiting symmetry, JQSRT 110:1460–1471 (2009).

"Optical Gas Bubble Management" at its Laser Thermo-Capillary Trapping in an Absorbing Liquid

A.D. BUTENKO, N.A. KAZACHKOVA, O.I. KOFMAN and V.I. LYMAR*

Physical Optics Chair, V.N. Karazin Kharkiv National University, Maidan Svobody, 4, Kharkiv, 61022, Ukraine

*Corresponding author: lymar@univer.kharkov.ua

Introduction

Light fields are subjected to substance distribution for most optical phenomena in nature, but, after nonlinear optics birth and, especially, after particles laser trapping experiments, it is clear that alternative contrary situations can be realized up to and including Bose-Einstein condensation. Microparticles with a relative refractive index of $n > 1$ are trapping easily by means of well-known Ashkin's dipole force technique. To trap particles with $n < 1$, *e.g.* gas bubbles in a liquid, it becomes rather more involved [1]. But because of a surface tension temperature dependence it is possible to trap the gas bubble easily using so-called dissipative thermo-capillary force in the absorbing liquids [2,3]. A broad size range of the bubbles, captured by a light beam, a large action radius and a high specific value of the capturing force are some of the useful thermo-capillary trap properties [4]. In the process they are evidently adjustable varying with the liquid medium absorbance. It is believed our results also can be treated as increasing an appeal of optical thermo-capillary gas bubble trap technique.

1 Experimental Technique

Our experimental setup is extremely simple (Figure 1). A linearly polarised laser beam is focused on the cell **C**, containing an absorbing liquid, by means of the converging lens **L**. The cell is arranged between the screens $\mathbf{S_1}$ and $\mathbf{S_2}$ to observe the interference patterns (see lower) in reflected (RL) and transmitted light (TL). The polarizer **P** is used to control over the laser beam power. There is some degree of freedom in the choice of laser types and liquids, but, evidently, laser light wavelength λ has to fall into the absorption band of the liquid. He-Ne-laser at $\lambda = 632.8$ nm and power $P \approx 15$ mW jointly with brilliant green ethanol solutions have been applied in our experiments. If the liquid transmittancy $T(\lambda)$ is roughly about 0.1 at 1-mm thick cell then conventionally such solution can be taken as being dense one, but at $T(\lambda)$~0.9 the term "dilute solution" will be used.

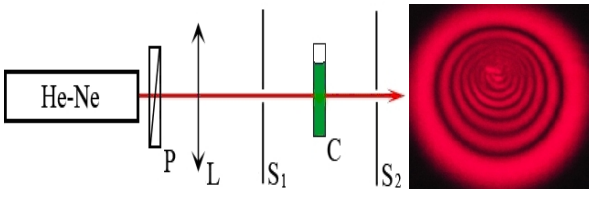


Figure 1. *Experimental scheme of the thermo-capillary gas bubble trap.* ***He-Ne*** *– laser used;* ***P*** *– linear polarizer;* ***L*** *– convergent lens;* ***C*** *– cell with an absorbing liquid;* $\mathbf{S_1}$ *and* $\mathbf{S_2}$ *– plane screens. Photo inset shows observed on screen* $\mathbf{S_2}$ *pattern of haussian laser beam thermal self-defocusing.*

Photo of Figure 1 demonstrates observed on screen $\mathbf{S_2}$ picture of a thermal self-defocusing, created by focused haussian laser beam in the dense solution. Lens **L** at **f**ocal distance 11 cm provides the beam crossover size about 50 microns at the entry of the cell **C.** The self-defocusing pattern testifies that the temperature of the liquid is highest in a centre of the beam and decays towards its periphery. The convective flows disturb a circular symmetry of the temperature distribution.

If the gas bubble is captured by the laser beam, then interference patterns shown on photos of Figure 2 are sharply appearing on screens $\mathbf{S_1}$ and $\mathbf{S_2}$. These interference

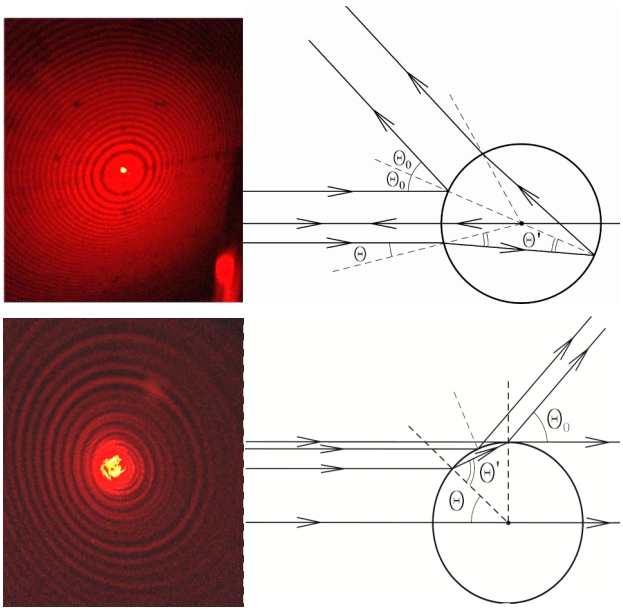


Figure 2. *The interference patterns observed on the screens* $\mathbf{S_1}$ *in reflected (upper) and* $\mathbf{S_2}$ *in transmitted (lower) lights after gas bubble capture. The drawing schemes explain the patterns in two–beam approach:* $\boldsymbol{\theta}$ *and* $\boldsymbol{\theta}'$ *are angles of incidence and refraction on the gas bubble surface;* $\mathbf{2\theta_0}$ *and* $\boldsymbol{\theta_0}$ *are angles of deflection in reflected and transmitted lights accordingly.*

patterns are moving in the process. As a rule, at laser power P ~10 mW diameters of the interference circles are growing if gas bubble is trapped in the dense solutions, but on the contrary, they are reducing if capturing in the dilute ones takes place. Interference pictures time evolution occurs because of the same of gas bubble size. It is remarkably that by means of the linear polarizer **P** this evolution process is under control. By the laser power increasing or decreasing the change of captured gas bubble size can be stopped and directed toward gas bubble growth or collapse at will. That is why we have used the term "optical gas bubble management" to present described above operations over the bubble size.

2 Two-beam Interference

Interference pictures of Figure 2 have both coarse (CFS) and fine fringe structure (only CFS is noticeable on the photos). Certainly, Mie theory [1,5] has to be applied to explain the structure completely. But CFS is described satisfactorily in approach of two-beam interference. Beam courses are sketched on schemes of Figure 2 at zero and maximum angles of deflection ($n = 1.360$ is taken as initial value for ethanol). If $2\theta_0$ and θ_0 are deflection angles in RL and TL accordingly, their magnitudes determine interference circles radiuses, θ and θ' are angles of incidence and refraction on a bubble surface (Figure 2), then there are the following relationships:

$$\theta_0 = 2\cdot\theta' - \theta \text{ in RL;}$$
$$\theta_0 = 2\cdot(\theta' - \theta) \text{ in TL.}$$

Besides of that the refraction law fulfils:

$$\sin\theta' = n\cdot\sin\theta\,. \qquad (1)$$

At a given θ value we have the corresponding values of θ' and θ_0. In doing so optical path differences are arising in RL

$$\Delta_r(\theta) = d\cdot\left(2\cdot\cos\theta' - n\cdot(\sin\theta_0 + \sin\theta)\cdot tg(\theta' - \theta)\right); \qquad (2)$$

and in TL

$$\Delta_t(\theta) = d\cdot(\cos\theta' - n\cdot\cos\theta)\cdot(1 - \sin\theta'), \qquad (3)$$

here d is a bubble diameter.

Obviously, the condition $\Delta = m\cdot\lambda$ corresponds to interferential minima in RL and maxima in TL. On the contrary, maxima in RL and minima in TL correspond to the condition $\Delta = (m + 1/2)\cdot\lambda$. Here, of course, m is integer.

Indicated above expressions are applicable to determine the bubble size with an accuracy of a few percent at least or even better in our experiments. But an essential error is possible if the difference of real relative refractive index n value from the initial one would be large enough. That is why the measurements of real n value are very important.

3 Doppler Effect

In the treatment of the previous section constant bubble diameter is suggested. If bubble diameter is variable, then optical path differences are changing in time also. Let time derivatives are specified by primes. From (2,3) at the limit of zero deflection angles

$$\left|\Delta_r'(0)/\Delta_t'(0)\right| = \frac{2}{n-1} = \left|\delta\omega_r/\delta\omega_t\right|. \qquad (4)$$

Here the last fraction is the ratio of Doppler frequency shifts for the waves reflected from and transmitted through the moving dielectric interface [6]. Hence, observed interference patterns time evolution can be treated as a manifestation of Doppler effect on the moving bubble walls. Measurements of Doppler shifts ratio (DSR) give the method to determine the refractive index n value in the vicinity of the bubble.

To carry out the measurements optical fibers were arranged instead of the screens **S**1 and **S**2 (Figure 1). By means of the fibers reflected and transmitted signals were communicated to photomultipliers and further to computer after an analogue-digital transformation. One of the measurement results is displayed on Figure 3. Transmitted signal I_T is sketched by red colour, reflected I_R—by the blue. In doing so the angle of observation ($n\cdot\theta_0$ for I_T and $2\cdot n\cdot\theta_0$ for I_R) was 1/15 rad. According to (4) at initial n value the DSR has to be equal about six, while from Figure 3 it results to $\mathbf{71/6}$, *i.e.* close to twelve. This two times disagreement can be explained by the following. The bubble centre is immobile with respect to a frame of reference in theoretical treatments discussed above. But in our trap it is the forward bubble wall that is immobile [2] and bubble centre is moving at its diameter variation. In laboratory frame of reference at the limit of zero deflection angle it will be used as before

$$\Delta_r'(0) = 2\cdot d'\,, \qquad (5)$$

but because of the bubble centre movement the variation of transmitted optical path difference is two times slower:

$$\Delta_t'(0) = d'/2\cdot(1 - n). \qquad (6)$$

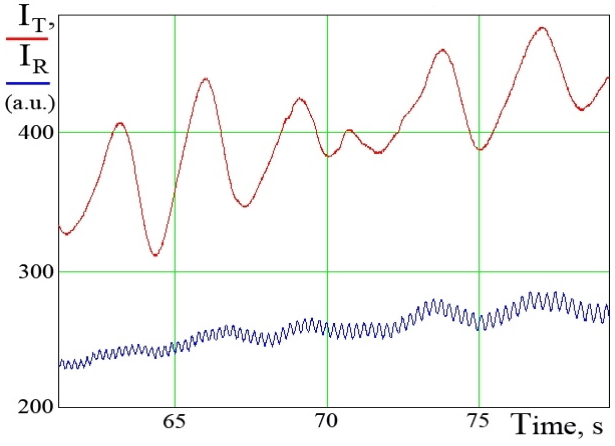


Figure 3. *The time dependences of the reflected* I_R *(blue) and transmitted* I_T *(red) signals at moving interference patterns. The observation angle (* $2\cdot n\cdot\theta_0$ *for* I_R *and* $n\cdot\theta_0$ *for* I_T*) is equal to* 1/15 *rad. Experimental value of Doppler frequency shifts ratio is* $\delta\omega_r/\delta\omega_t \approx 71/6$.

Hence, in case of our experiment we have instead of (4):

$$\left|\Delta'_r(0)/\Delta'_t(0)\right| = \frac{4}{n-1} = \left|\delta\omega_r/\delta\omega_t\right|. \quad (7)$$

Calculated by that value $n \approx 1.338$ is much better than by using (4). But we have take into account that our measurements were proceeded at non-zero observation (deflection) angles. It is following from (2,3) to the lowest degrees of θ_0:

$$\Delta_r \approx d\cdot\left(2-n^2\cdot\theta_0^2/(2\cdot n-1)\right); \quad (8)$$

$$\Delta_t \approx d\cdot(1-n)\cdot\left(1-n\cdot\theta_0/2\cdot(n-1)\right). \quad (9)$$

The latter explains the difference in outward appearance of RL and TL interference patterns on Figure 2. Hence the non-zero angle correction to DSR, defined by (4) in linear approach, is equal to $n\cdot\theta_0/(n-1)^2$. From some physical considerations we anticipate that this correction is conserving in passing to the laboratory frame of reference, *i.e.* it is suitable to correct the DSR value calculated by (7). Then after the first iteration step we receive $n \approx 1.356$, but after the repeating iteration process it results to $n \approx 1.3539$. It is the latter value that we suppose as final.

By means of the known ethanol table data it is possible to estimate a temperature coefficient of ethanol refractive index as $\partial n/\partial T \sim 4\cdot10^{-4}\ K^{-1}$. Therefore our final result corresponds to a temperature deviation $\delta T \sim 15K$ in the bubble vicinity. This magnitude may be considered as coincident with estimation $\delta T \sim 7.5K$ received in [2] by using the aberration circles number $N = 3$ on the pattern of thermal self-defocusing (see photo in Figure 1). As is seen $N = 6$ in our case.

We can estimate the effective value of nonlinear (Kerr) coefficient n^{nl} for the used solution. It is known that

$$\Delta n = n^{nl}\cdot I, \quad (10)$$

here Δn is the refractive index variation because of nonlinear Kerr effect; I is a laser beam intensity. At power $P \approx 10$ mW and haussian beam crossover $\sim 50\mu$ we have in the laser beam centre $\Delta n = 6\cdot10^{-3}$ at $I \sim 0.25$ kW/cm². Therefore $n^{nl} \sim 2.5\cdot10^{-2}$ cm²/kW is sought-for Kerr coefficient value. It is one of the highest known thermal nonlinearities. Perhaps by using the denser solutions it is possible to receive thermal nonlinearities just below the nonlinearities of liquid crystals.

4 Conclusions

The laser beam of treated above system serves the dual function of "optical bubble management" tool on the one hand and on the other – as a size-and-refractive index measuring tool. Obviously, this function could be subdivided between two lasers [1]. Moreover, the "bubble management" field could be of another, nonoptical nature, *e.g.* ultrasonic waves are used to capture gas bubbles in well-known sonoluminescence experiments. Then some degree of freedom would be provided to choose the measuring laser. But almost without exception it is possible, as in our experiment, to "tune" the liquid to laser wavelength by means of absorbing solvable dopants.

Certainly, the proposed method on refractive index measurements by means of DSR has an advantage because of its space-time locality comparatively to other known refractometric methods. If measured n value is perturbed by the nonlinearity or dispersion effects, then unperturbed initial value can be defined at the limits of low laser intensities or low dopant concentrations.

From thermodynamic viewpoint the gas bubble, trapped by a laser beam, is one of Prigogine's dissipative structure (DS) examples [3]. It is needed to note that another DS, known as optical heart-beating phenomenon and discovered by French scientists from Rouen in 1982 [7,8], is observable in our system also. Undoubtedly, both DS have the same thermo-capillary nature and hence their common synergetic exploration would ensure new scientific results.

5 Acknowledgement

In bright remembrance of Bogdan Kalinyak, Pavlo Mazurenko, Sergiy Nigoyan, Roman Senik, Mikhailo Zhiznevskiy and Yuriy Verbitskiy.

Authors are obligated to express their apology and gratitude to every man on EuroMaidan in Kiev and other cities, towns, villages of Ukraine, who comes out in cold and hot winter days to defend ideals of freedom, democracy and human rights against blind and deaf criminal power. We also are sincerely thankful to people of all countries, nationalities and religions for a support and understanding. Our hearts are beating together.

Slava Ukraini! -- Heroyam slava!

6 References

[1] Lankers M., Khaled E.E.M., Popp J., Rossling G., Stahl H., and Kiefer W., Determination of size changes of optically trapped gas bubbles by elastic light backscattering, Appl. Opt. 36(7):1638-43 (1997).

[2] Yarovaya R.G., Makarovskii N.A., and Lupashko N.A., Influence of a laser beam on the motion of gas bubbles in an absorbing liquid, Sov. Journ. Tech. Phys. 33(7):817-21 (1988).

[3] Bazhenov V.Yu., Vasnetsov M.V., Soskin M.S., and Taranenko V.B., Dynamics of laser-induced bubble and free-surface oscillations in an absorbing liquid, Appl. Phys. B 49:485-89 (1989).

[4] Ivanova N.A., Bezugliy B.A., Optical thermocapillary trap for a bubble, Pis'ma Zhurn. Tekhn. Fiz. 32(19):66-71 (2006) *(in Russian).*

[5] C.F. Bohren, and D.R. Huffman, *Absorption and scattering of light by small particles* (Wiley, New-York, 1983).

[6] I.Ye. Tamm, *Foundations of electricity theory* (Nauka, Moscow, 1989) *(in Russian).*

[7] Gouesbet G. and Lefort E., Dynamical states and bifurcations of a thermal lens using spectral analysis, Phys. Rev. A 37(12):4903-15 (1988).

[8] Gouesbet G., Simple model for bifurcations ranging up to chaos in thermal lens oscillations and associated phenomena, Phys. Rev. A 42(10):5928-45 (1990).

A NEW POLARIMETRIC INDICATOR IN SENSING APPLICATIONS BASED ON MAGNETO-DIELECTRIC NANOPARTICLES

Ángela I. BARREDA, Juan M. SANZ, José M. SAIZ*, Fernando MORENO and Francisco GONZÁLEZ

Departamento de Física Aplicada, Universidad de Cantabria, Santander, 39005, España

Corresponding author: saizvj@unican.es

Abstract

The spectral evolution of the linear polarization degree (P_L) is analytically studied at right-angle scattering configuration (θ=90º) for magneto-dielectric spherical nanoparticles. The behavior of $P_L(90º)$ is analyzed as a function of the refractive index of the surrounding medium, and it is compared with the extinction efficiency (Q_{ext}). This study has been done by focusing on the spectral pattern of quadrupolar magnetic, and dipolar electric and magnetic resonances of various semiconductor materials.

1 Introduction

Nanotechnology has revolutionized science of last years causing important theoretical and practical developments. Particularly, interaction of light with nanoparticles (NP's) has been a very active field in optics and sensing [1]. When incident light illuminates a metallic NP, free electrons start to oscillate generating localized surface plasmons (LSP's). These coherent oscillations of electronic plasma, which depends on optical properties, particle size and shape, and wavelength of incoming radiation, will originate surface charge distributions [2]. For certain frequencies, resonances can be observed and strong enhancements of the electric field in the surroundings of the nanoparticles happen. Although most studies have been based on metallic NP's due to their good response in visible range, its metallic nature also shows important disadvantages due to Joule's losses.

High refractive index dielectric NP's have been proposed as a solution for this problem because light can interact with these materials with negligible absorption [3]. In fact, instead of LSP's, whispering gallery modes are responsible for resonances in dielectric NP's. These resonances are located in well-defined spectral ranges, and depend on the NP's size and shape [4].

Another important feature is the magnetic response that these non-magnetic materials are able to exhibit. Although for these materials μ=1, being μ their magnetic permeability, magnetic resonances can be observed. During the last years this behavior has been vastly explored for some elements, such as Silicon or Germanium [5], while other semiconductor compounds are beginning to be studied recently [6], and all of them are so-called magneto-dielectric materials [7].

Depending on NP's size, resonances will be located at different spectral ranges. For a given magneto-dielectric material, resonances are red-shifted as NP's size increases. Resonances are also influenced by the relative refractive index of the NP and the surrounding media, but in this case twice: firstly, they can be red-shifted (blue-shifted) as the relative refractive index increases (decreases, respectively); and secondly, they are reinforced (weakened) [6].

In this research, spherical NP's of Silicon (Si), Germanium (Ge), Aluminum Arsenide (AlAs), Aluminum Antimonide (AlSb) and Gallium Phosphide (GaP) are theoretically analyzed for a set of refractive indexes of the surrounding media (m_{ext}) varying from 1 to 2. The spectral evolution of the linear polarization degree of the scattered light at right-angle detection, $P_L(90º)$ [8], is established as polarimetric observer for m_{ext} sensing. Although results have been obtained for the five former materials, Si has been chosen as the representative one for this presentation. The most important feature of these materials is their low absorption. In fact, in a range that varies from VIS to IR their absorption can be considered insignificant in most cases.

2 Theory

Following Mie's theory for scattering and absorption of light by small particles, scattering and extinction efficiencies by a NP can be defined as [9]:

$$Q_{ext} = \frac{2}{x^2}\sum_{n=1}^{\infty}(2\cdot n+1)\,\mathrm{Re}(a_n + b_n)$$
$$Q_{sca} = \frac{2}{x^2}\sum_{n=1}^{\infty}(2\cdot n+1)(|a_n|^2 + |b_n|^2) \qquad (1),$$

where a_n and b_n are the well-known diffusion coefficients of Mie's theory (which depend on the particle size and shape, and on the electric and magnetic properties of the NP and its surrounding medium), and x the size parameter, defined as $(2\pi\cdot m_{ext}\cdot R)/\lambda$, being λ the wavelength of incident light. Coefficients a_n and b_n, respectively, are related to electric and magnetic effects on the NP. In particular, a_1 (b_1) corresponds to the electric (magnetic) dipolar mode, and a_2 (b_2) corresponds to the quadrupolar one.

In the same way, intensities of light scattered by NP's are also related to a_n and b_n through the scattering matrix elements, which depends on the scattering direction. For linearly polarized light, the components parallel and perpendicular to the scattering plane of the scattered electric field are related to the incident ones by a diagonal scattering matrix. In this case, $P_L(90º)$ for a NP size smaller than the wavelength can be obtained in a straight-forward way [8]:

$$P_L(90°) = \frac{(9a_1 - 15b_2)^2 - (9b_1 - 15a_2)^2}{(9a_1 - 15b_2)^2 + (9b_1 - 15a_2)^2} \qquad (2)$$

Equation 2 may provide information about the NP's surrounding medium based on the value of the polarimetric observer $P_L(90º)$.

3 Results

3.1 Q_{ext} vs. $P_L(\theta = 90º)$

A recent study evaluates both the evolution and the sensitivity of Q_{ext} with the variation of m_{ext} for magneto-dielectric NP's [6]. Figure 1 shows the spectral behavior of Q_{ext} and $P_L(90º)$ for a Si NP (R=200 nm, m_{ext}=1.0). Resonances (a_1, b_1 and b_2) can be identified in both patterns for given R and m_{ext}, so that $P_L(90º)$ should be able to reproduce the information contained in Q_{ext}, but in a experimentally feasible way [7].

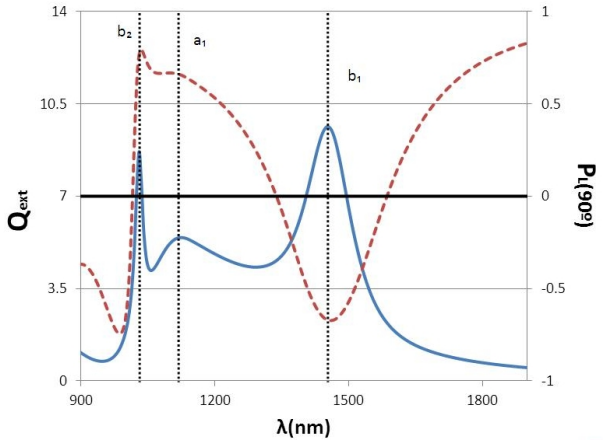


Figure 1 *Spectral behavior of Qext (red dashed line, left axis) and $P_L(90º)$ (blue line, right axis) for a Si NP (R=200 nm, m_{ext}=1). Resonances location is shown with vertical dotted lines.*

3.2 $P_L(\theta = 90º)$ as a sensing indicator.

Figure 2 shows the spectral evolution of $P_L(90º)$ as a function of m_{ext}. As can be seen, values of all resonances evolve with the refractive index of the surrounding media. An estimate of m_{ext} can be obtained through the evolution of $P_L(90º)$, for those wavelengths where resonances occur. Although Si has no absorption in the studied wavelength range, there are some materials, such as Ge, that have tiny absorption traces in the NIR region. The right choice of materials and sizes for each sensing application will lead to better results in sensing devices. Nevertheless, even in the worst case, electric resonances are less sensitive with the absorption than magnetic ones [10], so that their fingerprint in $P_L(90º)$ can still be followed in sensing.

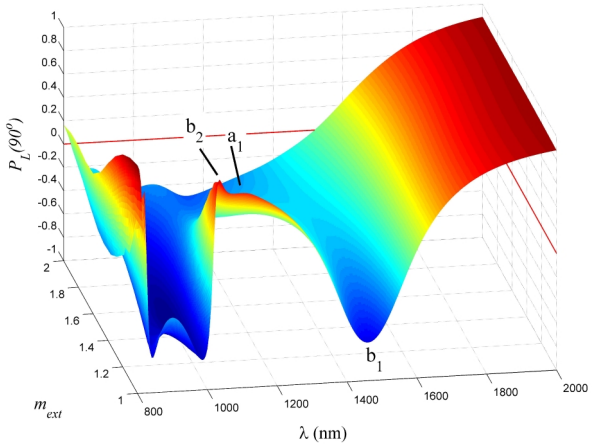


Figure 2 *Spectral evolution of $P_L(90º)$ for a Silicon nanoparticle (R=200 nm) as a function of m_{ext}.*

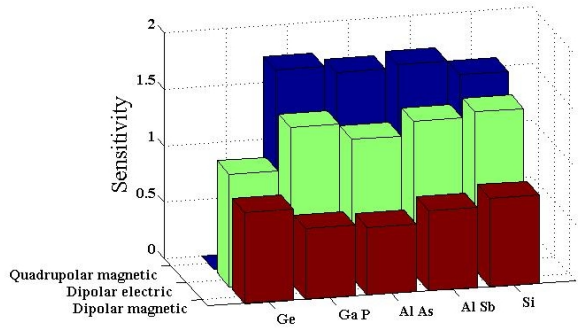
3.3 Sensitivity of $P_L(\theta = 90º)$

In order to establish the accuracy of $P_L(90º)$ as an indicator of m_{ext}, its sensitivity as a function of m_{ext} is evaluated by analyzing its values at the wavelengths where resonances take place. This can be done through the expression:

$$\frac{\partial P_L(90°)}{\partial m_{ext}} \qquad (3),$$

which evaluates the sensitivity in $P_L(90º)$ with respect to tiny changes in m_{ext}. Results of the average sensitivity in the studied spectral range for all semiconductors analyzed are shown in Fig. 3. As can be seen, Ge shows low sensitivity at short wavelengths (magnetic quadrupolar resonance). This is due to the absorption of Ge in this spectral range [11]. Apart from this, the main result is the high sensitivity values obtained for all the materials, regardless of the analyzed resonance, which are big enough as to consider $P_L(90º)$ an experimentally feasible indicator.

Figure 3 *Sensitivity of $P_L(90º)$ with m_{ext} at the wavelengths where resonances take place for isolated nanoparticles of Ge, GaP, AlAs, AlSb and Si (R=200 nm).*



4 Conclusions

The linear polarization degree of the scattered light at right-angle detection, $P_L(90^o)$, is proposed as a new polarimetric indicator for sensing applications by using magneto-dielectric nanoparticles. Its fingerprint is able to inform about the electric and magnetic effects in the NP, in the same way as Q_{ext}. Furthermore, its high sensitivity values made $P_L(90^o)$ an experimentally reliable indicator even for '*in vivo*' examinations. The right choice of materials and sizes may allow monitoring m_{ext} by means of $P_L(90^o)$, in spite of the spectral range or the chosen resonance.

5 Acknowledgements

This research was supported by USAITC-A (United States Army International Technology Center Atlantic) through grant W911NF-13-1-0245.

6 References

[1] P.N. Prasad, *Nanophotonics* (John Wiley & Sons, Inc., 2004).

[2] K.L. Kelly, E. Coronado, L.L. Zhao, and G. Schatz, The optical properties of metal nanoparticles: the influence of size, shape and dielectric environment, The Journal of Physical Chemistry B 107:668-77 (2003).

[3] A. Forouhi, and I. Bloomer, Optical properties of crystalline semiconductors and dielectrics, Physical Review B 38:1865 (1988).

[4] Y.H. Fu, A.I. Kuznetsov, A.E. Miroshnichenko, Y.F. Yu, and B. Luk'yanchuk, Directional visible light scattering by silicon nanoparticles, Nature Communications 4:1527 (2013).

[5] L. Shi, J.T. Harris, R. Fenollosa, I. Rodriguez, X. Lu, B.A. Korgel, and F. Meseguer, Monodisperse silicon nanocavities and photonic crystals with magnetic response in the optical region, Nature Communications 4:1904 (2013).

[6] B. García-Cámara, R. Gómez-Medina, J. J. Sáenz, and B. Sepúlveda, Sensing with magnetic dipolar resonances in semiconductor nanospheres, Optics Express 21(20):23007-20 (2013).

[7] J.M. Gefrin, B. García-Cámara, R. Gómez-Medina, P. Albella, L. Froufe-Pérez, C. Eyraud, A. Litman, R. Vaillon, F. González, M. Nieto-Vesperinas, J.J. Sáenz, and F. Moreno, Magnetic and electric coherence in forward-and back-scattered electromagnetic waves by a single dielectric subwavelength sphere," Nature Communications 3:1171 (2012).

[8] B. Setién, P. Albella, J.M. Saiz, F. González, and F. Moreno, Spectral behavior of the linear polarization degree at right-angle scattering configuration for nanoparticle systems, New Journal of Physics 12:103031 (2010).

[9] C.F. Bohren, and D.R. Huffman, Absorption and scattering of light by small particles (Wiley, New-York, 1983).

[10] J.M. Sanz, R. Alcaraz de la Osa, A.I. Barreda, J.M. Saiz, F. Gonzalez, and F. Moreno, Influence of pollutants in the magneto-dielectric response of silicon nanoparticles, Optics Letters (2014), *Article Under Review*.

[11] E.D. Palik, *Handbook of Optical Constants of Solids* (Academic Press: New York, 1998).

Scattering Matrix Measurements for Single Particles

Antti PENTTILÄ [1,*], Hanna PENTIKÄINEN [1], Daniel GUIRADO RODRÍGUEZ [2], Jouni PELTONIEMI [1,3], and Karri MUINONEN [1,3]

[1] Department of Physics, P.O. Box 64, FI-00014 University of Helsinki, Finland
[2] Instituto de Astrofísica de Andalucía - CSIC, Granada, E-18008, Spain
[3] Finnish Geodetic Institute, P.O. Box 15, FI-02431 Masala, Finland

Corresponding author: antti.i.penttila@helsinki.fi

Abstract

We are designing and developing an instrument for full Mueller matrix scattering measurements of single particles. The wavelength range for the measurements will be in visual and in near infrared. We are aiming at angle-resolved far-field scattering with target sizes down to the scale of microns or tens of microns.

1 Motivation

The far-field scattering properties of single particles are important in many application areas of electromagnetic radiation. In our atmosphere, the aerosol particles of natural or industrial origin are affecting the net radiation budget of the Sun to the Earth. These particles include, e.g., ice particles in cirrus clouds, sand and other small mineral particles, volcanic ash, and carbon contaminated particles from industrial processes. The level of understanding the scattering properties and their effect on the radiation budget should be in a high level so that global warming effects could be reliably estimated.

In astronomy the scattering of light, in visual and in other wavelengths, is an essential tool when interpreting the observations. Many fields of astronomy rely on observation of scattered electromagnetic radiation by a distant target. These fields are, e.g., studies of interstellar dust, studies of comets and their coma, and studies of regoliths on top of atmosphereless Solar System bodies such as asteroids.

In all of the abovementioned cases the knowledge of the scattering behaviour of singe particles is essential. The observed signal is often the net effect of vast amount of signals by single particles, which may be interacting with each other by multiple scattering. In the low-density cases the multiple scattering can be quite reliably treated with radiative transfer models, while in high-density cases an exact multiple scattering treatment might be necessary for a reliable modeling. In any case, the single scattering properties of the particles are the essential input for the model.

1.1 Single particle computations

The exact treatment of far-field scattering by a single particle and a group of interacting particles are not that different. The Maxwell equations to be solved are the same. A realistic particle target can easily be of shape other than a perfect sphere, so computations based on the Mie theory are often not sufficient. Furthermore, the scattering target can consist of several materials with different refractive indices, so there is anyway multiple scattering in a single particle. Often the single particle itself can be best modelled as an aggregate of smaller monomers, thus scattering from a single particle is a multiple scattering problem.

For the abovementioned reason, the same computational tools that can be used in exact multiple scattering computations are necessary in single particle scattering computations, too. These methods include, e.g. Finite Difference Time Domain, volume integral methods such as Discrete Dipole Approximation, surface integral methods such as *T*-matrix and nullfield method with discrete sources, among many [1].

To conclude the computational side, the scattering properties of single particle can, thanks to modern methods and computing power, be solved computationally for practically any single particle with moderate size parameter ($2\pi r/\lambda$ less than about 100) and refractive index or indices.

1.2 Scattering measurements

Experimental scattering studies, i.e., laboratory measurements of scattering, are needed in conjunction with computations, for two reasons. First, the exact computations are still very computationally intensive or even impossible when the particle's size parameter exceeds about 50 or 100. In blue light (λ = 0.45 μm), for example, this limit is reached with particles with diameter between ~7 μm and ~14 μm. For smooth, homogeneous particles much larger than that, the geometric optics treatment is valid and effective method, but unfortunately many naturally occurring particles are neither smooth nor homogeneous.

Second, the geometry, including the internal structure, and the material composition of small particles might be difficult to measure accurately for small particles. Electron microscopy and microtomography can reveal the structure of the particle quite well, but they are both laborious and expensive methods, and especially microtomography has its own resolution limit that might result in an imperfect model of the target.

For the abovementioned reasons, laboratory measurements of single particle scattering are needed. They can verify the computational results and give much needed realistic input to multiple scattering studies.

There are some groups conducting scattering experiments that produce valuable information in the form of angle-resolved Mueller matrices of single particles. We would like to mention here especially the Amsterdam-Granada scattering database, where this kind of data is collected and distributed to researches [2]. We aim to complement their work by offering single particle scattering matrices for single, well-documented particles in fixed orientation. The main difference to Amsterdam-Granada setup is that they measure the averaged scattering properties of multiple single particles in air flow, determining essentially the orientation-averaged scattering matrix for a particle collection. Our goal is the scattering matrix of one particle.

2 Proposed setup

We propose a setup where we need to control both the polarization state of the incident light and the position of the target, and measure the polarization state and intensity of the scattered radiation, as a function of the wavelength and the scattering angle.

The polarization state before and after the scattering event is controlled by a linear polarization filter and a wave retarder. By varying the angles of these four polarizing elements we can measure all the quantities needed to derive the full 4x4 Mueller matrix.

We are interested in the spectra of the target in the visual and near-infrared bands. In the minimal case we will employ a set of lasers with different wavelengths as the incident light source. A more ambitious setup can be reached with a wideband source with two possible options. First, the wavelength can be controlled by a monochromator before the polarizing elements and the target, and the measurement is done with a CCD camera after the target and the other set of polarizing elements. Second, the wideband radiation can be used as such, and the final intensity measurement after all the polarization controlling elements is done with a spectrometer.

The control of the particle is probably the most demanding part. Our options include, at least, using optical tweezers or mechanical control via nanoscale film, web or fibers, or with the micromanipulator device based on the Atomic Force Microscopy.

We are currently building the first version of the proposed setup with the possibility to verify and calibrate the device. We are using a droplet-generating device which will produce nearly spherical and very small water droplets as targets. The benefit of microdroplets is that we can use Mie calculations to calibrate the measured signal from our device.

3 Acknowledgement

The research is funded by the ERC Advanced Grant No. 320773 (SAEMPL).

4 References

[1] M.I. Mishchenko, L.D. Travis, and A.A. Lacis. *Multiple scattering of light by particles. Radiative transfer and coherent backscattering* (Cambridge University Press, 2006).

[2] O. Muñoz, F. Moreno, D. Guirado, D.D. Dabrowska, H. Volten, J.W. Hovenier, The Amsterdam–Granada Light Scattering Database, Journal of Quantitative Spectroscopy and Radiative Transfer 113(7):565-574 (2012).

Miscellaneous topics

Intrinsic Method for the Evaluation of Beam Shape Coefficients in Spheroidal Coordinates for Oblique Illumination

Lu HAN[1,*], Yi Ping HAN[1] , Gerard GOUESBET[2], and Jia Jie WANG[1]

[1] School of physics and optoelectronic engineering, Xidian University, Xi'an, shannxi 710071,China
[2] Département : Optique et Lasers, CORIA UMR 6614 CNRS/INSA et Université de Rouen, Saint-Etienne-du Rouvray, 76801, France

Corresponding author: luhan@stu.xidian.edu.cn

Abstract

In Generalized Lorenz-Mie theories (GLMTs), the most challenging issue concerns the evaluation of beam shape coefficients (BSCs). We provide a solution to the evaluation of spheroidal BSCs by using an intrinsic method in the general case of oblique illumination, including numerical results.

1 Introduction

A continued effort has been devoted to the development of generalized Lorenz-Mie theories (GLMTs) describing the interaction between electromagnetic arbitrary shaped beams with a class of regular particles having enough symmetry to allow for the solution of the scattering problem by using the method of separation of variables. One fundamental problem in the GLMT concerns the expansion of the incident shaped beam as a series of basic functions, with expansion coefficients named beam shape coefficients (BSCs). In any GLMT, the most challenging issue might concern the evaluation of BSCs. In spherical coordinates, the evaluation of BSCs may be carried out by using different kinds of methods, with a review in [1], and an important complement in [2]. Each of these methods to evaluate spherical BSCs is an intrinsic method, this means that the same kind of coordinate systems is used simultaneously both to solve the scattering problem under study and to evaluate the BSCs. Similarly, the intrinsic method has been used in cylindrical coordinates. Due to the intertwining between field components and spheroidal BSCs of different natures, and also due to the complexity inherent in the mathematics of vector spheroidal wave functions, GLMT for spheroid has been developed stepwise. Han and Wu [3] introduced an original method to evaluate spheroidal BSCs in terms of spherical BSCs. This is called an extrinsic method, in contrast with the more traditional intrinsic method. However, an intrinsic method in spheroidal coordinates is desirable because it is believed to be a necessary step to possibly develop localized beam models which have been found very efficient and enlightening in other coordinates, namely spherical and cylindrical coordinates. Then, Gouesbet et al. [4] presented a first formal solution to the evaluation of spheroidal BSCs, by using an intrinsic method in the most general off-axis case. Subsequently, we presented an intrinsic method in the case of an on-axis beam, including numerical results [5].

In this paper, we extend the above approach and provide a solution to the evaluation of spheroidal BSCs by using an intrinsic method in the general case of oblique illumination. A description of arbitrary shaped beam in the general case of oblique illumination is given by using addition theorem under coordinate rotations.

2 Theoretical background

Fig. 1 shows the geometry of the problem. The shaped beam propagates in free space and from the negative z'' to the positive z'' of $Ox''y''z''$, with the center of the beam waist as the origin O'' . The center of the scatter is located at the point O of the Cartesian coordinate system $Oxyz$ which is obtained by rotating the system $O''x''y''z'''$ at Euler angles of α, β, γ . In this paper, we assume that the time-dependent part of the electromagnetic fields is $e^{-i\omega t}$.

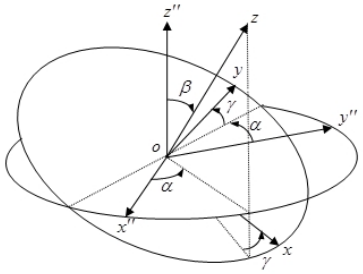


Figure 1. *Geometry of Cartesian coordinate system Oxyz of the incident shaped beam. Euler angles of rotation α,β,γ for transforming the Ox″y″z″ coordinate system into the Oxyz coordinate system.*

The incident shaped beam can be expanded in terms of spheroidal vector wave functions natural to the system $O''x''y''z'''$ [5]

where $g^1_{n,TE}$ and $g^1_{n,TM}$ are the spheroidal BSCs for the on-axis case, and can be derived by using an intrinsic method.

The description of the incident shaped beam from in its own Cartesian coordinate system $O''x''y''z'''$ can be

transformed to that in the accessory Cartesian coordinate system $Oxyz$ by the addition theorem.

$$\mathbf{E} = E_0 \sum_{m=0}^{\infty} \sum_{n=m}^{\infty} i^{n+1} \left[-2G_{n,TE}^{m} \mathbf{M}_{omn}(c;\xi,\eta,\phi) + 2G_{n,TM}^{m} \mathbf{N}_{emn}(c;\xi,\eta,\phi) \right] \tag{2}$$

$$G_{n,TE}^{m} = i^{n-1} \frac{2n+1}{n(n+1)} \rho(1,m,n) g_{n,TE}^{1} \tag{3}$$

$$G_{n,TM}^{m} = i^{n-1} \frac{2n+1}{n(n+1)} \rho(1,m,n) g_{n,TM}^{1} \tag{4}$$

where

$$\rho(1,m,n) = \sum_{\sigma=0}^{n-m} (-1)^{n-1-\sigma} \frac{(n-m)!}{(n-1-\sigma)!(m+1+\sigma)!} \times \frac{(n+1)!}{(n-m-\sigma)!\sigma!} \left(\cos\frac{\beta}{2} \right)^{2\sigma+1+m} \times \left(\sin\frac{\beta}{2} \right)^{2n-2\sigma-m-1} \exp\left[i(\alpha + m\gamma) \right] \tag{5}$$

3 Numerical validation

First, we compare the spheroidal BSCs obtained by the proposed method with those published by Xu et al. [6] for oblique incidence of the plane wave in Table 1. In the comparison, parameters are adopted directly from [6]. The wavelength is $0.6328\mu m$, incidence angle is 45°, polarization angle is 0°, and size parameter of the spheroid is 1. The agreement between the results from the four columns is perfect.

Consider a Gaussian beam with waist radius $w_0 = 3\lambda$ (the wavelength $\lambda = 0.6328\mu m$), polarization angle $\alpha = 0^\circ$, and incidence angle $\beta = 45^\circ$ incident on a spheroid of size parameter $c = 1$. The numerical results of spheroidal BSCs are listed in Table 2. We observe that the agreement between the results from the three columns is still very satisfactory.

m	n	$i\left(G_{n,TE}^{m}\right)_{Xu}$	$iG_{n,TE,\xi}^{m}$	$iG_{n,TE,\eta}^{m}$	$iG_{n,TE,\phi}^{m}$
0	1	(0,0)	(0,0)	(0,0)	(0,0)
0	2	(0,0)	(0,0)	(0,0)	(0,0)
0	3	(0,0)	(0,0)	(0,0)	(0,0)
1	1	(-0.7607,0)	(-0.7606709746,0)	(-0.7606709746,0)	(-0.7606709746,0)
1	2	(-0.3031,0)	(-0.3031496601,0)	(-0.3031496601,0)	(-0.3031496601,0)
1	3	(-0.1183,0)	(-0.1182577358,0)	(-0.1182577358,0)	(-0.1182577358,0)
2	2	(-0.1477,0)	(-0.1476609087,0)	(-0.1476609087,0)	(-0.1476609087,0)
2	3	(-0.0740,0)	(-0.0739856490,0)	(-0.0739856490,0)	(-0.0739856490,0)
3	3	(-0.0182,0)	(-0.0181834851,0)	(-0.0181834851,0)	(-0.0181834851,0)
m	n	$\left(G_{n,TM}^{m}\right)_{Xu}$	$G_{n,TM,\xi}^{m}$	$G_{n,TM,\eta}^{m}$	$G_{n,TM,\phi}^{m}$
0	1	(1.1079,0)	(1.1079082516,0)	(1.1079082516,0)	(1.1079082516,0)
0	2	(1.2124,0)	(1.2124015835,0)	(1.2124015835,0)	(1.2124015835,0)
0	3	(0.9845,0)	(0.9844851974,0)	(0.9844851974,0)	(0.9844851974,0)
1	1	(-0.5466,0)	(-0.5466066319,0)	(-0.5466066319,0)	(-0.5466066319,0)
1	2	(-0.0046,0)	(-0.0045772001,0)	(-0.0045772001,0)	(-0.0045772001,0)
1	3	(0.1698,0)	(0.1698136595,0)	(0.1698136595,0)	(0.1698136595,0)
2	2	(-0.1055,0)	(-0.1055120201,0)	(-0.1055120201,0)	(-0.1055120201,0)
2	3	(-0.0267,0)	(-0.0267363477,0)	(-0.0267363477,0)	(-0.0267363477,0)
3	3	(-0.0130,0)	(-0.0129518481,0)	(-0.0129518481,0)	(-0.0129518481,0)

Table 1: *Spheroidal BSCs: Oblique Incidence of a Plane Beam*

m	n	$iG^m_{n,TE,\xi}$	$iG^m_{n,TE,\eta}$	$iG^m_{n,TE,\phi}$
0	1	(0,0)	(0,0)	(0,0)
0	2	(0,0)	(0,0)	(0,0)
0	3	(0,0)	(0,0)	(0,0)
1	1	(0,0.7607747349)	(0,0.7607747354)	(0,0.7607747353)
1	2	(0,0.2997740922)	(0,0.2997740851)	(0,0.2997740851)
1	3	(0,0.1152299403)	(0,0.1152299404)	(0,0.1152299404)
2	2	(0,0.1460505560)	(0,0.1460505525)	(0,0.1460505525)
2	3	(0,0.0719455702)	(0,0.0719455703)	(0,0.0719455703)
3	3	(0,0.0176863396)	(0,0.0176863396)	(0,0.0176863396)
m	n	$G^m_{n,TM,\xi}$	$G^m_{n,TM,\eta}$	$G^m_{n,TM,\phi}$
0	1	(1.1083841622,0)	(1.1083841629,0)	(1.1083841628,0)
0	2	(1.1989768057,0)	(1.1989767771,0)	(1.1989767771,0)
0	3	(0.9581679980,0)	(0.9581679986,0)	(0.9581679985,0)
1	1	(-0.5464396926,0)	(-0.5464396929,0)	(-0.5464396929,0)
1	2	(-0.0043514139,0)	(-0.0043514138,0)	(-0.0043514138,0)
1	3	(0.1650126574,0)	(0.1650126575,0)	(0.1650126575,0)
2	2	(-0.1043193675,0)	(-0.1043193650,0)	(-0.1043193650,0)
2	3	(-0.0259713409,0)	(-0.0259713409,0)	(-0.0259713409,0)
3	3	(-0.0125932161,0)	(-0.0125932161,0)	(-0.0125932161,0)

Table 2: *Spheroidal BSCs: Oblique Incidence of a Gaussian Beam*

4 Conclusion

By virtue of the GLMT, the spheroidal BSCs are directly expressed in spheroidal coordinates by using an intrinsic method, for the case of general oblique illumination, including numerical results.

5 References

[1] G. Gouesbet, J.A. Lock, and G. Gréhan. Generalized Lorenz-Mie theories and description of electromagnetic arbitrary shaped beams: localized approximations and localized beam models, Journal of Quantitative Spectroscopy and Radiative Transfer, 112:1–27 (2011).

[2] G. Gouesbet, J.A. Lock, J.J. Wang, and G. Gréhan. Transformations of spherical beam shape coefficients in general Lorenz-Mie theories through rotations of coordinate system. V. Localized beam models, Optics Communications, 284:411–417 (2011).

[3] Y.P. Han and Z.S. Wu. Scattering of a spheroidal particle illuminated by a Gaussian beam, Applied Optics, 40(15):2501–2509 (2001).

[4] G. Gouesbet, J.J. Wang, and Y.P. Han. Solution to the intrinsic method for the evaluation of beam shape coefficients in spheroidal coordinates, Optics Communications, 294:29–35 (2013).

[5] L. Han, G. Gouesbet, Y.P. Han, G. Gréhan, and J.J. Wang. Intrinsic method for the evaluation of beam shape coefficients in spheroidal coordinates for on-axis standard configuration, Optics Communications, 310:125–137 (2014).

[6] F. Xu, K.F. Ren and X.S. Cai. Expansion of an arbitrarily oriented, located, and shaped beam in spheroidal coordinates, Journal of the Optical Society of America A, 24, 1:109–118 (2007).

Effect of Fractal Parameters of Soot Aggregates on their Absorption and Scattering Properties Simulated by Discrete Dipole Approximation

Gizem OKYAY[1-2*] and Franck ENGUEHARD [1-2]

[1] CNRS, UPR 288 Laboratoire d'Energétique Moléculaire et Macroscopique, Combustion (EM2C), Grande Voie des Vignes, 92295 Châtenay-Malabry, France
[2] Ecole Centrale Paris, Grande Voie des Vignes, 92295 Châtenay-Malabry, France
*Corresponding author: gizem.okyay@ecp.fr

Abstract

The objective of this study is to determine the impact of the fractal properties of methane soot issued from incomplete combustions on their absorption and scattering properties. The fractal properties are selected according to the bibliography. Sample numerical aggregates are generated accordingly. The absorption and scattering cross-sections, as well as the asymmetry factor are determined by our in-house developed DDA (discrete dipole approximation) code. Simulation results indicate a higher sensitivity of the radiative properties to the fractal dimension than to the prefactor. This sensitivity analysis aims to guide the choice of relevant characterization experiments of soot samples about the necessary precision on measurements and data collection, and also to decide on the extent of soot morphological properties to be considered in heat transfer simulations.

1 Introduction

The interaction of soot with radiation is of interest for the control of heat transfer within combustion chambers and the improvement of their design. The overall size of soot aggregates formed by incomplete combustions may reach several hundreds of nanometers. In high temperature applications, radiation is the main heat transfer phenomenon, and a strong interaction is expected between an incident radiation and soot aggregates reaching the size of the incident wavelength. Under such conditions, the complex morphology of these aggregates cannot be ignored in the radiation-aggregate interaction because the incident wave is able to probe the spatial arrangement of the material within the aggregate. In this work, the electromagnetic theory "DDA" is used to account for the complex shape of the aggregates in the computation of their radiative properties i.e. the features of their interaction with the electromagnetic radiation.

2 Soot aggregates

Inside a combustion chamber, the morphology, the composition and the number of monomers of a flame soot depend strongly on the operating conditions like the temperature, type of fuel, stoichiometry, type of flame.

This research focuses on soot aggregates from the combustion of methane with air and oxygen. These aggregates are of complex shape formed by hundreds of sphere like carbonaceous monomers.

A complete 3D description of the aggregate is needed as input for the electromagnetic modelling. Unfortunately, the current microscopy techniques do not allow access to this information, which is one of the fundamental input data for DDA simulation.

Studies found in the literature propose the application of the fractal theory for the 3D geometry description of soot aggregates [1,2]. It is therefore possible to correlate the geometrical parameters N (number of monomers in the aggregate), r (monomer radius), R_g (radius of gyration of the aggregate) by use of the dimensionless parameters k_f (prefactor) and D_f (fractal dimension) specific to the material and the conditions of its elaboration:

$$N = k_f (R_g / r)^{D_f} \quad (1)$$

Once the D_f, k_f and N parameters are decided, different aggregation algorithms like DLA (Diffusion Limited Aggregation) or DLCCA (Diffusion Limited Cluster Cluster Aggregation) are able to generate aggregates in a specific range of D_f, k_f and N.

Reference	r	N	D_f	kf
Zhang et al. (1998)	10	5-200	1.62	-
Koylu et al. (1995)	-	-	1.65	2.71
Cai et al. (1995)	-	-	1.74	1.23
Cai et al. (1995)	-	-	1.74	2.45
Sorensen et al. (1992)	-	-	1.73	-
Lee et al. (2000)	5 - 10	10-600	1.75	6.46

Table 1 *Bibliographic data on methane soot fractal properties*

A partial list of r, N, D_f and k_f values found in the literature for our study on methane soot is presented in Table 1. D_f values are all around 1.7 while the range of k_f values is much larger (from 1.2 to 6.5) depending on the experimental conditions. In order to quantify the impacts of these fractal parameters on the radiative properties, we generate, for each couple (D_f , k_f) examined, several samples of soot aggregates and calculate their interaction cross-sections with the DDA theory.

The reference case selected for methane soot has the parameters D_f = 1.7 and k_f = 2.0. The fractal properties are slightly modified around the reference values to observe the variations in the absorption and scattering cross-sections. The number of monomers per aggregate N ranges from a few tens to several hundreds and the monomer radius r from 5nm to 10nm according to the literature data. To represent correctly the methane soot and to ensure a high aggregate-radiation interaction, higher limits are selected as N = 500 and r = 10nm. Numerical soot aggregates are generated using the DLCCA algorithm of Mackowski [2], as represented in Figure 1.

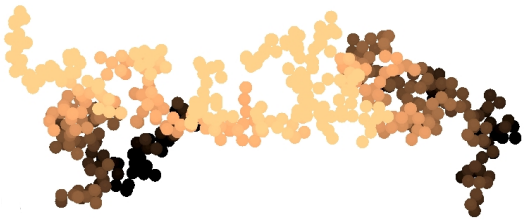


Figure 1 *Numerical aggregate with the reference parameters.*

3 DDA simulations

The DDA theory, originally proposed by Purcell and Pennypacker [3], is now a well-known modeling tool and the solution procedure is well established [4]. The method consists of material discretization into a sufficient number of dipoles where each dipole is polarized under the effect of the incident light. Each dipole contributes to the material-light interaction depending on its composition and its position in the discretized geometry. The limiting condition proposed by Draine [5] ensures a sufficient discretization under an incident wave :

$$|m|k\delta << 1 \qquad (2)$$

where m is the complex refractive index of the material, k is the wavenumber and δ is the characteristic size of the volume elements of the discretization.

Our research is focused on the radiation in combustion chambers at 1500-2000K. The DDA simulations are performed for an incident wavelength of λ = 1µm ; this wavelength is in the range of high temperature radiation and is of the same order of magnitude as the characteristic size of the soot aggregates, so that unconventional interaction effects can be expected. The non-polarized thermal radiation is modeled by averaging the simulations with 2 orthogonal polarizability directions for the same incident wave direction [6].

For our monomers of radius r = 10nm, the spatial discretization of one dipole per monomer satisfies the condition given in Eq. (2) under λ = 1µm and with a typical methane soot refractive index of m = 2.0+0.5i [7].

Soot being a highly absorbing material, errors may arise in DDA simulations due to the badly explained surface interactions (surface dipole polarizabilities) and the shading effect on inner dipoles at high refractive indices, even when the discretization condition is satisfied [8,9]. In a previous work, we have compared the Mie cross-sections of a soot monomer with the DDA solutions using different discretization finesses, and decided to consider one dipole per monomer in order to avoid such discretization errors [10]. Furthermore, the final aim is to obtain a qualitative comparison of the sensitivities to the fractal parameters.

4 Absorption and scattering from soot aggregates

It is to be reminded that the scope is to find the impacts of the morphology and fractal properties of numerically generated aggregates on their radiative properties, all other variables (material composition, r and N) being fixed. In the first part, a comparison with the Mie solution shows the relevance of considering complex aggregate shapes. In the second part, the evolution of the radiative properties is presented as a function of D_f and k_f.

4.1 Effect of complex aggregate geometry

Our present in-house heat transfer simulations consider Mie solution properties for the radiative properties of soot. The DDA results for the reference aggregate presented in Figure 1 are compared to the Mie solution for a sphere having an equivalent material volume.

Cross-section	*DDA (m²)*	*Mie (m²)*	$\lvert\Delta C\rvert/C_{DDA}$
$C_{Extinction}$	7.52e-15	9.18e-15	23 %
$C_{Absorption}$	7.10e-15	8.08e-15	14 %
$C_{Scattering}$	0.42e-15	1.10e-15	160 %
$g_{asymmetry}$	0.411	0.061	-

Table 2 *DDA compared to Mie solution for the reference case*

The results presented in Table 2 show the relevance of DDA simulations for the determination of the radiative properties of soot. Despite the well-known overestimation tendency of absorption by DDA [11], the DDA solution for absorption is more than 10% below the Mie solution. Also the asymmetry factor predicted by the DDA indicates a strong forward scattering unlike the Mie solution, which proves the sensitivity of the DDA to the morphology of the scatterer.

4.2 Effect of fractal properties

Aggregate samples are simulated first by varying D_f around its reference value with all other parameters fixed. The trends of the DDA results as a function of D_f are represented in Figures 3 and 4. As can be seen on these figures, several numerical aggregates are generated for the same fractal parameter in order to account for the random nature of the aggregation process.

The same procedure is applied to study the sensitivity of the radiative properties to the prefactor k_f. The trends extracted for k_f are globally similar to the ones presented in Figures 3 and 4. However, the sensitivities on D_f and k_f are slightly different, as summarized in Table 3.

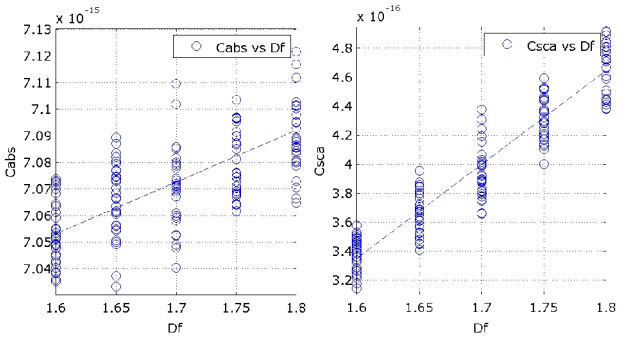


Figure 3 *Absorption (left), scattering (right) cross-sections of methane soot as a function of D_f (k_f, N and r are fixed).*

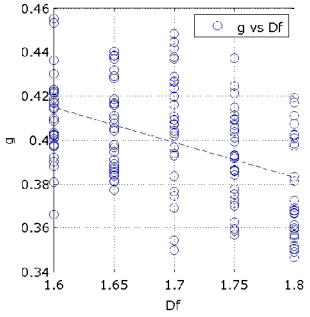


Figure 4 *Asymmetry factor for methane soot as a function of D_f (k_f, N and r are fixed).*

Results indicate that the interaction of soot with radiation is more affected by the value of the D_f parameter. In particular, varying D_f from 1.6 to 1.8 modifies the absorption by only 1.5% but the scattering by 46%. But as the absorption phenomenon dominates the scattering by soot, the sensitivity of soot radiative properties to the fractal parameters can be considered relatively small in the range of study if no particular interest is shown for scattering in the radiative heat transfer simulations.

	% change for 1% modification of D_f	% change for 1% modification of k_f
$C_{Absorption}$	0.12	0.04
$C_{Scattering}$	3.93	1.63
$g_{asymmetry}$	2.56	0.31

Table 3 *Variation of the radiative properties of methane soot aggregates due to modification of their fractal parameters.*

5 Conclusion and perspectives

In this study, the effects of the fractal properties on the radiative properties of methane soot are investigated. Methane soot is represented by numerically generated aggregates and the radiation-soot interaction is simulated using the DDA theory. Results indicate a small dependence for absorption but an important one for scattering versus the D_f and k_f parameters. If absorption is considered as the dominating phenomenon, the uncertainties on D_f and k_f around the reference values can be ignored.

The choice of our future characterization techniques and the necessary precision in data extraction depends on an extended version of the presented sensitivity study. Also, numerical soot aggregates will be gathered in groups of identical radiative properties merely dependent on the fractal parameters ; these groups are to be inserted as input for heat transfer simulations.

6 Acknowledgement

The authors kindly acknowledge the support of this research within the industrial chair OXYTEC of Ecole Centrale Paris, jointly conducted and funded by the laboratory EM2C, Air Liquide, CNRS and ANR.

7 References

[1] Megaridis C.M., Dobbins R.A., Morphological Description of Flame-Generated Materials, Combustion Science and Technology 71:95-109 (1990).

[2] Mackowski D.W., A simplified model to predict the effects of aggregation on the absorption properties of soot particles, J. Quant. Spectrosc. Radiat. Transfer 100:237-249 (2006).

[3] Purcell E.M., Pennypacker C.R., Scattering and absorption of light by nonspherical dielectric grains, Astrophys. J. 186:705-714 (1973).

[4] F. Enguehard, Mie Theory and the Discrete Dipole Approximation Calculating Radiative Properties of Particulate Media with Application to Nanostructured Materials, in S. Volz, *Thermal Nanosystems and Nanomaterials, Topics in Applied Physics* 118:151-212 (Springer Verlag Berlin Heidelberg, 2009).

[5] Draine B.T., Flatau P.J., The discrete dipole approximation for scattering calculations, J. Opt. Soc. Am. A 11:1491 – 1499 (1994).

[6] C.F. Bohren, and D.R. Huffman, *Absorption and scattering of light by small particles* (Wiley, New-York, 1983).

[7] Van-Hulle P., Caractérisation des Aérosols Emis par la Combustion des Hydrocarbures : Application à la Mesure de l'Indice de Réfraction des Suies, thèse de doctorat, INSA Rouen (2002).

[8] Collinge M., Draine B., Discrete-dipole approximation with polarizabilities that account for both finite wavelength and target geometry, J. Opt. Soc. Am. A 21 :2023-2028 (2004).

[9] Rahmani A., Chaumet P.C., Bryant G.W., On the importance of local-field corrections for polarizable particles on a finite lattice : Application to the discrete dipole approximation, Astrophys. J. 607:873-878 (2004).

[10] Okyay G., Enguehard F., Modélisation des propriétés radiatives des suies issues de combustions incomplètes au moyen de l'approximation dipolaire discrète, *Congrès Français de Thermique,* Lyon, 2014. [abstract accepted, paper in progress]

[11] K.A. Fuller and D.W. Mackowski, Electromagnetic Scattering by Compounded Spherical Particles, in Mischenko et al., *Light Scattering by Nonspherical Particles*, 225-272 (Academic Press, 2000).

Dynamic polarimeter for spectral imaging of scattering media

J. M. SANZ[1], F. CARMAGNOLA[1-2], A. FERNANDEZ[1], F. MORENO[1], F. GONZALEZ[1] and J. M. SAIZ[1,*]

[1] Departamento de Física Aplicada, Universidad de Cantabria, Santander 39005 Spain
[2] Dipartimento di Fisica, Università degli Studi di Milano.
Via Celoria 16, 20133 Milano (Italy)

Corresponding author: saizvj@unican.es

Abstract

The possibilities of a Dynamic Rotating Compensator Polarimeter (DRCP) for the accurate exploring of the polarimetric behaviour of dense media are explored. For the case of a rough surface, namely a surface standard like Spectralon®, its role as a depolarizer is analyzed over the visible spectrum by implementing and calibrating a multispectral source on the DRCP. For a scattering volume, a typical suspension of latex particles, a high dynamic range camera is added to the detection system of the DRCP, therefore allowing for a polarimetric imaging of the input surface. This is an external view of the scattering processes taking place inside the medium, a view that, for the simplest cases can be numerically simulated. However, when an object is embedded in such medium, this technique seems to be quite efficient in recognizing the position, depth, and even the nature of that object. Operations performed on the Mueller matrix (MM) image are able to distinguish absorbent, reflectant, and even highly-scattering objects, provided that a reference object-free polarimetric image can be also obtained.

The combination of spectral and imaging capabilities in the same DRCP instrument could offer the most complete "polarimetric fingerprint" of a dense media with optically inhomogeneous inclusions.

1 Depolarizing surfaces

Spectralon® is a white reflectance standard, and its Lambertian behavior, spectrally analyzed, stands over most of the visible spectrum. Regardless the angle of scattering, the brightness of a Lambertian surface to an observer is the same. That is why this kind of surfaces is essential to build diffuse reflectance standards, and for integrating sphere manufacture and other equipment calibration. It is also acquiring the role of a polarimetric standard in the sense of behaving as a *perfect depolarizer*. This has been shown recently for a multi-wavelength source in a variable-incidence experiment. The set-up geometry of the dynamic polarimeter and some important results obtained for this surface are summarized in Figs 1 and 2 as they are presented in [1]. In all cases the experimental reflectance (given by m_{11}) approaches very well a Lambertian curve, apart from Angles Of Incidence (AOI)>45° and θ>30°, and all comparisons between theoretical models and experimental results should be consistent with this experimental fact.

The purity of the matrix, P(M) is very close to zero in the range analyzed, as corresponding to an almost perfect depolarizer, with values under 0.02 for normal incidence over a large range of θ, regardless of the wavelength. This result stands for a high range of AOI.

In other words, Spectralon SRS-99 bounces off some [98-100]% of fully depolarized light in the wavelength range from 488.0 to 632.8 nm, independently of the AOI, for −60°<θ<30°

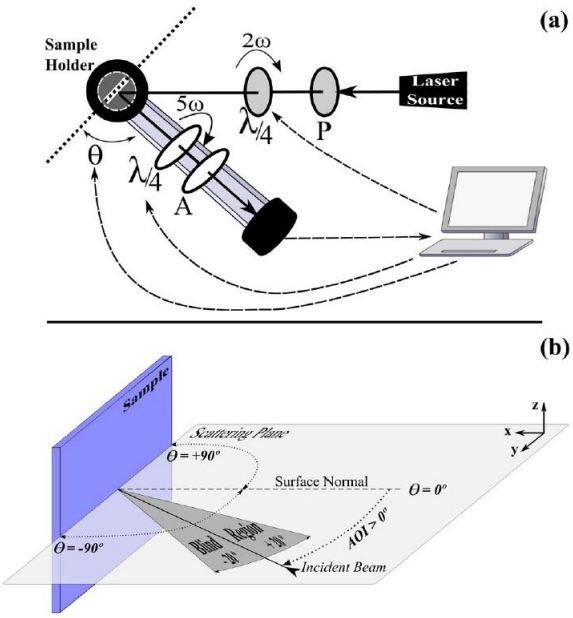


Figure 1 *(a) Experimental setup, where the synchronous rotation of the waveplates and the control of the angles is shown. (b)Scattering plane showing the criterion for the angles.*

outlining a Lambertian reflectance profile. At normal incidence more than 98% of the reflected light is fully depolarized in the scattering range −60°≤θ≤60°, with strong deviations when either θ≤−60° or θ≥60°. Such deviations increase dramatically for AOI>45° and θ>30°,

resulting in a low depolarizing surface for these conditions.

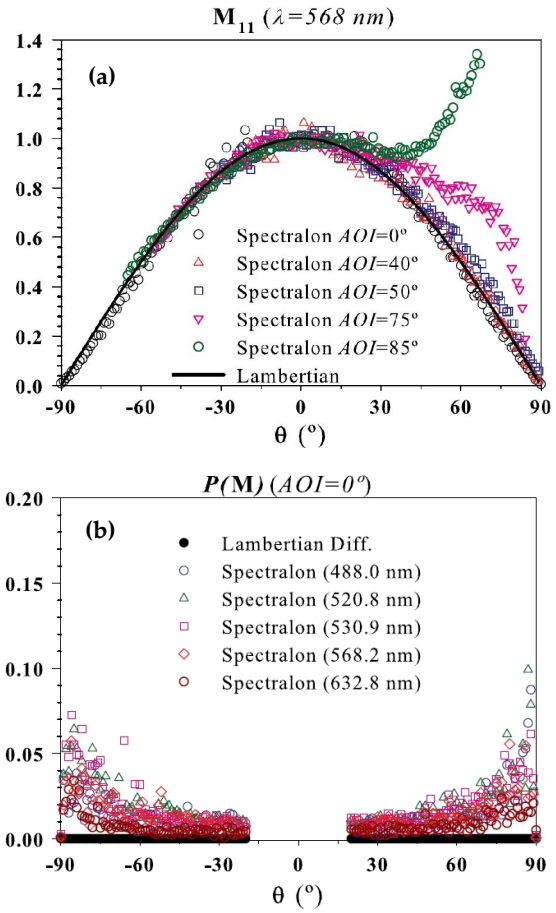


Figure 2 *Behavior of Spectralon® SRS-99 standard: (a) element m_{11} vs θ for at λ=568,2nm and for several AOI. (b)Purity of the matrix P(M) vs θ at normal illumination.*

2 Dense Media

In the case of a turbid medium, the outgoing scattered light exhibits, in general, substantial depolarization. In this situation, the surface of the medium, in the surroundings of the point where the incident beam hits such surface becomes very interesting. This is a considerable amount of light that travels through the medium, interacting with the matter, and can be monitored by a surface imaging system. Moreover, its polarization state keeps some record of such interactions, a fact that demands the use of a polarimetric imaging system for a proper analysis of such information (i.e. a 4x4 MM of the surface, or 16 images). From this point the approaches differ from some researchers to others, mainly because of the different purpose, medium, size or instrumentation. If an object embedded in a dense media interacts with light then it may leave its own mark in the output image polarization. In this sense it must be detectable. Although a complete MM analysis, like the so-called *polar decomposition* can extract the polarimetric information of the system in an understandable way, we have operated on the raw images, seeking a straight-forward way to find the polarimetric fingerprint of the embedded object.

2.1 Object-free medium

An experiment was performed with polystyrene spheres suspended in water. Fig 3(b), taken from [2], shows the MM for particles sized 1,1μm in diameter, with a concentration $3x10^{-3}\mu m^{-1}$, enough to have a few mm penetration and also to hide objects. For this system a Monte-Carlo simulation has been performed, based on the algorithm developed by Ramella-Roman et al [3]. Very briefly, the program tracks the path and polarization for every photon as it interacts (Mie scattering) with the latex particles (scattering coefficient μ_s), contributing to the polarization state at a given point of the surface. The result is shown in Fig 3 (a). The agreement is as good as the best found in the literature [4].

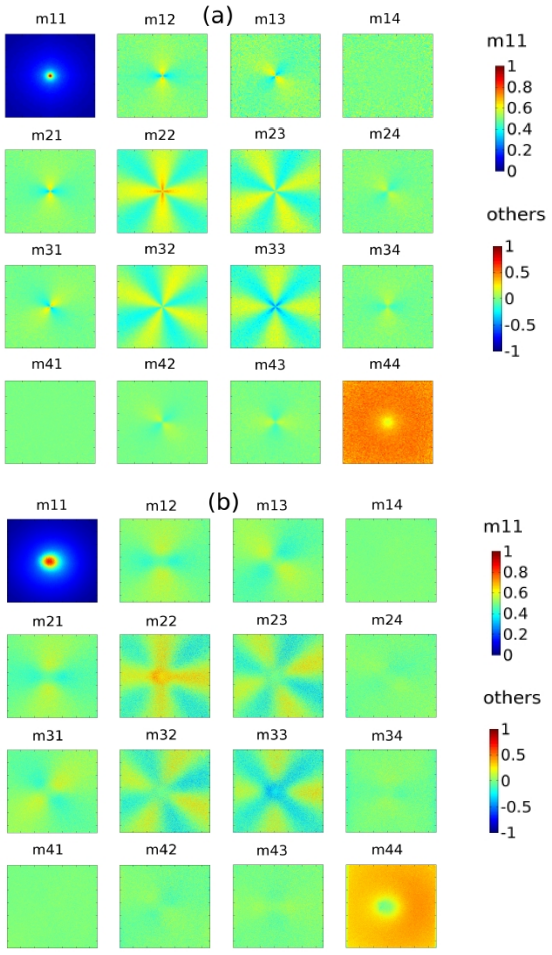


Figure 3 *MM's of a 1100nm diameter spheres suspension with concentration $3x10^{-3}\mu m^{-1}$ (picture dimensions are 10x10mm): (a) Simulated (μ_s=8,33mm^{-1}); (b)Measured (θ=20°).*

2.2 Polarimetric imaging with inmersed objects

Three different objects were embedded in the turbid media, all derived from a cylindrical glass tube with an external diameter of 0,75 mm that acts as a core. The reflective target is made with an external aluminum foil, the absorbing target is made adding a black felt cover, and the depolarizing target is made by gluing micrometer-sized glass powder. The glass tube is mounted on a stand, which allows us to control its position inside the cuvette, i.e. its lateral position and depth in the medium, as described in [2]. From the experimental MM obtained for these cases other *relative* matrices (subtraction matrices) are defined, in order to assess the sensitivity of the method to the presence of the object. The main conclusion of this study is that this operation applied to elements m_{11} and m_{44} allows the detection of the target, the assessment of its location, and also offers information about its nature (reflective, absorbent, scatter).

Fig 4 shows the map, 10x10mm of the surface for the relative matrix elements r_{11} and r_{44} when a reflecting object is located 4mm to the right and at several depths. Differences from zero are especially important both at the input spot and at the location of the object.

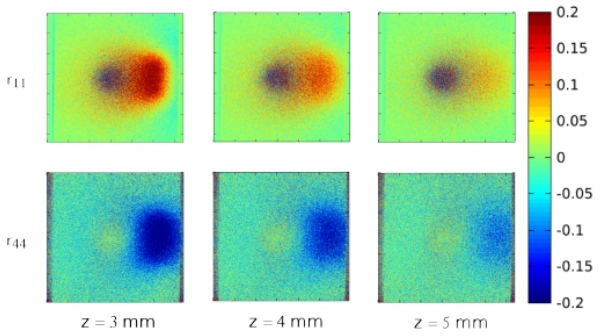


Figure 4 *"Relative" matrix elements r_{11} and r_{44} with the reflective target right-shifted 4mm and for three values of z.*

Fig 5 corresponds to the same two elements r_{11} and r_{44} for both depolarizing and absorbent targets, at the same lateral shift (x=4mm) and for a depth of z=3mm (this directly compares with the left images in Fig 4).

While in the case of reflecting and strongly scattering objects it is observed that $r_{44} < 0$), this is not the case for the absorbent object, for which r_{44} lies slightly over zero. Although the effects produced by the strongly depolarizing and reflecting objects are similar, the reflective one is much more localized. This behavior is somewhat reproducing that of its isolated counterpart. A reflecting object returns the light strongly polarized (the equivalent r_{44} for a mirror would be -1). The absorbing target shows a lack of backscattered light that can result in higher values of r44. This phenomenon can be understood as a lack of depolarized light. Lastly, for a depolarizing object, made of densely packed micron-sized glass particles, we have the case of a strong scatter inside a turbid (scattering) medium. Its effect is a non-local overall reduction of the values of r_{44}.

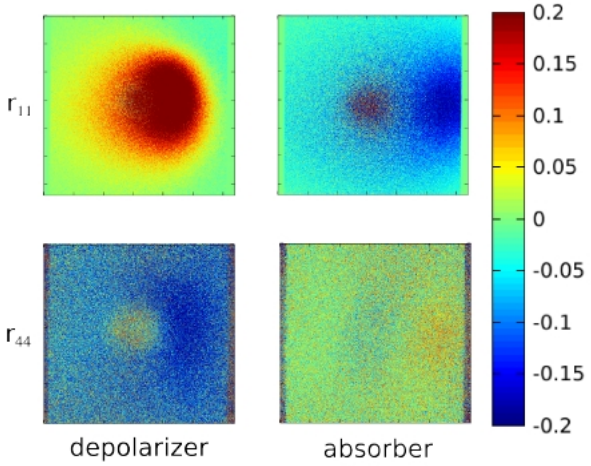


Figure 5 *"Relative" matrix elements r_{11} and r_{44} for the depolarizing and absorbent targets as in Fig4, with z=3mm.*

3 Spectral Imaging of turbid media

In principle, a dynamic polarimeter with an imaging system should provide a wide and accurate view of the output surface especially if the illumination and observation angles can be controlled. If the spectral sensitivity of a continuous source is added to the system, then its capabilities should increase, in particular for the cases in which the light-matter interaction is spectrally selective. This is the purpose of the upgrading that is being currently carried out in our dynamic DRCP, which performance and first results could presumably be shown by the time the congress takes place.

4 Acknowledgement

This research was supported by USAITC-A (United States Army International Technology Center Atlantic) through grant W911NF-13-1-0245. A. Fernández wishes to thank the Univ. of Cantabria for her research training grant.

5 References

[1] Sanz J.M., Extremiana C., Saiz J.M., Comprehensive polarimetric analysis of Spectralon white reflectance standard in a wide visible range, Applied Optics 52 (24): 6051-62 (2013)

[2] Carmagnola F., Sanz J.M., Saiz, J.M., Development of a Mueller matrix imaging system for detecting objects embedded in turbid media, Jour Quant Spect & Rad Transfer, in press.

[3] Ramella-Roman J. C., Prahl S. A., Jacques S. L., Three Monte-Carlo programs of polarized light transport into scattering media: part I, Opt. Express 13 (12), 4420-4438 (2005). [part II: Opt. Express 13 (25), 10392-10405 (2005)]

[4] He H., Zeng N., Li W., Yun T., Liao R., He Y., Ma H, Two dimensional backscattering Mueller matrix of sphere-cylinder scattering medium, Optic Letters 35 (14): 2323-25 (2010)

Diffusion of a Laser Pulse in a Particle Medium with Three-dimensional Geometry

Feng XU[1,*] and Anthony B. DAVIS[1]

[1] Jet Propulsion Laboratory, California Institute of Technology, Pasadena, CA 91109, USA

*Corresponding author: Feng.Xu@jpl.nasa.gov

Abstract

Light propagation in plane-parallel scattering particulate media has been well studied over the last decades in the regime of radiative transfer (RT). A number of numerical methods have been developed to achieve both computational efficiency and numerical accuracy [1]. While being fast, the plane-parallel model lacks the fidelity to the nature of some media in their shape. Moreover, the assumption of a spatially uniform light source does not reflect the nature of active laser-based measurement techniques. Although reliable numerical models for computing and interpreting the interaction of a light source with limited width and non-uniform intensity distribution against a three-dimensionally (3D) shaped medium are highly desirable, a very limited number of numerical methods have been developed (in comparison with the plethora of numerical solutions available for plane-parallel media). With few exceptions in the atmospheric optics literature, Monte Carlo methods [2] and the Spherical Harmonic Discrete Ordinate Method [3,4] have been developed and used as accurate methods to solve this problem.

However, to meet the requirements of computational efficiency for particle retrieval purposes, numerically faster models are still highly desirable. Therefore, diffusion-based models, as approximations for RT in optically thick media, have been and continue to be developed. Through inclusion of internal sources to the diffuse light field contributed by thermal emission and/or directly-transmitted sunlight with a first-order (i.e., 4-term) expansion of the radiance field and phase function into spherical harmonics, Davies [5], Liou [6] and coworkers [7] have derived and solved the resulting steady-state 3D diffusion equation, a Poisson-type partial derivative equation (PDE) with Robin-type boundary conditions (BCs). They used there efficient diffusion models to approximate RT in horizontally finite cuboidal clouds as well as internally variable cirrus and stratus clouds where the characteristic horizontal extension is mimicked by applying cyclical BCs.

Davis [8] did the same for a narrow pulsed laser beam illuminating a uniform plane-parallel medium that is representative of an optically thick stratus cloud to model the signals of multiple scattering lidar systems. By switching from the space-time domain to Fourier-Laplace space, he addressed the inherent time dependence and horizontal propagation of the signal at a laser wavelength such as 512 nm (2 x Nd:YAG) that is *not* absorbed by liquid water in cloud droplets. Specifically, he reduced it to a classic analytically tractable boundary-value problem in 1D "two-stream" RT with steady/uniform illumination, which is encoded in a pair of coupled ordinary differential equations (ODEs). In this case, however, it is for fictitious wavelengths with variable amounts of absorption. This strategy proved useful for developing a retrieval algorithm and estimating signal-to-noise ratios for the operational detection of laser pulses returned from optically thick stratiform clouds.

By forgoing the internal representation of the pulsed laser beam and instead representing it with a diffuse pulse of light emanating from at a single point on the cloud's boundary, and by using the same first order truncation of the spherical harmonics expansion of the space-time Green function, we simplify the diffusion model in the cw limit to Laplace or Helmholtz PDEs (respectively for non-absorbing and absorbing wavelengths) in general cloud geometry. Davis and Xu [9] then argue that the diffusion model will remain analytically tractable if it is generalized from media with plane-parallel slab geometry (1D RT) to media composed of any combination of constant-coordinate surfaces in any one of the standard curvilinear coordinate systems. We therefore have the potential for analytically tractable models for 3D RT, at least in the diffusion limit. The closed-form solution is then obtained by variable separation and point-matching methods for an arbitrary distribution of surface illumination, including a laser-like concentration at a single boundary point. While maintaining numerical accuracy to some extent with respect to the RT reference model, such a model has a significant advantage in computational efficiency.

We have explored so far a class of 3D media composed of spheres, oblate and prolate spheroids and assemblies of two hemi-spheroids with different aspect ratios, assuming uniform illumination by parallel beams of sunlight at any angle with respect to the axis of rotational symmetry [9].

Having such a foundation to build upon, we can return to the pulsed point source problem that approximates signal physics for multiple scattering lidars, now aimed at clouds with finite aspect ratios (ARs) viewing the standard plane-parallel cloud model as having an infinite AR. To this effect, we again use the Laplace transform of the pertinent time-dependent diffusion equation (heat-

type/parabolic PDE) to obtain the previously solved Helmholtz PDE where, in this case, the pseudo-absorption term captures time dependence in Laplace space. We thus obtain the solution for pulsed laser interaction with a cloud shaped as an assembly of two hemi-spheroids, a conveniently parameterized representation of 3D (finite AR) clouds that deviate strongly from slab geometry.

As an example of application, we compare predictions for quantities observable derived from raw multiple scattering lidar signals for the plane-parallel (AR = ∞) cloud [10] and horizontally finite (AR < ∞) ones of equal geometrical thickness (H) and optical (τ) thickness. We furthermore linearize our diffusion theoretical forward model to analyse the cloud information content of multiple scattering lidar signals in a statistical sense [11]. Following [7], we illustrate using instrument specs for two existing multiple scattering lidar systems, namely the Los Alamos National Lab's ground-based Wide-Angle Imaging Lidar (WAIL) [12] and NASA's shuttle-based Lidar-In-Space Technology Experiment (LITE) [13].

In the remainder of this summary, we describe our on-going research program in equations and figures.

1 Geometry, symbols, and equations

Figure 1 shows the parameterized geometry of the spheroidal optical medium M that will seek to probe with a pulsed laser aimed along its axis of rotational symmetry. Its shape and size can be represented either with the three semi-major axes (a,c_R,c_T). Alternatively, one can use the top-to-bottom thickness for size and two non-dimensional ones for shape: M(H,b,AR). Parameter $b = c_T/c_R$ thus quantifies the deviation of the 3D medium from an even more idealized shape, namely, the mirror-symmetric spheroid (b = 1). The aspect ratio parameter AR is given by $2a/(c_R+c_T)$. The (transport) extinction coefficient σ_t, or mean-free-path (MFP) $\ell_t = 1/\sigma_t$, must also be specified. Alternatively, one can use the transport (or "scaled" optical thickness) $\tau_t = \sigma_t H = H/\ell_t$. The figure also shows schematically (in green) the diffusion wave of scattered laser light propagating away from the isotropic point source at an early time. Finally, we can visualize the limiting case of a plane-parallel slab, namely, M(H,b,∞). The complete set of structural and optical parameters that we wish to retrieve from remotely observable responses to pulsed laser irradiation of M is the so-called state vector [11], denoted

$$\mathbf{x} = (H,\ b,\ \mathrm{AR};\ \tau_t)^{\mathrm{T}}, \qquad (1)$$

where superscript "T" means transpose. So $\mathbf{x} \in \mathbb{R}^n$ with, in this case, n = 4. In Fig. 1, we have set b = 1/4 and AR = 8/5.

We wish to compute the scalar flux of radiant energy $J(t,x,y,z)$ in M($\mathbf{x}$) and at its boundary ∂M($\mathbf{x}$). In the absence of internal sources and in the limit of RT when MFPs are small with respect to all the dimensions of the medium, in this case H, $J(t,\boldsymbol{x})$ obeys the classic 3+1D diffusion equation:

$$\left(\frac{\partial}{\partial t} + D\nabla^2\right) J = 0 \qquad (2)$$

where $D = c\ell_t/3$ is the diffusivity constant. The second-order PDE in (1) follows from

1) the conservation of radiant energy, $c^{-1}\partial_t J + \partial_x \boldsymbol{F} = -\sigma_a J$ in the absence of internal sources, where σ_a is the absorption coefficient (= 0, in this case), and
2) Fick's constitutive law for diffusion, $\boldsymbol{F} = -D\partial_x J$, which yields the vector flux.

The former expression is exact (0th-order angular moment of the integro-differential RT equation). The latter, however, is an approximation that results from the truncation of spherical harmonic expansion of the radiance field and the scattering phase function at 1st order. In the latter case, it reads as $p(\mu_s) = (1+3g\mu_s)/4\pi$ where μ_s is the cosine of scattering angle and the so-called asymmetry factor g is the mean value of μ_s averaged over the phase function. The previously used "transport" extinction coefficient $\sigma_t = (1-g)\sigma_s+\sigma_a$, where σ_s is the scattering coefficient. In RT theory, the differential cross-section for scattering is written as $\sigma_s p(\mu_s)$.

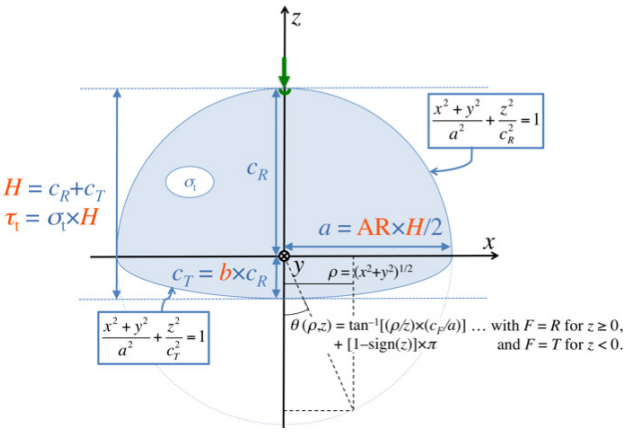


Figure 1 *Parametric geometry of the optical medium.*

BCs for (2) must specify the ingoing flux of radiant energy and therefore are of the 3rd or "Robin" type. For the present problem, we have:

$$F_{\mathrm{in}}(t,\boldsymbol{x}) = \frac{1}{4}\left(1 + \chi\ell_t \boldsymbol{n}(\boldsymbol{x})\cdot\nabla\right) J = \delta(t)\delta(x)\delta(y)\delta(z-c_R) \qquad (3)$$

where $\boldsymbol{n}(\boldsymbol{x})$ is the outgoing normal to ∂M($\mathbf{x}$) at boundary point $\boldsymbol{x}$, and χ is a numerical constant that controls precise value of the so-called extrapolation length scale, $\chi\ell_t$. This is not a variable per se it has been determined in the literature (primarily for neutron transport [e.g., 14]) to take values such as $1/\sqrt{3} \approx 0.577$, 2/3, or 0.7104··· by comparison between diffusion and RT predictions in one form or another. We usually adopt the intermediate value of 2/3.

We are particularly interested in the outgoing boundary fluxes

$$F_{\mathrm{out}}(t,\boldsymbol{x}) = \frac{1}{4}\left(1 - \chi\ell_t \boldsymbol{n}(\boldsymbol{x})\cdot\nabla\right) J = \frac{J(t,\boldsymbol{x})}{2} - F_{\mathrm{in}}(t,\boldsymbol{x}), \qquad (4)$$

especially those for

$$z = z_{\partial M}^{(R)}(x,y) = \frac{c_R}{a}\sqrt{x^2+y^2} \geq 0,$$

in Fig. 1, as they can be observed in reflective geometry (hence the subscript "*R*" in c_R, while "*T*" stands for the transmissive side of the medium). Therefore, a natural way of defining the forward model in this remote sensing inverse problem, $\mathbf{F}(\mathbf{x}) \in \mathbb{R}^m$, is to think of a large but finite number m of samples of the space-time reflected flux field:

$$R(t,\rho) = F_{\text{out}}(t,x,y,z_{\partial M}^{(R)}(x,y))|_{x=\rho,y=0}. \quad (5a)$$

Sampling can be at boundary points with $z_{\partial M}^{(R)}(\rho,0) \geq 0$ in the $y = 0$ plane. In short, we have

$$\mathbf{F}(\mathbf{x}) = (R(t_1,\rho_1),\ldots,R(t_m,\rho_m))^{\mathrm{T}}. \quad (5b)$$

However, to implement efficient retrievals of $\mathbf{x}$ using optimization techniques and/or perform a predictive error quantification, or a statistics-based information content analysis, we need to access the Jacobian matrix $\mathbf{K} = \partial\mathbf{F}/\partial\mathbf{x}$. Moreover, it is vastly preferable to be able to compute it analytically by linearizing the forward model $\mathbf{F}(\mathbf{x})$, i.e., enhancing it with the capability of delivering an accurate estimate of $\mathbf{K}$ at little cost in efficiency (finite differencing is not an option). It is not clear how to do that for the $\mathbf{F}(\mathbf{x})$ proposed in (5), but we do have a path forward if we turn to moments of $R(t,\rho)$.

2 Spatial and temporal moments as observables

More convenient and potentially more robust (less noisy) sets of observable quantities can be derived from $R(ct,\rho)$ or its discretized version in (5a,b), with enough samples, in the form of statistical moments. Letting

$$R_{\text{tot}} = 2\pi\frac{c_R}{a}\int_0^\infty\int_0^{\pi/2} R(ct,\rho_\theta)\rho_\theta\left|\frac{\mathrm{d}\rho_\theta}{\mathrm{d}\theta}\right|\mathrm{d}\theta\,\mathrm{d}ct \quad (5)$$

be the overall reflectivity (albedo) of the medium, $R(ct,\rho_\theta)/R_{\text{tot}}$ is a bi-variate probability density distribution (PDF), where we henceforth use path ct rather than time t per se (previous $R(\cdots)$ is simply divided by c). Radial distance from the z-axis of rotational symmetry (a.k.a. laser beam), ρ_θ is now expressed as a monotonic map from $[0,\pi/2]$ to $[0,a]$ defined implicitly in Fig. 1 for boundary points, i.e., when $z = z_{\partial M}(\rho,0) = c_R\times(1-(\rho/a)^2)^{1/2}$. From there, we define the marginal PDFs

$$p_R^{(\mathrm{t})}(ct) = \frac{2\pi}{R_{\text{tot}}}\times\frac{c_R}{a}\int_0^{\pi/2} R(ct,\rho_\theta)\rho_\theta\left|\frac{\mathrm{d}\rho_\theta}{\mathrm{d}\theta}\right|\mathrm{d}\theta, \quad (6)$$

for the time domain, and

$$p_R^{(\mathrm{s})}(\rho_\theta) = \frac{1}{R_{\text{tot}}}\int_0^\infty R(ct,\rho_\theta)\,\mathrm{d}ct, \quad (7)$$

for radial distance to the narrow collimated laser beam. We can now compute temporal moments,

$$\left\langle (ct)^q\right\rangle = \int_0^\infty (ct)^q\, p_R^{(\mathrm{t})}(ct)\,\mathrm{d}ct, \quad (8)$$

and spatial counterparts,

$$\left\langle \rho_\theta^{2q}\right\rangle = 2\pi\int_0^a \rho_\theta^{2q} p_R^{(\mathrm{s})}(\rho_\theta)\rho_\theta\,\mathrm{d}\rho_\theta, \quad (9)$$

for $q = 1,2,3,\ldots$.

An alternative vector of observables, with $m = 5 > n = 4$, could be $\mathbf{F}(\mathbf{x}) = (\langle ct\rangle, \langle (ct)^2\rangle, \langle (ct)^3\rangle, \langle \rho_\theta^2\rangle; R_{\text{tot}})^{\mathrm{T}}$. Or, better still,

$$\mathbf{F}(\mathbf{x}) = (\langle ct\rangle,\langle (ct)^2\rangle/\langle ct\rangle^2,\langle (ct)^3\rangle/\langle ct\rangle^3,\langle \rho_\theta^2\rangle/\langle ct\rangle^2;R_{\text{tot}})^{\mathrm{T}}. \quad (10)$$

Note that in the latter choice, we have one quantity with physical units of length and three non-dimensional ones, as for $\mathbf{x}$ in (1). Note also that we have isolated with a ";" the overall albedo R_{tot} since it is the only observed quantity that relies on absolute radiometric calibration, and knowledge of the transmitter's instantaneous power. So if we can avoid using it, thus reducing m from 5 to 4 in the moment-based scheme, it lessens significantly the burden on the instrument development effort. At any rate, these integrated quantities are much fewer, and will be far less noisy, than the relatively large set $\{R(t_i,\rho_i),\ i = 1,\ldots,m\}$ used to compute them in the discretized world.

Another significant advantage of working with spatial and temporal moments is that their forward model can be made analytically tractable in closed form. Indeed, we first note that the temporal moments in (9) can be derived directly from the Laplace transform of (7), known in probability theory as the moment generating function:

$$\hat{p}_R^{(\mathrm{t})}(s/c) = \left\langle \exp(-st)\right\rangle = \int_0^\infty p_R^{(\mathrm{t})}(ct)\exp(-(s/c)\times ct)\,\mathrm{d}ct. \quad (12)$$

We only need to know the Taylor series expansion of (12) at $s/c = 0$,

$$\begin{aligned}\hat{p}_R^{(\mathrm{t})}(s/c) &= \sum_{q=0}^\infty \frac{1}{q!}\times\left.\frac{\mathrm{d}^q\hat{p}_R^{(\mathrm{t})}}{\mathrm{d}(s/c)^q}\right|_{s=0}(s/c)^q \\ &= \sum_{q=0}^\infty (-1)^q\left\langle (ct)^q\right\rangle(s/c)^q\end{aligned}, \quad (12')$$

to obtain explicit expressions for the temporal moments, as functions of $\mathbf{x}$, using term-by-term identification, based on the definition of $\langle (ct)^q\rangle$ in (9).

Now, $\hat{p}_R^{(\mathrm{t})}(s/c)$ itself can be derived from the Laplace transform $\hat{J}(s/c,\boldsymbol{x})$ of $J(t,\boldsymbol{x})$ using the Laplace transforms of (4)–(5a,b) and normalization in (7). As it turns out, $\hat{J}(s/c,\boldsymbol{x})$ obeys a *steady-state* diffusion PDE for scattering and partially absorbing media that we already know how to solve:

$$\left(\nabla^2 - a^2\right)\hat{J} = 0, \quad (11)$$

where $a^2 = 3\sigma_{\mathrm{a}}\sigma_{\mathrm{t}}$ in our previous work [9], but here it is identified as $a^2 = s/D = (3/\ell_{\mathrm{t}})\times s/c$. BCs for $\hat{J}(s/c,\boldsymbol{x})$ are as in (3), but without the $\delta(t) = \delta(ct)/c$ that has become unity after Laplace transformation.

As for the spatial integrations in (6)–(7), as well as the estimation of the even-order moments of ρ_θ in (10), they are easily handled since the analytical solution of (13) in M(*H*,*b*,AR) is expressed in a Legendre series expansion generalized for the relevant elliptical coordinates. The main difference with [9] is that, here, Legendre coefficients for the singular BC in (2), without $\delta(t)$, must be computed analytically.

To summarize, we are in the process of deriving closed-form analytical expressions for moment-based version of $\mathbf{F}(\mathbf{x})$ in (11) in the form of truncated Legendre series expansions. This gives us the opportunity to compute analytically the Jacobian matrix $\mathbf{K} = \partial\mathbf{F}/\partial\mathbf{x}$. From there, one can follow Rodger's guidance in [11] to estimate the statistics-based information content of multiple scattering lidar observations of 3D optical media. That formalism requires a rational estimate of the measurement error, which in this case is dominated either by shot noise (Poissonian statsitics of photon counting) or by the noise (variability) of the background light entering the receiver at the laser wavelength (within the bandpass of the background rejection filter). Those noise levels will be computed following the methodology used in [8].

3 Validity of the plane-parallel slab assumption

One motivating application of our explicit knowledge of the forward model $\mathbf{F}(H,b,\mathrm{AR};\tau_t)$ is to compare it directly with $\mathbf{F}(H,b,\infty;\tau_t)$. That particular multiple scattering lidar signal model was first worked out by Davis et al. [10] for plane-parallel media as an approximation for stratiform clouds. We will denote it as $\mathbf{F}_\infty(\mathbf{x})$ for simplicity, and underscore the reduced set of unknown cloud parameters $\mathbf{x} = (H;\tau_t)^T$. The goal is to determine at what values of AR and b we need to worry about the 3D cloud geometry, and if deviations from the $\mathbf{F}_\infty(H;\tau_t)$ prediction are systematic.

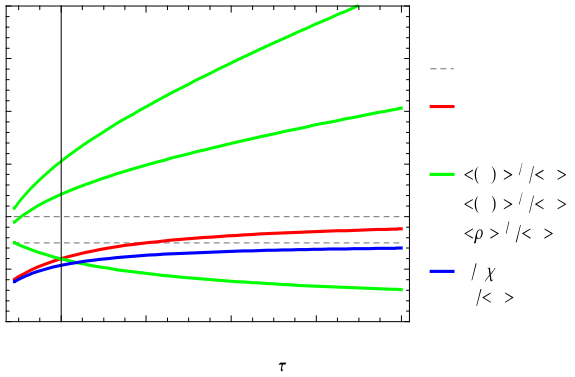


Figure 2 *Forward model elements* $\mathbf{F}_\infty(H;\tau_t)$ *versus scaled optical thickness* τ_t *when* $H = 1$ *and* $\chi = 2/3$.

In slab geometry (AR→∞, arbitrary b), there are no variables to separate. After a 2D Fourier transform in the (x,y) plane, hence $\partial_x^2+\partial_y^2 \mapsto -k^2$, the PDE problem in (13) with BCs in (3), without $\delta(t)\delta(x)\delta(y)$ after Fourier-Laplace transformation (denoted by an overscore "~"), becomes a boundary-value ODE problem. Specifically, we shall solve

$$\begin{cases} \left[\dfrac{\mathrm{d}^2}{\mathrm{d}z^2} - a^2\right]\tilde{J} = 0, \text{ with } a^2(s/c,k,\ell_t) = k^2 + \dfrac{3}{\ell_t}\times s/c \\ \left[\tilde{J} + \xi\dfrac{\mathrm{d}\tilde{J}}{\mathrm{d}z}\right]_{z=H} = 4, \left[\tilde{J} - \xi\dfrac{\mathrm{d}\tilde{J}}{\mathrm{d}z}\right]_{z=0} = 0, \text{ with } \xi(\ell_t) = \chi\ell_t \end{cases}, \quad (12)$$

where $\ell_t = H/\tau_t$. Based on (4), this leads to

$$R(s/c,k;\mathbf{x}) = \frac{\tilde{J}\left(a(s/c,k,\ell_t),\xi(\ell_t),H\right)}{2} - 1 = \frac{1-(\xi a)^2}{1+(\xi a)^2+2\xi a/\tanh(aH)}. \quad (13)$$

Series expansions of $R(s/c,k;\mathbf{x})$ up to order 3 in s/c, cf. (12′), and in k^2 lead to the following expressions for the moments in $\mathbf{F}_\infty(\mathbf{x})$:

$$\begin{aligned} R_{\mathrm{tot}}(\mathbf{x}) &= \frac{\tau_t/2\chi}{1+\tau_t/2\chi} = 1 - \frac{1}{1+\tau_t/2\chi} \\ \langle\rho^2\rangle(\mathbf{x}) &= H^2\times\left(\frac{8\chi}{3\tau_t}\right)\times\left[1+C_1(\tau_t/2\chi)\right] \\ \langle ct\rangle(\mathbf{x}) &= H\times(2\chi)\times\left[1+C_1(\tau_t/2\chi)\right] \\ \langle(ct)^2\rangle(\mathbf{x}) &= H^2\times\left(\frac{4\chi\tau_t}{5}\right)\times\left[1+C_2(\tau_t/2\chi)\right] \\ \langle(ct)^3\rangle(\mathbf{x}) &= H^3\times\left(\frac{24\chi\tau_t^2}{35}\right)\times\left[1+C_3(\tau_t/2\chi)\right] \end{aligned}, \quad (14)$$

where the scaling with H and (asymptotically) with τ_t is highlighted. The moment ratios used in (11) to form $\mathbf{F}_\infty(\mathbf{x})$ follow immediately. In the above expression for $R_{\mathrm{tot}} = 1 - T_{\mathrm{tot}}$ (in non-absorbing media), we recognize the well-known expression for total (diffuse+direct) transmission T_{tot} that goes back at least to Schuster's seminal paper [15].

The pre-asymptotic correction terms, $C_q(\tau_t/2\chi)$, are rational functions where the polynomial in the numerator is order q and order q+1 in the denominator. Figure 2 shows how the various elements of $\mathbf{F}_\infty(\mathbf{x})$ depend on τ_t when we set $H = 1$ and $\chi = 2/3$.

A practical algorithm to obtain $\mathbf{x} = (H;\tau_t)^T$ from $\mathbf{F}_\infty(\mathbf{x})$ in this 1D scenario is to first estimate τ_t from anyone of the red or green curves in Fig. 2, with the caveat that R_{tot} (in red) calls for absolute sensor calibration and the highest-order moment ($q = 3$) will be the most vulnerable to noise. So the rule-of-thumb is that, if only time-domain data is collected, use $\langle(ct)^2\rangle/\langle ct\rangle^2$, and if spatial as well as temporal data is available, use $\langle\rho^2\rangle/\langle ct\rangle^2$. Then the blue curve, at the same τ_t, is used as a multiplier to convert the observed value of $\langle ct\rangle$ into an estimate of H.

In the case of 3D media, To obtain $\mathbf{x} = (H,b,\mathrm{AR};\tau_t)^T$ from observed values of $\mathbf{F}(\mathbf{x})$, will likely call for a numerical minimization of a cost function in the least-squares sense, which will call for the Jacobian matrix.

4 Acknowledgments

We are grateful for sustained funding from NASA's Earth Radiation Sciences program office managed by Hal Maring and the Remote Sensing Theory program managed by Lucia Tsaoussi. AD acknowledges many fruitful discussions with Luc Bissonnette, Craig Bohren, Bob Cahalan, Frank Evans, Robin Hogan, Steve Love, Igor Polonsky, Nicola Pounder, Rob Sundberg, Tamás Varnái, Dave Winker, and Eleonora Zege. The research was carried out at the Jet Propulsion Laboratory, California

Institute of Technology, under a contract with the National Aeronautics and Space Administration.

5 References

[1] J. E. Hansen and L. D. Travis, Light scattering in planetary atmospheres, Space Science Reviews 16, 527-610 (1974).

[2] G. Marchuk, et al., *The Monte Carlo Methods in Atmospheric Optics* (Springer-Verlag, New-York, 1980).

[3] K. F. Evans, The spherical harmonics discrete ordinate method for three-dimensional atmospheric radiative transfer, J. Atmos. Sci. 55, 429-446 (1998).

[4] R. Pincus, and K. F. Evans, Computational cost and accuracy in calculating three-dimensional radiative transfer: Results for new implementations of Monte Carlo and SHDOM, J. Atmos. Sci. 66, 3131-3146 (2009).

[5] R. Davies, The effect of finite geometry on the three-dimensional transfer of solar irradiance in clouds, J. Atmos. Sci. 35, 1712-1725 (1978).

[6] K. N. Liou, *Radiation and Cloud Processes in the Atmosphere: Theory, Observation and Modelling* (Oxford University Press, Oxford, 1992).

[7] Y. Chen, K. N. Liou, and Y. Gu, An efficient diffusion approximation for 3D radiative transfer parameterization: Application to cloudy atmospheres, J. Quant. Spectrosc. Radiat. Transfer, 92, 189-200 (2005).

[8] A. B. Davis, Multiple-scattering lidar from both sides of the clouds: addressing internal structure, J Geophys Res 113, D14S10 (2008).

[9] A. B. Davis, and F. Xu, Toward a physics-based remote sensing of 3D clouds, Part 1: Fast forward radiative transfer modeling using diffusion theory, J. Atmos. Sci. (in preparation).

[10] A. B. Davis, R. F. Cahalan, J. D. Spinhirne, M. J. McGill, and S. P. Love, Off-beam lidar: An emerging technique in cloud remote sensing based on radiative Green-function theory in the diffusion domain, Phys. Chem. Earth (B) 24, 177-185 (1999). Erratum: pp. 757-765.

[11] C. D. Rodgers, *Inverse Methods for Atmospheric Sounding: Theory and Practice* (World Scientific, Singapore, 2000).

[12] I. N. Polonsky, S. P. Love, and A. B. Davis, The Wide-Angle Imaging Lidar (WAIL) deployment at the ARM Southern Great Plains site: Intercomparison of cloud property retrievals, J. Atmos. and Oceanic Techn. 22, 628-648 (2005).

[13] D. M. Winker, R. H. Couch, and M. P. McCormick, An overview of LITE: NASA's Lidar In-space Technology Experiment, Proc. IEEE 84, 164-180 (1996).

[14] K. M. Case, and P. F. Zweifel, *Linear Transport Theory* (Addison-Wesley Publ. Co., Reading, Mass, 1967).

[15] A. Schuster, Radiation through a foggy atmosphere, Astrophys. J. 21, 1-22 (1905).

© 2014 California Institute of Technology. Government sponsorship acknowledged.

Dynamics of laser excited colloidal Au nanoparticles conjugated with cysteine

Alexandra FALAMAS[1], Nicoleta TOSA[1,*] and Valer TOSA[1]

[1] National Institute for Research and Development of Isotopic and Molecular Technologies, 65-103 Donath, 400293, Cluj-Napoca, Romania

Corresponding author: nicoleta.tosa@itim-cj.ro

Abstract

The aim of this study was to investigate experimentally the ultrafast dynamics of Au colloidal nanoparticles when excited with femtosecond laser pulses. Also, their interaction with zwitterionic type molecules, such as cysteine and cystine is discussed. The time of the ground state population recovery of Au nanoparticles depends on the pump wavelength, with the highest value at the surface plasmon resonance excitation. In the same pump-probe conditions, the excited states life time of S-functionalized Au nanoparticles with zwitterionic molecules increases due to their chemisorption on the gold surface.

1 Introduction

The development of highly-sensitive, cost-effective, nanosensors for the detection of chemical and biological agents is of great interest in many areas, such as biomedical, forensic, biotechnology. Gold nanoparticles have attracted a great deal of interest due to their distinct physical and chemical properties that make them exceptional candidates for building biomedical nanosensors [1]. Colloidal Au nanoparticles can be synthesized rather easy and cheap, under a wide variety of shapes and sizes. The attachment of an analyte to the Au nanoparticles induces modifications of their physico-chemical properties, which can generate a detectable signal [2]. Functionalized nanoparticles with biologically interesting molecules can be used for applications in life sciences, chemical sensing, biomedicine.

Cysteine plays a critical role in various cellular functions, metabolism and even detoxification. It has a strong tendency to adsorb onto the surface of metals and it can be used to stabilize gold nanoparticles under different physiological conditions. Cysteine is widely used for the investigation of proteins and other biomolecules, which can be exploited by the attachment of a peptide to the surface of nanoparticles [3, 4].

In this study, we used a pump-probe method to investigate the picosecond dynamics of laser excited colloidal gold nanoparticles in aqueous solution, as well as their interaction with cysteine and cystine. The Au nanoparticles functionalized with these active sulphur containing molecules can enhance their selectivity for later reactions with other molecules, due to their -NH2, -COOH, SH groups of cysteine or S-S bonds of cystine [5].

2 Experimental section

Gold colloids were prepared by photochemical reduction of tetrachloroauric (III) acid ((HAuCl$_4$, 99.5%) in water (16.8 mM) with sodium citrate and polystyrene sulfonic acid (PSS), in order to limit the size of colloidal gold nanoparticles [6]. The reactants were purchased from Merck and used as received. The solution was firstly prepared by mixing tetrachloroauric (III) acid and sodium citrate with polystyrene sulfonic acid, and then it was irradiated by UV light at 254 nm for 20 minutes. The obtained solution was subjected to repeated centrifugal purification to obtain a concentrated colloidal solution.

The cysteine and cystine were dissolved in water to obtain $5 \cdot 10^{-3}$ M solutions. For each pump-probe experiments 20 µL of cysteine, respectively cystine aqueous solution was added to the Au colloid and the transient absorption spectra were recorded. The final Au colloid--sample ratio was 1:0.9.

The pump-probe set-up (Light Conversion Co. Ltd.) consists of a diode pumped Yb:KGW femtosecond laser delivering 180 fs laser pulses at a repetition frequency of 80 kHz, 75 nJ energy per pulse at 1030 nm wavelength. The laser is used to pump a collinear optical parametric amplifier delivering the wavelengths used here: 456, 480, 539, and 600 nm. The 539 nm pump used for the pump-probe experiments had a power of 20 mW, while at 456 nm the power was 35 mW.

In our pump-probe set-up, the pump pulse used to excite the sample is obtained in the optical parametric amplifier, and the probe pulse is a white light continuum (480-800 nm) produced by focusing 10% of the 1030 nm beam into a sapphire crystal. The transmitted white light is detected using a spectrograph with a 300 l/mm grating combined with an array detector, which gives a spectral window of approximately 310 nm.

The collected data were fit using the global target analysis technique [7], which describes the time-dependent population of the transient states and how they are connected, following a set of differential equations:

$$\frac{dc_1(t)}{dt} = I(t) - \frac{1}{\tau_1}c_1(t)$$
$$\frac{dc_i(t)}{dt} = \frac{1}{\tau_{i-1}}c_{i-1}(t) - \frac{1}{\tau_i}c_i(t), i \neq 1 \quad (1)$$

where c_i is the time-dependent population of state i, $I(t)$ is the excitation pulse, and τ_i is the time characteristic to the population decay from the ith excited compartment.

3 Results and discussion

The bare and the functionalized Au nanoparticles (GNPs) in their appropriate solutions were characterized by UV-Vis spectroscopy. The visible absorption spectra of the GNPs solution (Figure. 1) presents a well defined peak with a maximum at λmax = 539 nm, characteristic for surface plasmon resonance (SPR) absorbance of nanometric Au particles ascribed to an average size bellow 20 nm.

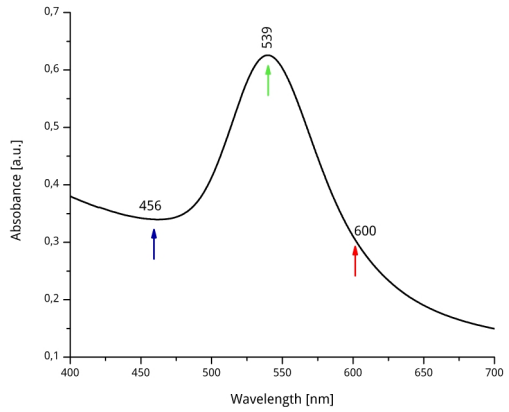


Figure 1 *UV-Vis absorption spectrum of Au nanoparticles. Arrows indicate the pump wavelength used in pump-probe experiment.*

3.1 Pump-probe experiment

The scope of the pump-probe experiment is to measure the sample absorbance differences in the presence and absence of the pump pulse. The pump pulse excites the sample and the probe pulse measures the sample transmittance. Thus, a difference absorbance signal is obtained as a function of both probe wavelength and the delay time between pump and probe pulses.

The picosecond dynamics behaviour of Au nanoparticles was investigated using three different pump wavelengths: 456, 539, and 600 nm. Figure. 2 shows the transient absorption spectra obtained at different time delays between pump and probe beams. The bleaching signal, assigned to the recovery of the ground state of the Au nanoparticles, is observed at 538 nm and recovers in less than 2 ps delay between pump and probe. In the pump-probe experiments the bleaching results from the optical excitation of the free electrons distribution within the nanoparticles. The spectra show two wings at 494 and 590 nm, respectively, assigned to the excited states of the "hot" electrons. The relaxation of the signal takes place through electron-electron scattering, and electron-phonon coupling [8].

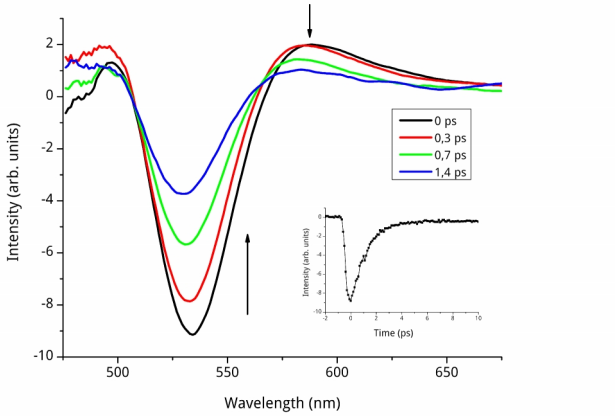


Figure 2 *Transient absorption spectra of Au nanoparticles excited with 456 nm. The inset shows the kinetics at the absorption plasmon band (539 nm).*

When processing the pump-probe data, we used a double exponential for the fitting of the kinetic traces and the same time was obtained for the bleach signal and the rise/ decay of the two wings. Therefore, we took into account only the decay of the signal for which a short time of 1.22 ps was obtained.

The Au colloidal nanoparticles were probed also using the 539 and 600 nm excitation wavelengths. A decay time of 1.30 and 1.19 ps, respectively, were obtained in these cases. This behaviour might be assigned to an increased number of nanoparticles, which absorb at 539 nm and contribute to the excited states population, compared to those absorbing at 600 or 456 nm.

3.2 Functionalization with cysteine derivatives

The Au nanoparticles were functionalized with cysteine and cystine respectively, in order to investigate the pump-probe behaviour of the nanoparticles under progressive surface coverage with S-derivative molecules. After the addition of cysteine to the colloidal solution, a decrease of the absorption maximum is recorded. In the case of cystine, a broadening of the plasmon band is also observed, as well as a weak red-shifted broad band around 800 nm. This indicates the chemisorption of cystine molecules to the Au surface and therefore the aggregation of the nanoparticles.

The functionalized Au nanoparticles were investigated using pump-probe spectroscopy for each addition of the given amount of cysteine/cystine solution. The chemisorption of the S-derivative molecules on the Au nanoparticles induced a rise of the excited states life time

in conjunction with the increase of the surface coverage. This can be assigned to additional oscillations of the free electrons in the functionalized nanoparticles induced by the newly formed S-Au bond.

4 Conclusions

The decay time of the transient absorption signal of the Au nanoparticles is dependent on the pump wavelength, with the highest time value at the surface plasmon resonance excitation. The fit of the decay signal gave a short time of 1.19-1.30 ps, assigned to both the bleaching of the ground state signal and the rise/ decay of excited states of the "hot" electrons. The covering of the Au nanoparticles surface with the S-derivative molecules increases the excited states life time, due to the S- Au bond.

5 Acknowledgement

This work was supported by the grants of the Ministry of National Education, CNCS - UEFISCDI, Romania, project number 169/25.07.2012 (project code the project PN-II-PT-PCCA-2011-3.2-0210) and project number 31/2013 (project code PN-II-ID-PCE-2012-4-0342).

References

[1] R. Bhattacharya, P. Mukherjee, *Biological properties of "naked" metal nanoparticles*, Advanced Drug Delivery Reviews, 60(11):1289-1306 (2008)

[2] P. K. Jain, I. H. El-Sayed, M. A. El-Sayed, *Au nanoparticles target cancer*, Nano Today, 2(1): 18-29 (2007)

[3] F. Wang, X. Liu, C.H. Lu, I. Wilner, *Cysteine-mediated aggregation of Au nanoparticles: The development of a H2O2 sensor and oxidase-based biosensors*, ACS Nano, 7(8):7278-7286 (2013)

[4] P. Tengvall, M. Lestelius, B. Liedberg, I. Lundstrom, *Plasma protein and antisera interactions with L-cysteine and 3-mercaptpropionic acid monolayers on gold surfaces*, Langmuir, 8:1236-1238 (1992)

[5] C. Jing, Y. Fang, *Experimental (SERS) and theorethical (DFT) studies on the adsorption behaviors of L-cysteine on gold/silver nanoparticles*, Chemical Physics, 332:27-32 (2007)

[6] F. Toadere, N. Tosa, *Functioning of the protective UV filters based on gold nanoparticles*, AIP Conference Proceedings, 1425:93-97 (2011)

[7] I. H. M. van Stokkum, D. S. Larsen, R. van Grndelle, *Global and target analysis of time-resolved spectra*, Biochimica et Biophysica Acta, 165:82-104 (2004)

[8] T. S. Ahmadi, S. L. Logunov, M. A. El-Sayed, *Picosecond dynamics of colloidal gold nanoparticles*, J. Phys. Chem, 100:8053-8056 (1996)

Optical properties of core–shell gold–iron oxide and iron oxide–gold nanoparticles for near UV and visible radiation wavelengths

Victor PUSTOVALOV[1], Liudmila ASTAFYEVA[2,*] and Galina LEDNEVA[2]

[1]Belorussian National Technical University, Minsk, 220013, Belarus
[2] Laboratory of Physical Optics, B.I. Stepanov Institution of Physics of National Academy of Sciences, Minsk, 220072, Belarus

Corresponding author: astafev@dragon.bas-net.by

Abstract

During past years many research efforts have been focused on preparation and investigation of spherical hybrid core-shell nanoparticles because of their unique size-dependent physical and chemical properties [1-4]. First of all, core-shell silica –gold [1-3] and silver-gold and vice-versa gold-silver [4] nanoparticles were prepared and experimentally investigated and applied in nanomedicine, imaging, labeling and laser medicine. Furthermore, for the purposes of laser medicine two-layered nanoparticles such as dielectric-metal and metal-dielectric are deeply used.Among them are silica-gold and gold-silica as well as some oxides (Fe_3O_4, ZnO, TiO_2 and others). Use of system dielectric-metal allows to shift the peak of plasmon resonance in IR spectrum.

1 Computer modelling of optical properties of spherical two-layered nanoparticles

It is assumed that spherical two-layered nanoparticle consists of a spherical homogeneous core of radius r_0 with the complex refractive index $m_0=n_0-i\kappa_0$ of gold, enveloped by spherically symmetric homogeneous shell of radius r_1 with the complex refractive index $m_1=n_1-i\kappa_1$ of iron oxide (Fe_3O_4). Particle is located in the homogeneous non-absorbing medium with a refractive index n_2. The set of geometrical and optical parameters of core - r_0, m_0, shell - r_1, m_1, medium - n_2 determines optical properties of two-layered nanoparticle placed in some medium. Optical characteristics of two-layered sphere (absorption, scattering and extinction effective cross sections) are expressed in terms of amplitude coefficients given by theory of diffraction of radiation on two-layered spherical particle [5,6]. Calculations of such characteristics for two-layered particles are much more cumbersome than for homogeneous spherical particles [5].

Consider two-layered spherical nanoparticles with gold (Au) core and iron oxide (Fe_3O_4) shell. We used gold for core material because gold has appropriate properties for many applications and is widely used in experiments. Optical indexes of Au were used from [7]. Optical indexes for shell material were used from [8].

Figure 1 presents the spectral dependencies of efficiency factors of absorption K_{abs}, scattering K_{sca} and extinction K_{ext} of radiation by two-layered gold core with the radii r_0=40 nm and iron oxide shell spherical nanoparticles with thicknesses Δr=5(a), 20 (b) and 40 (c) nm, placed in water.

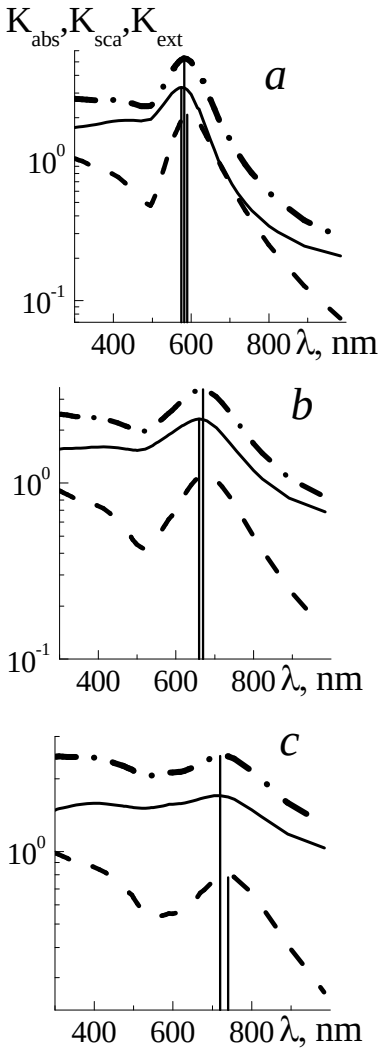


Figure 1 *Spectral dependences of efficiency factors of absorption K_{abs} (solid), scattering K_{sca} (dash) and extinction K_{ext} (dash-dot) of by two-layered gold core and iron oxide shell spherical nanoparticles.*

Gold nanoparticles have strong plasmon resonance in the spectral interval 520-540 nm. In our case for r_0=40 nm gold nanoparticle has plasmon resonance at 540 nm. It

follows from figure 1 that the occurrence and rise of the thickness of iron oxide shell leads to the shift of plasmon resonances of two-layered nanoparticles in the spectral interval 575-670 nm in the dependence of the shell thickness values. Figure 2 gives the spectral dependencies of efficiency factors of absorption K_{abs}, scattering K_{sca} and extinction K_{ext} of radiation by two-layered iron oxide core with the radii r_0=40 nm and gold shell spherical nanoparticles with thicknesses ar=5(a), 20 (b) and 40 (c) nm, placed in water.

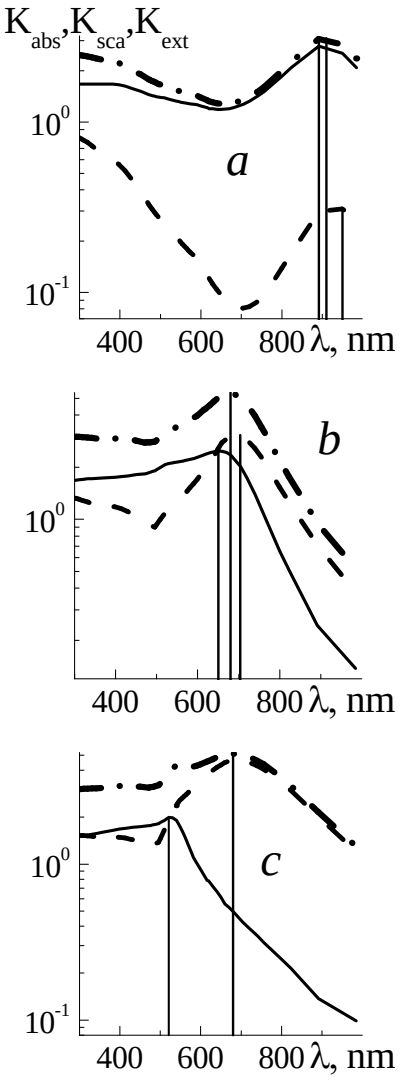


Figure 2 *Spectral dependences of efficiency factors of absorption K_{abs} (solid), scattering K_{sca} (dash) and extinction K_{ext} (dash-dot) of by two-layered iron oxide core and gold shell spherical nanoparticles.*

When the iron oxide is in the two-layered nanoparticle core and gold is in the shell, plasmon resonance peaks are shifted in the IR spectrum, especially for thin shells. For ar=5 nm plasmon resonance peaks are situated in the spectral intervak 890-950 nm. For ar=40 nm plasmon resonance peaks are situated for absorption at 520-525 nm, for scattering and extinction – at 675-685 nm. Such shifts of the location of plasmon resonance peaks are due to the influence of iron oxide shell rise in Fidure 1 and the influence of the gold shell rise in Figure 2. In the first case increasing the iron oxide thickness is beginning to mask optical properties of gold core, in the second case, vice versa, increasing the gold shell masks the jhnical properties of iron oxide core.

Our results can be used for experimental optical detection and investigation of stages of material shell formation and increasing on NP core and determination of geometrical parameters of core and shell of two-layered NPs during chemical preparation. Novel approach presented here possibly allows substitute complicated microscopy procedures by more simple optical extinction and scattering procedure.

2 References

[1] Hirsch L.R., Stafford R.J., Bankson J.A., Sershen S.R., Rivera B., Price R.E., Hazle J.D., and Halas N.J. Nanoshell-mediated near-infrared thermal therapy of tumors under magnetic resonance guidance, PNAS 100(23):13549-6 (2003)

[2] Hirsch L.R., Gobin A.M., Tam F., Drezek R.A., Halas N.J., West J. Metal nanoshells, Ann Biomed Eng. 34(1): 15-22 (2006)

[3] Barhoumi A., Huschka R., Bardhan R., Knight M., Halas N.J.. Light-induced release of DNA from plasmon-resonant nanoparticles: towards light-controlled gene therapy, Chem Phys Lett. 482(4): 171-6 (2009)

[4] Steinbrück A., Csaki A., Festag G., Fritzsche W. Preparation and optical characterization of core-shell bimetal nanoparticles, Plasmon 1(1):79-85 (2006)

[5] C.F. Bohren, and D.R. Huffman, *Absorption and scattering of light by small particles* (Wiley, New-York, 1983).

[6] Pustovalov V., Astafyeva L,. Jean B. Computer modeling of the optical properties and heating of spherical gold and silica-gold nanoparticles for laser combined imaging and photothermal treatment, Nanotechnol 20:225105 (2009)

[7] Johnson P.B, Christy R.W. Optical constants of the noble metals, Phys Rev B 6(12):4370-9 (1972)

[8] Database of Optical Constants for Cosmic Dust: www.astro-uni-jena.de/

IDEAL ABSORPTION DESIGN IN NANOPARTICLES

Brian STOUT[1,*], Nicolas BONOD[1] , Jérôme WENGER[1], and Victor GRIGORIEV[1]

[1] Université Aix-Marseille, Institut Fresnel, Marseille, 13397, France

Corresponding author: brian.stout@fresnel.fr

Abstract

Analytic formulas and precise semi-numerical methods are introduced for the practical design of Ideal Absorption (IA) in nano-particles. We will show that IA allows a sub-wavelength particle to completely stop the propagation of a given mode in an incident beam, and we discuss possible applications in beam shaping.

1 Introduction

Ideal Absorption (IA) provides a means to efficiently transform electromagnetic energy into another form (joule heat, photo-electric, fluorescence). This unique property of IA particles can be optimized by placing them at the positions of high beam intensity, like "hot-spots" in inhomogenenous media and meta-materials, or in the focal zones of beams in high numerical aperture optics.

We derive formulas permitting the design of IA in spherically symmetric particles. These formula predict that IA is achievable for specific frequencies and particle sizes with known materials. Furthermore, extensions of this technique predict that one can design core-shell particles to produce Ideal Absorption at virtually any frequency in the visible and near visible range.

2 Designing Ideal Absorption.

2.1 General theoretical considerations

IA can be conveniently described in the context of an S-matrix theory.[1] In this context, the absorption cross can be written as:

$$\sigma_{n,\mathrm{a}}^{(e,h)} = \frac{\pi}{2k^2}(2n+1)\left(1-\left|S_n^{(e,h)}\right|^2\right), \qquad (1)$$

where $S_n^{(e,h)}$ is the S-matrix element of an nth order electric (e) or magnetic (h) mode. The (2n+1) factor comes from the degeneracy of the projection angular momentum modes in a spherically symmetric particle. Since unitarity (*i.e.* flux conservation) requires that $|S_n^{(e,h)}|\leq 1$, one sees directly from Eq.1 that the absorption cross section in an nth order orbital channel must satisfy:

$$\sigma_{n,\mathrm{a}}^{(e,h)} \leq \frac{(2n+1)}{8\pi}\lambda^2 , \qquad (2)$$

with IA occurring when the upper limit of the absorption cross section is reached, *i.e.* $S_n^{(e,h)}=0$.

Even though the absorption cross section in a given channel is limited to a finite value, one can show that IA can completely stop the propagation of an incident field mode. This property has lead to IA being referred to as time reversed lasing and (somewhat misleadingly) as "perfect" absorption.[2] We show that point-like models of scatterers[3,4] predict that IA should occur when the dielectric function of the scatterer, ε_s , divided by the background medium dielectric constant, ε_b , is given by:

$$\bar{\varepsilon}_s \equiv \frac{\varepsilon_s}{\varepsilon_b} = \frac{2+\frac{2}{3}(kR)^2\left[1-ikR\right]}{1-\frac{2}{3}(kR)^2\left[1-ikR\right]} . \qquad (3)$$

Although this formula yields a reasonable approximation for the IA condition in extremely small particles, it proves inaccurate for larger subwavelength particles, and we provide improved approximations based on the analytic structure of the IA conditions.

2.2 IA conditions as a function of particle size.

The S-matrix of a homogeneous spherical particle has an explicit analytic form obtainable from Mie theory. We show that solving for the IA condition takes the form of a complex transcendental equation, and that these solutions can readily be determined via Weierstrass factorization.[5] As an example, we plot in Figure 1, the required IA permittivity for the electric dipole mode in a spherical scatterer as a function of the particle's size parameter, *ka* where *k* is the host medium wavenumber, and *a* the particle radius.

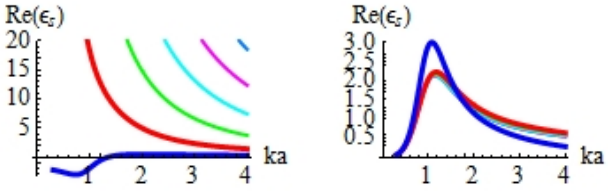


Figure 1 . *Permittivity required for electric dipole IA as a function of the size parameter ka.*

Although there are an infinite number of IA solutions, as one can see from Figure 1, there is only one solution (blue curve)for which $\mathrm{Re}(\varepsilon_s)<1$, and that this is the only viable solution for extremely sub-wavelength particles. Nevertheless, Figure 1 indicates that electric dipole IA can occur in sub-wavelength particles with $\mathrm{Re}(\varepsilon_s)>1$ at values that one can potentially find in real materials.

2.3 IA for realistic materials

Plasmonic materials like silver and gold appear as good candidates for achieving IA in the lowest electric dipole IA mode since these materials are renown for having Re(ε_s)<1. However, the fact that for a given particle size, IA is only satisfied for a given complex value of $\overline{\varepsilon}_s$ means that even for these materials, IA can only be satisfied at specific frequencies and particle sizes.

The specific frequencies and sizes for IA in silver and gold suspended in homogeneous dielectric medium of refraction index N_b=1.5,can be determined by plotting $\overline{\varepsilon}_s$ in the complex plane as the wavelength varies over the near ultra-violet to mid-visible range. The values of $\overline{\varepsilon}_s$ required for IA are plotted in blue as the particle size parameter, *kR*, varies from 0 to 4. For comparison, the theoretical predictions for IA by a point-like model are plotted in Green as *kR*, varies from 0 to ∞.

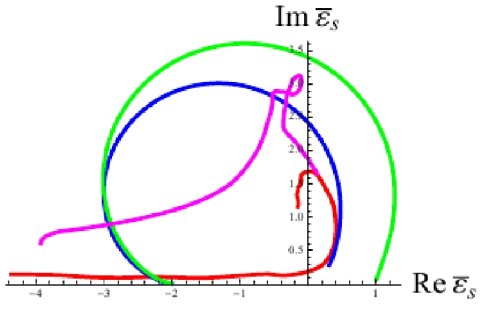


Figure 2 . *Values of $\overline{\varepsilon}_s$ for variations in the vacuum wavelength λ_0 for silver (red - $\lambda_0 \in$ {188-500}nm) and gold (magenta - $\lambda_0 \in$ {206-600}nm). Values of $\overline{\varepsilon}_s$ required for IA are plotted in blue as kR varies from 0 to 4.*

In Figure 2, IA occurs at those particles sizes and frequencies at which the blue curve intercepts the particle dielectric functions of $\overline{\varepsilon}_s$ of gold or silver. One readily determines then that IA occurs for very small Silver and slightly larger gold particles at visible frequencies (gold even has 2 additional IA conditions, and silver a range of near IA in the ultra-violet).

3 Core-shell designs for IA at arbitrary frequency

We saw in section 2, that in order to observe IA, one needs a tunable laser and particle of the adequate composition and size. In applications, one may wish to design IA to occur at a specific frequency. We extended our calculations in an effective permittivity context to design subwavelength core-shell designs which satisfy IA at a given wavelength. The results for IA to occur in core-shell designs of silver or gold enveloping a high index core (N_b=2.8 are presented in Figure 3.

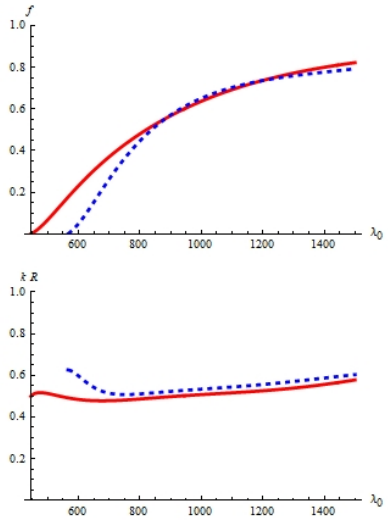


Figure 3 . *Plots of the filling fraction, f, (a) and the size parameter kR (b), required to achieve IA in a core shell structure immersed in a N_b =1.5 background material. The core is considered to be a lossless high index material, N_c =2.8, and the shell either silver (red-solid line) or gold (blue-dashed line). f,*

4 Conclusion

We found that IA can be designed to occur in realistic subwavelength particles, and that it can have dramatic effects on the shape of an incident beam. IA may also prove to be a sensitive test of the validity of using bulk permittivity parameters to describe nano-scale particles. Since IA corresponds to a fundamental theoretical limit, it may also serve as a guide to a better understanding of this absorption in quantum systems like molecules and quantum dots.

5 Acknowledgements

The research leading to these results has received funding from the European Research Council under the European Union's Seventh Framework Programme (FP7/2007-2013) / ERC Grant agreements 278242 (ExtendFRET) and from the French Agence Nationale de la Recherche under Contract No. ANR-11-BS10-002-02 TWINS."

6 References

[1] R.G. Newton, *Scattering Theory of Waves and Particles* (Dover, 1982).

[2] Y.D. Chong *et al.*, Coherent Perfect Absorbers: Time-Reversed Lasers, PRL. **105,** 053901 (2010).

[3] Y.-P.~Pellegrini, P.~Thibaudeau, B.~Stout, J. Phys. Condens. matter, **9**, 177-191 (1997).

[4] G.Colas~des~Francs, et al, Opt. Express, **16**, 17654-17666 (2008).

[5] V.Grigoriev *et al.*, Optimization of resonant effects in nanostructures via Weierstrass factorization, Ph.Rev.A, **88** , 011803 (2013).

POLARIZED LIGHT EXTRACTION FROM LIGHT EMITTING DIODES USING METALLIC NANOSTRUCTURES

Örs SEPSI[1,*], Tibor GÁL[1] and Pál KOPPA[1]

[1] Department of Atomic Physics, Budapest University of Technology and Economics, Budapest, 1111, Hungary

Corresponding author: sepsi.ors@gmail.com

Abstract

We investigate metallic nanostructures by electromagnetic modeling for polarized light extraction from light emitting diodes (LEDs). We show two nanostructures as possible polarization selective filters.

Aluminum wire grid polarizers (WGPs) are investigated using rigorous coupled wave analysis (RCWA). The result of the model is used in conjunction with a ray tracing calculation in order to build up a complete LED model. With this model extinction ratio over 2.72 is obtained with extraction efficiency surpassing an unpolarized LED + external polarizer setup.

Silver nanoellipsoids are studied using a quasistatic approximation in layered environment. The degree of polarization and the total transmittance spectra are calculated. The effect of parameters like lattice period, axial ratio and particle size are considered. Optimization procedure shows that particles in the size range of 100 nm are optimal to reach 50% degree of polarization and less than 15% absorbance for an uncollimated and unpolarized dipole source.

Introduction

Polarized light plays a major role in many applications such as liquid crystal displays [1], automotive lighting [2], microscopy [3] and communications [4]. Using polarization selective devices in combination with light emitting diodes (LEDs) provides a cost effective solution for these applications. Usually one uses external polarizers for these applications, however in this case more than half of the light is lost due to absorption and reflection. Several papers deal with polarized light extraction from light emitting diodes [5-8], using geometrical optical concepts as well as with photonic crystals and nanostructures placed onto the LED chip.

In the present paper we cover the modeling of polarized light extraction from light emitting diodes and investigate the polarization dependence of light scattering on metallic nanostructures. First the performance of wire grid polarizer (WGP) is examined for the purpose of polarized LED applications. Based on the results of the RCWA calculations a complete AlGaInP LED model is built up using a ray tracing software.

As a second approach we exploit the shape introduced anisotropy of silver nanoellipsoids. It is well known that the response of such particles will depend on the polarization of the exciting light due to the anisotropy [9]. Recently ellipsoidal metallic nanoparticles embedded in a transparent host were suggested for ultrathin polarizers [10]. We use this idea to obtain polarized light extraction from conventional LED chips. To calculate the scattering on the nanoellipsoids we use the quasistatic approximation in a layered system. Optimization is carried out to obtain optimal particle size, axial ratio and particle-particle distance.

Polarized light extraction with wire grid polarizers

We have investigated two possible placement of the wire grid polarizer on the complete LED structure. In the first one the WGP is placed onto the encapsulation, in the second one the WGP is placed onto the LED chip.

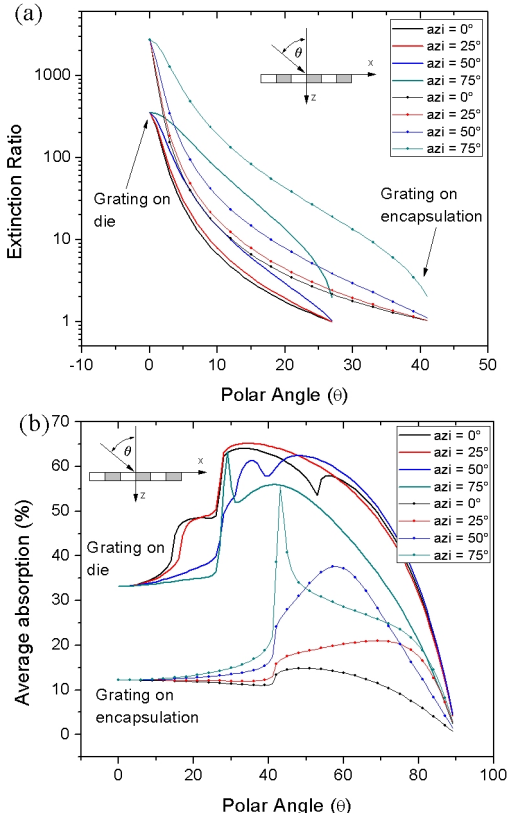


Figure 1 *(a) Extinction ratio and (b) average absorption for unpolarized incident wave. The WGP is placed onto the encapsulation (Grating on encapsulation: line + symbol) or onto the LED die (Grating on die: solid line).*

The optical properties of the wire grid polarizer on planar interfaces are investigated using the rigorous

coupled wave analysis [11, 12]. The wire grid polarizer is illuminated at conical incidence with an unpolarized plane wave. The extinction ratio as well as the average absorption is shown on Figure 1.

It can be seen from the figures, that the WGP achieves better performance when put onto the encapsulation both in extinction ratio and in extraction efficiency. From the geometry of the LED source it is clear, that the wave coming from the chip and hitting the encapsulation surface falls nearly at normal incidence onto the surface. On the contrary inside the chip, the waves fall on the interface of the chip and the encapsulation in polar angles uniformly distributed. Consequently a large amount of light is trapped inside the LED die by total internal reflection. Thus one can conclude that if these conditions hold, it is reasonable to put the WGP onto the encapsulation rather than onto the chip surface.

Complete LED model with wire grid polarizers

We have used a commercial ray tracing program in conjunction with the RCWA calculations to model the complete LED source with nanostructures. For illustration purposes we have chosen to model a high efficiency transparent substrate AlGaInP LED. Three different configurations were investigated: an unpolarized LED source with an external polarizer, an LED source with WGP put onto the LED chip and an LED source with WGP put onto the encapsulation surface.

For the unpolarized LED source the extraction efficiency was about 23% which is in good agreement with the results found in the literature. In the unpolarized case the extinction ratio was very close to 1 as expected. Using an external polarizer to produce polarized light the efficiency of the system dropped to 9.6%, i.e. more than the half of the light was lost compared to the previous case. Putting the WGP onto the LED chip resulted in an extraction efficiency of 5.6% and extinction ratio of 2.04. Putting the WGP onto the LED encapsulation the extinction ratio increased to 2.72 moreover the extraction efficiency increased to 12.9%.

To summarize the previous results it can be seen that placing the WGP onto the encapsulation provides the best configuration of polarized light extraction with WGP.

Investigation of the polarization properties of silver nanoellipsoids

Using ordered or disordered array of nanoparticles at surfaces to produce polarized light enables us to further fine tune the optical response of the system. The investigated setup consists of a planar chip/encapsulation interface and a square array of silver nanoellipsoids oriented in the same direction. The ellipsoids are placed into the encapsulation material. The light scattering is calculated using the periodic layered Green's tensor formulation, where the particles are considered as polarizable dipoles, with multiple scattering between the particles taken into account [13-15]. The light source in this case is the farfield of a radiating dipole emitter with random polarization.

We investigate the degree of polarization (DOP), reflectance and absorbance of the interface as a function of the geometrical parameters of the nanoparticle lattice for the visible spectral range. The nanoparticle lattice provides polarization selection as expected and in the 10-100 nm size range the maximum degree of polarization depends mainly on the particle size, not on the axial ratio or lattice period. The axial ratio influences only the peak position in the wavelength spectrum.

Figure 2 shows the degree of polarization, absorbance, transmittance and reflectance of the investigated setup as a function of the semi-major axis. The wavelength was 620 nm. The period was set to $p = 2.1\ l_x$ and the axial ratio was equal to 2.2.

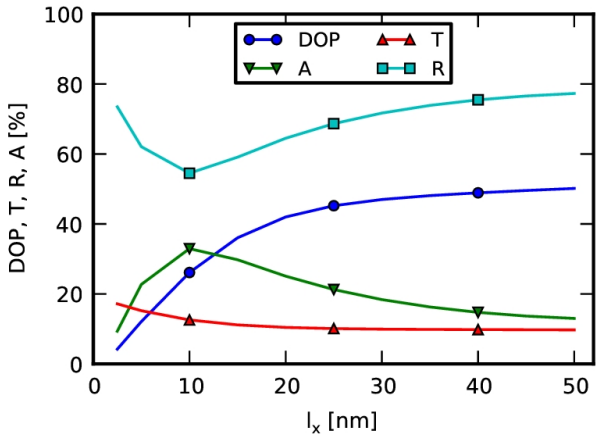


Figure 2 *DOP, absorbance, transmittance and reflectance at 620 nm as function of particle semi-major axis. The axial ratio was equal to 2.2, the period was $p = 2.1\ l_x$.*

It can be seen that by increasing the particle size the degree of polarization increases and reaches a relatively constant range above 30 nm semi-major axis length. The absorbance reaches a maximum around 10 nm semi-major axis length and with increasing particle size it decreases. The reflectance also increases with increasing particle size.

At around 50 nm semi-major axis the DOP is high enough and the absorbance is low enough for practical applications. The high reflectance of the lattice can be exploited by suitable polarization recycler below the nanoparticle structure in order to increase the extracted power.

Conclusion

One dimensional aluminum periodic array of nanowires showed excellent polarizing properties by placing on material interfaces. By putting these wire grid polarizers onto the curved encapsulation of an LED extinction ratio of 2.72 and extraction efficiency of 12.9%

can be obtained. The investigated setup also compares favorably with the currently existing solutions.

Silver nanoellipsoids are promising too for polarized LED application. For the best configurations the degree of polarization values were near 50%, while the absorbance was below 15% for the unpolarized dipole emitter. The transmittance and reflectance was about 10% and 75% respectively. Using a proper polarization recycler to recover the reflected waves, the extracted power can largely surpass the LED + external polarizer configuration.

Acknowledgement

This work has been supported by the grants TAMOP – 4.2.2.B-10/1 – 2010-0009 and VKSZ-12-1-2013-80.

References

[1] P. Yeh, C. Gu, *Optics of Liquid Crystal Displays*, (John Wiley, Canada, 1999).

[2] B. H. Billings, E. H. Land, A Comparative Survey of Some Possible Systems of Polarized Headlights, JOSA, **38,** (1948) 819-823

[3] S. Inoué, R. Oldenbourg, *Microscopes, Handbook of Optics*, 2nd ed. (McGraw-Hill, New York, 1995), Vol. II, Chap. 17.

[4] R. Otte, L. P. de Joung, A. H. M. van Roermund, *Low-Power Wireless Infrared Communications* (Kluwer Academic Publishers, 1999).

[5] M. F. Schubert, A. Noemaun, S. Chhajed, J. K. Kim, E. F. Schubert, Ch. Sone, Encapsulation shape with non-rotational symmetry designed for extraction of polarized light from unpolarized sources, Opt. Express **15**, (2007) 10452-10457.

[6] M. F. Schubert, S. Chhajed, J. K. Kim, E. F. Schubert, J. Cho, Linearly polarized emission from GaInN light-emitting diodes with polarization-enhancing reflector, Opt. Express **15**, (2007) 11213-11218.

[7] A. Rizzo, C. Nobile, M. Mazzeo, M. De Giorgi, A. Fiore, L. Carbone, R. Cingolani, L. Manna, G. Gigli, Polarized Light Emitting Diode by Long- Range Nanorod Self-Assembling on a Water Surface, ACS Nano, **3**, (2009) 1506-1512.

[8] C. Lai, J. Chi, H. Yen, H. Kuo, C. Chao, H. Hsueh, J. Trevor Wang, C. Huang, W. Yeh, Polarized light emission from photonic crystal light-emitting diodes, Appl. Phys. Lett., **92** (2008), 243118

[9] C. F. Bohren, D. R. Huffman, *Absorption and Scattering of Light by Small Particles* (Wiley, 1998).

[10] S. G. Moiseev, Thin-film polarizer made of heterogeneous medium with uniformly oriented silver nanoparticles, Appl. Phys. A 103, 775–777 (2011).

[11] M. G. Moharam, E. B. Grann, D. A. Pommet, T. K. Gaylord, Formulation for stable and efficient implementation of the rigorous coupled-wave analysis of binary gratings, J. Opt. Soc. Am. A **12**, (1995) 1068-1076.

[12] L. Li, Use of Fourier series in the analysis of discontinuous periodic structures, J. Opt. Soc. Am. A **13** (1996) 1870-1876.

[13] B. Gallinet, A. M. Kern, and O. J. F. Martin, Accurate and versatile modeling of electromagnetic scattering on periodic nanostructures with a surface integral approach, J. Opt. Soc. Am. A 27, 2261–2271 (2010).

[14] M. Paulus, P. Gay-Balmaz, and O. J. F. Martin, Accurate and efficient computation of the Green's tensor for stratified media, Phys. Rev. E 62, 5797–5807 (2000).

[15] Ö. Sepsi, T. Gál, P. Koppa, Polarized light emitting diodes using silver nanoellipsoids, Optics Express, 22 (2014) A1190-A1196

Near-field and resonances

Laser Emission from Random Gain Media with Bubble Structures

Takashi OKAMOTO*, Shouhei MATSUSHITA and Masanori TAKABAYASHI

Department of Systems Design and Informatics, Kyushu Institute of Technology,
680-4, Kawazu, Iizuka, Fukuoka 820-8502, Japan

Corresponding author: okamoto@ces.kyutech.ac.jp

Abstract

We study experimentally the lasing properties of dye-doped polymer random media in which scattering particles and spacer particles with spherical shape are distributed. The intensity of emitted light and the distribution of spikes in the emission spectrum are analyzed. Experimental results show that the bubble-structured random laser exhibits a higher peak in the emission spectrum than conventional random lasers. The mode analysis of random lasers is carried out to reveal the feature of this new type of random structures.

1 Introduction

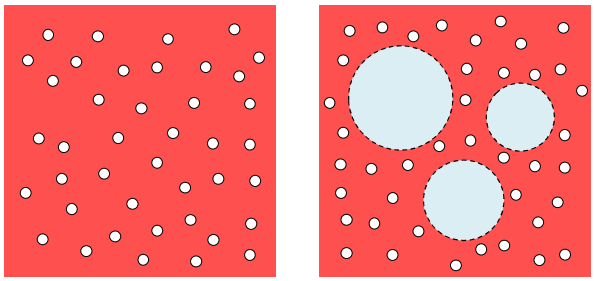
The random laser is a mirrorless laser in which multiple scattering of light provides long optical paths and feedback necessary for laser action [1-6]. Most of random lasers consist of small particles distributed in an amplifying medium or powder particles which themselves have gain properties. In recent years, several novel structures of random gain media have been investigated for controlling the spectrum and efficiency of random laser emission [7–9]. For example, monodisperse scattering particles allow us to control the emission spectrum [7], and when there is a defect in the distribution of monodisperse particles, the light is concentrated and enhanced in the defect region [8]. These two studies have revealed that the laser emission can be controlled by adding some regularity to the random structure. Another variation in the structure is the shape of the scattering particles, which has been found to affect the efficiency of random lasing [9].

In a previous study [10], we investigated the random laser emission from random media with a "bubble structure" which have non-scattering regions distributed randomly. We found that the peak of emission spectrum is enhanced under certain conditions. In this study, a systematic control of spacer particles (SPs) constituting non-scattering regions is carried out. Although this structure seems to be similar to that of superdiffusive media [11], the non-scattering regions in our model do not necessarily realize a Lévy flight for light

2 Experiment

Figure 1 shows a schematic of the random structures we used for random lasers. Random media with a bubble structure are fabricated by using silica particles with diameters of 30, 40, 60, and 100 μm as SPs. TiO_2 scattering particles with a diameter of 180 nm and the SPs are dispersed in light curable photopolymer (Adell K40) which is doped with rhodamine 6G laser dye with a density of 6.7×10^3 mol/l. The volume filling fraction of scattering particles is 10%. The refractive index of TiO_2 particles, silica particles, and K40 polymer are 2.7, 1.52, and 1.5, respectively, so that scattering from silica particles is almost negligible. The liquid polymer medium is then put on a slide glass with a cover glass on top, and cured by illuminating it with 405 nm violet laser light for 8 min. The thickness of the fabricated random media is 0.2 mm.

A schematic diagram of the experimental setup is shown in Figure 2. The sample is pumped by a frequency-



(a) (b)

Figure 1 *(a) homogeneous and (b) inhomogeneous distributions of scattering particles in dye doped polymer media. Dashed circles in (b) represent spacer particles.*

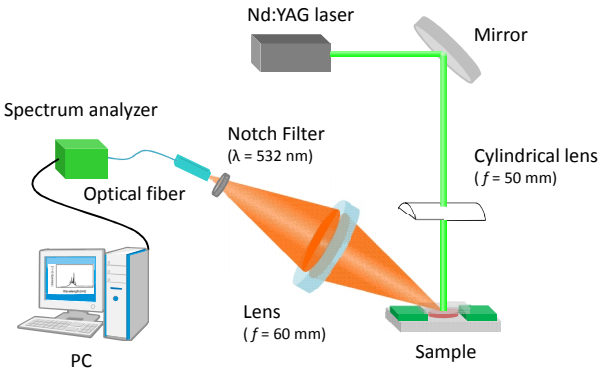


Figure 2 *Schematic diagram of the experimental setup for measuring the emission spectrum.*

doubled Nd:YAG laser beam with a wavelength of 532 nm and a pulse duration of 10 ns. The pump beam is focused vertically onto the surface of the sample using a cylindrical lens of 50 mm focal length. The light emitted from the sample is detected by a spectrometer (Ocean Optics HR2000) through a collective lens and an optical fiber at an observation angle of about 45°. A notch filter in front of the fiber end removes the pump light. The emission spectrum is measured with a spectral resolution of 0.2 nm. 200 spectral data were obtained for each sample configuration by changing the position of the pump spot.

3 Results

Typical emission spectra obtained from the homogeneous and bubble structures are shown in Figure 3(a) and 3(b), respectively. Some spikes are seen to appear in the spectra, showing that random lasing with resonant feedback occurs in the samples. We found that some spikes grow higher than others in the bubble medium, whereas all the spikes look alike for the homogeneous medium.

We performed experiments with all the combinations of SPs: monodisperse particles of 30, 40, 60, and 100 μm diameters, and polydisperse particles of two, three, and four different sizes. The volume filling fractions of SPs are 5 and 10%, and the volume fraction of each particle size is the same for the polydisperse SPs. The average intensity in the wavelength range of 560–590 nm and the average value of the maximum peak intensity in the emission spectrum are plotted as a function of the volume fraction of SPs in Figure 4(a) and 4(b), respectively. The volume fraction of 0% and the diameter of 0 μm denote a homogeneous medium schematically shown in Figure 1(a). As seen from Figure 4(a), there is little difference in the average intensity between the homogeneous medium and the monodisperse and polydisperse bubble media. In this respect, the emission efficiency is almost the same. On the other hand, almost all the bubble structures exhibit higher maximum intensity than the homogeneous medium. In particular, a random laser with polydisperse SPs of 30–100 μm diameters and 5% filling fraction presents up to 1.4 times higher emission intensities than the homogeneous one. The other size groups (monodisperse) of the SPs show lower maximum intensities than that of polydisperse one, indicating that the size range of SPs should be wider for high emission peak.

The emission peak intensity in the spectrum is higher for the filling fraction of SPs of 5% than for 10%. Light cannot be amplified in the SPs so that the gain volume reduces as the SPs increase. The result suggests that the optimal fraction of SPs for strong peak emission exist between 0% and 10%.

We studied the mode properties of bubble random media to examine the reason for the high emission spikes in the spectrum. We pumped at the same region of the sample and took a series of emission spectra. The intensity correlation between different pairs of spikes in the

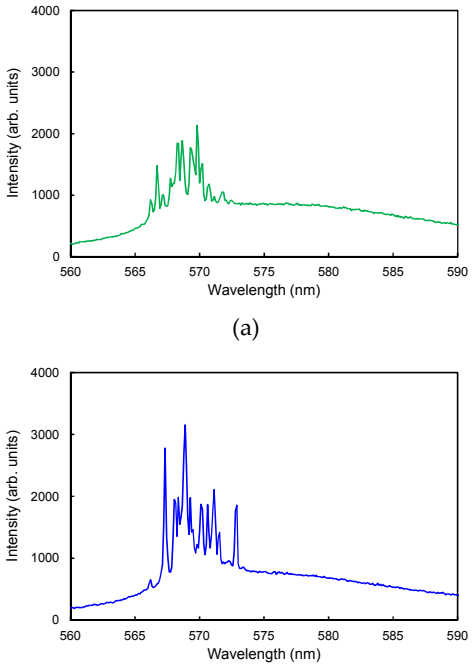


Figure 3 Emission spectra from (a) a homogeneous medium (SP: 0%) and (b) a medium with a bubble structure (SP: 1.25% each for 30, 40, 60, 100 μm).

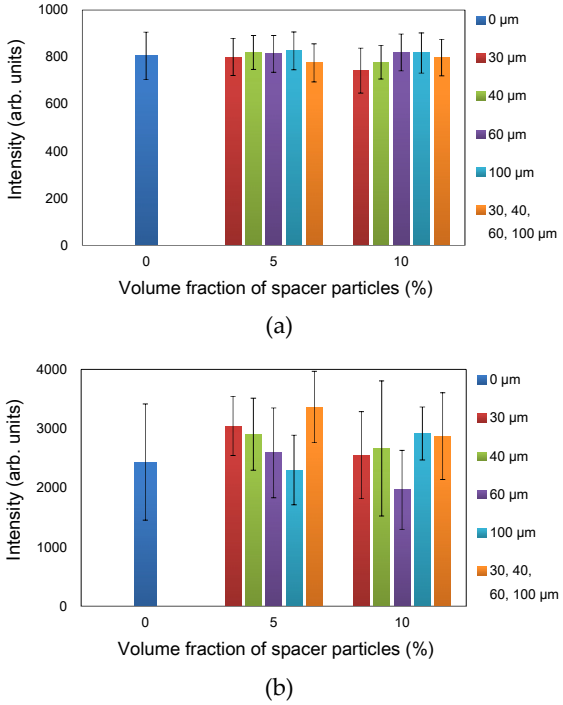


Figure 4 (a) Average and (b) maximum intensity in the emission spectrum for various sizes and volume fractions of spacer particles.

emission spectrum was then evaluated [12] for the homogeneous medium and the bubble media containing 5% of the SPs with various sizes. We set the criteria that the spikes which have the correlation coefficient of more than 0.7 with each other belong to the same resonator.

Figure 5 shows the average number of resonators and the average number of resonant frequencies in a resonator obtained by pumping 20 different regions for each sample configuration. As seen from Figure 5(a) and 5(b), the number of resonators is small and the number of resonant frequencies per resonator is large for the monodisperse SPs, compared to those for the homogeneous medium and the polydisperse SPs. Large values of the standard deviations, however, make it difficult to compare the difference between the average values. It is to be noted that the variation in the number of resonators caused by a change in the pump position is larger for the bubble media than for the homogeneous one. This indicates that the position of the SPs in the gain volume has a large effect on the resonant mode of the random laser.

We cannot see a distinct difference between the mode properties of the homogeneous medium and that of the bubble one with polydisperse SPs. However, the properties of photon diffusion should be different between the two. Further experimental analysis is needed to elucidate the emission properties of the bubble-structured random laser.

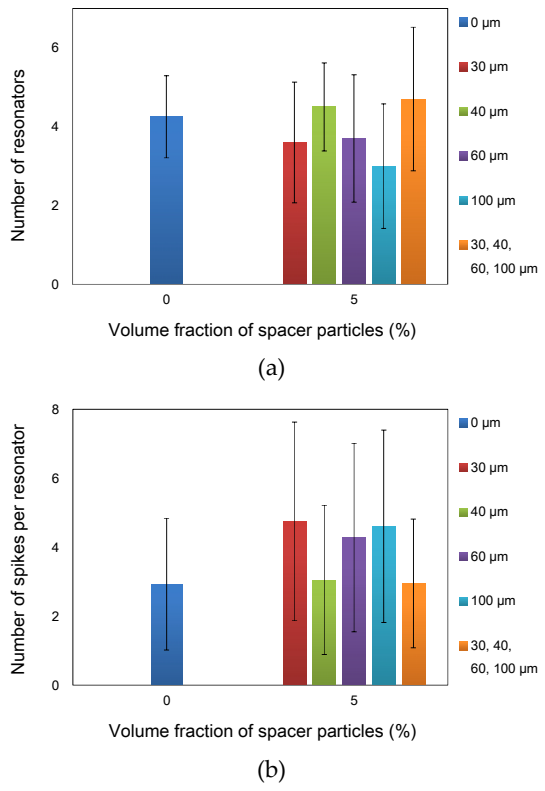


Figure 5 *(a) Number of resonators in the sample media and (b) the number of resonant frequencies of a resonator.*

4 Conclusion

We investigated the spectral and mode properties of random lasers in which scattering particles are distributed inhomogeneously. We found that dispersing spacer particles in a random gain medium results in an increase in the emission intensity at certain wavelengths. It is suggested that the spacer particles contribute to the selection of modes in which stimulated emission is effectively enhanced. A simulation study is planned to further explore the mechanisms of resonant modes of the random laser with bubble structures.

5 Acknowledgement

This work was supported by JSPS KAKENHI Grant Number 24560048

6 References

[1] Cao H., Random lasers with coherent feedback, *Optical Properties of Nanostructured Random Media*, ed. Shalaev V.M. (Springer, Berlin, 2002) pp. 303-328.

[2] Cao H, Lasing in disordered media, *Progress in Optics*, Vol. 45, ed. E. Wolf (North-Holland, Amsterdam, 2003) pp. 317-370.

[3] Noginov M., *Solid-State Random Lasers* (Springer, New York, 2005).

[4] Cao H., Review on latest developments in random lasers with coherent feedback, J. Physics A: Math. Gen., 38: 10497-10535 (2005).

[5] Wiersma D.S., The physics and applications of random lasers, Nature Physics, 4: 359-367 (2008).

[6] Wiersma D.S., Random lasers explained?, Nature Photonics, 3: 246-248 (2009).

[7] Gottardo S., Sapienza R., García P.D., Blanco A., Wiersma D.S., López C., Resonance-driven random lasing, Nature Photonics 2: 429-32 (2008).

[8] Fujiwara H., Niyuki R., Ishikawa Y., Koshizaki N., Tsuji T., Sasaki K., Low-threshold and quasi-single-mode random laser within a submicrometer-sized ZnO spherical particle film, Applied Physics Letters 102: 061110 (2013).

[9] Okamoto T. and Adachi S., Effect of particle size and shape on nonresonant random laser action of dye-doped polymer random media, Optical Review 17: 300-4 (2010).

[10] Okamoto T. and Yoshitome R., Emission properties of random laser media with a bubble structure, *CLEO/Europe - IQEC 2013* (IEEE Catalog Number: CFP13ECL-ART, ISBN: 978-1-4799-0594-2), JSIII-1.1, 12-16 May, Munich, Germany, 2013.

[11] Barthelemy P., Bertolotti J., Wiersma D.S., A Lévy flight for light, Nature 453: 495-8 (2008).

[12] Leonetti M., Conti C., Lopez C., The mode-locking transition of random lasers, Nature Photonics 5: 615 (2011).

Influence of sinter necks on the spectral behaviour of ITO aggregates

Thomas WRIEDT [1,*], Jens HELLMERS [2], Krzysztof SKORUPSKI [3] and Janusz MROCZKA [3]

[1] Institut für Werkstofftechnik, 28359 Bremen, Germany
[2] Process and Chemical Engineering, University of Bremen, 28359 Bremen, Germany
[3] Chair of Electronic and Photonic Metrology, Wroclaw University of Technology, 50-317 Wroclaw, Poland
Corresponding author: thw@iwt.uni-bremen.de

Abstract

Different degrees of sintering between nanoparticles lead to different interparticle rigidity and thereby to different material properties. Here, we extend our recent study regarding nano-scaled sintered dimers of ITO to monodisperse fractal-like aggregates and investigate possible approaches for a fast measurement method to characterize the size of connections between the primary particles.

1 Introduction

Fractal-like aggregates are commonly modelled as assemblies of primary particles (spheres) positioned in point contact only. On the other hand, sintered nano-particles can be divided into two groups [1]: 'soft agglomerates' which are characterized by weak van der Waals forces holding the particles together and 'hard agglomerates' (aggregates) where the particles are bound chemically. Depending on their state such agglomerates or aggregates can show quite different behaviour for conductivity, appearance, stability, etc. It follows that the necking can be expected to have a significant impact and should not be neglected. Now, the morphological parameters of fractal-like aggregates can be characterized using different light scattering methods [2]. Here, we would like to present actual results for light scattering simulations for aggregates of Indium Tin Oxide (ITO).

2 Optical properties of ITO

Fig. 1 shows the refractive index, the reflectance and the permittivity (see e.g. [3]) for ITO. The material data is taken from Franzen [4] (Drude model parameters). One can see that the real part of the refractive index n constantly drops until ≈1200nm while the imaginary part k steeply increases starting from ≈1000nm. As a result the reflectance of the bulk material goes up starting from 1000nm, reaching its maximum around ≈1500nm. Now, as a rule of thumb plasmonic resonance for nanospheres occur around $\varepsilon_{real} \approx -2$, and for nanorods at more negative values (see e.g. Cortie et al. [5]). For ITO, $\varepsilon_{real} \approx -2$ is found at ≈1300nm. As a result one can expect interesting spectral behaviour of ITO in the wavelength area from 1000nm to roughly 1700nm.

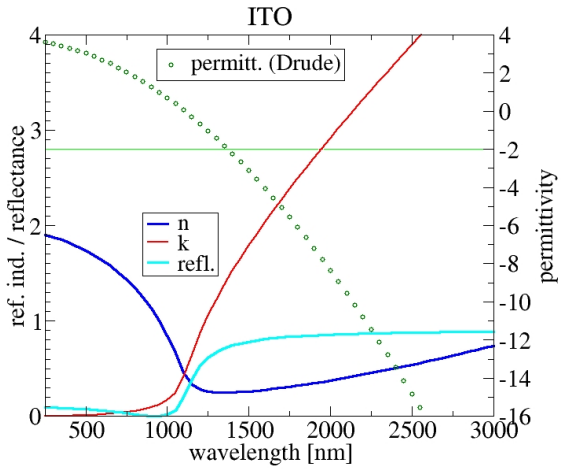


Figure 1 *Optical properties of ITO.*

3 Investigated geometries

Starting from sintered nano-scaled dimers we successively increase the number of particles to create fractal-like aggregates. For the investigations of sintered dimers we use a Cassini-oval curve to describe the shape [6]. For the clusters we assume that the primary particles are bonded by a cylinder-like neck between them. This is outlined in Fig. 2.

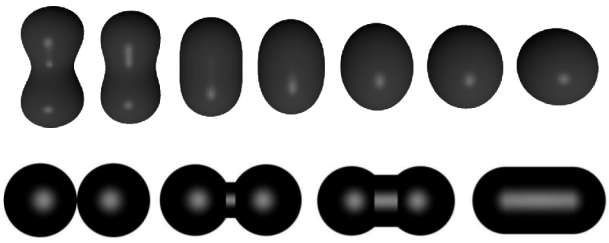


Figure 2 *Particle shapes. Top: Cassini-oval based dimers. Bottom: primary particles connected together by a cylindrical neck. The diameter of the cylinder in relation to the primary particle diameter is (from left to right) Y_{con}=0.00, Y_{con}=0.50, Y_{con}=0.75 and Y_{con}=1.00. The volume of the structure is constant for the calculations (the scaling of the presentations here differs).*

A factor Y_{con} defines the relation between the diameter of the connecting cylinder to the diameter of the primary particle: $Y_{con} = d_{cyl} / d_{particle}$. Therefore Y_{con}=0.0 means point-contact while Y_{con} =1.0 describes a cylinder with rounded ends.

The fractal-like aggregates were generated by the Cluster-Cluster algorithm proposed by Filippov et al. [7]. An exemplarily structure is presented in Fig. 3.



Figure 3 *Fractal-like aggregate models. Parameters: Rp=25nm, Np=50, D f=1.8 and Kf=1.3. The size of the connections presented here: Y_{con}=0.0, Y_{con}=0.5 and Y_{con}=1.0. The volume of the structure is constant for the calculations.*

4 Light scattering calculations

For the light scattering calculations for the sintered dimers we use the Nullfield Method with Discrete Sources (NFM-DS) [8]. This is a variant of the conventional Nullfield Method [9] that allows overcoming the usual numerical restrictions regarding the scatterer's aspect ratio and concave shape [10].

For the light scattering calculations for fractal-like aggregates we use the Discrete Dipole Approximation (DDA) [11]. Here, the DDScat code by Draine and Flatau [12] was applied to the investigations.

5 Results

In the following we would like to present results for the Cassini-based dimers (Fig. 2) as well as the cluster structure (Fig. 3) with cylinder-shaped necks.

5.1 Cassini-oval based dimers

The two original primary particles for this investigations have a diameter of d=50nm. Fig. 4 shows the spectral intensity for a wavelength range of 250-3000nm. These are the orientation averaged results for parallel polarization in forward direction.

One can observe a shift to longer wavelengths the more concave the shape gets. This happens between wavelengths from ≈1400nm to ≈1800nm and thereby corresponds with the expectation regarding the optical properties of the bulk material (see section 2). Note that the curve for the most concave shape shows a pattern that implies that this calculation was on the border of what is numerically possible [10].

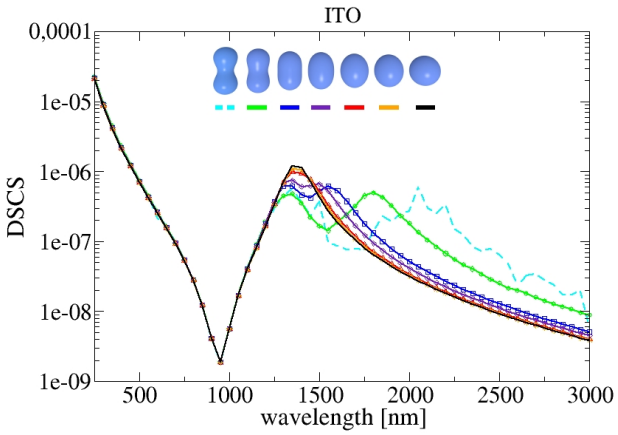


Figure 4 *Results for Cassini-based dimers. The primary particle diameter is d=50nm, orientation averaged results for the Differential Scattering Cross Section (DSCS).*

5.2 Fractal-like aggregates

In Fig. 5 the results for the cluster outlined in Fig. 3 are presented. The investigated necks are Y_{con}=0.5 and Y_{con}=1.0, the primary particle diameter is d=50nm again. Plotted are the orientation averaged extinction, scattering and absorption cross sections.

One can see that the thickness of the sinter-neck has a significant influence on the spectral behaviour in the domain of plasmon resonances, driven by the absorption.

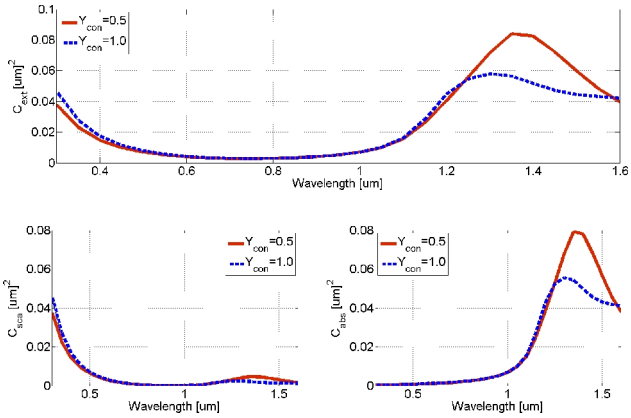


Figure 5 *Results for a cluster (Fig. 3) with Y_{con}=0.5 and Y_{con}=1.0, primary particle diameter d=50nm. Shown are the orientation averaged extinction (top), scattering (bottom left) and absorption cross sections (bottom right).*

6 Outlook

The observed effects for the spectral behaviour might be of interest for the development of a fast, in situ measurement method for the degree of sintering during a

production process. For example the intensity difference for specifically chosen wavelengths could be used for this.

7 Acknowledgement

We like to acknowledge support of this work by Deutsche Forschungsgemeinschaft DFG, WR 22/43-1.

8 References

[1] Tsantilis S., and Pratsinis S.E., Soft- and hard-agglomerate aerosols made at high temperatures, Langmuir 20(14):5933–39 (2004).

[2] Sorensen C.M., Light scattering by fractal aggregates: A review, Aerosol Science and Technology 35:648–87 (2001).

[3] E. Hecht, *Optics* (Addison Wesley, 2002).

[4] Franzen S., Surface plasmon polaritons and screened plasma absorption in indium tin oxide compared to silver and gold, J Phys Chem C 112:6027-32 (2008).

[5] Cortie M.B., Giddings J., Dowd A., Optical properties and plasmon resonances of titanium nitride nanostructures, Nanotechnology 21:115201 (2010).

[6] Hellmers J., and Wriedt T., Applicability of T-matrix light scattering simulations for the spectral investigation of sintered nanoparticles, JQSRT 123:53-61 (2013).

[7] Filippov A., Zurita M., Rosner D., Fractal-like aggregates: Relation between morphology and physical properties, Journal of Colloid and Interface Science 229:261–73 (2000).

[8] Doicu A., Eremin Yu., Wriedt T., *Light scattering by systems of particles. Null-field method with discrete sources: theory and programs* (Springer, 2006).

[9] Waterman P.C., Matrix formulation of electromagnetic scattering, Proc IEEE 53:805-12 (1965).

[10] Hellmers, J., Schmidt, V., Wriedt, T., Improving the numerical stability of T-matrix light scattering calculations for extreme particle shapes using the nullfield method with discrete sources, JQSRT 112(11): 1679-86 (2011).

[11] Purcell E.M., and Pennypacker C.R., Scattering and absorption of light by nonspherical dielectric grains, Astrophys J 186:705-14 (1973).

[12] Draine B.T., and Flatau P.J., Discrete-dipole approximation for scattering calculations, J Opt Soc Am A 11:1491-99 (1994).

PHOHOTONIC JET GENERATED BY SPHEROIDAL PARTICLE

Yiping HAN*, Lu HAN and Wenjuan ZHAO

School of physics and optoelectronic engineering, Xidian University, Xi'an, Shaanxi 710071, China

*Corresponding author: yphan@xidian.edu.cn

Abstract

A photonic jet corresponds to the high-intensity optical flux with rather narrow transverse dimensions and very low divergence angle emerging from the shadow surface of a dielectric microparticle illuminated by a light wave. Here we report the demonstration of photonic jet generated by spheroidal particle, within the framework of generalized Lorenz-Mie theory (GLMT). Specific attention is paid to the study of the influences of spheroid's ellipticity as well as the refractive index on the intensity enhancement and focal distance. It reveals that simply varying the ellipticity, it is possible to obtain localized photon fluxes having different characteristics.

1 Introduction

Optical properties of dielectric microparticles have attracted a lot of attention during last decade due their ability to squeeze light and enhance laser intensity on the shadow side. The localization does not just exist in very close vicinity to the surface of the particle but stretches beyond. The narrow high-intensity beam is called as a "photonic jet", which emerges from the shadow surface of illuminated dielectric cylinder, sphere, or spheroid with a diameter comparable or somewhat larger than the wavelength of the incident beam [1-5]. By properly selecting the optical properties of particulate material and the particle geometry, it is possible to obtain the photonic jet that can maintain a subwavelength full-width at half-maximum transverse beamwidth along a path. This fact attracts a particular interest to the photonic jet in wide practical applications, e.g., in high-resolution (nanometer scale) optical sensors [6, 7], in ultra-high density optical data storage devices [8, 9], in subdiffraction-resolution optical virtual imaging [10, 11], and in ultra-directional optical antennas [12]. Due to the distinctive features of photonic jet, the feasibilities of using photonic jet to design tools for precision cell surgery and tumor detection [13, 14], and optical tweezers [15, 16], as well as to achieve enhanced Raman scattering [17-19] were reported. Most of previous work has focused on photonic jets from spheres or cylinders, the use of a spheroid however offers many advantages. The size and shape of spheroid can be easily controlled to high precision in the fabrication process. Thus, the main goal of this paper is to investigate the photonic jet generated by spheroidal particle, within the framework of generalized Lorenz-Mie theory (GLMT). GLMT can serve as a rigorous theory in describing the interaction between the incident beam and spheroid. Proceeding from numerical calculations, we investigated the intensity enhancement and focal distance of photonic jet from spheroidal particles of different ellipticity.

2 Theoretical background

Through this paper, the propagation axis of the incident beam coincides with the revolution axis z of the spheroidal particle, the center of the spheroid is located at the middle of the beam, and the time-dependent part of the electromagnetic fields is $\exp(-i\omega t)$. According to GLMT of spheroid, the incident, scattered and internal fields in prolate spheroidal coordinates can be expanded in terms of the spheroidal vector wave functions as follows (for a TE mode): [20-22]

incident field,

$$\mathbf{E}^i = \sum_{n=1}^{\infty} i^n \left[G_n(c_1)\mathbf{M}_{e1n}^{r(1)}(c_1,\xi,\eta,\phi) + iF_n(c_1)\mathbf{N}_{o1n}^{r(1)}(c_1,\zeta,\eta,\phi) \right] \tag{1}$$

$$\mathbf{H}^i = -\frac{k_1}{\omega\mu_1}\sum_{n=1}^{\infty} i^n \left[G_n(c_1)\mathbf{M}_{o1n}^{r(1)}(c_1,\xi,\eta,\phi) - iF_n(c_1)\mathbf{N}_{e1n}^{r(1)}(c_1,\xi,\eta,\phi) \right] \tag{2}$$

scattered field,

$$\mathbf{E}^s = \sum_{n=1}^{\infty} i^n \left[\beta_n \mathbf{M}_{e1n}^{r(3)}(c_1,\xi,\eta,\phi) + i\alpha_n \mathbf{N}_{o1n}^{r(3)}(c_1,\xi,\eta,\phi) \right] \tag{3}$$

$$\mathbf{H}^s = \frac{k_1}{\omega\mu_1}\sum_{n=1}^{\infty} i^n \left[\alpha_n \mathbf{M}_{o1n}^{r(3)}(c_1,\xi,\eta,\phi) - i\beta_n \mathbf{N}_{e1n}^{r(3)}(c_1,\xi,\eta,\phi) \right] \tag{4}$$

internal field,

$$\mathbf{E}^w = \sum_{n=1}^{\infty} i^n \left[\delta_n \mathbf{M}_{e1n}^{r(1)}(c_{\text{II}},\xi,\eta,\phi) + i\gamma_n \mathbf{N}_{o1n}^{r(1)}(c_{\text{II}},\xi,\eta,\phi) \right] \tag{5}$$

$$\mathbf{H}^w = \frac{k_2}{\omega\mu_2}\sum_{n=1}^{\infty} i^n \left[\gamma_n \mathbf{M}_{o1n}^{r(1)}(c_{\text{II}},\xi,\eta,\phi) - i\delta_n \mathbf{N}_{e1n}^{r(1)}(c_{\text{II}},\xi,\eta,\phi) \right] \tag{6}$$

In the above equations, the field strength E_0 has been set equal to unity. Also, c is equal to kf, with k as the wavenumber and f as the semi-interfocal distance of the

spheroid. The subscripts Ⅰ, Ⅱ on c refer to outer or inner region of the particle, respectively. $G_n(c_{\mathrm{I}})$ and $F_n(c_{\mathrm{I}})$ are the expansion coefficients of incident beam, i.e. the beam shape coefficients [21, 23, 24]. As the incident field is known, the unknown coefficients of the scattered and internal electromagnetic fields can be determined by using the well-known boundary conditions of continuity of the tangential electromagnetic field over the spheroidal surface.

In the external near-surface field, the intensities of scattered field may be expressed as [20-22]:

$$I^s = E^s E^{s*} = E_\eta^s E_\eta^{s*} + E_\xi^s E_\xi^{s*} + E_\phi^s E_\phi^{s*} \qquad (7)$$

while the intensities in the internal electromagnetic field can be written as:

$$I^w = E^w E^{w*} = E_\eta^w E_\eta^{w*} + E_\xi^w E_\xi^{w*} + E_\phi^w E_\phi^{w*} \qquad (8)$$

in which the superscript * is the complex conjugate.

It is important to note that the results for the oblate spheroid can be evaluated in analogy with the method used above for the prolate spheroid by the transformations [21, 25]

$$c_{\mathrm{I}} \to -ic_{\mathrm{I}}, \quad c_{\mathrm{II}} \to -ic_{\mathrm{II}}, \quad \xi \to i\xi \qquad (9)$$

3 Numerical validation

The ellipticity of the spheroid is defined as the ratio of the horizontal length a to its vertical length b, similar definitions were used by Han et al. [26]. Prolate spheroid with $a/b>1$ is elongated along a line, whereas oblate spheroid with $a/b<1$ is contracted. The case of $a/b=1$ reduces to a sphere. Figure 1 presents the intensity spatial distributions over the $x-z$ plane for the Gaussian beam focused by polystyrene spheroids (refractive index equal to 1.59), while the surrounding medium is water (refractive index equal to 1.33). The horizontal length a is a constant equal to $2\mu m$ while the vertical length b is a variable. The wavelength λ of the incident Gaussian beam is $0.633\mu m$, and the waist radius is chosen to be $w_0 = 2\lambda$. The particle border is represented by the white solid line and the black dashed line, and gradations of the intensity are given by the color-bars. We can see that the polystyrene spheroid likes a lens and results in the strong three-axis confinement of light field intensity, with a large reduction of the beam extent along the propagation axis. Localized high-intensity beam called photonic jets emerges from the shadow-side surface of the spheroid, mainly due to the focusing effect of the curvature surface of the spheroidal particle. With each increase of the ellipticity, the maximum value of the optical intensity enhancement increases, the point of maximum intensity shifts close to the centre of the spheroid along the $z-$ direction, and the photonic jet significantly shortens in the $z-$ direction. The intensity maximum outside the spheroid is multiplied by more than 10 (see Figure 1(e) $a/b=1.5$). It is evident that the intensity enhancement of the photonic jet depends significantly on the spheroids' ellipticity.

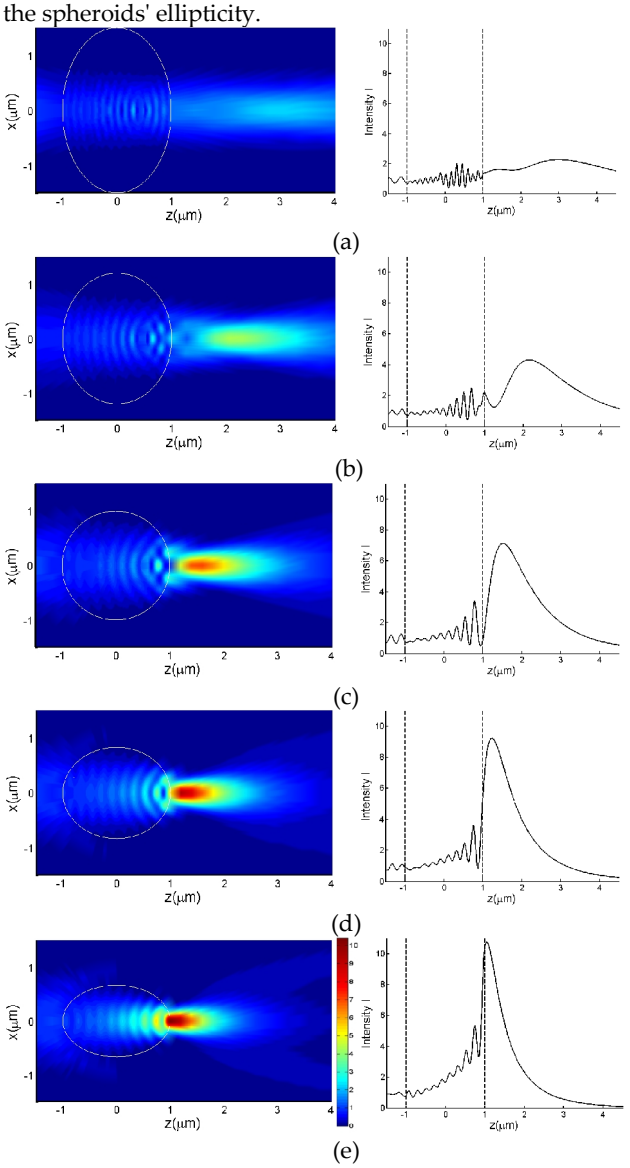


Figure 1. *Spatial distributions of the photonic jet relative intensity formed in the vicinity of polystyrene spheroids with different ellipticities placed in water and illuminated by a TE polarized Gaussian beam: (a)* $a/b=0.6667$, *(b)* $a/b=0.8333$, *(c)* $a/b=1$, *(d)* $a/b=1.2$, *and (e)* $a/b=1.5$.

These results offer good evidence that the oblate spheroid ($a/b<1$) can generate lower intensity, but longer focal distance than the corresponding sphere ($a/b=1$). On the other hand, the prolate spheroids ($a/b>1$) demonstrate shorter longitudinal waists, but higher intensity than the various realizations of the sphere ($a/b=1$). It may be advantageous to choose a jet-producing particle to obtain the photonic jet with desired properties in application. For example, in technologies of direct-write nanopatterning, the preferred photonic jet from prolate spheroid has maximal intensity, and in live

probe, oblate spheroid could be selected to generate maximally extended photonic jet.

4 References

[1]. Z. Chen, A. Taflove, and V. Backman, "Photonic nanojet enhancement of backscattering of light by nanoparticles: a potential novel visible-light ultramicroscopy technique," Optics express **12**, 1214-1220 (2004).

[2]. A. Itagi and W. Challener, "Optics of photonic nanojets," JOSA A **22**, 2847-2858 (2005).

[3]. S. Lecler, Y. Takakura, and P. Meyrueis, "Properties of a three-dimensional photonic jet," Opt Lett **30**, 2641-2643 (2005).

[4]. A. Devilez, B. Stout, N. Bonod, and E. Popov, "Spectral analysis of three-dimensional photonic jets," Optics express **16**, 14200-14212 (2008).

[5]. P. Ferrand, J. Wenger, A. Devilez, M. Pianta, B. Stout, N. Bonod, E. Popov, and H. Rigneault, "Direct imaging of photonic nanojets," Optics express **16**, 6930-6940 (2008).

[6]. X. Li, Z. G. Chen, A. Taflove, and V. Backman, "Optical analysis of nanoparticles via enhanced backscattering facilitated by 3-D photonic nanojets," Optics express **13**, 526-533 (2005).

[7]. P. Ghenuche, H. Rigneault, and J. Wenger, "Photonic nanojet focusing for hollow-core photonic crystal fiber probes," Applied optics **51**, 8637-8640 (2012).

[8]. S. C. Kong, A. Sahakian, A. Taflove, and V. Backman, "Photonic nanojet-enabled optical data storage," Optics express **16**, 13713-13719 (2008).

[9]. S. C. Kong, A. V. Sahakian, A. Heifetz, A. Taflove, and V. Backman, "Robust detection of deeply subwavelength pits in simulated optical data-storage disks using photonic jets," Appl Phys Lett **92**(2008).

[10].Z. Wang, W. Guo, L. Li, B. Luk'yanchuk, A. Khan, Z. Liu, Z. Chen, and M. Hong, "Optical virtual imaging at 50 nm lateral resolution with a white-light nanoscope," Nature communications **2**, 218 (2011).

[11].Y. Duan, G. Barbastathis, and B. Zhang, "Classical imaging theory of a microlens with super-resolution," Opt Lett **38**, 2988-2990 (2013).

[12].A. Devilez, B. Stout, and N. Bonod, "Compact metallo-dielectric optical antenna for ultra directional and enhanced radiative emission," ACS nano **4**, 3390-3396 (2010).

[13].H. Seidfaraji, M. Hasan, and J. J. Simpson, "A Feasibility Study of Microjets Applied to Breast Cancer Detection," 2012 International Conference on Electromagnetics in Advanced Applications (Iceaa), 949-951 (2012).

[14].V. N. Astratov, A. Darafsheh, M. D. Kerr, K. W. Allen, N. M. Fried, A. N. Antoszyk, and H. S. Ying, "Photonic nanojets for laser surgery," SPIE Newsroom **12**, 32-34 (2010).

[15].X. Cui, D. Erni, and C. Hafner, "Optical forces on metallic nanoparticles induced by a photonic nanojet," Opt. Express **16**, 13560-13568 (2008).

[16].V. Yannopapas, "Photonic nanojets as three-dimensional optical atom traps: A theoretical study," Optics communications **285**, 2952-2955 (2012).

[17].K. J. Yi, H. Wang, Y. F. Lu, and Z. Y. Yang, "Enhanced Raman scattering by self-assembled silica spherical microparticles," Journal of Applied Physics **101**(2007).

[18].C. L. Du, J. Kasim, Y. M. You, D. N. Shi, and Z. X. Shen, "Enhancement of Raman scattering by individual dielectric microspheres," J Raman Spectrosc **42**, 145-148 (2011).

[19].J. Kasim, T. Yu, Y. M. You, J. P. Liu, A. See, L. J. Li, and Z. X. Shen, "Near-field Raman imaging using optically trapped dielectric microsphere," Optics express **16**, 7976-7984 (2008).

[20].G. Gouesbet and G. Gréhan, *Generalized Lorenz-Mie Theories* (Springer, 2011).

[21].Y. Han and Z. Wu, "Scattering of a spheroidal particle illuminated by a Gaussian beam," Applied optics **40**, 2501-2509 (2001).

[22].L. Han, Y. Han, J. Wang, and G. Gouesbet, "Internal and near-surface field distributions for a spheroidal particle illuminated by a focused Gaussian beam: on-axis case," Journal of Quantitative Spectroscopy and Radiative Transfer (2012).

[23].F. Xu, K. Ren, G. Gouesbet, G. Gréhan, and X. Cai, "Generalized Lorenz-Mie theory for an arbitrarily oriented, located, and shaped beam scattered by a homogeneous spheroid," JOSA A **24**, 119-131 (2007).

[24].G. Gouesbet, F. Xu, and Y. Han, "Expanded description of electromagnetic arbitrary shaped beams in spheroidal coordinates, for use in light scattering theories: a review," Journal of Quantitative Spectroscopy and Radiative Transfer **112**, 2249-2267 (2011).

[25].C. Flammer, *Spheroidal wave functions* (Stanford University Press, 1957).

[26].Y. Han, L. Méès, K. Ren, G. Gouesbet, S. Wu, and G. Gréhan, "Scattering of light by spheroids: the far field case," Optics communications **210**, 1-9 (2002).

Near and Far Field Light scattering from silcon nitride microdisks

David McCLOSKEY* and John F. DONEGAN

[1] School of Physics Trinity College Dublin and AMBER, CRANN, Trinity College Dublin, Dublin 2, Ireland.

*Corresponding author: mccloskd@tcd.ie

Abstract

High intensity sub-wavelength spots and low divergence nanojets are observed in a system of Si_3N_4 microdisks illuminated with linearly polarised coherent light of wavelength 532 nm. The disks are of height 400 nm with diameters ranging from 1µm to 10µm. Light scattered from the disk and substrate is observed by imaging from above. In free space light is focused inside the disks and a sub wavelength spot is observed. The angular distribution of the intensity compares well to numerical 3D FEM results. The diameter and polarisation dependence of the scattering is explored and matches well with theory.

1 Introduction

Near-field light scattering from cylindrical and spherical particles in the Mie regime is receiving renewed interest due to the formation small high intensity sub wavelength spots and low divergence lobes on the shadow side of these particles. The main lobe can have sub-diffraction limited waist and propagate with much lower divergence than a Gaussian beam of the same waist. This has been attributed to the fact that some of the light is scattered at large angles [1]. This main diffraction lobe has been termed a photonic nanojet [2]. Much of the experimental work thus far has centred on dielectric microspheres, primarily due to the fact that high quality mono-disperse microspheres are widely available commercially. Many applications have been developed including direct write photolithography [3], high resolution optical data storage [4] and single molecule fluorescence [5].

This work shows the formation of high intensity spots and photonic nanojets in lithographically defined planar structures [6]. Using standard processing techniques adapted from the microelectronics industry allows us to change the size and shape of the structures and observe the effect on the scattering distribution. The scattering distributions are measured experimentally by imaging from above using a microscope objective. The propagating components of the near-field are mapped by secondary scattering from the substrate. The angular far-field distribution is mapped by imaging the back focal plane of the objective.

2 Experimental measurements and results

The structures were fabricated using electron beam lithography (EBL) and inductively coupled plasma (ICP) etching. An SEM image of a typical structure is shown in Fig.1 (a), with a 90° side wall angle shown in Fig.1 (b). The experimental setup is depicted in Fig.1(c). Linearly polarised light from a 532 nm diode pumped solid state laser is input at 80° from the normal. Light from the sample was collected using a 100x infinity corrected microscope objective with an NA of 0.7. Reflected light from the substrate is not within the collection angle of the objective and only scattered light is collected.

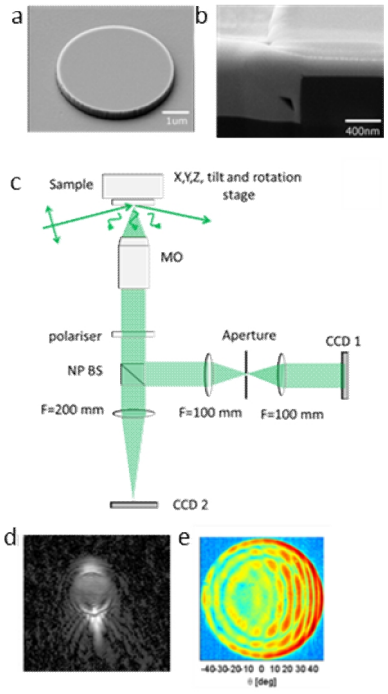


Figure 1. *(a) SEM image of a microdisk of diameter 5 µm (b) SEM image of sidewall angle after FIB milling. (c) Experimental setup: Linearly polarised collimated light is introduced with an angle of incidence of 80°. The scattered light from the structure is collected using the microscope objective (MO) and imaged onto a CCD as indicated by the marginal ray bundle in green. (d) Single shot image from a microdisk of diameter 6.5µm, with 532 nm incident wavelength. Light is incident from the top of the image. (e) Back focal plane image showing angular far field distribution of scattering.*

Imaging the microdisk shows the angular distribution of the near field due to secondary scattering from the substrate shown in Fig.1(d). A typical back focal plane image representing the angular far field scattering out of plane is shown in Fig. 1 (d).This gives a map of the angular dependence of the far-field scattering.

Mie theory for an infinite cylinder shows that the number of scattering lobes depends only on the size parameter, which is the ratio of the circumference of the cylinder to the incident wavelength, and the ratio of the refractive index of the scatter to its surroundings. The size parameter dependence for these finite height cylinders is explored experimentally by varying the diameter of the lithographically defined microdisks shown in Fig. 2.

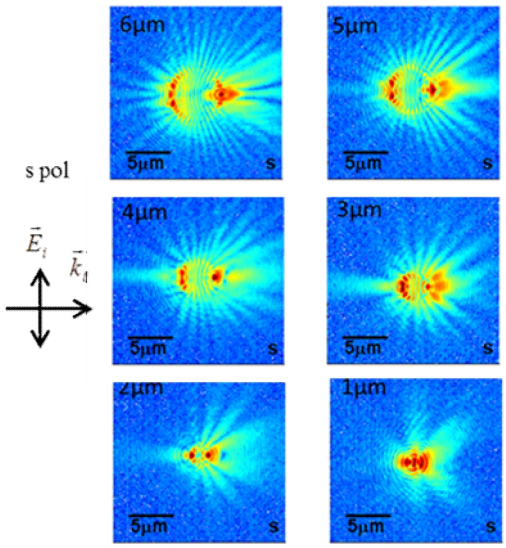


Figure.2: *Experimental images on log scale for scattering from individual disks. Light is incident from the left of the image with a fixed input angle of θ_i=80°with a wavelength of 532 nm. Disk diameter is varied from 6 μm to 1 μm as labelled.*

The images contain bright diffraction limited spots at the edge of the disk which are due to out of plane scattering, and a patterned intensity distribution outside the disk which is three orders of magnitude weaker due to secondary scattering. A high dynamic range imaging method was used to capture all the scattering information. The images are all displayed on a normalised log scale in order to display both the bright areas and the detail in low intensity regions in the same image. For the case of Si_3N_4 microdisks in air the refractive index contrast is such that a small high intensity spot is formed on, or just inside the surface of the disk. Scattering lobes are observed outside of the disks with increasing number with increasing disk diameter.

This experimental technique can be applied to characterise more complex 2D focusing elements based on a combination of refraction and scattering. We recently demonstrated diffraction limited 2D focusing elements based on a Cartesian Oval (Fig.3).

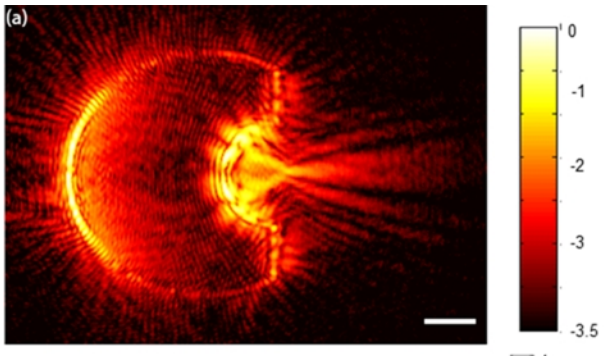


Figure.3: *Experimental image of focusing by a truncated oval with parameter a=20 μm and a cylindrical cut out with d= 10 μm is shown on log scale. Incident light is s-polarised (along y-axis).*

3 Conclusions

Under certain conditions high intensity spots and photonic nanojets can be created using Si_3N_4 microdisks. Due to the relatively high refractive index compared with polymer and SiO_2 microspheres, these microdisks may provide an improvement on techniques currently shown with microspheres. A relatively simple imaging technique was demonstrated which gives a great deal of information about the scattering structures. Using EBL the size and shape of the scatterers can be controlled with high precision to control the near-field intensity distribution.

4 References

[1] A. Devilez, B. Stout, N. Bonod, and E. Popov, "Spectral analysis of three-dimensional photonic jets," Opt.Express 16(18), 14200–14212 (2008).

[2] Z. Chen, A. Taflove, and V. Backman, "Photonic nanojet enhancement of backscattering of light by nanoparticles: a potential novel visible-light ultramicroscopy technique," Opt. Express 12(7), 1214–1220 (2004).

[3] E. McLeod, and C. B. Arnold, "Subwavelength direct-write nanopatterning using optically trapped microspheres," Nat. Nano **3**, 413-417 (2008).

[4] S.-C. Kong, A. Sahakian, A. Taflove, and V. Backman, "Photonic nanojet-enabled optical data storage," Opt. Express **16**, 13713-13719 (2008)

[5] Cuifang Kuang, Yong Liu, Xiang Hao, Ding Luo, Xu Liu, Creating attoliter detection volume by microsphere photonic nanojet and fluorescence depletion, Optics Communications, Volume 285, Issue 4, 15 February 2012, Pages 402-406, ISSN 0030-4018, 10.1016/j.optcom.2011.10.021.

[6] D. McCloskey, J. Wang, and J. Donegan, "Low divergence photonic nanojets from Si_3N_4 microdisks," Opt. Express 20, 128-140 (2012).

[7] D. McCloskey and J. Donegan, "Planar Solid Immersion Lens based on a Cartesian Oval," APL 091101 (2013).

Laser-Bubble Interactions under the Acoustic Field

Honoh SUZUKI* and I-Yin Sandy LEE

Department of Chemistry, University of Toyama, 3190 Gofuku Toyama 930-8555 Japan

*Corresponding author: honoh@sci.u-toyama.ac.jp

Abstract

Bubbles in the acoustic field have attractive optical properties that are potentially useful in photochemical and biomedical applications. As a step toward realization of such possibilities, translational dynamics of acoustically driven bubbles and the laser-induced cavitation under the acoustic field have been investigated. Computational results on the optical near field of Mie scattering are also discussed in the context of photochemical enhancement.

1 Introduction

Bubbles play an essential role in sonochemistry and sonoluminescence. When driven by an external acoustic field, they can expand and shrink in resonance, and generate a hot spot with catalytic activity and light emission [1]. Extensive research has been carried out to elucidate the mechanism of sonoluminescence [2].

Bubbles can also be important in laser-induced processes. During our research on carbon nanotube suspensions in water, we found that short-lived, transient bubbles are generated by laser irradiation, which leads to nonlinear optical scattering, photoacoustic emission, and acoustic resonance of a bubble swarm [3,4]. Such transient cavitation is also crucial in laser-induced rupture of liposomes, in which transient bubbles (with a lifetime of several microseconds) act as a 'micro-hammer' to break the liposome membrane and trigger the drug delivery [5]. In these cases, bubbles show promise as photoacoustic and mechanical devices for biomedical applications.

Bubbles are generally biocompatible (unless there are too many of them). They have a high refractive index contrast, and are flexible in their size crossing over Fresnel and Fraunhofer regions. Therefore, it is reasonable to envision them also as an optical device for biomedical, photonic, and photochemical applications. Indeed, optics of bubbles is a long and well established field of research, especially in the context of physical optics [6,7]. To explore the possibility for such applications, however, it is mandatory that we sustain and control the position of the bubbles in the ultrasonic field with a high precision, and that we understand the interactions of the acoustically driven bubble with laser pulses.

In this paper, we describe our recent results on the translational dynamics of acoustic bubbles, and the laser-induced cavitation under the acoustic field. We also discuss computational results on the optical near field of Mie scattering, with photochemical perspectives in mind.

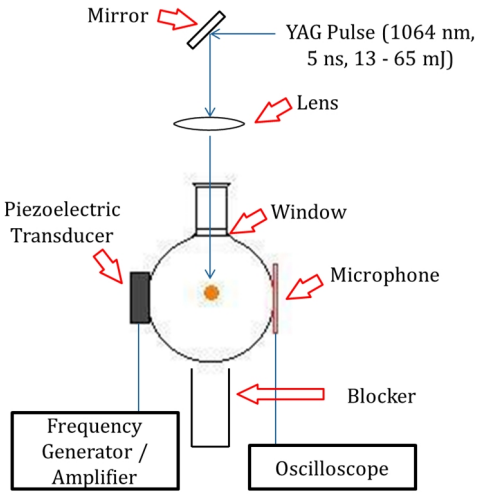


Figure 1 *Acoustic bubble trap.*

2 Experimental

Our set-up (Fig. 1) closely follows that for single-bubble sonoluminescence [8]. A 50-mL flask filled with water is sonicated with a ceramic piezoelectric transducer, and monitored with a shielded piezofilm microphone (Measurement Specialties SDT1-028K). A combination of a digital frequency generator (Strawberry Linux USB-DDS), a home-built preamplifier, a power amplifier, and an LC oscillator is used to drive the transducer. A computer-controlled scan of the frequency, the input voltage, and the inductance determines the optimal condition for trapping a single bubble at the anti-node of the standing acoustic wave (typically around 36 kHz). During each experiment, the phase drift between the driving and monitored signals is compensated by adjusting the frequency in 10 Hz intervals, which has improved the stability of the trapped bubble.

The trapped bubble is imaged by using a microscope with a long working distance (79 mm) (Specwell M0616) and a Koehler illuminator. Mie scattering measurements are done with a diode-pumped laser (cw, 532 nm, 40 mW), an optical fiber, and a photomultiplier tube.

Laser-induced cavitation is performed with a YAG laser (1064 nm, pulse duration 5 ns, maximum pulse energy 450 mJ).

Computation of the Mie near field inside and around a bubble, which is illuminated with a plane wave of monochromatic light, is done with our program [9].

3 Results and Discussion

3.1 Dynamics and Control of the Translational Motion of the Bubble

The trapped bubble can be driven into quasiperiodic and chaotic modes by applying perturbation to the acoustic frequency or pressure. The trajectories are qualitatively classified as circle, helix, eddy, irregular, oval, and flicker. Two hypotheses on the cause for the periodic dancing exist: (i) bubble growth/shrinkage [1], and (ii) nonlinear coupling between translation and hydrodynamics [10]. Our result is consistent with the latter.

The trapped bubble position can also be controlled (to some extent) by tuning the acoustic frequency and pressure, with a precision estimated to be less than 80 μm. However, there still exist obstacles against reproducibility, such as acoustic streaming and possible drifts in the concentration of dissolved gas.

3.2 Laser-Induced Cavitation under the Acoustic Field

Irradiation of a single laser pulse focused at the acoustic anti-node creates a stable bubble. The threshold in the pulse energy compares well with those for laser-induced breakdown (LIB), although LIB without an external acoustic field generally only leads to transient (short-lived) cavitation [11]. Laser-induced plasma formation is likely to provide a bubble seed, followed by its growth and stabilization via "rectified diffusion" in the acoustic field [1].

When a second pulse hits the vicinity of the first bubble, a second bubble is created and rapidly fused into the first. The strong attraction between them is interpreted in terms of transient Bjerknes forces (acoustic radiation forces).

3.3 Mie Field Calculation

Recently, the optical near field is attracting much attention with the interest for morphology-dependent resonances (MDR) [12] and photonic jets [13]. To examine the possibility of photochemical enhancements near the surface of the bubble, we have computed the near field inside and around a bubble (with a diameter of 1 μm) in water, irradiated with the 1064-nm light (Fig.2). The top and middle figures depict irradiance, which indicates significant deformation and enhancement near the bubble surface. Also, the small size of the bubble allows penetration of the field into it, which may be analysed in terms of evanescent wave and optical tunnelling [6].

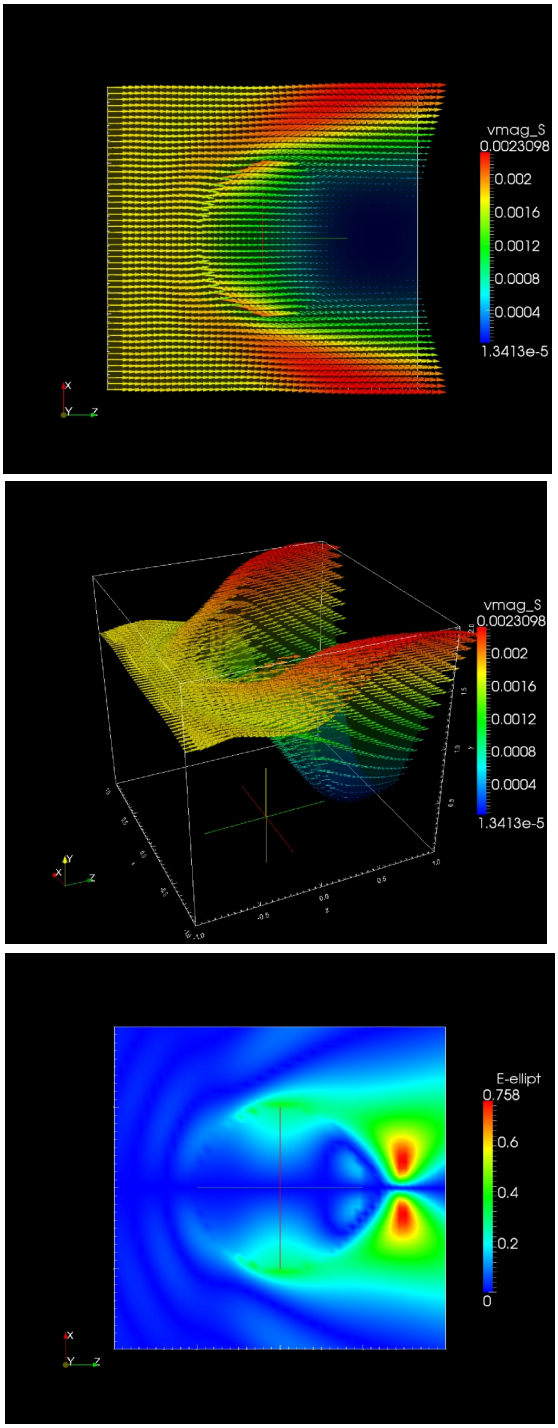


Figure 2 *Mie field around a 1-μm bubble (the refractive index n = 1) in water (n = 1.3206) irradiated with the plane-wave light of 1.064μm. Incident direction = z-axis (from left to right); linear polarization = x-axis; x-z plane (y = 0) spanning +-1μm is shown. (Top) Surface map of irradiance (I); (middle) 3D map plotting I as the height (y-axis); and (bottom) surface map of ellipticity of the electric field.*

The bottom figure shows ellipticity of the electric vector field [14], which clearly indicates that elliptic polarization

is generated from the incident linear polarization; thus, the bubble acts as a sort of a wave plate or retarder. However, the vibration ellipse is not perpendicular to the Poynting vector but nearly sitting on the x-z plane, and highly localized at the side faces of the bubble. Similar behaviour in ellipticity has been found in the case of other scatterers. Its significance (or insignificance) in relation with photochemical enhancement is yet unclear to us at the moment. (It is also noted that the strong ellipticity in the 'shadow' region is misleading and actually insignificant, because there is little irradiance there.)

4 Acknowledgement

We thank M. Takeda, Y. Ina, and H. Maekita for their experimental support. This work is supported by the Japanese Ministry of Education, Science and Culture (Grant no. 23550010).

5 References

[1] T. Leighton, *The acoustic bubble* (Academic Press, 1994). .

[2] K.S. Suslick, K.S., Flannigan, D.J., Inside a collapsing bubble: sonoluminescence and the conditions during cavitation, Annu. Rev. Phys. Chem. 59: 659-683 (2008).

[3] Lee, I-Y.S., Matsuo, T., Suzuki, H., Photosensitization of nonlinear scattering and photoacoustic emission from single-walled carbon nanotubes, Appl. Phys. Lett. 92: 103122 (2008).

[4] Lee, I-Y.S., Hayama, Y., Suzuki, H., Osawa, T., Photoacoustic sensitization and laser-induced cavitation in polymer solutions by carbon nanotubes, J. Phys. Chem. C 114: 22392-22397 (2010).

[5] Suzuki, H., Lee, I-Y.S., Sakai, T., Laser-Induced Rupture of Infrared Dye-Doped Liposomes, *Nanomaterials for Biomedicine* (Ed. by R. Nagarajan), ACS Publications, Chapter 8, pp 175-189 (2012).

[6] Marston, P.L., Kingsbury, D.L., Scattering by a bubble in water near the critical angle: interference effects, J. Opt. Soc. Am. 71: 192-196 (1981).

[7] Onofri, F.R.A., Radev, S., Sentis, M., Barbosa, S., Physical-optics approximation of near-critical-angle scattering by spheroidal bubbles, Optics Letters, 37: 4780-4782 (2012).

[8] Steer, W.A., Sonoluminescence experiment: sound into light, http://www.techmind.org/sl/ (2007).

[9] H. Suzuki, BHFIELD: A Fortran program for the Mie field calculation (Open Source), University of Toyama (2009). [available at http://www.scattport.org/]

[10] Mettin, R., A.A. Doinikov, Translational instability of a spherical bubble in a standing ultrasound wave, Applied Acoustics 70: 1330-1339 (2009)

[11] Vogel, A., et al., Energy balance of optical breakdown in water at nanosecond to femtosecond time scales, Applied Physics B: Lasers and Optics 68: 271-280 (1999).

[12] Lock, J.A., Excitation efficiency of a morphology-dependent resonance by a focused Gaussian beam, JOSA A 15: 2986-2994 (1998).

[13] Chen, Z., Taflove, A., Backman, V., Photonic nanojet enhancement of backscattering of light by nanoparticles: a potential novel visible-light ultramicroscopy technique, Optics express 12: 1214-1220 (2004).

[14] M. Born, and E. Wolf, *Principles of optics: electromagnetic theory of propagation, interference and diffraction of light*. Cambridge University Press (1999).

Optical Particle Characterization

Fast Nanoparticle Sizing By Image Dynamic Light Scattering

Chengze XU[1], Xiaoshu CAI[1,*], Jie ZHANG[1], Lili LIU[1]

[1] Institute of Particle and Two-phase Flow Measurement, University of Shanghai for Science & Technology, Shanghai 200093, China

*Corresponding author: usst_caixs@163.com

Abstract

In this paper, an Image Dynamic Light Scattering method (IDLS) for nanoparticle sizing is introduced. Here, the spatial distribution of scattered light from nanoparticles undergo Brownian motion was captured by CCD camera. It took an acquisition time of milliseconds to achieve a real-time sizing, much faster than conventional DLS from tens of seconds to several minutes for acquisition. The diameter was obtained via Stokes-Einstein relation. Dilute dispersions of latex spheres were tested and the results showed the feasibility of this real-time Image DLS technique. The requirements in hardware and algorithm by using Image DLS measurements were discussed.

1 Introduction

Dynamic Light Scattering (DLS) technique based on particles' Brownian motion is widely used in nanoparticle sizing. During the development of DLS technique, different researchers also used other academic terms like Intensity Fluctuation Spectroscopy (IFS) [1], Quasi-Elastic Light Scattering (QELS) [2], Photon Correlation Spectroscopy (PCS) [3]. The terms used depend largely on the background and philosophy of the practitioner. Now PCS and DLS are widely accepted. It can be applied to Chemistry, Biology and Physics etc [4]. The schematic drawing of DLS apparatus is shown in Fig.1. A photon multiplier tube (PMT) or avalanche photodiode is usually employed to collect the signals of scattered light. Then the time intensity autocorrelation function (ACF) is calculated in digital correlators to extract the information of particles' translational diffusion coefficient D_T. For spherical particles, the Stokes-Einstein relation relates D_T to particle's hydrodynamic diameter d :

$$D_T = \frac{k_b T}{3\pi\eta d} \quad (1)$$

Where k_b is Boltzmann's constant, T is the absolute temperature and η is the dynamic viscosity of the suspending medium. Thus, the particle diameter is derived from Eq.1.

However, in order to get sufficient data for intensity autocorrelation function, DLS measurements require an acquisition time from tens of seconds to several minutes [5,9], which is far way from real-time acquisition. On the other hand, the Brownian motion is sensitive to the viscosity of the suspending medium, which is related to its temperature. Thus, a temperature-control unit is applied to stabilize the sample temperature during the long acquisition time. It is not optimized for real-time and in-situ measurements of nanoparticles, especially in the fields of nanofluids in microchannels, synthesis of nanoparticles, and chemical reaction processes, etc. For those reasons, a fast Image DLS (IDLS) method with compact and smart packages is introduced in this work to explore the possibility of real-time nanoparticle sizing.

2 Difference

In fact, nanoparticles scatter the incident laser beam in all directions. DLS (shown in Fig.1) collects signals at one spot (about one coherence area large restricted by a pinhole) for a high coherence factor [6]. Thus, DLS requires a long acquisition time to get sufficient data as mentioned. Here in IDLS (Fig.2), a spatial distribution of scattered light was captured (Fig.3). The speckle pattern of scattered light was captured by CCD camera at scattering angle of 45°. Millions of pixels on imaging chip were equivalent to large amounts of sensors collecting different coherence areas simultaneously. Thus, it had large amounts of information in one frame to carry out a statistic intensity ACF result and was able to shorten the acquisition time to milliseconds. It takes an acquisition time nearly a thousand times shorter than conventional way. Then it is possible to carry out a real-time nanoparticle sizing, especially real-time acquisition. Firstly, real-time acquisition is of fundamental importance for real-time monitoring. The computing of intensity autocorrelation was executed in software by a personal computer with an Intel Core i5 processor. Real-time computing can be achieved by using digital correlator arrays or upgrading the hardware. In such short acquisition time about milliseconds to sub-second, it may also lessen the danger of appreciably heating the sample or having local thermal convection when using medium-powered laser to work with weakly scattering systems (small particle). The requirements of apparatus and data processing in IDLS measurement will be discussed.

3 Experiment

A schematic diagram of this IDLS apparatus is shown in Fig.2. A diode laser of wavelength 532 nm was utilized

to illuminate the diluted suspension of monodisperse latex spheres. The camera was placed at the scattering angle θ of 45° .

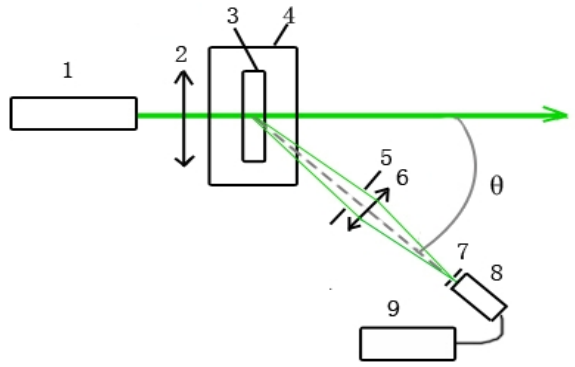


Figure 1. *Schematic diagram of conventional DLS apparatus. (1- Laser; 2-Lens; 3-Sample cell; 4-Temperature-control slot; 5-Aperture; 6-Lens; 7-Pinhole; 8-Photon multiplier; 9-Digital correlator + Computer)*

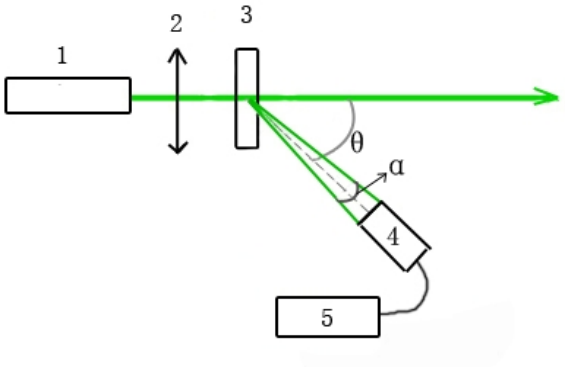


Figure 2. *Figure 2. Schematic diagram of IDLS apparatus. (1- Laser; 2-Lens; 3-Sample cell; 4- camera; 5-Computer)*

The intensity fluctuations due to particles' Brownian motion (diffusion) are usually not readily to observed because they take place on a rapid time scale (μs-ms) and take place at a point [7]. The first part means a high speed detection must be applied. Here a high-speed motion camera (Redlake's MotionPro X3, 8-bit monochrome) was applied for experimental research. Fame rates can be set from 1000 fps at full resolution (1280×1024 pixels) to over 64,000 fps at reduced resolution. Solutions were found to use a normal CCD camera in IDLS measurement instead of an expensive high-speed motion camera. The second part is related to the spatial coherence factor (β) of DLS measurement. As noted by [6], the intensity of the whole frame appears constant. In order to get a maximum signal-to-noise ratio of the intensity fluctuation (a high coherence factor), DLS keeps the detector aperture (pinhole) just small enough to see one coherence area. In IDLS, the smallest area for this approach could be set to one pixel (12μm×12μm) in algorithm, much smaller than a typical DLS detector aperture for consideration of coherence factor. So, the whole frame was divided into small units of pixel areas in algorithm before carrying on intensity ACF calculations.

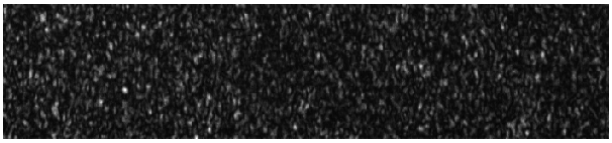


Figure 3. *Frame of scattered light (352nm latex spheres) captured by IDLS apparatus.*

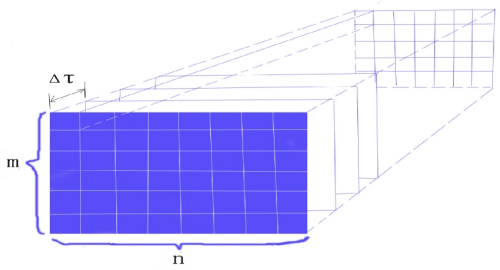


Figure 4. *Grid dividing for frames captured*

Firstly, a series of frames were captured at fixed frame rate. Then each frame was first divided into m×n grids in algorithm, forming m×n tunnels of autocorrelation functions (illustrated in Fig.4). Each grid had an area that was small enough to see only one coherence area to achieve a high coherence factor. In the experiments, we calculated 3000 correlation functions with a grid size of 4×4 pixels. And the coherence area can be calculated by follow equation [8]:

$$A_{coh} = 4\frac{\lambda^2 R^2}{\pi w^2} \qquad (2)$$

In our experiments, λ was 532 nm, R was 0.18 m, w was 1 mm. Thus, coherence area A_{coh} was equal to 11,676 μm². The area of one grid A_d was 2304 μm² (4×4×12μm×12μm), much smaller than A_{coh}. Theoretically, if $A_d \leqslant A_{coh}$, the coherence factor β of the experiments can be equal to one [3]. But due to the dark count of the camera, the gray valve of the pictures were not purely caused by the signals (scattered light). Thus the real coherence factor was reduced. The coherence factor of our experiments were around 0.8. It can be calculated from Eq.4. In another words, if $A_d \gg A_{coh}$, β will decrease to zero; the signals will be uncorrelated.

Totally, 3000 tunnels (3000 grids) of intensity signals generated 3000 autocorrelation functions:

$$G_i^{(2)}(\tau) = < I_i(t) I_i(t+\tau) > \qquad (3)$$

Here i is the number of each tunnel. $I(t)$ and $I(t+\tau)$ are the intensities of scattered light at the moment of 't' and '$t+\tau$'. A normalized form was utilized to fit the autocorrelation function of monodisperse nanoparticles, written as

$$g^{(2)}(\tau) = \frac{\langle I(t) I(t+\tau) \rangle}{\langle I(t) \rangle^2} = 1 + \beta \exp(-2\Gamma \cdot \tau) \qquad (4)$$

Where β denotes the coherence factor. To extract the information of the reciprocal decay time Γ, using the simplified form $G(t) = \exp(-2\Gamma \cdot t)$.

4 Results and discussion

In acquisition time less than one second, different diameters (27nm/ 80nm/ 352nm) of standard polystyrene latex spheres were tested. Catalog numbers are HMn-27, HMn-80, GBW12010. The autocorrelation functions were showed in Fig.5. And the results were shown in Table 1.

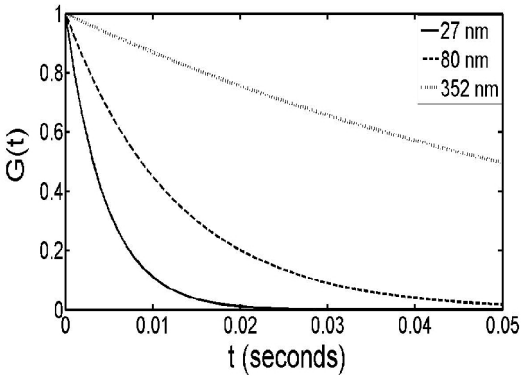


Figure 5. *Autocorrelation functions for latex nanospheres of different diameters in 75%(V) glycerol solution. (n=1.44, η =0.02773 pa • s, T=298 K, Frame rate=1000 fps)*

Diameter (nm)	Mean measured value (nm)	Standard deviation
27	28	±2 nm
80	79	±4 nm
352	357	±12 nm

Table 1 *Calculated diameter of different latex spheres*

The results showed acceptable precision in verifying the possibility of this IDLS method, realizing a real-time acquisition. Glycerol solution of 75% volume concentration was chosen to achieve a detecting speed of 1000 frames per second, which was available to a normal CCD camera at reduced resolution. Also, a sample of nano-silver was tested and the result was compared with the analysis of TEM result.

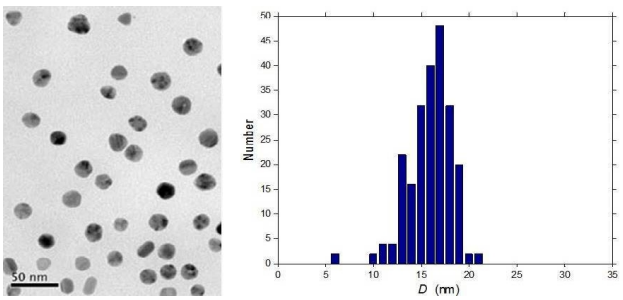


Figure 6. *TEM photograph and diameter analysis of the nano-silver sample.*

The mean diameter value of 112 particles analyzed by TEM photograph was 15.9 nm. And the mean measured value given by IDLS measurement was 18 nm ± 2 nm. Suspending medium was 75%(V) glycerol solution (η=0.03162 pa·s, *T*=296 K, *Frame rate*=2000 fps). 1000 fps to 2000 fps is available for normal CCD cameras at reduced resolution. The standard deviation of the mean measured value could be slightly reduced by raising the frame rate. And to extend the lower limit of the measurement, higher frame rate is recommended. Further, a 16-bit camera can improve the accuracy of the measurement. The average diameter value was tested for monodisperse system in this work to verify the feasibility of IDLS detecting. For polydisperse system, There are many mathematic methods [10] to perform the inverse Laplace transform like the 'CONTIN' program, which will not be discussed here.

5 Conclusions

The experimental results showed an acceptable accuracy and the mean value was tested to verify the feasibility of the IDLS method, which shortening the acquisition time from conventional tens of seconds to milliseconds. It will become feasible to achieve real-time and in-situ nanoparticle monitoring in the fields of chemical reaction process, nanoparticle generating, etc. Furthermore, it gives out an impact and smart apparatus with the fast developments of tiny CCD camera and its performance, which will also indicate the future of real-time nanoparticle monitoring.

6 Acknowledgement

This work is supported by the Specialized Research Fund for the Doctoral Program of Higher Education of China (20113120130001), the Nanotech Initiative Project of Shanghai Science and Technology Commission (11nm0507100).

7 References

[1] R. Food, E. Jakeman, C. Oliver and E.R. Pike, Determination of Diffusion Coefficients of Haemocyanin at Low Concentration by Intensity Fluctuation Spectroscopy of Scattered Laser Light, Nature Vol.227 (1970).

[2] B.E. Dahneke etc, *Measurement of Suspended Particles by Quasi-Elastic Light Scattering* (Wiley, New York, 1983).

[3] R. Pecora, *Dynamic Light Scattering: Applications of Photon Correlation Spectroscopy* (Plenum, New York, 1985).

[4] B.J. Berne, R. Pecora. *Dynamic Light Scattering with Applications to Chemistry, Biology, and Physics* (Wiley, New York, 1976).

[5] T. Allen, *Powder Acquisition and Particle Size Determination* (Elsevier, Amsterdam, 2003).

[6] John C. Thomas, Photon correlation spectroscopy: technique and i-nstrumentation, *Proc. SPIE 1430, Photon Correlation Spectroscopy: Multico mponent Systems, 2* (June 1, 1991).

[7] N.C. Ford, "Theory and Practice of Photon Correlation Spectroscopy." in *Measurement of Suspended Particles by Quasi-Elastic Light Scattering*, B.E. Dahneke (Wiley, New York, 1983).

[8] P.N. Pusey and J.M. Vaughan, "Light scattering and Intensity Fluctuation Spectroscopy." in *Dielectric and Related Process, Vol.2,* M. Davies ed. , (Chemical Society, London, 1975).

[9] W. Brown, *Dynamic Light Scattering-The method and some applications* (Clarendon, Oxford, 1993).

[10] Jiaqi Shen, Xiaoshu Cai, Optimized inversion procedure for retrieval of particle size distributions from dynamic light scattering signals in current detection mode, Optics Letters, Vol.35(12), (2010).

High-sensitivity low-coherence dynamic light scattering and particle sizing for nanoparticles (Ⅲ): Particle size distribution of pigment particles

Katsuhiro ISHII[1,*], Sohichiro NAKAMURA[2] and Yuki SATO[2]

[1] The Graduate School for the Creation of New Photonics Industries,
1955-1 Kurematsucho, Nishiku, Hamamatsu, Shizuoka, 432-1202, Japan
[2] Analysis Technology Center, Research & Development Management Headquarters, FUJIFILM Corporation,
210, Nakanuma, Minamiashigara, Kanagawa, 250-0123, Japan

Corresponding author: ishii@gpi.ac.jp

Abstract

High-sensitivity low-coherence DLS is applied to measurement of particle size distribution of pigments suspended in a ink. We show the changes of particle size distribution of thixotropy and sedimentary pigments with time. Moreover, we show the dependence of particle size distribution of pigments particles on the concentration.

1 Introduction

We have been proposed and developed low-coherence dynamic light scattering(DLS), which is heterodyne DLS using a broadband light source instead of a laser. Because of characteristics of low-coherence interferometer, path-length resolved measurement can be taken. By choosing the pathlength of scattered light to be shorter than the mean-free-path-length, the influence of multiple scattering can be neglected and the DLS measurement can be performed even for dense scattering media[1-3]. However, its application was limited to particles with a diameter larger than 100 nm since the primary system with Michelson interferometer has not high sensitivity. Adopting a Mach-Zehnder interferometer, a balance detector, and a confocal system, the sensitivity of the new system, named high-sensitivity low-coherence DLS, is considerably improved and lower the limit of detectable particle size is extended to less than 10 nm[4].

In this paper, by using high-sensitivity low-coherence DLS, we measurement particle size distribution of pigment particles suspended in a ink. We measure the change of particle size distribution of sedimentary and non-sedimentary pigment particles with time. We investigate the influence of dilution to the particle size distribution.

2 High-sensitive low-coherence DLS

Figure 1 shows a schematic of the developed low-coherence DLS system. A superluminescent diode (SLD), with a central wavelength of 835.7 nm and a spectral width of 18 nm is used as a low-coherent light source. The coherence length of it is about 34 μm. The light is divided by a coupler into 99% probe light and 1% reference light. The probe light illuminates the sample via a circulator, a collimator, and a 10x objective lens. The backscattered light is coupled again into the optical fiber, and sends to the other coupler with a coupling ratio of 50:50. We adopt a confocal optical system to efficiently detect the scattered light but a numerical aperture of the incident light is not so high. A beam waist size of the incident light is about 100 μm. A large number of particles is inside the scattering volume. The influence of the confocal optical system on the scattering angle is insignificant because the wave front of the incident light is plane near the beam waist and a numerical aperture of the incident light is not so high. The focal point of the incident light is inside the sample and 100μm away from a wall of a cuvette to avoid the wall-drag effect on Brownian motion.

The reference light undergoes sinusoidal phase modulation by an electro-optic modulator placed between two collimators and sends to the second coupler. The modulation frequency varied from a few kHz to a few hundreds of kHz, depending on the bandwidth of the scattered light. The distance between two collimators is adjusted so that the path length of the light scattered at the focal point coincides with that of the reference light. Therefore, the light scattered from the region around the focal point can interfere with the reference light. The depth of the region is coherence length of the light source.

The scattered light and the phase modulated reference light is combine and divided by the second coupler with a coupling ratio of 50:50 and fed to a balanced detector. The detector amplifies the difference of two signals that is the interference signal between the scattered light and reference light. The intensity of interference signal oscillates with the modulation frequency of the reference light. The power spectrum and the temporal autocorrelation function of the detected signal is calculated by a PC.

The temporal autocorrelation function of the detected signal is given by [3]

$$G(\tau)=(I_r+I_s)^2+(<I_s^2(t)>-I_s^2)g_2(\tau) + 2I_r\sum_{n=-\infty}^{\infty}J_n^2(\phi_m)\cos(n\omega_m\tau)\int_0^{\infty}I_s(s)g_1(\tau,s)\left|\gamma(\Delta l/c+s/c)\right|^2 ds, \quad (1)$$

where I_r, I_s, $<I_s^2(t)>$, and $I_s(s)$ denote the intensity of the reference light, the time-averaged intensity of the total scattered light, time average of the square of the intensity

of the total scattered light, and the time-averaged intensity of the scattered light with the path length s. s means the path length in side the scattering medium and, then, the light scattered at the boundary of scattering medium has the path length s=0. $g_2(\tau)$ denotes the temporal autocorrelation function of the intensity of the total scattered light. $g_1(\tau,s)$ denotes the temporal autocorrelation function of the amplitude of the scattered light with the path length s. $\gamma(\tau)$ means the complex coherence function of the light source. Δl means path length difference between the reference light and the light scattered at the boundary. ϕ_m and ω_m denote the modulus and frequency of the phase modulation. The temporal autocorrelation function in Eq. (1) is similar to that of the conventional heterodyne DLS. The third them corresponds to the temporal autocorrelation function of the conventional heterodyne DLS. The second term is negligible in conventional heterodyne DLS but it is substantial in low-coherence DLS. The second term is proportional to the intensity of the total scattered light but the third term is proportional to the amplitude of the scattered light with the path length s.

When a coherent light source such as laser is used, the complex coherence function is regarded as unity and the temporal autocorrelation function is reduced to $g_1(\tau)=\int_0^\infty I_s(s)g_1(\tau,s)ds$. It is identical to that of the conventional heterodyne DLS. On the other hand, when the coherence length is quite short and the complex coherence function is regarded as delta function $|\delta(\Delta l/c+s/c)|$, we can obtain the temporal autocorrelation function of the amplitude of the scattered light with the path length $s=\Delta l$

$$\int_0^\infty I_s(s)g_1(\tau,s)\left|\delta(\Delta l/c+s/c)\right|^2 ds = I_s(\Delta l)g_1(\tau,\Delta l). \quad (2)$$

Because the coherence length of actual light sources is finite, the path length of the detected scattered light is broadened and its width is coherence length of light source. As a result the width and the depth of the scattering volume are beam waist size and coherence length in low-coherence DLS measurement, respectively.

By set path length of detected scattering light shorter than few times of mean-free-math-length, low-coherence DLS can obtain the temporal autocorrelation function of single scattering even for extremely dense media[2]. Particle size distribution can be analyzed from the temporal autocorrelation function by the conventional method such as CONTIN method, weighted histogram analysis method, and cumulant expansion.

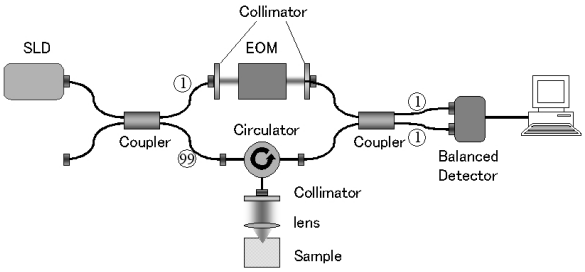


Figure 1 *Experimantal setup.*

3 Results and discussion

Figure 5 shows particle size distribution of thixotropy and sedimentary pigments estimated by the weighted histogram analysis method. The primary particle size of the pigments is a few tens nm. The vertical axis denotes the scattering intensity. The scattering intensity from one particle is proportional to the sixth power of particle diameter according to Rayleigh scattering. We can find 4 peaks in the particle size distribution just after dispersing. The peak around 10-20nm corresponds to primary particle. Other peaks show aggregate or agglomerate of pigments. It should be noted that a large number of primary particles and a few aggregates and agglomerates are in the suspension because the scattering intensity from primary particle is quite weak. One month after dispersing, the number of primary particle decrease drastically due to the aggregation or agglomeration. Moreover, aggregates larger than 1 μm disappear due to the sedimentation.

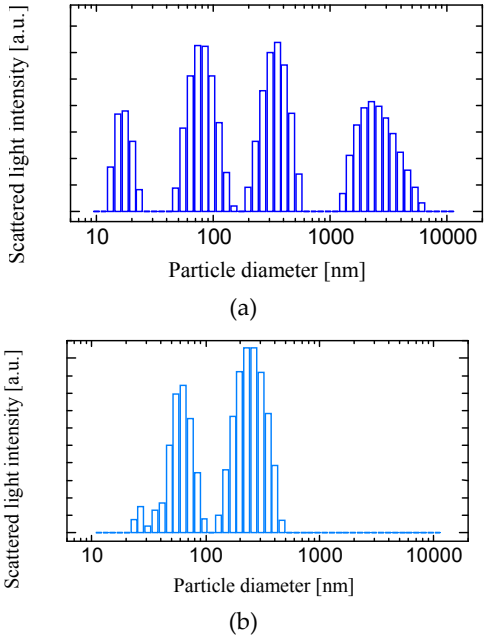


Figure 2 *Particle size distributions of thixotropy and sedimentary pigments measured (a) just after and (b) one month after dispersing, respectively. They are estimated by the weighted histogram analysis method.*

Figure 6 shows particle size distribution of other kind of pigments estimated by the weighted histogram analysis method. The weight fraction of the pigments is 15wt %. Three diluted solutions with weight fraction of 0.15wt%, 5wt%, and 10wt% are prepared. The pigments with weight fraction 15wt % has broad particle size distribution from 50nm to 10000nm. By diluting the ink, large size particles vanishes and width of size distribution decreases. This indicate that the diluting the solution influence to the dispersion of particles and great care must be taken to dilute solution in DLS measurement. The low-coherence DLS which can apply to dense and turbid medium without dilution is available method to evaluate the dispersion of particles.

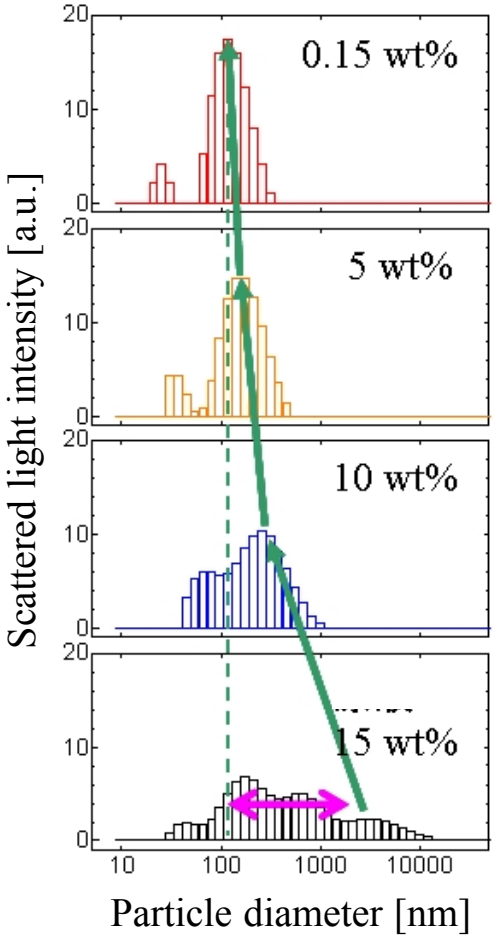


Figure 3 *Particle size distributions of thixotropy and sedimentary pigments measured (a) just after and (b) one month after dispersing, respectively. They are estimated by the weighted histogram analysis method.*

4 Conclusion

We measurement particle size distribution of pigments suspended in a ink by using high-sensitivity low-coherence DLS. The temporal variation of particle size distribution of thixotropy and sedimentary pigments due to aggregation, agglomerate, and sedimentation is demonstrated. Moreover, we demonstrate the influence of dilution of ink to particle size distribution. In a kind of ink, the dilution of ink strongly influence to the dispersion of particles. The low-coherence DLS which can apply to dense and turbid medium without dilution is available method to evaluate the dispersion of particles.

5 References

[1] Ishii K., Yoshida R., Iwai T., Single-scattering spectroscopy for extremely dense colloidal suspensions by use of a low-coherence interferometer, Optics Letters:555-557 (2005)

[2] Xia H., Ishii K., Iwai T., Hydrodynamic radius sizing of nanoparticles in dense polydisperse media by low-coherence dynamic light scattering, Japanese Journal of Applied Physics 44:6261-6264 (2005)

[3] Ishii K., Iwai T., Theoretical analysis of path-length resolved power spectrum measurement using low-coherence dynamic light scattering, Japanese Journal of Applied Physics 47:8397-8401 (2008)

[4] Ishii K., Nakamura S., Sato Y., High-sensitivity low-coherence dynamic light scattering and particle sizing for nanoparticles, Proceddings of SPIE 8082:80821z-1-8 (2011)

Light Scattering in Highly Concentrated Mono- and Bimodal Dispersions

Lena BRESSEL[1,*], Miren AGUIRRE[2], Mariano BARRADO[3], Jose Ramon LEIZA[2] and Oliver REICH[1]

[1]innoFSPEC Potsdam, Institute of Chemistry - Physical Chemistry, University of Potsdam, Potsdam, 14476, Germany

[2]POLYMAT, Kimika Aplikatua Saila, Kimika Zientzien Fakultatea, University of the Basque Country UPV/EHU, Joxe Mari Korta Zentroa, 20018, Donostia-San Sebastian, Spain

[3]SGIker, University of the Basque Country UPV/EHU, Joxe Mari Korta Zentroa, 20018, Donostia-San Sebastian, Spain

Corresponding author: bressel@uni-potsdam.de

Abstract

In this work the reduced scattering coefficient μ_s' of highly concentrated mono- and bimodal dispersions is investigated by Photon Density Wave spectroscopy. The measured μ_s' are found to be in good agreement with theoretical values from Mie theory up to volume fractions of 0.4 if dependent scattering is considered applying the hard sphere model in the Percus-Yevick approximation either for mono- or bimodal systems. Particle sizes (and in case of bimodal systems additionally the relative amount of small to large particles) are obtained by comparison of the measured with calculated μ_s' at different volume fractions and wavelengths. An excellent agreement is found between these particles sizes (even for bimodal systems) and reference values determined by DLS or TEM at high dilution. A short introduction to dependent scattering in mono- and bimodal dispersions is given.

1 Introduction

Light scattering in highly concentrated dispersions is a challenging topic but nevertheless important for particle sizing in such materials. Due to multiple light scattering, well-known sizing techniques as DLS, SLS or turbidity measurements are bound to fail. However, Photon Density Wave (PDW) spectroscopy [1] based on multiple light scattering is able to determine the reduced scattering coefficient at high particle concentrations and hence provides an access to the particle size without dilution. Nevertheless, due to dependent scattering at high concentrations spatial particle correlation has to be considered for correct sizing. In the following models for dependent scattering in mono- and bimodal dispersions will be verified and determined particles sizes will be compared to reference values obtained at high dilution.

2 Theory and Experiment

2.1 Reduced Scattering Coefficient and Dependent Scattering

The reduced scattering coefficient μ_s' for monodisperse samples is connected to the particle radius a by the well-known relationship [2, p.84]:

$$\mu_{s,\mathrm{indep}}' = \frac{3\phi Q_s}{4a}\left[1-g\right], \tag{1}$$

where ϕ is the volume fraction of the particles and Q_s and g are the scattering efficiency and anisotropy factor, respectively, accessible by Mie theory. Hence, for known ϕ Eq. (1) can be used for particle size determination. However, Eq. (1) is only valid for low particle concentrations. At high concentrations the inter-particle distance becomes small leading to an interaction between the particles due to e. g. volume exclusion or electrostatic interaction. Hence, spatial particle ordering occurs resulting in interference of the scattered light from different particles. In case of monomodal systems only interference of the scattered light from particles of the same size arises and can be taken into account by the static structure factor S. The reduced scattering coefficient then reads [3]

$$\mu_{s,\mathrm{dep}}' = \frac{3\phi\pi Q_s}{2a}\int_{-1}^{1} f(\cos\theta)S(\theta,\phi)\left[1-\cos\theta\right]\mathrm{d}\cos\theta\,, \tag{2}$$

where f is the normalized scattering phase function and θ is the scattering angle. If no particle interaction takes place $S(\theta)=1$ reducing Eq. (2) to Eq. (1). In bimodal systems interference of the scattered light from particles of the same size (S_{11}, S_{22}) and of different sizes (S_{12}) occurs. The reduced scattering coefficient reads for this case [4]

$$\mu_{s,\mathrm{dep}}' = \frac{3\phi\lambda^2}{16\pi^2 n_M^2\left(x_1a_1^3+x_2a_2^3\right)}\int_{-1}^{1} FS(\theta,\phi)\left[1-\cos\theta\right]\mathrm{d}\cos\theta\,, \tag{3}$$

with refractive index of the medium n_M, wavelength λ and

$$\begin{aligned} FS(\theta,\phi) = {} & x_1\left(\left|f_{S,1}\right|^2+\left|f_{P,1}\right|^2\right)S_{11} + x_2\left(\left|f_{S,2}\right|^2+\left|f_{P,2}\right|^2\right)S_{22} \\ & + 2\sqrt{x_1x_2}\,\mathrm{Re}\left(f_{S,1}f_{S,2}^* + f_{P,1}f_{P,2}^*\right)S_{12} \end{aligned}, \tag{4}$$

where x_1 and x_2 are the relative number densities of the small and large particles, respectively, with $x_1+x_2=1$. $f_{S,1}$, $f_{P,1}$ $f_{S,2}$ and $f_{P,2}$ are the complex single scattering amplitudes of the two polarization states (S, P) for the small (1) and large (2) particles (f^* being the complex conjugates) and S_{11}, S_{22} and S_{12} are the static structure factors. Hence, if the structure factors are known, μ_s' can be calculated for mono- (Eq. (2)) and bimodal (Eq. (3)) dispersions and particle sizes can be determined even at high

concentrations. In the following only hard sphere interactions between the particles are considered which is sufficient for polymer dispersions of high ionic strength. For this case the static structure factors for the mono- [3] and bimodal [5,6] systems can be calculated analytically for the hard sphere model in the Percus-Yevick approximation (HSPYA).

2.2 Experimental and Data Analysis

PDW spectroscopy [1,3] measurements are carried out on two monomodal polystyrene latices PS_1 and PS_2, a mixture of these two latices with $x_2 = 0.0514$, a monomodal (CP_1) and a bimodal (CP_2) methylacrylate-butylacrylate-copolymer. For all samples the reduced scattering coefficient μ_s' was determined as a function of volume fraction and wavelength λ (ranging from 638 to 982 nm). In the following only results at one wavelength are shown exemplarily. However, data analysis and determination of particle radii has been carried out including all wavelengths. Refractive indices of the particles n_P and the surrounding water n_M, essential for data evaluation [7], are taken from [8] or measured using an ATR-refractometer. The refractive index of the dispersion at each ϕ is calculated from n_P and n_M [7]. Particle sizes are determined from the measured μ_s' by comparison to calculated μ_s' applying either the monomodal (Eq. (2)) or bimodal (Eq. (3)) HSPYA. For an error estimation in the monomodal dispersions particle sizes are determined at each volume fraction and the standard deviation is taken. Error estimation for the bimodal systems is still under investigation. Here, particle sizes for the best agreement between experimental and calculated μ_s' are given only. Reference particle sizes are determined by DLS or cryo-TEM at high dilution.

3 Results

3.1 Monomodal Systems

The measured reduced scattering coefficient of PS_1 and PS_2 at $\lambda = 833$ nm and of CP_1 at $\lambda = 935$ nm are shown in Figure 1 and Figure 2, respectively. μ_s' increases in the range from $0 < \phi < 0.2$ for all samples deviating from the linearity due to dependent scattering. For CP_1 μ_s' decreases for larger ϕ exhibiting a maximum at $\phi \approx 0.2$. Here, the effect of dependent scattering has a huge influence on μ_s'. For comparison calculated μ_s' applying the monomodal HSPYA (Eq. (2)) are shown. Best overlap between experimental and calculated values is obtained for $a = (253 \pm 10)$ nm for PS_1, $a = (106 \pm 2)$ nm for PS_2 and $a = (128 \pm 1)$ nm for CP_1. For PS_1 and PS_2 calculated and measured μ_s' agree very well over the whole investigated range. However, for CP_1 the experimental μ_s' are slightly larger for $\phi > 0.4$ than expected from calculations. One possible reason for the discrepancy is that the Percus-Yevick approximation is valid quantitatively only up to volume fractions of 0.4. Particle radii obtained individually at each ϕ above 0.4 therefore range from 128 nm to 135 nm and are not included in the standard deviation. However, below $\phi = 0.4$ the determined particle radii of all samples are in good agreement with reference values obtained by DLS and cryo-TEM ($a_{PS1}^{DLS} = (268 \pm 53)$ nm, $a_{PS2}^{DLS} = (106 \pm 31)$ nm, $a_{CP1}^{TEM} = (125 \pm 30)$ nm). The small standard deviation of the particle size obtained by PDW spectroscopy indicates the possibility of correct particle sizing by wavelength dependent measurements at a single ϕ.

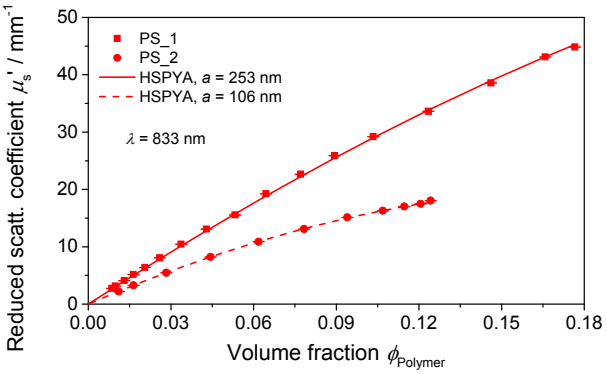


Figure 1 *Experimental μ_s' of PS_1 and PS_2 (symbols) and calculated μ_s' applying monomodal HSPYA (lines).*

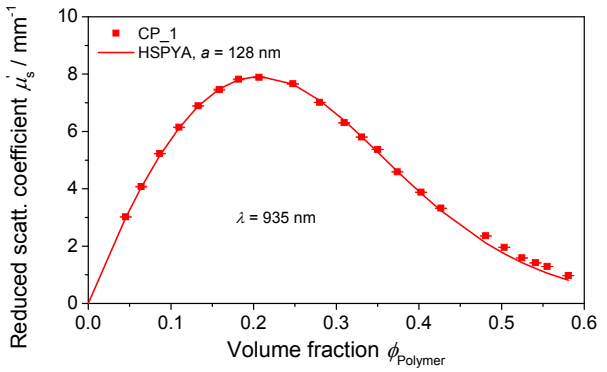


Figure 2 *Experimental μ_s' of CP_1 (symbols) and calculated μ_s' applying monomodal HSPYA (line).*

3.2 Bimodal Systems

The measured μ_s' at $\lambda = 833$ nm of the mixture of PS_1 and PS_2 ($x_2 = 0.0514$) is shown in Figure 3. The values are smaller than those obtained for the pure latex PS_1 and larger than those for pure PS_2. Here, a linear volume-fraction-weighted combination of calculated μ_s' applying the monomodal HSPYA with $a = 106$ nm and $a = 253$ nm does not agree with the experimental results as the particle correlation between small and large particles is not considered. However, the bimodal HSPYA for $a_1 = 106$ nm, $a_2 = 253$ nm and $x_2 = 0.0514$ results in a good overlap for the experimental and calculated values.

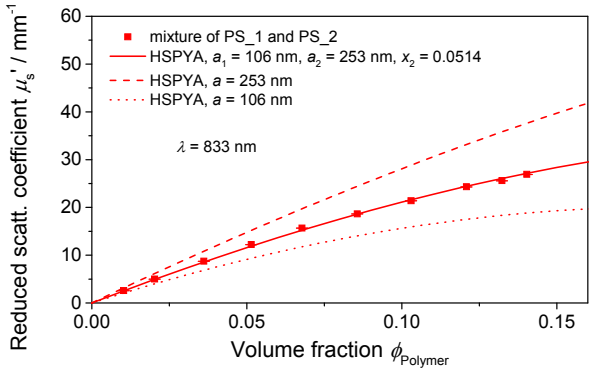


Figure 3 *Experimental μ_s' of a mixture of PS_1 and PS_2 (symbols) and calculated μ_s' applying bimodal (solid line) or monomodal (dashed and dotted lines) HSPYA.*

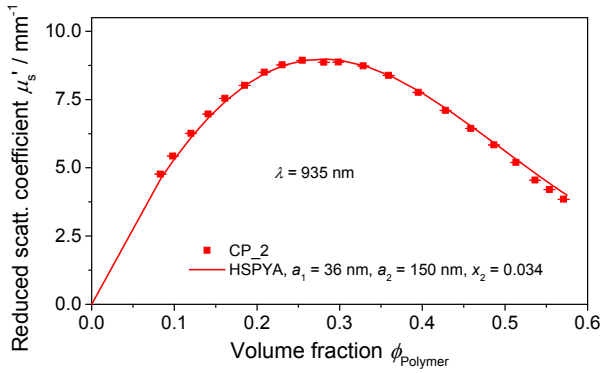


Figure 4 *Experimental μ_s' of CP_2 (symbols) and calculated μ_s' applying bimodal HSPYA (line).*

The experiment indicates that μ_s' can be calculated correctly if the particle radii of the two components and their relative amount are known. However, also the inversion, i. e. the determination of the particle sizes and their relative amount in such bimodal dispersions, is possible from measured μ_s'. As CP_2 was synthesized as a bimodal latex μ_s' could not be measured for the two sub-distributions and hence their particle size could not be determined individually. In Figure 4 the measured reduced scattering coefficient at $\lambda = 935$ nm is shown for CP_2. Even though μ_s' exhibits a similar behaviour as CP_1 no overlap is obtained if the monomodal HSPYA is applied. In contrast incorporating the bimodal HSPYA model with $a_1 = 36$ nm, $a_2 = 150$ nm and $x_2 = 0.034$ results in an excellent agreement between experimental and calculated values. Only at very high volume fractions the calculated μ_s' differ from the experimental ones possibly due to the limit of validity of the Percus-Yevick approximation. The obtained radii agree very well with reference values from cryo-TEM ($a_{1,CP2}^{TEM} = (36 \pm 6)$ nm, $a_{2,CP2}^{TEM} = (150 \pm 13)$ nm). The TEM analysis also suggests a higher amount of small particles being present in the sample ($x_2 = 0.097$) corresponding to the value of $x_2 = 0.034$ obtained by PDW spectroscopy. Even though the here given radii and x_2 are obtained by comparison of experimental with calculated μ_s' over the whole range of ϕ and all λ, the results suggest that the determination at constant ϕ is also possible. This will be further investigated.

4 Conclusion

In this work the reduced scattering coefficient of highly concentrated mono- and bimodal polymer latices was investigated by PDW spectroscopy. Dependent scattering was considered applying the hard sphere model in the Percus-Yevick approximation. An excellent agreement was found between measured and calculated μ_s' up to volume fractions of 0.4. Particle sizes determined from measured μ_s' in this range agree very well with reference data from DLS or TEM. In case of monomodal dispersions particle sizes determined individually at each ϕ were nearly constant up to a volume fraction of 0.4. Further data analysis will reveal if particle sizes in bimodal dispersion can also be obtained from $\mu_s'(\lambda)$ at a single ϕ. Additionally, influence of the relative amount in bimodal dispersions on μ_s' will be presented.

Acknowledgement

We gratefully thank Dr. B.-R. Paulke, Fraunhofer Institute for Applied Polymer Research, Potsdam, Germany, for providing the polystyrene dispersions. We like to thank the German BMBF program Unternehmen Region (grant no. 03Z2AN12) and the Land Brandenburg, MWFK, for financial support of innoFSPEC Potsdam.

5 References

[1] O. Reich, *Photonendichtewellenspektroskopie mit intensitätsmodulierten Diodenlasern*, Dissertation, University of Potsdam (2005).

[2] M. Kerker, *The scattering of light and other electromagnetic radiation* (Academic Press, New York, 1969).

[3] Bressel L., Hass R., Reich O., Particle sizing in highly turbid dispersions by Photon Density Wave spectroscopy, J Quant Spectrosc Radiat Transf 126:122-9 (2013).

[4] Sun Z., Sevick-Muraca E.M., Investigation of Particle Interactions in Dense Colloidal Suspensions Using Frequency Domain Photon Migration: Bidisperse Systems, Langmuir 18(4):1091-7 (2002).

[5] Ashcroft N.W., Langreth D.C., Structure of Binary Liquid Mixtures. I, Phys Rev 156(3):685-92 (1967).

[6] Ashcroft N.W., Langreth D.C., Structure of Binary Liquid Mixtures. I. Errata, Phys Rev 166:934 (1968).

[7] Hass R., Münzberg M., Bressel L., Reich O., Industrial applications of Photon Density Wave spectroscopy for in-line particle sizing, Applied Optics 52(7):1423-31 (2013).

[8] Sultanova N.G., Nikolov I.D., Ivanov C.D., Measuring the refractometric characteristics of optical plastics, Optical and Quantum Electronics 35:21–34 (2003).

Diffusing Wave Spectroscopy: A Modern Light Scattering Technique to Characterize Mixtures/Soft Matter Systems

Frédéric Mondiot, Mathias Reufer, and Andreas C. Voelker*

LS Instruments AG, Passage du Cardinal 1, 1700 Fribourg, Switzerland

*Corresponding author: charles.voelker@lsinstruments.ch

Abstract

Diffusing Wave Spectroscopy (DWS) is a modern light scattering technique that allows the quantitative measurement of microscopic motion in soft mater systems, from which the rheological properties can be extracted via the so-called microrheology approach.

In this presentation, we will first review the fundamentals of DWS microrheology. Next, we will show examples of soft matter systems including mixtures (suspensions and emulsions) on which we successfully applied microrheology. Specifically, we will show that one can obtain the same results as with a mechanical rheometer, if certain requirements are fulfilled. Finally, we will demonstrate how DWS can also accurately measure the mean hydrodynamic radius of solid, liquid, or gaseous particles in turbid mixtures.

1 Diffusing Wave Spectroscopy

DWS can be applied to highly turbid media such as concentrated particle suspensions, emulsions, foams, or gels. In such opaque mixtures, light is scattered multiple times by solid particles, liquid droplets, or gaseous bubbles. These scatterers perform Brownian motion, which makes the intensity of scattered light fluctuate over time. By assuming a diffusive propagation of light within the sample, the path length distribution $P(s)$ of the scattered photons can be determined. When the diffusion approximation is applied to the intensity correlation function of the scattered light, the mean square displacement (MSD) of the scattering particles, droplets or bubbles, can be then extracted [1]. Moreover, the rheological properties of the surrounding medium, namely the storage (G') and loss (G'') moduli, can be derived from the particle MSD upon application of the Generalized Stokes-Einstein Relation [2]. The MSD could also be obtained using other methods such as video-based particle tracking. From our experience DWS is, however, the technology that obtains the most precise MSD, if the boundary conditions are well chosen. Microrheology thus represents the most frequent application of DWS. A far less known application of DWS is particle sizing, which uses the particle MSD and the standard Stokes-Einstein relation to calculate the mean hydrodynamic radius of particles in Newtonian fluids [3]. Only few publications have discussed this topic, because the precision of DWS particle sizing was often considered inferior to dynamic light scattering (DLS) sizing. A recent study conducted by us shows, however, that DWS precision is comparable to that of DLS, and results are highly reproducible.

2 DWS Microrheology

This section focuses on experiments we carried out using the DWS technology for microrheology applications. Using a DWS-based optical rheometer equipped with the DWS Echo technology [4], we show, in particular, that accurate and reliable measurements of the storage and loss moduli have been achieved over angular frequencies as high as 10^6 rad.s^{-1} and in a matter of minutes. By contrast, typical rheometers are limited to angular frequencies up to ~ 10^2 rad.s^{-1}, and may take several hours to complete a frequency sweep. Figure 1 compares the angular-frequency dependence of the storage and loss moduli of an aqueous solution containing 0.55 % wt/v of xanthan, obtained by a mechanical rheometer (Malvern Bohlin Gemini) and a DWS-based optical rheometer (DWS RheoLab from LS Instruments). To perform microrheology with the latter, 980-nm-diameter polystyrene particles, used as tracer particles, were added to the aqueous solution at 1% wt/v. The data obtained from DWS microrheology are in excellent agreement with the data obtained from mechanical rheology within the overlapping angular frequency range. We note, moreover,

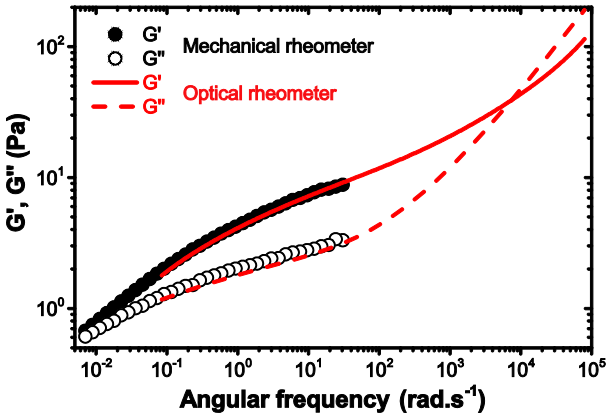


Figure 1 *Storage (G') and loss (G'') moduli of an aqueous solution containing 0.55 % wt/v of xanthan, measured by a mechanical rheometer (Malvern Bohlin Gemini) and a DWS-based optical rheometer (DWS RheoLab from LS Instruments). To perform microrheology with the latter, 980-nm-diameter tracer polystyrene particles were added to the aqueous solution at 1% wt/v.*

that DWS microrheology extends the measurements of G' and G'' to considerably higher angular frequencies.

Other examples of soft matter systems such as everyday-life products (yogurt, gelatin, mayonnaise, etc.), which we have applied DWS microrheology to, will be discussed.

3 DWS Particle Sizing

The well-established state-of-the-art imaging techniques to measure particle size such as scanning (SEM) or transmission electron microscopy (TEM), require tedious sample preparation and are typically sample destructive. By contrast, DWS is a non-destructive and a non-invasive technique that can be applied to many samples with no sample preparation at all. While some advanced DLS techniques allow measurement at very high particle volume fractions, nearly all standard commercial instruments require dilution of the sample. DWS, however, only works in systems containing high-enough particle volume fractions.

We have successfully applied the DWS technology to the measurement of the mean hydrodynamic radius of particles in highly-concentrated suspensions in a very accurate and reproducible manner. Figure 2 shows the accuracy of DWS sizing measurements as a function of turbidity, here characterized by the inverse of the transport mean free path, l^*, for different particle materials, sizes, and volume fractions. Figure 2 not only demonstrates that DWS sizing is able to measure particle sizes over a broad range of radii, typically in the range of radii [100nm, 1µm], but also at very high particle volume fractions.

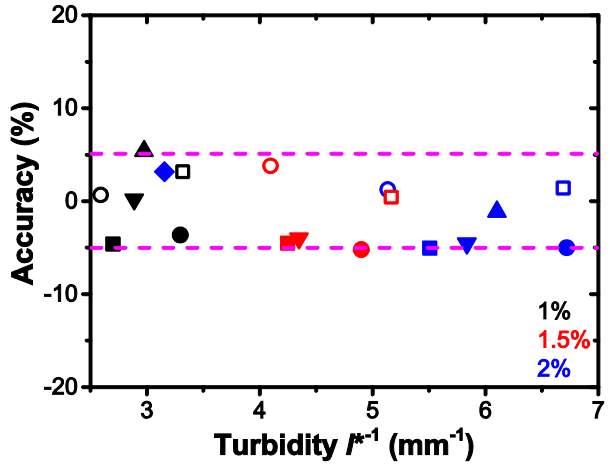


Figure 2 *Accuracy of DWS sizing measurements as a function of turbidity, characterized by the inverse of the transport mean free path, l*. Measurements were carried out on aqueous suspensions of spherical polystyrene particles with radii of (■) 111nm, (●) 220nm, (▲) 280nm, (▼) 385nm, and (◆) 960nm, and on melamine particles with radii of (□) 296nm, and (○) 516nm, at different volume fractions (indicated by the colored numbers in the bottom right-hand corner). Within the size range [100nm, 1µm] and the turbidity range shown, an accuracy of ± 5% is achieved.*

We present, in addition, other experiments where we have successfully applied DWS sizing (characterization of the Ostwald ripening in concentrated emulsions, determination of the bubble size in a shaving cream, etc.).

4 References

[1] D.A. Weitz, and D.J. Pine, *Diffusion Wave Spectroscopy*. In Dynamic Light Scattering; Brown, W., Ed.; Oxford University Press: New York, 652-720 (1993).

[2] Mason T.G., Weitz, D.A., *Optical Measurements of Frequency-Dependent Linear Viscoelastic Moduli of Complex Fluids*, Physical Review Letters 74, 1250-1253 (1995).

[3] Scheffold F., *Particle Sizing with Diffusing Wave Spectroscopy*, Journal of Dispersion Science and technology 23, 591-599 (2002).

[4] Zakharov P., Cardinaux F., Scheffold F., *Multispeckle Diffusing-Wave Spectroscopy with a Single-Mode Detection Scheme*, Physical Review E 73, 011413 (2006).

Digital In-line Holography for the Characterization of Inclusions in a Suspended Water Droplet

Wisuttida WICHITWONG, Sébastien COETMELLEC, Denis LEBRUN, Daniel ALLANO, Gérard GREHAN, and Marc BRUNEL*

UMR CNRS 6614 CORIA, Avenue de l'Université, 76801 Saint-Etienne du Rouvray Cedex, France

*Corresponding author: marc.brunel@coria.fr

Abstract

Inclusions in a suspended water droplet are investigated using digital in-line holography. Holograms are numerically reconstructed by using the two-dimensional fractional-order Fourier transform (2D-FRFT). The reconstructed images are analyzed to extract the size of the particles and their 3-D locations within the droplet. Using a long exposure regime, some trajectories of the inclusions are further experimentally extracted.

1 Introduction

The study of water droplets with inclusions is very important in many areas. In atmospheric and climate science, water droplets in atmosphere can contain small aerosol particles. In biology, small organisms in a liquid coat can be considered as droplets with inclusions.

In this work, we study inclusions within a suspended millimetric water droplet. The inclusions that we consider are calibrated spherical glass particles (of diameters 2, 5, 10 or 20 micrometers). We use digital in-line microholography [1] to record the diffraction patterns created by the inclusions present inside the droplet. From theoretical point of view, the intensity of the diffracted field in the plane of the CCD sensor is derived theoretically under Fresnel approximation using the generalized Huygens-Fresnel integral formalism based on optical transfer matrices which describe the whole imaging system. Using a long exposure time, we further show that we can reconstruct directly some portions of the trajectories of the inclusions inside the droplet.

2 Results

The experimental set-up is as follows: calibrated particles are located within a millimetric droplet. The incident beam is a Gaussian beam emitted by a Continuous Wave laser (wavelength 642nm). The beam propagates through an optical system and is focused with a microscope objective within the suspended water droplet. A CCD camera is positioned at the output of the droplet. Digital reconstruction of the holograms is realized using the two-dimensional fractional-order Fourier transform (2D-FRFT). The numerical reconstruction can be viewed as a numerical refocusing on the diffracting element (particle inside the droplet in this study) [2].

Fig. 1 (a) and (b) show simulated and experimental holograms of 20µm particles dispersed within a millimetric water droplet, respectively. Using an optical transfer matrices based-model, we can evaluate the optimal order of reconstruction of a particle versus the distance between the corresponding particle and the CCD sensor. The optimal order of reconstruction is indeed linked analytically to the position of the inclusion within the droplet [2]. Different planes of reconstruction correspond to different fractional orders. The holograms of Fig. 1(a) and (b) have thus been numerically reconstructed by using the 2D-FRFT. Fig. 1 (c) and (d) are the reconstructed images of (a) and (b) with optimal fractional orders equal to 0.5 and 0.48, respectively. The calibration curve giving the longitudinal position of the inclusion versus the order of reconstruction is given in figure 2.

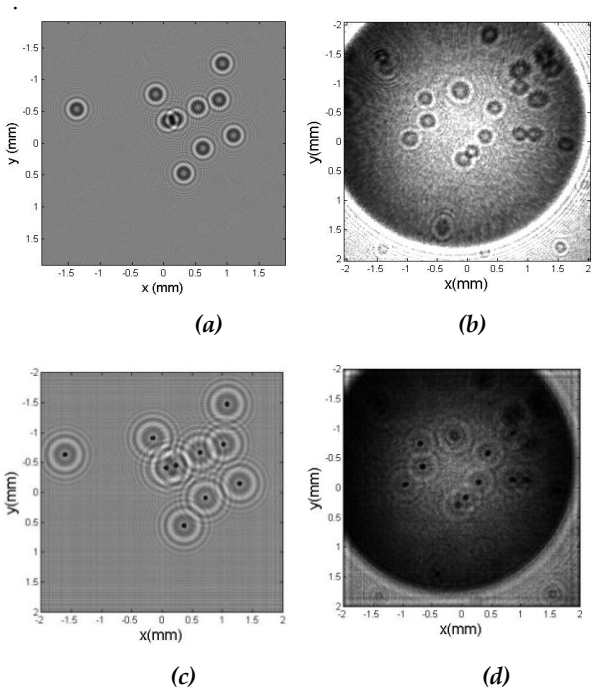


Figure 1 *Simulated (a) and experimental (b) holograms of 20µm particles. (c) and (d) are the reconstructed images of (a) and (b), respectively. (e) and (f) are the intensity profiles along x of a reconstructed particle (from (c) and (d))*

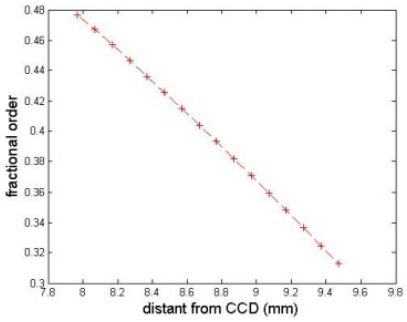
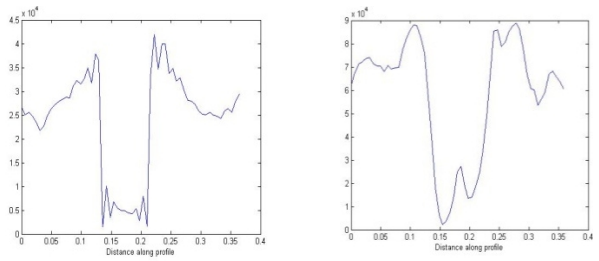


Figure 2 *Optimal fractional order of reconstruction versus the distance between the inclusion and the CCD sensor.*

The diameter of each particle can be finally measured by plotting the intensity profile of the reconstructed particles as shown in Fig. 3 (a) and (b).



(a) (b)

Figure 3 *(a) and (b) are the intensity profiles along x of a reconstructed particle (from Fig 1 (c) and (d) respectively).*

When the exposure time is much longer than the time necessary for grabbing the particle at one location, the diffraction pattern is spread along the trajectory of the particle [3]. Fig. 4(a) shows an experimental hologram recorded when the exposure time is 0.20s. After optimal reconstruction, we can further observe the trajectories of different inclusions in different longitudinal planes (Fig. 4 (b)-(d)), which correspond to the different axial positions of the inclusions from the CCD sensor. The axial positions of the reconstructed particles in Fig. 4 (b), (c), and (d) are 13.81mm, 13.76mm, and 13.60mm, respectively. From the trajectory of the particles and the value of the exposure time, we can finally evaluate the transverse velocity of the inclusions.

3 Conclusion

By using digital in-line holography, the 3D-position and the trajectory of particles inside a droplet can be obtained. This technique should allow the 3D vizualisation of the capture of particles by droplets in real-time in the future.

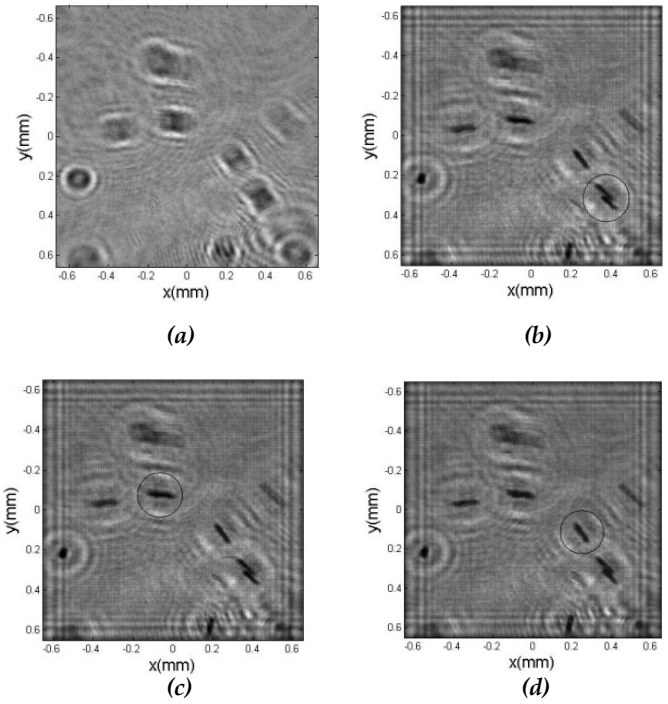


Figure 4 *(a) is the hologram of 20µm particles inside a millimetric droplet, with a long 0.20s exposure time. (b),(c), and (d) are the reconstructed images in different longitudinal planes corresponding to the fractional orders 0.73, 0.735, and 0.75,respectively.*

4 References

[1] Xu W., Jericho M.H., Kreuzer H.J., Meinertzhagen I.A., Tracking particles in four dimensions with in-line holographic microscopy, Optics Letters 28(3):164-166 (2003)

[2] Verrier N., Coëtmellec S., Brunel M., Lebrun D., Digital in-line holography in thick optical systems: application to visualization in pipes, Applied Optics 47:4147-4157 (2008)

[3] Lebrun D., Méès L., Fréchou D., Coëtmellec S., Brunel M., Allano D., Long time exposure digital in-line holography for 3-D particle trajectography, Optics Express 21(20):23522-23530 (2013)

Energy redistribution in single particle interference microscopy

Markus SELMKE[1,*], Irene NEUGEBAUER[1] and Frank CICHOS[1]

[1] Molecular Nanophotonics, Universität Leipzig, Leipzig, 04103, Germany

Corresponding author: selmke@rz.uni-leipzig.de

Abstract

Transmission microscopy represents a sensitive method to detect and characterize single nanoparticles. A tightly focused laser beam induces a scattered field, which interferes with the illuminating field in its propagation direction [1]. The far-field detected transmission signal under this seemingly simple situation of interference exhibits a rich phenomenology. We study the energy-redistribution and absorption characteristics of focused-beam interference both for Rayleigh and arbitrarily sized Mie scatterers.

1 Interference Microscopy

Substantial work has been done in the experimental application of interference detection schemes. Sensitive techniques such as spatial modulation spectroscopy (SMS [2]) and photothermal single particle microscopy [3] provide the means to quantitatively measure extinction and absorption cross-sections of individual nanoparticles from the transmission signal of a tightly focused coherent laser. Despite this progress, the way in which the key parameters which determine the signal, i.e. the collection angle $\theta_{\max}$, the particle's complex-valued polarizability α and its placement in the focal region, have not yet been described in a coherent picture. Only the signal in the strict forward direction has been discussed in some detail [4]. While a few rigorous treatments of the phenomenon exist [5], a simple interpretation is spoiled by their complex nature. We propose a minimal yet accurate model based on the generalized Lorenz Mie theory and find revealing dependencies on the polarizability of the particle and the collection angle used to detect the signal. Especially the simplification for Rayleigh-scatterers promises to be a useful tool for future studies in this field.

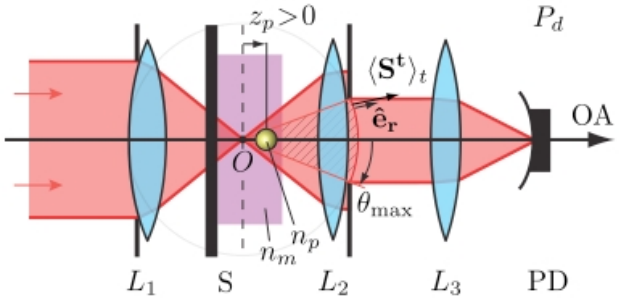


Figure 1 *Schematic setup for transmission microscopy. L: lenses (microscope objectives), PD: photodiode, z_p : particle position, OA: optical axis.*

1.1 Axial transmission signal characteristics

To describe relative transmission signals, i.e. the background normalized change in transmission, we generalize the notion of extinction and scattering cross-sections to fractional cross-sections. These depend on the collection angle and, similar to the complete cross-sections, on the particle placement in the beam.

$$\frac{\Delta P_d}{P_{inc}} = \frac{\sigma_{sca}(\theta_{\max}) - \sigma_{ext}(\theta_{\max})}{\sigma_{inc}(\theta_{\max})} \tag{1}$$

We provide exact analytical expressions for the signal (1) for arbitrary and possibly multilayererd Mie scatterers in terms of sums over multipoles. Thereby, the signal of large metallic particles, gradient refractive index particles and other microspheres can be accurately predicted. Absorption cross-sections may also be inferred from the signal in photothermal single particle microscopy [3].

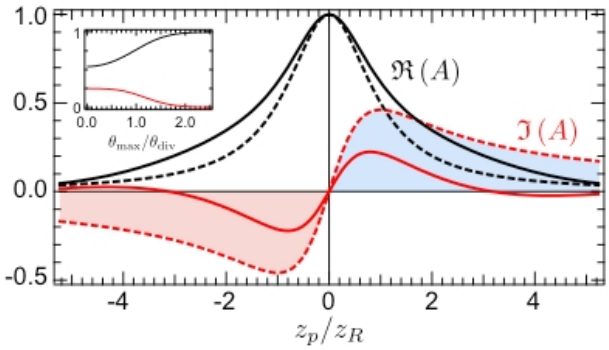


Figure 2 *The two generic contributions to a transmission signal, Eq. (2), normalized to a maximum of $\Re(A)=1$. Dashed lines: $\theta_{\max} \approx 0$, solid lines: $\theta_{\max} = \theta_{div}$. The inset shows their maximum amplitudes.*

Assuming scatterers of small size parameters $x = kR$, Rayleigh particles, one finds that for moderate collection angles the signal shape is determined by interference only, $\Delta P_d = -\sigma_{ext}$, and is made up of two generic contributions:

$$\sigma_{ext} = -k\left(\mathrm{Im}(\alpha)\mathrm{Re}(A) + \mathrm{Re}(\alpha)\mathrm{Im}(A)\right) \tag{2}$$

The first component of the signal exhibits a dispersive axial shape and is connected to the real part of the polarizability. It is the consequence of the changing phase relation of the interfering illuminating beam and the scattered field as the position of the particle within the focal region changes. Revealingly, this contribution decays

and finally disappears as the collection angle exceeds about twice the incident beam's angle of divergence $\theta_{\max} \geq 2\theta_{div}$. It is hereby seen as an energy redistribution phenomenon.

Conversely, the second contribution is related to the imaginary part of the polarizability and is dip-like in its axial dependence on the particle's coordinate. For a Gaussian beam the shape is Lorentzian and thus follows the intensity profile. However, at intermediate collection angles, the signal deviates and broadens up. Only at collection angles exceeding the incidents beam's spread of propagation directions, i.e. its angle of divergence, this part of the signal again follows the intensity profile of the beam and quantifies the occurring absorption.

If the collection angle exceeds twice the beam's angle of divergence only the absorption signal will remain, see the inset of Fig. 2. The energy redistribution will no longer provide a contrast since the energy that was removed (added) in the forward direction will then be collected in the periphery with opposite sign, leading to a cancellation. Perfect dielectric scatterers will then only provide a contrast due to scattering, see Eq. (1). They are therefore best visible by interference in the near forward direction, while the absorption is accurately quantified only if the collection angle is large. Intermediate or equal collection angles when compared to the illumination angle will introduce errors if the signal is directly translated into an absorption cross-section σ_{abs}.

Eq. (1) also provides the means to tell the particle position in the focal region for any metallic nanoparticle based on the transmission signal. Accurate absorbed powers and induced temperatures may then be found.

1.2 Transverse transmission signal characteristics

The quantitative analysis of transmission scans requires knowledge of the incident beam. If a Gaussian beam is assumed, this is tantamount to knowledge of the beam waist ω_0 or its Rayleigh-range $z_R = n_m \pi \omega_0^2 / \lambda$. We therefore provided an appropriate extension of the previous considerations to off-axis particle placements. For Rayleigh scatterers the signal is again composed of two generic contributions, each connected to the real and imaginary part of the particle's polarizability.

An expression analogous to Eq. (2) again describes the relative transmission signal. Fig. 3 shows their behaviour as a function of the particle placement x_p, z_p relative to the focus. Only for absorbing particles with a finite imaginary part of their polarizability and for large detection angles will the signal follow the intensity distribution of the incident beam. Especially for perfect dielectrics rich interference structures are obtained. An understanding of these allows an assessment of the incident beams field's structure in addition to the particle's optical properties.

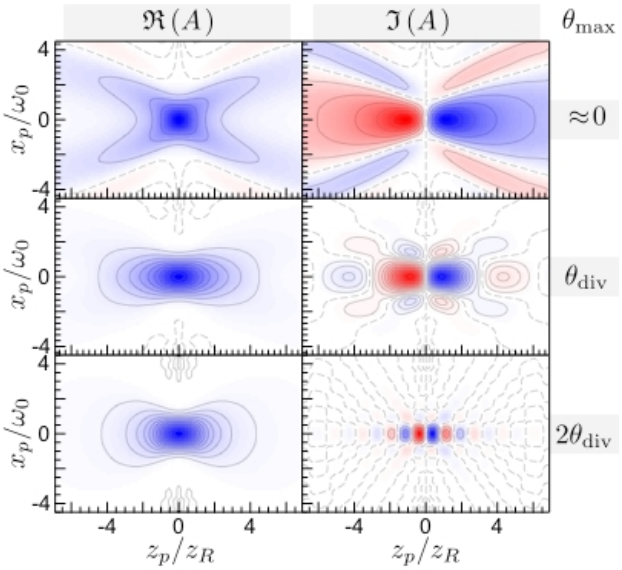


Figure 3 *The two generic transmission scan contributions for an arbitrary off-axis positioning of the particle.*

2 Conclusion

Generalizing total to fractional cross-sections in the generalized Lorenz-Mie framework, a convenient description of transmission signals is achieved. A thorough understanding of the discussed effects allows for signal optimization and tailored spatial signal detection functions for specific applications, such as scattering interference correlation spectroscopy (SICS [6]) and particle velocimetry in the spirit of twin-focus photothermal correlation spectroscopy [7].

3 References

[1] Taubenblatt M. A., Batchelder J. S., Measurement of the size and refractive-index of a small particle using the complex forward-scattered electromagnetic field, Appl. Optics 30(33):4972–4979 (1991)

[2] Lermé J. et al., Optical response of a single spherical particle in a tightly focused light beam: application to the spatial modulation spectroscopy technique, J. Opt. Soc. Am. A 25(2):493–514 (2008)

[3] Selmke M., Braun M., Cichos F., Photothermal Single Particle Microscopy: Detection of a Nanolens, ACS Nano 6(3):2741-2749 (2012)

[4] Hwang J., Moerner W. E., Interferometry of a single nanoparticle using the gouy phase of a focused laser beam, Opt. Commun. 280(2): 487–491 (2007)

[5] Rohrbach A., Stelzer E. H. K., Three-dimensional position detection of optically trapped dielectric particles, J. Appl. Phys. 91(8): 5474–5488 (2002)

[6] Wennmalm S., Widengren J., Interferometry and Fluorescence Detection for Simultaneous Analysis of Labeled and Unlabeled Nanoparticles in Solution, J. Am. Chem. Soc., 134(48):19516–19519 (2012)

[7] Selmke M., Schachoff R., Braun M., Cichos F., Twin-Focus Photothermal Correlation Spectroscopy, RSC Adv. 3:394-400 (2013)

Identification and Characterization of Cell-Derived Microparticles Using Light Scattering

Anastasiya I. KONOKHOVA[1,*], Darya N. CHERNOVA [1-2], Dmitry I. STROKOTOV [1], Maxim A. YURKIN [1,2], and Valeri P. MALTSEV [1,2]

[1] Laboratory of Cytometry and Biokinetics, Institute of Chemical Kinetics and Combustion SB RAS, Novosibirsk, 630090, Russia

[2] Novosibirsk State University, Novosibirsk, 630090, Russia

Corresponding author: konokhova_a@mail.ru

Abstract

We describe a method for identification and characterization of cell-derived microparticles in plasma, using the scanning flow cytometer, which measures light scattering patterns (LSPs) of individual particles. The identification of MPs in plasma is performed based on shape differences of spherical MPs and other non-spherical plasma particles. Using light-scattering information from LSPs and additionally measured side-scattering we solve the inverse-scattering problem for each measured particle and rigorously characterize it, determining size and refractive index including errors of these estimates. This method allows us to characterize individual MPs larger than 300 nm with median precisions (standard deviations) of 7 nm and 0.0018 for size and refractive index respectively.

1 Introduction

Cell-derived microparticles (MPs) are spherical phospholipid particles, which are present in peripheral blood and body fluids and constitute a heterogeneous population of particles highly variable in size, composition, concentration, cellular origin, and functional properties [1]. Being involved in a variety of physiological processes MPs are considered as potential diagnostic or prognostic biomarkers. That attaches importance to determination of MPs characteristics, which may contain significant clinical information. But detection and analysis of MPs is challenging due to their small sizes (typically defined in ranges between 100 nm and 1 μm) and low (with respect to the medium) refractive indices. It motivates development of new techniques and methods to identify MPs in biological fluids distinguishing them from other constituents of similar size and to characterize MPs both by their size and refractive index.

Scanning flow cytometry is a technique capable of measuring angle-resolved light-scattering patterns (LSPs) for individual particles [2,3]. The LSP contains valuable information, which can be used to deduce particle size, shape, and refractive index. Since a homogeneous sphere is an adequate optical model of MPs a complete characterization (determination of size and refractive index) is possible by solving the inverse light-scattering (ILS) problem using Mie theory for light-scattering simulation. Moreover, it provides unambiguous separation of MPs from other non-spherical plasma constituents on the basis of similarity of their LSPs to that of a sphere. Additional light-scattering data from side-scattering measured using a different wavelength can also be used to improve the accuracy of MPs characterization.

2 Methods

2.1 Light-scattering measurements

Within the Mueller-matrix formalism [4] for description of light scattering by a particle, the LSP and side-scattering intensity (SSC) measured by Scanning Flow Cytometer are expressed as:

$$\mathbf{I}_{\text{th}}^{\text{LSP}}(\theta) = k_1 \int_0^{2\pi} [S_{11}(\theta,\varphi) + S_{14}(\theta,\varphi)] d\varphi \,, \tag{1}$$

$$\mathbf{I}_{\text{th}}^{\text{LSP}}(\theta) = k_2 \int_{apert.} d\varphi d\theta \sin\theta [S_{11}(\theta,\varphi) - S_{12}(\theta,\varphi)\cos(2\varphi) - S_{13}(\theta,\varphi)\sin(2\varphi)] \tag{2}$$

where $S_{ij}(\theta,\varphi)$ are elements of the Mueller matrix, θ and φ are the polar and azimuthal scattering angles, k_1 and k_2 are the scaling coefficients, determined from calibration of the SFC. The LSP is measured at the wavelength of 405 nm in the polar angular range from 5° to 70° and the SSC is measured at the wavelength 488 nm and integrated over circular aperture that is 90±17.5° for both polar and azimuthal diametric angles respectively. SSC is also used to trigger the electronics of SFC and thus its sensitivity determines the detection limit of the instrument.

2.2 Inverse light-scattering problem solution, microparticle identification and characterization

Applying the model of homogeneous sphere to MPs we reduce the solution of the ILS problem to simultaneous fitting of experimental LSPs and SSC signals by theoretical ones. Thus the problem is transformed into the global minimization of the following sum of squares:

$$S(\boldsymbol{\beta}) = \sum_I \left[w(\theta_i)\right]^2 \left[I_{\text{exp}}^{\text{LSP}}(\theta_i) - \eta I_{\text{th}}^{\text{LSP}}(\theta_i, \boldsymbol{\beta})\right]^2 + \\ + \left[I_{\text{exp}}^{\text{SSC}} - I_{\text{exp}}^{\text{SSC}}(\boldsymbol{\beta})\right]^2 \quad (3)$$

where $\boldsymbol{\beta}$ is the vector of characteristics consisting of a diameter d and RI n of a MP, θ_i is the polar scattering angle, $\mathbf{I}_{\text{exp}}^{\text{LSP}}(\theta_i)$ and $\mathbf{I}_{\text{th}}^{\text{LSP}}(\theta_i, \boldsymbol{\beta})$ are the intensities of experimental and theoretical LSP at angle θ_i respectively, $\mathbf{I}_{\text{exp}}^{\text{SSC}}$ and $\mathbf{I}_{\text{th}}^{\text{SSC}}(\boldsymbol{\beta})$ are experimental and theoretical SSC signals respectively, η is the coefficient that compensates an effect of the non-central particle trajectory in the flow cell of the SFC. The theoretical LSP and SSC are calculated from Eqs. (1) and (2) using the Mie theory.

The global minimization is performed by DiRect algorithm [5], which provides an extensive search of global minima $S(\boldsymbol{\beta})$ over the parameter space confined by parameter bounds $d \in [0.1, 2]$ μm, $n \in [1.35, 1.7]$, which amply cover the range of MPs.

Using this solution we separate MPs from other plasma constituents, such as platelets and cellular debris, supposed to have non-spherical shape, by similarity of their LSPs structure to that of sphere, and perform residual correlation analysis to quantitatively describe these differences. In particular, number of intersections of experimental and best-fit theoretical LSPs is used, which has smaller values for non-spherical particles due to larger correlation between neighboring residuals [6]. Also based on the solution of the ILS problem we rrigorously characterize each measured particle, determining its size and refractive index including errors of these estimates.

3 Results

The developed method was applied to analyse MPs populations in three differently prepared samples of untreated, centrifuged and filtered trough 1.2 μm pore filter platelet plasma. Typical results of individual MPs characterization with determined characteristics and their uncertainties are shown in Figure 1.

Polystyrene microspheres of 400 nm and 1 μm were also measured and analyzed, showing a good agreement in their size and refractive index determination and thus confirming the method adequacy. The MPs and polystyrene microspheres distributions over size and refractive index are shown in Figure 2. The major part of detected MPs falls in the range of 400 – 800 nm for size and 1.46–1.50 for the refractive index, and the median precisions in determination of each parameter for single measured particle are 7 nm and 0.0018, respectively.

Details of the obtained results are described in [7].

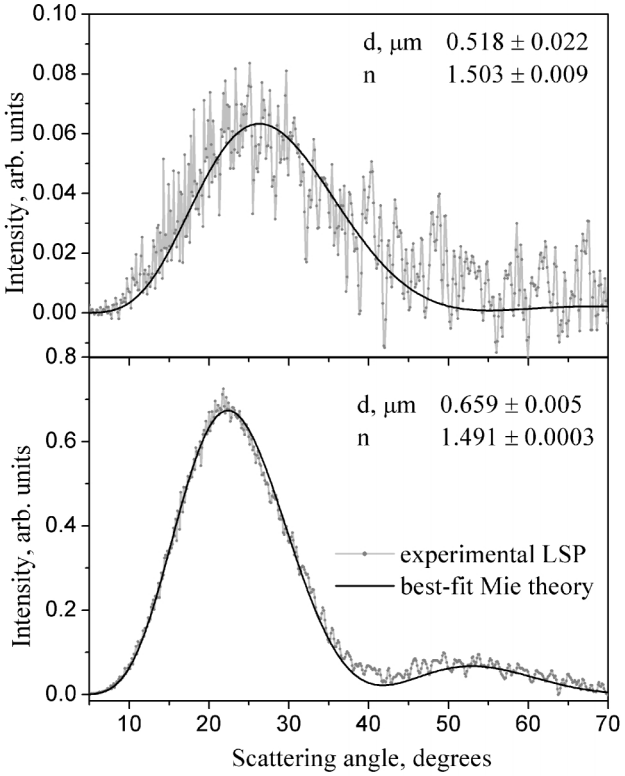


Figure 1 *Typical results of characterization of single MPs, depicting weighted experimental and best-fit Mie theory LSPs. Estimates of particles size d and refractive index n (mathematical expectation ± standard deviation) are also shown.*

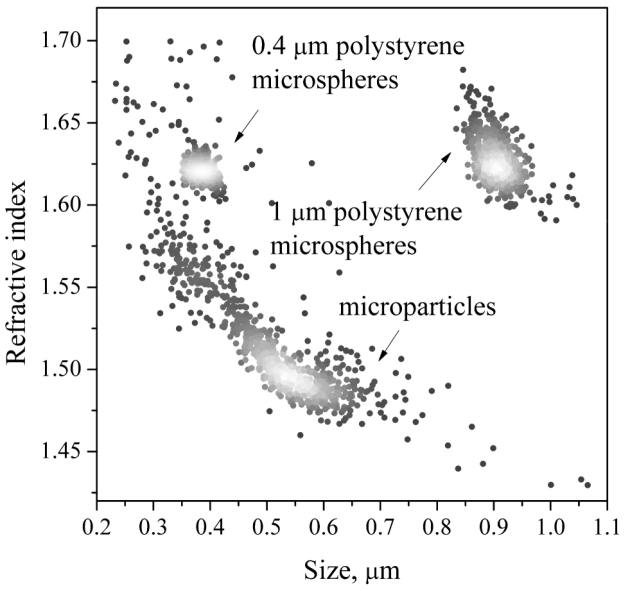


Figure 2 *Distributions over size and refractive index for MPs and polystyrene microspheres of 0.4 and 1 μm.*

4 Conclusion

Here we describe a method for identification and characterization of blood microparticles using angle-resolved light scattering measured with the SFC. The identification of spherical MPs among other measured non-spherical sample constituents, including platelets and cellular debris, is based on the structure of their LSPs, that could be described by Mie theory for MPs, and shows large disagreement with theory for other particles. Each MPs is characterized by size and refractive index obtained from the inverse light-scattering problem solution with uncertainties of these parameter estimations. The accuracy of particle parameter estimations is improved by using an additional to LSP scattering information from side-scattering measured on the other laser wavelength and in different angular range.

The only limitation of this approach is size detection limit - the current optical set-up of the SFC can reliably analyze MPs larger than 400 nm. But the detection limit could be further decreased to 300 nm using higher-power lasers and middle-angle light scattering instead of SSC.

5 References.

[1] Piccin, A., Murphy, W.G., Smith, O.P. Circulating microparticles: pathophysiology and clinical implications. Blood Reviews 21, 157–171 (2007)

[2] Maltsev, V.P. Scanning flow cytometry for individual particle analysis. Rev Sci Instrum 71, 243–255 (2000)

[3] Strokotov, D.I., Moskalensky, A.E., Nekrasov, V.M., Maltsev, V.P., 2011. Polarized light-scattering profile-advanced characterization of nonspherical particles with scanning flow cytometry. Cytometry A 79, 570–579 (2011)

[4] C.F. Bohren, and D.R. Huffman, *Absorption and scattering of light by small particles* (Wiley, New-York, 1983).

[5] Jones, D.R., Perttunen, C.D., Stuckman, B.E., 1993. Lipschitzian optimization without the Lipschitz constant. J Optim Theory Appl 79, 157–181 (1993)

[6] Konokhova, A.I., Yurkin, M.A., Moskalensky, A.E., Chernyshev, A.V., Tsvetovskaya, G.A., Chikova, E.D., Maltsev, V.P., 2012. Light-scattering flow cytometry for identification and characterization of blood microparticles. J Biomed Opt 17, 057006.

[7] Konokhova, A.I., Chernova, D.N., Strokotov, D.I., Yurkin, M.A., Chernyshev, A.V., Maltsev, V.P., 2014. Cell-derived microparticles in platelet-rich plasma: label-free identification and characterization with flow cytometry. Submitted to J Thromb Haemost.

Interferometric out-of-focus imaging simulator for irregular multi-emitters. Application to the characterization of irregular rough particles

Marc BRUNEL*, Sébastien COETMELLEC, Gérard GREHAN and Huanhuan SHEN

UMR CNRS 6614 CORIA, Avenue de l'Université, 76801 Saint-Etienne du Rouvray Cedex, France

Corresponding author: marc.brunel@coria.fr

Abstract

We present the development of an original simulator to predict interferometric out-of-focus patterns generated by particles that can be assimilated to a wide number of punctual Dirac emitters. This simulator allows to predict quantitative properties of the speckle-like patterns, in particular the dimension of the central peak of the 2D-autocorrelation of the pattern. This parameter can then be linked to the size and the shape of the particle projected on the CCD sensor, in cases where there is no exact theoretical formulation to calculate the scattered intensity. An experimental illustration is performed with interferometric out-of-focus images of rough NaCl salt crystals.

1 Elaboration of a simulator for complex scattering objects

Interferometric out-of-focus imaging is a robust technique that has important potentiality for the characterization of droplets or bubbles [1,2]. Assuming that a bubble or a droplet can be assimilated as an emitter composed of two punctual Dirac sources (the so-called "glare points" [3]), it is possible to describe any imaging configuration in terms of optical transfer matrices, in such a way that the characteristics of the interferometric patterns can be linked analytically to the different parameters of the droplets and of the imaging system [4]. The potentiality of this technique to study irregular scattering objects exists but much has to be done in this direction. The main difficulty is that we need first to be able to describe the scattering properties of irregular objects. Unfortunately, this problem has no analytical solution in the framework of the Lorenz-Mie theory and can not be resolved in most of the cases.

In the present study, we present the development of a simulator to predict the interferometric out-of-focus patterns produced by irregular objects. As the rigorous description of the scattering properties of many complex objects has no exact solution, we consider complex irregular objects that can be assimilated to an ensemble N_{gp} punctual Dirac emitters (which is an extension of the case of spherical droplets where only two glare points are necessary). Generalizing the relations developed in [4] for spherical droplets, it is then possible to predict the speckle-like patterns generated by such complex objects [5,6]. We have thus developed a wide library of complex objects (sticks, hexagons, spheres, ellipsoids, hexagonal plates…). In each case, the object is defined by a random location of N_{gp} glare points over the global form of these objects (N_{gp} to be defined). Figure 1 shows some examples of objects that we can define.

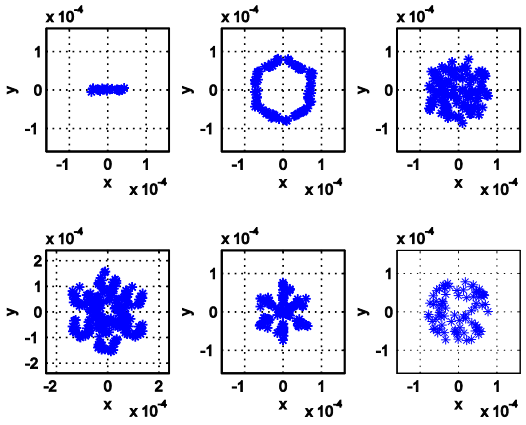


Figure 1 *Examples of objects assimilated to an ensemble of N_{gp} Dirac emitters randomly located over a global form.*

We are then able to simulate the interferometric out-of-focus image predicted for this object. In our simulator, the imaging system is described by optical transfer matrices. We can thus describe a wide variety of imaging systems. In a first part of this communication, we propose to present the elaboration of this simulator of interferometric out-of-focus imaging experiments for complex objects. In a second step, we will use this simulator to analyze the patterns observed experimentally using irregular rough NaCl salt crystals.

2 Example of interpretation of experimental results with NaCl salt crystals

We have performed interferometric out-of-focus imaging experiments. NaCl salt crystals are illuminated by a collimated frequency-doubled Nd:YAG laser emitting 10 mJ, 4 ns pulses at 532 nm. The CCD sensor is a Marlin camera. Out-of-focus imaging is realized with a spherical lens. This experimental set-up is presented in figure 2.

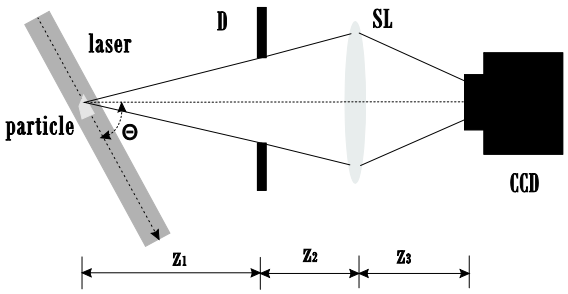


Figure 2 *Experimental set-up*

Figure 3(a) shows the typical out-of-focus image recorded. It is a speckle-like pattern. In order to estimate, the statistical dimension of the speck of light of this speckle-like pattern, figure 4 shows the x-cut and y-cut of the central peak of the 2D-autocorrelation of this speckle-like pattern (in dotted lines) [5,6]. We can observe that the speck of light is not circular but ellipsoidal, which traduces a global ellipticity of the salt crystal [5,6]. Figure 3 (b) shows the out-of-focus image predicted for an object composed of 80 Dirac emitters randomly located over an half-ellipsoid of dimensions 600 micrometers along x and 400 micrometers along y. These dimensions allow the best-fitting of the x-cut (a) and y-cut (b) of the central peak of the 2D-autocorrelation of the experimental pattern, as can be seen on figures 4(a) and 4(b) (in plain lines). Note that all parameters used in our simulator are those of the experimental set-up. If the dimension of the simulated object was smaller, the speck of light of the simulated speckle-like pattern would be larger than in the experimental case. Reciprocally, if the dimension of the simulated object was bigger, the speck of light would be smaller. In addition, this best-fitting does not depend significantly on the number of Dirac emitters to be considered (30, 60…) and on their exact positioning on the global ellipsoid (if the global form of the ellipsoid is entirely covered by the Dirac emitters) [5,6].

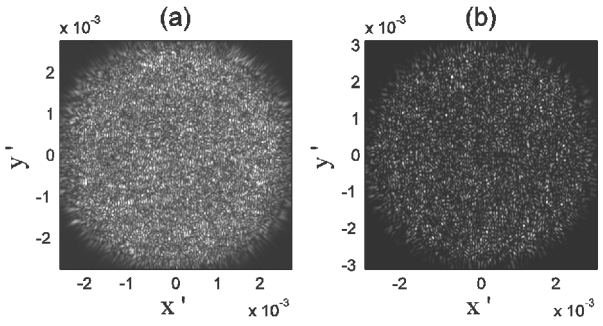


Figure 3 *Experimental out-of-focus image of a NaCl salt particle (a) and simulated out-of-focus image of an ensemble of 80 Dirac emitters randomly distributed on a half-ellipsoid of dimensions 600x400 micrometers (b).*

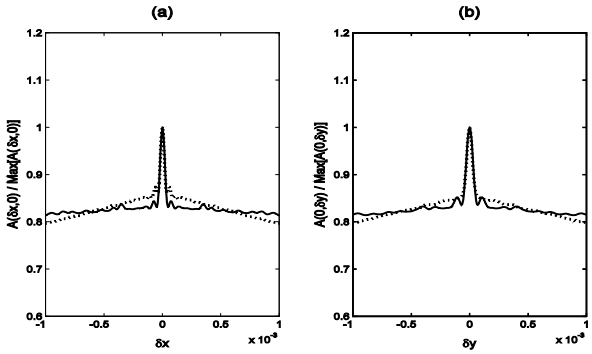


Figure 4 *x-cut (a) and y-cut (b) of the central peak of the 2D-autocorrelation of the experimental pattern presented in Fig1(a) (dotted). x-cut (a) and y-cut (b) of the central peak of the 2D-autocorrelation of the simulated pattern presented in Fig1(b) (plain) (b).*

In this communication, we will detail the elaboration of our simulator, discuss its domain of validity and its possible use for the interpretation of experimental images recorded with irregular rough particles, and thus its applicability for the characterization of irregular rough particles. As the imaging system is described in our simulator by optical transfer matrices, we will show that it is possible to establish analytical expressions that link characteristics of the speckle-like patterns to the parameters of the imaging system and to the dimensions of the rough particle under study.

3 References

[1] Glover A.R., Skippon S.M., and Boyle R.D., Interferometric laser imaging for droplet sizing: a method for droplet-size measurement in sparse spray systems, Applied Optics 34:8409-8421 (1995).

[2] Kawaguchi T., Akasaka Y., and Maeda M., Size measurements of droplets and bubbles by advanced interferometric laser imaging technique, Measurement Science and Technology 13:308-316 (2002).

[3] van de Hulst H.C., and Wang R.T., Glare points, Applied Optics 30:4755-4763 (1991).

[4] Shen H., Coëtmellec S., Gréhan G., Brunel M., ILIDS revisited: elaboration of transfer matrix models for the description of complete systems, Applied Optics 51:5357-5368 (2012).

[5] Brunel M., Shen H., Coëtmellec S., Gréhan G., Delobel T., Determination of the Size of Irregular Particles Using Interferometric Out-of-Focus Imaging, International Journal of Optics, 143904 (2014).

[6] Brunel M., Coëtmellec S., Gréhan G., Shen H., Interferometric out-of-focus imaging simulator for irregular rough particles, J. Europ. Opt. Soc.: Rap. Public. Vol. 9, 14008 (2014).

Simultaneous Mapping of Droplets Size and Concentration in Sprays using Structured Laser Illumination Planar Imaging

Yogeshwar Nath MISHRA*, Elias KRISTENSSON and Edouard BERROCAL

Division of Combustion Physics, Department of Physics, Lund University, Lund, SE-22100, Sweden

*Corresponding author: yogeshwar.mishra@forbrf.lth.se

Abstract

Structured Laser Illumination Planar Imaging (SLIPI) is used in combination with LIF/Mie ratio and two-side Mie imaging (dual-SLIPI) for a two-dimensional mapping of both the droplet Sauter Mean Diameter (SMD) and the extinction coefficient (μ_e). By means of combining the two techniques simultaneously, the local distribution of droplet concentration as well as the liquid volume fraction can also be deduced. This approach is for the first time tested for the characterization of a steady hollow-cone water spray.

1 Introduction

Atomising sprays are used for large numbers of applications, spanning in a variety of fields such as medicine, agriculture, combustion, and industrial processes. Each spray process must deliver the desired droplets size and concentration at a desired location. Therefore there is a clear need for rapid and accurate 2D or even 3D characterization of the spray region. Such characterization consists in extracting a measurement map of both the droplet size and concentration with high spatial resolution.

In the past, various light sheet based 2D imaging techniques have been developed for example LIF/Mie ratio technique proposed by Yeh *et* al.[1] can rapidly extract droplet relative SMD in 2D. This has been further developed as an Optical patternator by Sankar *et* al. [2] and other researchers to extract droplet SMD combined with laser extinction measurements [3]. However, these conventional techniques could not resolve the errors induced by multiple scattering when applied to image a spray plane consisting of dense clouds of micro-sized droplets. In addition, sources of errors such as light extinction and signal attenuation also bring discrepancies in measurements but these are easier to correct with bidirectional illumination and compensation scheme based on Beer-Lambert law [4].

SLIPI present a solution to suppress efficiently the intensity from multiple light scattering [5]. The Dual-SLIPI geometry ishowever, capable of also correcting for laser extinction and signal attenuation [6].

Here, we show simultaneous SLIPI-LIF/Mie and Dual-SLIPI measurements performed on a hollow-cone spray for a rapid 2D-mapping of droplets SMD and extinction coefficient in-between two illuminated planes.

2 Description of imaging techniques

2.1 SLIPI

Structured Laser Illumination Planar Imaging (SLIPI) is based on using a spatial modulation in conventional laser sheet imaging. A sinusoidal modulation is imprinted on the light sheet by using a Ronchi grating and a spatial filter [5]. This is used as a signature to recognise the singly scattered photons. Such photons leaving the illuminated plane will maintain this modulation while the multiply scattered photons will lose it. A planar image of spray of intensity $I(x,y)$ with a sinusoidal pattern imprinted on it is described as:

$$I(x,y) = I_C(x,y) + I_S(x,y)\cdot\sin(2\pi x\nu + \phi) \qquad (1)$$

where ϕ is the spatial phase and ν represents the modulation frequency. Here, $I_C(x,y)$ is the intensity corresponding to singly and multiply scattered photons and $I_S(x,y)$ represents the amplitude of the modulation from the singly scattered photons only. To be able to experimentally generate a SLIPI image, a minimum of three modulated sub-images with a spatial phase of $0°$, $120°$, and $240°$ is recorded.

A SLIPI image (consisting of singly scattered photons only) can be constructed by means of taking the root mean square of differences between each modulated images. Similarly, a conventional image (consisting of both the singly and multiply scattered photons) can be generated by averaging the three sub-images [5]. Details regarding SLIPI technique and its application in spray diagnostics can be found in [7].

2.2 LIF/Mie droplet sizing:

The SMD of droplet in sprays can be measured by taking the ratio of laser induced fluorescence signal (proportional to droplet volume) and Mie scattered signal (proportional to droplet surface area) [1].

However, there are three main conditions need to be addressed while performing LIF/Mie technique:

First, the spray droplets must be spherical. Second, all photons arriving at the CCD chip should be singly scattered. Third, the evaporation rate should be slow enough in order to minimize the fluorescence contribution from the gaseous phase.

2.3 Dual-SLIPI

Dual SLIPI is extended version of SLIPI where two Mie images are recorded simultaneously on two cameras positioned at ± 90 degrees to light sheet. By moving the laser sheet in-between two positions, a final set of four images is recorded. From these images an average extinction coefficient (μ_e) using Beer-Lambert relation can be calculated. A detailed description of the Dual-SLIPI technique theory and its application in sprays is reported in [6]

3 Experimental setup

The experimental setup is shown in Figure 1. The centre of the spray is crossed by the modulated light sheet (a) (λ=448 nm) created by the SLIPI setup shown in (b).

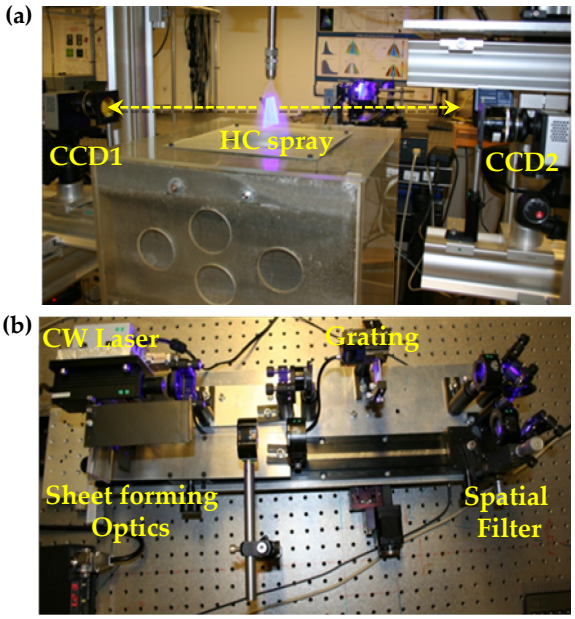


Figure 1 *(a) Experimental setup for LIF/Mie and Dual-SLIPI. (b) Optical arrangement of SLIPI setup (top-view)*

The injected water (20 bars pressure) is mixed with Pyranine dye from yellow highlighter's ink. When excited with 448 nm, it gives a broad-band fluorescence (LIF) signal peaking at 517 nm. Prior to reaching at detector, these two wavelengths are spectrally separated using adequate optical filters. Two EM-CCD cameras (of similar characteristics) used for image recording can be seen in figure 1(a). For SMD measurement (LIF/Mie ratio), one camera record LIF and other camera record Mie signal. Whereas for the extinction coefficient measurement (based on Dual-SLIPI), two cameras record Mie images simultaneously. Similar image recording routine is followed on a second location of the spray by changing the position of laser sheet. From the images acquired in-between two locations, relative SMD and μ_e is deduced.

4 Results

Relative SMD image shown in figure 2 is extracted from the LIF/Mie ratio while the extinction coefficient image shown in figure 3 is obtained from four Mie images.

4.1 Relative SMD of droplets

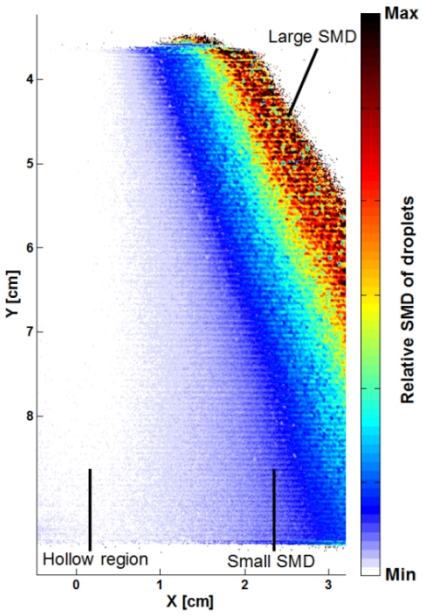


Figure 2 *Image of relative SMD of droplets. Note that only half portion of the HC spray is considered here. To obtain the absolute SMD, recently shown in [8], a calibration procedure using for rxample PDI, is needed.*

4.2 Extinction coefficient

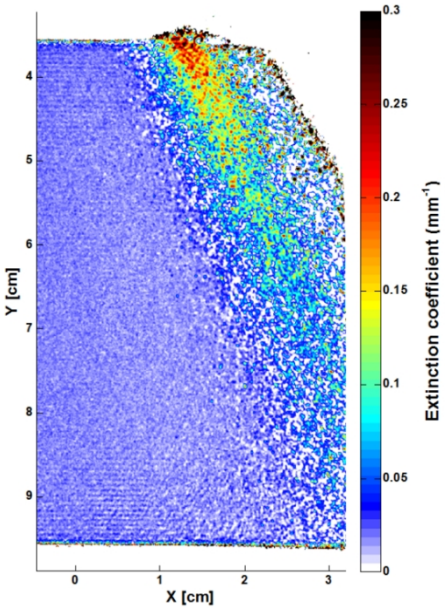


Figure 3 *Image of the extinction coefficient*

5 References

[1] C. N. Yeh, H. Kosaka, and T. Kamimoto, A fluorescence/scattering imaging technique for instantaneous 2-D measurements of particle size distribution in a transient spray, in Proceedings of the 3rd Congress on Optical Particle Sizing, pp. 355-361(1993).

[2] S. V. Sankar, K. E. Maher, and D. M. Robart, W.D. Bachalo, Rapid characterization of fuel atomizers using an optical patternator, J. Eng. Gas Turbines Power 121 (3):409-414 (1999).

[3] H. Koh, D. Kim, S. Shin, and Y. Yoon, Spray characterization in high pressure environment using optical line patternator, Meas. Sci. Technol. 17: 2159 (2006)

[4] H. Koh, J. Jeon, D. Kim, Y. Yoon, and J-Y Koo, "Analysis of signal attenuation for quantification of planar imaging technique," Meas. Sci. Technol. 14:1829-39 (2003).

[5] E. Berrocal, E. Kristensson, M. Richter, M. Linne, and M. Aldén, Application of structured illumination for multiple scattering suppression in planar laser imaging of dense sprays, Optics Express 16:17870 (2008).

[6] E. Kristensson, E. Berrocal and M. Aldn, Extinction coefficient imaging of turbid media using dual structured laser illumination planar imaging, Opt. Letters 36:1656-1658 (2011).

[7] E. Kristensson, Structured Laser Illumination Planar Imaging: Applications for spray diagnostics (Ph.D. Thesis, Lund University, 2012).

[8] Y. N. Mishra, E. Kristensson, and E. Berrocal, "Reliable LIF/Mie droplet sizing in sprays using structured laser illumination planar imaging," Opt. Express 22, 4480-4492 (2014)

Determination of droplet velocity and size immediately before impacting into a liquid pool

Norbert ROTH[1,*] and Bernhard WEIGAND[1]

[1] Institut für Thermodynamik der Luft- und Raumfahrt, Universität Stuttgart, Stuttgart, 70569, Germany

Corresponding author: norbert.roth@itlr.uni-stuttgart.de

Abstract

A method is presented, which allows determining the velocity and size of droplets impacting onto a liquid surface. The measurement is performed very close to the surface just before the impact. The principle of the measurement, which is based on a modified Doppler technique, is explained. The experimental setup is described and a few examples, showing the feasibility of the method, are presented.

1 Introduction

The impact of droplets onto liquid surfaces plays an important role in many natural and technical systems. The surface may belong to a liquid film or a pool. The knowledge of the impact parameters like droplet size and droplet velocity is very important for instance, when parameter studies or comparisons with numerical results are performed. It is preferable to obtain the parameters as close to the surface as possible, especially, when the droplets are small and may undergo an acceleration or deceleration just before the impact.

The principle of the method presented here for liquid surfaces has been orally presented for solid surfaces on the 9th International Conference on Laser-Light and Interactions with Particles in Rouen 2012 [1]. The solid surface was then a reflecting mirror. An example is shown in Figure. 1. The droplets were generated by a droplet on demand generator and impact perpendicularly on a mirror positioned at distance h. As the droplets undergo a deceleration on their path to the mirror their impact velocity decreases for larger distances.

However, as soon as a droplet has impacted onto a solid surface it sticks in many cases on the surface depending on the contact angle and impact parameters. The following droplets impact then on a liquid surface. Therefore the application of the technique for liquid surfaces is even more important [2].

In the following the rather simple method is explained again, the experimental setup is described, and first results of velocity measurements of droplet impacting perpendicularly onto a liquid surface are presented. The measurements are performed in a distance below 100 µm to the liquid surface as will be shown in the examples. For spherical droplets it is possible to determine the droplet size applying the phase Doppler technique [3].

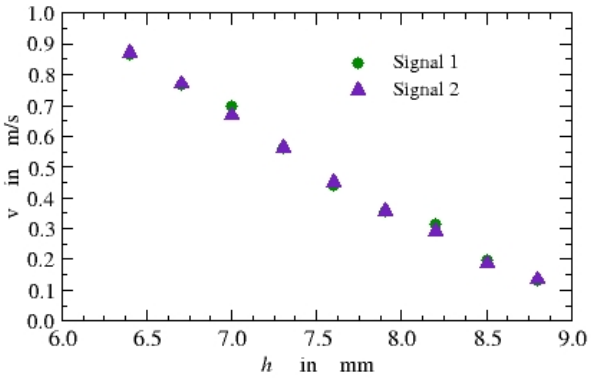


Figure 1 *Impact velocity as a function of the distance to the mirror surface. Shown results from two different sensors.*

2 Principle of the Measurement Technique

The method is based on the principle of a Laser Doppler Anemometer (LDA). A laser beam, in this case with a wavelength of $\lambda = 633$ nm, is directed under an angle α to a liquid surface. The laser beam is reflected by the surface and forms, as shown in the schematic view of Figure 2, half of a measurement volume, which is similar to the measurement volume of a normal LDA.

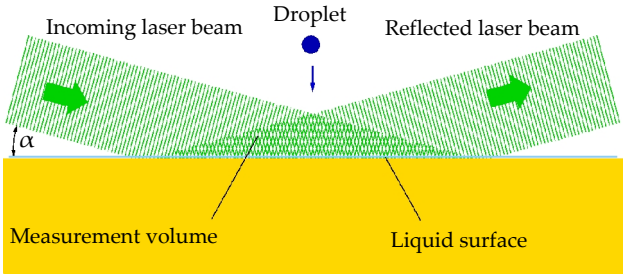


Figure 2 *Illustration of the principle of the measurement method. Shown is the intersection in the x,z-plane, defined by the incoming and reflected laser beam.*

An observer on a droplet arriving with velocity v observes from the incoming laser beam light with a frequency shifted a little bit to the red and from the reflected beam a frequency shifted a little bit to the blue. Therefore, similar to a normal LDA, a sensor detecting the light scattered by the droplet registers an alternating intensity with time at a frequency (beat frequency,

Doppler signal) proportional to the droplet velocity. In the case a second sensor is applied detecting the scattered light at a different angle comparable to a regular Phase Doppler Anemometer (PDA), the phase shift between the two Doppler signals gives information about the droplet size as with a normal PDA system.

3 Experimental Setup

This method is realized with an experimental setup shown in Figure. 3. The optical axis of lens A with a focal length of f = 300 mm is identical with the z-axis; its distance to the x,y-plane is exactly the focal length f. The liquid surface is in the y,z-plane. The illuminating laser beam runs in the x,z-plane, as shown in Figure. 2.

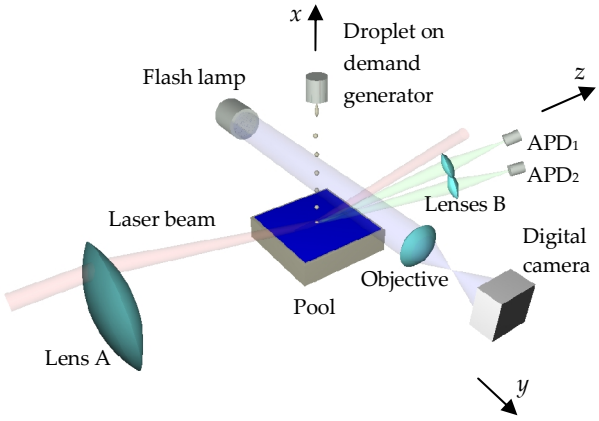


Figure 3 *Schematic view of the experimental setup.*

Before interacting with lens A the incoming laser beam is parallel to the optical axis and has a distance of a = 19.1 mm to it. Therefore the incoming laser beam interacts with the mirror surface at an angle α = 3.65° and a measurement volume is generated, as depicted schematically in Figure 2, in the origin of the coordinate system.

Using a droplet on demand generator, described in [4], single droplets are generated, which interact with the liquid surface. The path of the droplets is approximately along the x-axis. Therefore the droplets enter the measurement volume, when they approach the liquid surface. Part of the laser light scattered by the droplets is gathered by the lenses B_1 and B_2 and then focused on the avalanche photodiodes APD_1 and APD_2 respectively. The optical axis of these lenses and photodiodes is rotated by the scattering angle Θ around the x-axis and by the elevation angle Ψ_1 and Ψ_2 respectively around the y-axis. The orientation of this optical axis within the coordinate system is illustrated in Figure. 4. For more clearness only the light path of APD_1 is depicted.

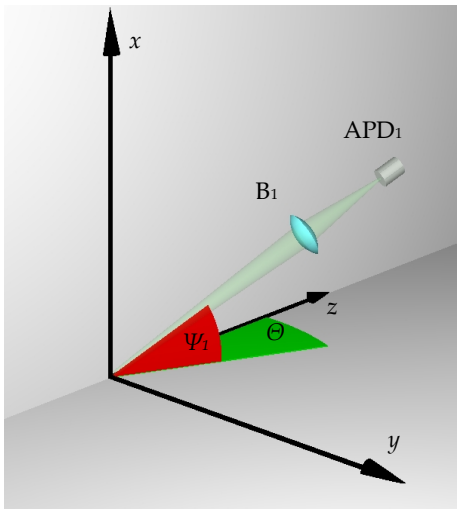


Figure 4 *Orientation of* APD_1 *and lens* B_1 *in the coordinate system.*

While the droplets interact with the surface shadowgraphs are taken by a digital camera. For the illumination a flash lamp is used, producing flashes short enough for sharp images. The shadowgraphs are used to observe the impact process and to measure the droplet size and correlate this size measurement to the phase shift between the two Doppler signals obtained by the photodiodes. In the following section a few results are presented.

4 Results

In Figure 5 the image of a hexadecane droplet immediately before impacting in a pool of hexadecane is shown. In addition a mirror image due to reflection at the liquid surface can be seen.

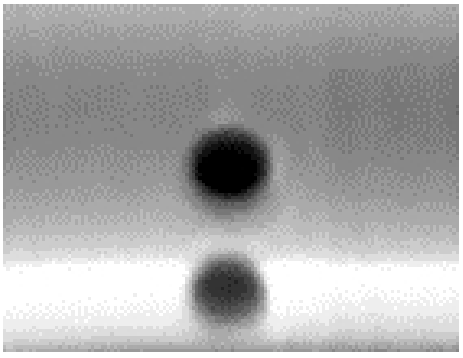


Figure 5 *Image of a hexadecane droplet just before impacting in a pool of hexadecane.*

The diameter of the droplet was D = 52 µm derived from Figure 5. This results in a phase shift of the Doppler signals detected by APD_1 and APD_2 of $\Delta\varphi$ = -296°. From these Doppler signal shown in Figure 6 an impact velocity of v = 0.65 m/s has been evaluated. The time t = 0 µs

indicates the time in the diagram of Figure 6, when the image of Figure 5 has been taken.

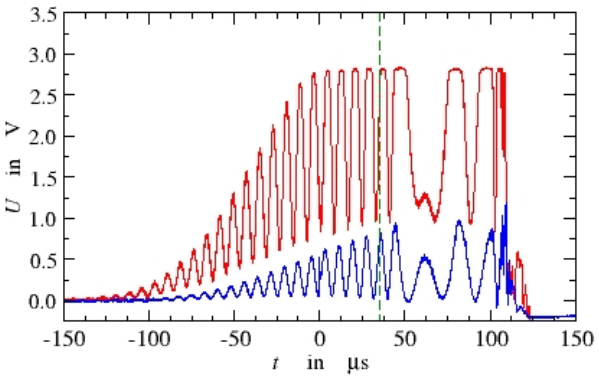


Figure 6 *Doppler signals from* APD_1 *in red (in this case the photodiode was saturated) and* APD_2 *in blue. At the time t = 0µs the image of Figure 5 has been taken. The vertical dotted line indicates the time the droplet hits the liquid surface.*

In the Doppler signals small disturbances can be seen on an enlarged view not shown here, which seem to indicate, when the droplet hits the pool surface. When hitting the pool surface the droplet seems not to immerge immediately into the pool but to remain a very short time at the surface while deforming it. This will be studied in future in detail using a high speed camera. Of special interest is for which range of impact parameters this phenomenon can be observed. The impact velocity must be rather low.

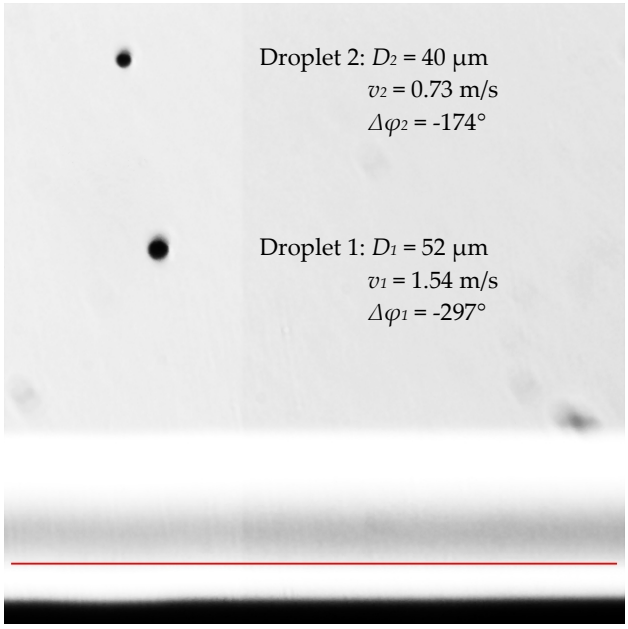


Figure 7 *Image of two droplets impacting on a liquid surface. The horizontal red line indicates the position where the droplets will contact the surface.*

In Figure 7 an image of two droplets of different size and velocity impacting in the pool is shown. The parameters of the droplets are given in the Figure. The velocities and the phase shifts of the Doppler signals are obtained from the Doppler signal much closer to the pool surface as the image has been taken. As the droplet size is different the phase shift is different as expected.

The examples presented above show the feasibility of this method for liquid surfaces. After some further tests a fast and rather simple method for the determination of velocity and size of droplets impacting on a liquid surface will be available. The main advantage is, that the measurement takes place immediately before the impact.

5 References

[1] Roth N., Weigand B., Technique to determine particle velocity and size immediately before impacting perpendicularly on a solid surface, *Int. Conf. on Lasers and Interactions with Particles* (*LIP-2012*), paper 4.4, 26- 30 March., Rouen, France, 2012.

[2] Moreira A.L.N., Moita A.S., Panão M.R., Advances and challenges in explaining fuel spray impingement: How much of single droplet impact research is useful?, Progress in Energy and Combustion Science 36:554-580 (2010).

[3] H.E. Albrecht, M. Borys, N. Damaschke, and C. Tropea, *Laser Doppler and Phase Doppler Measurement Techniques*, Experimental Fluid Mechanics (Springer Verlag, Berlin Heidelberg, 2003).

[4] A. Frohn, and N. Roth, *Dynamics of Droplets*, Experimental Fluid Mechanics (Springer Verlag, Berlin Heidelberg, 2000).

Particle Characterization With Digital Holography

Matthew BERG[1,*], Nava SUBEDI[1] and Nicholas FOWLER[2]

[1] Department of Physics & Astronomy, Mississippi State University, Mississippi State, MS, 39762, USA
[2] Department of Physics, Kansas State University, Manhattan, KS, 66502, USA

Corresponding author: matt.berg@msstate.edu

Abstract

This work describes the design and application of an apparatus to image aerosol particles using digital holography in a flow-through, contact-free manner. Particles in an aerosol stream are illuminated by a triggered, pulsed laser and the pattern produced by the interference of this light with that scattered by the particles is recorded by a digital camera. The recorded pattern constitutes a digital hologram from which an image of the particles is computationally reconstructed using a fast Fourier transform. This imaging is validated using a cluster of ragweed pollen particles. Examples involving mineral-dust aerosols demonstrate the technique's *in situ* imaging capability for complex-shaped particles over a size range of roughly 15-500 micrometers.

1 Introduction & Background

The *in situ* characterization of small particles is a persistent objective in applied physics and engineering contexts. Examples include the determination of atmospheric aerosol compositions for climate modeling and the detection of biological weapons agents for defense applications. Countless measurements and calculations of single and multiple-particle scattering-patterns can be found in the literature. The overall goal of such work is to infer information relating to the particles' physical form, such as size and shape, by analyzing the angular structure of these patterns [1]. Unfortunately, a fundamental limitation of this approach is the absence of an unambiguous quantitative relationship between a pattern and the corresponding particle properties, i.e., the so-called "inverse problem." Consequently, the inference of these properties from the patterns has proved to be very difficult in practice, except for the simplest of cases.

Ideally, one would prefer to image the particles directly, thus eliminating the complexity and ambiguity associated with interpretation of the scattering patterns. However, the typical particle size range of interest for many applications is roughly 0.1 to 10 micrometer [1,2]. Because of this, direct images are possible in part of this range only with high numerical-aperture (NA) optics and correspondingly small focal volumes. This typically requires collection and immobilization of particle samples, and thus, such imaging is not a practical technique for particle characterization in applications requiring high sample thru-put or images of the particles in their undisturbed form, i.e., *in situ* images.

Holography is an alternative technique that combines useful elements of both conventional imaging and scattering. Fundamentally, this is a two-step process: First, an object is illuminated with coherent light and the intensity pattern resulting from the interference of this light with that scattered by the particle is recorded. This pattern constitutes the hologram, from which an image of the object is reconstructed. Traditionally, holograms are recorded with photographic film due to the film's high resolution, which is required to capture the finer features of the interference pattern. The subsequent chemical development of the film is costly and time consuming, and this greatly limits the practical utility of the technique. For this reason, Charged Coupled Device (CCD) detectors are used to record the interference pattern digitally. The resulting digital hologram can then be computationally processed, rather than chemically, to reconstruct an image of the object.

2 Digital Holography

Recent work by the authors demonstrates the viability of a holographic technique to image aerosol particles *in situ* in a flowing sample-stream [3]. This is done by digitally recording a hologram of a particle using the arrangement shown in Fig. 1 below. An aerosol stream is delivered via a nozzle to a measurement volume where an optical trigger senses the presence of a particle. When sensed, a pulsed laser fires, illuminating the particle and forming a hologram on a Charged Coupled Device (CCD) sensor. Here, the triggered laser is a 70 ns pulsed Nd:YAG, frequency doubled to 532 nm. After passing through a linear polarizer (a), the beam is focused onto a 50 micron diameter pinhole (c) followed by an iris (d), which improves the beam's spatial coherence and the subsequent hologram. The beam is then re-focused several mm from the nozzle outlet. Thus, the particle is illuminated by (approximately) a diverging spherical wave emerging from the beam waist. Then the expanding beam interferes with the particle's forward-scattered light across the sensor to produce the hologram, I^{holo}.

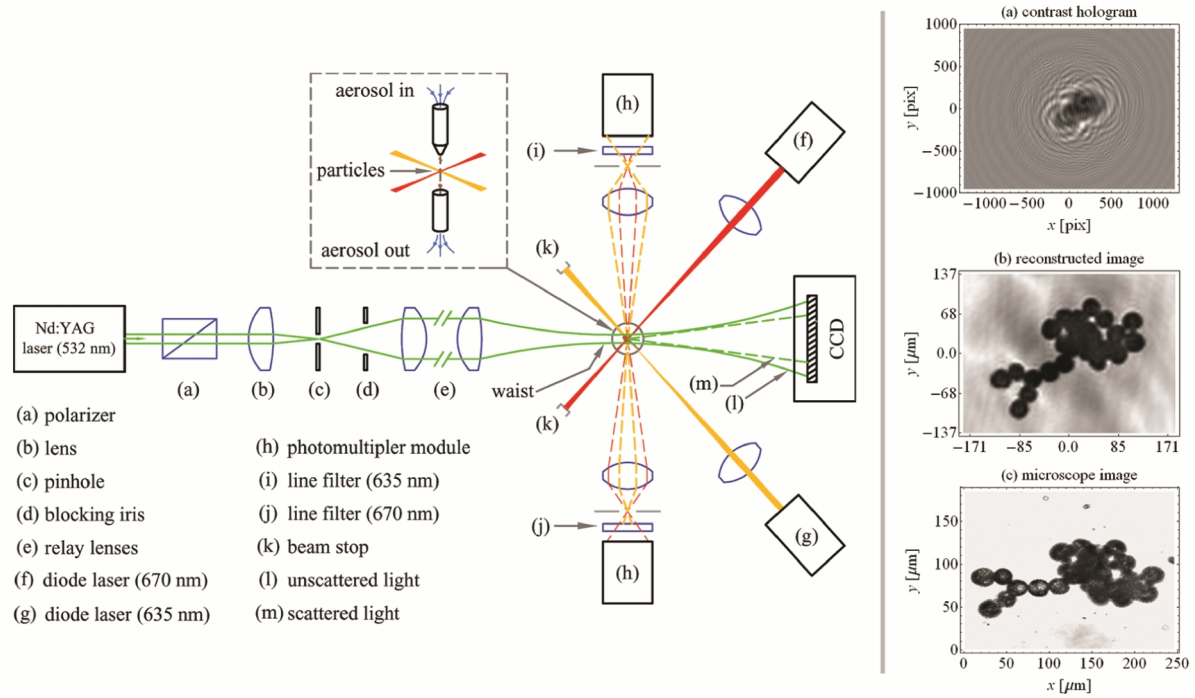


Figure 1 *Apparatus developed to capture digital holographic images of flowing aerosol particles in situ. The inset shows the aerosol nozzle, trigger beams, and eduction tube. Plot (a) shows the measured contrast hologram* I^{con} *for a ragweed pollen-cluster, which is processed via Eq. (1) to yield the image in (b). For validation, the same cluster is imaged with an optical microscope in (c).*

From I^{holo}, the particle-free background, or reference intensity I^{ref}, across the sensor is subtracted to yield a contrast hologram I^{con}. This step removes most imperfections in the illumination-beam profile and greatly improves the particle image. To obtain the image, the particle's forward-scattered wave amplitude, K, is computationally reconstructed, inclusive of its phase information, using the Fresnel-Kirchhoff (FK) diffraction integral:

$$K(\mathbf{r}) = \alpha \iint_S I^{\text{con}}(\xi,\eta) \exp\left\{\frac{ik}{2z}\left[(x-\xi)^2 + (y-\eta)^2\right]\right\} \mathrm{d}\xi \mathrm{d}\eta \qquad (1)$$

where $k = 2\pi/\lambda$, α is a constant, and S, is the two-dimensional sensor data-set [4]. Here, the coordinate origin is located at the nozzle outlet in Fig. 1, (x, y) is a point on the reconstruction plane and (ξ, η) is a point on the sensor S. A particle is illuminated along the $z-$axis and the particle-sensor separation is $z = L$. If Eq. (1) is evaluated at a distance of $z = 2L$, the particle's near-field wave is regenerated. Taking the absolute square $|K|^2$, then yields an unambiguous image of the particle analogous to that obtained from conventional light-microscopy [5].

Figure 1 also shows a demonstration of this imaging involving a cluster of ragweed pollen particles on a microscope slide at the intersection of the trigger beams. Other particle types were investigated, but were done in aerosol form, i.e., with no slide, to establish the flow-through, on-the-fly capability of the technique. Examples here include Tunisian and Saharan sand fragments and are shown in [3]. More recently, this technique has been successfully extended to utilize backscattered light [6].

3 Applicatons

The ability of Eq. (1) to reconstruct a particle's near-field wave amplitude creates the possibility to do more with the hologram than imaging alone. For example, consider the particle's extinction cross section C^{ext}. This quantity represents the combined effect of scattering and absorption resulting in a loss of energy flowing along the forward direction in a beam. More precisely, this redistribution of energy is a consequence of the *interference* between the incident and scattered waves. Recent work by the authors in [7] shows that C^{ext} can be directly related to this interference pattern around the forward direction. But, this pattern is *exactly* what is measured in the digital contrast hologram. Thus, the hologram need only be integrated to obtain an estimate for C^{ext}. In this presentation, we will describe how the cross section can be extracted from an particle's hologram simultaneous with an image of the particle. We will also discuss the possibility of extracting other scattering observables from digital holograms.

4 Acknowledgement

The authors are grateful for support from the US Army Research Office, Young Investigator Program.

5 References

[1] K.B. Aptowicz, R.G. Pinnick, S.C. Hill, Y.L. Pan, R.K. Chang, Optical scattering patterns from single urban aerosol particles at Adelphi, Maryland, USA; a classification relating to particle morphologies, J. Geophys. Res., 111:D12212 (2006).

[2] Y.-L. Pan, J. D. Eversole, P. H. Kaye, V. Foot, R. G. Pinnick, S. C. Hill, M. W, Mayo, J. R. Bottiger, A. Huston, V. Sivaprakasam, R. K. Chang, Bio-aerosol fluorescence; detecting and characterizing bio-aerosols via UV light-induced fluorescence spectroscopy, in A. Hoekstra, V. Maltsev, G. Videen (eds.), Optics of Biological Particles, NATO Science Series II: Mathematics, Physics, Chemistry, 238, 63-164, Springer, Dordrecht (2000)

[3] M. J. Berg, G. Videen, Digital holographic imaging of aerosol particles in flight, J. Quant. Spectrosc. Ratiat. Transfer 112:1776-83 (2011).

[4] T. Kreis, *Handbook of Holographic Interferometry; Optical and Digital Methods*, (Wiley, Germany, 2005).

[5] W. Xu, M. H. Jericho, I. A. Meinertzhagen, H. J. Kreuzer, Digital in-line holography of microspheres, Appl. Opt., 41:5367-75 (2002).

[6] N. R. Subedi, N. B. Fowler, M. J. Berg, Backscatter digital holography of microparticles, Opt. Ex., 21:12611-16 (2013).

[7] M. J. Berg, C. M. Sorensen, A. Chakrabarti, Extinction and the optical theorem. Part I. Single particles, J. Opt. Soc. Am. A, 25:1504-13 (2008).

Measurement Of Bubbles Inside A Droplet By Digital In-Line Holography

Darawan PEJCHANG[1,*], Sébastien COETMELLEC[1], Gérard GREHAN[1], Daniel ALANO[1], Denis LEBRUN[1] and Marc BRUNEL[1]

[1] UMR 6614/CORIA, CNRS/Université et INSA de Rouen, 76800 France

*Corresponding author: darawan.pejchang@coria.fr, coetmellec@coria.fr

Abstract

A model of an air bubbles hologram inside a water droplet is studied. Here, we assume that the spherical-shaped of the bubble is considered as an opaque annular (ring). We show that the opaque ring disk can produce a diffraction pattern like the diffraction pattern from a bubble. The simulations of diffraction pattern of a fully opaque disk and an opaque ring disk will be shown and will be compared with the diffraction pattern from the experiment.

1 Introduction

Digital in-line holography (DIH) is an attractive tool to localize small particles in 3-dimension and to realize a metrology. It records in the form of light wave front, the intensity and phase informations. The recorded hologram of particles can be refocused by computer's process to many 2D images in various planes and distances. Therefore, DIH has an ability to determine the size and the location of a particle. Based on Fresnel's integral and ABCD matrix, the holograms can be simulated for various systems such as an object in the air medium with lenses [1] or some inclusions in fluid flow system [2]. Here, DIH can adapt well with the opaque disk [3,4]. Generally, the spherical object is considered as an opaque disk. If the opaque spherical object is measured, there is no problem because the scattering light was created from the object's edge very close to an opaque disk [3-5]. But with a transparent object, the light is transmitted partly and this part will affect the diffraction pattern recorded by the CCD sensor. However, the authors in [6] have simulated with success the holograms of individual phase disks.

The challenge of this work is to accurately describe the hologram of a spherical air bubble that floats in the water droplet.

2 Description of Model

The schematic of system is shown in Figure.1. The air bubble is considered as a phase object but due to its spherical shape, the diffraction pattern is not similar with the case of phase disk. We have to consider the refractive indices ratio of the object and the droplet. When the ratio less than one (case of bubble, ratio n_b/n_d = 1/1.33), there is a part of the light reflected due to the total reflection. So one sphere bubble will act like an opaque ring disk with the opaque part and transparent part (see Figure.2). From this idea this work will show you a possible interpretation of the opaque ring disk which produces a theoretical diffraction pattern close to the experimental diffraction pattern of bubble.

3 Results

To confirm our theoretical model, in presentation in LIP 2014, we will show the experimental results compared to the numerical simulation of the fully opaque disk and opaque ring disk.

In a first step, the theory will be presented. The optical system composed of the droplet can be explained by ACBD matrix. On the object field (i.e., the bubble), we determine the width of opaque ring from the optical geometry. Then the intensity distribution in the CCD plane will be calculated based on Fresnel diffraction integral. The numerical simulations will be performed. In a second step, we will explain the experimental observation by DIH. The holograms which are recorded by CCD camera will be shown.

In final step, we will compare the results between numerical simulations and experimental. In the Figure.3a and 3b are the simulations of intensity distribution and profile graphs of the fully opaque disk and opaque ring disk respectively. Figure.3c shows the diffraction pattern from experiment that looks close similar to the opaque ring disk than the fully opaque disk.

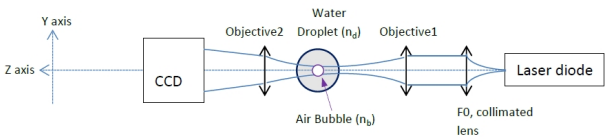


Figure 1 *Schematic set-up of DIH imaging the droplet with bubbles.*

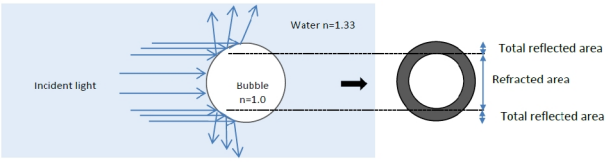


Figure 2 *Bubble acts like the opaque ring disk.*

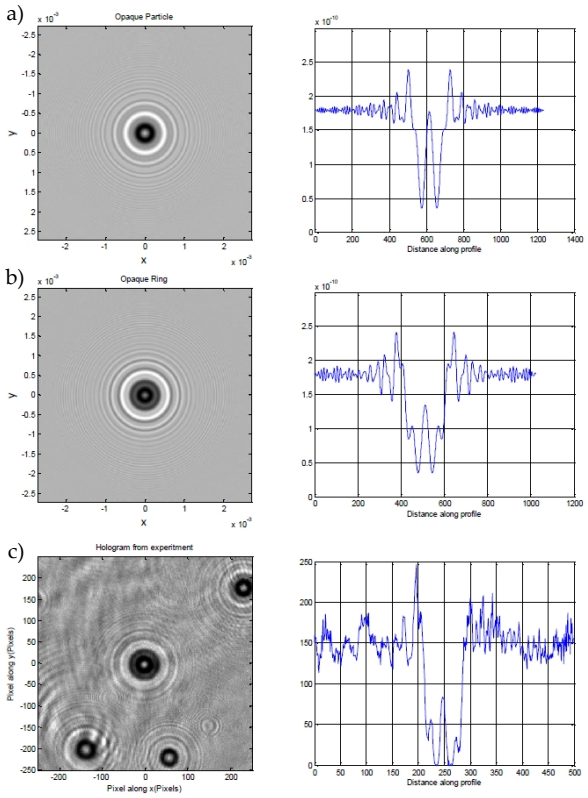


Figure 3 *a) Simulated intensity distribution of a fully opaque disk and its profile, b) simulated intensity distribution of an opaque ring disk and its profile, c) experimental diffraction pattern and its profile.*

4 Conclusion

We will give the details of mathematical model, simulation results and experimental results in the presentation in LIP 2014. These results prove that the opaque ring disk model can simulate for the bubble with a better accuracy than the fully opaque disk.

5 Acknowledgement

This work was partially supported by the French National Agency under grant ANR – 2011 – NANO – 008 "NANOMORPH" and Le Centre national de la recherche scientifique.

6 References

[1] Verrier N., Coëtmellec S., Brunel M. and Lebrun D., Digital in-line holography in thick optical systems: application to visualization in pipes, Applied Optics 47(22):4147–4157 (2008)

[2] Verrier N., Ramacha C., Brunel M., Lebrun D. and Coëtmellec S., Micropipe flow visualization using digital in-line holographic microscopy, Opt. Express 18(8):7807–7819 (2010)

[3] Nicolas F., Coëtmellec S., Brunel M., Allano D. and Lebrun D., Application of the fractional Fourier transformation to digital holography recorded by an elliptical, astigmatic Gaussian beam, J. Opt. Soc. Am. A 22(11):2569–2577 (2005)

[4] Verrier N., Coëtmellec S., Brunel M., Lebrun D. and Janssen A. J. E. M, Digital in-line holography with an elliptical, astigmatic Gaussian beam: wide-angle reconstruction, J. Opt. Soc. Am. A 25(6):1459–1466 (2008)

[5] Guildenbecher D. T., Gao J., Reu P. L. and Chen J., Digital holography simulations and experiments to quantify the accuracy of 3D particle location and 2D sizing using a proposed hybrid method, Applied Optics 52(16):3790–3801 (2013)

[6] Brunel M., Coëtmellec S., Lebrun D. and Ameur K. A., Digital phase contrast with the fractional Fourier transform, Applied Optics 48(3):579–583 (2009)

Measurement of spray characteristics by FII: Experimental validation on calibrated multijet

Sawitree SAENGKAEW*, Siegfried MEUNIER-GUTTIN-CLUZEL and Gerard GREHAN

UMR CNRS 6614/CORIA, Normandie Université, Saint Etienne du Rouvray, 73800, FRANCE

*Corresponding author: sawitrees@coria.fr

Abstract

The characterization of clouds of droplets under thermo-chemical evolution is still a challenge which have an importance for fundamental studies as well as for industrial applications, as for example in multicomponent fuels evaporation, CO_2 capture by sprays, injection in the vicinity of critical pressure, flash evaporation, ...

A large number of measurement techniques exist, based on different physical properties. Limiting us to the optical techniques, it is possible to sort these techniques as follows:

- Techniques measuring an individual particle, as for example Imaging, Phase Doppler Velocimetry, Particle Image Velocimetry, Holography and then repeat this measurement to obtain a statistical description of the discrete phase.
- Techniques measuring an average value on a section of a cloud, as diffractometry, turbidimetry, global rainbow refractometry...

These techniques have the following properties:

- The signal is a strong function of the particle size (d^2), strongly limiting the measurement range.
- Any information on the cloud structure is obtained as the distance between droplets,
- Each particle is measured one time.
- These techniques are limited to geometrical characterization of the particles, except the rainbow refractometry which via the refractive index value gives access to droplet temperature and/or composition.

1 Objectives

In our presentation at LIP 2014, we will present a new concept of measurement, called Fourier Interferometric Imaging (FII). This concept is based on the recording of the interference field created by the light scattered by the particles located in the control volume and its processing in the associated 2D FFT space. The approach can be seen as Holography without reference beam or as holography where the wave scattered by each particle is the reference for all other particles.

The concept can be shortly explained as follows:

- The particles located inside the control volume scatter light towards the detector surface where the light coming from the different particles interferes. On a pixel of the camera, the amplitude A_t is the sum of the amplitudes of the light issue from each particle: $A_t = \sum_{i=1}^{N} A_i$ where N is the number of particles in the control volume.
- The light intensity on the pixel is expressed by: $I_t = \sum_{i=1}^{N} A_i \bullet A_i^* + \sum_{i=1}^{N} \sum_{j=1|_{j\neq i}}^{N} A_i \bullet A_j^*$. FII exploits the second term of this expression. More precisely, the computation of the 2D FFT of I_t permits to isolate the $A_i A_j^*$ terms. The main advantages are:
  - Each particle is measured *N-1* times
  - To each couple of particles corresponds a trace. The trace intensity is proportional to $\sqrt{I_1 I_2}$, where I_1 and I_2 are the scattered intensity by each particles in the couple.
  - The distance between a trace center and the image center is a direct measurement of the distance between the two particles.
  - From three interacting traces, the scattering function of each particle can be extracted, and then accurate processing strategies can be applied to extract key information as particle size and refractive index (which gives the temperature or the composition of the droplet).

The series of images in Figure 1 exemplifies a typical FII measurement carried out on a line of mono dispersed droplets of N-heptane, recorded at the rainbow angle. The line of mono-dispersed N-Heptane droplets is created by a FMP drop generator. Figure 1-a is the interference field recorded by a CCD camera located around the rainbow angle. Figure 1-b is the 2D FFT of the Fig. 1-a. Figure 1-c is the inverse 2D FFT of the central trace of fig 1-b (the red rectangle) while Fig. 1-d is the inverse 2D FFT of the first lateral trace of fig 1-b (the blue rectangle).

In our presentation at LIP 2014, the validity of this approach will be proved numerically and experimentally on a spray of droplets created by a multi-lines mono-disperse droplets generator. Figure 2 is a view of such a multi-lines of mono-dispersed droplets .

2 REFERENCES:

[1] P. Briard, S. Saengkaew, X. C. Wu, S. Meunier-Guttin-Cluzel, L. H. Chen, K. Cen and G. Gréhan, Measurements of 3D relative locations of particles by Fourier Interferometry Imaging (FII), Opt. Express 19, 12700-12718 (2011)

[2] P. Briard, S. Saengkaew, X. C. Wu, S. Meunier-Guttin-Cluzel, L. H. Chen, K. Cen and G. Gréhan, Droplet characteristic measurement in Fourier interferometry imaging and behavior at the rainbow angle, Appl. Opt. 52, A346-A355 (2013)

[3] X. C. Wu, S. Meunier-Guttin-Cluzel, Y. C. Wu, S. Saengkaew, D. Lebrun, M. Brunel, L. H. Chen, S. Coetmellec, K. F. Cen and G. Gréhan, Holography and micro-holography of particle fields: a numerical standard. Optics Communications, 285, 3013-3020 (2012).

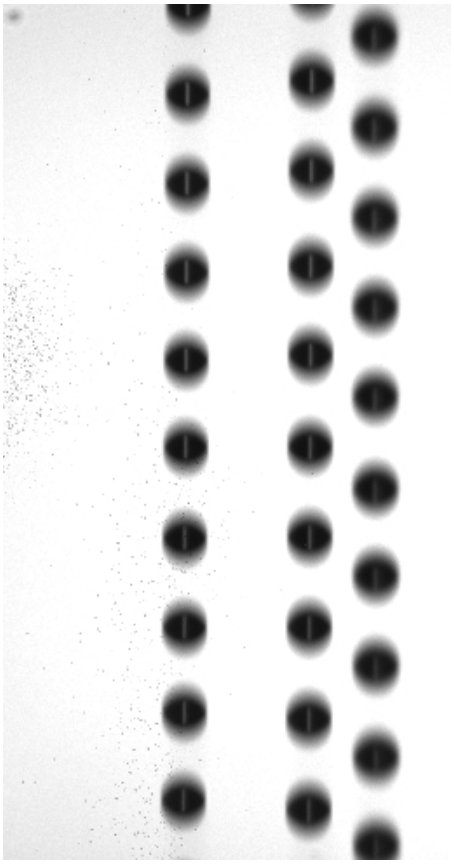
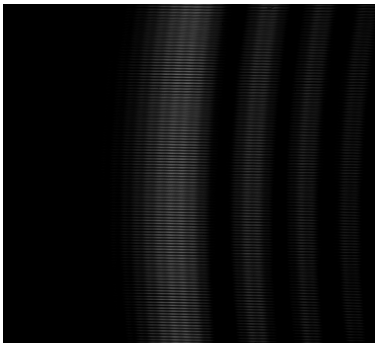
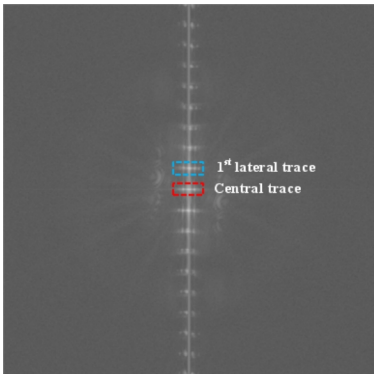


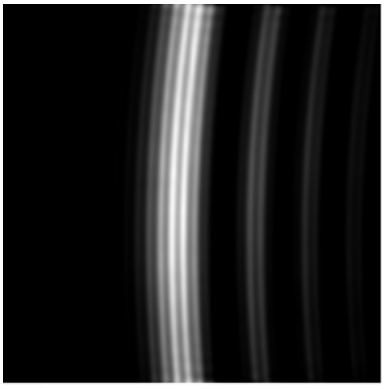
Figure 2 : *Three lines of mono-dispersed droplets created by one orifice.*



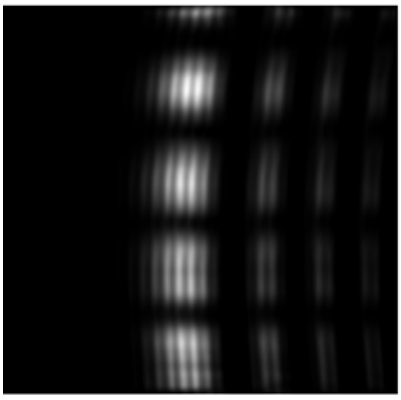
a



b



c



d

Figure 1: *A typical FII measurement sequence on a line of mono-dispersed droplets. a) the recorded interference field, b) the associated 2D FFT, d) the scattering field reconstructed from the central trace, e) the scattered field reconstructed from the first lateral trace.*

Transient evolution of refractive index gradients inside single isolated droplets with rainbow refractometry

Christopher ROSEBROCK[1], Thomas WRIEDT[2] and Lutz MÄDLER[1,2,*]

[1] Dept. of Production Engineering, University of Bremen, Bremen, 28359, Germany
[2] Foundation Institute of Material Science (IWT), University of Bremen, Bremen, 28359, Germany
Corresponding author: lmaedler@iwt.uni-bremen.de

Abstract

Rainbow refractometry has been applied to combusting and cooling droplets, showing an unexpected shift of the rainbow structure as combustion and cooling is initiated. This unexpected shift correspond to temperature gradients within the liquid droplets, which can be determined assuming diffusion limited heat transfer and applying the Lorenz-Mie theory for stratified spheres.

1 Introduction

Rainbow refractometry (RRF) is a versatile nonintrusive laser-based diagnostic technique for determining refractive indices and sizes for both, single liquid droplets [1,2] and in entire sprays [3,4].

RRF uses the shift of the rainbow structure in the elastic light scattering pattern of spherical droplets due to refractive indices changes with temperature in the liquid droplet (considering only pure liquids). In a first approximation the rainbow structure shifts towards lower scattering angles with decreasing refractive index of the liquid droplet. The refractive index of pure liquids decrease with increasing temperature. Therefore, by knowing the functional relation between temperature and refractive index the latter can be determined by detecting the positional change of the rainbow structure.

However, there are certain limitations of the RRF due to the change of the rainbow structure with the size for droplet diameters below $1000\mu m$ and with refractive index profiles within the liquid droplet. While the former can be commonly avoided, using an additional droplet size measurement technique, the uncertainties accompanied with refractive index profiles remain challenging. Especially during combustion, where high temperatures and fast vaporization rates occur, temperature differences between the surface and the interior of droplets can sustain throughout the droplet lifetime [5].

In order to take into account the refractive index profiles within the liquid droplet, a stratified sphere model for the Lorenz-Mie theory [6], geometrical optics [7], generalized Airy theory [8] or the complex angular momentum theory in combination with the FSSM [9] have been applied.

However, there is still a lack of experimental evidence of refractive index profiles within droplets. The aim of the present study is the time-resolved detection and determination of refractive index profiles within burning or cooling single isolated droplets.

2 Experimental setup and theoretical models

For observation of refractive index profiles within liquid droplets, the experimental setup schematically shown in Figure 1 is used. It consists of a droplet-on-demand generator (piezodropper [10]) that produces single isolated droplets operated with a mean separation distance of $s/d_0 \approx 1800$ between the droplets, where d_0 is the initial droplet diameter. The droplets are ejected either upwards or downwards through a laser sheet to follow continuously the light scattering of the droplets. The upward ejected droplets are ignited by means of a synchronized spark discharge, following the internal temperature profile (refractive index) as combustion proceeds. To promote a spherical flame shape and assuring radial heat transfer to the droplet surface, coflowing oxygen surrounds the droplets. In contrast, the downward ejected droplets are passing a heating coil that preheats the droplets close to the boiling point. After passing the heating coil the droplets cool down in the colder atmosphere, enabling the detection of temperature profiles during the cooling process.

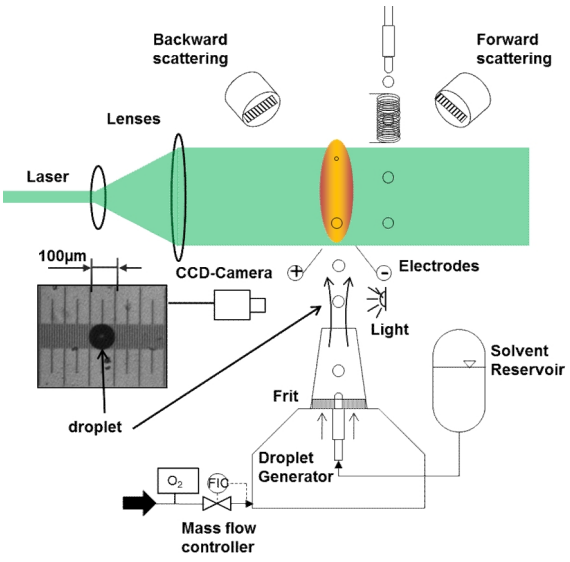


Figure 1 *Experimental setup of radial refractive index measurements.*

In order to evaluate the shift of the rainbow structure in backward scattering region due to the temperature profiles within the liquid droplets, the droplet size is simultaneously measured by means of interference fringes occurring in the forward scattering region due to refraction and reflection. With the known droplet size and the assumption of diffusion limited heat transfer within the droplet, i.e. an approximately parabolic temperature profile, the transient evolution of the refractive index gradients can be evaluated by applying the LMT for stratified spheres [10].

3 Results and discussion

Figure 2 shows the droplet diameter and the first two positions of the rainbow maxima for a single dodecane droplet during cooling at room temperature preheated beforehand with a heating coil (Figure 1). The position of the rainbow maxima are determined after applying a low pass filter to the rainbow pattern for removing both the higher frequency of the interference of the second order refraction and the reflection (ripple structure) and the high frequency noise.

Figure 2 shows that the droplet diameter decreases slightly due to evaporation of the preheated droplet after leaving the heating coil. However, the positions of the rainbow maxima shift towards lower positions, passing through minima and increase again. Since the refractive index of dodecane increases linearly with decreasing temperature, one would expect solely an increasing rainbow positions throughout the cooling, if the droplet has a uniform temperature at every instance, i.e. ideal mixed. Contradicting the initial decrease would suggest an increasing droplet temperature, which has no physical meaning. Therefore, the droplet temperature cannot be uniform throughout the droplet interior but possess a temperature and refractive index profile intially.

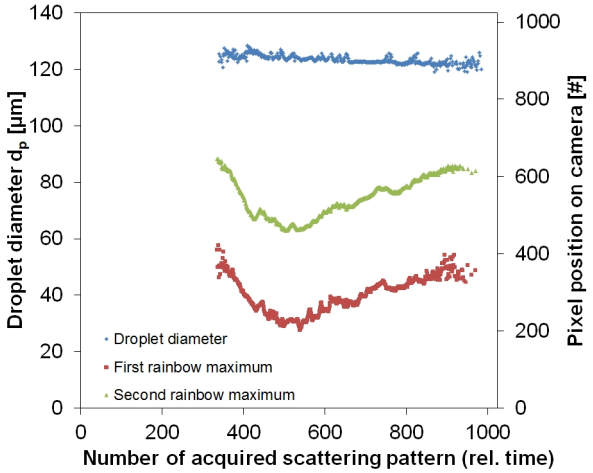


Figure 2 Droplet diameter and pixel position of the first two rainbow maxima for a single isolated dodecane droplet cooling at room temperature.

Comparable conclusion can be drawn for burning droplets, representing the reverse case of the aforementioned cooling dodecane droplet.

Figure 3 shows the droplet diameter and the first two rainbow maxima for a single dodecane droplet burning in a coflowing oxygen stream. The positions of the rainbow maxima have been determined similarly to the previous case. Note that the combustion is not completed within the laser sheet. However, the ignition and heating of the droplet is clearly visible. Figure 3 shows that the droplet diameter decreases quadratically according to the D^2-Law for droplet combustion after the ignition, which is indicated by the scatter of the data points around the 180th acquired scattering pattern. The scatter is due to the ignition spark that induces surface wave onto the droplet, distorting the scattering pattern for a brief period.

In accordance with the previous case, both rainbow maxima possess again a turning point, which are now maxima. Similarly to the cooling dodecane droplet, one would expect solely a decreasing shift of the rainbow positions throughout the combustion, since the refractive index decreases with increasing temperature. However, the initial increase of the rainbow positions suggests again a non-physical behaviour, i.e. a decreasing droplet temperature while heat is transferred from the combustion to the droplet. Thus, even for combustion where high temperatures and a fast heat transfer occur, the temperature within the droplet interior is initially nonuniform.

By using either of the applied theories [6,7,8,9], it was shown that assuming solely diffusional transport within the droplet, these initially non-physical shifts of the rainbow structure corresponds to refractive index gradients within the droplet. That means, by following the position of the rainbow structure and assuming diffusion limited transfer processes, gradients within the droplet can be determined with rainbow refractometry.

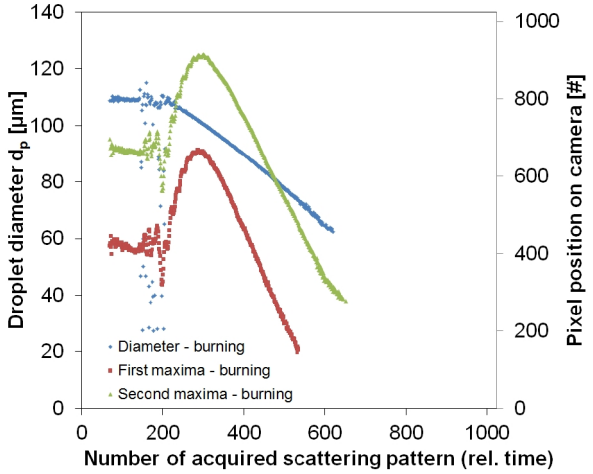


Figure 3 Droplet diameter and pixel position of the first two rainbow maxima for a single isolated dodecane droplet burning in a coflowing oxygen stream.

Since diffusion transfer processes are similar to each other, the non-dimensionalized gradients should be the same for all. This can be used as a verification for both proving diffusion processes as well as determine temperature and concentration gradients within liquid droplets. The turning points result from diffusional heat transport within the droplet that can be approximated by parabolic refractive index profiles.

4 Acknowledgement

The authors would like to thank the Deutsche Forschungsgemeinschaft (DFG) for funding this project under grants of MA 3333/4-1.

5 References

[1] Roth N., Anders K. , Frohn A., Refractive-index measurements for the correction of particle sizing methods, Applied Optics 30(33):4960-65 (1991)

[2] van Beeck J.P.A.J., Riethmuller M.L., Nonintrusive measurements of temperature and size of single falling raindrops, Applied Optics 34(10):1633-39 (1995)

[3] Sankar S.V., Buermann D.H., Bachalo W.D., Application of rainbow thermometry to the study of fuel droplet heat-up and evaporation characteristics, Journal of Engineering for Gas Turbines and Power 119(3):573-84 (1997)

[4] van Beeck J.P.A.J., Giannoulis D., Riethmuller M.L., Global rainbow thermometry for droplet-temperature measurement, Optics Letters 24(23):1696-98 (1999)

[5] Law C.K., Sirignano W.A., Unsteady droplet combustion with droplet heating – II: Conduction limit, Combustion and Flame 28:175-86 (1977)

[6] Kai L., Massoli P., Scattering of electromagnetic-plane waves by radially inhomogeneous spheres: a finely stratified sphere model, Applied Optics 33(3):501-11 (1994)

[7] Anders K., Roth N., Frohn A., Influence of refractive index gradients within droplets on rainbow position and implications for rainbow refractometry, Particle & Particle Systems Characterization 13(2):125-29 (1996)

[8] Vetrano M.R., van Beeck J.P.A.J., Riehtmuller M.L., Generalization of the rainbow airy theory to nonuniform spheres, Optics Letters 30(6):658-60 (2005)

[9] Saengkaew S., Charinpanitkul T., Vanisri H., Tanthapanichakoon W., Biscos Y., Garcia N., Lavergne G., Mees L., Gouesbet G., Grehan G., Rainbow refracometry on particles with radial refractive index gradients, Experiments in Fluids 43(4):595-601 (2007)

[10] Ulmke H., Wriedt T., Bauckhage K., Piezoelectric droplet generator for the calibration of particle-sizing instruments, Chemical Engineering & Technology 24(3):265-68 (2001)

[11] Wu Z.S., Guo L.X., Ren K.F., Gouesbet G., Gréhan G., Improved algorithm for electromagnetic scattering of plane waves and shaped beams by multilayered spheres, Applied Optics 36(21):5188-98 (1997)

MEASUREMENT OF LASER RAINBOW OF ELLIPTICAL LIQUID JET

Ruliang ZHONG, Xiang'e HAN* and He LIU

School of Physics and Optoelectronic Engineering, Xidian University, Xi'an, 710071, China

*Corresponding author: xehan@mail.xidian.edu.cn

Abstract

Light scattering by nonspherical particles has been issues of interest for reseachers in many areas. Elliptical cylinder, as the most simple approximation model, is the preferred object of study. Light scattering of elliptical cylinder has analytical solution based on rigorous boundary conditions, but it is only used to analysis of elliptical cylinder with small dimension and small aspect ratio. Recently, geometrical optics and Vectorial Complex Ray Model have received great attention and developed quickly, they compensate the limitation of analytical methods. In this article, we mainly carry out the measurement of light scattering of elliptical liquid jet. When the incident light is perpendicular to the liquid jet axis, the distribution of the first-order rainbow of liquid jet is measured by laser rainbow measuring system of liquid jet. We select the liquid jet with major axis of 500-1000 μm and aspect ratio of 1-1.3 at different incident light, including parallel and oblique to minor and major axes of the ellipse. Finally, we compare the measurement results with the numerical results calculated by geometrical optics and Vectorial Complex Ray Model.

1 Introduction

In experimental studies, due to the difficulty of making spheroidal particles of various spectroscopic aspect ratio, few experimental studies on elliptical droplets or elliptical jet are conducted[1]. In this paper, a metal tube with squashed spout is used to generate desired elliptical liquid jet [2]. The first-order rainbow of liquid jet is measured with laser rainbow measuring system of liquid jet(LRMSLJ) [3]. Figure.1 illustrates the schema of ray when it interacts with an elliptical cylinder[4], where a and b are respectively the axes of the ellipse in x and y directions. the liquid jet is illuminated by laser in the direction perpendicular to its axis, and it is given in the schema that how laser emergents after reflecting on the inner surface of the elliptical cylinder once. The emergent ray makes an angle θ with the incident ray, which is the scattering angle, and the incident wave propagating direction makes an angle α with the x-axis. When α=0°, 90°, 180° or 360°, it is called normal incidence, otherwise called oblique incidence.

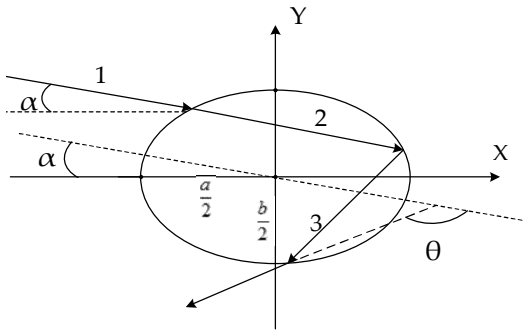


Figure.1 *schema of ray interaction with elliptical cylinder*

2 Laser rainbow measuring system of liquid jet

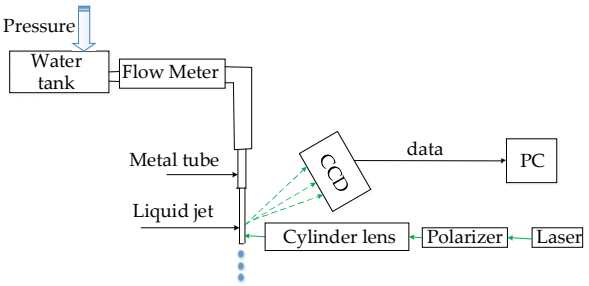


Figure. 2 *Laser rainbow measuring system of liquid jet*

Figure. 2 shows a functional block diagram of LRMSLJ. We give a pressure to distilled water of the tank, it will form elliptical cylinder after passing elliptic orifice of the metal tube. Laser (20mW, 532nm) goes through the polarizer and cylindrical lens, it comes up light scattering with the axis of elliptical cylinder vertically. Using CCD to receive reflected and scattered light, and transfer data to the computer. Finally, finishing data processing with PC.

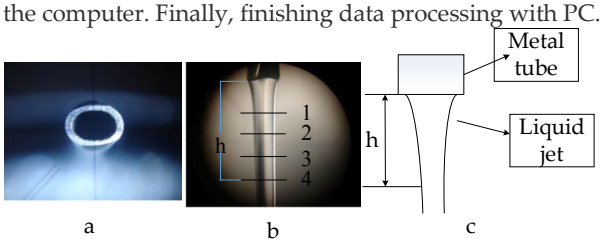


Figure. 3 *Sketch map for elliptical cylinder.*

Figure. 3 (a) shows a sectional view of the metallic orifice, Figure. 3 (b) shows the liquid jet observed by measuring microscope, Figure. 3 (c) shows a sketch map of the liquid jet, h is the height from orifice to observation point. With h increased under surface tension, the shape of section changes from ellipse to circle. Its physical dimension also changes with h increased. Using measuring microscope, we measure major axis a, minor

axis b and aspect ratio a/b of the liquid jet with different h. Measuring results are shown in Table 1.

Location	h (mm)	a (μm)	b (μm)	a/b
1	5	990	791	1.251
2	8	900	751	1.198
3	12	806	728	1.107
4	15	705	705	1.000

Table 1 *Measuring results with different* h

3 Experiment results and analysis

This paper mainly measures the first-order rainbow of elliptical cylinder. We give measurement results in two cases, while room temperature T=25℃, laser wavelength λ=532nm, liquid flow rate v=40ml/min, the refractive index of water m=1.3348.

(1) Along major axis by normal incidence (α=0°), different aspect ratios corresponding angular distribution of the rainbow.

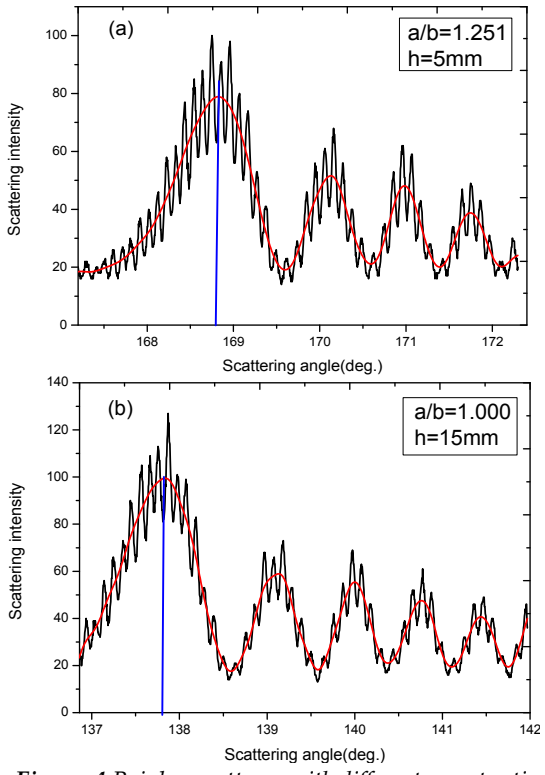


Figure. 4 *Rainbow patterns with different aspect ratios.*

Figure. 4 shows the first-order Airy-Rainbow angle changes from large to small with aspect ratio decreased. This trend is consistent with theoretical analysis[4].

(2) Umder the oblique incident condition, different tilt angles α corresponding angular distribution of the rainbow. h=5mm, $a=990\mu$m, $b=791\mu$m, a/b=1.251.

Due to space limitations, we give angular distribution of the rainbow when $\alpha=25^{\circ}$ and 45°.

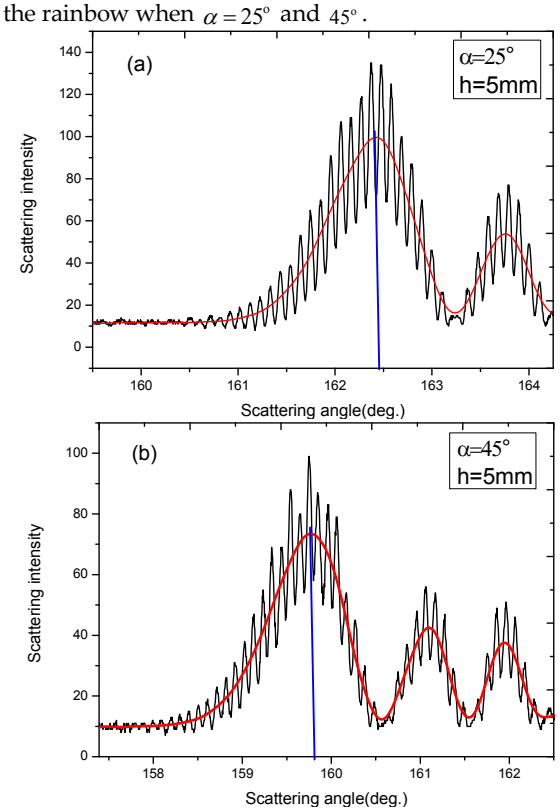


Figure. 5 *Rainbow patterns with* $\alpha=25^{\circ}$ *and* 45°.

Figure 5 shows the first-order Airy-Rainbow angle changes from large to small with the tilt angle α increasing. This trend is consistent with theoretical analysis[4].

4 Conclusions

There is some theoretical analysis of rainbow phenomenon on elliptical structures, including geometrical optics and Vectorial Complex Ray Model, but empirical validation is still absent. By setting up LRMSLJ in the laboratory, rainbows of elliptical liquid jet are measured. After getting the angular distribution of rainbows of elliptical liquid jet at different incident angles and preliminarily comparing it with the calculated values by geometrical optics theory, it is validated that the change trend agrees with the theoretical analysis. Further researches have yet to be carried out.

5 References

[1] Huifen Jiang, and Xiang'e Han, Study on measurement of refractive index profile of GI-POF by light scattering, Optics Communications 282: 1243-46 (2009)

[2] Yue Hu, Research on laser rainbow measurement of the liquid jet and its application. Master dissertation. Xidian University. 2007.

[3] X. Han, Study of refractometry of rainbow and applications to the measurement of instability and temperature gradient of a liquid jet. Ph. D. dissertation. University of Rouen. France. 2000.

[4] Xiangzhen Li, Geometrical-optics approximation of light scattering by particles. Ph. D. dissertation. Xidian University. 2009.

[5] Thormahlen, J. Straub, and U. Grigull, Refractive index of water and its dependence on wavelength, temperature, and density. J. Phys. Chem. Ref. Data 14(4):933-45 (1985)

[6] K. F. Ren, C. Rozé, and T. Girasole, Scattering and transversal divergence of an ellipsoidal particle by using Vectorial Complex Ray Model. Journal of Quantitative Spectroscopy & Radiative Transfer 113:2419-23 (2012)

[7] Keli Jiang, Xiang'e Han, and Kuan Fang Ren, Scattering of a Gaussian beam by an elliptical cylinder using the Vectorial Complex Ray Model. J. Opt. Soc. Am. A 30(8): 1548-56 (2013)

DIGITAL IN-LINE HOLOGRAPHY FOR NEAR FIELD OBSERVATION OF LIQUID-LIQUID FLOWS

Fabrice LAMADIE[1,*], Laurent BRUEL[2] and Lila OULDARBI[3]

[1] CEA, DEN/DTEC/SGCS, 30207 Bagnols-sur-Cèze, France
[2] CEA, DEN/DTEC/SEPE, 30207 Bagnols-sur-Cèze, France
[3] CORIA, 76801, Saint-Etienne du Rouvray, France

Corresponding author: fabrice.lamadie@cea.fr

Abstract

Liquid-liquid extraction is used in many industrial processes. Such processes involve liquid-liquid flows, called emulsions, which can be successfully characterized by especially suited holographic techniques. Because the droplets are millimeter size, a near-field diffraction regime is observed. This regime departs from conventional holography and requires adapted numerical solutions. Due to droplets transparency positioning could not be achieved by usual focusing methods based on research of singularities. The only suitable method is based on calculating an indicator. To be effective a segmentation of the image into individual diffraction patterns is needed. As initial reconstruction can lead to errors, to further improve robustness, the hologram restitution is checked, and then the four parameters, radius and position, are optimized to fit the acquired hologram. If some missing droplets are found, they are identified and included. As a result about slightly less than twice as many drops are included, leading to a shadow density of 20%. Results presented in this communication are on a dedicated device. Outlooks are regarding the adaptation to cylindrical geometry of industrial columns. To address this point a prospect study, using fractional Fourier transform and transfer matrix models, has been conducted.

1 Introduction

Digital holography (DH) is a suitable technic, by which particles can be positioned in 3D space using a single camera. It is used for a broad range of applications including particle image velocimetry (PIV) and particle tracking velocimetry (PTV) [1], live cell imaging [2], and microscopy [3]. The first applications this technique to the characterization of dispersed phases in a two-phase flow were recently described [4], demonstrating that it is capable of simultaneously measuring the size and 3D position of droplets in rapid motion in the continuous phase [5]. Regardless of their applications, most of the examples reported in the literature refer to diffracting objects typically ranging in size from a few micrometers to a few hundred micrometers, observed at distances of the order of ten millimeters. This corresponds to a Fresnel number ($N_f = \pi d^2/4\lambda z$, where d is the particle diameter, λ the laser wavelength, and z the distance between the particle midplane and the observation plane) not exceeding 10^{-2}, i.e. to diffraction conditions intermediate between Fresnel diffraction and Fraunhofer diffraction.

Moreover, the small particle size allows the presence of a large number of elements in the field of view without any significant degradation of the signal to noise ratio, as defined by Royer's criterion [6]. According to this criterion, holograms remain usable as long as the shadow density ($SD = \pi \sum_i d_i^2/4S$ if S is the sensor area) remains below 10%. Conversely, when characterizing emulsions the droplets range in diameter from a few hundred micrometers to two or three millimeters and are observed from a distance of a few tens of centimeters [7]. The Fresnel number is then between 0.5 and 15, which corresponds to nearfield diffraction of transparent objects and requires special hologram processing.

In this communication we propose a hologram processing method to address these issues. The specifics of observing phase objects in the very near field are outlined and the hologram processing method is then presented. This is a two-step process: initial focusing followed by optimization, in which the holograms are processed in sections. The measurement of millimetric transparent droplets ascending in a liquid-liquid flow is then described as an example of processing experimental results. Finally an outlook addressing measurements in astigmatic conditions induced by the geometry of industrial columns is presented.

2 Characterization of nearfield transparent droplets in holographic images

The use of digital holography to characterize millimeter-size transparent droplets observed in the near-field requires taking into account the refraction effect. As illustrated in Figure. 1, synthetic holograms produced by using exact electromagnetic calculations, based on generalized Lorenz–Mie theory (GMLT) [8], exhibit a refraction effect for millimeter-size transparent droplets. It could prevent hologram processing. Taking refraction into account requires an addition to the opaque disk model usually used in digital holography. Fitting on the experimental results have demonstrated that refractive effect could be simulated by adding a phase term at the center of the opaque disk model [7].

Moreover By reconstructing GLMT synthetics holograms using free-space transfer function in the Fresnel approximation [9], differences in the size and structure of the diffraction patterns appear for both the phase and intensity (Figure. 1). For small to intermediate size droplets, which holograms are rather similar to ones of fully opaque disks, the intensity is virtually constant, dropping to a single local minimum at the position of the droplet. The phase varies with 1/z [10], with a characteristic jump on the droplet midplane. For millimeter-size droplets, the intensity varies according to the reconstruction distance with two local extrema, a minimum on the focusing plane (in the direction of reconstruction) and a maximum on the focal plane. Apart from these extrema, the evolution of the function is not monotonic as in the case of small droplets. The phase exhibits a much more complex structure that is no longer symmetrical with respect to the midplane and has multiple jumps.

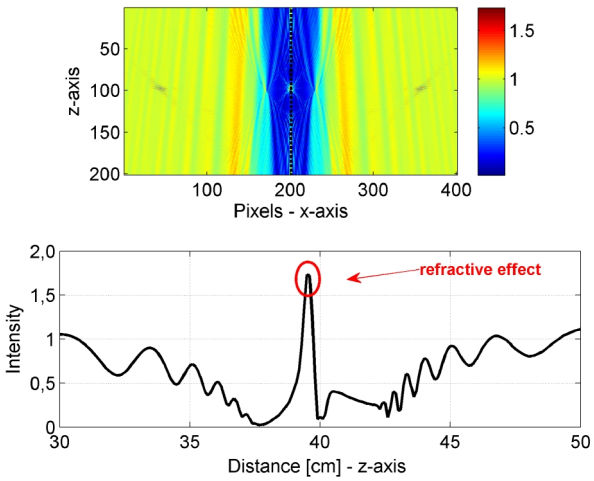


Figure 1 *Cross sections of modulus of the field reconstructed from simulations calculated with the generalized Lorenz-Mie theory (the section plane passes through the center of the droplet and contains the z axis) – Case of a 1 mm droplet observed at 40 cm, Nf ≈ 3.*

These characteristics make it difficult to achieve positioning on the optical axis by searching for singularities. Similarly, the existence of a local maximum intensity will require modification of most of the focusing methods described in the literature, which are generally based on an opaque disk model. The only suitable focusing method is based on calculating an indicator [7]. Two scalar indicators can be used, one based on calculating the sum of the Laplacian of the imaginary part of the reconstructed field (Eq. (1)), the other on calculating the sum of the variance (Eq. (2)) of the imaginary part of the reconstructed field.

$$LAP(z)=\sum_{x,y}\left\{\nabla^2\Im\left(A(x,y;z)\right)\right\}^2 \qquad (1)$$

$$VAR(z)=\frac{1}{N}\sum_{x,y}\left\{\Im\left(\mathrm{A}(x,y;z)\right)-\Im\left(\bar{\mathrm{A}}(z)\right)\right\}^2 \qquad (2)$$

where $\Im\left(\mathrm{A}(x,y;z)\right)$ is the imaginary component of the field reconstructed at distance z, and $\Im\left(\bar{\mathrm{A}}(z)\right)$ is the mean value of the imaginary component of the reconstructed field. Focused plane corresponds to a minimum of the variation of these indicators versus z [7].

3 Hologram processing

Holograms are processed in sections based on the information around each diffraction pattern. First, each diffraction pattern is identified by image processing [11]. An initial position is then assigned after calculating the indicators on the reconstructions. The final optimization step deals with poorly positioned or missing droplets.

Obviously, the precision on the z axis depends on the selected reconstruction step. Thanks to initial focusing about 50 droplets can be correctly positioned on each hologram. When there are more than approximately 50 droplets in the field of view, initial reconstruction can lead to positioning errors or to missing droplets. This limitation is mainly caused by a low SNR of the focus function as soon as many droplets are overlapped. It is therefore necessary to verify their positions and optimize the reconstruction.

Using a transmission model mixing the opaque disk model with a phase term at the droplet center, an hologram synthesized from the expected positions and diameters is built [7]. It's then compared with the acquisition. As a result, missing and poorly reconstructed droplets are identified and can be optimized. For this purpose the simplex method, proposed by George Dantzig in 1947 [12], is particularly suitable. This algorithm is efficient in finding the minimum of a merit function of several variables. This function is minimal as the difference between acquisition and restitution is low. The Euclidean matrix norm is used for this study but sequentially on one droplet mask at a time. The whole hologram optimization is finally the result of the optimization of each droplet restitution. On numerical simulations, this optimization, even if it increases significantly processing time, raises the number of well-positioned droplets in a hologram from around 50 to 80.

4 Experimental results

Acquisitions were conducted on an experimental setup designed to produce droplets of known diameter and velocity as well as an unknown polydisperse droplet population. A detailed description of this setup can be found in [7]. In order to verify the relevance of droplet positions and sizes assessed by holography, all measurements were performed by a dual acquisition set-up. This set-up is as follow: a classical holography

assembly on the first axis and a shadowgraphic setup on the second one, perpendicular to the first one. In comparison with the conventional methods [13–15] used to characterize emulsions (shadowgraphy, laser induced fluorescence, etc.), we obtained on this device the following results:

- The maximum number of droplets measurable (around 80 droplets assuming a mean diameter of 1mm) concurrently is practically the same as with other field measurement techniques (Figure. 2). In this respect, holography is equivalent to the other techniques.
- The measured diameter range is adapted to the requirements of liquid-liquid extraction devices: from 50 µm to 3 mm.
- When the number of droplets is limited (fewer than 30 droplets with a mean diameter of 1 mm), the shadow density is less than 10% and the Royer [6] criterion is met. The paths of droplets with polydisperse diameters can then be reconstructed by successive acquisitions.

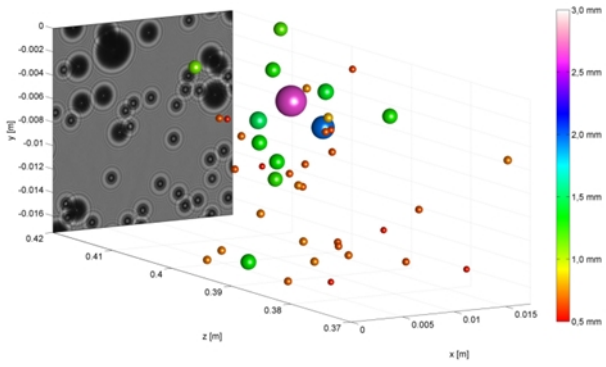


Figure 2 *3D visualization of 43 droplets cloud processed from a single shot hologram.*

5 Outlooks: measurement under astigmatic conditions

As mentioned in introduction, the cylindrical geometry of the columns induces a strong astigmatism and perturbs the acquisition of holograms. This issue could be addressed by using the Fractional Fourier Transform (FrFT) to process the holograms [16]. A first successful prospective test has been conducted, with the experimental setup in cylindrical configuration, on a monodisperse droplets train. It has confirmed the suitability of FrFT for astigmatic holograms processing. However, as the FrFT impose a quadratic phase term, indicators defined in paragraph 2 cannot be directly used. It's a key point currently under study.

6 Acknowledgement

The authors would like to thank the teams at the Interprofessional Aerothermochemistry Research Complex (CORIA) at the University of Rouen for the use of their computer code based on the generalized Lorenz-Mie theory to simulate nearfield holograms of millimetersize transparent droplets [8].

7 References

[1] G. Pan, H. Meng, Digital in-line holographic PIV for 3D particulate flow diagnostics, *4th international symposium on particle image velocimetry*, Göttingen, Germany, 2001.

[2] Y-S Choi, S-J Lee, Three-dimensional volumetric measurement of red blood cell motion using digital holographic microscopy, Appl. Opt. 48:2983-2990 (2009).

[3] F. Dubois, L. Joannes, J.C. Legros, Improved three-dimensional imaging with digital holography microscope using a partial spatial coherent source, Appl. Opt. 38:7085–7094 (1999).

[4] N. Salah, G. Godard, D. Lebrun, P. Paranthoën, D. Allano, S. Coëtmellec, Application of multiple exposure digital in-line holography to particle tracking in a Bénard–von Kármán vortex flow, Meas. Sci. and Tech. 19 (074001):7pp (2008).

[5] L. Tian, N. Loomis, J.A. Dominguez-Caballero, G. Barbastathis, Quantitative measurement of size and three-dimensional position of fast-moving bubbles in air-water mixture flows using digital holography, Appl. Opt. 49:1549–1554 (2010).

[6] H. Royer, An application of high-speed microholography : the metrology of fogs, Nouv. Rev. d'Opt. 5:87-93 (1974).

[7] F. Lamadie, L. Bruel, M. Himbert, Digital holographic measurement of liquid-liquid two-phase flows, Opt. and Laser in Eng. 50:1716–1725 (2012).

[8] X.Wu, S. Meunier-Guttin-Cluzel, Y. Wu, S. Saengkaew, D. Lebrun, M. Brunel, L. Chen, S. Coetmellec, K. Cen, G. Grehan, Holography and micro-holography of particle fields: A numerical standard, Optics Communications, 285: 3013-3020 (2012).

[9] D. Voelz, *Computational Fourier Optics* (SPIE, Bellingham, 2011).

[10] W.D. Yang, A.B. Kostinski, R.A. Shaw, Phase signature for particle detection with digital in-line holography, *Opt. Lett*. 31:1399–1401 (2006).

[11] F. Lamadie, L. Bruel, Processing method for near-field in-lines holograms (Fresnel number ≥ 1), Opt. and Laser in Eng. 57:130–137 (2014).

[12] J.C. Lagarias, J.A. Reeds, M. Wright, P. Wright, Convergence properties of the nelder-mead simplex method in low dimensions. SIAM Journal of Optimization 9:112–147 (1998).

[13] M. J. Sathea, I. H. Thakerb, Tyson E. Strandc, Advanced PIV/LIF and shadowgraphy system to visualize flow structure in two-phase bubbly flows, Chemical Engineering Science 65(8):2431-2442 (2010).

[14] F.R. A. Onofri, M. Krzysiek, J. Mroczka, K-F. Ren, St. Radev, J-P. Bonnet, Optical characterization of bubbly flows with a near-critical-angle scattering technique, Experiments in Fluids 47(4-5):721-732 (2009).

[15] S. Dehaeck, J. P. A. J. van Beeck and M. L. Riethmuller, Extended glare point velocimetry and sizing for bubbly flows, Experiments in Fluids 39(2):407-419 (2005).

[16] N. Verrier; S Coetmellec, M. Brunel, Marc; and D. Lebrun, Digital in-line holography in thick optical systems: application to visualization in pipes, Applied Optics, 47 (22):4147-4157 (2008).

On the measurement of nano and micro particles by Fourier Interferometric imaging

Sawitree SAENGKAEW*, Annie GARO, Siegfried MEUNIER-GUTTIN-CLUZEL and Gérard GREHAN

UMR CNRS 6614/CORIA, Normandie Université, Saint Etienne du Rouvray, 76800, FRANCE

*Corresponding author: sawitrees@coria.fr

Abstract

According with the European Community report [1], a Nano-material is defined as:

- nanomaterial means a natural, incidental or manufactured material containing particles, in an unbound state or as an aggregate or as an agglomerate and where, for 50% or more of the particles in the number size distribution, one or more external dimensions is in the size range 1 nm-100nm.
- In specific cases and where warranted by concerns for the environments, health, safety or competitiveness the number of size distribution threshold of 50% may be replaced by a threshold between 1 and 50%.

Accordingly, developments of techniques to measure few nano particles in the vicinity of largest particles are a challenge. In our contribution to LIP 2014, a new approach based on the use of the Fourier Interferometric Imaging will be described and validated both numerically and experimentally.

1 FII Concept

1.1 Generalities

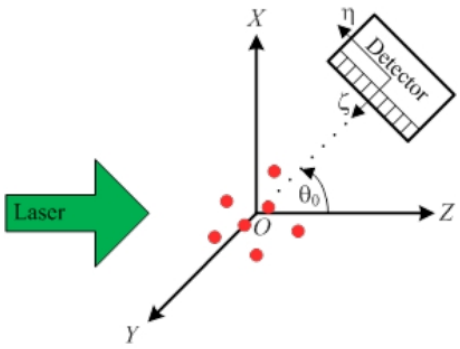


Figure 1: *Scheme of the problem understudy.*

The FII approach has been introduced in [2]. Here we only recall the main lines. Let us assume a cloud of particles illuminated by a pulse laser and a CCD camera to collect the scattered light. On one pixel of the detector the total amplitude is given by:

$$A_t = \sum_{i=1}^{N} A_i \quad (1)$$

Where A_i is the amplitude of the light scattered by one particle. Accordingly, the total intensity is:

$$I_t = A_t . A_t^* = \sum_{i=1}^{N} A_i A_i^* + \sum_{i=1}^{N} \sum_{j=1|_{j\neq i}}^{N} A_i A_j^* \quad (2)$$

The fundamental principle of FII is to work with only the terms $A_i A_j^*$ which have the following properties:

- The distance between the particles *i* and *j* is directly measured.
- Each particle is measured *N-1* times, where *N* is the number of particles in the control volume.
- The signal intensity is proportional to the square root of the product of the intensities scattered by each particle.

To extract the terms $A_i A_j^*$, the 2DFFT of the recorded field of interference is computed. Figure 2 illustrates that procedure.

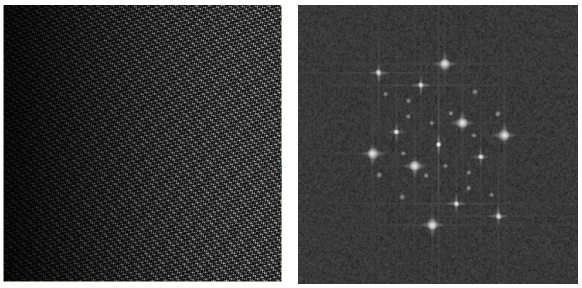


Figure 2: *An interference field and its associated 2DFFT.*

In figure 2, each spot of the 2DFFT (right image) corresponds to the contribution of two particles.

1.2 Application to Brownian particles.

For one particle, the Brownian motion is characterized by the diffusion coefficient which is related to the mean squared displacement. Then the measurement of mean squared displacement defined by:

$$\left\langle X^2(t) \right\rangle = N^{-1} \sum_{i=1}^{N} (x_i(t) - x_i(0))^2 \quad (3)$$

where N is the number of measurements of one particle, x_i is the particle location at measurement i and x_0 is the particle location at the first measurement, is a measurement of the diffusion coefficient which is a function of the particle size.

In FII approach, the particle location is not measured but the distance between two particles is measured. It is possible to show that the mean squared distance variation between the two particles is related to the mean squared displacement of each particle by:

$$\left\langle X^2_{1,2} \right\rangle = \left\langle X_1^2 \right\rangle + \left\langle X_2^2 \right\rangle \quad (4)$$

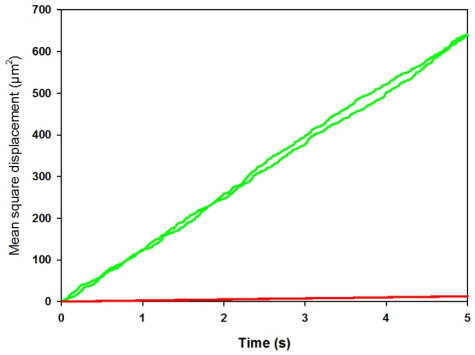


Figure 3: *The mean squared displacement for individual particles (from numerically simulated coordinates).* In *green 20 nm particles, in red 1 µm particles*

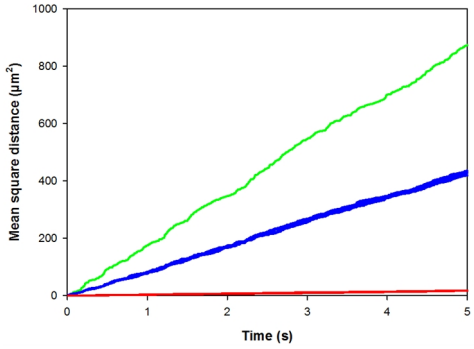


Figure 4: *The mean squared distance variation between particles couple (from numerically simulated coordinates). In green two 20 nm particles, in blue one 20 nm and one 1 µm particles, in red two 1 µm particles*

1.3 Numerical Validation of Brownian motion

In the following part of the paper we will detail the example of a set of six silica particles (2 of diameter 20 nm and 4 of diameter 1 micron) in water.

Validation of the Brownian movement simulations is confirmed by the computed behaviour of particles as shown on figure 3.

From the same series of numerical simulations, the squared distance variation has been computed from their coordinates. Figure 4 presents the squared distance variations versus time. We observe that the squared distance variation of particles are gathered in 3 classes: the largest displacement corresponds to a pair 20 nm-20 nm, then the 8 pairs 20 nm-1micron, and finally the 6 pairs 1micron-1micron.

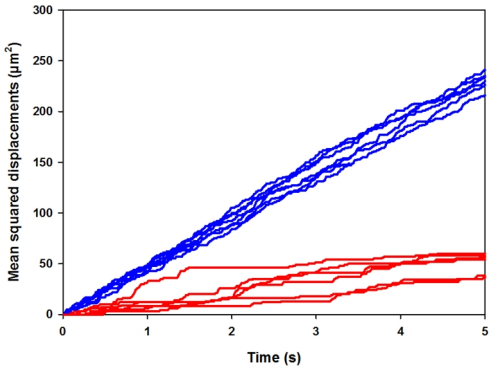


Figure 5: *The mean squared distance variation measured from the 2DFFT FII image. In blue 1 of 20 nm and one of 1 µm, in red two of 1 µm*

1.4 FII field simulations

For each time step (delay 0.01 s), from the series of simulated coordinates, the field of interference is computed by using the Lorenz-Mie code described in [3]. Then at each time step we associate a couple of images as display in figure 2. We notice that one trace is missing: the 20 nm-20 nm pair is not observable directly. From the visible spots locations versus time, the squared distance variation is plotted on Figure 5.

The analysis of the curves plotted in figure 5 proves that the slope of the curve is a measurement of the sum of the mean squared displacement of both particles (see Formulae (4)).

To be able to measure each particle individually, the couple interaction must be identified. Then from three spots corresponding to three interacting particles, the size of individual particles can be obtained. This procedure will be described in our contribution to LIP 2014.

2 References

[1] T. Linsinger, G. Roebben, D. Gilliland, L. Calzolai, F. Rossi, N. Gibson and C. Klein, Requirements on measurements for the implementation of European Commission definition of the term "nanomaterial', JRC Reference reports, EUR 25404 EN (see page 7).

[2] P. Briard, S. Saengkaew, X.C. Wu, S. Meunier-Guttin-Cluzel, L.H. Chen, S. Coetmellec, K.F. Cen and G. Grehan, Measurements of 3D relative locations of particles by Fourier Interferometry Imaging (FII), Optics Express, 2011, 19, 12700-12718

[3] X.C. Wu, S. Meunier-Guttin-Cluzel, Y.C. Wu, S. Saengkaew, D. Lebrun, M. Brunel, L.H. Chen, S. Coetmellec, K.F. Cen and G. Grehan, Holography and Micro-holography of particle fields: a numerical Standard, Optics Communications, 2012, 285, 3013-3020

Numerical Considerations on Measurements of Light-Absorbing Particles Using Polarized-Type Phase Doppler Method

Naomichi YOKOI[1,*] and Yoshihisa AIZU[2]

[1] Department of Mechanical Systems Engineering, Asahikawa National College of Technology, Asahikawa, 071-8142, Japan
[2] Division of Engineering for Composite Functions, Muroran Institute of Technology, Muroran, 050-8585, Japan

**Corresponding author: yokoi@asahikawa-nct.ac.jp*

Abstract

We have proposed so far a polarized-type phase Doppler method for particle sizing by using polarization properties of scattered light. In order to verify the usefulness of the present method for sizing light-absorbing particles, we numerically investigate the phase-diameter properties in relation to an extinction coefficient of a particle by using the generalized Lorenz-Mie theory.

1 Introduction

Various optical techniques have been studied so far for non-intrusive measurements of particle dynamics and characteristics. Among them, historically speaking, the phase Doppler method (PDM) was proposed by Durst and Zaré [1] in 1975 as an extension of laser Doppler velocimetry (LDV) [2] for measuring size and velocity of a moving particle simultaneously. The PDM, however, annoys users with error due to the particle trajectory effect [3] and difficulty in optical alignment. To overcome these problems, we developed the polarized-type phase Doppler method (PPDM) in 2001 [4].

To extend this method, in the present study, we investigate the phase-diameter properties in PPDM in relation to the extinction coefficient of a light-absorbing particle by numerical simulation using the generalized Lorenz-Mie theory (GLMT) [5,6].

2 Principle

Figure. 1 shows a schematic diagram of the PPDM. Two incident laser beams in the x-z plane pass through the $\lambda/2$ plate and change their polarization angles to be ω_p with respect to the scattering plane (y-z plane). These two beams intersect with angle 2α to form a probe volume. Light scattered by a spherical particle passing through the probe volume along x axis from its negative to positive side is received in a direction with an off-axis angle ϕ from z axis and an elevation angle ψ from y-z plane. The light passes through a detecting aperture and then is divided into two equivalent light fields in power by a dual prism. Each of the two fields enters an analyzer P_0 or P_1, which is respectively set to be an appropriate angle ω_{h0} or ω_{h1} with

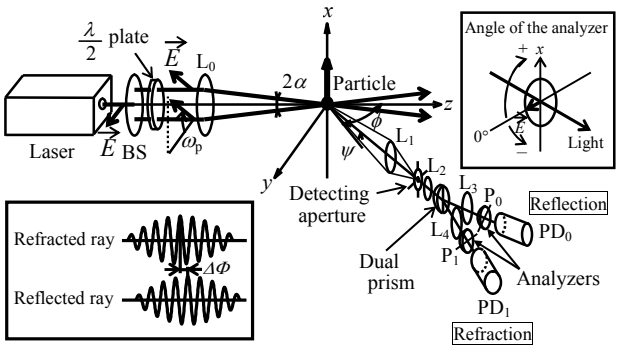


Figure 1 *Optical geometry of the PPDM system. BS, beam splitter. PD, photodetector.*

respect to the scattering plane, and, then, the reflected ray is obtained from the analyzer P_0 and the refracted ray from P_1. Each of ω_p, ω_{h0} and ω_{h1} is defined to be positive for counterclockwise rotation toward the light-propagating direction as shown in the upper inset of Fig.1.

The phases Φ_0 and Φ_1 of reflected and refracted rays, respectively, can be determined individually on the basis of geometrical optics approximation as [7]

$$\Phi_0 = d_p \cdot \frac{k\sin\alpha\sin\psi}{\sqrt{2(1-\cos\alpha\cos\psi\cos\phi)}}, \tag{1}$$

$$\Phi_1 = d_p \cdot \frac{-kn\sin\alpha\sin\psi}{\sqrt{2(1+\cos\alpha\cos\psi\cos\phi)\left[1+n^2-\sqrt{2}n\sqrt{1+\cos\alpha\cos\psi\cos\phi}\right]}}, \tag{2}$$

where k is the wave number, d_p is the particle diameter, and n is the particle refractive index relative to the surrounding medium. Thus, under the known particle refractive index n, the particle diameter is determined from the difference between Φ_0 and Φ_1, i.e. phase difference $\Delta\Phi$ between two Doppler beat signals detected by PD_0 and PD_1 as shown in the lower inset of Fig.1.

3 Numerical simulation and discussion

To estimate the usefulness of the PPDM for sizing light-absorbing particles, we carried out GLMT simulations of the signal phase of the reflected and refracted rays for several water-black-ink droplets with different extinction coefficients. Here the extinction coefficient is an imaginary part of the complex refractive

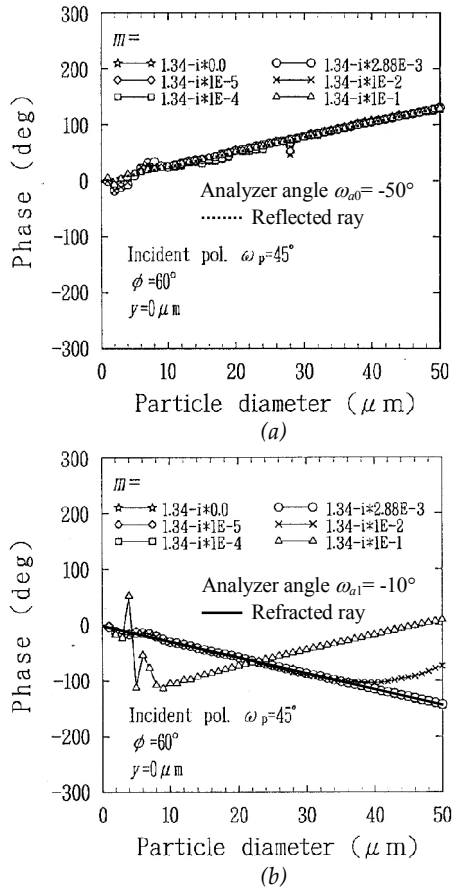


Figure 2 *Simulated results of phase-diameter relations as a function of the extinction coefficient for the analyzer angles of ω_{a0}=-50 deg and ω_{a1}=-10 deg, respectively.*

index of the particle, *m*. Figures. 2(a) and (b) show the phase-diameter relations as a function of the extinction coefficient for the analyzer angles of ω_{a0}=-50 deg and ω_{a1}=-10 deg, respectively, which are almost equal to the predicted optimum angles for transmitting the reflected and refracted rays from the preceding geometrical optics considerations [4]. For these simulations, we employed six published values [8] of extinction coefficients as shown in Figs. 2(a) and (b) for the mass percentage of ink in water of 0%, 0.05%, 0.5%, 12%, 44% and 100%, respectively, for the wavelength of illuminating laser light of 632.8nm. For a comparison purpose, the theoretical phase-diameter relations of the reflected and refracted rays computed from Eqs. (1) and (2) are also plotted by dotted and solid lines in Figs. 2(a) and (b), respectively. The results in Fig. 2(a) demonstrate that any phase-diameter relation has almost no dependence on extinction coefficient and shows good agreement with the theoretical line of the reflected ray. Thus the reflected ray is always effective for sizing absorbing particles. On the other hand, the results in Fig. 2(b) demonstrate that if the extinction coefficient is larger than the order of 1.0×10^{-2}, the simulated phase-diameter relation deviates from the theoretical line of the refracted ray. Particularly for extinction coefficient of 1.0×10^{-1}, apart from an irregular phase jump at around 5μm in the particle diameter, the slope of the phase versus diameter curve is rather similar to that of the theoretical line of the reflected ray as seen in Fig. 2(a). This property suggests that the absorption in the refracted ray becomes substantial and only the reflected ray remains. Therefore, it is clear that the refracted ray cannot be used for sizing absorbing particles having the extinction coefficient larger than the order of 1.0×10^{-2} in the condition treated in the present study.

4 Conclusion

In this study, we numerically estimated the usefulness of the PPDM for sizing light-absorbing particles. Although the PPDM has some problems such as the limitation on particles applicable (refractive particle) and on the scattering region (near forward directions), we consider that it can be certainly an alternative to the PDM.

5 Acknowledgement

Part of this work was supported by a Grant-in-Aid for Scientific Research from the Japan Society for the Promotion of Science.

6 References

[1] Durst F., and Zaré M., Laser Doppler measurements in two-phase flows, LDA-75 Symposium Copenhagen: *The Accuracy of Flow Measurements by the Laser Doppler Method*, pp.403-429, Copenhagen, Denmark, 1975.

[2] Yeh Y., and Cummins H.Z., Localized fluid flow measurements with an He-Ne laser spectrometer, Applied Physics Letters 4(10):176 (1964)

[3] Yokoi N., Aizu Y., Mishina H., Estimation of particle trajectory effects and their reduction using polarization in phase Doppler particle measurements, Optical Engineering 38(11):1869-1882 (1999)

[4] Yokoi N., Aizu Y., Mishina H., Unidirectional phase-Doppler method for particle-size measurements, Applied Optics 40(7):1049-1064 (2001)

[5] Gouesbet G., Maheu B., Gréhan G., Light scattering from a sphere arbitrarily located in a Gaussian beam, using a Bromwich formulation, Journal of Optical Society of America A5(9):1427-1443 (1988)

[6] Gouesbet G., Gréhan G., Maheu B., Localized interpretation to compute all the coefficients g_n^m in the generalized Lorenz-Mie theory, Journal of Optical Society of America A7(6):998-1007 (1990)

[7] Naqwi A., and Durst F., Light scattering applied to LDA and PDA measurements, Part 2: Computational results and their discussion, Particle & Particle Systems Characterization 9:66-80 (1992)

[8] Manasse U., Wriedt T., Bauckhage K., Phase-Doppler sizing of optically absorbing liquid droplets: comparison between Mie theory and experiment, Particle & Particle Systems Characterization 9:176-185 (1992)

Ultrathermometry of Evaporating Droplets

Giennadiy DERKACHOV, Daniel JAKUBCZYK*, Mariusz WOŹNIAK, Justice ARCHER and Maciej KOLWAS

Institute of Physics, Polish Academy of Sciences, Warsaw, 02-668, Poland

Corresponding author: jakub@ifpan.edu.pl

Abstract

In view of recent works [1, 2], it has become possible to determine reliably the temperature of a steadily evaporating/condensing droplet, relative to ambient temperature. The accuracy of determination of temperature difference between the droplet and the ambient atmosphere reaches fractions of mK. We determined droplet temperature evolutions for different cases of growing complexity: (i) a two-component mixture of pure liquids, (ii) solutions of solid in liquid: a non-surface-active and surface-active and (iii) suspensions: non-light-absorbing and light-absorbing. In case of non-light-absorbing droplets, the droplet temperature is always lower than the ambient temperature and is controlled by the droplet composition and the ambient atmosphere parameters (temperature, vapour content) while in case of light-absorbing droplets, the droplet temperature can rise above the ambient temperature and is additionally controlled by the incident light irradiance and by the droplet absorption cross-section. Therefore, the droplet temperature can be, to some extent, programmed by engineering the droplet composition and absorption cross-section and remotely controlled with incident light irradiance.

1 The outline of the used model

For a micro or even a nanodroplet of a liquid (pure, mixed, solution or suspension) the steady evolution of droplet radius $a(t)$ can be described effectively with a very simple differential equation(s). The derivation can be found in [1,3] (compare [2] for nanoscale considerations). It must be stressed that the parametrisation introduced in [1] uses the temperature of droplet interior rather than the temperature of vapour near the droplet surface [4]:

$$\frac{da}{dt} = \frac{P_{1k}}{a + P_2}, \tag{1}$$

where $k = m,t$ with:

$$P_{1m} = \frac{DM}{R\rho_L}\left\{\frac{Sp_{sat}(T_\infty)}{T_\infty} - \frac{p_a(T_L)}{T_L}\right\}, \tag{2}$$

when the transport of mass is considered and

$$P_{1t} = \frac{\lambda \Delta T}{q_{eff}\rho_L}, \text{ where } \Delta T = T_L - T_\infty, \tag{3}$$

when the transport of heat from the ambient atmosphere (non-light-absorbing droplet) is considered. In both cases

$$P_2 = Al_{mfp}. \tag{4}$$

M, ρ and q_{eff} are the molecular mass, the liquid density and the effective enthalpy of evaporation of the evaporating component respectively, D is its diffusion coefficient in the surrounding gaseous medium, p_{sat}, p_a, and S are its saturated vapour pressure, vapour pressure at the droplet surface and the relative saturation far from the droplet respectively, λ and l_{mfp} are the thermal conductivity coefficient and the mean free path of the surrounding gaseous medium respectively, T_∞ and T_L are the temperature far from the droplet and the temperature of (the liquid in) the droplet interior respectively and R is the universal gas constant. According to [1], $A = 2.35$.

In principle, equation(s) Eq. (1) enable predicting droplet temperature evolution *a priori*, provided all the parameters of the model are known with sufficient accuracy. If some parameters are not known with sufficient accuracy, like in case of mixtures and suspensions, the droplet temperature can be determined from the observed droplet radius evolution. The adopted procedure depends on the complexity of the case (see next sections). It must be once more underlined, that the accuracy of finding T_L is, in practice, always limited by the accuracy of T_∞ measurement, though the accuracy of ΔT (the precision of T_L) finding is very high.

2 Temperature of evaporating non-light-absorbing droplet

2.1 Pure liquids mixture

For pure single-component liquids, $P_{1t} = P_{1m} = const$. This implies that ΔT remains constant as long as other parameters are constant. Then, if those parameters are known, ΔT can be calculated. Otherwise, ΔT can be retrieved from experimental $a(t)$ by means of the heat transport equation (Eq.(1) with Eq.(3)). For single component liquids, equation Eq.(1) can be integrated analytically and solved for ΔT. For multi-component liquid, the droplet temperature reflects the changes of mass transport caused by the evolution of composition. In this case the differential form of Eq.(1) must be used and the evolution of composition must be accounted for in model equations. In the extreme case of very large $|\Delta T|$, other temperature-dependent parameters of the model equations may get significantly modified. Then the model equations, together

with all relevant parameter-describing equations, must be integrated numerically. Here we illustrate the case of a multi-component liquid and a very small $|\Delta T|$. In figure 1, we present the radius evolution of a droplet of diethylene glycol/glycerol mixture and the droplet temperature retrieved from this evolution. The P_{1t} parameter was modified to account for two-component liquid and the experimentally obtained droplet radius was differentiated. This enabled retrieving ΔT without integration of Eq.(1). The procedure is straightforward, but the minute errors of the radius retrieval method are magnified by differentiation (see figure 1) and require post-filtering.

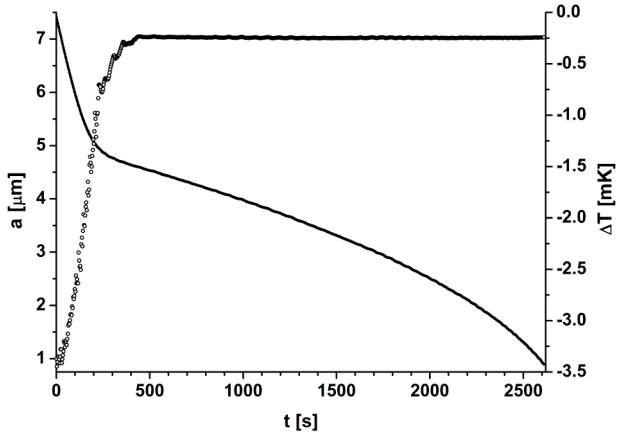


Figure 1 *The temporal evolution of droplet radius (solid circles merged into line) and of relative temperature (open circles) for a droplet of 1:5 glycerol/diethylene glycol mixture evaporating into nitrogen atmosphere, at STP conditions.*

2.2 Solution and transparent suspension

The presence of dissolved/dispersed phase influences the evaporation and, in consequence, has impact on ΔT. In case of non-light-absorbing droplet, it is enough that just the mass transport equation (Eq.(1) with Eq.(2)) is modified. We found it sufficient that the exponential Köhler term (compare [4,5]) is introduced into P_{1m} parameter in the following manner:

$$P_{1m} = \frac{D \cdot M}{R \cdot \rho_L} \cdot \left\{ \frac{S \cdot p_{sat}(T_\infty)}{T_\infty} - \frac{p_a(T_L)}{T_L} \cdot \exp\left[\frac{-n_S}{(a/a_0)^3 - n_S} \right] \right\}, \tag{5}$$

where a_0 is the initial droplet radius and n_S reflects (but is not exactly equal to) the initial mass concentration of solute/dispersed phase [4]. In order to retrieve $\Delta T(t)$, the set of equations Eq.(1), Eq.(3), Eq.(5) must be integrated numerically and fitted to experimental $a(t)$ by means of S and n_s optimisation. This is feasible as long as S is constant throughout the whole evolution.

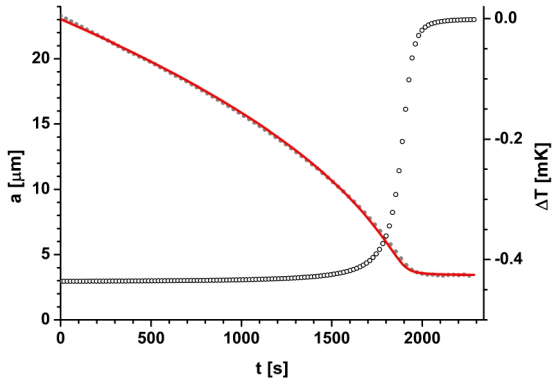
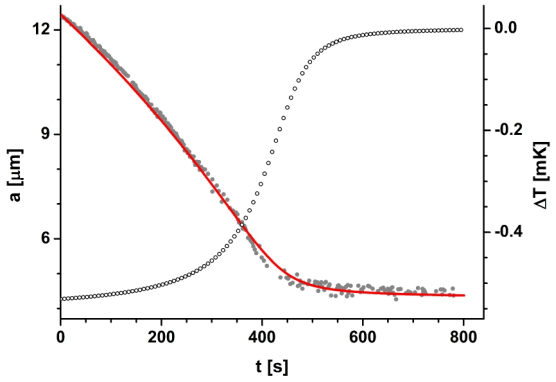


Figure 2 *The temporal evolution of droplet radius (gray, solid circles) and the resulting relative temperature evolution (open circles) for a droplet of solution of surface active agent (sodium dodecyl sulfate) in diethylene glycol. Model equations fit is represented with red, solid line.*



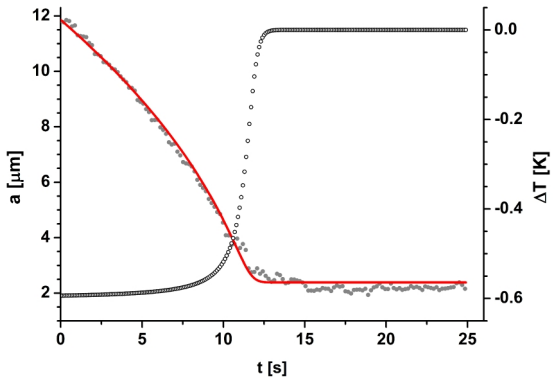


Figure 3 *The temporal evolution of droplet radius (gray, solid circles) and the resulting relative temperature evolution (open circles) for a droplet of: (top panel) suspension of SiO_2 225-nm-radius nanospheres in (sodium dodecyl sulfate/diethylene glycol solution; (bottom panel) aqueous suspension of SiO_2 225-nm-radius nanospheres. Model equations fit is represented with red, solid line.*

We applied the procedure to: (i) surface-active compound solution (sodium dodecyl sulfate in diethylene glycol, figure 2) and non-light-absorbing coarse suspensions (figure 3): (ii) SiO_2 nano-spheres in diethylene glycol (with sodium dodecyl sulfate) and (iii) SiO_2 nano-spheres in water.
In all cases presented in figures 2 and 3, the evaporation finally stopped and so the final $\Delta T = 0$.

3 Temperature of evaporating droplet of light-absorbing suspension

The case of evaporating droplet of light-absorbing suspension is still more complicated. Both transport equations must be modified and used. The mass transport equation, as previously, comprises the Köhler term, while the heat transport equation must account for the presence of internal heat source(s) (light absorption). The internally released heat can, in our case, be calculated with the aid of Mie formulas for absorption cross-section Q_{abs} (see e.g. [6]). Then

$$P_{1t} = \frac{I_0 \cdot Q_{abs}(a)/(4 \cdot \pi \cdot a) + \lambda \cdot \Delta T}{q_{eff} \cdot \rho_L}, \qquad (6)$$

where I_0 is the incident light irradiance. The changes in refractive index, which follow the changes of composition due to evaporation, must also be accounted for. Again, it is important for the presented method that S remains constant throughout the evolution. We applied the developed model to a light-absorbing droplet of fine aqueous dispersion of C_{60} fullerene nanocrystallites evaporating into humid atmosphere. As previously, in this case the equations were numerically integrated and fitted to experimental $a(t)$ with S and n_S optimisation. The results are presented in figure 3. The raise of temperature due to heating by light is plainly visible. Further on, the final temperature of the droplet is significantly higher than the temperature of the chamber ($\Delta T > 0$).

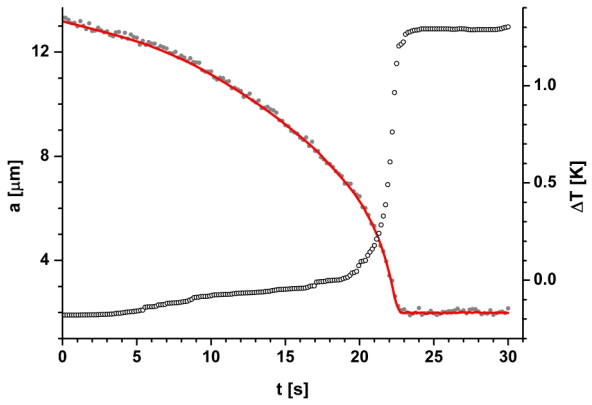


Figure 3 *The temporal evolution of droplet radius (gray, solid circles) and the resulting relative temperature evolution (open circles) for a droplet of aqueous C_{60} fullerene suspension. Model equations fit is represented with red, solid line.*

4 References

[1] Hołyst *et al.*, Nanoscale transport of energy and mass flux during evaporation of liquid droplets into inert gas: computer simulations and experiments, Soft Matter 9: 7766-74 (2013).

[2] Zientara M., Jakubczyk D., Litniewski M., Hołyst R., Transport of mass at the nanoscale during evaporation of droplets: the Hertz-Knudsen equation at the nanoscale, J. Phys. Chem. C 117: 1146–50 (2013).

[3] Hołyst *et al.*, Evaporation of freely suspended single droplets: experimental, theoretical and computational simulations, Rep. Prog. Phys. 76: 034601–20 (2013).

[4] Pruppacher H. and Klett J., *Microphysics of Clouds and Precipitation* (Kluwer, Dordrecht, 1997).

[5] Friedlander S., *Smoke, Dust and Haze Fundamentals of Aerosol Dynamics* (Oxford University Press, New York, 2000).

[6] Bohren C.F. and Huffman D.R., *Absorption and scattering of light by small particles* (Wiley, New-York, 1983).

Laser Speckle of Nanofluids and its Application in Velocity Distribution Measurement

*Chuanlong XU, Zhihong DU, Shimin WANG
Key Laboratory of Energy Thermal Conversion and Control of Ministry of Education, Southeast University, Nanjing 210096, P. R. China
*Corresponding author: chuanlongxu@seu.edu.cn

Abstract

Nanofluids are dilute suspensions of functionalized Nanoparticles smaller than 100nm, which belong to a new type of functional composite materials developed about a decade ago with the specific aim of increasing the thermal conductivity of heat transfer fluids. However, the mechanistic understanding on Nanofluids for its heat transfer enhancement is still quite limited due to the complex influence of Nanoparticle shape, size, concentration, Nanoparticle aggregation, morphology and Brownian motion effect. So it is desirable to investigate and visualize the particles flow behaviour, concentration distribution, and particle aggregation effect in the base liquid for in-depth understanding of Nanofluids mechanism. This paper aims to study the speckle characteristics of Nanofluids illustrated by a laser source numerically and experimentally, and apply the speckle for the measurement of Nanofluids velocity distribution.

Figure 1 shows the computed speckle based on Rayleigh scattering theory. The Histogram of intensity distribution corresponding to Figure 1 is illustrated in Figure 2. It can be seen from Figures 1-2 that the commutated image and its intensity distribution has the characteristics of speckle pattern, which is a result of the interference of many waves scattered by the Nanoparticles in base liquid. These waves have different phases and amplitudes, which add together to give a resultant wave whose amplitude and intensity varies randomly.

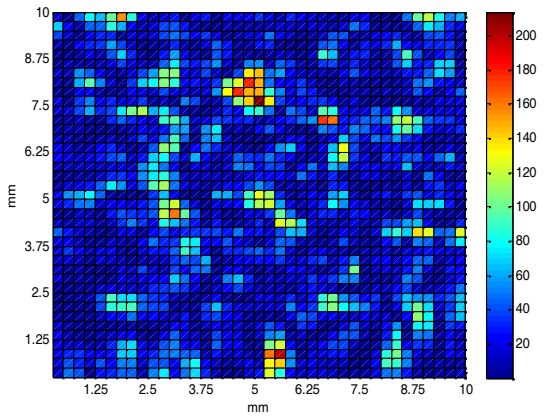


Figure 1 *Computed scattering speckle (Particle size: 20nm, concentration: 0.01%)*

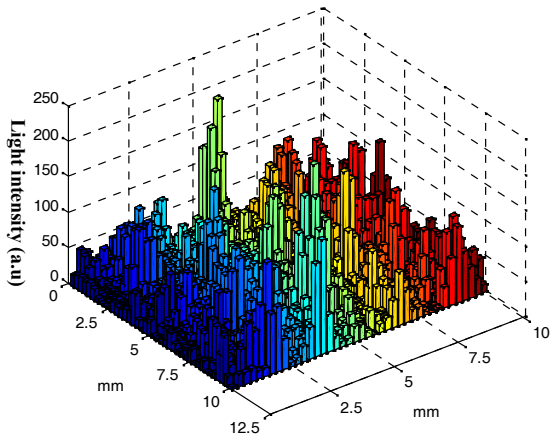


Figure 2 *The intensity distribution Histogram of the light speckle in Figure 1*

Figure 3 shows the average light intensity of the speckle patterns produced by Nanofluids (Nanoparticle concentration: 0.01%, size ranging from 5 nm to 45 nm). From Figure 3, with increasing Nanoparticle size, the average intensity of the speckle pattern decreases. This may be caused by decreasing nanoparticles number in base liquid at the same particle concentration (0.01%), and thus the scattered light intensity in speckle pattern becomes weak.

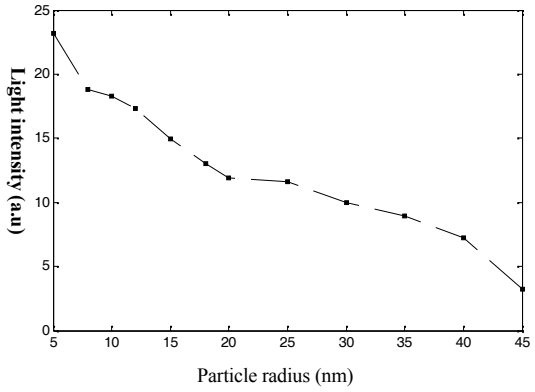


Figure 3 *The average intensity of the speckle patterns by Nanofluids (Nanoparticle concentration: 0.01%)*

The laser speckle of Naoparticles is further proposed to measure the velocity distribution measurement of

Nanofluids based on spatial cross-correlation algorithm. An experimental system is built and a series of speckle photographs are caught by a CCD under dynamic Nanofluids with different particle concentrations. Figure 4 shows a raw speckle of Nanofluids with the naoparticles of Fe_3O_4. The nanoparticle size is 20 nm. A homomorphic filter is employed to reduce the speckle noises produced by nanopartiles motion blur. Figure 5 represents the filtered speckle corresponding to Figure 4. By comparisons between the raw and filtered speckles, we can see that the homomorphic filter not only eliminates the uneven illumination of the raw speckle, but also effectively enhances its details, making the vague and scattered spots more clear. The filtered speckles are then converted into binary images through Otsu's method (Figure 6). The Otsu algorithm assumes that the image to be thresholded contains two classes of pixels (objects and background) and calculated the optimum threshold separating these two classes. As can be seen from the Figure 6, the useful spots can be efficiently separated from the background in the binary speckle, which makes the spatial-correlation processing for speckles more convenient and faster.

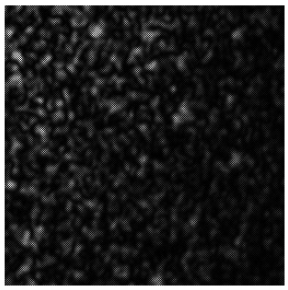


Figure 4 *Raw speckle pattern*

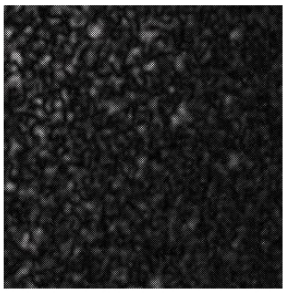


Figure 5 *Filtered speckle pattern*

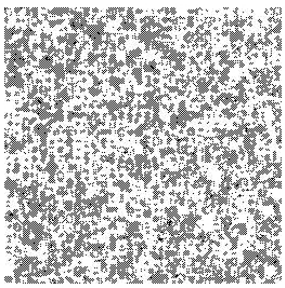


Figure 6 *Binary speckle*

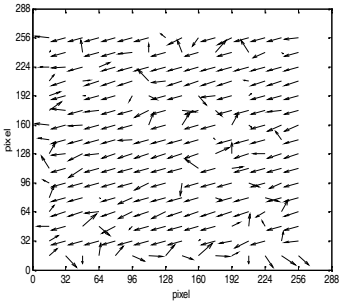


Figure7 *Velocity distribution vectors*

The Nanofluid velocity distribution vectors are further determined by the block motion matching based cross-correlation algorithm for processing the binary speckles. Figure 7 shows the velocity distribution vectors of the Nanofliuds with the flowrate of 140 mL/min. The corresponding average velocity of Nanofluids in the pipe is 2.33 cm/s. After the individual erroneous velocity vectors are excluded, the average magnitude (the displacement of speckle motion) of the vectors is calculated as 4.5 pixels. As the pixel size is 8.3μm, the displacement corresponding to 4.5 pixels is 37.1μm. The magnification and frame rate of the lens for the CCD are 8.57 and 67, respectively. The calculated velocity of the Nanofluids is 2.13 cm / s.

Acknowledgement

The authors wish to express their gratitude to the National Natural Science Foundation of China (No. 51376049) for supporting the research as reported in this paper.

References

[1] Choi, S. U. S. Enhancing thermal conductivity of fluids with nanoparticles. In Proceedings of the 1995 ASME International Mechanical Engineering Congress and Exposition San Francisco, CA, USA (1995).

[2] Wen D., Lin G., Vafaei S., Zhang K. Review of nanofluids for heat transfer applications. Particuology, 7: 141–150 (2009)

[3] Hong H. P., Wright B., Wensel J., et al. Enhanced thermal conductivity by the magnetic field in heat transfer nanofluids containing carbon nanotube [J]. Synthetic Metals, , 157(10-12): 437-440 (2007).

[4] Chicea D. Nanoparticle sizing by coherent light scattering-computer simulation results. Journal of Optoelectronics and Advanced Materials, 10(4): 813-818 (2008).

[5] Qian M., Ni X. W., Shen Z., et al. Key issues in measuring the velocities of nanoparticles in nanofluids. Key Engineering Materials, 364-366: 1111-1116 (2008)

Ionisation of Soot Aggregates and Primary Particles In a Laser Field

Vivien BEYER[3], Doug GREENHALGH[2]
Yannis HARDALUPAS[1], Christopher HONG[1]*, Alex TAYLOR[1]

[1]Imperial College London, London, SW7 2AZ, UK

[2]Glasgow Caledonian University, Glasgow, G4 0BA, UK

[3]Heriot Watt University, Edinburgh, EH14 4AS, UK

Corresponding author: christopher.hong03@imperial.ac.uk

Abstract

Carbon atoms have been shown to ionise when subjected to a laser field. By applying a laser field to soot particles, the strength of this ionisation can be tested to provide information on the morphology of soot aggregates and primary particles. This is carried out by applying an electric field to carbon black particles when exposed to a pulsed laser beam. From this experiment, the difference in the carbon particles' trajectory with and without the electric field can be used to determine the Coulombic forces involved, the temperature threshold for the thermionic property and the mass/charge ratio for the particles. With this information, a model on this laser-induced carbon thermionic property can be devised.

1 Introduction

The morphology and physical properties of soot aggregate are important for application of techniques such as Laser Induced Incandescence (LII) on measuring soot primary particle sizes in flames and optical engines. Soot morphology has a bearing on its formation, growth and oxidation, better understanding of which allows for possible reduction of it in combustion processes. It enables more accurately devised models and interpretation of results.

When carbon particles are heated up to a suitably high temperature, it has been observed that these fragment and appear to "explode" and break up into smaller particles[1]. The increase in temperature and energy in the carbon particles causes the electrons in the particles to escape by thermionic emission, which is well known[2]. The positively charged carbon particles then repel each other and move in opposing directions, hence appearing to "explode". This ionisation in a laser field of clusters[3] and carbon atoms is well understood and multiple experiments have been carried out to characterise these, including their ionization potentials[4]. Studies on electron emission has also been carried out on larger carbon fullerene molecules[5]. Ionisation of soot has been shown to be important in the process of soot formation [6] and study of ionisation directly contributes to the modelling of soot formation[7]. The effect of soot ionisation has also been applied to soot detection [8].

This ionisation process can be used to determine the morphology and physical properties of soot aggregates. High resolution TEM images of soot particles show hollow primary particles consisting of fractured graphene-like fragments[9, 10]. These primary particles, when promptly abstracted from flames, are made up of large chains of primary particles bound by tens to hundreds of carbon atoms across graphite like planes. It is a reasonable hypothesis that these 'bound' primary particles have bond strengths of order of 35meV per atom, as compared to a typical C-C bond strength in a graphene-like layer of order of 1.5 eV[11]; because hundreds of carbon atoms constitute the fusion points on the primary particles [10] these are likely to be held by a strength of order 3-30 eV. These chains may then condense or aggregate in the post flame or exhaust as aggregates, weakly bound by van der Waals forces. This study is aimed at elucidating the binding forces between primary particles and soot aggregates, which will lead to better understanding of the morphology of soot aggregates and primary particles.

2 Method

The experiment was conducted in a vacuum chamber and carbon particles were introduced through a series of aerodynamic lenses. An intensified charge-coupled device (ICCD) camera was used to record the signal from soot particles heated by the laser beam from a R4-25 400W continuous wave fibre laser at a wavelength of 1070nm. The carbon particles were produced by an aerosol generator with black toner mixed with water, driven by compressed air.

Figure 1 shows the experimental setup. The carbon black was then passed through the laser beam and a pair of metal plates with a high potential difference between them. This distorted the fragmentation pattern as the ionised particles were attracted to one of the plates. This provided information on charge/mass ratio of the particles.

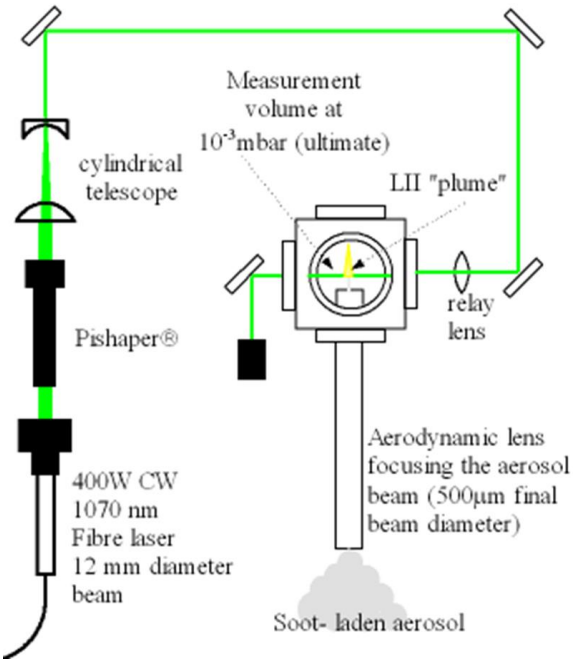


Figure 1 *Experimental setup showing the laser path and measurement volume.*

3 Results and Discussion

This study has shown that soot aggregates under high intensity laser pulses undergo a two stage "explosion", the first of which is presumbed to be the weaker force holding the aggregates together and the second is the fracturing of the individual, tightly packed graphite layers of the primary particles. The velocities and direction of this fragmentation can be seen in Figure 2. This fragmentation of the particles is caused by the ionisation of carbon under the laser field with the ejection of electrons, causing the positively charged carbon molecules to repel each other and fragment.

For a comparatively large particle subjected to the laser field, this produces many electrons locally. In the vicinity of the particle there is likely to be, effectively, a weak plasma which interacts with and absorbing light. This has been shown in this study where a continuous wave laser and the continued energising of carbon particles eventually blocks any signal being detectable by the ICCD camera.

Along with the current findings, this study will perform the study of carbon aggregates and primary particles in a laser field and subjected to an electric field. The trajectory of fragments of carbon can be recorded and compared with a second set of trajectories when the fragments are subjected to the electric field. The difference between these trajectories, along with the known strength of the electric field, can be used to determine the Coulombic forces in the soot aggregates and primary particles, the temperature threshold for the ionisation and the mass/charge ratio for the particles. With this information, a model on this laser induced soot aggregate ionisation can be devised.

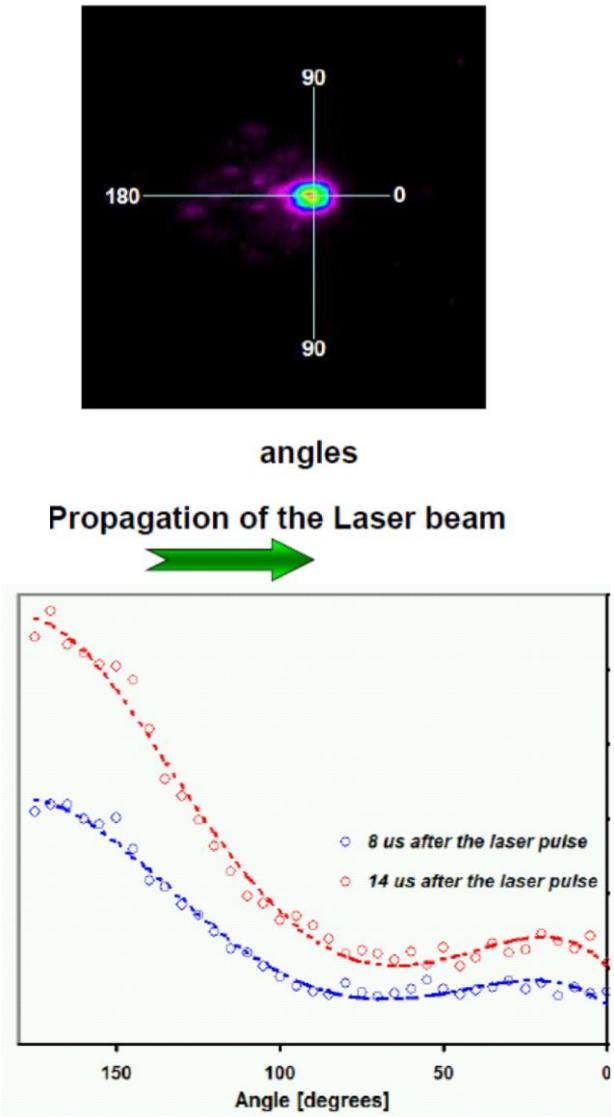


Figure 2 *Explosion velocities from a dual sequenced images, measured using particulate image velocimetry (PIV).*

4 Acknowledgement

C.H. thanks the EPSRC for the award of a CASE studentship.

5 References

[1] Beyer, V. and D. Greenhalgh, Laser induced incandescence under high vacuum conditions. Applied Physics B, 2006. 83(3): p. 455-467.

[2] Langmuir, I., The Effect of Space Charge and Residual Gases on Thermionic Currents in High Vacuum. Physical Review, 1913. 2(6): p. 450-486.

[3] Joachain, C.J., N. J. Kylstra, and R.M. Potvliege., Atoms in Intense Laser Fields2011: Cambridge University Press.

[4] Jaroń-Becker, A., A. Becker, and F.H. Faisal, Ionization of N 2, O 2, and linear carbon clusters in a strong laser pulse. Physical Review A, 2004. 69(2): p. 023410.

[5] Johansson, J., et al., Anisotropic hot electron emission from fullerenes. The Journal of Chemical Physics, 2012. 136(16): p. 164301.

[6] Smyth, K.C. and W. Gary Mallard, Laser-Induced Ionization and Mobility Measurements of Very Small Particles in Premixed Flames at the Sooting Limit. Combustion Science and Technology, 1981. 26(1-2): p. 35-41.

[7] Balthasar, M., F. Mauss, and H. Wang, A computational study of the thermal ionization of soot particles and its effect on their growth in laminar premixed flames. Combustion and flame, 2002. 129(1–2): p. 204-216.

[8] Manzello, Samuel L., Eui J. Lee, and George W. Mulholland, Use of laser-induced ionization to detect soot inception in premixed flames. Applied Optics, 2005. 44(24): p. 5105-5111.

[9] Apicella, B., et al., Soot structure by high resolution electron transmission microscopy (HR-TEM) image analysis: current potentialities and perspectives.

[10] Vander Wal, R.L., Soot Nanostructure: Definition, Quantification and Implications, 2005, SAE International.

[11] Benedict, L.X., et al., Microscopic determination of the interlayer binding energy in graphite. Chemical Physics Letters, 1998. 286(5–6): p. 490-496.

Fine Particles Sampling of Light-Scattering Laser Photometer and Air Sampler with Impaction Sizer

C-H HUANG* and Y-Y CHANG

Department of Environmental Engineering and Health, Yuanpei University, Hsinchu, 300, Taiwan

*Corresponding author: chhuang@gm.ypu.edu.tw

Abstract

In this study, the fine particle concentrations by the light-scattering laser photometer and air sampler with impaction sizer were sampling in the field. The particle capture efficiency of the impaction sizer were examined first due to the particle capture efficiency of impaction sizer in the air sampler is important for fine particles sampling. This study used the tested particles and the aerodynamic particle sizer to measure the particle capture efficiency of the impaction sizer. Results show that the particle capture efficiencies of the impaction sizer with foam material of 9mm thickness are higher than those with of 3mm foam material for the jet diameter of 10mm. The numerical results of the particle capture efficiencies of the impaction sizer will compare with those of the experimental data. The fine particle concentrations obtained using the light-scattering laser photometer will be compared to those of air sampler with the impaction sizer.

1 Introduction

The light-scattering laser photometer is a portable monitor for measuring fine particle concentrations in different air environments. Several studies pointed out that the particle concentrations by the light-scattering laser photometer were higher than those by the manual method [1,2]. The concentrations of respirable particulates were measured using the light-scattering laser photometer and a gravimetric method in the indoor environment. Results also showed that the particle concentrations of the light-scattering laser photometer were high correlated with the Federal Reference Method [3]. Their results reported that the particle concentrations by the light-scattering laser photometer were found to be about twice as high as those of air sampler. In addition, the relationships between particle concentrations from a beta gauge monitor and by the light-scattering laser photometer were evaluated at different ambient environments [4]. The results indicated that the fine particle concentrations of the light-scattering laser photometer were higher than those of the beta gauge monitor, whenever the inlet heater of the beta gauge was turned on or off. The particle concentrations of the adjusted light-scattering laser photometer were compared to those of the beta gauge monitor. Results showed that the estimated concentration measurements by the adjusted light-scattering laser photometer can be recalibrated to improve the accuracy of the particle concentrations. Beside, studies have pointed out that collection plat coated with oil in the impaction sizer can keep the particle capture efficiency of the impaction sizer. The collected particles were accumulated on the grease material till long-time loading conditions. Thus, foam impaction sizer has been applied for the fine particles sampling. The impaction sizer with foam substrate inside the air sampler has the characteristics of reducing particulate rebound effect. Its particulate capture efficiency curve does not follow the steep theoretical curve. The particle capture efficiencies of the impaction sizer with larger thickness were found to be higher than those with smaller thickness [5]. In this study, the particle capture efficiency of an impaction sizer were studied experimentally first. Numerical methods will be also used to obtain the particle capture efficiency of the impaction sizer. This work attempts to compare the fine particle concentrations obtained using the light-scattering laser photometer to those of air sampler with the impaction sizer.

2 Methods

Liquid particles were generated by using an ultrasonic atomizing nozzle. An aerodynamic particle sizer was used to measure the aerosol number concentrations at the inlet and outlet of the impaction sizer to test the particle capture efficiency. The flow field in the impaction sizer was then simulated by solving the Navier-Stokes equations in the cylindrical coordinate. The governing equation was discretized by means of the finite volume method. After obtaining the flow field, the particle equations of motion were solved numerically to obtained particle capture efficiency of the impaction sizer. The light-scattering laser photometer and the air sampler with impaction sizer were collocated on a laboratory room to compare the fine particle concentrations. The photometer and the air sampler were placed at about 1.5m above the floor to determine fine particle concentration. The components of the air sampler include an impaction sizer with foam substrate and filter.

3 Results and discussion

In this study, the particle capture efficiency of the impaction sizer were studied experimentally first. Foam substrates were used as the collection material of the impaction sizer with different thicknesses. Foam porosity

of the impaction sizer is 100ppi. Figure 1 displays the particle capture efficiency of the impaction sizer for various jet diameters and foam thicknesses. Results demonstrate that the particle capture efficiencies of the impaction sizer with foam material of 3mm thickness are lower than those with foam material of 9mm thickness for jet diameter of 10mm. Findings also show that the particle capture efficiencies of impaction sizer with foam material decrease as the aerodynamic particle diameter decreased.

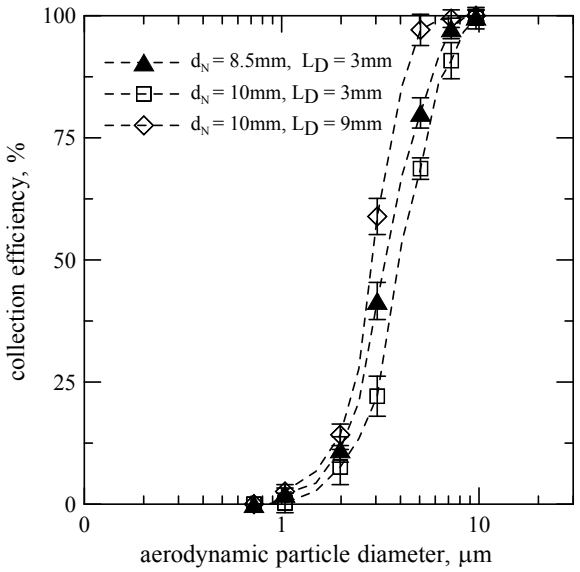


Figure 1 *Particle capture efficiency of impaction sizer for different conditions.*

The particle capture efficiencies of the impaction sizer using the foam material are higher than those of the flat substrate. In addition, the cut-size of the impaction sizer with foam material for the jet diameter of 8.5mm is found to be smaller than those with foam material of 3mm thickness for the jet diameter of 10mm at same flow rate. This study will perform the numerical calculations for the particle capture efficiencies of the impaction sizer with the foam material. The numerical results of the particle capture efficiencies of the impaction sizer will compare with those of the experimental data. The fine particle concentrations from the light-scattering laser photometer will be compared to those of air sampler with the impaction sizer.

4 Acknowledgement

The authors would like to thank the National Science Council of the Republic of China, Taiwan, for partly supporting this research.

5 References

[1] Yanosky, J.D., Williams, P.L., MacIntosh, D.L.A., Comparison of two direct-reading aerosol monitors with the Federal reference method for PM2.5 in indoor air, Atmos. Environ. 36:107–113 (2002)

[2] Tung, T.C.W., Chao, C.Y.H., Burnett, J., A methodology to investigate the particulate penetration coefficient through building shell, Atmos. Environ. 33:881–893 (1999)

[3] Niu, J., Lu, B.M.K., Tung, T.C.W., Instrumentation issue in indoor air quality measurements: the case with respirable suspended particulates, Indoor Built. Environ. 11:162–170 (2002)

[4] Huang, C. H., Tai, C. Y., Improving estimation of real-time concentration for inhalable particles<10μm from a light scattering monitor, Journal of Environmental Science and Health, Part A, 45:332-338 (2010)

[5] Huang, C. H., Lin, Y. C., Influence of substrate porosity and thickness on the collection efficiency of an impactor stage, Journal of Aerosol Science, 41:364-372 (2010)

Aerosol optical and microphysical properties retrieved from combination LIDAR with Sun/sky photometer: Preliminary results over Lille

Valentyn BOVCHALIUK [1,*], Thierry PODVIN [1], Augustin MORTIER [1], Philippe GOLOUB [1], Oleg DUBOVIK [1], Didier TANRE [1], Igor VESELOVSKII [2], Stéphane VICTORI [3]

[1] Laboratoire d'Optique Atmosphérique, Université de Lille 1, Villeneuve d'Ascq, 59650
[2] Physics Instrumentation Center, 142190, Troitsk, Moscow, Russia
[3] Cimel electronics, Paris, 75011, France

*Corresponding author: valentyn.bovchaliuk@ed.univ-lille1.fr

Abstract

In December 2013, a multiwavelength elastic (|| and _|_) and RAMAN LIDAR (LILAS: Lille Lidar AtmosphereS) has been assembled and started regular observation in LOA atmospheric platform located in Lille with the main objective to improve aerosol characterization in various atmospheric conditions. We present both the characteristics of this new instrument, the first data and data processing methodologies used to invert aerosol properties from the combination of LIDAR and sun/sky photometer (BASIC and GRASP-GARRLIC approaches).

1 Introduction

Many atmospheric stations have vertical sounding capabilities thanks to LIDAR system. LOA atmospheric station, located in the Campus of University of Lille 1, is one of them, thanks to vertical soundings performed, since 2006, on a routine basis [1]. Several studies have demonstrated the relevance to combine sun/sky photometer and LIDAR observation to monitor aerosol characteristics [1,2]. In LOA station, both automatic sun/sky photometer and automatic elastic back-scattering CAML (Cloud Aerosol Micro Lidar, one wavelength 532 nm) are operated for long time. However, recently (December 2013), LILAS, a multiwavelength and Raman LIDAR has been assembled in the framework of a cooperation between PICS (Russia), CIMEL-Avanced monitor SME and LOA and started regular observation. Lille atmosphere is mainly composed of urban and industrial aerosols. However, biomass burning particles (Canada) and mineral dust particles (Sahara region) events are detected several times a year thanks to LIDAR observations. Volcanic ash particles have been rarely detected with the noticeable exception in 2010. Nevertheless the amount and accuracy of the height-dependent aerosol properties remain limited due the reduced amount of information provided by mono-wavelength CAML. For this reasons LOA recently setup a more powerful LIDAR system to enable measurement of more relevant aerosol parameters such as fine/coarse modes, LIDAR ratio and single scattering albedo vertical distributions. In this paper, we present LILAS main characteristics, as well as the methodology to retrieve aerosol optical and microphysical properties in under cloud free conditions or in the vicinity of cloud.

2 Instrumentation

LIL S presented in Figure. 1 was designed for more precise observation. LILAS has 9 wavelengths – 3 Raman, 3 elastic and 3 depolarized. Pulse energy for all emitting wavelengths is close to 100mJ. More LILAS's characteristics are presented in Table 1.



Figure 1 *LILAS system (telescope, LASER, RADAR and acquisition system).*

Energy(1064/532/355 nm)	100/100/100 mJ
Pulse Width	5-8 nsec
Divergence	0.5 mrad
Beam Diameter after	50 mm
Beam Pointing	100 ± μrad
Rate repetition	20 Hz
Telescope Newton	0.4 m
Range resolution	7.5 m
Elastic scattering	355, 532, 1064 nm
Nitrogen Raman Scattering	387, 608 nm
Raman Scattering water wapor	408 nm
Depolarisation channels	532, 355, 1064 nm

Table 1 *Instrument characteristics*

3 Methodology and preliminary results

Our methodology is based on the use of the coincident measurements from LIDAR (single or multiwavelength irradiances) and sun/sky-photometer (spectral Aerosol Optical Depth (AOD) and radiances). Two codes have been considered in our study to process LIDAR data. First of them called BASIC [1] is based on Klett method constrained by sun-photometer AOD and provide aerosols extinction profile at 532 nm and an effective LIDAR ratio. In this case, spectral angular radiances measured by the sun/sky photometer are not used.

For inverting simultaneously all measurements performed by LIDAR and sun/sky photometers GARRLiC (Generalized Aerosol Retrieval from Radiometer and Lidar Combined data) code has been recently developed [2]. In this case, a set of aerosol parameters describing both columnar and vertical aerosol properties are derived. Depending on the available technologies (single or multiwavelength LIDAR) and observation scenario (AOD and/or sky radiance), different aerosol properties can be derived. For example, if LIDAR operates only at one wavelength then, using the entire measurements provided by sun/sky-photometer, vertical distribution of coarse and fine mode particles cannot be retrieved. Conversely, when multiwavelength LIDAR measurements are performed (355, 532 and 1064 nm) vertical distribution of coarse and fine mode particles but also vertical distribution of single-scattering albedo, LIDAR ratio can be retrieved.

In our preliminary work both BASIC and GARRLiC are used only for elastic channels but, in the future, the 2 Raman channels and 3 depolarized channels (355, 532 and 1064nm) will be accounted for in the retrieval scheme.

3.1 Preliminary results

During the initial setup phase (December 2013 – April 2014) LILAS system operated in Lille station with only 2 elastic channels (355 and 532 nm) including additional depolarization measurement at 355 nm. Time series of extinction (532nm) and Angström exponent (355/532) inverted following BASIC approach are presented in Figures 2 and 3. The data have been acquired at the beginning of February 2014 (4th). The atmosphere was cloud-free from 9 to 10:30 UTC, average AOD at 532 nm and Angström exponent around 0.08 and 0.3 (440/870) respectively, according to sunphotometer measurements (AERONET). Moreover, the AERONET size distribution retrieved at 9h is dominated by coarse mode particles which is consistent with the low Angström exponent measured by the sunphotometer. In cloud free condition LIDAR ratio varied between 20 and 55 sr and mean value equal 33 sr (Figure 4). It corresponds maritime particles or less absorbing urban particles [3]. Backtrajectory analysis shows that air mass came from Atlantic ocean cross North coast of France.

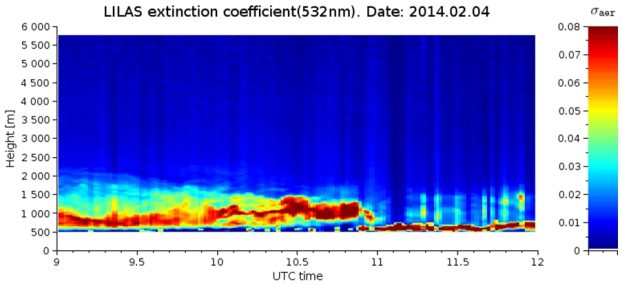


Figure 2 *Time series of aerosol extinction coefficient (km-1) at 532 nm for 04/02/2014 (LILAS).*

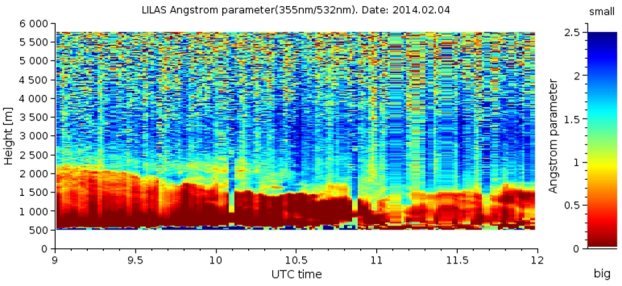


Figure 3 *Time series of aerosol Angström exponent (355/532 nm) for 04/02/2014.*

Aerosol vertical profiles show that aerosols are all located in the boundary layer (<1500m). The vertical profile of the Angström exponent (<0.5 for altitude below 1000 m) clearly indicates domination of coarse particles in the boundary layer. This result is in agreement with the columnar value measured by the sunphotometer.

Additionally, we observed a good agreement between extinction measured by LILAS and CAML, both data inverted with BASIC algorithm [4].

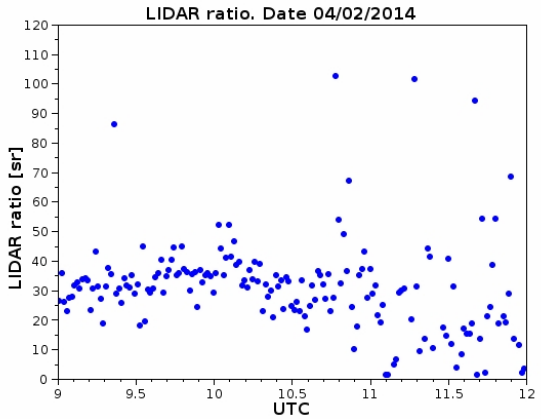


Figure 4 *Time series of retrieved LIDAR ratio at 532 nm for 04/02/2014.*

3.2 Data processing with GARRLiC

As mentioned above, GARRLiC algorithm inverts coincident LIDAR and sunphotometer (AOD and sky radiances) observations. Both data types enhance information about each other, LIDAR improve sensitivity to the columnar properties and photometer observation derive amount and type of aerosol. GARRLiC code is a

part of GRASP (Generalized Retrieval of Aerosol & Surface Properties) project [5]. GRASP is the general code for processing ground-based and satellite measurements and their combination. Although GARRLIC is designed for processing multi-wavelength LIDAR data, it can also be used for processing mono-wavelength CAML LIDAR and AERONET data. Example of results is presented on Figure 5.

Measured and inverted LIDAR signals show good agreement. But for separation coarse and fine modes of particles needed LIDAR observations from three wavelengths. Analysis of various atmospheric conditions (clear sky, polluted and near cloud situations) from CAML and LILAS instruments will be presented during the conference.

4 Conclusion / perspectives

First results of LILAS were shown. The instrument is designed to provide detailed information on aerosols in various conditions. Several numerical inversion codes were used to retrieve aerosol properties. Preliminary analysis is shown here. Both inversion codes and instrumentation will be implemented. There are ongoing development GARRLIC methodology that will use a larger set of observations and will retrieve altitude dependent parameters such as LIDAR ratio, concentrations of coarse and fine mode particles, extinction and backscatter coefficients, single scattering albedo, size distribution as well as all column integrated properties like the ones provided by the current AERONET inversion scheme.

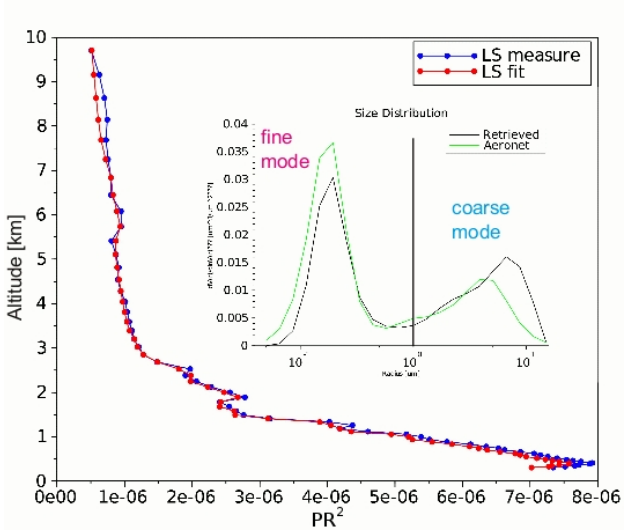


Figure 5 *CAML retrieval of LIDAR signal (blue – measurements; red – retrieved) and size distribution (green – AERONET retrieval without LIDAR data, black – retrieval with CAML LIDAR data) by GARRLiC algorithm for 07/07/2013.*

In the near future, LILAS observations will contribute to ORAURE national observatory (http://www.icare.univ-lille1.fr/drupal/?q=/oraure/) and to EARLINET-ACTRIS in the coming years. LILAS will be deployed during several field campaigns in 2014 (China, Beijing) and 2015 (Senegal, Dakar) in the Framework of CaPPA (http://labex-cappa.univ-lille1.fr/).

5 Acknowledgement

This study supported by Labex CaPPA, ACTRIS European project (http://www.actris.net/). Authors are very grateful AERONET (http://aeronet.gsfc.nasa.gov/), Service d'Observation PHOTONS teams and NOAA HYSPLIT Air Ressource Laboratory model (http://ready.arl.noaa.gov/HYSPLIT.php).

LIDAR data can be seen at http://www-loa.univ-lille1.fr/Instruments/lidar/fr/index.php.

6 References

[1] A. Mortier et al., Detection and characterization of volcanic ash plumes over Lille during the Eyjafjallajokull eruption, Atmos. Chem. Phys. Discuss., 12, 31031–31070, 2012.

[2] A. Lopatin et al., Enhancement of aerosol characterization using synergy of lidar and sun-photometer coincident observations: the GARRLiC algorithm, Atmos. Meas. Tech., 6, 2065–2088, 2013.

[3] Claus Weitkamp, Lidar: range-resolved optical remote sensing of the atmosphere, (Springer series in optical sciences, 2005).

[4] V. Bovchaliuk et al., Aerosol properties in cloudy environment, 1st CaPPA scientific meeting, Lille, January 2014.

[5] http://grasp.catalysts.cc/

In Situ Individual Aerosol Particle Composition: Combining IR Spectroscopy and Coherent Heterodyne Scattering

Jay EVERSOLE[1],*, Brian SAAR[2], David WOLINSKI[2], Adam SHABSHELOWITZ[2], Matthew HART[1] and William HERZOG[2]

[1] Naval Research Laboratory, Washington, DC, 20375, USA
[2] Lincoln Laboratory, City, Postal Code, Country

Corresponding author: jay.eversole@nrl.navy.mil

Abstract

Optical interrogation offers the possibility of rapid characterization of individual suspended aerosol particles. However, a general method for determination of particle composition has remained elusive. Infrared (IR) absorption spectroscopy has become a widely accepted analytical tool for chemical identification and material characterization for a broad range of bulk gas, liquid and solid samples. However, application of this spectroscopic method to aerosol particle analysis faces a couple of main obstacles. First, IR illumination in commercial instruments is typically a broadband continuum extended source, such as a glow-bar. Interrogation of individual aerosol particles will require both high fluence and tight focus that only a laser source can provide. Both rapidly tuneable and broadband laser light sources in the IR spectral region are starting to make their appearance. Therefore, the near-term possibility of applicable IR laser sources suggests the feasibility of direct IR characterization of airborne particles. Second, a more fundamental impediment is that determining absorption by measuring incident beam attenuation becomes invalid for highly turbid or heterogeneous samples including single particles for which attenuation of the incident radiation may be dominated by scattering rather than true absorption.

In the LIP2012 conference we introduced a new approach using spectral scattering signatures from individual aerosol particles as a means to acquire a IR spectrum that is dominated by material properties rather than particle properties. The connection between radiation absorption and scattering comes through the complex refractive index of the particle material in which the real and imaginary parts must conform to the Kramers-Kronig spectral relationship. Therefore, the total scattering cross section of a particle of a given material will necessarily go through a characteristic spectral oscillation whenever an absorption peak of the material occurs. This is shown schematically in Figure 1 in which a hypothetical Lorentzian absorption peak is generated over a wavelength range from 7 to 10 microns in the top graph, and the resultant real refractive index is computed as shown in the second graph. The bottom (third) graph shows the integrated scattered light intensity from a spherical particle (using Mie theory) for the optical arrangement shown in Figure 2 in which forward scattered light is collected over a symmetric azimuthal angular range (0–2π) for scattering angles between 5 and 17 degrees.

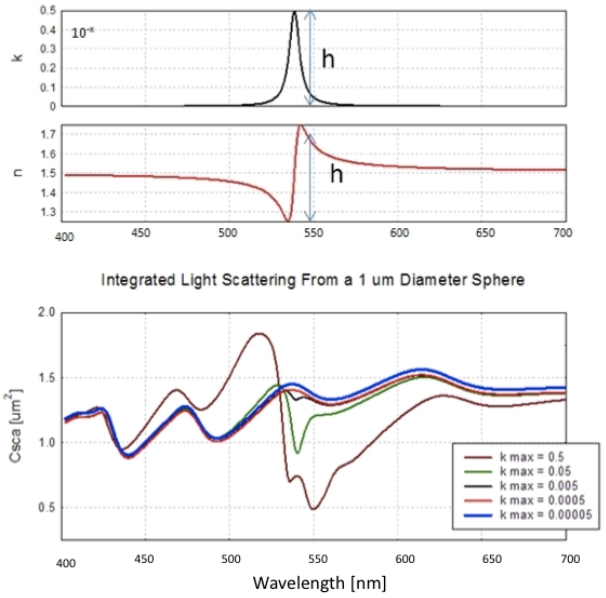


Figure 1 *An absorption resonance peak in the imaginary part of the refractive index (top graph) is associated with a change in the real refractive index (middle graph), and can be observable in elastic scattering cross section (bottom graph).*

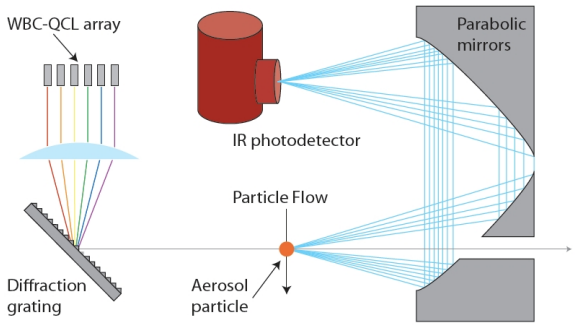


Figure 2 *A schematic diagram of multiple wavelength-beam-combined (WBC) incident QCL light on single aerosol particles and collected forward scattering.*

One can readily see that the integrated scattered light follows the real refractive index closely, so that this type of measurement could be used to infer an absorption peak position and width. We showed data using an array composed of eight commercially available quantum cascade lasers (QCLs) at specific wavelengths in a range from 7 to 11 micrometers to provide a course IR spectrum.

Using this arrangement, we have demonstrated an ability to differentiate aerosol particles based on the absorption profiles of their material composition[1].

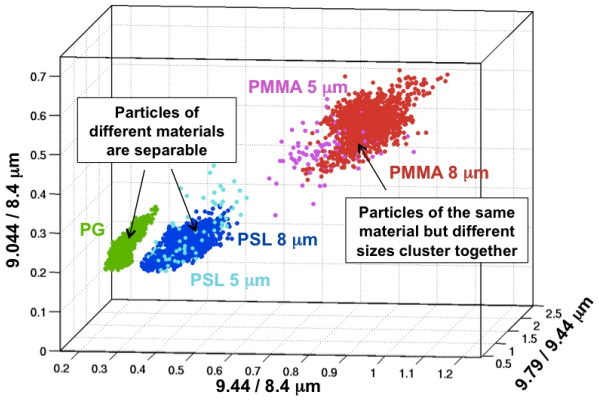


Figure 3 *Scattered light intensities from 3 aerosol samples: polymethylmethacrylate (PMMA), propylene glycol (PG), and polystyrene latex (PSL) in terms of 3 wavelength ratios*

As an example, Figure 3 shows data from different samples of aerosol particles, shown in different colors in a 3-dimensional plot where the axes are ratios of scattering intensities from three different wavelengths. In this scatter plot example, individual particles are represented as separate data points. For this set of samples one can see that data of each sample material clusters tightly and is distinct from others, while for particles of different size, but the same material, their data clusters overlap. Clearly, classification of aerosol particles would normally be performed computationally with a full set of scattering data from all eight of the QCL wavelengths, but we used only the three ratios carrying the most information for the purposes of visual illustration. In practical application, we envision aerosol particle classification based on validated training sets to search for materials of interest. The eight QCL wavelengths that were chosen were placed throughout the mid-IR spectral region, but as technology improves we anticipate the possibility of increasing the number of wavelengths and hence, increased spectral resolution and identification capability.

In the past year, there have been many practical and technical hurdles that have needed to be addressed to improve the feasibility and practicality of this approach. One of the most significant changes since our original design has been development of coherent heterodyne signal detection from the particle scattering. In our original demonstration, direct scattered light intensities were measured from each QCL, which required time-multiplexing the QCL array. Using an interferometric optical arrangement, each of the different wavelength lasers can be frequency modulation at a distinctive (MHz band) modulation tone. This permits all of the array lasers to be operated simultaneously with a single photo-detector. In addition, the weak scattering intensity from a single aerosol particle is now amplified by mixing with the reference beam, so that an improvement in the signal-to-noise ratio of about a factor of 100 is also realized. In optimizing the optical design with regard to aerosol particle interrogation, there are a significant number of trade-offs that must be determined. For example, the throughput of the instrument can be increased only at the expense of signal-to-noise. The complexity of these considerations was sufficient, that a detailed computational model was constructed that starts with a Monte Carlo approach to picking aerosol particles out of a range of sizes and trajectories, and computes the spatially dependent illumination, scattering and coherent mixing based on the specific optical train using ray tracing, in order to predict the signal intensities. This model is being used to optimize the optical design and flow velocity of the next iteration of the aerosol IR spectrometer. This presentation will discuss the latest results and progress of the new method for single aerosol particle IR scattering spectroscopy.

Acknowledgement

We gratefully acknowledge the Defense Threat Reduction Agency (DTRA) Joint Science and Technology Office (JSTO) for their support.

References

[1] Brian Saar, David Wolinski, Jason Jonga, Matt Hart, Jay Eversole and William Herzog, Infrared elastic scattering spectroscopy of individual aerosol particles (Electromagnetic and Light Scattering XIV 2013 (ELS-2013), paper C1-5, 17- 21 June, Lille, France, 2013.

Conformable Organic Photo Sensors for Particle Systems Chacaterization

Matthias SENTIS[1], Fabrice R.A. ONOFRI[2], Fabien CHAUCHARD[3], Olivier DHEZ[4], Jean-Yves LAURENT[5]

[1] Aix-Marseille University, CNRS, IUSTI, UMR 7343, 13453 Marseille, France
[2] INDATECH, 34730 Prades-le-Lez, France
[3] ISORG, Minatec, 38040 Grenoble Cedex 09, France
[4]LITEN, CEA / Grenoble, 38054 Grenoble Cedex, France,
Corresponding author: fabrice.onofri@univ-amu.fr

Abstract

The interest of organic photo sensors to develop efficient, cost effective and complex photo sensitive geometries is investigated with the aim, *in fine*, to propose innovative optical particle and particle systems characterization methods. These investigations are carried out with Monte Carlo simulations as well as laboratory experiments.

1 Introduction

According to all experts OLED (organic light-emitting diode) technology is close to fully revolution the lighting sector. While lesser-known and developed, the technology of Organic Photo Sensors (OPS, eg. [1]) is also rapidly developing with promises of bringing totally new solutions for our day-to-day life, for manufacturing process control as well as for scientific instrumentation.

Metal-semiconductor photodetectors (Si, GeSi, PbSn,...) offer fast and high sensitivity responses over a large electromagnetic spectrum [2]. Nearly all sensors (APDs, photomultipliers, CCD or C-MOS sensors) currently in use for particle systems and flow diagnoses are based on Silicon since the latter offers the best performances in the visible range. However, the production of Silicon photo sensors with large, complex-shaped and multiple photosensitive area(s) is delicate and extremely costly. The aforementioned limitations of the metal-semiconductor technology are connected, among other reasons, to the complex manufacturing process of the wafers as well as their crystalline structure and mechanical properties.

On the other side, with organic photo sensors obtained by a fully inkjet-printed process, one can expect to produce, on demand, and for a reasonable price, arbitrary sized and shaped photosensitive areas. Furthermore, these plastic-like photosensitive films are conformable, so that they can be bent, without a significant loss or performance, down to curvature radiuses of few centimetres. Hower

In this communication, we present the work conducted by a French industry/academic consortium, called OPTIPAT, to develop innovative OPS based light scattering methods to characterize [3-4] dilute to dense particle systems encountered in industrial processes and laboratory experiments.

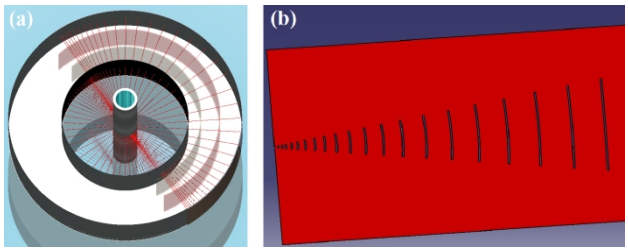


Figure 1 *Schematic of an (a) OPS based Multi-Angle Light Scattering (MALS, or nephelometer) system for the characterization of particles flowing inside a cylindrical spectrophotometer cell; (b) Exemplify design of an OPS.*

2 Material and method

At this step, and for confidentiality reasons, little can be said on the photosensitive and electronics characteristics of the OPS under development. However, in few words, they are comparable to those of Silicon technology, except that the response time of organic sensors is far inferior (about tens of millisecond).

A Monte Carlo type code was developed to evaluate and optimize the response of OPS when recording the scattering diagrams of particle systems inside a cylindrical spectrophotometer cell, see Figure 1 (a). To fully take advantage of the conformable capabilities of OPS, optical lenses are replaced by, and modelled as, pinhole lenses and curved slits grouped on a thin optical mask, see Figure 1 (b). The latter mask was optimized for the sizing of small to intermediate size particles (D=0.5-50µm) from the analysis of the asymmetry parameter (e.g. [3-4]). This Monte Carlo code allows taking account and investigating many effects of interest like, among other things: the laser beam profile, dimensions and inclination; the contributions of higher order rays and internal reflections within the cylinder; the effect of the cylinder curvature on extinction measurements; the angular resolution of the system and the validity of the remote sensing approximations; the effective probe volume characteristics, multiple scattering effects (e.g. [5]), etc.

To validate our numerical tools and models as well as the concept of the proposed methods, an experimental setup was developed and tested on various particle

systems ranging from colloidal suspensions to gas-solid particulate systems.

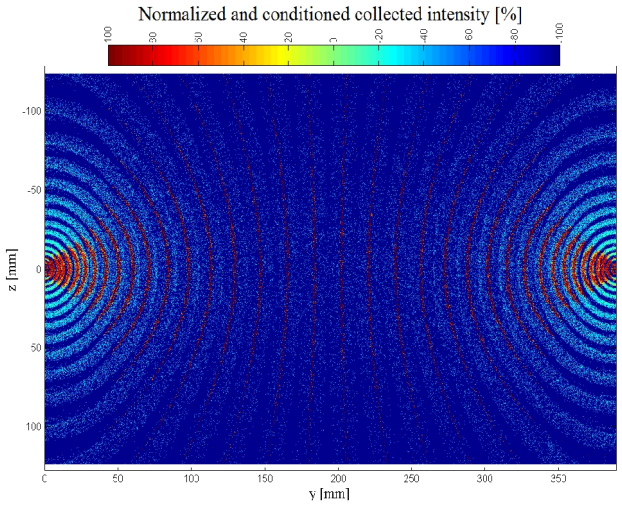


Figure 2 *Monte Carlo simulation of the normalized distribution of virtual photons scattered by an optically dilute aqueous suspension of silica nanoparticles within a cylindrical spectrophotometer cell. This 2D map corresponds to the detection cylinder unfolded - when cylindro-conic slits are used to control the angular resolution of the system. The red and dark blue areas indicate where the nominal angular resolution is satisfied and where the photons are totally filtered out.*

3 Results and discussion

Figure 2 shows a typical scattering intensity map corresponding to photons that have successfully passed through a geometrically optimized optical mask and that were collected onto an OPS film folded around a cylindrical cell. For understandable reasons, the intensity map is numerically unfolded onto a 2D plan. The red areas correspond to regions where the collected photons satisfy the desired angular resolution of cylindro-conic to circular shaped photosensitive areas (see Figure 1 b).

By varying the shape and height of the photosensitive areas, one can decrease by several orders of magnitude the dynamics of the collected signals. Extensive simulations show that with actual OPS printing technology, an angular resolution of ±1° throughout the full angular range is easily achievable for a reasonable size of the whole system. One other key advantage of OPS is that they allow covering large angular ranges. Figure 2 presents numerical predictions for the evolution of a light scattering intensity based ratio (R) that is highly sensitive to the mean diameter (D) of log-normal particle size distributions (PSD). Basically, R is the ratio of the average intensity collected in the first rainbow region over the intensity collected near the forward diffraction zone. A rather good agreement is found between Lorenz-Mie Theory (LMT) and the Monte Carlo model, which both predict a simple power law relation between R (quantity to be measured) and D (quantity to be determined). However, the Monte Carlo simulations account for many effects that are neglected by LMT based model: arbitrary laser beam shape and position, sensors photosensitivity, shape and near-field location, false reflections at the pipe interfaces and between the particles, etc. In fact, the agreement find here is the result of a long optimization process of essentially three key parameters: the laser beam waist, OPS and optical masks distances and shapes. Nonetheless, the LMT based model allows faster and more cost effective estimation of D. In fact, the Monte Carlo calculations, which are really more time consuming, should be reserved to improve the final resolution on the PSD parameters.

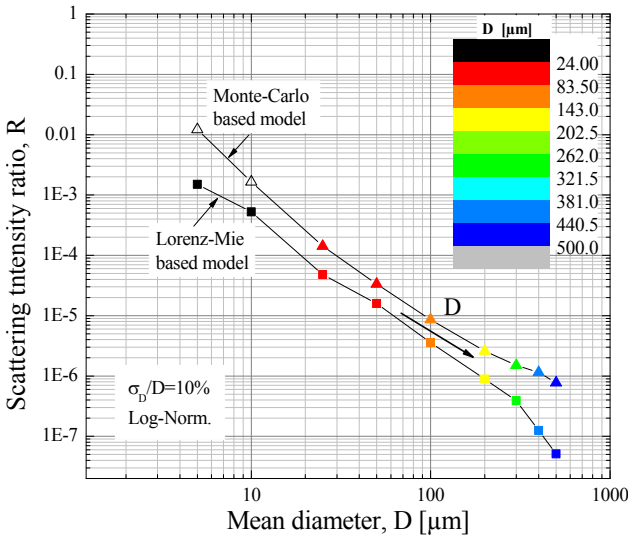


Figure 3 *Numerical predictions for the evolution of a particular light scattering intensity ration (R) versus the mean diameter of an optically dilute flow of glass beads.*

4 Acknowledgements

This work was partially funded by OSEO, the CG13 and PACA, under the grant FUI-AAP12 "Optipat".

5 References

[1] Bass M. et al (Ed), Handbook of Optics, Volume 1: Fundamentals, Techniques, and Design, Mac Graw-Hill, New-York (1995)

[2] Azzellino G., Grimoldi A., Binda M., Caironi M., Natali D., Sampietro M., Fully Inkjet-Printed Organic Photodetectors with High Quantum Yield, Advanced Materials 25(47):6829-33 (2013)

[3] Xu R, Particle Characterization: Light Scattering Methods, Kluwer Academic, Dordrecht, The Netherlands, 20012.

[4] Onofri F., Barbosa S., "Chapter II: Optical particle characterization", in "Laser Metrology in Fluid Mechanics", Boutier, A (ed.), ISTE Ltd and John Wiley & Sons Inc, London, 2012

[5] Onofri F., Bergounoux L., Firpo J-L., Mesguish-Ripault J., Velocity, size and concentration measurements of optically inhomogeneous cylindrical and spherical particles, Applied Optics 38(21):4681-4690 (1999).

An Improved Analysis of the Scattering Properties to the Half-Space Problem with Multiple Defect Particles for Optical Surface

Lei GONG[1,*], Zhen-Sen WU[2]

[1] School of Photoelectric Engineering , Xi'an Technological University, Xi'an, shaanxi 710021,China
[2] School of Science , Xidian University, Xi'an, shaanxi 710021,China

Corresponding author: zzgonglei@126.com

Abstract

Combing the practical situation of nondestructive examination, an improved analysis of the scattering properties to the multiple defect particles for optical surface are shown, such as the sphere, column or ellipsoidal particle in/below/inlay the optical surface. Based on the Finite Difference Time Domain(FDTD) method, the Generalized Perfectly Matched Lays (GPML) can work very well against the half-space problem about the optical surface and defect particles. The connect boundary condition is educed by three waves method. The reciprocity theorem is applied to near-far field extrapolation. The results are compared with Method of Moment (MOM) method firstly, both of which are identical very well. It proves the reliability of the method in this paper. Secondly, the angle distributions of double particles with different positions are shown. Some selected calculations on the effects of the size parameter and the sphere separation distance are described. The position factor as the most important factor is discussed particular. The theory and the model are valuable to inspect materials such as optical surface. In the optical nondestructive examination project, the defect position and shape can be diagnosed by the way.

1 Introduction

The optical system performance is directly influenced by the optical surface quality. Extracting effectively the defect characterization has important realistic value to improve the optical system efficiency. In order to meet the increasing requirements of high-quality optical system, the pure and roughness of optical surface has to be improved.

Light scattering is a powerful tool in optical surface quality control. The scattering sources such as particles above the surface or defects below the surface give rise to polarizations and scattering intensity that differ from those predicted by microroughness. It can help to derive some information about the defect particle such as sizes, materials, shapes and so on. With this goal in mind, a number of theories have been developed to predict the scattering by defects on or inlay surfaces:BV theory[1], null-field method(NFM) [2], discrete dipole approximation (DDA) [3], discrete sources method (DSM) [4]. Validation of those theories, however, has been carried out only in a limited number of cases, and the composite scattering field among the particles and the factor influence rules are not simulation and analysis. For this researchers from our group studied by the Finite Difference Time Domain(FDTD) method[5].Because the FDTD is applied directly to Maxwell equations, there has been a strong trend towards it in the last few decades. FDTD is a simple technique, because it does not require profound knowledge of Maxwell theory. It is based on simple mathematical operations, which can be handled even by very simple computers.

It is worthwhile to note that the theory and the numerical arithmetic described in this paper are applicable to the randomly distributed aggregated spherical particles whose radii are comparable to the incident wavelength, including aggregation particles statistically distributed in spatial coordinate such as soot aggregation particles.

2 Scattering model and half space FDTD method

2.1 Scattering model

In the optical system manufacture industry, many steps have been experienced such as deposit, polish and so on. During the procedures, multi-body defect particles with different position may be leaded-in. The multi-body defect particles are regarded as sphere in the paper for the length liminted(see Figure1.).

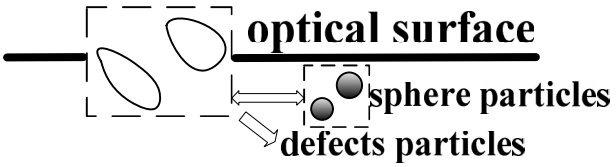


Figure 1 *Schematic view of defect particle with many shapes in different position*

2.2 Half space FDTD method

There are some half space problems in optics and electromagnetics which is based on upon or down space with different mediums. In the half space problem of the optical system manufacture, incident wave will produce reflectance and transmission wave. There are incident field and reflectance field in upon space. Transmission filed exist in down space. The method above is called three wave approach. Figure.2 shows the schematic of incident angle and azimuth angle geometry. The incident angle of wave is θ_i and ϕ.

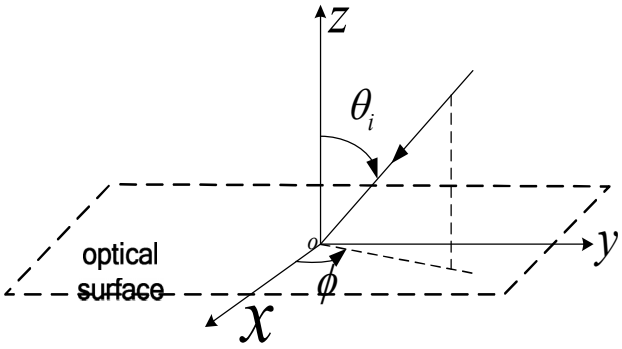


Figure 2 *Schematic of incident angle and zone azimuth angle geometry*

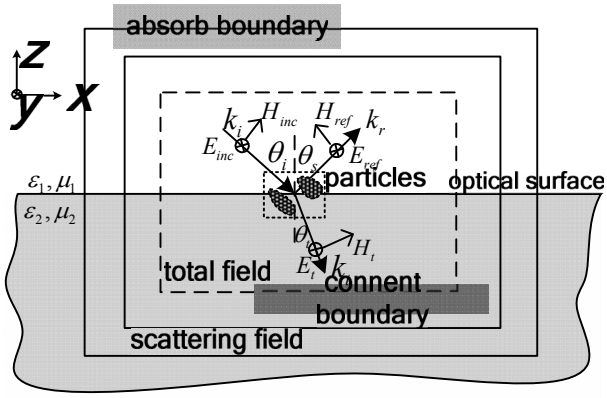


Figure 3 *Schematic of half-space scattering zone and field about s polarization light*

Fig.3 shows schematic of half-space scattering zone and field about s polarization light. The incident electric field can be written as $\overline{E}_{inc}, \overline{H}_{inc}$; the reflectance electric field as $\overline{E}_{ref}, \overline{H}_{ref}$;the transmission electric field as $\overline{E}_t, \overline{H}_t$; the scattering electric field as $\overline{E}_s, \overline{H}_s$ .The upon field can be obtained: $\overline{E} = \overline{E}_{inc} + \overline{E}_{ref} + \overline{E}_s$ and $\overline{H} = \overline{H}_{inc} + \overline{H}_{ref} + \overline{H}_s$ .The down field can be obtained: $\overline{E} = \overline{E}_t + \overline{E}_s$ and $\overline{H} = \overline{H}_t + \overline{H}_s$ .In the subsequent depiction, a time dependence of the form $exp(-i\omega t)$ is assumed and suppressed, where ω is the circular frequency. The incident field can be written as follows:

$$\vec{E}^{inc}(\vec{r}) = \left[E_{\perp}(\vec{r})\hat{s} + E_{\parallel}(\vec{r})\hat{p}\right] \quad (1)$$

The s polarization light will be analyzed in detail. The electric field and electromagnetic field will be decomposed along x,y,z axis. The decomposition variable can be expended as follows:

$$E_y^{i(p)}(\vec{r}) = E_{\perp} exp\left[i\left(k_{xi}x + k_{zi}z - \omega t\right)\right] \quad (2)$$

$$E_y^{r(p)}(\vec{r}) = R^p E_{\perp} exp\left[i\left(k_{xr}x + k_{zr}z - \omega t\right)\right] \quad (3)$$

$$E_y^{t(p)}(\vec{r}) = T^p E_{\perp} exp\left[i\left(k_{xt}x + k_{zt}z - \omega t\right)\right] \quad (4)$$

Where R^p and T^p represent the Fresnel reflection and transmission coefficient individually.

3 Numerical simulation and discussion

In this section, the results are compared with Method of Moment (MOM) method firstly, both of which are identical very well. It proves the reliability of the method in this paper.

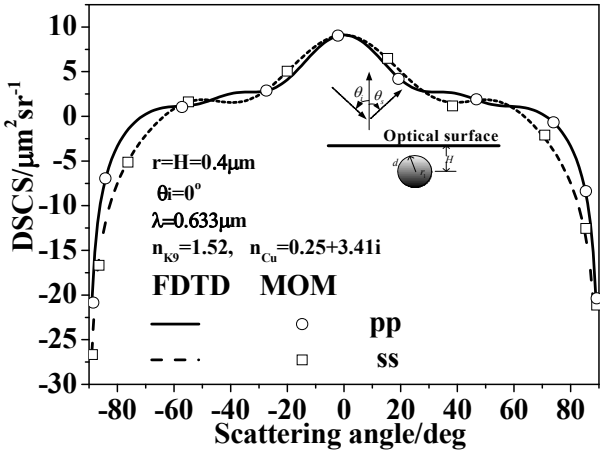


Figure 4 *Distribution of DSCS compared with that obtained by MOM method*

In addition, the angle distributions of double particles with different positions are shown. Some selected calculations on the effects of the size parameter and the sphere separation distance are described. The effect of size parameter will be derived. And the effective distance of composite scattering between two spheres will be researched.

4 Acknowledgement

We acknowledge support form the Natural Science Foundation of China(61308071 and 61172031), the Natural Science Foundation in Shaanxi Province of China (2013JQ8018) and the Special Natural Science Fund Projects in Shaanxi Province of China (2013JK0633).

5 References

[1] Germer T. A. and Asmail C. C., Goniometric optical scatter instrument for out-of-plane ellipsometry measurements, Review of Scientific Instruments 70(9):3688-3695 (1999)

[2] Mishchenko M.I., Videen G., Khlebtsov N.G., Wriedt T., Zakharova N.T., Comprehensive T-matrix reference database: a 2006–07 update. Journal of Quantitative Spectroscopy and Radiative Transfer109(8):1447-1460(2008)

[3] Karlsson A., He J. P., Swartling J., and Andersson-Engels S., Numerical simulations of light scattering by red blood cells, IEEE Trans. Biomed. Eng. 52(1):13–18 (2005)

[4] Eremina E., Light scattering by an erythrocyte based on Discrete Sources Method: shape and refractive index influence, Journal of Quantitative Spectroscopy and Radiative Transfer 110(14-16):1526–1534 (2009)

[5] Gong Lei,Wu Zhensen.Analysis of composite light scattering properties between wafers and many shapes of particles with different positions[J].Acta optica sinica, 32(6):0629003-1~0629003-6,(2012)

MULTIPLEX SINGLE PARTICLE AND BIOLOGICAL CELL ANALYSIS IN MICROFLUIDICS

David DANNHAUSER [1,*], Domenico ROSSI [1], Filippo CAUSA [1-2] and Paolo, A. NETTI [1-2]

[1] Center for Advanced Biomaterials for Healthcare@CRIB, Istituto Italiano di Tecnologia (IIT), Largo Barsanti e Matteucci 53, 80125 Naples, Italy

[2] Interdisciplinary Research Centre on Biomaterials (CRIB), Università degli Studi di Napoli "Federico II", Piazzale Tecchio 80, 80125 Naples, Italy

Corresponding author: david.dannhauser@iit.it

Abstract

We report on a cost-effective way to measure separated micrometric sized particles and biological cells in microfluidic flow conditions. The scattering profile of single particles/cells is fully characterized by a CMOS-based light scattering apparatus with a range of 3-30°. For this purpose, we created a collimated incident laser with a beam width of ~110µm at the measurement position; also, we implemented a precise hydrodynamic 3D alignment effect by viscoelastic-induced particle migration in order to ensure a controlled particle passage. We measured different polystyrene particle sizes and T-lymphocyte cells and matched their scattering profiles with Mie theory.

We describe a light scattering apparatus able to analyse precisely the scattering profile of single particles in microfluidic flows. A continuous scattering profile was achieved thanks to a narrow incident beam collimation and an optimized scattered light collection system. Multiplex particle sizes were measured in a rectangular-shaped low-cost particle alignment section. Matching the measured scattering profile of a particle to that predicted by theory, it is possible to obtain simultaneously particle size and refractive index of the measured unknown single particle.

1 Introduction

Biological particles such as blood cells play an important role in respect of human health. In particular, white blood cells such as lymphocytes of the immune system help to defend the body from invading micro-organisms. Lymphocytes represent 20-45% of peripheral blood, have an almost spherical shape with a diameter of 6-9 µm by and an eccentric nucleus encased by cytoplasm, which is considered to be transparent. A changing number of lymphocytes in our blood, as well as varied cell characteristics (size and refractive index), are often an indicator of diseases such as leukemia, to name one.

The characterization of micrometric particles from scattering patterns obtained by light interaction is a well-known measurement technique. The achieved scattering profile over a wide angular range provides a fast and accurate measurement of particle properties, e.g., refractive index, size and shape. The polymorphism and complexity of biological particles need a specific approach in measurement and interpretation of light scattering data. Viscoelastic-induced particle migration in a round shaped capillary can be used to obtain precise 3D particle alignment in microfluidic flows.[1] This simple alignment technique - combined with particle or cell specific physiological fluids (RPMI 1640) and an adjustable particle velocity range - makes this approach interesting for biological single cell measurements. The combination of a light scattering measurement over a wide continuous scattering range and the 3D alignment opens up the possibility for precise characterization of unknown geometrical features of a single particle without changing its physiological medium or adding fluorescence probes.

2 Experimental Setup

Our apparatus measures single particles/cells at forward scattering angles θ in microfluidic flow condition. (see schematically illustration in Figure. 1)

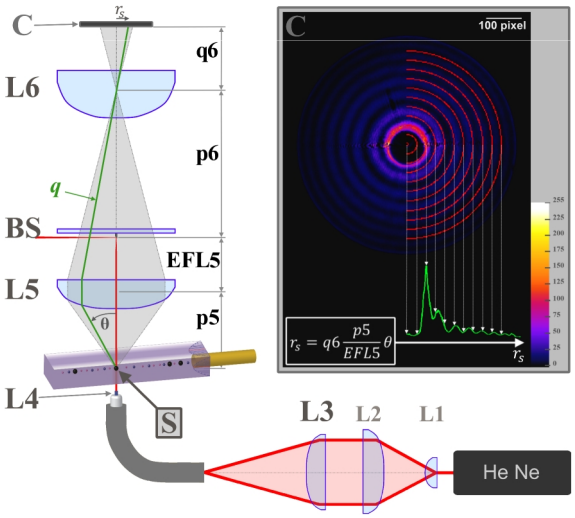


Figure 1 *Schematic diagram of the apparatus. L1 & L2 expand the laser beam, while L3 focuses the laser in the optical fibre. L4 indicates the collimation lens and S the position of the target particle in the microfluidic device. L5 & L6 collect and map the scattered light on the camera sensor C. BS shows the beamstop. In inset C, the scattering pattern after the background subtraction is overlaid with red rings each corresponding to a certain pixel radius value obtaining the final scattering profile (green curve) over the whole θ-range.*

The distinguishing advantage of this setup, compared to systems known in literature[2-5], is the in-flow measurement of a single micrometric particle over a continuous scattering range spanning from $3° < \theta < 30°$.

The used light source was a 5mW linear polarized HeNe laser directly aligned into a beam expander (L1 & L2) that enlarged the beam waist 20 times before an achromatic lens (L3) focused the laser in the entrance of a single mode fibre. To obtain a small and quasi-collimated laser beam size at the sample region (*S*), a GRIN-lens (L4) with a working distance equal to zero is glued to the exit of the optical fibre. This procedure resulted in a beam diameter of ~110μm at S. The expected laser divergence was calculated to be 7.46mrad. Such small divergence combined with the obtained beam diameter enabled a precise single particle analysis.

To ensure 3D particle alignment along the central axis, a specific microfluidic device was designed using the presence of normal stress differences in a viscoelastic liquid (0.2wt% PEO, 4MDa), which induced particle migration in a certain range of shear rates.[1] Alignment was achieved by a round capillary (ID=25μm) that induced particle migration towards the central axis. The capillary entered a rectangular-shaped measuring chamber (h:400μm & w:382μm) from the side, resulting in a coincident central axis. The obtained 3D aligned particle stream was kept along the central axis flowing through the measurement chamber, thus allowing the laser beam to efficiently interrogate the particles one at a time at S. The microfluidic device was placed on a XY- and Z-stage for accurate positioning of the flowing particle axis with respect to the incident beam centre.

An aspheric lens (L5) -with NA=83 and magnification M6=8.54- collected the emitted forward scattering of each particle passing through the laser beam. The limitation of the measureable θ was mainly due to NA and the absolute distance from L5 to S. A beamstop (BS) of 2 mm -placed at the back- focal plane of L5- and the clear aperture of L5 further restricted the measurable scattering range. At the end of the scattered light collecting-system, a plano-convex lens (L6) mapped the scattered light on the CMOS-sensor (C). By knowing all optical distances, it became then entirely possible to calculate the scattering profile over the measureable θ-range.

3 Materials and Methods

The functionality of the apparatus was tested with polystyrene latex (PSL) particles of different radii, spanning from 0.947 up to 4.010μm.

In this study we focused our attention on the most important sub-population of the human white blood, the T-lymphocytes (donated by a 29 year old healthy man). The white blood cells was first separated from the whole blood by a standard density gradient method; then, a specific nylon-wool filter was used to separate the T-lymphocytes. All measurements were carried out with strongly diluted particle solutions, reducing multi-particle scattering effects.

Typically, each light speckle collected by the camera corresponded to the same magnitude of the scattering wave-vector $q \equiv |q|$, but different azimuthal orientations, and was collected in a single scattering ring $rs=q6(p5/EFL5)\theta$. The average intensity of these rings was plotted over the q-range of the camera, where the acquired scattering profile is generally defined as $q=4\pi\lambda^{-1}m_m \cdot sin(\theta/2)$, with $\theta=rs/(EFL5 \cdot M6)$ corresponding to the pixel ring radius and m_m to the refractive index of the medium. The measured scattering profiles were compared to calculations based on the un-polarized Mie theory[6] calculations by a self written Matlab routine. The correlation between measured profile and predictions made it possible to obtain simultaneously particle size and refractive index. As to PSL particles, the refractive index was fixed to 1.58722; therefore, we extracted only the particle size from the scattering profile. The refractive index of the PEO solution (0.2wt% PEO in RPMI) was assumed to be ~1.327.

We used a frame rate of 25 fps for each measurement and calculated the average intensity of each pixel over 3 successive frames during particle passage, thus reducing the thermal noise effects of the sensor. For each sample the background intensity was subtracted and the scattering profile was calculated. Growing pixel-rings with the width of one pixel starting from r_s=1 up to a value of 330 pixels were used to average the q-value at each pixel distance. For optimal analysis, the used scattering range was limited to a θ-range of 3-30°, reducing possible optical aberration or vignetting effects. Particle characteristics were established by overlaying the best fitting Mie scattering profile.

4 Results

4.1 PSL particle

We measured all PSL particle sizes in order to prove the efficiency and multiplex ability of the apparatus. A comparison with theoretical Mie calculations confirmed the accuracy of our measurements in the entire meaningful θ-range. As an example, we show PSL results illustrating three different 4.010μm measurements overlaid by corresponding Mie theory in Figure 2.

The scattering profiles match theory, where most scattering peaks are correctly measured in their position and height. The absolute intensity of the scattering minima is surprisingly well measured. Indeed, an almost perfect match between the measured profiles and theory is achieved showing the possibility to measure small variations in particle size or refractive index.

The first peak of each measurement illustrates a slight mismatching, caused by the BS presence. Note that small

microfluidic misalignments of the particles can result in altered background noise values, effecting mainly $\theta < 7°$. At $\theta > 25°$, measurements may show inaccuracy caused by optical vignetting effects from the microfluidic device.

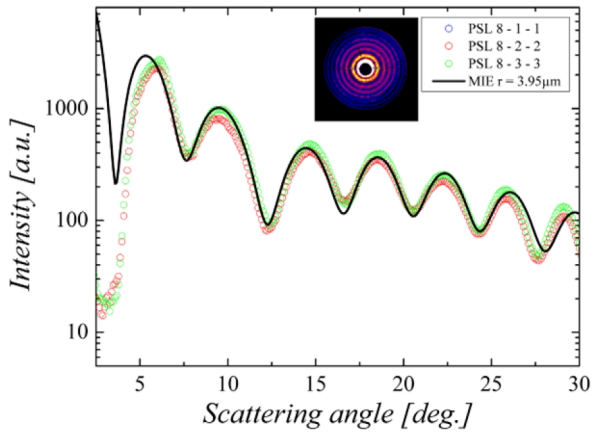


Figure 2 *PSL scattering profiles of particles with nominal radius of 4.010µm. Mie theory is overlaid in black for the corresponding particle properties. The image at the top illustrates the scattered light pattern of a single particle at the sensor.*

4.2 T-lymphocyte cells

The scattering profiles of T-lymphocyte cells were measured and analyzed. Mie scattering profile for un-polarized light and spherical cell shape was applied for the data analyses. Good agreement with literature[7] was found. Figure. 3 shows five representative scattering profiles.

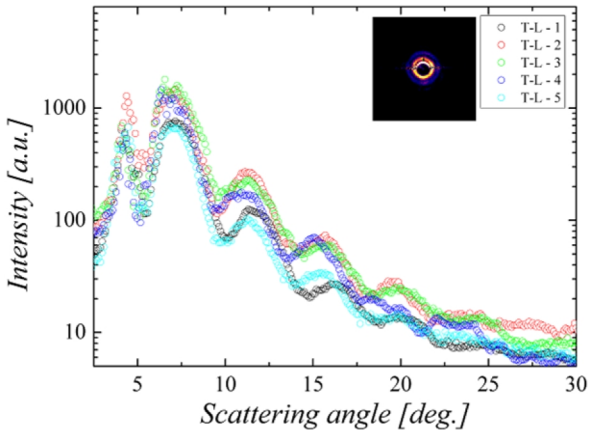


Figure 3 *Human T-lymphocyte scattering profiles. The image at the top illustrates the scattered light pattern of a single particle at the sensor.*

Results show an average cell radius of 3.154±0.07µm with a complex refractive index of 1.37 + i0.0577±0.0274. The corresponding Mie theory curves are not shown for better readability. Precise cell radius measurement of healthy T-lymphocytes shows a minor influence of the real part of the complex refractive index, while the imaginary part -related to the cell absorption- significantly influences results.

5 Conclusion

We report a reliable, robust and cost-effective technique to measure geometrical features of micrometric sized particles and biological cells in microfluidic flows. The light scattering system is combined with a precise hydrodynamic particle alignment system. Reliable results are obtained for both PSL particles and healthy T-lymphocyte cells and match theoretical values.

The precise characterization and detection of pathological T-Lymphocytes as well as from general RBC cells is from significant interest. We expect that this apparatus can be useful in analysis of more complex particle shapes with different refractive indices and absorption coefficients.

6 References

[1] Romeo G., D'Avino G., Greco F., Netti P.A., and Maffettone P.L., Viscoelastic flow-focusing in microchannels: scaling properties of the particle radial distributions, Lab Chip 13: 2802-2807 (2013)

[2] Ferri F., Use of a charge coupled device camera for low-angle elastic light scattering Rev. Sci. Instrum. 68: 2265-2274 (1997)

[3] Wong A., and Wiltzius P., Dynamic light scattering with a CCD camera, Rev. Sci. Instrum. 64(9): 2547-2549 (1993)

[4] Cipelletti L., and Weitz D.A., Ultralow-angle dynamic light scattering with a charge coupled device camera based multispeckle, multitau correlator, Rev. Sci. Instrum. 70(8): 3214-3221 (1999)

[5] Tamborini E., and Cipelletti L., Multiangle static and dynamic light scattering in the intermediate scattering angle range, Rev. Sci. Instrum. 83(9): 093106-093106-8 (2012)

[6] Mätzler C., Matlab function for Mie scattering and absorption, IAP Res. Rep 8, (2002)

[7] Maltsev, V.P., and Semyanov K.A., Characterisation of bio-particles from light scattering (Walter de Gruyter, 2004).

Observation of Red Blood Cells in Blood Coagulation Using Digital Holographic Microscopy

Hideki FUNAMIZU*, Yuki WATANABE and Yoshihisa AIZU

Division of Mechanical Systems and Materials Engineering, Muroran Institute of Technology,
27-1 Mizumoto, Muroran, Hokkaido 050-8585, Japan

*Corresponding author: funamizu@mmm.muroran-it.ac.jp

Abstract

Blood coagulation is an important role in hemostasis process. In microscopic observation, an aggregation structure of red blood cells (RBCs) indicates the degree of blood coagulation. In the present paper, we demonstrate an observation of a spatial distribution of RBCs in blood coagulation using digital holographic microscopy. Digital holograms are obtained for blood of several hematocrit values, and intensity and phase distributions of reconstructed images are observed.

1 Introduction

Blood coagulation is an important role in hemostasis process corresponding to the cessation of blood loss from a damaged blood vessel [1]. Coagulation disorders increase a risk of hemorrhage or thrombosis, which leads to severe diseases related with blood circulation. Many different techniques have been proposed and developed to detect the degree of blood coagulation or to observe a spatial distribution of RBCs. Behaviours of blood coagulation can be observed at various scales ranging from macroscopic to microscopic levels. In macroscopic level, blood coagulation is evaluated quantitatively from a blood viscosity [2]. In an observation using microscopic technique, such as electron microscopy, conventional and confocal optical microscopy and atomic force microscopy, a spatial distribution of RBCs indicates the degree of blood coagulation.

In the present paper, we demonstrate the observation of a spatial distribution of RBCs in bloods coagulation using digital holographic microscopy. The observation using this microscopy has several advantages in that the three-dimensional information of an object can be obtained from a single hologram by a numerical refocus using computer, which implies the feasibility of the observation of the three-dimensional coagulation process in real time.

2 Mechanism of blood coagulation

Blood coagulation results from many changes in chemical and physical properties of blood. The mechanism of blood coagulation is a complex series of cascading enzymatic reactions involving proteins, called them blood coagulation factors. When a blood vessel is damaged, a prothrombin, which is a protein involved in plasma, activates and is converted into thrombin. Subsequently, thrombin converts fibrinogen, which is a blood coagulation factor dissolved in blood, into fibrin that radiates from the clumped platelets. The fibrin forms a meshwork and traps a number of platelets and RBCs, and then produces an aggregation structure of RBCs. The reactions in blood coagulation are balanced by a cessation of coagulation process and dissolve coagulation after the blood vessel has healed. Without this control system, minor injuries of a blood vessel could trigger widespread coagulation throughout the body, which actually happens in some severe diseases, such as cerebral hemorrhage, cardiac episode, and pulmonary embolism.

3 Experimental setup and results

Figure 1 shows an experimental setup of digital holographic microscopy for observing blood coagulation [3,4]. In this setup, a Mach-Zehnder type interferometer is used. An optical source is a laser diode (Mitsubishi ML101J27) with the wavelength of 660 nm and the output power of 130 mW. The operation temperature is kept to 25.00 ± 0.01 ˚C by means of a laser driver (Thorlab ITC502) and a temperature-controlled mounter (Thorlab TCLDM9). Coherent light emitted from the laser diode is collimated by an objective lens OB_1, and is split by a half mirror HM_1. One of the split light waves is reflected by HM_2, and is cleaned by OB_2 and a spatial filter SF. It is then collimated by a lens L again and is used as a reference wave. The light transmitted through HM_1 is reflected by a mirror M_3, and is incident on a test object, where an object wave is produced. The object wave is magnified by OB_3 (Newport MV-60X, ×60, NA = 0.85). The object and reference waves are coupled by a beam splitter BS again, and then these two waves interfere each other. The interference pattern, called it hologram, is detected on CCD camera (AVT, Guppy F-146B) with 1392×1040 pixels and a pixel pitch 4.65 μm. The hologram is reconstructed by numerical reconstruction using angular spectrum method [5]. To separate DC terms and a twin image from a real image in the reconstruction plane, a spatial carrier phase is added to hologram by adjusting the angle of BS. A horse blood is used as the test object. The blood is adjusted to a hematocrit 2% and 4%. It is withdrawn into a syringe by 0.02 ml, and is put on a glass slide. To coagulate the blood, we use a blood coagulant reagent (Axis-Shield PoC AS,

NC 031021). The coagulant reagent or plasma 0.04 ml, which is made for a comparison purpose, is added to the blood on the glass slide, and then a cover glass is put on the glass slide.

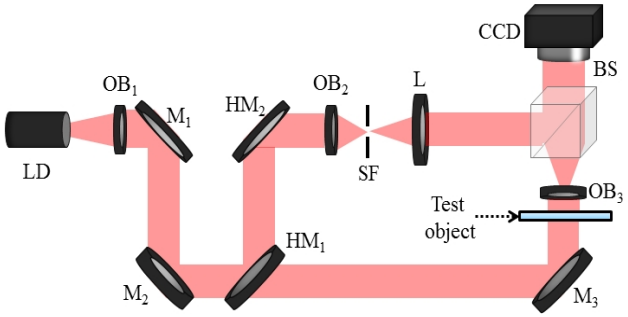


Figure 1 *Experimental setup of digital holographic microscopy.*

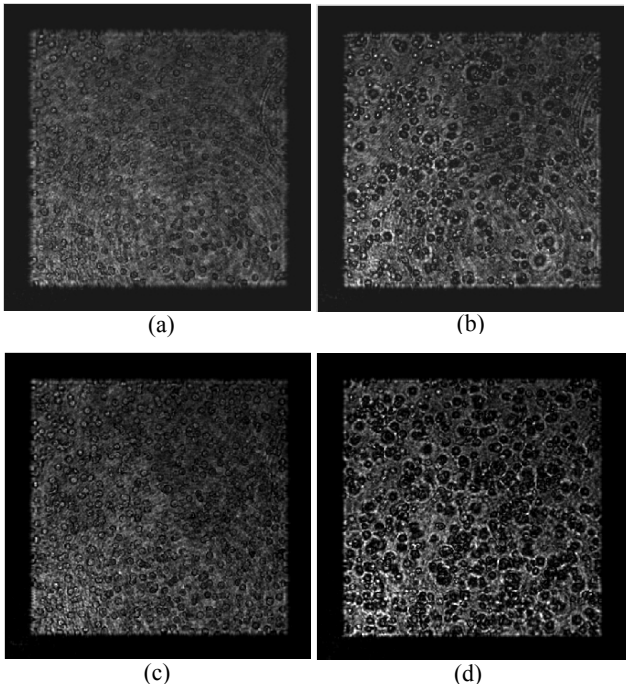


Figure 2 *Intensity distributions of reconstructed images of horse blood in normal condition and blood coagulation. The upper and bottom figures are in the case of hematocrit 2% and 4%. (a), (c) are in normal condition, and (b) and (d) are in blood coagulation.*

Figure 2 and 3 shows experimental results of intensity and phase distributions of reconstructed images obtained from digital holographic microscopy. The reconstruction distance is determined by the minimum of the contrast of reconstructed images obtained from numerical refocusing at a range of distance, which implies they are reconstructed at the average focal plane in the field of view. It is found in Fig. 2 that the defocused RBCs increase in the use of the coagulation agent, which implies the three-dimensional aggregation structure of RBCs is formed by blood coagulation. In addition, it is seen in Fig. 3 that aggregation structure is produced in the horse blood using coagulation reagent in comparison with that of normal condition.

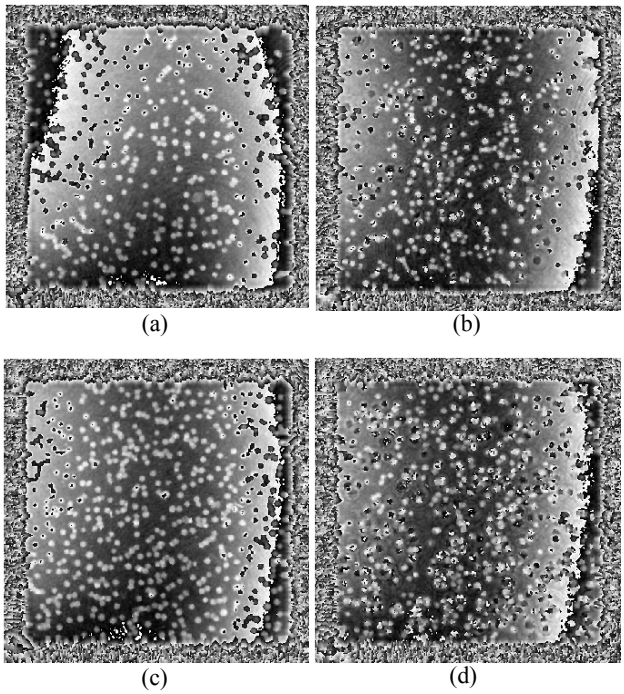


Figure 3 *Phase distributions of reconstructed images of horse blood in normal condition and blood coagulation. The upper and bottom figures are in the case of hematocrit 2% and 4%. (a), (c) are in normal condition, and (b) and (d) are in blood coagulation.*

4 Reference

[1] J. Antovic and M. Blomback, Essential Guide to Blood Coagulation (Wiley-Blackwell, Oxford, ,2013).

[2] M. Faivre, P. Peltie, A. P.-Chretian, M.L. Cosier, M. Cubizolles, C. Nougier, C. Negrier, and P. Pouteau, Coagulation dynamics of a blood sample by multiple scattering analysis, Journal of Biomedical Optics 16, 057001 (2011).

[3] T. Zhang and I. Yamaguchi, Three-dimensional microscopy with phase-shifting digital holography, Optics Letters 23, 1221-1223 (1998).

[4] E. Cuche, P. Marquet, and C. Depeursinge, Simultaneous amplitude-contrast and quantitative phase-contrast microscopy by numerical reconstruction of Fresnel off-axis holograms, Applied Optics 38, 6994-7001 (1999).

[5] M. K. Kim, Digital Holographic Microscopy (Springer, NewYork, 2011).

Measurement of collected polarised light across a liquid-liquid extensional flow

Arab BELKADI[1], Dominique TARLET[1*], Agnès MONTILLET[2], Jérôme BELLETTRE[1] and Patrizio MASSOLI[3]

[1] LTN UMR CNRS 6607,LUNAM Université, 1 rue Christian Pauc, 44306 Nantes, France
[2] GEPEA UMR CNRS 6144, LUNAM Université, CRTT Bd de l'Université, 44602 Saint Nazaire, France
[3] Istituto Motori - CNR, Napoli, 80125, Italy

Corresponding author: dominique.tarlet@univ-nantes.fr

Abstract

An extensional flow involving water-in-oil emulsification is created in an impinging micro-channel. A focalised beam of laser light is polarised in the direction of the channel, and its amount of collected light through the emulsion is measured. Polarised light is expected to be more interacting with stretched and elongated droplets. The obtained mappings of four different flow patterns confirm the observations of Segre and Silbergerg in suspensions across micro-channels.

1 Introduction

The laser extinction technique is well known to be used for solids particles sizing [1] or droplets characterization in multiphase environment as it is the case in atomization and spray control [2]. This light-matter interaction is also used to study the stability of an emulsion using this technique [3].

In the present work the laser collected light is applied for a micro-emulsifier system. The studied device is presented in the form of two micro-channels engraved on Plexiglas slab which intersect to form a cross. This configuration shown Fig. 1 allows obtaining one water inlet, one oil inlet and two outlets for the made emulsion. Finally, water in oil (w/o) emulsion is produced using confined impinging jets flow patterns.

2 Materials and methods

2.1 Micro-channel facility

The test facility was designed to study the production of w/o emulsion, using jets confined in micro-channel impact is shown in "Figure. 1".

This facility is equipped with two double-piston pumps (Armen-APF-100-25-1). The maximum pressure and flow rate of these pumps are respectively 25 bar and 100 mL/min for water using. Each pump is reserved for pumping only one liquid to supply to the micro-channel.

To allow very accurate flow measurements, the test bench is equipped with two weighing scales (Sartorius - mse2203) with an accuracy of $\pm 10^{-3}$ g. The pressure measurement is ensured by two compact pressure sensors

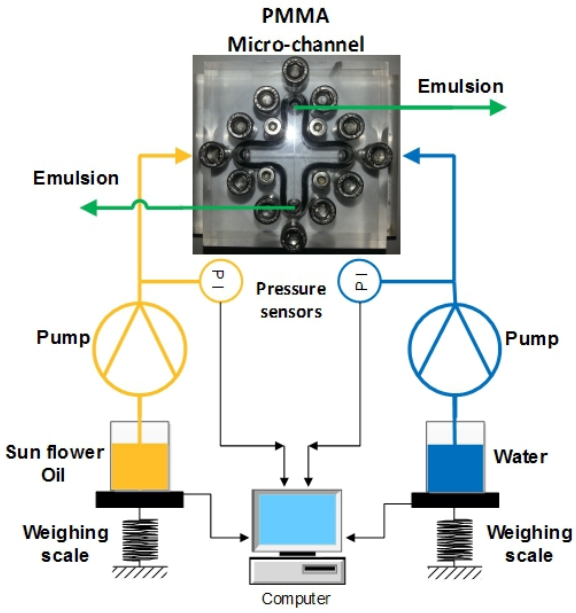


Figure 1: *Experimental set-up – microchannel*

(Gems-3100). The measuring range for this sensors is between 0-25 bar with an accuracy of ±0.25% of full scale.

These pressure sensors measure the static and relative pressure for each of the two mixed liquids (see These "Figure. 1").

The studied micro-channel has the water inlet section (300 x 300 µm) smaller than the oil inlet and emulsion outlets (600 x 600 µm). The length of channels on all sides of the crossroads is 20 mm.

2.2 Optical test bench

Optical techniques based on the properties of scattered light are widely utilized to study disperse flows [4]. However, these techniques generally require the knowledge of the optical properties of the liquid forming the droplets [5]. Laser light scattering, considered as an in-situ and non-intrusive measurement, is used for mapping scattered light intensity within flames of raw fuel and of water-in-oil emulsified fuel [6, 2]. In the present work, this technique is adapted to perform a mapping of the water droplets presence, both

in the impinging area where emulsification is actually going on, and in the overall flow pattern.

The experimental set-up is designed to measure the amount of polarized light collected through the liquid-liquid flow. It brings a qualitative information about the different flow patterns since it is a function of all the encountered droplets in the line of sight.

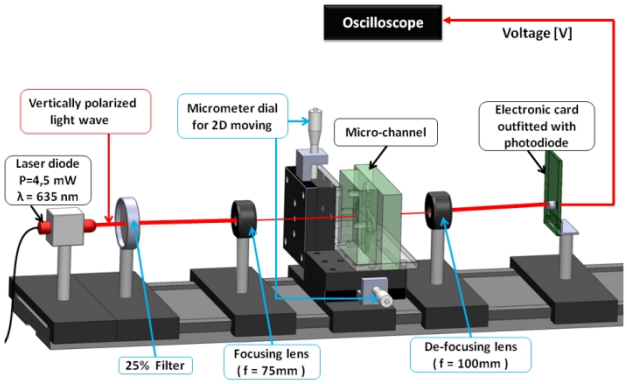


Figure 2 : *Optical test facility for the measurement of collected light through the transparent micro-channel.*

This optical test bench described in "Table 1" comprises in order of beam propagation shown Fig. 2 : A red laser diode, a 25% neutral density filter, a focusing plano-convex lens, the transparent micro-channel, a de-focusing plano-convex lens and the photodiode. The photodiode delivers a tension that is checked to be a linear function of the incoming light power, using neutral density filters of different attenuations. The mini-channel is mounted on a base moving with micrometer screws, allowing a very precise 2D translation control through the channel. This allows to obtain a mapping of the collected light measurement along the channels. The role of the de-focusing lens shown Fig. 3 must be explained. First, it increases the beam diameter from less than 150 µm to 3 mm, preventing the photodiode from being damaged. Secondly, it rejects the beams coming out from the mini-channel with an angle superior to 5 degrees. Since the Plexiglas wall of the mini-channel deviates the light paths by 50% in itself due to a refractive index near 1.49 [8], the collection angle is actually less than 2.5 degrees.

Perpendicularity of the beam with respect to the Plexiglas surfaces was carefully checked, and the energetic diameter of the beam was measured to be less than 150 µm. The negligible influence of roughness at the bottom of the channels (less than 7 % of irradiance) are checked. The detailed procedure is reported in [9] with a complete calibration of the collected light measurement in the central channel using premixed emulsion flow. , as a function of its water volume fraction f and mean diameter of droplets Dd. Because the size parameter $\alpha = \pi Dd/\lambda$ is greater than 15 in the present case, the scattering cross section is approximated as proportional to the squared diameter of droplet Dd^2. Thus, in the case of a constant water fraction f the irradiance is expressed as $It/I0 = e^{-(C/Dd)}$ with C constant. And in the case of constant droplet diameters, the irradiance is expressed as $It / I0 = e^{-C' \times f}$ with C' constant since the total number of droplets is inversely proportional to the droplet volume, i.e. Dd^3. Experimental calibration consists in fitting measurements with this exponential behavior [11]. Thus, the collected light results are presented under the well-known formulation log(It/I0) in the present paper. A test was conducted at an acquisition frequency of 500 Hz, 1 kHz and 2 kHz to check that the measured signal does not depend on the acquisition frequency. The co-polar correlation coefficient ρ_{hv} is measured and found equal to 1.2%, indicating a highly polarized laser beam. It is expected to be more sensitive to the stretched and elongated droplets, so the direction of polarization is always put in the channel direction.

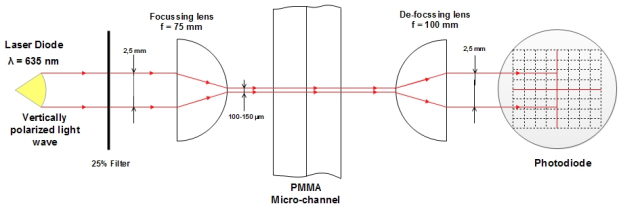


Figure 3 : *Simplified optical diagram.*

3 Mappings of four different flow patterns

The experiments with the 150 µm laser beam consist in mapping $\log(I_t/I_0)$ all over one half of the impinging channel and 9 Dh downstream (Dh = 600 µm), to see where the flow becomes steady. Four experimental cases labeled as A, B, C and D in Fig. 4 were performed by varying the fluid and flow parameters, excepted the oil flow rate that is maintained at 69 ± 7mL/min :

A - is considered as a reference case with a low water fraction (8.7%wt.), and without addition of SPAN surfactant or Butanol. The water and oil streams are impinging in a smooth interface.

B - is a case with a high flow rate of water (15%wt.), where the flow becomes apparently disordered.

C - is a case with 59 % less interfacial tension using SPAN surfactant and a higher flow rate of water (12.6%wt.).

D - is a case with 23 % less viscosity, a high water flow rate (15.38%wt.) and 54 % less interfacial tension because

of 5% wt. addition of Butanol in oil.

To sum up, the four tested cases («Table 2") are : (A) Reference case, (B) Faster case with locally disordered flow structures, (C) Low interfacial tension case, and (D) Low-viscosity, apparently disordered case. The obtained mappings can be seen in Fig. 4. . In case (A), the first striking result is the presence of water droplets crossing the channel downward the water inlet, and grouped close to the opposite wall when flowing downstream.

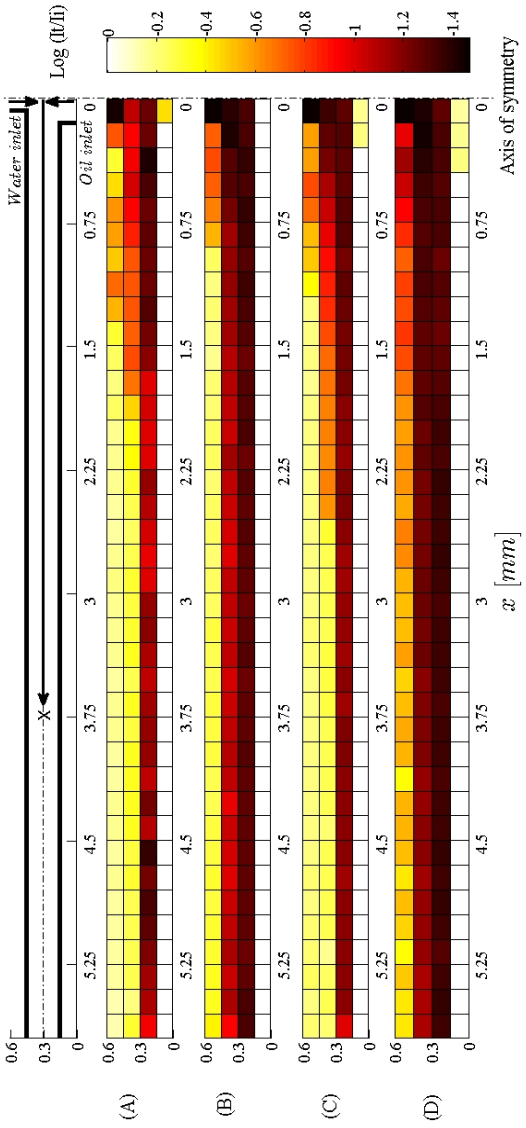


Figure 4 : *The liquid/liquid flow patterns, obtained by mapping the measurement of polirezed light all over the central channel.*

In case (B) with a higher water flow rate, the presence of water droplets is detected on an area twice as large as in case (A). Although the water to oil superficial velocity ratio steps from 9.6% to 17.6% from case (A) to (B), the obtained disperse flow has a more homogeneous distribution of water in case (B). In case (C) with a lower interfacial tension, the presence of water droplets is noticed, as in case (A), close to the opposite wall and almost no water is detected elsewhere. Comparing to case (B), the main change is the dramatic decrease in interfacial tension (-59%). Lastly, the case (D) shows a flow where water droplets are invading two thirds of the channel length, and significantly occupying the last third.

To explain that, the Reynolds number in case (D) steps from 16-19 in the three other cases to a value of 26. This explains why the water droplets are invading a larger area across the channel: The inertia effects in the flow become dominant and move the droplets away from their equilibrium location observed at a lower Reynolds number. Following the work of Segre and Silberberg [10] about suspensions, other authors [11] investigated this kind of effects in confined channels, using the Reynolds number as an important criterion. In this extent, the present emulsions are considered as similar to suspensions because of a low water fraction.

4 References

[1] Jones A. R. Light scattering for particle characterization. *Progress in Energy and Combustion Science, 25*(1), 1–53(1999).

[2] Calabria R., Massoli P., Mateo M.-P., Ctvrtnickova T., Yanez A., Nicolas G., Paa W., Haisch C., Somandepalli V. S. R., Morse T. L., Grisch F., *Laser diagnostic in Combustion* (ProcessEng Engineering GmbH, 2009).

[3] Dalmazzone C., Characterization of the morphology and stability of water-in-oil petroleum emulsions, *25èmes entretiens du centre Jaques Cartier, Emulsification, Modelling, Technologies and Application*(Lyon, 2012).

[4] Tadros T., Izquierdo P., Esquena J., Solans C., Formation and stability of nano-emulsions. *Advances in Colloid and Interface Science, 108-109*, 303–18(2004).

[5] Calabria R., Massoli P., Generalised scattering imaging laser technique for 2-D characterization of non-isothermal sprays. *Experimental Thermal and Fluid Science, 31*(5), 445–451(2007).

[6] Mattiello, M., Cosmai, L., Pistone, L., Beretta, F., Massoli, P., Exerimental evidence for microexplosions in water/fuel oil emulsion flames inferred by laser light scattering. *Symposium (International) on Combustion*, 24, 1573–1578 (1992.)

[7] De Gennes, P.G., Brochard-Wyart, F., Quéré, D., *G outtes, bulles, perles et ondes*. (Belin, 2005).

[8] Nikolova, K.S., Georgieva, S.N., Dimitrov, I.C., Dechev, N.I.. *Analysis of the dispersion of optical plastic materials*. Optical Materials 29, 1481– 1490 (2007).

[9] Belkadi, A., Tarlet, D., Montillet, A., Bellettre, J., Massoli, P., High-speed w/o emulsification within impinging and cross-flowing mini-channels, *Proceedings of the 3rd European Conference on Microfluidics,* Heidelberg, Germany (2012).

[10] Segre, E., Silberberg, A., Behaviour of macroscopic rigid spheres in Poiseuille flow: Part 2. experimental results and interpretation. *J. Fluid Mechanics* 13,136 (1962).

[11] Chun, B., Ladd, A., Inertial migration of neutrally buoyant particles in a square duct: An investigation of multiple equilibrium positions. Physics of Fluids 18,1093–1096 (2006).

Coupling environmental acoustic levitation cell and Micro-Raman spectroscopy for monitoring photoevolution and hygroscopicity of single particles with atmospheric interest.

Myriam MOREAU*, Yeny TOBON, Sophie SOBANSKA and Jacques BARBILLAT [1]

[1] Laboratoire de Spectrochimie Infrarouge et Raman, UMR CNRS 8516, Université de Lille 1 Sciences et Technologies, Bât. C5, 59655 Villeneuve d'Ascq Cedex, France

Corresponding author: myriam.moreau@univ-lille1.fr

1 Introduction

In atmospheric chemistry, aerosols play an essential role mainly concerning the heterogeneous chemistry in the atmosphere [1]. However, studying the aerosol properties remains a challenge and it's indispensable to try to understand the chemical processes which occur at the particle or at the surface scale. Laboratory experiments are the most common way to go towards to real processes under controlled conditions, and it's necessary to look for techniques or combination of techniques which permit to simulate the conditions occurring in the atmosphere.

Raman spectroscopy is a non-destructive technique that provides detailed molecular and structural information with a spatial resolution of about 1µm^3, and it is a valuable tool to follow real-time evolutions of volume or surface structures under controlled conditions. Micro-Raman spectroscopy, coupled to an environmental levitation cell, is especially useful for studying, at micrometric scale, the in-situ modifications of aerosol when exposed to reactive environments or humidity without the influence of a contacting surface [2]. Moreover, photochemical transformation can be followed by irradiation of the particles.

In this presentation, we used an environmental acoustic levitation cell coupled to the micro-Raman spectroscopy to monitor the physical and chemical processes occurring in particles of atmospheric interest when exposed both, to humidity and UV-Vis light. Physical and chemical changes can be followed at the interface or deeper depending on the optical properties of the particle. Particles, as small as 20 µm, can be levitated and studied by micro-Raman spectroscopy. Hygroscopic property evolution of nitrate containing aerosols ($NaNO_3$) when irradiated with UV-Vis light was investigated by using this experimental set up.

2 Environmental levitation cell coupled to micro-Raman spectroscopy

An ultrasonic levitator (APOS BA 10, Tec5, Germany) was modified to be installed within a small dimension environmental levitation cell and was horizontally coupled to the Raman microscope as shown in figure 1. The cell consists of 4 optics accesses, and transparent quartz windows allowing the exposure to UV radiation. Two inlet/outlet valves are used for gas supplies to modify the environment inside the cell. The relative humidity and the temperature are measured within the cell by using an adapted sensor.

The spectrometer used for the coupling is a Horiba Scientific LabRam HR visible, equipped with a CW 633 nm laser and a Liquid Nitrogen-cooled CCD camera. We used the micro arrangement in backscattering mode.

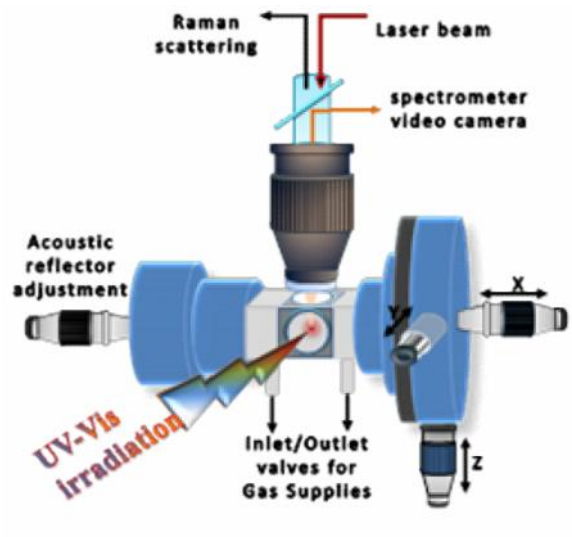


***Figure 1**. Schematic diagram of environmental levitation cell coupled to the Raman microscope*

The size evolution of the particles was measured by using a speed high resolution video camera (Basler Ace NIR, 2048x2048 pixels) with a ms time resolution and the growth factor was calculated by comparing geometric diameter evolution for various RH. The chemical evolution, i.e liquid versus solid and NO_3^- to NO_2^-, was followed through Raman spectra acquired with time steps ranging between 2 and 10 s. The photochemical evolution i.e. NO_3^- to NO_2^- conversion of the particle was evaluated using Raman measurements after exposition with UV lamp in the 250-280 nm range.

3 Photochemical transformation and hygroscopicity of individual particles

Deliquescence and efflorescence processes of $NaNO_3$ were evidenced by the transformation of the Raman spectra. The shift on the NO_3^- symmetric stretching vibration

from 1069 to 1052 cm^{-1} is the most common change reported on the literature as an evidence of the transitions. In addition, our experiments showed that deliquescence and efflorescence values are altered after irradiation of the particles as consequence of the photochemical products. By using spectral data treatments the transformation rate was drawn. By irradiating in the UV range the nitrate into nitrite particle conversion was demonstrated and showed similar trend that described previously for $NaNO_3$ particles [3].

4 Acknowledgement

This work was supported by funds from the "Laboratoire d'Excellence (LABEX) -CaPPA- (ANR-11-LABX-0005-01) and IRENI program.

5 References

[1] Andreae, M. O., and Crutzen, P. J., Atmospheric Aerosols: Biogeochemical Sources and Role in Atmospheric Chemistry, Science 276, 1052-1058. (1997)

[2] Krieger, U. K., Marcolli, C., and Reid, J. P., Exploring the complexity of aerosol particle properties and processes using single particle techniques, Chem. Soc. Rev. 41, 6631-6662, (2012).

[3] Asher, S. A., D. D. Tuschel, T. A. Vargson, L. Wang and S. J. Geib, Solid State and Solution Nitrate Photochemistry: Photochemical Evolution of the Solid State Lattice, Journal of Physical Chemistry A 115(17): 4279-4287 (2011).

On the Routine Characterization of Nanopaticles by Static Light Scattering

Cedric MONTET[1,2], Mariusz WOZNIAK[1], Matthias SENTIS[1] and Fabrice ONOFRI[1,*]

[1] Aix-Marseille Université, CNRS, UMR 7343 IUSTI, 13453, Marseille, France
[2] CILAS, 8 Avenue de Buffon, 45100, Orléans, France

Corresponding author: fabrice.onofri@univ-amu.fr

Abstract

This paper review the work in progress to develop a multi-angle light scattering apparatus allowing routine characterization of liquid suspensions of nanometer-sized particles in freely exchangeable sampling cells.

1 Introduction

"Multi-angle light scattering" (MALS) or "Static Light Scattering (SLS)" techniques (e.g. [1]) are widely used for the characterization of micro-particulate systems, see Fig. 1. The so-called laser diffractometry, the rainbow angle and critical angle techniques (e.g. [1-3]) may be considered as variants requiring only a narrow angular range to be analyzed and thus, a simple optical setup (basically, a CCD camera and a Fourier lens).

For submicron particulate systems in general, and more particularly for nanoparticle systems (aerosols, sooty flames, colloidal suspensions,...) in which we are mostly interested in, the extremely low intensity and low modulation of the scattered signal made multi-angle analyses particularly difficult. One fundamental reason for that is that, asymptotically, the angular dependency of the scattering patterns of very small size-parameter particles tends to be independent on the particle size. The use of a non-optical radiations, such as X-rays ("small-angle X-ray scattering", SAXS, e.g. [4]), or even the use of fundamental particles such as neutrons ("small-angle neutron scattering", SANS, e.g. [5]), allows to overcome this problem by increasing by several orders of magnitude, with respect to visible light, the size parameters of the particles under study. The SAXS technique also benefits from the development of asymptotic scattering models (i.e. Rayleigh-Debye-Gans (RDG, e.g. [6-10]), which make possible the inversion of the scattering diagrams of complex shaped nanoparticles and their aggregates. However, it is quite obvious that synchrotron light source are not designed for routine characterizations, as well as to perform online and real time analyses of the dynamics of aggregation processes for instance. Therefore, the development of MALS systems operating in the visible range and with freely exchangeable sampling cells is still a subject of interest, provided that a few set of basic and practical points are revisited.

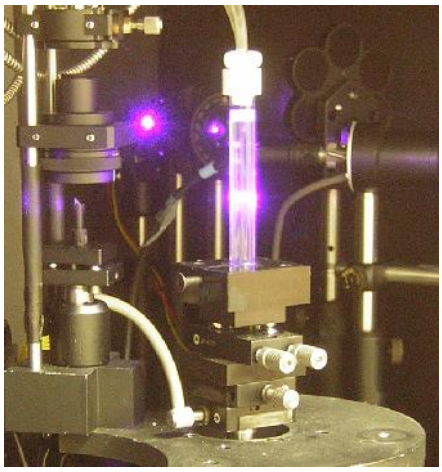


Figure 1 Multi-angle light scattering setup for recording the scattering diagrams slightly below the conventional scattering plane. The colloidal suspensions is placed into a cylindrical spectrophotometer cell.

2 Scattering models, inversion methods

Numerous comparisons were performed to evaluate the validity of RDG predictions compared to T-Matrix ones, for fractal [8, 11-13] as well as Buckyball [13-14] shaped aggregates. For T-Matrix calculations, we have parallelized the code developed Mackowski and Mishchenko [15]. Fig. 2 exemplifies the limits of RDG by comparing its predictions for the cross-sections of fractal aggregates of carbonaceous nanoparticles with those of the T-Matrix, where n_p, r_p, R_g and D_f stand for the number and radius of the nanoparticules, the radius of gyration and the fractal dimension of the aggregate respectively [12-13, 16].

Our inversion methods are either algebraic ones (based on Tikhonov and Phillips-Twomey regularization methods [13-14]) or based on the automatic extraction of the asymptotic behavior of the scattering patterns [12]. By automatic, we mean that the extraction of the Guinier zone (i.e. forward angle plateau length strongly correlated to the radius of gyration) and fractal zone properties (i.e. decay slope strongly correlated to the fractal dimension) are performed with a given set of parameters and no human intervention [12].

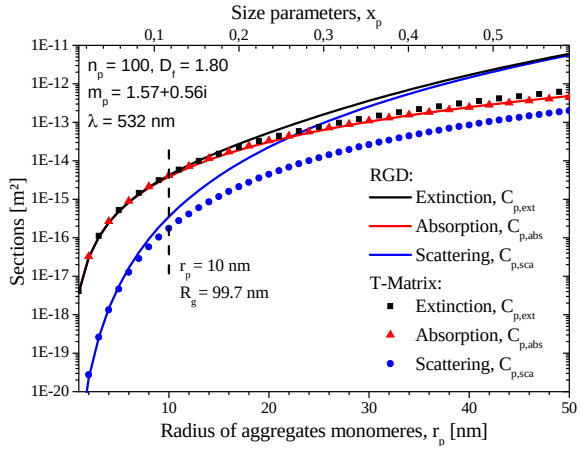


Figure 2 RDG and T-Matrix predictions for the cross-sections of fractal aggregates of the same morphology but for nanoparticles of increasing size [12-13].

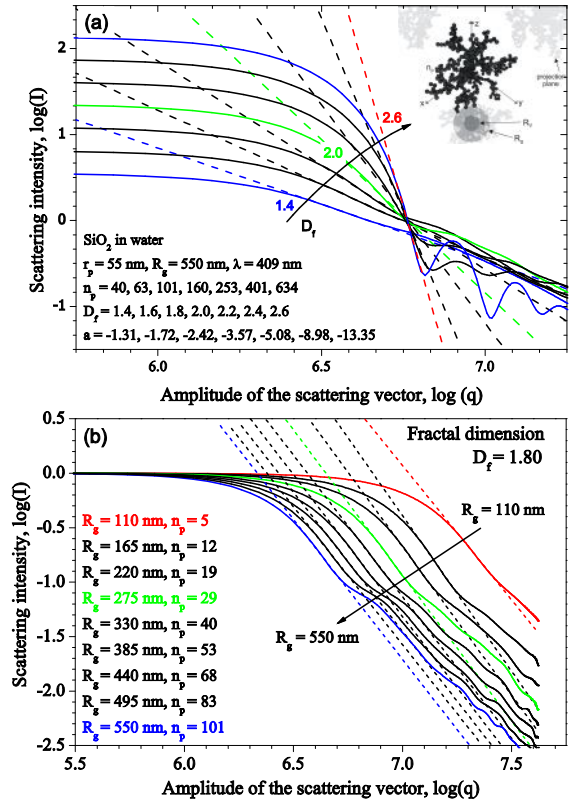


Figure 3 T-Matrix results for the scattering diagrams of water suspensions of SiO_2 particle aggregates with various (a) fractal dimensions or (b) radiuses of gyration [12-13] - Perp. polar.

Figs. 3 (a) and 3 (b) show, in log-log scale, the calculation of the intensity scattered by fractal aggregates of a silicon dioxide nano beads in aqueous suspension, versus the scattering vector q, for various fractal dimension and radiuses of gyration respectively. Figure 4 shows the results of the automatic analysis of the diagrams of synthetic aggregates [16] when two level of white noise are added. A similar agreement was obtained for the estimation of R_g [12].

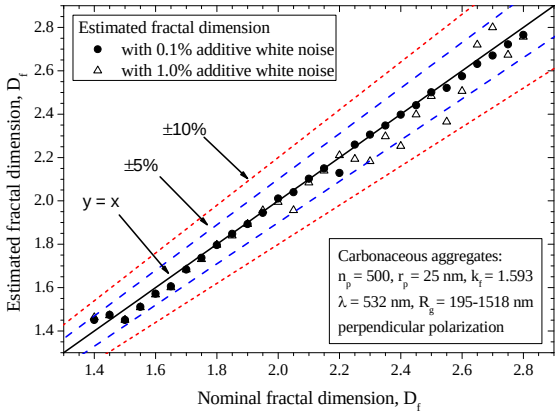


Figure 4 Comparison of nominal and estimated fractal dimensions of synthetic aggregates [16] which scattering diagrams were processed automatically [11-12].

3 Experimental setup and examplifyng results

For the routine characterization of liquid suspensions of nanometer-sized particles in freely exchangeable sampling cells, one has to take into account for various potential biases, and more particularly:

- The low angular modulation of the scattering signal, which requires a perfect linearity of the acquisition chain and minimizing any distortion of the signal (due to refraction effects at the cell interfaces, variations of the measurement volume shape and size with the observation angle,...)

- The weakness of the scattered signal requires a perfect calibration of the system and minimizing any false scattering effects (reflections within the sampling cell, laser source, molecular diffusion, surface nano-rugosities and positioning of the cell,...), see Fig. 1).

To overcome most of the problems pointed above, we are developing a setup where the spectrophotometer cell is cylindrical and the scattering diagrams are collected slightly above the conventional scattering plane, see Fig. 1. The cylindrical shape allows to prevent distortions and false reflections occurring with usual square or rectangle shaped cells. The latter are also cost effective, and easy to replace (which is a decisive advantage for users). The detection slightly above the scattering plane allows minimizing the collection of the direct beam and of in plane false rays which contributions may strongly exceeds the intensity of the light scattered by nano suspensions. The latter solution, in combination with the use of an elliptical laser beam, allow minimizing the variation of the probe volume shape and dimensions with the collection angle. So that, the calibration of the probe volume angular dependency is no more strictly necessary. All other components are quite standard. The scattering pattern is recorded with a photomultiplier rotating thanks to a high precision goniometer. The laser beam properties of a few milliwatts UV laser diode with a center wavelength at 405 nm are controlled via spherical and cylindrical lenses,

polarizer and neutral density filters. It will be shown that Lorenz-Mie theory and Monte Carlo simulations did show promising performances and a good agreement with preliminary experimental results.

4 Acknowledgements

This work was partially funded by the French National Research and Technology Agency (ANRT) and the French National Research Agency (ANR, under the grant ANR-2011-NANO-008).

5 References

[1] Xu, R., *Particle characterization : Light scattering methods* (Kluwer Academic Publishers, Dordrecht, Nederland, 2002).

[2] van Beeck, J.P.A.J., Giannoulis, D., Zimmer, L., Riethmuller, M.L., « Global Rainbow Thermometry for Droplet-Temperature Measurement », Optics Letters, 24: 1696-1705 (1999).

[3] Onofri, F., Krzysiek, M., Mroczka J., « Critical Angle Refractometry and Sizing for Bubbly Flow Characterization », Optics Letters, 32:2070-2072 (2007).

[4] Glatter O, Kratky O (eds.) *Small Angle X-ray Scattering* (Academic Press, London, 1982).

[5] Kostorz, G. (ed.) *Neutron Scattering*. in Treatise on Materials Science and Technology, Vol. 15. (Academic Press, London, 1982).

[6] C.F. Bohren, and D.R. Huffman, *Absorption and scattering of light by small particles* (Wiley, New-York, 1983).

[7] Pecora, R., *Dynamic Light Scattering: Applications of Photon Correlation Spectroscopy* (Plenum Press, New-York, 1985).

[8] Koylu, U. O., Faeth, G. M., Farias, T. L., Carvalho, M. G. Fractal and projected structure properties of soot aggregates. Combustion and Flame, 100(4), 621-633 (1995).

[9] Puri, R., Richardson, T. F., Santoro, R. J., Dobbins, R. A. Aerosol Dynamic Processes of Soot Aggregates in a Laminar Ethene Diffusion Flame. Combustion and Flame, 92(3), 320–333 (1993).

[10] Sorensen, C. M. Light Scattering by Fractal Aggregates: A Review. Aerosol Science and Technology, 35, 648–687 (1997).

[11] Witten, T. A., Sander, L. M.. Diffusion-Limited Aggregation, a Kinetic Critical Phenomenon. Physical Review Letters, 47(19), 1400–1403 (1981).

[12] Mroczka J., Wozniak M., Onofri F., Algorithms and methods for the analysis of the optical structure factor of fractal aggregates, Metrology and Measurement Systems XIX(3): 459-470 (2012)

[13] Woźniak, M., *Characterization of nanoparticle aggregates with light scattering techniques* (PhD thesis, Aix-Marseille University, Marseille, 2012).

[14] Onofri F.R.A, Barbosa S., Touré O., Woźniak M., Grisolia C., Sizing highly-ordered buckyball-shaped aggregates of colloidal nanoparticles by light extinction spectroscopy, Journal of Quantitative Spectroscopy & Radiative Transfer 126:160-168 (2013)

[15] Mackowski DW, Mishchenko MI. Calculation of the T-Matrix and the scattering matrix for ensembles of spheres. JOSA A 13:2266-78 (1996).

[16] Wozniak M., Onofri F.R.A., Barbosa S., Yon J., Mroczka J., Comparison of methods to derive morphological parameters of multi-fractal samples of particle aggregates from TEM images, Journal of Aerosol Science 47: 12–26 (2012)

Plasmonics

Au-Fluorophore Nanohybrids: Experimental Evidence of the Plasmonic Dicke Effect

Pierre FAUCHÉ[1,*], Miguel COMESAÑA-HERMO[1], Brahim LOUNIS[2], Serge RAVAINE[1] and Renaud VALLÉE[1]

[1] CRPP, UPR 8641, CNRS – Univ. Bordeaux, Pessac, 33600, France
[2] LP2N, UMR 5298, CNRS – IOGS - Univ. Bordeaux, Talence, 33400, France
Corresponding author: fauche@crpp-bordeaux.cnrs.fr

Abstract

Experimental evidence of the plasmonic Dicke effect is presented from the fluorescence ensemble characterization of different concentrations of organic emitters grafted to plasmonic nanoparticles.

1 Introduction

Nanohybrids formed by the combination of emitters and plasmonic nanostructures have attracted the attention of the scientific community during the last years thanks to the relevant applications that such systems may find in different fields like the design of novel optoelectronic devices or biosensors [1,2]. Nevertheless, the physical interactions between these entities are of complex nature and numerous studies have been developed in order to fully understand them [3,4].

It has been recently postulated that, for an ensemble of dipoles situated at the surface of a plasmonic nanoparticle (NP), the interaction between emitters is mainly of plasmonic character rather than radiative. The emission of a photon becomes a cooperative process involving all the dipoles and the metal nanoparticle. This plasmonic coupling leads to the formation of collective states known as "superradiant states" [5]. These results are an extension of the previous work by Dicke, in which he postulated the existence of such states for an ensemble of dipoles confined in a spatial volume small with respect to the radiation wavelength [6]. In the presence of a plasmonic resonator cross-talking between emitters leads to an extremely fast desexcitation process. At a sufficiently large distance from the plasmonic core (d≥10nm for a 32nm-NP), a progressive enhancement reaching a saturation of the ensemble quantum efficiency is expected when the number of coupled emitters is increased. This is directly related to a radiative decay rate that scales with the number of emitters placed in close vicinity to the core in a purely cooperative regime. Moreover, the authors also point out that the role played by FRET between neighbor emitters is negligible in this process.

To the best of our knowledge, there has been no experimental demonstration of the plasmon-mediated superradiance near metal nanoparticles, this being a consequence of the difficulty to create a system in which the number of emitters per plasmonic core and the distance between the different components are precisely controlled. In our work we show experimental evidence for the formation of plasmonic superradiant states from the decay rate studies of an ensemble of such nanohybrids in solution.

2 Materials and methods

The nanohybrids have been designed by the coating of Au NPs with a homogeneous silica shell that works as a spacer while endowing the system with an improved colloidal stability. The structural integrity of the obtained system was characterized by TEM. The system has then been decorated with organic emitters. To avoid problems of reproducibility during the characterization of the nanohybrids, a covalent bond between the different components has to be granted. In such conditions, an irreversible adsorption of the emitters at the surface of the silica shell is ensured, even under harsh conditions like strong sonication. In our systems, such strong bond is provided by the silane coupling agent aminopropyltriethoxysilane.

The optical response of the nanohybrids in ethanol dispersion was acquired with a spectral- and time-resolved setup consisting of a streak camera pre-fitted with a spectrograph with a grating of 150 gr/mm. Acquiring the fluorescence of a whole population, the temporal decay profile deviates from a single exponential decay. We accordingly fitted the decay profiles with a stretched exponential function (Eq. (1)) convoluted to the instrumental response function of the system, in order to estimate the mean decay time of the nanohybrids population.

$$I(t) = I_0 e^{(-\frac{t}{\tau_K})^{\beta}} \quad (1)$$

The mean decay time is obtained from the relation

$$< \tau >= \frac{\tau_K}{\beta} \Gamma(\frac{1}{\beta}) \quad (2)$$

3 Experimental Results

Figure 1 shows the normalized temporal decay profiles obtained for the nanohybrids dispersed in an ethanol solution with a various number of labeled

emitters. As clearly observable in the figure, the decay profiles shorten and become less and less exponential as the concentration in emitters per particle is increased. A comparison with the mono-exponential decay profile of pure RhB in solution is also provided in the figure. Accordingly, a decrease of the mean decay time $< \tau >$ is determined when N (the number of emitters per plasmonic core) is increased, in agreement with theoretical predictions (Figure 1). The comparison with the decay profile of bare Rhodamine B shows that the long time decay observed for hybrid samples corresponds to non-labeled emitters released into the solution.

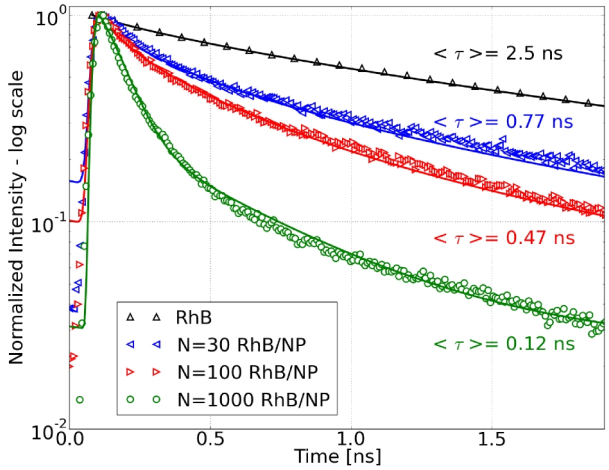


Figure 1 *Normalized temporal decay profile of bare Rhodamine B (in black) and of Au-Rhodamine B nanohybrids where the number of molecules per plasmonic core (N) has been varied (in red, green and blue). The symbols are measured data points and the solid lines are stretched exponential fits convoluted with the instrumental response function of the setup.*

Unfortunately, the use of organic molecules does not allow an easy quantification of the total amount of emitters used and thus direct correlation with simulations is not straightforward. To overcome this limitation, we are currently replacing Rhodamine B with QDs, nano-objects that can be observed with electron microscopy techniques (Figure 2). More precisely, 3D electron tomography will be used to unequivocally ascertain the exact number of QDs adsorbed on each nanohybrid. The combination of this technique with single-particle spectroscopy will allow the characterization of single nanohybrids, an ideal scenario to prove the validity of the theoretical predictions presented by V.N. Pustovit and T.V. Shahbazyan [5].

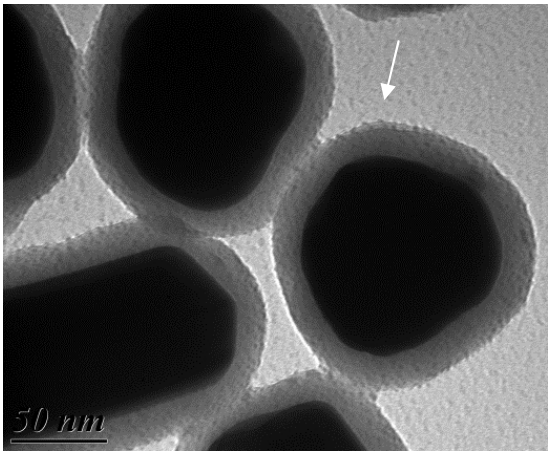


Figure 2 *Transmission electron microscopy image of a nanohybrid composed by QDs (small spots attached to the silica shell) surrounding the Au NPs (in black).*

4 References

[1] Wang Z., Zhan X., Wang Y., Muhammad S., Huang Y., He J., A flexible UV nanosensor based on reduced graphene oxide decorated ZnO nanostructures, Nanoscale 4(8): 2678-84 (2012)

[2] Pan W., Zhang T., Yang H., Diao W., Li N., Tang B., Multiplexed detection and imaging of intracellular mRNAs using a four-color nanoprobe, Analytical Chemistry, 85(21): 10581-88 (2013)

[3] G. Sun, and J.B. Khurgin, Plasmonic Enhancement of optical properties by isolated and coupled metal nanoparticles, in *Plasmonics and plasmonic metamaterials : analysis and application,* G. Shverts and I. Tsukerman, (World Scientific, vol.4, 2011)

[4] Schaadt D.M., Feng B., Yu E.T., Enhanced Semiconductor Optical Absorption via Surface Plasmon Excitation in Metal Nanoparticles, Applied Physics Letters 86(6):063106 (2005)

[5] Pustovit V.N., Shahbazyan T.V., Cooperative Emission of Light by an Ensemble of Dipoles near a Metal Nanoparticle: The Plasmonic Dicke Effect, Physical Review Letters, 102(7):077401 (2009)

[6] Dicke R.H., Coherence in Spontaneous Radiation Processes, Physical Review 93(1):99-110 (1954)

Enhanced Spin-Hall and Goos-Hänchen shift(s) mediated by scattering in plasmonic nanoparticles

Jalpa SONI[1,*], Shampy MANSHA [2], S. Dutta GUPTA[3], Ayan BANERJEE[1] and Nirmalya GHOSH[1]

[1]Dept. of Physical Sciences, Indian Institute of Science Education and Research (IISER) Kolkata, Mohanpur Campus, Mohanpur 741 252, India
[2] Division of Physics and Applied Physics, School of Physical and Mathematical Sciences, Nanyang Technological University, Singapore, 637371 Singapore
[3]School of Physics, University of Hyderabad, Hyderabad 500046, India
Corresponding author: jalpa1120@iiserkol.ac.in

Abstract

The Goos-Hänchen (GH) and Spin-Hall (SH) shifts have been studied extensively at planer interfaces. We present a general framework to study these shifts in scattering from Plasmon resonant systems by making use of the Poynting vector. We further show that these shifts can be highly enhanced by the interfering modes in plasmonic nanoparticles. We also establish the correlation of these shifts with experimentally measurable polarimetry parameters, namely, *diattenuation (d)* and *retardance (δ)*. The results reveal that each of the shifts can be controllably tuned and enhanced by exploiting the interference of neighbouring modes, which can be experimentally measured easily by the *d* and *δ* parameters.

1 Introduction

Originally studied for the case of total internal reflection, the GH shift is observed in the plane of incidence while the SH shift is observed in the plane perpendicular to the plane of incidence [1-2]. These shifts are typically in the sub-wavelength domain and are rapidly gaining attention due to the development of nano-optics employing light evolution at sub-wavelength scales [3]. It has been shown that, in addition to reflection/refraction and tight focusing, these shifts can also be observed in scattering from dielectric spheres [3]. More recently, in plasmonic systems, a spin-dependent splitting of the focal spot of a plasmonic focusing lens was demonstrated and explained in terms of a geometric phase [4]. Although GH and SH shifts have been observed in the context of various plasmonic systems, a thorough and detailed investigation of these shifts observed in scattering process is absent in the literature. In this work, we present a theoretical model where the GH and SH shifts for scattering have been defined and calculated in terms of the Poynting vector. We show that since these shifts are polarization dependent, a direct and interesting correlation of the origin of these shifts can be drawn with polarimetry parameters like *diattenuation (d,* differential attenuation of orthogonal polarizabilities) and *retardance (δ,* phase difference between orthogonal polarizabilities). We also show that both GH and SH shifts can be significantly enhanced/optimized in plasmonic metal nano-particles/nanostructures.

2 Theoretical model

We consider scattering of plane waves by a spherical particle in Cartesian coordinate system with the incident plane wave propagating in the Z direction. The polar angle of scattering θ and the azimuthal angle ϕ are assigned with respect to the Z and the X-axes respectively. Now, the eigenmodes of the GH shift are linearly polarized waves and those for SH shift are circularly (or elliptically) polarized waves [5]. Therefore, we consider scattering of X-polarized wave to calculate GH shift and scattering of right circularly polarized waves to calculate SH shift. The scattered electric and magnetic fields (radial, angular and azimuthal components) are derived using Mie theory []. These can then be used to obtain the corresponding Poynting vector components. Since the GH and SH shifts are conventionally defined in the plane of incidence and in the plane perpendicular to the plane of incidence respectively, we define these shifts in the scattering plane (θ-plane, P_θ) and in the plane perpendicular to the scattering plane (i.e., azimuthal plane which is Φ-plane) respectively. We use the θ-component of the Poynting vector to define the GH shift (Δ_{GH} for Φ = 0°) and the Φ-component of the Poynting vector as to define the SH shift (Δ_Φ) as;

$$\Delta_{GH} = \lim_{r\to\infty} r\left(\frac{P_\theta}{|P_r|}\hat{\theta}\right) = -\frac{1}{k}\sin\theta\,\frac{\mathrm{Im}\left\{S_2^*\left[\sum_{n=1}^{\infty}(2n+1)a_n\pi_n\right]\right\}}{|S_2|^2}$$

$$\Delta_{SH} = \lim_{r\to\infty} r\left(\frac{P_\varphi}{|P_r|}\hat{\varphi}\right)$$

$$\Delta_{SH} = \frac{\sigma}{k}\left(\frac{\left|\mathrm{Re}\left(S_1^*\left[\sum_{n=1}^{\infty}(2n+1)a_n\pi_n\right] + S_2\left[\sum_{n=1}^{\infty}(2n+1)b_n\pi_n\right]^*\right)\right|}{|S_1|^2+|S_2|^2}\right)\sin\theta$$

Where, σ = ±1 denote that incident RCP/LCP light gives

opposite SH shifts. Here, S_1 and S_2 are the amplitude scattering matrix elements, defined as;

$$S_1 = \sum_{n=1}^{\infty} \frac{(2n+1)}{n(n+1)}(a_n\pi_n + b_n\tau_n), S_2 = \sum_{n=1}^{\infty} \frac{(2n+1)}{n(n+1)}(a_n\tau_n + b_n\pi_n)$$

and a_n and b_n are the coefficients of the normal scattering modes (TM (electric) and TE (magnetic) modes respectively) and τ_n, π_n are the corresponding angle (θ) dependent functions. Note that the radial component of the Poynting vector ($P_r\hat{r}$) signifies energy flow along the direction of the propagation of the scattered wave, whereas, both the angular ($P_\theta\hat{\theta}$) and the azimuthal components ($P_\phi\ \hat{\phi}$) imply transversal energy flow and accordingly lead to shifts (parallel and perpendicular to the scattering plane respectively) in perceived location of the source (scatterer). We then calculated the GH and SH shifts for plasmonic nano-particles (nano-spheres and nano-rods) using the derived expressions. Note that, the above expression of the SH shift includes the contribution from both TM (a_n) and TE (b_n) modes. However, we will consider only the lowest order TM modes (a_1, electric dipole mode) for the scattering from plasmon resonant structures. We correlate GH and SH shifts with polarimetry parameters retardance and diattenuation respectively, which are defines as,

$$\delta(\theta) = \cos^{-1}\left[\frac{\mathrm{Re}(S_2^*(\theta)S_1(\theta))}{|S_2(\theta)||S_1(\theta)|}\right], d(\theta) = \left\{\frac{|S_2(\theta)|^2\cos^2\theta - |S_1(\theta)|^2}{|S_2(\theta)|^2\cos^2\theta + |S_1(\theta)|^2}\right\}$$

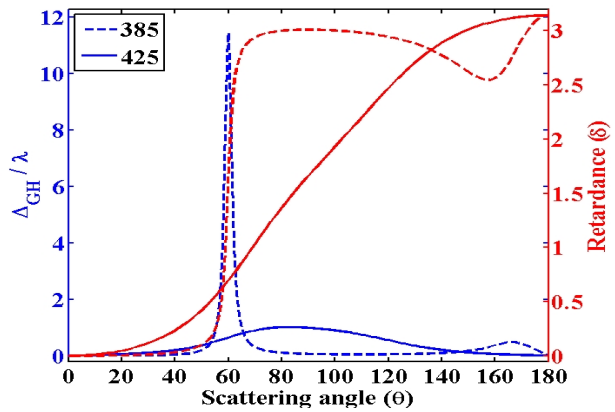


Figure 1: *Angular variation of GH shift (left axis, blue lines) for 50 nm Ag nanosphere for two wavelengths, λ=385 nm (blue dashed line), 425 nm (blue solid line). The angular variation of retardance δ is shown on the right axis for same wavelengths with red dashed and solid line respectively.*

3 Results

In **Fig. 1**, we show the GH equivalent shift (left axis, blue lines) (for x-polarized incident light, in the plane φ=0) for scattering from metal (silver, Ag) nano-spheres of radius 50 nm with surrounding medium as water. These nano-spheres exhibit two resonances: quadrupolar at λ ~ 365 nm and dipolar at λ ~ 480 nm. Shifts are shown for two wavelengths: (1) λ = 385 nm, where the interference between the two modes is strong and (2) λ = 425 nm, near the weak interference region.

The corresponding retardance values are shown on the right axis with red lines. Since retardance is the phase difference between two orthogonal polarizabilities, it is sensitive to the interference. Notice that the GH shift is larger when the retardance is changing sharply from 0 to π and weaker when the retardance is varying slowly. We also did the similar calculations for silver nano rods, where the GH shift was further enhanced (~ 15λ) at spectral overlap (interference) region of the two orthogonal electric dipolar plasmon resonance modes of the nano rods.

In **Fig. 2**, the SH shift (left axis, blue lines) (for RCP incident light) for scattering from same nano-spheres as of Fig. 1 is shown. Local angular maxima of Δ_{SH} is accompanied with local maxima of *d*. This was also observed for the nano-rods with similar calculations. Details of this work and interesting observations of obtained results will be presented in the conference.

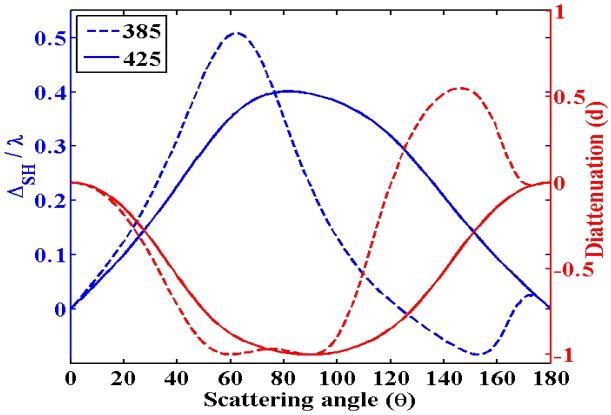


Figure 2: *Angular variation of SH shift (left axis, blue lines) for 50 nm Ag nanosphere for two wavelengths, λ=385 nm (blue dashed line), 425 nm (blue solid line). The angular variation of diattenuation d is shown on the right axis for same wavelengths with red dashed and solid lines respectively.*

4 Conclusion

We have developed a Poynting vector based framework to study both the longitudinal Goos-Hänchen and the transverse Spin Hall shifts, which can be observed in scattering of plane waves from nano particles. Moreover, interesting correlations between the shifts and the *retardance* and the *diattenuation* parameters is shown, which may open up interesting avenues for analysis and

interpretation of the shifts via these polarimetry parameters.

5 References

[1] F. Goos and H. Hänchen, Ann. Phys. 1, 333 (1947).

[2] F.I. Fedorov, Dokl. Akad. Nauk SSSR 105, 465 (1955).

[3] K Y Bliokh and A Aiello, *J. Opt.* **15** 014001 (2013).

[4] Y. Gorodetski, A. Niv, V. Kleiner, and E. Hasman, Phys. Rev. Lett. 101, 043903 (2008).

[5] C.F. Bohren, and D.R. Huffman, *Absorption and scattering of light by small particles* (Wiley, New-York, 1983).

Tailoring the spectral efficiency of gold nanospheres using size dependence of plasmon resonance frequencies and damping rates

Krystyna KOLWAS*, and Anastasiya DERKACHOVA
Institute of Physics, Polish Academy of Sciences, Warszawa 02-668, Poland
**Corresponding author: Krystyna.Kolwas@ifpan.edu.pl*

Abstract

Tailoring the spectral performance of gold nanospheres using size dependence of multipolar plasmon resonance frequencies and damping rates is studied in the range of particle radius from one to hundreds of nanometres. The formalism of Mie theory is used. Careful choice of the material parameters is made for realistic description of plasmonic activity of nanoparticles. Changes in scattering abilities with increasing particle radius are explained by transformation of "dark" plasmon modes of small nanoparticles into radiative, brilliant modes of larger ones. Increasing radiative damping with size is found to compete with the energy dissipative (nonradiative) damping channel. This effect suppresses absorption and increases radiation abilities of larger particles within plasmon mechanism. This is manifested in the corresponding absorption and scattering efficiencies.

1 Introduction

The development of the methodology of synthesis of metal nanoparticles (NPs), as well as of capability of controlling NPs properties by size, shape and composition, has opened a variety of possibilities for applications of NPs in diverse domain of sciences and technology. The exceptional features of NPs result from their ability to resonate with light leading to excitation of localized surface plasmon (LSP) waves. At resonance, light squeezed into sub-wavelength volumes in particle proximity have a profound effect on the efficiency of many optical processes. LSP resonances (LSPR) manifest as the intense absorption or/and scattering of light, depending on the particle size, shape and optical properties of particle environment. The sensitivity of LSPR to these parameters is the basis of colour effects of NP's colloids applied in colorimetric detection methods in biology and medicine.

Understanding the fundamentals of resonant interaction of light with plasmonic nanoparticles is essential for studying LSP properties and for their optimal use. Practically, optimisation is possible, if one has a simple prescript telling how to tailor nanoparticle parameters to optimise plasmon features in divers application. The presented study delivers direct characteristics of absorption and scattering efficiencies of gold nanoparticles and the analysis of their LSP spectral performance in terms of size dependent plasmon resonance frequencies and damping rates. *R*.

2 Direct size characteristics of surface plasmons

Mie scattering theory [1] can correctly reproduce the positions of maxima in the spectra of nanoparticles of chosen radius. Maxima in the absorption or scattering spectra resulting from Mie theory are often interpreted as LSPR. However, scattering and absorption spectra of nanoparticles fall in different spectral ranges, as illustrated in Figure 1. Spectral positions of peaks in these spectra do not coincide and undergo shift with increasing *R* (see Figure 1 and 3). Therefore, in general, such peaks cannot serve as a definition of LSPR.

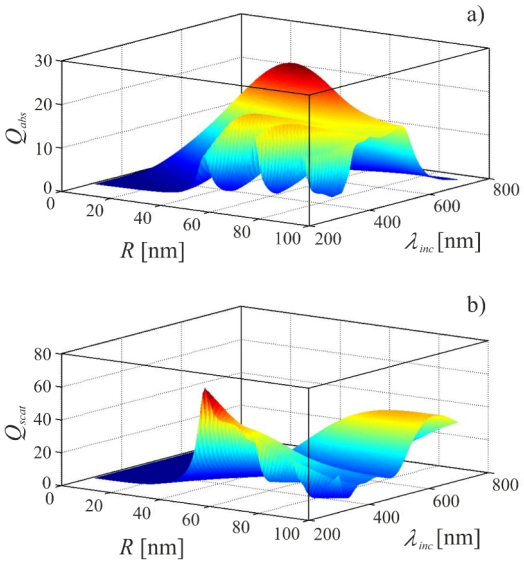


Figure 1 *Visualisation of the spectral performance of gold nanoparticles in the range of radii up to R=100nm: Maxima of a) absorption efficiencies $Q_{abs}(R,\lambda_{inc})$ and of b) scattering efficiencies $Q_{scat}(R,\lambda_{inc})$ fall in different spectral ranges of LSP performance. λ_{inc} is the wavelength of the incoming light, n_{out}=1.*

LSPR size characteristics can be directly predicted by solving the eigenmode problem [2,3,4] of a metal nanosphere, by finding the solutions of Maxwell's equations in absence of the incoming light [1]. Direct dependencies of plasmon resonance frequencies and resonance spectral width and strength (defined by plasmon damping rates (DRs)) versus particle size for noble-metal NPs embedded in diverse dielectric media follow from the modelling [2,3,4]. In the present study we used more specifically parameterized dielectric function of

gold with the effective parameters, which account for the contribution of bound electrons to the polarizability, the additional absorption of bulk gold over 1.8 eV [5] and the effect of the additional, size dependent relaxation of free electrons by scattering on the nanoparticle surface [6].

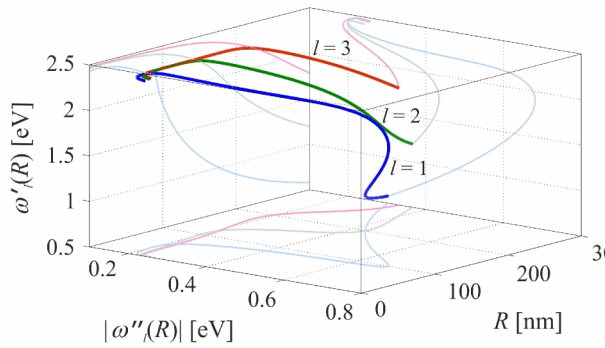


Figure 2 *Plasmon resonance frequencies $\omega'_l(R)=\hbar\omega(R)$ and plasmon damping rates $|\omega''_l(R)|=\hbar/T_l(R)$ for the dipole (l=1), quadrupole (l=2) and hexapole (l=3) plasmon mode.*

Figure 2 shows a 3D plot of LSPR frequencies $\omega'_l(R)=\hbar\omega(R)$ and DRs $|\omega''_l(R)|=\hbar/T_l(R)$, expressed in units of energy (electronvolts) as a function of particle radius. Such plot allows to demonstrate not only size dependence of $\omega'_l(R)$ and $|\omega''_l(R)|$, but also a relationship of ω'_l and $|\omega''_l|$ in addition. $T_l(R)$ are damping times of plasmon oscillations of the plasmon mode l (from the range of (1-20 fs)).

$\omega'_l(R)$ is a decreasing function of radius (with exception of the smallest nanoparticles of few nm radius), as shown on the section on the left wall of the box in Figure 2. $\omega'_l(R)$ dependence starts from the values $\omega_{0,l}$ in the corresponding modes l (see [6] for more details). LSPR resonances at $\omega'_l(R)$ on gold nanoparticles in air (n_{out}=1) is expected to be excited by light of frequency $\omega=\omega'_l(R)$. The corresponding wavelength of the incoming light wave $\lambda_l(R)=2\pi\cdot c\hbar/(e\cdot\omega'_l(R))$. $\lambda_l(R)$ dependence is shown in Figure 3 a)-d) with black solid lines. The first dipole (l=1), quadrupole (l=2) and hexapole (l=3) plasmon modes are presented. The shortest LSP wavelength is that of the dipole plasmon mode $\lambda_{l=1}$=509 nm. Figure 3 d) shows the spectral range and "strength" of the corresponding modes expressed by the Lorentz profiles with the amplitudes and half-widths defined by the corresponding damping rates $|\omega''_l(R)|$. Colours represent summed amplitudes of Lorentz profiles.

However, LSP modes of nanoparticles up to R~50nm are not radiative active. Their scattering efficiencies $Q_{scat}(R)$ are negligible, as seen in Figure 3 b). In this region of sizes LSP modes are dark modes; they are not able to radiate EM energy. This effect can be explained by the fact, that the LSP damping rates $|\omega''_l(R)|$ in this size range (see Figure 1 or 3 b) violet solid lines) are due mainly of nonradiative (dissipative) losses [6]; the contribution of the radiative damping $\gamma^{rad}(R)$ to the total damping rate $|\omega''_l(R)|$ is

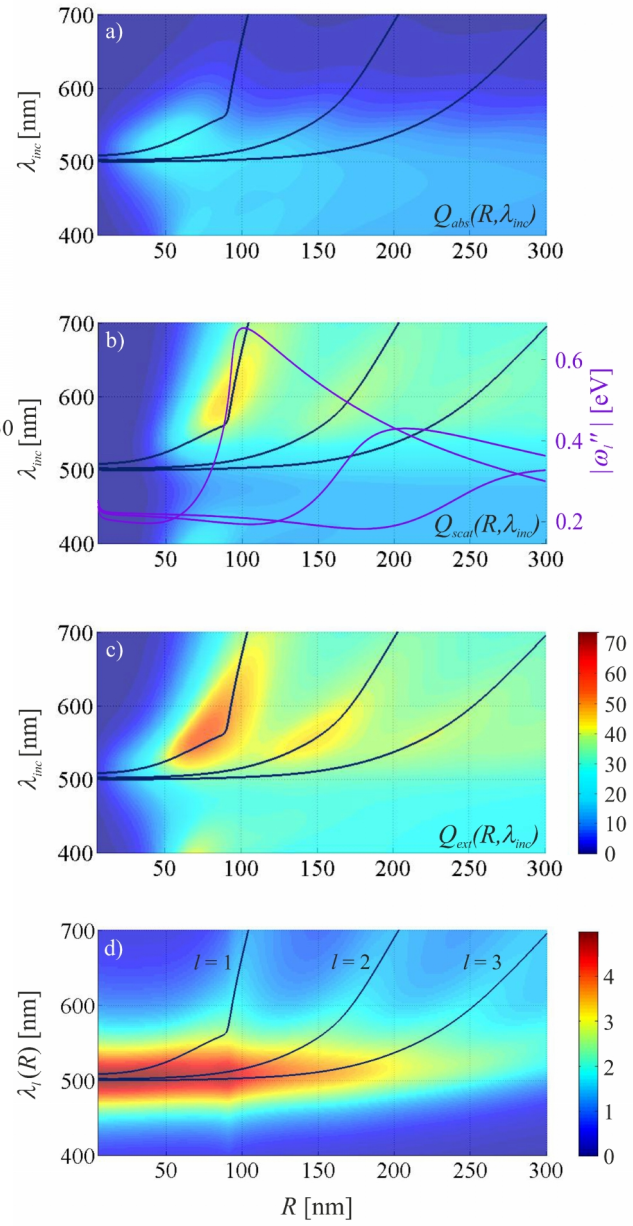


Figure 3 *Maps representing a) absorption $Q_{abs}(R,\lambda_{inc})$, b) scattering $Q_{scat}(R,\lambda_{inc})$ and c) extinction $Q_{ext}(R,\lambda_{inc})$ cross-section efficiencies for gold nanoparticles (n_{out}=1) versus particle radius R after excitation of light at wavelength, λ_{inc}. Colours in figs. a)-c) represent the amplitudes of the corresponding efficiencies, according to the colour scale in fig. c). Black solid lines represent the wavelength λ_l of the light exciting LSRP at $\omega'_l(R)$. for the first dipole (l=1), quadrupole (l=2) and hexapole (l=3) plasmon modes. Solid violet lines in figure b) show the dependence of the corresponding total damping rates $|\omega''_l(R)|$. Colours in fig. d) represent the spectral range and "strength" of LSP modes defined by the corresponding damping rates $|\omega''_l(R)|$.*

negligible. $|\omega''_l(R)|$ dependence results from a specific interplay of radiative and nonradiative contributions. In our modelling, the nonradiative processes consist of ohmic

losses, resulting from the bulk electron relaxation rate γ of the Drude-Lorentz model, and of the surface scattering in small nanoparticles, increasing effective electron relaxation rate proportionally to $1/R$. This kind of processes leads to absorption of light and particle heating. For larger R, radiation damping becomes fast increasing function of particle size, as demonstrated in Figure 2 (see the section presented on the bottom of the 3D box) and Figure 3 b), violet lines. This effect has a tremendous impact on spectral performance of metal nanoparticles, while it competes with the energy dissipative (nonradiative) plasmon damping mechanism causing suppression of absorption [6]. This explains, while the absorption abilities of larger particles are weak in LSP modes of low l. In return, larger nanoparticles scatter light effectively in those modes.

Figure 3 a)-c) which show absorption $Q_{abs}(R,\lambda_{inc})$, scattering $Q_{scat}(R,\lambda_{inc})$ and extinction $Q_{ext}(R,\lambda_{inc})$ cross-section efficiencies, confirm these expectations: smallest nanoparticles are optically weakly active. Their spectral performance is mainly due to absorption; scattering efficiencies Q_{scat} are negligible in this size range, due to the negligible contribution of radiative damping to the total damping rate $|\omega''_l(R)|$. Figure 3 b) proves, that the region of sizes characterised by the increase of damping rates $|\omega''_l(R)|$ in the mode l, (supposed to be due to the increasing contribution of radiative damping $\gamma^{rad}(R)$), correspond to the increase in the scattering efficiency of a nanoparticle.

3 Conclusions

Understanding the fundamentals of resonant interaction of light with plasmonic nanoparticles is essential for studying LSP properties and for their optimal use. The aim of the study was a better understanding of the fundamentals of LSP basis in terms of size characteristics of the most important LSP parameters: plasmon resonance frequencies and the corresponding damping rates. Size dependence of both, with the realistic description of dielectric material properties of a metal nanoparticle, is sufficient in predicting all the plasmon features in applications. When expressed in function of the incoming light wavelength $\lambda_l(R)$ designed to excite LSPR at $\omega'_l(R)$, the derived characteristics can serve as a convenient tool in tailoring the spectral performance of metal nanoparticles in applications by practitioners. In addition to the practical issues, we discuss the LSPR basis: the possibility of converting dark plasmon mode into bright radiant mode by changing the nanoparticle size or plasmon polarity l. Using elaborated spectral characteristics it is possible e.g. to predict the spectral performance of colloids, explain the observed colours and interpret their changes. Also, it is possible to control the changes in performance of plasmonic nanoantennas from good absorbing to good scattering devices, and to optimise their near-field strength. Such kind of study is of use e.g. in tailoringing properties of optoelectronic devises. Also, these characteristics provide basic predictions for studying plasmon dynamics probed with femtosecond laser pulses.

.

4 Acknowledgement

We acknowledge the financial support for this work by the Polish Ministry of Science and Higher Education (Grant No N N202 126837).

5 References

[1] C. F. Bohren and D. R. Huffman, *Absorption and scattering of light by small particles*, (Wiley, New-York, 1983).

[2] A. Derkachova and K. Kolwas, Size dependence of multipolar plasmon resonance frequencies and damping rates in simple metal spherical nanoparticles, Eur. Phys. J. Spec. Top., 144(1): 93–99(2007)

[3] K. Kolwas, A. Derkachova, and M. Shopa, Size characteristics of surface plasmons and their manifestation in scattering properties of metal particles, JQSRT, 110(14–16):1490–1501(2009)

[4] K. Kolwas and A. Derkachova, Plasmonic abilities of gold and silver spherical nanoantennas in terms of size dependent multipolar resonance frequencies and plasmon damping rates, Opto-Electronics Rev., 18(4):429–437(2010)

[5] A. Derkachova, K. Kolwas *to be published*

[6] K. Kolwas and A. Derkachova, Damping rates of surface plasmons for particles of size from nano- to micrometers; reduction of the nonradiative decay, JQSRT,114:45–55(2013)

Analysis of the scattering behaviour of two spherical plasmonic particles

Wen FENG[1,*], Jens HELLMERS[1] , Vladimir SCHMIDT[1] , Lutz MÄDLER[1] and Thomas WRIEDT[2]

[1] Process and Chemical Engineering, Universität Bremen, 28359 Bremen, Germany
[2] Institut für Werkstofftechnik, 28359 Bremen, Germany

Corresponding author: w.feng@iwt.uni-bremen.de

Abstract

The T-matrix method is used to calculate the extinction cross section of two ITO particles resulting from incoming fields with different polarizations in the plasmonic region. We investigate the influence of the interparticle distance between two spherical particles, the incident direction and the size of scatterers on their scattering behaviour.

1 Introduction

The T-matrix method [1] is used to calculate scattering cross sections of two spherical particles close to each other. Much work has been performed to compute light scattering properties on bispherical clusters [2, 3]. But there are still some problems when merging two spheres together. Here, we would like to present results of light scattering simulations for dimers of Indium Tin Oxide (ITO) in the plasmonic region. The Drude model approach is used to calculate the corresponding values for the real and imaginary parts of the reflective index which is presented in Figure 1.

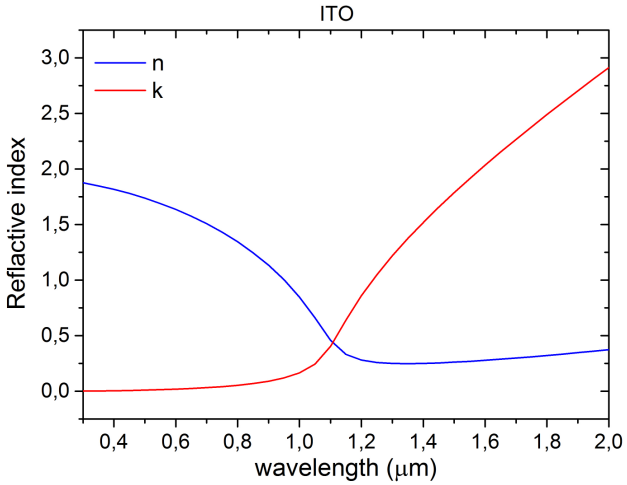


Figure 1 *Refractive index (n,k) of ITO. The corresponding data for a Drude-model approach was taken from [4].*

2 Parameter choices

Figure 2 shows the extinction cross sections of two ITO particles with an identical diameter of d = 50 nm and separated by a distance D varying from 0.5 nm to 10 nm. These are the orientation averaged results for wavelengths from 500 nm to 2000 nm. When D is sufficiently small (approximately 5 nm), there is an additional peak for wavelengths above 1500 nm. This peak is red-shifted when the interparticle distance decreases. In order to analyse the influence of the interparticle distance, the incident direction and the size of the scatterers on the extinction cross section, we consider the scatterers aligned along the y-axis (henceforth termed the scatterer axis). Two different diameters, d = 20 nm, and d = 100 nm, and a varying interparticle distance D from 0.2 nm to 3 nm are investigated for wavelengths in the range from 1500 nm to 2000 nm.

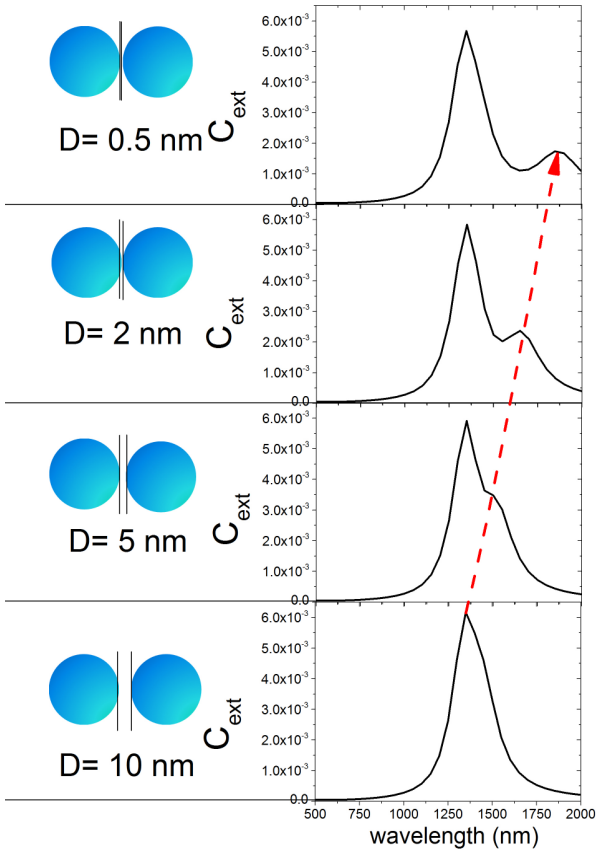


Figure 2 *Evolution of the extinction cross section of two ITO particles with a diameter of 50 nm irradiated by a plane wave with wavelength increasing from 500 nm to 2000 nm, orientation averaged results. The interparticle distance increases from 0.5 nm to 10 nm.*

Concerning the incident field, we consider three configurations, specified by the direction of the incident light **k** and the polarization shown in Table 1.

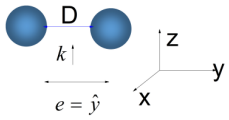
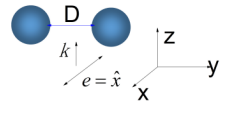
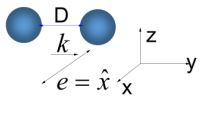
i. Perpendicular: k perpendicular to the scatterer axis, polarization parallel to the scatterer axis: $\mathbf{k} = k\hat{z}, \mathbf{e} = \hat{y}$	
ii. Transverse: k perpendicular to the scatterer axis, polarization perpendicular to the scatterer axis: $\mathbf{k} = k\hat{z}, \mathbf{e} = \hat{x}$.	
iii. Parallel: k parallel to the scatterer axis, polarization perpendicular to the scatterer axis: $\mathbf{k} = k\hat{y}, \mathbf{e} = \hat{x}$.	

Table 1 *Different configurations used in the simulation.*

Extinction cross sections of dimers for three configurations are calculated for different interparticle distances in order to investigate the influence of the interparticle distance and the incident direction on the convergence of light scattering calculations.

3 Method

To simulate the light scattering by ITO dimers we use the Null-Field Method (commonly known as the T-matrix method) [5]. This is a very accurate method based on the semianalytical solution of Maxwell equations. Over the years it was extended to more complex cases such as cluster of particles, particles near the surface, anisotropic scatterers [6, 7].

In the frame of the T-matrix method the incident and scattered fields are expressed in terms of spherical vector wave functions (SVWF):

$$\mathbf{E}_{inc}(\mathbf{r}) = \sum_{n=1}^{\infty}\sum_{m=-n}^{n} a_{nm}\mathbf{M}_{nm}^{(1)}(k\mathbf{r}) + b_{nm}\mathbf{N}_{nm}^{(1)}(k\mathbf{r}) \quad (1)$$

$$\mathbf{E}_{scat}(\mathbf{r}) = \sum_{n=1}^{\infty}\sum_{m=-n}^{n} p_{nm}\mathbf{M}_{nm}^{(3)}(k\mathbf{r}) + q_{nm}\mathbf{N}_{nm}^{(3)}(k\mathbf{r}) \quad (2),$$

where $k = k_0\sqrt{\varepsilon\mu}$ is the wave number. The expansion coefficients (a_{nm}, b_{nm}) and (p_{nm}, q_{nm}) are interconnected by the linear transformation, the T-matrix. Here, in the computations we limited the summation in (1) by the expansion order N_{rank} and the azimuthal order M_{rank} as follows:

$$\sum_{n=1}^{\infty}\sum_{m=-n}^{n} \cdots \rightarrow \sum_{n=1}^{N_{rank}}\sum_{-min(n,M_{rank})}^{min(n,M_{rank})} \cdots \quad (3)$$

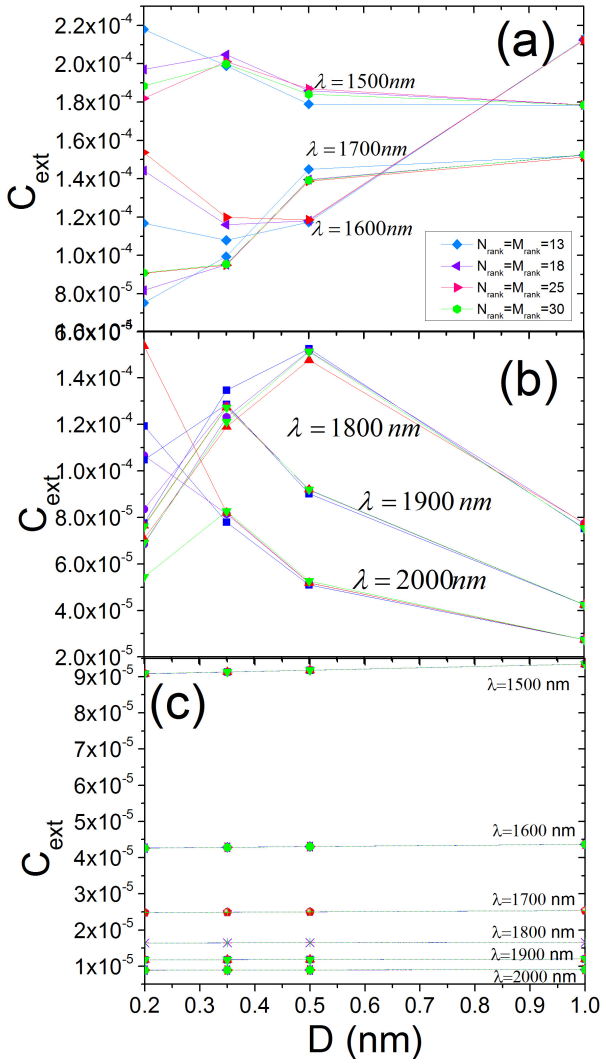


Figure 3 *Dependence of the extinction cross sections of ITO dimers on the expansion order N_{rank} and azimuthal order M_{rank}, diameter d=20 nm, wavelength increasing from 1500 nm to 2000 nm. (a), (b) show the results for configuration iii as mentioned above, (c) for configuration i and ii. N_{rank} and M_{rank} are identical varying from 13 to 30. The interparticle distance ascends from 1.0 nm to 0.2 nm. Numerical precision is QUAD.*

T-matrix light scattering calculations using the Null Field Method for extreme particle shapes e.g. concavities and highly non-spherical particles with large aspect ratios show an increasingly unstable numerical behaviour. The results for an increasing expansion order N_{rank} start to behave unpredictably, usually never reaching convergence [8].

4 Results

In the following, we would like to present results for ITO dimers with fixed d varying the interparticle distance from 0.2 nm to 3 nm.

4.1 d = 20 nm

The extinction cross sections for the configuration iii are shown in Figure 3 (a) and (b), for the configuration i and ii in Figure 3 (c).

For the configuration iii, all diagrams indicate that when the interparticle distance decreases below 0.35 nm, there are convergence problems of the solution. The calculations become numerically unstable. On the other hand this does not happen for the configuration i and ii. The simulation of the spectral behaviour of the dimers for configuration iii corresponding to Figure 3 (a) and (b) is presented in Figure 4. A minimal distance of D= 0.5 nm is chosen to stay clear of the observed numerical difficulties.

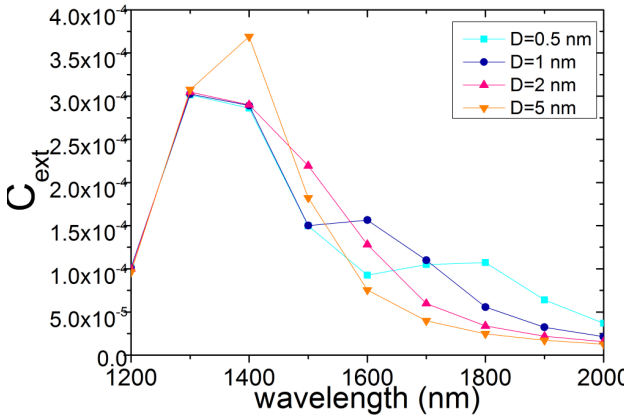


Figure 4 *Simulation of spectral behaviour of approaching ITO dimers for parallel polarization, the value D is the distance between the spheres' surfaces.*

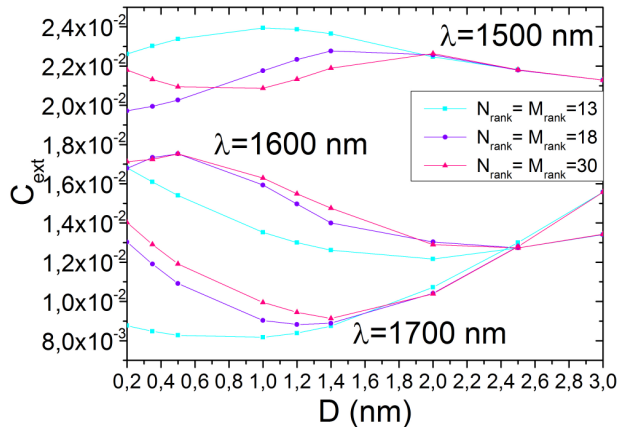


Figure 5 *Dependence of the extinction cross sections of ITO dimers on N_{rank} and M_{rank}, diameter d= 100 nm, wavelength increasing from 1500 nm to 1700 nm. N_{rank} and M_{rank} are identical varying from 13 to 30. The interparticle distance ascends from 3.0 nm to 0.2 nm.*

4.2 d = 100 nm

The results presented in Figure 5 show convergence problems occur below an interparticle distance of about 2 nm. Overall they become larger than those observed for d=20 nm.

5 Summary

In this preliminary investigation we have demonstrated that the interparticle distance of two ITO nanoparticles does have an appreciable effect on the extinction cross section. Convergence problems occur when the direction of incident light is parallel to the scatterer axis and a small interparticle distance. The critical interparticle distance depends on the size of particles. In our simulation, the ratio of the critical distance to the size of particles is approximately 2 %. Further investigations are needed to clarify this numerical problem, which has also been observed with other T-matrix computer programs based on a similar theoretical approach.

6 Acknowledgement

This work was supported by Graduate School MIMENIMA (GRK 1860) through Deutsche Forschungsgemeinschaft (DFG).

7 References

[1] A. Doicu, T. Wriedt and Y. Eremin, *Light Scattering by Systems of Particles. Null-Field Method with Discrete Sources–Theory and Programs.* (Springer Verlag, Berlin, Heidelberg, New York, 2006).

[2] Mishchenko M.. I., Hovenier J.W. and Travis L.D., *Light scattering by nonspherical particles.* (Academic Press, New York 2000).

[3] Mackowski D.W., Analysis of radiative scattering for multiple sphere configurations. Proceedings of the Royal Society of London A 433, 599-614 (1991).

[4] Franzen S., Surface plasmon polaritons and screened plasma absorption in indium tin oxide compared to silver and gold. Journal of Physical Chemistry C 112:6027–32 (2008).

[5] Waterman P. C., Matrix formulation of electromagnetic scattering. Proceedings of the IEEE 53, 805-812 (1965)

[6] Doicu A., Eremin Y., Wriedt T., *Acoustic and electromagnetic scattering analysis using discrete sources.* (Academic Press, 2000)

[7] Mishchenko M. I., Travis L. D, Lacis A. A., *Scattering, absorption and emission of light by small particles.* (Cambridge University Press, Cambridge 2002)

[8] Hellmers J., Schmidt V., Wriedt T., Improving the numerical stability of T-matrix light scattering calculations for extreme particle shapes using the nullfield method with discrete sources. Journal of Quantitative Spectroscopy & Radiative Transfer 112, 1679–1686 (2011)

Multiple Light Scattering From Ordered and Disordered Atomic Clouds

Philippe COURTEILLE* and Romain BACHELARD

Instituto de Física de São Carlos, Universidade de São Paulo, Av. Trabalhador São-carlense, 400, São Carlos 13566-590, SP, Brazil

*Corresponding author: philippe.courteille@ifsc.usp.br

Abstract

The scattering of light from macroscopic material objects can be described in terms of Maxwell's equations solved for a given set of boundary conditions. In contrast, for point-like targets such as atoms in a dilute gas, the scattering is understood in terms of Bohr's atomic model. Since any macroscopic object is formed from elementary scatterers (atoms or molecules), it is an interesting question how the scatterers must cooperate to produce macroscopic scattering phenomena such as refraction or Mie scattering. The cooperation can be studied in confined cold atomic clouds, which exhibit micro- as well as macroscopic scattering features. We will discuss a microscopic approach to cooperative scattering able to grasp apparently contradictory features of both, micro- and macroscopic scattering. In a regime called single-photon superradiance it reproduces Rayleigh, Bragg or Mie scattering, whereas in a regime dominated by multiple scattering it predicts coherent backscattering or the formation of photonic band structures. In ultracold clouds, correlations between subsequent scattering processes can even cause collective instabilities called matter wave superradiance and collective atomic recoil lasing depending on whether the correlations are sustained by long-lived matter wave coherences or mediated by long-lived modes of a high finesse ring cavity. We support the validity of our model by experimental observations.

1 Introduction

The interaction of light with macroscopic objects like prisms or crystals is described by Maxwell's equations and uses the notion of quantities such as the "index of refraction" or "nonlinear susceptibility". On another scale, it is quite well known how atoms and molecules scatter light, absorbing photons and reemitting them isotropically. Difficulties arise as one tries to reunite these two images into a complete theory in order to understand, for example, how the atoms or molecules of the macroscopic body must "cooperate" to scatter, diffract or refract light the way they do, thus generating the illusion of a homogeneous refractive index. An interesting system to study these issues are clouds of atoms, which are macroscopic when we consider the cloud as a whole, but microscopic when we look at individual atoms. Cold atoms are particularly useful because they can easily be controlled and manipulated in the laboratory.

However, a precise definition of "cooperativity" is not simple as there are various manifestations of cooperativity. A simple limit, which already captures phenomena such as diffraction, refraction or Bragg scattering, is *single scattering*, when photons are scattered only once. The opposite case, more challenging from the point of view of cooperativity, is the *multiple scattering* limit. Obviously, if a photon entering a sample is scattered many times, more atoms cooperate in diffusing the photon. Finally, we are also interested in the case where the *cooperative optical forces* induce a coherent reorganization of the atomic density distribution, which in turn provides a coherent feedback to the light.

2 Cooperative scattering phenomena

Our group at the Instituto de Física de São Carlos developed together with research groups from the Institut Non Linéaire de Nice and from the Universitá degli studi di Milano a theory of cooperative light scattering by atomic clouds that is, in principle, able to operate in the mesoscopic regime [1,2]. We are currently in the process of applying this theory to physically relevant systems to obtain experimentally testable predictions of collective effects.

2.1 Cooperative radiation pressure force

In cold and ultracold atomic clouds it is very easy to measure the *radiation pressure* force. We have observed dramatic alteration of this force due to cooperative effects [3,4] even in the single-scattering regime. Under certain circumstances cooperative optical forces may lead to the emergence of self-organized structures. For instance, the so-called “Collective Atomic Recoil Laser” (CARL) is a phenomenon in which a matter wave grating and a standing light wave build up each other self-consistently [5]. CARL has been observed with cold atomic clouds [6] and Bose-Einstein condensates interacting with high-finesse optical ring cavities [7,8].

2.2 Mie resonances

Another effect we aim at evidencing are *Mie resonances in atomic clouds*, an effect expected to occur in the multiple scattering regime. Much can be learned from comparing the light scattering by large objects with continuous density distributions and disordered samples of small scatterers, such as atomic clouds. The first case can be treated by Mie theory [9], which considers propagating

waves inside and outside of a continuous dielectric medium. The second case can be handled by a theory of generalized Rayleigh scattering that may be applied because of the microscopic size of the atom (much smaller than the wavelength of incident light) assuming that all atoms in the sample participate altogether in the scattering process, i.e., the *light is scattered cooperatively* [1,10-12]. We showed in a recent work [12-13] that the theory of collective scattering can be mapped to the Mie theory, restoring the well-known refractive index. Hence, we may now use the results of Mie theory and Mie resonances [14] for clouds of cold atoms. Such resonances arise from some phase matching condition between the propagating wave and the cavity created by the microscopic particles. Despite the absence of sharp boundaries for the clouds, we have recently shown that some types of Mie resonances are to be expected in dense atomic clouds [13]. They have, however, not been observed experimentally yet.

2.3 Photonic bandgaps in optical lattices

Differently from the phenomena discussed so far, which are expected in disordered media, photonic bandgaps are observed in periodically ordered structures, such as photonic crystals. Atomic clouds can be periodically ordered in so-called optical lattices. In contrast to dielectric photonic crystals, they can be tuned in real time and they can be made to have perfect periodicity. We have recently been able to demonstrate photonic bands in one-dimensional optical lattices [15,16] and are now starting to look for omnidirectional bandgaps. It is interesting to note that the phenomenon of photonic bandgaps can be understood in terms of cooperative multiple scattering [17].

3 References

[1] Ph.W. Courteille et al., Modification of radiation pressure due to cooperative scattering of light, Eur Phys . J. D 58, 69 (2010).

[2] R. Bachelard , N. Piovella , and Ph.W. Courteille , Cooperative scattering and radiation pressure force in dense atomic clouds, Phys . Rev. A 84, 013821 (2011).

[3] T. Bienaimé, S. Bux, E. Lucioni, Ph.W. Courteille, N. Piovella, R. Kaiser, Observation of cooperative radiation pressure in presence of disorder, Phys. Rev. Lett. 104, 183602 (2010).

[4] H. Bender et al., Observation of cooperative Mie scattering from an ultracold atomic cloud, Phys. Rev. A 82, 011404(R) (2010).

[5] R. Bonifacio and L. de Salvo, Nucl. Instrum Methods Phys. Res. A 341, 360 (1994).

[6] D. Kruse, C. von Cube, C. Zimmermann and Ph.W. Courteille, Observation of Lasing Mediated by Collective Atomic Recoil, Phys. Rev. Lett. 91, 183601 (2003).

[7] S. Slama, S. Bux, G. Krenz, C. Zimmermann, Ph.W. Courteille, Superradiant Rayleigh scattering and collective atomic recoil lasing in a ring cavity, Phys. Rev. Lett. 98, 053603 (2007).

[8] S. Bux, Ch. Gnahm, R.A. Maier, C. Zimmermann, Ph.W. Courteille, Cavity-controlled matter wave superradiance at the recoil limit Phys. Rev. Lett. 106, 203601 (2011).

[9] G. Mie, Beiträge zur Optik trüber Medien, speziell kolloidaler Metallösungen, Ann . Phys. 330, 377 (1908).

[10] M.O. Scully , E. Fry , C.H.R. Ooi , and K. Wodkiewicz , Directed Spontaneous Emission from an Extended Ensemble of N Atoms: Timing Is Everything, Phys . Rev. Lett. 96, 010501 (2006).

[11] J.H. Eberly, Emission of one photon in an electric dipole transition of one among N atoms, J. Phys. B 39, 599 (2006).

[12] R. Bachelard, H. Bender, Ph.W. Courteille, N. Piovella, C. Stehle, C. Zimmermann, S. Slama, Role of Mie scattering in the seeding of matter-wave superradiance, Phys. Rev. A 86, 043605 (2012).

[13] R. Bachelard , Ph.W. Courteille , R. Kaiser and N. Piovella , Resonances in Mie scattering by an inhomogeneous atomic cloud, Europhys. Lett. 97, 14004 (2012).

[14] C.F. Bohren, and D.R. Huffman, Absorption and scattering of light by small particles (Wiley, New-York, 1983).

[15] A. Schilke, C. Zimmermann, Ph.W. Courteille, W. Guerin, Photonic band gaps in one-dimensionally ordered cold atomic vapors, Phys. Rev. Lett. 106, 223903 (2011).

[16] A. Schilke, C. Zimmermann, Ph.W. Courteille, W. Guerin, Optical parametric oscillation with distributed feedback in cold atoms, Nature Phot. 6, 101 letter (2012).

[17] M. Samoylova, N. Piovella, R. Bachelard, Ph.W. Courteille, Microscopic theory of photonic bandgaps in optical lattices, Opt. Comm. 312, 94 (2014).

Surface Plasmon Polaritons in Linear Chains of Silver Nanospheroids

Ilia L. RASSKAZOV[1-2,*], Sergei V. KARPOV[1-3] and Vadim V. MARKEL[4-5]

[1] L.V. Kirensky Institute of Physics, Russian Academy of Sciences, Krasnoyarsk, 660036, Russia
[2] Siberian Federal University, Krasnoyarsk, 660041, Russia
[3] Siberian State Aerospace University, Krasnoyarsk, 660014, Russia
[4] Department of Bioengineering, University of Pennsylvania, Philadelphia, Pennsylvania, 19104, USA
[5] Department of Radiology and Graduate Group in Applied Mathematics and Computational Science, University of Pennsylvania, Philadelphia, Pennsylvania, 19104, USA

Corresponding author: il.rasskazov@gmail.com

Abstract

We consider propagation of surface plasmon polaritons in linear chains of silver nanospheroids. We show that, for suitably chosen parameters, the propagation is free of spatial decay in spite of the full account of absorptive losses in the metal.

1 Introduction

Propagation of surface plasmon polaritons (SPPs) in chains of metallic particles has attracted significant attention due to the number of potential applications in waveguiding and nanoplasmonics [1,2], as well as in spectroscopy and chemical sensing [3,4]. Chains of nanoparticles have also attracted attention in quantum information processing and it was recently demonstrated that such chains can serve as unidirectional single-photon or single-plasmon emitters [5]. In this work, we investigate the spatial decay of SPPs in chains of spheroidal particles and evaluate ways to mitigate this decay by manipulating the aspect ratio of the particles.

2 Model

Consider a linear periodic chain of N identical silver spheroids with b and a being the shorter and longer semi-axes. The spheroids can be either prolate or oblate, and we assume that the longer semi-axis is perpendicular to the chain in both cases. We will consider only the SPPs that are polarized transversely to the chain. For oblate spheroids, the two mutually orthogonal transverse polarizations are equivalent. In case of prolate spheroids, we will consider only the polarization aligned with the longer axis. In all cases, the shorter semi-axis is taken to be $b = 8$ nm and the center-to-center interparticle distance is $h = 3b = 24$ nm. Thus, the surface-to surface distance between two nearest neighbours in the chain is equal to b. For transversely polarized SPPs, these parameters are within the range of validity of the dipole approximation [6], which will be used in all simulations.

The principal values of the polarizability tensor of each spheroid are given by well-known expressions [7] with the account of the first nonvanishing radiative correction [8]. We use the Drude formula to define the dielectric permittivity ε of silver with the contribution to the permittivity due to the interband transitions.

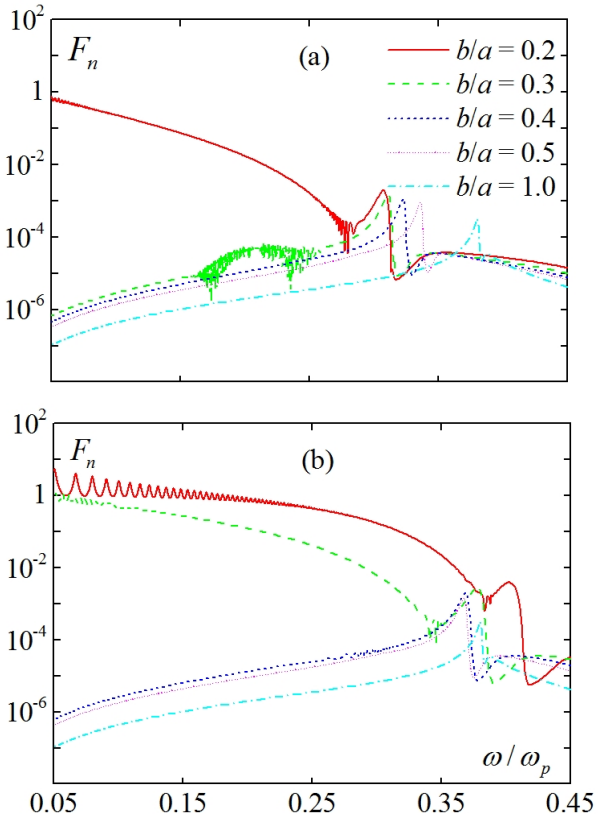


Figure 1 *Transmission spectra for transversely polarized SPPs in chains built from prolate spheroids (a) and oblate spheroids (b) for different aspect ratios b/a*

3 Numerical results

Assume that the first particle in the chain ($n = 1$) is illuminated by a near-field external source, which creates a fixed and known amplitude of the electric field. We will use the formalism of normalized Green's function [9], $F_n = |D_{n,1} / D_{1,1}|$ which can be obtained in finite chains numerically by solving the coupled-dipole equations [9].

We will refer to the quantity F_n as the transmission of the chain.

Figure. 1 shows that SPPs tend to propagate with less decay for smaller values of b/a. The transmission F_n is of the order of unity when $0.05 < \omega/\omega_p < 0.15$ (for prolate spheroids) or $0.05 < \omega/\omega_p < 0.25$ (for oblate spheroids).

The above finding is radically different from the results previously obtained for chains of spherical particles. Still, it can be seen from Figure. 2 that, in the case of spheres, F_n drops precipitously with n. The curves for spheroids exhibit much slower decay.

The data of Figures. 1,2 do not contradict conservation of energy. When the decay of the Green's function is slow or absent, all spheroids dissipate energy approximately at the same rate and, correspondingly, this energy must be supplied by an external source. Therefore, to maintain a given amplitude of the external field, one must supply the system with the optical energy, which is proportional to the length of the chain, N.

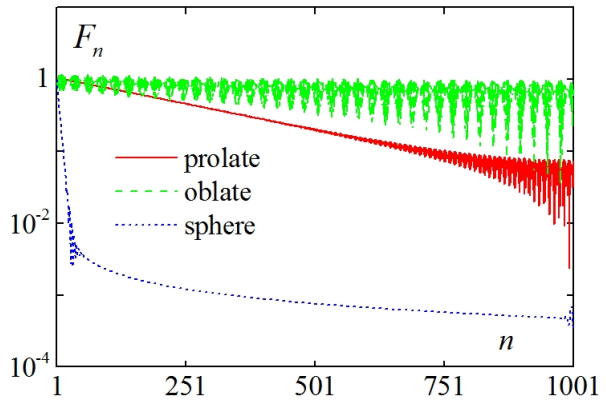


Figure 2 *Normalized Green's function F_n for linear chains of spheroids with aspect ratio $b/a = 0.2$ at the frequency $\omega/\omega_p = 0.15$ and for a chain of spheres at $\omega/\omega_p = 0.38$*

In Figure. 3, we plot $\eta = Q_s/Q_e$ (where Q_s and Q_e are the efficiencies of scattering and extinction [7]) as a function of frequency for chains of spheroids and spheres. For both prolate and oblate spheroids, we have $\eta \approx 1/N \approx 10^{-3}$ at $\omega = 0.15\omega_p$. This indicates that, in the case of spheroids, almost all energy supplied by the source is absorbed and the absorption is equally divided between the spheroids comprising the chain; hence, we see no significant spatial decay of F_n.

The slow decay of SPPs reported above can be explained from a physical point of view. Replacing spherical particles by spheroids increases the strength of electromagnetic interaction of neighbouring particles because the coupling coefficients (polarizabilities) can be increased while keeping $h = \text{const}$. This results in a significant increase of the group velocity of SPPs, as was already predicted in [10]. A wave packet spends less time travelling from one end of the chain to another. If we assume that the amplitude of the wave packet decays with time at a constant rate, then we can expect a larger amplitude of the SPP at Nth spheroid. Another helpful factor is that the introduction of nonsphericity allows one to shift the Frohlich frequency of the spheroids toward the red, where metal nanoparticles are known to be better (higher-quality) resonators.

Using previously known theoretical results [9] we can estimate the SPP propagation length for the parameters used in this work. We have $l \approx 44\mu m$ (oblate spheroids), $l \approx 9.1\mu m$ (prolate spheroids), and $l \approx 0.6\mu m$ (spheres), which are in a good agreement with the data of Figure. 2.

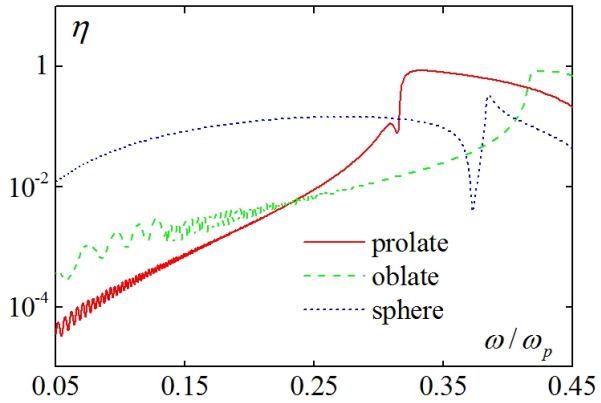


Figure 3 *Quality factor $\eta = Q_s/Q_e$ for chains of spheres and spheroids with the aspect ratio $b/a = 0.2$*

4 Conclusion

We conclude that the use of nonspherical particles can be advantageous for the design of nanoparticle waveguides. Gaussian SPP wave packets can propagate along a chain of spheroids with negligible spatial decay. These two features are desirable in many of the applications considered in the literature. Unfortunately, this regime of propagation requires large energy input: the fraction of incident energy converted to the useful signal scales as $1/N$.

5 References

[1] Evlyukhin A.B., Bozhevolnyi S.I., Stepanov A.L., Kiyan R., Reinhardt C. et al., Focusing and directing of surface plasmon polaritons by curved chains of nanoparticles, Optics Express 15(25):16667-80 (2007)

[2] Udagedara I.B., Rukhlenko I.D., Premaratne M., Complex-ω approach versus complex-k approach in description of gain-assisted surface plasmon-polariton propagation along linear chains of metallic nanospheres, Physical Review B 83(11):115451-57 (2011)

[3] Evlyukhin A.B., Bozhevolnyi S.I., Pors A., Nielsen M.G., Radko I.P., et al., Detuned electrical dipoles for plasmonic sensing, Nano Letters 10(11):4571-77 (2010)

[4] Kravets V.G., Schedin F., Jalil R., Britnell L., Gorbachev R.V., et al., Singular phase nano-optics in plasmonic metamaterials for label-free single-molecule detection, Nature Materials 12:304-309 (2013)

[5] Koenderink A.F., Plasmon Nanoparticle Array Waveguides for Single Photon and Single Plasmon Sources, Nano Letters 9(12):4228-33 (2009)

[6] Rasskazov I.L., Karpov S.V., Markel V.A., Nondecaying surface plasmon polaritons in linear chains of silver nanospheroids, Optics Letters 38(22):4743-46 (2013)

[7] C.F. Bohren, and D.R. Huffman, *Absorption and scattering of light by small particles* (Wiley, New-York, 1983).

[8] Draine B.T., The discrete-dipole approximation and its application to interstellar graphite grains, Astrophysics. Journal 333:848-872 (1988)

[9] Markel V.A., Sarychev A.K., Propagation of surface plasmons in ordered and disordered chains of metal nanospheres, Physical Review B 75(8):085426(11) (2007)

[10] Govyadinov A.A., Markel V.A., From slow to superluminal propagation: Dispersive properties of surface plasmon polaritons in linear chains of metallic nanospheroids, Physical Review B 78(3):035403(12) (2008)

Multiple particle scattering approach applied to coupling effects in plasmonic aggregates: from hybrid dimer modes to quadrumer Fano resonances

Saïd BAKHTI[1], Nathalie DESTOUCHES[1] and Alexandre TISHCHENKO[1,*]

[1] Université de Lyon, F-42023 Saint-Etienne, France; CNRS, UMR 5516, Laboratoire Hubert Curien, Université Jean-Monnet, 18 rue Pr. Lauras F-42000 Saint-Etienne

Corresponding author: alexandre.tishchenko@univ-st-etienne.fr

Abstract

The extension of the T-Matrix method to multiple particle systems is used together with an efficient numerical resonance extractor to study the coupling effects in interacting metal particles. In small dimers, identic particles exhibit only parallel and perpendicular (with respect to the dimer axis) symmetric dipolar modes, whereas asymmetric modes can be excited by breaking the system symmetry, e.g. when considering different particle sizes. Combining two dimers brings up Fano resonances resulting from destructive interferences between dimer hybrid modes. Tuning such asymmetric line profile is achieved by tuning hybrid modes of each dimer taken separately.

1 Introduction

Metal nanoparticles (NPs) are well known for their particular optical properties. Under optical excitation, such particles exhibit localized surface plasmon resonances (LSPRs) due to collective oscillations of free electrons and characterized by an enhancement of both radiative (scattering) and non-radiative (absorption) particle response [1]. In the case of noble metals, LSPRs occur in the visible spectrum with a strong dependence on the particle morphology and distribution in its spectral response. In particular, coupling effects in interacting particles are well suited to tune the resonance position over a broad spectral domain. Fano resonances occurring in specific nanostructures [2], like particle oligomers, appear as a promising way to control the spectral behavior of plasmonic devices. Such resonances appear as an asymmetric spectral line shape in the system optical response and are physically related to destructive interferences between broad and narrow resonances.

We report in this work a numerical investigation of coupling effects in dimers and characterization of the Fano resonances in quadrumers as resulting of interacting dimer modes. We use the rigorous solution of multiple particle scattering based on the T-Matrix approach [3, 4] to model the optical response of metal NPs, combined with an accurate pole finding algorithm [5] to extract the resonance characteristics and study the plasmon coupled modes.

2 Numerical methods

2.1 Multiple particle scattering

The multiple particle scattering problem (Figure 1) is solved using the T-Matrix approach extended to an ensemble of particles. All electromagnetic fields, i.e. incident and scattered by each particle, are expanded into infinite series in the basis of weighted vector spherical wave functions. The problem is formally solved by applying, for each particle, the T-Matrix operator on the total incident wave on this particle (including the incident field and the fields scattered by the other particles). The interaction equations are then expressed as:

$$\mathbf{f}_i = \mathbf{T}_i \left(\mathbf{a}_i + \sum_{i \neq j} \mathbf{H}^{ij} \mathbf{f}_j \right) \quad (1)$$

where $\mathbf{f}_i$ and $\mathbf{a}_i$ are expansion coefficient vectors respectively related to the field scattered by the ith particle and to the incident wave centered on this particle. $\mathbf{T}_i$, the ith particle T-Matrix, is founded by applying the boundary conditions on the particle surface. $\mathbf{H}^{ij}$ is the translation matrix which transforms the scattered expansion coefficient from the jth particle's coordinate system center to the ith one.

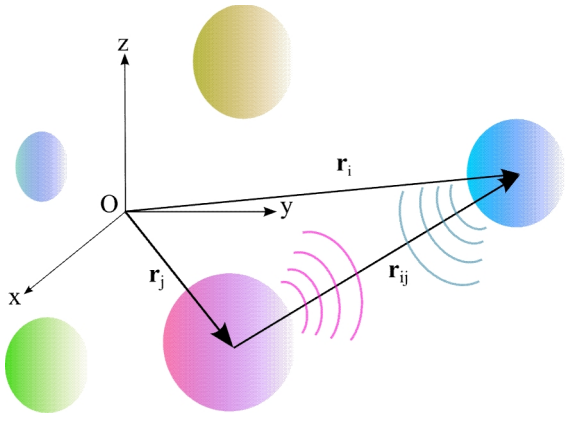


Figure 1 *Geometry of the multiple particle scattering problem.*

2.2 Extraction of resonance characteristics

When considering metal particles, plasmon resonances occur in form of different spectral resonance bands related to different modes. We propose an efficient method to extract the resonance characteristics of each excited resonant mode. The key idea of our approach, based on precedent studies [5, 6], is an analytical representation of the particle response (in our case the complex-valued extinction cross section) as a singular function of the pulsation with J poles corresponding to the J resonances in the particle response:

$$C(\omega) = \sum_{j=1}^{J} \frac{p_j \omega_j}{\omega - \omega_j} + \sum_{k=0}^{\infty} q_k \omega^k \qquad (2)$$

Each pole, i.e. resonance, is spectrally characterized by complex pulsation ω_j whose real part corresponds to the spectral position and imaginary part to the bandwidth.

An efficient algorithm [7] is used to compute the complex pulsation of each mode by filtering the regular part of Eq. (2). This is done by discretizing the particle response in function of the pulsation, and by applying the Newton's divided differences to perform a numerical derivation of Eq. (2) in order to nullify the regular part and to find the resonance characteristics. The number of discretization points determines the derivation order and in practice, only few points (about five per mode) are needed to obtain accurate results.

3 Results

3.1 Hybrid modes on sphere dimers

We consider first silver sphere dimers embedded in glass (n = 1.5). In the case of similar particles (e.g. 5 nm in radius), a split of dipolar resonance into parallel and perpendicular (respective to the dimer axis) modes occurs (Figure 1). These two modes correspond to a symmetric polarization of the spheres. The parallel mode is strongly red-shifted when the inter-particle distance decreases, whereas the perpendicular mode is slightly blue-shifted. This behavior can be physically related to energetically favorable (parallel mode case) and unfavorable (perpendicular case) coupled dipoles.

When breaking the dimer symmetry, i.e. by considering different sphere sizes, different polarization configurations appear for each mode (Fig. 3). For the parallel mode (Fig. 3a) symmetric (favorable) and anti-symmetric (unfavorable) configurations are red- and blue-shifted, respectively. In the case of the perpendicular mode (Fig. 3b), the situation is reversed and the anti-symmetric configuration is red-shifted.

This behavior observed using rigorous computations is consistent with the hybridization theory for plasmon modes developed by Nordlander et al. [8].

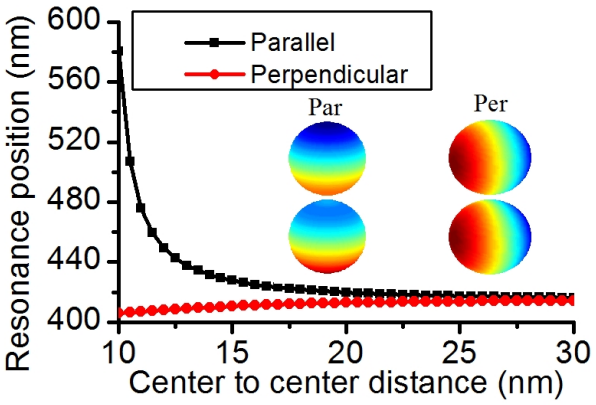


Figure 2 *Split of dipolar mode in the case of two similar silver spheres (5 nm in radius) versus inter-particle distance, with field distribution of these modes.*

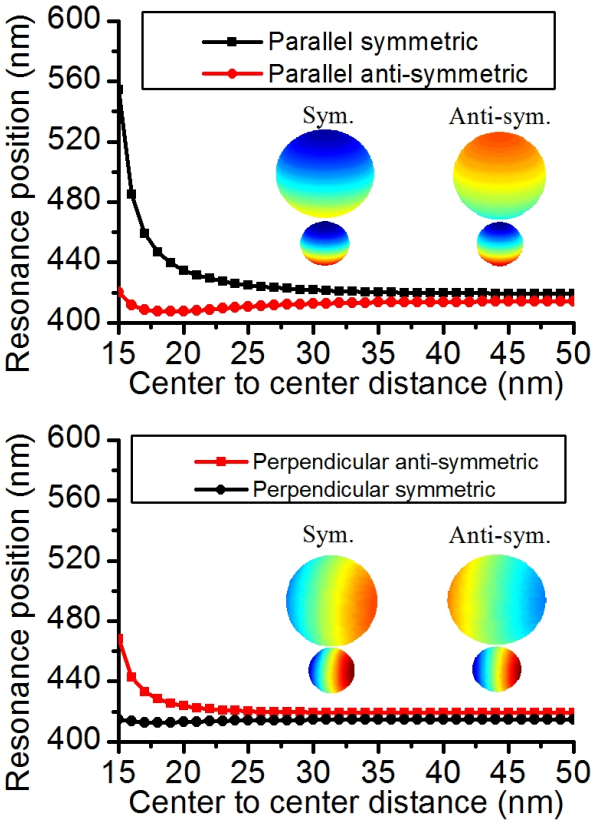


Figure 3 *Resonance positions and field mapping of the different polarization configurations for the dipolar (a) parallel and (b) perpendicular modes in a heterodimer system (spheres of 5 nm and 10 nm in radius).*

3.2 Fano resonances on quadrumers

We consider next silver sphere quadrumers as a combination of horizontal and vertical dimers, with the

configuration given in Figure 4 and illuminated with an incident polarization along the horizontal dimer. The destructive interferences between the perpendicular mode of vertical dimer and the parallel mode of horizontal dimer form a Fano resonance in the extinction spectra. Since the resonance position of horizontal dimer involved is sensitive to the particle separation, this last parameter can be used to tune the position of Fano resonance. As an example, Figure 4 shows the red-shift of the Fano resonance with the decrease of horizontal dimer particle gap.

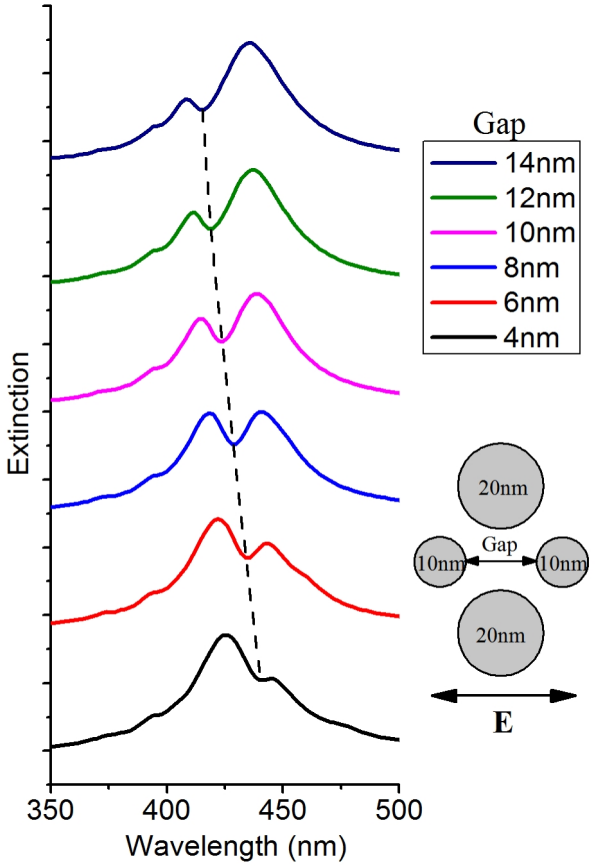


Figure 4 *Extinction spectra of silver quadrumers, with the given configuration, depending on the gap between the two small particles. The dashed line indicates the evolution of Fano resonance position.*

4 Aknowledgments

This work was supported by the LABEX MANUTECH-SISE (ANR-10-LABX-0075) of Université de Lyon, within the program "Investissements d'Avenir" (ANR-11-IDEX-0007) operated by the French National Research Agency (ANR). The authors thank the French ANR for its financial support in the framework of project Photoflex ANR-12-NANO-0006-01, and the Rhône-Alpes region for the thesis grant of S.B.

5 References

[1] U. Kreibig, M. Vollmer. *Optical Properties of Metal Clusters* (Springer, Berlin, 1995).

[2] B. Luk'yanchuk, N.I. Zheludev, S.A. Maier, N.J. Halas, P. Nordlander, H. Giessen, C.T. Chong, *The Fano Resonance in Plasmonic Nanostructures and Metamaterials*, Nat. Mater. 9:707-15 (2010).

[3] D.W. Mackowski, *Analysis of Radiative Scattering for Multiple Sphere Configurations*, Proc. R. Soc. Lond. A 8:599-614 (1991).

[4] A. Doicu, T. Wriedt, Y.A. Eremin. *Light Scattering By System of Particles: Null-Field Method with Discrete Sources – Theory and Programs* (Springer, Berlin, 2006).

[5] S. Bakhti, N. Destouches, A.V. Tishchenko. *Analysis of Plasmon Resonances on a Metal Particle*, JQSRT, in press (2014).

[6] S. Benghorieb, R. Saoudi, A.V. Tishchenko. *Extraxtion of the 3D Plasmon Field*, Plasmonics 6:445-55 (2011).

[7] A.V. Tishchenko, M. Hamdoun, O. Parriaux, *Two-Dimensional Coupled Mode Equation for Grating Waveguide Excitation by a Focused Beam*, Opt. Quant. Electron. 35:475-91 (2003).

[8] P. Nordlander, C. Oubre, E. Prodan, K. Li, M.I. Stockman, *Plasmon Hybridization in Nanoparticle Dimers*. Nano Lett. 4:899-903 (2004).

Sponsors & exhibitors pages

The inventor of
Laser Particle Size
Technology

Particle Size and Shape Analyzers

PRODUCT RANGE

Expert in laser particle size and shape analysis for over 40 years, CILAS provides reliable instruments for accurate results



Shape Analyzer
Size range: 0.5 µm – 2500µm

- For emulsions, suspensions and dry powders
- Particle size and shape are measured simultaneously on the same sample
- Direct connection to the liquid mode of the PSA

Laser particle size analyzers
Size range: 0.04µm – 2500µm

- Patented compact optical bench, mounted on a cast-iron base plate
- Liquid and dry mode in the same device
-Tri laser design






YOUR PARTNER IN PARTICLE ANALYSIS

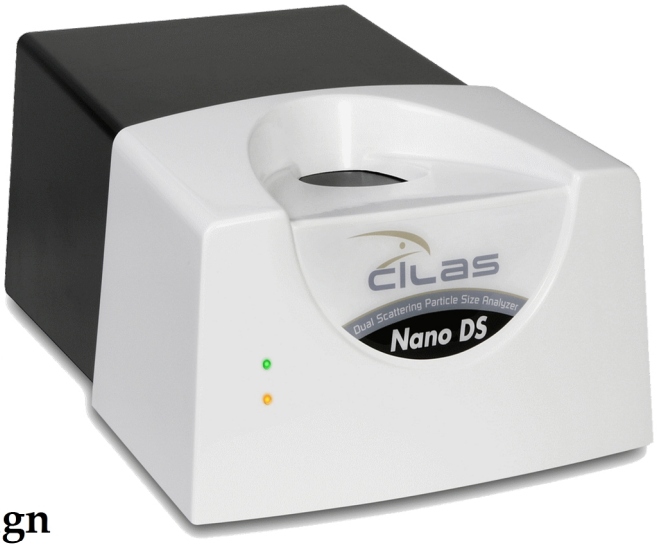
CILAS - 8 avenue Buffon - 45063 ORLEANS Cedex 2 - France
Tel: +33 (0)2 38 64 15 55

www.cilas.com
Info.particle@cilas.com

The inventor of
Laser Particle Size
Technology

Nano DS

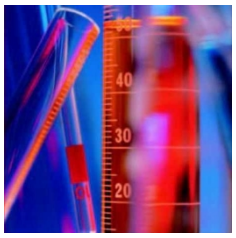
Dual Scattering Particle Size Analyzer



- **Multi-angle DLS**
- **Dual Technology**
- **Range 0.3 nm to 10µm**
- **Repeatability <1%**
- **Maintenance-free design**
- **Multi-peak size distribution measurements**

CILAS Nano DS Dual Light Scattering Particle Size Analyzer features a breakthrough technology **that makes nanoparticle characterization more accurate** even if your **sample is agglomerated or has a multi-peak size distribution.** This technology provides you with the best **accuracy, repeatability and resolution** over the entire 0.3 nm to 10 µm size range.









YOUR PARTNER IN PARTICLE ANALYSIS

CILAS - 8 avenue Buffon - 45063 ORLEANS Cedex 2 - France
Tel: +33 (0)2 38 64 15 55
www.cilas.com
Info.particle@cilas.com



ELSEVIER

www.elsevier.com

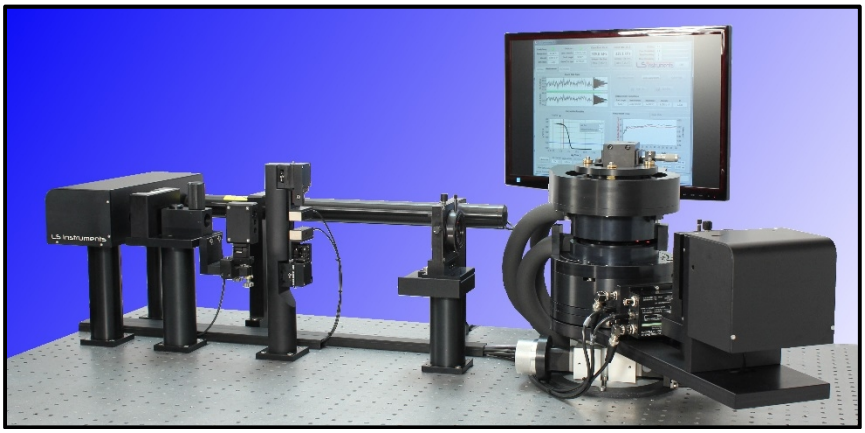
LS Instruments is a Swiss company which is committed to supply scientists in academia and industry with instruments that are equipped with the latest light scattering technologies.
We are experts for:

- Dynamic Light Scattering (DLS)
- Static Light Scattering (SLS)
- Diffusing Wave Spectroscopy (DWS)
- Ultra Small Angle Light Scattering (USALS)

We offer a range of innovative products that harness these technologies to deliver high quality measurements.

LS Spectrometer: DLS & SLS

The LS Spectrometer by LS Instruments is the most sophisticated system for both Dynamic and Static Light Scattering (DLS & SLS) available. The modular design of the instrument allows an individual configuration suited for the customer's specific requirements, without compromising neither precision nor quality.



The LS Spectrometer (with options) for DLS and SLS measurements

Dynamic light scattering (DLS) is a widely used particles sizing technique to determine hydrodynamic radius (R_h) and size distribution. It has become an industry standard for sizing nanoparticles (metals, polymers, proteins, emulsions…) in the range of several nanometers to several microns. Because most common DLS instruments only measure at one or two fixed scattering angles, they only supply precise measurements for a limited range of samples, since each scattering angle can only measure a certain particle size precisely, depending on the particle material. Furthermore they are only suited for spherical particles. The LS Spectrometer however can measure DLS at any scattering angle from 8°-155° and is thus suited for a much larger range of particle shapes and sizes.

Static Light Scattering (SLS) measures the intensity of scattered light in dependence of the scattering angle. Using SLS one can obtain important sample characteristics such as radius of gyration (R_g), molecular weight (M_w), second viral coefficient (B_2), structure and form factor or the inter particle distance. In the past SLS data treatment was a complex procedure that required specialized expertise. This is no longer the case. LS Instruments has developed user friendly solutions, such as the fully automated Zimm Plot to facilitate data treatment and thus enable a wider range of scientist to benefit from the many SLS techniques available.

It is important to note that the LS Spectrometer offers both SLS and DLS. It thus benefits from the synergy effect of combining these two techniques thus making it a far more powerful tool for particles characterization than each of these techniques applied separately.

Unique solutions: 3D cross correlation

DLS and SLS experiments are based on the assumption that only singly scattered light is detected. Already a small amount of multiple scattering however can result in significant measurement errors, which the user will be unaware of, since none of the commercial DLS/SLS instruments can identify the presence of multiple scattering. This is why they always require strong dilution of the sample to ensure that only single scattering is present. To solve this problem, LS Instrument has developed the advanced **3D cross-correlation technology** which suppresses multiple scattering efficiently, thus allowing measurements of many turbid samples in their natural undisturbed state, without any need for dilution. By combining this technology with other modules such as the modulation unit or the sample goniometer, the range of measureable samples can be even further increased. This is only one of the many specific solutions offered exclusively by LS Instruments. Please do not hesitate to contact us to learn more about our wide range of SLS or DLS solutions.

DWS RheoLab II: microrheology and particle sizing

The RheoLab II is compact stand-alone laboratory instrument which performs both microrheology and particle sizing of turbid samples (turbidity exceeding the turbidity accessible limit by the DLS technologies).

Microrheology and particle sizing are based on the Diffusing Wave Spectroscopy technique (DWS). It measures the temporal fluctuations of laser light that is scattered from particles embedded in the sample undergoing Brownian motion. The statistical analysis of these fluctuations allows the extraction of the microrheological properties of the sample. For suited samples these are in agreement with bulk rheology obtained from a mechanical oscillatory rheometer. DWS is however faster, contact-free, has a higher reproducibility and measures in a frequency range that surpasses mechanical rheometry by several decades.



DWS RheoLab II

New: NanoLab 3D

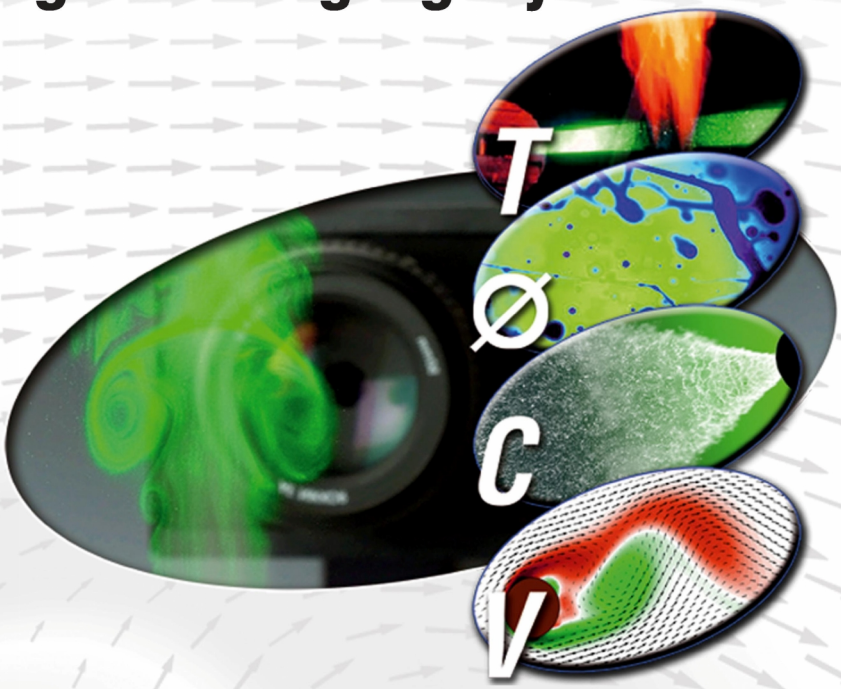
Scientists at LS Instruments have succeeded at making DLS particle sizing experiments easier than ever. Operating the NanoLab 3D is as simple as pressing a button: no sample preparation required! This unique fixed-angle DLS system is based on the patented 3D modulation technology that enables accurate determination of the hydrodynamic radius (R_h) even in extremely turbid samples.

The NanoLab 3D is a robust standalone device unique of this kind and will be available by the end of the 2014.



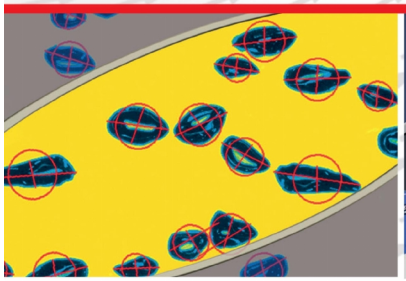
NanoLab 3D

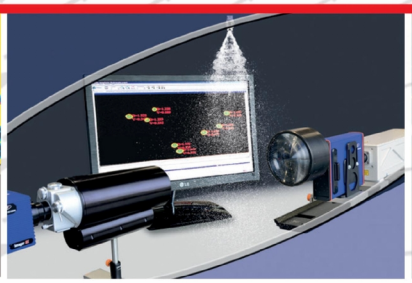
Intelligent Imaging Systems



Laser Imaging Systems

for Simultaneous Determination of Size and Velocity of Individual Particles or Droplets in Fluids or Multi-phase Flows with High Spatial Resolution





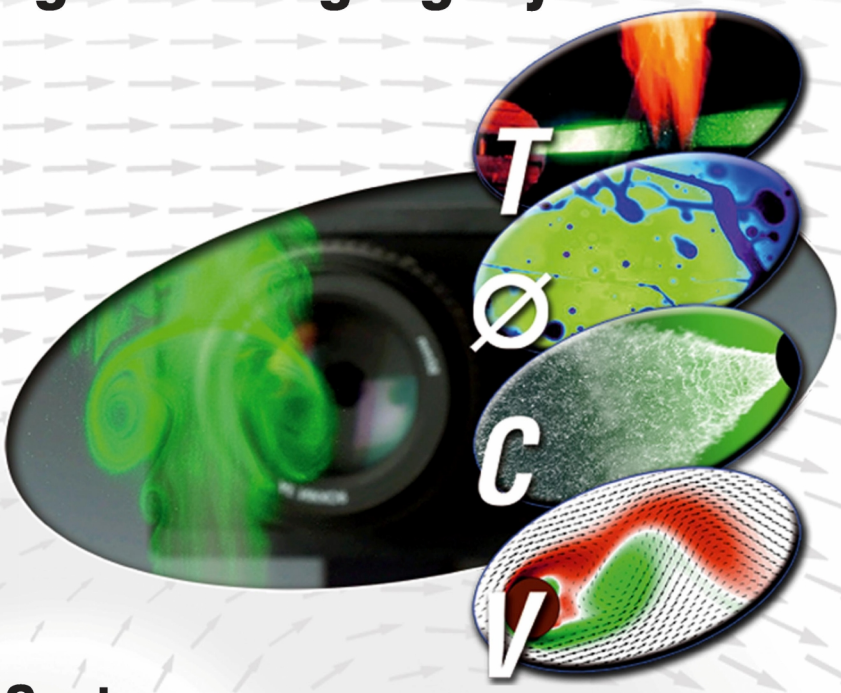


LaVision GmbH
Anna-Vandenhoeck-Ring 19
37081 Goettingen

Phone: +49 (0)551 9004 0
Email: sales@lavision.com
www.lavision.com

LaVision
We count on Photons

Intelligent Imaging Systems



Sensor Systems

for the Real-Time, Non-Intrusive Measurement of Individual Droplet Size and up to 3 Velocity Components in Spray Applications with Phase Doppler Interferometry and Laser Doppler Velocimetry



LaVision GmbH
Anna-Vandenhoeck-Ring 19
37081 Goettingen

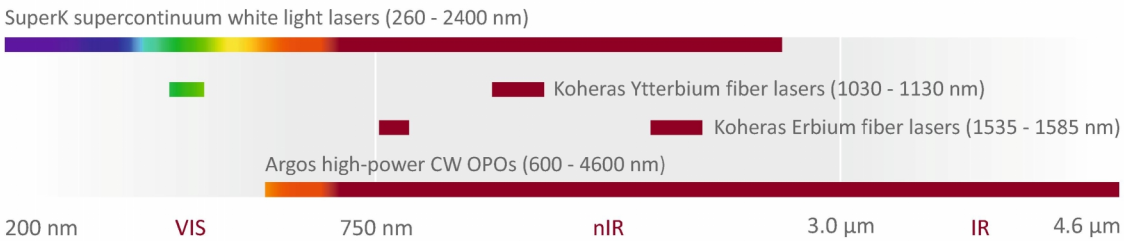
Phone: +49 (0)551 9004 0
Email: sales@lavision.com
www.lavision.com

LaVision
We count on Photons



Call now:
+33 (0) 64898 3976

Get all the wavelengths you need from NKT Photonics



www.nktphotonics.com
laser_sales@nktphotonics.com

NKT Photonics
the power of light

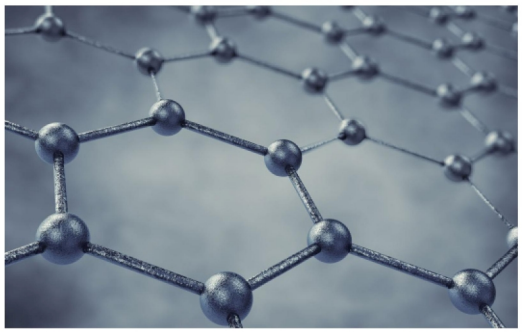
Characterization of

Nanostructures

What are nanostructures?

Nanostructures simply refer to physical structures with features on a nanometer scale. Structures relevant for optical characterization include such diverse fields as:

- Metamaterials
- Graphene and carbon nanotubes
- Photonics bandgap structures
- Surface plasmon waveguides
- Nanofibers, spheres, rods etc.
- Quantum dots





"The SuperK is a great source for characterization of plasmonic structures and optical metamaterials. It is very broad-band and suitable for characterization both in the visible and near infrared ranges, high power (which is very important for characterization of lossy plasmonic structures), very stable, flexible and easy to use."

Prof. Alexandra Boltasseva
Birck Nanotechnology Center, Purdue University

How can I use a SuperK for characterization?

Have you ever needed a different wavelength, wider tunability or are more convenient, stable or reliable light source? Then the SuperK white light laser is for you.

The SuperK supercontinuum laser can give you light anywhere in the 260-2400 nm region, making it a great tool for optical characterization of nanostructures. Many researchers around the World use the SuperK for measurements on nanoparticles, plasmonic waveguides, metamaterials and many other small structures. The lasers are compatible with a variety of characterization techniques like Raman spectroscopy, Brillouin light scattering spectroscopy, spectroscopic ellipsometry, SNOM and s-SNOM where it replaces single-line lasers and traditional broadband sources.

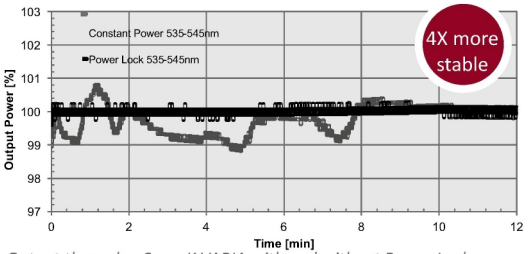
A SuperK supercontinuum source replaces all of these light sources:

- ASE sources
- Lamps
- Single line lasers
- SLEDs
- Dye lasers

Stability is the key

When characterizing very small structures, the stability of the light source is critical (e.g. for coupling to plasmonic waveguides). As the only supercontinuum source on the market, the SuperK EXTREME comes with our uniqe Power Lock feature that lets you lock the power anywhere in your setup. This lets you compensate for drift and instabilities in mirrors, lenses etc. and gives you power stability at you sample in the 0.2-0.5 % range.

Power stability is important, but without good pointing stability of the beam, it is worthless. The SuperK EXTREME has the best pointing stability on the market and it is single-mode in the entire spectral range of the source. This ensures not only stable transmission through our own filtering accessories, but also stable coupling to your sample resulting in less noise and better measurements.



Output through a SuperK VARIA with and without Power Lock. Power Lock improves stability to fractions of a percent.



"We use the SuperK for measuring photodetectors based on graphene and 2d materials. Because it's broadband and it's very easy to select a single or multiple wavelengths, it's perfect for our work. In addition, the SuperK is very stable and reliable; it has never broken down in 4 years.»

Dr. Frank Koppens
ICFO- The Institute of Photonic Sciences

Contact us now

+33 (0) 64898 3976
www.nktphotonics.com/nano
laser_sales@nktphotonics.com

Selected SuperK nano customers:

STANFORD UNIVERSITY · PURDUE UNIVERSITY · DTU · JOHANNES KEPLER UNIVERSITY LINZ | JKU

NKT Photonics
the power of light



Optical Cooling and Trapping (OT)

This group is concerned with the physics of laser cooling, electromagnetic trapping and other radiative manipulation of neutral atoms, ions, dielectric particles and nanostructures. These fundamental studies are used to develop applications to new kinds of physics measurements and processes such as high resolution spectroscopy, atomic clocks, atomic collisions, atom optics, bio-molecular interactions, and atomic-scale and nano-scale fabrication. Basic studies involve Bose-Einstein condensates, cold collisions, optical lattices, optomechanics, and soft-matter interactions.

GROUP LEADERSHIP | UPCOMING MEETINGS | RECENTLY PUBLISHED

Name	Affiliation	Title
Onofrio Marago	CNR-IPCF	Advisor/Chair
Philip H. Jones	UCL, London, United Kingdom	
Antonio A. R. Neves	UFABC, Santo André, Brazil	
Le Luo	IUPUI, Indianapolis, USA	

www.osa.org

VisiSize Systems

Oxford Lasers

Oxford Lasers was founded in 1977 by physicists from Oxford University whose research had been directed towards the study of new, yet practical, laser devices. Initially the company focused on the manufacture of Excimer - and Copper Vapor lasers. Since 1990 we have manufactured laser-based systems incorporating lasers of all types, with an increasing emphasis on solid state lasers.

We offer a wide range of systems, contract services, R&D and technical support for high speed imaging, using digital high speed cameras, lasers and software to offer complete imaging solutions.

The VisiSize products offer our customers a unique integrated platform to determine drop size and droplet velocity information. The VisiSize system uses a Particle Droplet Image Analysis (PDIA) technique This image-based technique provide a system with a unique range of benefits:

- Ability to work in extreme conditions
- Unaffected by change in the refractive index
- Not just a measurement system
  - Data on particle size and velocity
  - Images on drop formation and sheet breakup
- Measure any material
  - Paint, Water, Fuel, Volatile Liquids, Powders and Bubbles

Non-Intrusive Measurement
The VisiSize technique works by capturing images of the spray using a high-resolution camera together with short pulse light source to freeze the motion. VisiSize software inspects the images to identify the particles from the background. The software then interrogates each particle to assess the particle position relative to the in-focus position. Once the particle position has been determined, VisiSize can report the diameter and shape and calculates the diameter distribution. The non-contact online measurement means that you can add a VisiSize particle sizing system to your current process without causing disruption, providing that there is suitable optical access.

Model	Portable	D30 Range		N60 Range	
Application	Analysis of particles in a portable, cost-effective package	Analysis of sprays in a cost-effective package		Analysis of fast moving small droplet sprays	
Measure Velocity/Direction	No	D30S: No	D30: Yes	N60S: No	N60V: Yes
Size Range	>15 µm	>5 µm		>2 µm	
Typ. Working Distance	Fixed	40 – 1500 (subject to lens option)			
Max. Particle Velocity (Ø50 µm Particle)	15m/s	25m/s		1500m/s	
Image Source	Online or high resolution camera, up to 15,000 particles/second in real-time mode				
Spray Protection	Splash-proof enclosure, suitable for use with sprays	Multi-element splash cover for use in spray without disrupting flow			

VisiSize Systems

- Online Real-Time measurement
- Intuitive set-up
- Non-intrusive
- Droplets, Bubbles and Solids
- Particle size, Velocity and Direction
- Image based – visualise your process

OXFORD LASERS
IMAGING DIVISION

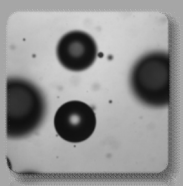


PORTABLE | N60 RANGE | D30 RANGE

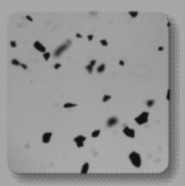
- Measure particle size, shape and velocity
- Correlate particle size against velocity
- Capture images of your spray or particle stream to see what's really happening - it's not just a particle sizing system.
- Fully integrated solution
- Statistics reported include: Mean diameter (by number, area or volume); Sauter mean diameter; 10%, 50% and 90% volume percentiles; Deviation; Relative span; Absolute concentration



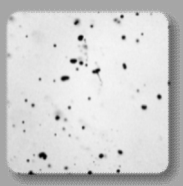
Air inclusions in Agricultural spray



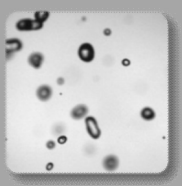
Liquid in liquid droplets



Solid particles



Paint spray



Droplets

Oxford Lasers Ltd
Unit 8, Moorbrook Park
Didcot
Oxon, OX11 7HP, UK
Tel: +44 (0) 1235 812255
Fax:+44 (0) 1235 810060

Oxford Lasers Inc
D201, 2 Shaker Road
Shirley, MA 01464
USA
Tel: (978) 425 0755
Fax: (978) 425 4487

Oxford Lasers France
5 rue des Suisses
75014 Paris
France
Tel: +33 (0)1 5688 2963
Fax: +33 (0)1 5376 0365

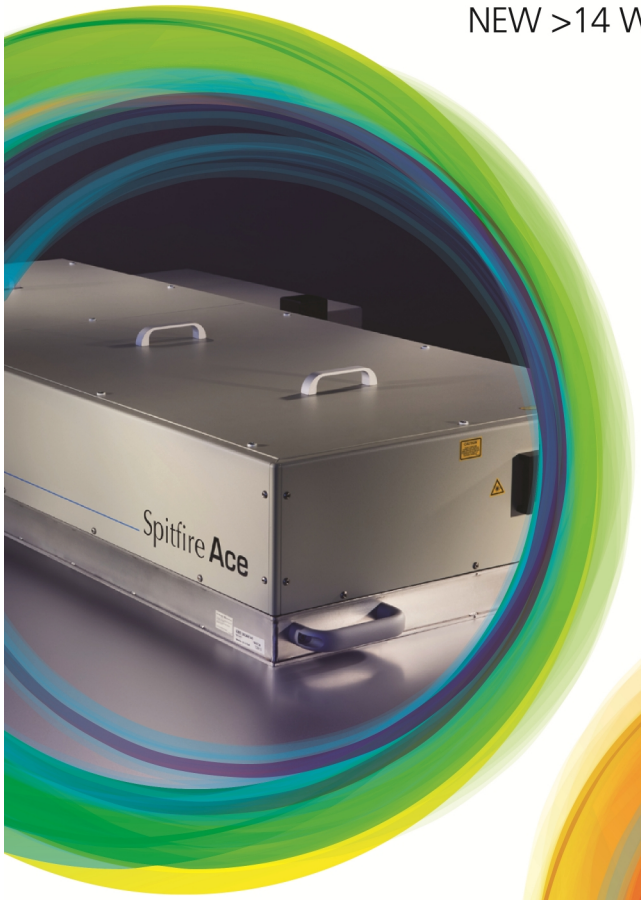
VISIBLE AND INVISIBLE LASER RADIATION AVOID EYE OR SKIN EXPOSURE TO DIRECT OR SCATTERED RADIATION CLASS 4 LASER PRODUCT

lip2014@oxfordlasers.com
www.oxfordlasers.com

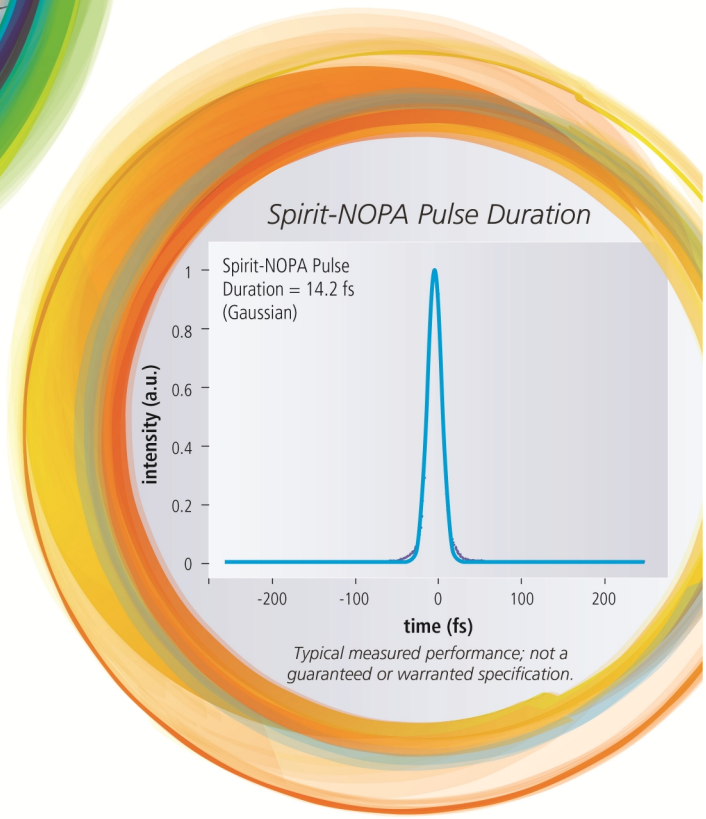
unbounded ultrafast potential

NEW >14 W, 12 mJ

NEW SUB-20 fs AT HIGH REP RATES



- THz generation, time resolved spectroscopy, high energy physics, etc.
- Output power range >6 W to >14 W
- High pulse energy up to >12 mJ
- Wide wavelength range UV to IR
- High repetition rate up to 1 MHz



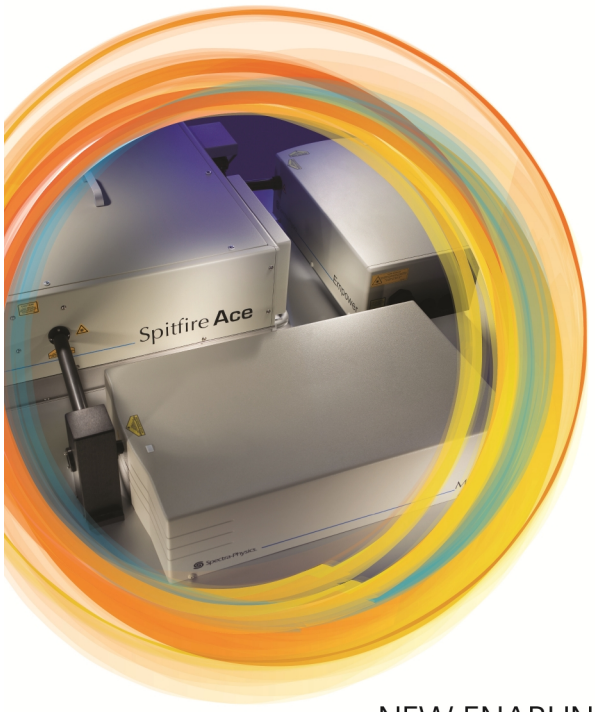
Spectra-Physics is dedicated to breaking through boundaries and unleashing ultrafast capabilities—from THz generation and high energy physics to time-resolved spectroscopy and beyond. We recently added three new amplifiers to further extend our Ultrafast portfolio. Discover why with Spectra-Physics, the potential for Ultrafast is unbounded. For more information on our *Number 1 in Ultrafast* line of lasers, visit

www.spectra-physics.com/ultrafast-lasers

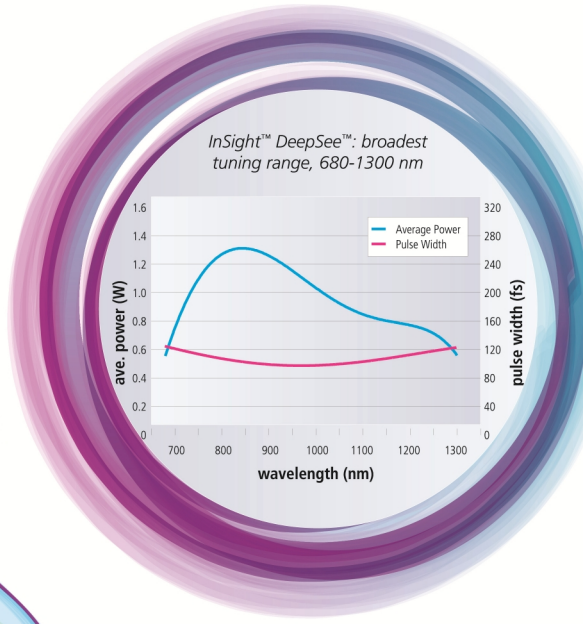
or contact us at **+49 6151-708-0** or **europe@spectra-physics.com**.

Spectra-Physics®
A Newport Company

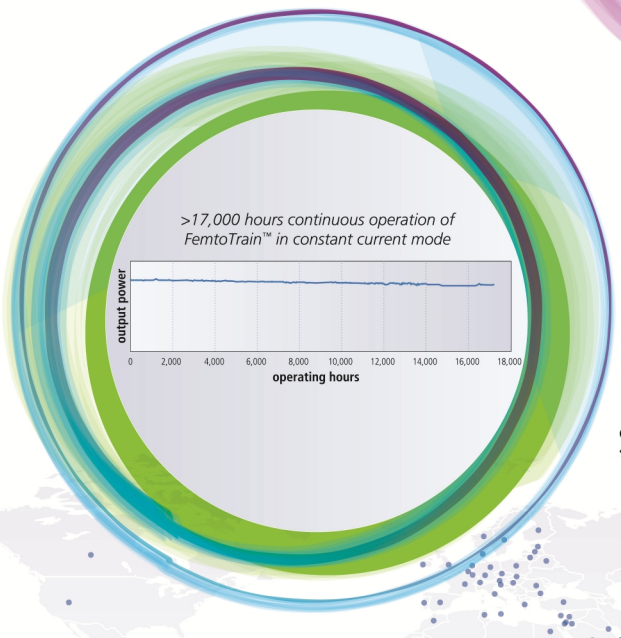
breakthrough lasers drive results



BROADEST PORTFOLIO



NEW ENABLING PERFORMANCE



UNPRECEDENTED ROCK-SOLID STABILITY

WORLD'S LARGEST INSTALLED BASE

Spectra-Physics®
A Newport Company

Authors index

ADAM, John A.	(FF-5)			
AGUIRRE, Miren	(PC-3)			
AIZU, Yoshihisa	(PC-18)	(PC-28)		
ALLANO, Daniel	(PC-5)	(PC-12)		
AMBROSIO, Leonardo A.	(BS-4)			
ARCHER, Justice	(CP-2)	(CP-10)	(PC-19)	
ARTONI, P.	(ME-16)			
ASAVEI, Theodor	(ME-20)			
ASTAFYEVA, Liudmila	(MT-6)			
BACHELARD, Romain	(PL-5)			
BACIA, Marcin	(ME-7)			
BAI, Lu	(FF-6)			
BAKHTI, Saïd	(PL-7)			
BANERJEE, Ayan	(PL-2)			
BARBILLAT, Jacques	(PC-30)			
BARRADO, Mariano	(PC-3)			
BARREDA, Ángelal.	(ME-22)			
BARTOLINO, R.	(ME-11)			
BECERRA-CARRILLO, Rodrigo	(CP-14)			
BELKADI, Arab	(PC-29)			
BELLETTRE, Jérôme	(PC-29)			
BERG, Matthew	(PC-11)			
BERNS, Michael W.	(ME-12)	(ME-17)		
BERROCAL, Edouard	(PC-9)			
BESCOND, Alexandre	(CP-12			
BEYER, Vivien	(PC-21)			
BONOD, Nicolas	(MT-7)			
BORK, Benjamin	(CP-11)			
BOVCHALIUK, Valentyn	(PC-23)			
BOX, Stuart	(ME-9)			
BRESSEL, Lena	(PC-3)			
BRUNEL, Marc	(PC-5)	(PC-8)	(PC-12)	(PC-16)
BUI, Anna.M.	(ME-17)	(ME-12)		
BUTENKO, A.D.	(ME-21)			
CAI, Xiaoshu	(PC-1)			
CARMAGNOLA, F.	(MT-3)			
CAUSA, Filippo	(PC-27)			
CHANG, Y.-Y.	(PC-22)			
CHAUCHARD, Fabien	(PC-25)			
CHERNOVA, DaryaN.	(PC-7)			
CHVÁTAL, Lukáš	(ME-6)			
CICHOS, Frank	(PC-6)			
CIPPARRONE, G.	(ME-11)			
COETMELLEC, Sébastien	(PC-5)	(PC-8)	(PC-12)	
COILLET, Elodie	(FF-8)	(FF-10)		
COMESAÑA-HERMO, Miguel	(PL-1)			
COPPALLE, Alexis	(CP-12			
COURTEILLE, Philippe	(PL-5)			
D'ANDREA, C.	(ME-1)			
DANNHAUSER, David	(PC-27)			
DAVID, Gregory	(FF-8)	(FF-10)		
DAVIS, AnthonyB.	(MT-4)			
DEBONO, Luke	(ME-9)			
DERKACHOV, Genadij	(CP-2)	(CP-10)	(PC-19)	
DERKACHOVA, Anastasiya	(PL-3)			
DESTOUCHES, Nathalie	(PL-7)			
DEUMIE, Carole	(CP-3)			
DHEZ, Olivier	(PC-25)			
DING, Chunying	(ME-18)			
DLUGACH, Janna M.	(CP-5)			
DONATO, M. G.	(ME-1)	(ME-11)	(ME-15)	
DONEGAN, John F.	(NR-4)			
DREIZLER, Andreas	(CP-11)			
DU, Zhihong	(PC-20)			
DUBOVIK, Oleg	(PC-23)			

ENGUEHARD, Franck	(MT-2)					
ENOCH, Stefan	(CP-3)					
EREMIN, Y.	(FF-9)					
EVERSOLE, Jay	(PC-24)					
FALAMAS, Alexandra	(MT-5)					
FAUCHÉ, Pierre	(PL-1)					
FAVRE-BULLE, Itia	(ME-10)					
FAZIO, B.	(ME-1)					
FENG, Wen	(PL-4)					
FERNANDEZ, A.	(MT-3)					
FOWLER, Nicholas	(PC-11)					
FUNAMIZU, Hideki	(PC-28)					
GÁL, Tibor	(MT-8)					
GANSMANN, A.-K.	(CP-13)					
GARO, Annie	(PC-17)					
GHOSH, Nirmalaya	(PL-2)					
GIGAN, Sylvain	(ME-13)					
GJONAJ, Erion	(CP-9)					
GOLOUB, Philippe	(PC-23)					
GONG, Lei	(FF-2)	(FF-6)	(FF-11)	(ME-19)	(PC-26)	
GONZALEZ, F.	(MT-3)					
GONZÁLEZ, Francisco	(ME-22)					
GOUESBET, Gérard	(BS-1)	(MT-1)				
GREENHALGH, Douglas	(PC-21)					
GREHAN, Gérard	(PC-5)	(PC-8)	(PC-12)	(PC-13)	(PC-17)	(PC-21)
GRIER, David G.	(ME-5)					
GRIGORIEV, Jérôme	(MT-7)					
GRYNKO, Yevgen	(CP-8)					
GUCCIARDI, P. G.	(ME-1)	(ME-11)	(ME-15)			
GUO, Lixin	(ME-18)					
GUPTA, S.Dutta	(PL-2)					
HAN, Lu	(FF-7)	(MT-1)	(NR-3)			
HAN, Xiang'e	(MT-1)	(NR-3)	(PC-15)			
HANNA, Simon	(ME-9)	(ME-16)				
HARDALUPAS, Yannis	(PC-21)					
HART, Matthew	(PC-24)					
Hebert, Damien	(CP-12					
HELLMERS, Jens	(NR-2)	(PL-4)				
HERNANDEZ, J.	(ME-11)					
HERZOG, William	(PC-24)					
HIM, Kam	(PC-21)					
HONG, Christopher	(PC-21)					
HUANG, C.-H.	(PC-22)					
HUNTEMANN, Marcus	(FF-1)					
IATI, M.A.	(ME-11)					
IRRERA, A.	(ME-1)	(ME-15)	(ME-16)			
ISHII, Katsuhiro	(PC-2)					
JÁKL, Petr	(ME-6)					
JAKUBCZYK, Daniel	(CP-2)	(CP-10)	(PC-19)			
JEŽEK, Jan	(ME-6)					
JONES, P.H.	(ME-1)	(ME-9)	(ME-15)	(ME-16)		
KARPOV, SergeiV.	(PL-6)					
KAZACHKOVA, N.A.	(ME-21)					
KE, Xizheng	(FF-12)					
KHATIBZADEH, Nima	(ME-12)					
KOFMAN, O.I.	(ME-21)					
KOLWAS, Maciej	(CP-2)	(CP-10)	(PC-19)			
KOLWAS, Krystyna	(CP-10)	(PL-3)				
KÖNIG, Thomas	(CP-11)					
KONOKHOVA, Anastasiya	(PC-7)					
KOPPA, Pál	(MT-8)					
KRISTENSSON, Elias	(PC-9)					
KUO, Mao-Kuen	(ME-4)					
LAMADIE, Fabrice	(PC-16)					
LAMANNA, Grazia	(CP-11)					

LAURENT, Jean-Yves	(PC-25)					
LAVEN, Philip	(FF-5)					
LEBRUN, Denis	(PC-5)	(PC-12)				
LECUREUX, Marie	(CP-3)					
LEDNEVA, Galina	(MT-6)					
LEE, I-YinSandy	(NR-5)					
LI, Renxian	(ME-18)					
LI, Hai-Ying	(FF-6)					
LI, Zheng-Ju	(FF-2)	(FF-6)	(FF-11)	(ME-19)		
LIAW, Jiunn-Woei	(ME-4)					
LIU, He	(PC-15)					
LIU, Lili	(PC-1)					
LO, Wei-Jiun	(ME-4)					
LOCK, James A.	(BS-1)	(BS-2)	(FF-5)	(CP-1)		
LOKE, Vincent L.Y.	(CP-15)	(ME-20)				
LOUDET, Jean-Christophe	(ME-8)					
LOUNIS, Brahim	(PL-1)					
LYMAR, V.I.	(ME-21)					
MÄDLER, Lutz	(PC-14)	(PL-4)				
MAGAZZU, A.	(ME-1)	(ME-11)	(ME-15)	(ME-16)		
MALTSEV, Valeri P.	(PC-7)					
MANSHA, Shampy	(PL-2)					
MARAGÓ, Onofrio M.	(ME-1)	(ME-9)	(ME-11)	(ME-16)		
MARKEL, VadimV.	(PL-6)					
MARKKANEN, Johannes	(CP-6)					
MARSTON, PhilipL.	(AK-1)					
MASAJAD, Jan	(ME-7)					
MASSOLI, Patrizio	(PC-29)					
MATSUSHITA, Shouhei	(NR-1)					
MAZZULLA, A.	(ME-11)					
McCLOSKEY, David	(NR-4)					
MESSINA, E.	(ME-1)					
MEUNIER-GUTTIN-CLUZEL, Siegfried	(PC-13)	(PC-17)				
MIFFRE, Alain	(FF-8)	(FF-10)				
MIHIRETIE, Besira	(ME-8)					
MISHCHENKO, Michael I.	(AK-4)	(CP-1)	(CP-5)			
MISHRA, YogeshwarNath	(PC-9)					
MITRI, Farid G.	(BS-3)					
MOLINA-TERRIZA, Gabriel	(CP-4)					
MONDIOT, Frédéric	(PC-4)					
MONTET, Cedric	(PC-31)					
MONTILLET, Agnès	(PC-29)					
MOREAU, Myriam	(PC-30)					
MORENO, Fernando	(MT-3)	(ME-22)				
MORTIER, Augustin	(PC-23)					
MROCZKA, Janusz	(NR-2)					
MUINONEN, Karri	(CP-6)					
NAKAMURA, Sohichiro	(PC-2)					
NETTI, PaoloA.	(PC-27)					
NEUGEBAUER, Irene	(PC-6)					
NEVES, Antonio A.R.	(ME-2)					
NIEMINEN, Timo A.	(ME-3)	(ME-10)	(ME-12)	(ME-17)	(ME-20)	(CP-15)
OKAMOTO, Takashi	(NR-1)					
OKYAY, Gizem	(MT-2)					
ONOFRI, Fabrice R.A.	(PC-25)	(PC-31)				
OULDARBI, Lila	(PC-16)					
PEJCHANG, Darawan L	(PC-12)					
PELTONIEMI, Jouni	(CP-6)					
PENTTILÄ, Antti	(CP-6)					
PFEILSTICKER, Klaus	(CP-7)					
PINGHAN, Yi	(FF-7)					
PODVIN, Thierry	(PC-23)					
POULIGNY, Bernard	(ME-8)					
PREECE, Itia	(ME-10)					
PRIOLO, F.	(ME-15)	(ME-16)				

PROVENZANO, C.	(ME-11)				
PUSTOVALOV, Victor	(MT-6)				
QI, Xiaoqiong	(CP-15)				
QU, Tan.	(FF-2)	(FF-6)	(FF-8)	(FF-11)	(ME-19)
RAIROUX, Patrick	(PC-21)				
RAMONLEIZA, Jose	(PC-3)				
RASSKAZOV, Ilia L.	(PL-6)				
RAVAINE, Serge	(PL-1)				
REICH, Olivier	(PC-3)				
REN, Kuan-Fang	(AK-3)	(FF-4)	(FF-13)	(FF-14)	
REUFER, Mathias	(PC-4)				
RICHARDS, C.J.	(ME-15)				
ROBBIE, Kevin	(CP-14)				
ROSEBROCK, Christopher	(PC-14)				
ROSSI, Domenico	(PC-27)				
ROTH, Norbert	(PC-10)				
ROZE, Claude	(CP-12	(FF-4)			
RUBINSZTEIN-DUNLOP, Halina	(CP-15)	(ME-10)	(ME-12)	(ME-17)	(ME-20)
RUFFNER, David B.	(ME-5)				
SAAR, Brian	(PC-24)				
SAENGKAEW, Sawitree	(PC-13)	(PC-17)			
SAIJA, R.	(ME-11)				
SAIZ, José M.	(MT-3)	(ME-22)			
SANZ, Juan M.	(MT-3)	(ME-22)			
SATO, Yuki	(PC-2)				
SCHMIDT, V.	(FF-9)	(PL-4)			
SCOTT, Ethan K.	(ME-10)				
SELMKE, Markus	(PC-6)				
SENTIS, Matthias	(PC-25)	(PC-31)			
SEPSI, Örs	(MT-8)				
SHABSHELOWITZ, Adam	(PC-24)				
SHANG, Qing-Chao	(FF-11)	(ME-19)			
SHEN, Huanhuan	(PC-8)				
SHEN, Jianqi	(FF-3)				
SHENG, Xin-Qing	(FF-13)				
ŠILER, Martin	(ME-6)				
SILVA, Glauber T.	(ME-14)				
SIMPSON, S.H.	(ME-9)	(ME-16)			
SKORUPSKI, Krzysztof	(NR-2)				
SMART, T. J.	(ME-15)				
SOBANSKA, Sophie	(PC-30)				
SONI, Jalpa	(PL-2)				
STEGMANN, Patrick	(CP-9)	(CP-13)			
STILGOE, Alexander	(ME-12)	(ME-17)	(CP-15)		
STROKOTOV, Dmitryl.	(PC-7)				
STOUT, Brian	(MT-7)				
SUBED, Nava	(PC-11)				
SUZUKI, Honoh	(NR-5)				
TAKABAYASHI, Masanori	(NR-1)				
TANRE, Didier	(PC-23)				
TARLET, Dominique	(PC-29)				
TAYLOR, Alex M.K.P.	(PC-21)				
TISHCHENKO, Alexandre	(PL-7)				
TOBON, Yeny	(PC-30)				
TOSA, Nicoleta	(MT-5)				
TOSA, Valer	(MT-5)				
TRICOLI, Ugo	(CP-7)				
TROPEA, Cameron	(CP-9)	(CP-13)	(FF-3)		
VALLÉE, Renaud	(PL-1)				
VESELOVSKII, Igor	(PC-23)				
VOELKER, Andreas C.	(PC-4)				
VOLPE, Giorgio	(ME-13)				
VOLPE, Giovanni	(ME-13)				
WANG, Mingjun	(FF-12)				
WANG, JiaJie	(MT-1)	(FF-7)			

WANG, Shimin	(PC-20)					
WATANABE, Yuki	(PC-28)					
WECKENMANN, Florian	(CP-11)					
WEIGAND, Bernhard	(PC-10)					
WRIEDT, Thomas	(FF-9)	(NR-2)	(PC-14)	(PL-4)	(PC-14)	
WU, Zhen-Sen	(FF-2)	(FF-6)	(FF-7)	(FF-11)	(ME-18)	(ME-19)
WU, Pengfei	(FF-12)					
WU, Yue-Qian	(FF-13)					
WU, Zhen-Sen	(PC-26)					
XU, Chuanlong	(PC-20)					
XU, Feng	(MT-4)					
XU, Chengze	(PC-1)					
XU, Renliang	(AK-5)					
YANG, Jian	(CP-14)					
YANG, Ming-Lin	(FF-13)					
YANG, Ruiping	(ME-18)					
YOKOI, Naomichi	(PC-18)					
YON, Jérôme	(CP-12					
YU, Haitao	(FF-3)					
YUAN, Yijia	(FF-4)					
YURKIN, MaximA.	(FF-1)	(PC-7)				
ZAMBRANA-PUYALTO, Xavier	(CP-4)					
ZEMANEK, Pavel	(AK-2)	(ME-6)				
ZHANG, Huayong	(FF-12)					
ZHANG, Jie	(PC-1)					
ZHAO, Wenjuan	(NR-3)					
ZHONG, Ruliang	(PC-15)					



ISBN 978-2-9548080-0-0



10th Int. conf. series on

LASER-LIGHT AND INTERACTIONS WITH PARTICLES (LIP2014)

August 25-29th, 2014, Marseille, France.